

December 2018

## Deconvolution of Membrane Protein-Detergent Complex Interactions

Aaron Wolfe  
Syracuse University

Follow this and additional works at: <https://surface.syr.edu/etd>



Part of the [Physical Sciences and Mathematics Commons](#)

---

### Recommended Citation

Wolfe, Aaron, "Deconvolution of Membrane Protein-Detergent Complex Interactions" (2018). *Dissertations - ALL*. 979.

<https://surface.syr.edu/etd/979>

This Dissertation is brought to you for free and open access by the SURFACE at SURFACE. It has been accepted for inclusion in Dissertations - ALL by an authorized administrator of SURFACE. For more information, please contact [surface@syr.edu](mailto:surface@syr.edu).

## **Abstract**

Membrane proteins are important in many biological functions such as cell-cell recognition, transport, and signaling; yet the study of these proteins is stunted due to their excessive aggregation in aqueous solutions. Detergents have been extensively exploited to mitigate this aggregation, and accomplish this by protecting the hydrophobic exterior of the membrane protein with their hydrophobic tails, while the polar heads of the detergents interact with the surrounding aqueous environment. Although detergents are of fundamental importance in many membrane protein studies, their selection is primarily done by trial and error screening. In this thesis, I will describe a method to utilize steady state fluorescence polarization to look at the desolvation of detergents from various membrane proteins. The overall goal is to create a methodology that can be employed broadly to map the kinetic fingerprints of various detergents with distinct membrane proteins. This map could potentially be used to build a model that would allow for the better selection and design of amphipols and detergents. Using this newly described fluorescence polarization anisotropy method, I examine the quantitative contributions of the adhesive protein-detergent and the cohesive detergent-detergent interactions for four beta barrel proteins in five distinct detergents. Further highlighting the generalizable nature of this method, I show the feasibility of this method by using two single pass alpha helical membrane proteins SELENOK and SELENOS. Next, we utilize real time kinetic reads of detergent desorption by describing two distinct phases of the desorption process. The kinetic reads allow the exploration of these interactions and the description of the inferred rate constants of association and dissociation of various detergent-protein complexes. Taken together, I will also explore the intricacies of these protein detergent complexes by describing their dependence on both the biophysical architecture of the membrane protein and the physiochemistry of the detergent itself.

# **Deconvolution of Membrane Protein-Detergent Complex Interactions**

by

Aaron J Wolfe

B.S., State University of New York Environmental Science and Forestry, 2007

Dissertation

Submitted in partial fulfillment of the requirements for the degree of  
Doctor of Philosophy in Structural Biology, Biochemistry, and Biophysics

Syracuse University  
December 2018

Copyright © Aaron J Wolfe 2018

All Rights Reserved



## **Acknowledgments**

I would like to thank my thesis committee Drs. Matthew LaHaye, Stewart Loh, Christopher Noumura, Eric Schiff, Mark Braiman, and Ivan Korendovvch for dedicating their time to assess this work.

I have been extremely fortunate in the fact that many people have contributed to my scientific development, definitely too many to enumerate a full list in this document. But a few individuals have stood out and helped shape who I am and the way that I look at the world around me. I would like to take the time to thank them individually here.

I would like to thank the Syracuse University Physics department and all the staff who has made my time there extremely rewarding, especially Penny Davis, Lou Buda, Charles Brown and Phil Arnold with whom I spent a lot of time pontificating life and whose open ears have helped me through long days in the basement.

Ever since I can remember, my Grandfather Mike Molnar has guided me in innumerable ways from teaching me, "*You are who you are by the books that you read and the people you know,*" to guiding my ethos and trajectory in every way conceivable. For that, my deepest of thanks; I plainly would be a different person without his guidance.

I am grateful for the countless hours of communications with Dr. Adam Blanden. The late-night bantering and crazy we-can-do-anything out-of-the-box thinking that has resulted in many papers and companies. I would not be the scientist/person I am today if it were not for his sharp wit, guidance, and dry to the fact council which has made many things possible.

To my wife Kimberly Wolfe who has consistently supported me with love and compassion since the first day we met and is my major motivation.

For Kelsey Moody, who has pushed the completion of this thesis to a business endpoint, knowing that this would be the only thing that would get me to commit.

Most importantly, Professor Liviu Movileanu, whom I met as an undergraduate in 2005. We have worked on many projects together and collaborated on 10 papers during these years. Liviu and I have gone through all the stages of the classic 1965 Tuckerman group development: forming, storming, norming, and performing (Citation Skipped!), and now, I wholeheartedly consider a friend. Thank you for all the effort and leniencies you have provided me during the various stages of our dynamic. I will be forever grateful for the efforts and the time that you have invested in me.

## Table of Contents

<i>Acknowledgments</i> .....	<i>iV</i>
<i>Lists of Illustrative material</i> .....	<i>iX</i>
<i>List of Figures</i> .....	<i>iX</i>
<i>List of Tables</i> .....	<i>XXiV</i>
<b>Chapter 1:</b>	
<i>Introduction: Development of a scalable method for the quantification of protein-detergent complexes</i> .....	<i>1</i>
<i>References</i> .....	<i>9</i>
<b>Chapter 2:</b>	
<i>Global Redesign of a Native <math>\beta</math>-barrel Scaffold</i> .....	<i>12</i>
<i>References</i> .....	<i>51</i>
<b>Chapter 2.1:</b>	
<i>Supplement for Global Redesign of a Native <math>\beta</math>-barrel Scaffold</i> .....	<i>56</i>
<i>References</i> .....	<i>105</i>
<b>Chapter 3:</b>	
<i>Interrogating Detergent Desolvation of Nanopore-Forming Proteins by Fluorescence Polarization Spectroscopy</i> .....	<i>108</i>
<i>References</i> .....	<i>133</i>
<b>Chapter 3.1:</b>	
<i>Supplement for Interrogating Detergent Desolvation of Nanopore-Forming Proteins by Fluorescence Polarization Spectroscopy</i> .....	<i>136</i>
<i>References</i> .....	<i>165</i>
<b>Chapter 4:</b>	
<i>Quantification of Membrane Protein-Detergent Complex Interactions</i> .....	<i>167</i>
<i>References</i> .....	<i>222</i>
<b>Chapter 4.1:</b>	
<i>Supplement for Quantification of Membrane Protein-Detergent Complex Interactions</i> .....	<i>228</i>
<i>References</i> .....	<i>259</i>
<b>Chapter 5: Detergent Desorption of Membrane Proteins</b>	
<i>Exhibits Two Kinetic Phases</i> .....	<i>260</i>
<i>References</i> .....	<i>289</i>
<b>Chapter 5.1: Supplement for Detergent Desorption of Membrane Proteins</b>	
<i>Exhibits Two Kinetic Phases</i> .....	<i>293</i>
<i>References</i> .....	<i>338</i>

<b>Chapter 6:</b>	
<b><i>Kinetics of Membrane Protein-Detergent Interactions Depend on Protein Electrostatics</i></b> .....	<b>339</b>
<b><i>References</i></b> .....	<b>384</b>
<b><i>Chapter 6.1: Supplement for Kinetics of Membrane Protein-Detergent Interactions Depend on Protein Electrostatics</i></b> .....	<b>389</b>
<b><i>References</i></b> .....	<b>475</b>
<b>Chapter 7:</b>	
<b><i>Concluding Remarks</i></b> .....	<b>476</b>
<b><i>References</i></b> .....	<b>481</b>
<b>Vita:</b>	
.....	<b>483</b>

## List of Figures

<b>Figure 1.1</b> <b>Anisotropy equation .....</b>	<b>8</b>
<b>Figure 2.1</b> <b>Homology molecular structures created by Swiss-model to visually compare the global mutational alterations of the <math>\beta</math>-barrel scaffold of FhuA with respect to wild-type FhuA (WT-FhuA). .....</b>	<b>16</b>
<b>Figure 2.2</b> <b>Representative current blockades observed with globally mutated FhuA derivatives at very high positive potentials. ....</b>	<b>26</b>
<b>Figure 2.3</b> <b>Representative single-channel electrical signature of FhuA <math>\Delta C/\Delta 7L</math>-30N at a medium applied potential. ....</b>	<b>31</b>
<b>Figure 2.4</b> <b>FhuA <math>\Delta C/\Delta 7L</math>-30N shows a distinctive signature from the other truncation FhuA mutants. ....</b>	<b>32</b>
<b>Figure 2.5</b> <b>Discrete current blockades observed with FhuA <math>\Delta C/\Delta 7L</math>-30N in the presence of Syn B2. ....</b>	<b>34</b>
<b>Figure 2.6</b> <b>Representative 33% current blockades observed with FhuA <math>\Delta C/\Delta 5L</math>-25N_ELP. ..</b>	<b>39</b>
<b>Figure 2.7</b> <b>Conserved single-channel features of the truncation FhuA mutants. ....</b>	<b>42</b>
<b>Figure 2.S1</b> <b>This amino acid alignment involves a cork-deletion mutant of the native FhuA (FhuA <math>\Delta C</math>) as well as three globally-mutated polypeptides FhuA <math>\Delta C/5L</math>, FhuA <math>\Delta C/5L</math>-25N, and FhuA <math>\Delta C/7L</math>-30N. ....</b>	<b>61</b>
<b>Figure 2.S2</b> <b>Topology of the cork-free, wild-type FhuA protein (WT-FhuA <math>\Delta C</math>). ....</b>	<b>63</b>
<b>Figure 2.S3.</b> <b>Topology map of FhuA <math>\Delta C/\Delta 5L</math> showing in red the loops that have been altered from the WT-FhuA structure. ....</b>	<b>66</b>

<b>Figure 2.S4</b>	
<b>Single-channel current of FhuA <math>\Delta C/\Delta 5L</math> as a function of the KCl concentration. ..</b>	<b>71</b>
<b>Figure 2.S5</b>	
<b>Engineered FhuA <math>\Delta C/\Delta 5L</math> nanopores are stable under low-salt concentration conditions.....</b>	<b>72</b>
<b>Figure 2.S6</b>	
<b>Engineered FhuA <math>\Delta C/\Delta 5L</math> pores are stable under extreme pH and greater transmembrane potential conditions. ....</b>	<b>74</b>
<b>Figure 2.S7</b>	
<b>Spectral density of the current noise of single FhuA <math>\Delta C/\Delta 5L</math> nanopores under different pH conditions. ....</b>	<b>76</b>
<b>Figure 2.S8</b>	
<b>Topology map of FhuA <math>\Delta C/\Delta 4L-N25</math> highlighting the residues in red that represent the 25 charge neutralizations with respect to the WT-FhuA protein. ....</b>	<b>77</b>
<b>Figure 2.S9.</b>	
<b>FhuA <math>\Delta C/\Delta 5L-25N</math> shows a closely similar single-channel electrical signature to FhuA <math>\Delta C/\Delta 5L</math>. ....</b>	<b>80</b>
<b>Figure 2.S10</b>	
<b>Engineered FhuA <math>\Delta C/\Delta 5L-25N</math> pores are stable under a broad range of conditions. ....</b>	<b>82</b>
<b>Figure 2.S11</b>	
<b>Representative long-lived current blockades observed with globally mutated FhuA derivatives at greater negative applied transmembrane potentials. ....</b>	<b>85</b>
<b>Figure 2.S12</b>	
<b>The current transitions between the long-lived and discrete sub-states of FhuA <math>\Delta C/\Delta 5L</math> are reversible under extreme applied transmembrane potentials. ....</b>	<b>86</b>
<b>Figure 2.S13</b>	
<b>Representative single-channel electrical recordings of TL-FhuA <math>\Delta C/ 5L</math> in 1M KCl, 10 mM potassium phosphate, pH 7.4. ....</b>	<b>88</b>
<b>Figure 2.S14</b>	
<b>Topology map of FhuA <math>\Delta C/\Delta 7L-30N</math>. ....</b>	<b>90</b>

<b>Figure 2.S15</b>	
<b>Single-channel electrical signature of FhuA <math>\Delta C/\Delta 7L</math>-30N at lower applied potentials.</b>	
.....	<b>93</b>
<b>Figure 2.S16</b>	
<b>FhuA <math>\Delta C/\Delta 7L</math>-30N showed brief current fluctuations when Syn B2, a cationic, 23-residue polypeptide, was added to the trans side at +120 mV.</b>	
.....	<b>95</b>
<b>Figure 2.S17</b>	
<b>Demonstration that engineered FhuA <math>\Delta C/\Delta 5L</math> pore has a bimolecular interaction with the Syn B2 polypeptide.</b>	
.....	<b>97</b>
<b>Figure 2.S18</b>	
<b>Discrete long-lived current blockades were observed with FhuA</b>	
.....	<b>99</b>
<b>Figure 2.S19</b>	
<b>The demonstration of the reversibility of the long-lived current blockades among long-lived sub-states observed with FhuA <math>\Delta C/\Delta 5L</math>-N25_ELP.</b>	
.....	<b>101</b>
<b>Figure 2.S20</b>	
<b>FhuA is characterized by heterogeneous positive and negative charge distribution throughout the <math>\beta</math> turns, <math>\beta</math> barrel, and extracellular loops.</b>	
.....	<b>103</b>
<b>Figure 3.1</b>	
<b>Side view of the FhuA <math>\Delta C/\Delta 5L</math> protein</b>	
.....	<b>113</b>
<b>Figure 3.2</b>	
<b>Time-dependent anisotropy showing the protein–detergent complex (PDC) interfacial dynamics of FhuA <math>\Delta C/\Delta 5L</math>.</b>	
.....	<b>118</b>
<b>Figure 3.3</b>	
<b>Concentration–response anisotropy changes recorded with protein nanopores of varying isoelectric point pI.</b>	
.....	<b>124</b>
<b>Figure 3.4</b>	
<b>Unusual thermostability of LPPG-refolded protein nanopores and functional reconstitution of LysoFos-, DDM-, and OG-refolded protein nanopores.</b>	
.....	<b>127</b>
<b>Figure 3.S1</b>	
<b>SDS-PAGE gel of purified FhuA <math>\Delta C/\Delta 5L</math></b>	
.....	<b>138</b>
<b>Figure 3.S2</b>	
<b>SDS-PAGE analysis of Texas Red labeled OmpG</b>	
.....	<b>141</b>

<b>Figure 3.S3</b> Some examples of concentration-dependent anisotropy endpoints of FhuA determined after 24 hours incubation at 4C. ....	146
<b>Figure 3.S4</b> Specific fluorescence anisotropy signature of LPPG-refolded FhuA $\Delta C/\Delta 5L$ at higher detergent concentrations. ....	151
<b>Figure 3.S5</b> Time- and concentration-dependent anisotropy traces acquired with anionic and zwitterionic detergents. ....	152
<b>Figure 3.S6</b> Time-dependent changes in anisotropy produced by the dissociation of steroidal group-containing detergents from FhuA .....	154
<b>Figure 3.S7</b> Time-dependent changes in anisotropy produced by the dissociation of neutral, maltoside-containing detergents of varying tail from FhuA $\Delta C/\Delta 5L$ .....	155
<b>Figure 3.S8</b> Time- and concentration-dependent anisotropy traces acquired with OG using four protein nanopores .....	157
<b>Figure 3.S9</b> Time- and concentration-dependent anisotropy traces acquired with FhuA $\Delta C/\Delta 5L$ in OTG. ....	158
<b>Figure 3.S10</b> Single-channel electrical signature of the engineered FhuA $\Delta C/\Delta 5L$ protein pores refolded in different detergents. ....	160
<b>Figure 3.S11</b> Comparison of the single- and multi-channel electrical traces produced by the FhuA $\Delta C/\Delta 5L$ proteins under various voltages .....	162
<b>Figure 3.S12</b> Schematic model of the detergent desolvation-induced protein unfolding. ....	164
<b>Figure 4.1</b> Cartoons showing the backbone homology structures of the four $\beta$ -barrel proteins inspected in this work .....	172



<b>Figure 4.2</b>	
<b>Graphic illustrating the three hypothetical scenarios of the balance between adhesive and cohesive interactions of PDCs. ....</b>	<b>187</b>
<b>Figure 4.3</b>	
<b>Dose-response changes in fluorescence anisotropy for neutral maltoside-containing detergents. ....</b>	<b>189</b>
<b>Figure 4.4</b>	
<b>Dose-response changes in fluorescence anisotropy recorded with zwitterionic detergents and proteins of varying isoelectric point pI. ....</b>	<b>196</b>
<b>Figure 4.5</b>	
<b>Dose-response changes in fluorescence anisotropy acquired with DM under acidic conditions ....</b>	<b>203</b>
<b>Figure 4.6</b>	
<b>MD simulations of DDM binding to the <math>\beta</math>-barrel proteins. ....</b>	<b>205</b>
<b>Figure 4.7</b>	
<b>Dose-response in fluorescence anisotropy acquired with SELENOK U92C and SELENOS U188S, two short single <math>\alpha</math>-helical transmembrane proteins solubilized in DDM. ....</b>	<b>210</b>
<b>Figure 4.S1</b>	
<b>Characterization of SELENOK U92C and SELENOS U188S prior to and following labeling with Texas Red. ....</b>	<b>229</b>
<b>Figure 4.S2</b>	
<b>Time-dependent fluorescence anisotropy traces acquired with (DM). ....</b>	<b>231</b>
<b>Figure 4.S3</b>	
<b>Anisotropy readout was collected after 24 hours ....</b>	<b>233</b>
<b>Figure 4.S4</b>	
<b>Time-dependent changes in the FP anisotropy when the four proteins were incubated in CHAPS ....</b>	<b>240</b>
<b>Figure 4.S5</b>	
<b>Time-dependent changes in the FP anisotropy when the four <math>\beta</math>-barrel proteins were incubated in n-dodecyl-N,N-dimethylglycine. ....</b>	<b>242</b>

<b>Figure 4.S6</b>	
<b>MD simulations of DDM molecules binding to <math>\beta</math>-barrel proteins .....</b>	<b>250</b>
<b>Figure 4.S7</b>	
<b>Differential affinity of DDM molecules to residues of <math>\beta</math>-barrel proteins .....</b>	<b>252</b>
<b>Figure 4.S8</b>	
<b>DDM binding versus residue type. ....</b>	<b>254</b>
<b>Figure 5.1</b>	
<b>Side-view of the molecular structures of OmpG and truncation FhuA mutant. ...</b>	<b>265</b>
<b>Figure 5.2</b>	
<b>Time-dependent alterations in the FP anisotropy when the membrane proteins were incubated at different concentrations of LysoFos, a zwitterionic detergent .....</b>	<b>271</b>
<b>Figure 5.3</b>	
<b>Time-dependent alterations in the FP anisotropy .....</b>	<b>273</b>
<b>Figure 5.4</b>	
<b>Time-dependent alterations in the FP anisotropy when the membrane proteins were incubated at different concentrations of DM, a neutral maltoside-containing detergent. ....</b>	<b>278</b>
<b>Figure 5.5</b>	
<b>Time-dependent alterations in the FP anisotropy when the membrane proteins were incubated at different concentrations of CYMAL-4, a neutral maltoside-containing detergent. ....</b>	<b>280</b>
<b>Figure 5.6 Cartoon showing different FP anisotropy-based trajectories of the proteodemicellization. ....</b>	<b>283</b>
<b>Figure 5.S1</b>	
<b>Illustration of the time-dependent predesolvation and desolvation of OmpG solubilized with 20 mM LysoFos .....</b>	<b>297</b>
<b>Figure 5.S2</b>	
<b>Illustration of the time-dependent predesolvation and desolvation of FhuA 25N solubilized with 20 mM LysoFos .....</b>	<b>299</b>
<b>Figure 5.S3</b>	
<b>Illustration of the time-dependent predesolvation and desolvation of FhuA <math>\Delta</math>C/<math>\Delta</math>7L_30N solubilized with 20 mM LysoFos. ....</b>	<b>301</b>

<b>Figure 5.S4</b>	
<b>Illustration of the time-dependent predesolvation and desolvation of OmpG solubilized with 5 mM UM .....</b>	<b>303</b>
<b>Figure 5.S5</b>	
<b>Illustration of the time-dependent predesolvation and desolvation of FhuA <math>\Delta C/\Delta 5L_{25N}</math> solubilized with 5 mM UM .....</b>	<b>305</b>
<b>Figure 5.S6</b>	
<b>Illustration of the time-dependent predesolvation and desolvation of FhuA <math>\Delta C/\Delta 7L_{30N}</math> solubilized with 5 mM UM .....</b>	<b>307</b>
<b>Figure 5.S7</b>	
<b>Illustration of the time-dependent desolvation of OmpG solubilized with 5 mM DM. ....</b>	<b>309</b>
<b>Figure 5.S8</b>	
<b>Illustration of the time-dependent predesolvation and desolvation of FhuA <math>\Delta C/\Delta 5L_{25N}</math> solubilized with 5 mM DM .....</b>	<b>311</b>
<b>Figure 5.S9</b>	
<b>Illustration of the time-dependent predesolvation and desolvation of FhuA <math>\Delta C/\Delta 7L_{30N}</math> solubilized with 5 mM DM .....</b>	<b>313</b>
<b>Figure 5.S10</b>	
<b>Illustration of the time-dependent predesolvation and desolvation of OmpG solubilized with 50 mM CYMAL-4. ....</b>	<b>315</b>
<b>Figure 5.S11</b>	
<b>Illustration of the time-dependent predesolvation and desolvation of FhuA <math>\Delta C/\Delta 5L_{25N}</math> solubilized with 50 mM CYMAL-4. ....</b>	<b>317</b>
<b>Figure 5.S12</b>	
<b>Illustration of the time-dependent predesolvation and desolvation of FhuA <math>\Delta C/\Delta 7L_{30N}</math> solubilized with 50 mM CYMAL-4. ....</b>	<b>319</b>
<b>Figure 5.S13</b>	
<b>Illustration of the dependence of the observable desolvation rate .....</b>	<b>327</b>
<b>Figure 5.S14</b>	
<b>Logarithmic plot showing that the observable desolvation rate .....</b>	<b>330</b>

<b>Figure 5.S15</b>	
<b>Logarithmic plot showing that the observable desolvation rate, <math>k_{obs}^{des}</math>, recorded with FhuA <math>\Delta C/\Delta 7L_{30N}</math> scales with the detergent concentration of dodecyl-<math>\beta</math>-D-maltoside (DDM) at values below the <math>CMC^{DDM} = 0.17</math> mM. ....</b>	<b>332</b>
<b>Figure 5.S16</b>	
<b>Logarithmic plot showing that the observable desolvation rate, <math>k_{obs}^{des}</math>, recorded with FhuA <math>\Delta C/\Delta 7L_{25N}</math> scales with the detergent concentration of UM at values below the <math>CMC^{UM} = 0.59</math> mM .....</b>	<b>334</b>
<b>Figure 6.1</b>	
<b>Structural homology models of the four proteins explored in this work. ....</b>	<b>344</b>
<b>Figure 6.2</b>	
<b>Cartoon illustrating the two phases noted as a result of detergent depletion within the sample well. ....</b>	<b>346</b>
<b>Figure 6.3</b>	
<b>Time-dependent anisotropy showing the DM desolvation of OmpG at various pH values. ....</b>	<b>356</b>
<b>Figure 6.4</b>	
<b>Time-dependent FP anisotropy showing the CYMAL-4 desolvation of OmpG at various pH values .....</b>	<b>358</b>
<b>Figure 6.5</b>	
<b>Time-dependent FP anisotropy showing the DM desolvation of FhuA <math>\Delta C/5\Delta L</math> at various pH values. ....</b>	<b>363</b>
<b>Figure 6.6</b>	
<b>Time-dependent FP anisotropy showing the DM desolvation of FhuA <math>\Delta C/5\Delta L_{25N}</math> at various pH values .....</b>	<b>365</b>
<b>Figure 6.7</b>	
<b>Time-dependent FP anisotropy showing the DM desolvation of FhuA <math>\Delta C/7\Delta L_{N30}</math> at various pH values .....</b>	<b>367</b>
<b>Figure 6.8</b>	
<b>Dependence of the observed desolvation rate constants, <math>k_{obs}^{des}</math>, on the protein charge. ....</b>	<b>370</b>

<b>Figure 6.9</b>	
<b>The apparent rate constants of the interfacial PDC interactions of proteomicelles.</b>	
.....	<b>374</b>
<b>Figure 6.S1</b>	
<b>Time-dependent desolvation of FhuA <math>\Delta C/\Delta 5L</math> incubated in CYMAL-4.</b>	<b>391</b>
<b>Figure 6.S2</b>	
<b>Time-dependent desolvation of FhuA <math>\Delta C/\Delta 5L_{25N}</math> incubated in CYMAL-4.</b>	
.....	<b>393</b>
<b>Figure 6.S3</b>	
<b>Time-dependent desolvation of FhuA <math>\Delta C/\Delta 5L_{25N}</math> incubated in CYMAL-4.</b>	
.....	<b>395</b>
<b>Figure 6.S4</b>	
<b>Time-dependent predesolvation and desolvation of OmpG and FhuA <math>\Delta C/\Delta 5L</math> incubated with DM at pH 4.6.</b>	
.....	<b>397</b>
<b>Figure 6.S5</b>	
<b>Time-dependent predesolvation and desolvation of OmpG and FhuA <math>\Delta C/\Delta 5L</math> incubated with DM at pH 5.6.</b>	
.....	<b>399</b>
<b>Figure 6.S6</b>	
<b>Time-dependent predesolvation and desolvation of OmpG and FhuA <math>\Delta C/\Delta 5L</math> incubated with DM at pH 6.8.</b>	
.....	<b>401</b>
<b>Figure 6.S7</b>	
<b>Time-dependent predesolvation and desolvation of OmpG and FhuA <math>\Delta C/\Delta 5L</math> incubated with DM at pH 8.2.</b>	
.....	<b>403</b>
<b>Figure 6.S8</b>	
<b>Time-dependent predesolvation and desolvation of OmpG incubated with DM at pH 10.0.</b>	
.....	<b>405</b>
<b>Figure 6.S9</b>	
<b>Time-dependent predesolvation and desolvation of FhuA <math>\Delta C/\Delta 5L_{25N}</math> incubated with DM at pH 4.6.</b>	
.....	<b>407</b>
<b>Figure 6.S10</b>	
<b>Time-dependent predesolvation and desolvation of FhuA <math>\Delta C/\Delta 5L_{25N}</math> and FhuA <math>\Delta C/\Delta 7L_{30N}</math> incubated with DM at pH 5.6.</b>	
.....	<b>409</b>

<b>Figure 6.S11</b> Time-dependent predesolvation and desolvation of FhuA $\Delta C/\Delta 5L_{25N}$ and FhuA $\Delta C/\Delta 7L_{30N}$ incubated with DM at pH 6.8 .....	411
<b>Figure 6.S12</b> Time-dependent predesolvation and desolvation of FhuA $\Delta C/\Delta 5L$ and FhuA $\Delta C/\Delta 7L_{30N}$ incubated with DM at pH 8.2. ....	413
<b>Figure 6.S13</b> Time-dependent predesolvation and desolvation of FhuA $\Delta C/\Delta 5L$ incubated with CYMAL-4 at pH 4. ....	415
<b>Figure 6.S14</b> Time-dependent predesolvation and desolvation of OmpG and FhuA $\Delta C/\Delta 5L$ incubated with CYMAL-4 at pH 5.6. ....	417
<b>Figure 6.S15</b> Time-dependent predesolvation and desolvation of OmpG and FhuA $\Delta C/\Delta 5L$ incubated with CYMAL-4 at pH 6.8 .....	419
<b>Figure 6.S16</b> Time-dependent predesolvation and desolvation of OmpG and FhuA $\Delta C/\Delta 5L$ incubated with CYMAL-4 at pH 8.2. ....	421
<b>Figure 6.S17</b> Time-dependent desolvation of OmpG incubated with CYMAL at pH 10.0. ....	423
<b>Figure 6.S18</b> Time-dependent predesolvation and desolvation of FhuA $\Delta C/\Delta 5L_{25N}$ and FhuA $\Delta C/\Delta 7L_{30N}$ incubated with CYMAL-4 at pH 5.6. ....	425
<b>Figure 6.S19</b> Time-dependent predesolvation and desolvation of FhuA $\Delta C/\Delta 5L_{25N}$ and FhuA $\Delta C/\Delta 7L_{30N}$ incubated with CYMAL-4 at pH 6.8 .....	427
<b>Figure 6.S20</b> Time-dependent predesolvation and desolvation of FhuA $\Delta C/\Delta 5L_{25N}$ and FhuA $\Delta C/\Delta 7L_{30N}$ incubated with CYMAL-4 at pH 8.2. ....	429
<b>Figure 6.S21</b> Time-dependent predesolvation and desolvation of FhuA $\Delta C/\Delta 5L_{25N}$ incubated with CYMAL-4 at pH 10.0 .....	431

**Figure 6.S22**  
The observed kinetic rates of desolvation of OmpG scale linearly with the DM detergent concentrations at values below the  $CMC^{DM} = 1.8$  mM ..... 456

**Figure 6.S23**  
The observed kinetic rates of desolvation of FhuA  $\Delta C/\Delta 5L$  scale linearly with the DM detergent concentrations at values below the  $CMC^{DM} = 1.8$  mM. .... 458

**Figure 6.S24**  
The observed kinetic rate constants of desolvation of FhuA  $\Delta C/\Delta 5L_{25N}$  scale linearly with the DM detergent concentrations at values below the  $CMC^{DM} = 1.8$  mM at pH 8.2. .... 460

**Figure 6.S25**  
The observed kinetic rates of desolvation of FhuA  $\Delta C/\Delta 7L_{30N}$  scale linearly with the DM detergent concentrations at values below the  $CMC^{DM} = 1.8$  mM. .... 462

**Figure 6.S26**  
The observed kinetic rates of desolvation of OmpG scale linearly with the CYMAL-4 detergent concentrations at values below the  $CMC^{CYMAL-4} = 7.6$  mM. .... 464

**Figure 6.S27**  
The observed kinetic rates of desolvation of FhuA  $\Delta C/\Delta 5L$  scale linearly with the CYMAL-4 detergent concentrations at values below the  $CMC^{CYMAL-4} = 7.6$  mM ..... 466

**Figure 6.S28**  
The observed kinetic rates of desolvation of FhuA  $\Delta C/\Delta 5L_{25N}$  scale linearly with the CYMAL-4 detergent concentrations at values below the  $CMC^{CYMAL-4} = 7.6$  mM. .... 468

**Figure 6.S29:**  
The observed kinetic rates of desolvation of FhuA  $\Delta C/\Delta 7L_{30N}$  scale linearly with the CYMAL-4 detergent concentrations at values below the  $CMC^{CYMAL-4} = 7.6$  mM. .... 470

## List of Tables

<b>Table 2.S1</b>	
<b>Features of the extracellular loops of the WT-FhuA protein. ....</b>	<b>64</b>
<b>Table 2.S2</b>	
<b>Details of the truncation FhuA <math>\Delta C/\Delta 5L</math> mutant. ....</b>	<b>64</b>
<b>Table 2.S3</b>	
<b>Comparison of the unitary conductance and oligomeric state of FhuA <math>\Delta C/\Delta 5L</math> pore with those of other protein nanopores. ....</b>	<b>67</b>
<b>Table 2.S4</b>	
<b>Comparison of the unitary conductance of globally engineered FhuA-based protein pores under various experimental conditions. ....</b>	<b>68</b>
<b>Table 2.S5.</b>	
<b>This table lists all of the point mutations in FhuA <math>\Delta C/\Delta 5L</math>-25N with respect to the sequence of FhuA <math>\Delta C/\Delta 5L</math>. ....</b>	<b>78</b>
<b>Table 2.S6</b>	
<b>Details of the truncation FhuA <math>\Delta C/\Delta 7L</math>-30N mutant ....</b>	<b>89</b>
<b>Table 2.S7. The point mutations table highlights all of the point mutations that differentiate the FhuA <math>\Delta C/\Delta 7L</math>-N30 polypeptide from the FhuA <math>\Delta C/\Delta 5L</math> ....</b>	<b>91</b>
<b>Table 2.S8</b>	
<b>Loop modifications table highlighting the deletions and point modifications which make up the reduction of the specified loops in FhuA <math>\Delta C/\Delta 7L</math>-N30 ....</b>	<b>92</b>
<b>Table 3.S1</b>	
<b>Physical features of the detergents ....</b>	<b>142</b>
<b>Table 3.S2</b>	
<b>Table showing the acquired minima and maxima of anisotropy and rotational diffusion coefficients ....</b>	<b>148</b>
<b>Table 3.S3</b>	
<b>Table showing the fitting parameters derived from dose-response dissociation phases of detergent tori from FhuA <math>\Delta C/\Delta 5L</math> ....</b>	<b>150</b>
<b>Table 4.1</b>	
<b>Physical properties of the detergents examined in this work.....</b>	<b>175</b>



<b>Table 4.2</b>	
<b>Biophysical properties of the <math>\beta</math>-barrel proteins used in this study. ....</b>	<b>176</b>
<b>Table 4.3</b>	
<b>The recorded minima and maxima of the anisotropy with neutral and zwitterionic detergents and proteins .....</b>	<b>191</b>
<b>Table 4.S1</b>	
<b>Table that summarizes the recorded minima and maxima of the anisotropy readout with neutral, maltoside-containing detergents and the four proteins. ....</b>	<b>235</b>
<b>Table 4.S2</b>	
<b>Summary of the fitting results of the two-state, concentration-dependent anisotropy curves acquired with neutral, maltoside-containing detergents .....</b>	<b>236</b>
<b>Table 4.S3</b>	
<b>Table that summarizes the recorded minima and maxima of the anisotropy readout with DM and the four <math>\beta</math>-barrel proteins under conditions of varying pH .....</b>	<b>244</b>
<b>Table 4.S4</b>	
<b>Summary of the fitting results of the two-state, concentration-dependent anisotropy curves acquired with three FhuA derivatives and OmpG under conditions of varying pH.a,b DM was the detergent used in this case .....</b>	<b>247</b>
<b>Table 4.S5:</b>	
<b>Biophysical properties of the <math>\alpha</math>-helical proteins used in this study .....</b>	<b>256</b>
<b>Table 4.S6</b>	
<b>Table that summarizes the recorded minima and maxima of the anisotropy readout with the SELENOK U92C and SELENOS U188S <math>\alpha</math>-helical membrane proteins solubilized in DDM .....</b>	<b>257</b>
<b>Table 4.S7</b>	
<b>Summary of the fitting results of the two-state, concentration-dependent anisotropy curves acquired with SELENOK U92C and SELENOS U188S <math>\alpha</math>-helical transmembrane proteins. ....</b>	<b>258</b>
<b>Table 5.S1</b>	
<b>Characteristics of the <math>\beta</math>-barrel proteins examined in this study .....</b>	<b>295</b>
<b>Table 5.S2</b>	
<b>Physicochemical features of the detergents .....</b>	<b>296</b>

<b>Table 5.S3</b>	
<b>Determination of the observed predesolvation rates (kobs) .....</b>	<b>321</b>
<b>Table 5.S4</b>	
<b>Determination of the observed desolvation rates, <math>k_{\text{obs}}^{\text{des}}</math> .....</b>	<b>323</b>
<b>Table 5.S5</b>	
<b>Determination of the kinetic rate constants of association (kon) and dissociation (koff) of proteomicelles formed by LysoFos with truncation FhuA derivatives .....</b>	<b>329</b>
<b>Table 5.S6</b>	
<b>The dissociation rate scaling with the final detergent concentration in the sample well. ....</b>	<b>337</b>
<b>Table 6.S1</b>	
<b>Determination of the observed predesolvation rates, <math>k_{\text{obs}}^{\text{pre}}</math>, of OmpG when was incubated in 5 mM DM. ....</b>	<b>434</b>
<b>Table 6.S2</b>	
<b>Determination of the predesolvation observed rates of FhuA <math>\Delta C/\Delta 5L</math> when was incubated in 5 mM DM. ....</b>	<b>434</b>
<b>Table 6.S3</b>	
<b>Determination of the predesolvation observed rates of FhuA <math>\Delta C/\Delta 5L_{25N}</math> when was incubated in 5 mM DM .....</b>	<b>435</b>
<b>Table 6.S4</b>	
<b>Determination of the predesolvation observed rates of FhuA <math>\Delta C/\Delta 7L_{30N}</math> when was incubated in 5 mM DM. ....</b>	<b>436</b>
<b>Table 6.S5</b>	
<b>Determination of the predesolvation observed rates of OmpG when was incubated in 50 mM CYMAL-4 .....</b>	<b>437</b>
<b>Table 6.S6</b>	
<b>Determination of the predesolvation observed rates of FhuA <math>\Delta C/\Delta 5L</math> when was incubated in 50 mM CYMAL-4 .....</b>	<b>438</b>
<b>Table 6.S7</b>	
<b>Determination of the predesolvation observed rates of FhuA <math>\Delta C/\Delta 5L_{25N}</math> when was incubated in 50 mM CYMAL-4 .....</b>	<b>439</b>

<b>Table 6.S8</b>	
<b>Determination of the predesolvation observed rates of FhuA <math>\Delta C/\Delta 7L_{30N}</math> when was incubated in 50 mM CYMAL-4. ....</b>	<b>440</b>
<b>Table 6.S9</b>	
<b>The observed desolvation rate constants, <math>k_{obs}^{des}</math>, of OmpG refolded in 5 mM DM .....</b>	<b>442</b>
<b>Table 6.S10</b>	
<b>The observed desolvation rate constants, <math>k_{obs}^{des}</math>, of FhuA <math>\Delta C/\Delta 5L</math> refolded in 5 mM DM .....</b>	<b>443</b>
<b>Table 6.S11</b>	
<b>The observed desolvation rate constants, <math>k_{obs}^{des}</math>, of FhuA <math>\Delta C/\Delta 5L_{25N}</math> refolded in 5 mM DM .....</b>	<b>444</b>
<b>Table 6.S12</b>	
<b>The observed desolvation rate constants, <math>k_{obs}^{des}</math>, of FhuA <math>\Delta C/\Delta 7L_{30N}</math> refolded in 5 mM DM .....</b>	<b>445</b>
<b>Table 6.S13</b>	
<b>The observed desolvation rate constants, <math>k_{obs}^{des}</math>, of OmpG refolded in 50 mM CYMAL-4. ....</b>	<b>446</b>
<b>Table 6.S14</b>	
<b>The observed desolvation rate constants, <math>k_{obs}^{des}</math>, of FhuA <math>\Delta C/\Delta 5L</math> refolded in 50 mM CYMAL-4. ....</b>	<b>447</b>
<b>Table 6.S15</b>	
<b>The observed desolvation rate constants, <math>k_{obs}^{des}</math>, of FhuA <math>\Delta C/\Delta 5L_{25N}</math> refolded in 50 mM CYMAL-4 .....</b>	<b>448</b>
<b>Table 6.S16</b>	
<b>The observed desolvation rate constants, <math>k_{obs}^{des}</math>, of FhuA <math>\Delta C/\Delta 5L_{30N}</math> refolded in 50 mM CYMAL-4 .....</b>	<b>449</b>
<b>Table 6.S17</b>	
<b>Initial desolvation rates, <math>R_{in}^{des}</math>, of the DM- and CYMAL-4-containing proteomicelles that include acidic and basic <math>\beta</math>-barrel membrane proteins. ....</b>	<b>450</b>

**Table 6.S18**  
**Determination of kinetic rate constants of association and dissociation of DM-based proteomicelles as well as the equilibrium dissociation constant,  $K_d$  ..... 472**

**Table 6.S19**  
**Determination of kinetic rate constants of association and dissociation of CYMAL-4-based proteomicelles as well as the equilibrium dissociation constant,  $K_d$  ..... 474**



# Chapter 1. Introduction

**Development of a scalable method for the quantification of protein-detergent complexes.**

**Aaron J. Wolfe**

<sup>1</sup>Department of Physics, Syracuse University, 201 Physics Building, Syracuse, New York 13244-1130, USA

<sup>2</sup>Structural Biology, Biochemistry, and Biophysics Program, Syracuse University, 111 College Place, Syracuse, New York 13244-4100, USA

## 1.1 Membrane Proteins : A Primer

A defining feature of cells is the plasma membrane which separates the cell's internal contents from the surrounding environment [1]. These membranes are composed of both lipids and proteins, where the protein components are often the active units involved in a myriad of functions including signal transduction[1], transport [2] and enzymatic reactions[3], [4]. They are the gate keepers of the cell and as such, are extremely attractive targets in drug development. Membrane proteins currently represent 60% of drug targets but only ~1% of the solved protein structures [5].

It was not until 1985 that Johann Deisenhofer solved the first crystal structure of a membrane protein: the photosynthetic reaction center from the bacterium *Rhodospseudomonas* [6]. Highlighting the importance of this work, Dr. Deisenhofer, along with Hartmut Michel and Robert Huber, was awarded the Nobel Prize in Chemistry in 1988. To build a bit of perspective on the hurdles of handling membrane proteins in biophysical assays, this first membrane protein structure was solved 27 years after the first soluble protein structure, myoglobin, was solved by Kendrew et al.[7]. Membrane proteins are difficult to study for many reasons, but it is almost ubiquitously understood that detergent selection and solubilization is a limiting factor. Some solubilization detergents can extract these proteins well from the membrane, but they may in turn reduce the stability and therefore deactivate the protein of interest. These complex relationships between structure, function, and handling ease seem to be at the crux of the membrane protein biophysics field [7].

Detergents are vital in all steps of membrane protein handling in the laboratory from solubilization, purification, and experimentation. Their structure and concentration is important to maintaining the functionality and solubility of membrane proteins when they are being

handled outside of a membrane[8]. Though the importance of detergents and membrane proteins is known, the selection of the proper detergent at the proper concentration for each membrane protein is still an exercise in trial and error[9].

## **1.2 A Narrative Introduction**

My work in membrane protein biophysics began in 2007, when I worked on characterizing mutations of alpha-hemolysin, with respect to its transport of various small peptides, at single molecule resolution [10][11]. Alpha-hemolysin is assembled in red blood cells[12], and after this assembly, becomes water soluble. This attribute makes alpha-hemolysin a favorite among single channel electrophysiologists, including myself and Dr. Movileanu [11], [13].

The fact that alpha-hemolysin is water soluble is not unique amongst membrane proteins in the nanopore field. As early as 2003, Dr. Hagan Bayley described a water soluble OmpG monomer [14]. Researchers strive to increase the solubility of nanopore sensors, as being water-soluble imparts many very favorable attributes to a nanopore. Primarily, using a water-soluble sensor obviates the need for detergents to hold the nanopore in solution, which allows researchers to focus solely on designing experiments that can elucidate the fundamentals of transport physics. I would now like to admit that my experience with the alpha-hemolysin nanopore system spoiled me when it came to working with membrane proteins; I was under the naive impression that you can simply take a protein, add it to the reaction chamber, and data would come out.

My third publication [15] was my first interaction with a membrane protein that needed solubilizing detergents. Fortuitously, this work was a collaboration with Bert Van Den Berg who is one of the world's leading experts on beta-barrel crystallography. Dr. Van den Berg, at the time of this writing, is credited with solving all of the 16 known outer membrane carboxylate



channel (Occ) structures, as shown on the database of UC Irvine's Dr. Stephen White (url: <http://blanco.biomol.uci.edu/mpstruc/>). As I was receiving proteins from Dr. Van Den Berg the conditions for handling and studying the OccD channels were elucidated well before I received any proteins. It was not until late 2011 that I had to start thinking about the nuances of detergents and how they interact with proteins. In the lab, I was genetically modifying the Ferrichrome outer membrane transporter/phage receptor (FhuA) Which was previously modified by Dr. Mohammad and Dr. Movileanu to make a large ion conducting nanopore [16] [17]. I was recombinantly expressing my modifications and purifying them in denatured conditions in inclusion bodies and refolding them in various detergents after simple affinity chromatography purification. It was at this time that I saw my first "puff" of precipitate when I added a newly created mutation to the refolding buffer. This precipitate appeared suddenly and was promptly removed by a short spin on the microcentrifuge, leaving, at best, nanograms of my protein of interest. This first experience with proteins falling out of solution spurred my interest in understanding and improving protein solubilization. I began reading and came across Dr. Paula Booth's work on protein folding and detergent interactions[18]–[22]. Her work, amongst others, greatly influenced the trajectory of how I went about mitigating my protein precipitation issue and helped guide my thinking as I was making my first mutations in FhuA.

As time went on, I became more aware that there seemed to be a lack of a quantitative readout to guide detergent selection, and the field was relying on an ineffective trial and error system. I was finding this to be very frustrating as I watched week after week of my efforts fall out of solution. I found no solace in the literature, as it seemed to indicate the best approach was to try many detergents and perhaps some of them would work. I continued to return to the problematic lack of a systematic method for determining what is driving the interfacial forces

between various greasy proteins and detergents. I toiled for over a year to generate a manuscript describing the single channel characteristics of four genetically engineered pores[23] (Chapter 2 of this thesis), hindered by the ineffective solubilization methods common for membrane protein field. As I was working primarily in the world of single molecule electrophysiology, one must wait until a channel inserts into the membrane before a recording can be made and functionality confirmed. As such, during this period, there were long wait times between the start of an experiment and a successful recording. However, I was unable to determine if these delays were caused by pores being lost due to unfavorable insertion kinetics, or a lack of solubility in the reaction chamber, or other non-determined errors on my part. This lack of understanding led to the utilization of these wait times to explore the measurement of the protein detergent interaction.

Handling membrane proteins in aqueous solutions is required for many applications in general biochemistry and biophysics. Outside of my desire to do single molecule electrophysiological recordings on my mutational work, it should be noted that membrane proteins are increasingly important in medicine. Currently, 60% of drugs in development target membrane proteins[24] and although they represent 30% of the proteome, they account for only ~1% of the solved protein structures[25]. It is commonly believed that one reason for the disparity in structural knowledge is these proteins are exceedingly difficult to handle in solution once their hydrophobic patches are exposed. In contrast, soluble proteins sequester their hydrophobic patches in the core region to stabilize their structure. Membrane proteins are stabilized inside the hydrophobic interior of the lipid membrane. Therefore, their hydrophobic regions are exposed to the milieu, allowing them to freely interact with the hydrophobic interior of the membrane. Dealing with this inside-out nature of the membrane protein in a laboratory

setting, where most systems and experiments on biological matter are carried out in aqueous environments, is usually mitigated by the addition of an amphiphilic compounds mixtures thereof. These compounds use their dual nature to coat the hydrophobic patches of the proteins while allowing water to interact with the hydrophilic regions to maintain solubility and structural integrity of the membrane proteins under study, while these proteins are displaced from their native lipid environments. In general, these amphiphilic molecules are lipids, detergents, bile acid salts, or amphipols[20]. The use of novel solubilization techniques including amphipols[26] or nanodiscs[27] usually require the addition of a solubilizing detergent as an intermediate steps, as does the extraction of membrane proteins from their native lipid environments[28] [29]. Due to the nearly ubiquitous usage of detergents in membrane protein handling, I decided to focus my thoughts and work on creating methods to further elucidate a detailed understanding of protein-detergent complex (PDC) interactions.

Though it is known that solubilizing agents are essential in much of membrane protein biophysics, I found no systematic, high throughput, quantitative method to understand the forces involved in these protein-detergent complex interactions. Trial and error screening methods are routinely employed in discovering what detergents are to be selected for functional or structural studies[20]. The poorly soluble nature of membrane proteins makes sensitive biophysical measurements of the PDC utilizing techniques difficult to perform, primarily because they become misfolded, aggregated, and heterogeneous when not in the proper detergent. Although this is true for elucidating the interfacial forces of the PDC, there are a multitude of examples where these techniques are used to study membrane protein structure, in general: SAXS[30], DSC [31], and NMR [32], [33].

The trial and error selection of detergents is commonly accomplished simply by visually determining whether the protein remained in solution. This low-tech, stand-alone analysis is effective in the short term, but these experiments have no quantitative way to inform the researcher on what drives the interfacial forces of the PDC and are therefore not beneficial in accumulating new and useful information for future condition or reagent selection, drastically hindering long term success.

In this thesis, I set out to describe the creation of a semiquantitative method to describe the thermodynamic and kinetic description of the protein-detergent complex interactions using steady state fluorescence anisotropy.

### **1.3 Introduction to Anisotropy**

Fluorescence polarization (FP) as an analysis technique is based on the finding that emission from a fluorophore excited by plane polarized light is depolarized by rotational diffusion of the molecule during the emission lifetime of the fluorophore. This theory was first described by Francis Perrin in 1926 [34]. FP can be used to determine shifts in molecular mass, as mass changes will alter the molecular rotation of the labeled molecule and therefore change the intensity of the FP readout in either the parallel or perpendicular channel. Below is the equation for FP denoted  $P$  for polarization. The equation for anisotropy is similar, with the only exception being that the intensity ( $I$ ) horizontal in the denominator is multiplied by a factor of two. Therefore, the terms FP and fluorescence anisotropy (FA) can be used interchangeably, although they are slightly different mathematically.

$$P = \frac{I_{\text{vertical}} - I_{\text{horizontal}}}{I_{\text{vertical}} + I_{\text{horizontal}}}$$

FIGURE 1

It can be clearly seen in the above equation that concentration is not a factor as long as the fluorescent signal is within the limits of detection for the experimental instrument[35]. In general, a greater anisotropy signal is due to more light being emitted in the parallel intensity and therefore slower diffusion, which can then be related to a relatively larger hydrodynamic radius. This is useful in determining protein protein interactions (PPI) and their inhibitors in a high throughput manner. When associated, protein -protein complexes will be larger and therefore rotate slower than when the complex is disrupted by the addition of a molecule. Upon disruption, the labeled species is free of its partner and will therefore be smaller and rotate faster, emitting more light in the perpendicular plane leading to a reduced anisotropy value [36], [37]. This ability to deduce the relative change in hydrodynamic radius, and the concentration independence of the readout, are at the heart of the following chapters, as we build a case for utilizing FA in determining and quantifying the interfacial forces of the protein-detergent complex.

## REFERENCES

- [1] J. T. Groves and J. Kuriyan, "Molecular mechanisms in signal transduction at the membrane.," *Nat. Struct. Mol. Biol.*, vol. 17, no. 6, pp. 659–665, Jun. 2010.
- [2] M. A. Hediger, B. Cl  men  on, R. E. Burrier, and E. A. Bruford, "Molecular Aspects of Medicine The ABCs of membrane transporters in health and disease," *Mol. Aspects Med.*, vol. 34, no. 2–3, pp. 95–107, 2013.
- [3] D. J. Riese II, "Ligand-based receptor tyrosine kinase partial agonists: New paradigm for cancer drug discovery?," *Expert Opin. Drug Discov.*, vol. 6, no. 2, pp. 185–193, 2011.
- [4] A. I. S  galiny, M. Tellez-Gabriel, M. F. Heymann, and D. Heymann, "Receptor tyrosine kinases: Characterisation, mechanism of action and therapeutic interests for bone cancers," *J. Bone Oncol.*, vol. 4, no. 1, pp. 1–12, 2015.
- [5] H. Yin and A. D. Flynn, "Drugging Membrane Protein Interactions," *Annual review of biomedical engineering*, vol. 18. pp. 51–76, Jul-2016.
- [6] J. Deisenhofer and H. Michel, "Nobel lecture. The photosynthetic reaction centre from the purple bacterium *Rhodospseudomonas viridis*." *The EMBO Journal*, vol. 8, no. 8. pp. 2149–2170, Aug-1989.
- [7] J. C. KENDREW, G. BODO, H. M. DINTZIS, R. G. PARRISH, H. WYCKOFF, and D. C. PHILLIPS, "A three-dimensional model of the myoglobin molecule obtained by x-ray analysis.," *Nature*, vol. 181, no. 4610, pp. 662–666, Mar. 1958.
- [8] D. Linke, "Detergents: an overview.," *Methods Enzymol.*, vol. 463, pp. 603–617, 2009.
- [9] I. Moraes, G. Evans, J. Sanchez-weatherby, S. Newstead, and P. D. Shaw, "Biochimica et Biophysica Acta Membrane protein structure determination — The next generation ☆☆," *BBA - Biomembr.*, vol. 1838, no. 1, pp. 78–87, 2014.
- [10] R. Bikwemu, A. J. Wolfe, X. Xing, and L. Movileanu, "Facilitated translocation of polypeptides through a single nanopore," *J. Phys. Condens. Matter*, vol. 22, no. 45, p. 454117, 2010.
- [11] A. J. Wolfe, M. M. Mohammad, S. Cheley, H. Bayley, and L. Movileanu, "Catalyzing the translocation of polypeptides through attractive interactions," *J. Am. Chem. Soc.*, vol. 129, no. 45, pp. 14034–14041, 2007.
- [12] N. Tobkes, B. A. Wallace, and H. Bayley, "Secondary structure and assembly mechanism of an oligomeric channel protein.," *Biochemistry*, vol. 24, no. 8, pp. 1915–1920, Apr. 1985.
- [13] L. Movileanu and H. Bayley, "Partitioning of a polymer into a nanoscopic protein pore obeys a simple scaling law," vol. 98, no. 18, 2001.
- [14] S. Conlan and H. Bayley, "Folding of a monomeric porin, OmpG, in detergent solution.," *Biochemistry*, vol. 42, no. 31, pp. 9453–9465, Aug. 2003.
- [15] J. Liu *et al.*, "Cation selectivity is a conserved feature in the OccD subfamily of *Pseudomonas aeruginosa*," *Biochim. Biophys. Acta - Biomembr.*, vol. 1818, no. 11, pp.

- 2908–2916, 2012.
- [16] M. M. Mohammad, K. R. Howard, and L. Movileanu, “Redesign of a Plugged  $\beta$ -Barrel Membrane Protein \*  $\beta$ ,” vol. 286, no. 10, pp. 8000–8013, 2011.
- [17] M. M. Mohammad, R. Iyer, K. R. Howard, M. P. Mcpike, P. N. Borer, and L. Movileanu, “Engineering a Rigid Protein Tunnel for Biomolecular Detection,” 2012.
- [18] P. J. Booth, “The trials and tribulations of membrane protein folding in vitro,” *Biochim. Biophys. Acta - Biomembr.*, vol. 1610, no. 1, pp. 51–56, 2003.
- [19] P. J. Booth, R. H. Templer, W. Meijberg, S. J. Allen, A. R. Curran, and M. Lorch, “In Vitro Studies of Membrane Protein Folding,” *Crit. Rev. Biochem. Mol. Biol.*, vol. 36, no. 6, pp. 501–603, 2001.
- [20] A. M. Seddon, P. Curnow, and P. J. Booth, “Membrane proteins, lipids and detergents: Not just a soap opera,” *Biochim. Biophys. Acta - Biomembr.*, vol. 1666, no. 1–2, pp. 105–117, 2004.
- [21] P. J. Booth and P. Curnow, “Membrane proteins shape up: understanding in vitro folding,” *Curr. Opin. Struct. Biol.*, vol. 16, no. 4, pp. 480–488, 2006.
- [22] N. J. Harris and P. J. Booth, “Folding and stability of membrane transport proteins in vitro,” *Biochim. Biophys. Acta - Biomembr.*, vol. 1818, no. 4, pp. 1055–1066, 2012.
- [23] A. J. Wolfe, M. M. Mohammad, A. K. Thakur, and L. Movileanu, “Global redesign of a native  $\beta$ -barrel scaffold,” *Biochim. Biophys. Acta - Biomembr.*, vol. 1858, no. 1, pp. 19–29A, 2016.
- [24] J. P. Overington, B. Al-Lazikani, and A. L. Hopkins, “How many drug targets are there?,” *Nat. Rev. Drug Discov.*, vol. 5, no. 12, pp. 993–996, 2006.
- [25] A. Doerr, “Membrane protein structures,” *Nat. Methods*, vol. 6, no. 1, pp. 35–35, 2009.
- [26] P. Champeil *et al.*, “A robust method to screen detergents for membrane protein stabilization, revisited,” *Anal. Biochem.*, vol. 511, pp. 31–35, 2016.
- [27] J. Borch and T. Hamann, “The nanodisc: A novel tool for membrane protein studies,” *Biol. Chem.*, vol. 390, no. 8, pp. 805–814, 2009.
- [28] A. E. Speers and C. C. Wu, “Proteomics of integral membrane proteins--theory and application,” *Chem. Rev.*, vol. 107, no. 8, pp. 3687–3714, Aug. 2007.
- [29] Y. Arinaminpathy, E. Khurana, D. M. Engelman, and M. B. Gerstein, “Computational analysis of membrane proteins: the largest class of drug targets,” *Drug Discov. Today*, vol. 14, no. 23–24, pp. 1130–1135, Dec. 2009.
- [30] P.-C. Chen and J. S. Hub, “Structural Properties of Protein-Detergent Complexes from SAXS and MD Simulations,” *J. Phys. Chem. Lett.*, vol. 6, no. 24, pp. 5116–5121, Dec. 2015.
- [31] Z. Yang and C. G. Brouillette, “A Guide to Differential Scanning Calorimetry of Membrane and Soluble Proteins in Detergents,” *Methods Enzymol.*, vol. 567, pp. 319–

- 358, 2016.
- [32] I. Kucharska and L. K. Tamm, “Solution NMR Provides New Insight into Lipid-Protein Interaction,” *Biochemistry*, vol. 56, no. 33, pp. 4291–4292, 2017.
- [33] A. Manuscript, “Protein NMR Techniques,” vol. 831, no. 41, pp. 1–18, 2012.
- [34] F. Perrin, *Polarisation de la lumière de fluorescence. Vie moyenne des molécules dans l'état excité*, vol. 7. 1925.
- [35] W. A. Lea and A. Simeonov, “Fluorescence polarization assays in small molecule screening.,” *Expert Opin. Drug Discov.*, vol. 6, no. 1, pp. 17–32, Jan. 2011.
- [36] M. D. Hall, A. Yasgar, T. Peryea, J. C. Braisted, A. Jadhav, and N. P. Coussens, “and drug discovery : a review,” vol. 4, no. 2, pp. 1–41, 2017.
- [37] D. M. Jameson, “Fluorescence Polarization : Past , Present and Future,” no. October, 2015.



## Chapter 2. Global Redesign of a Native $\beta$ -barrel Scaffold

Aaron J. Wolfe,<sup>1,2</sup> Mohammad M. Mohammad,<sup>1</sup> Avinash K. Thakur,<sup>1,2</sup> and Liviu Movileanu<sup>1,2,3</sup>

<sup>1</sup>Department of Physics, Syracuse University, 201 Physics Building, Syracuse, New York 13244-1130, USA

<sup>2</sup>Structural Biology, Biochemistry, and Biophysics Program, Syracuse University, 111 College Place, Syracuse, New York 13244-4100, USA

<sup>3</sup>The Syracuse Biomaterials Institute, Syracuse University, 121 Link Hall, Syracuse, New York 13244, USA

This section was originally published as:

**Aaron J. Wolfe**, M.M. Mohammad, A.K. Thakur, and L. Movileanu. Global Redesign of a Native Beta-barrel Scaffold, 2016, *Biochim. Biophys. Acta Biomembranes* 1858(1), 19-29.

<https://doi.org/10.1016/j.bbamem.2015.10.006> © 2015 Elsevier B.V.

Author contributions:

AJW: Designed experiments, performed experiments, analyzed data, co-wrote manuscript.

MMM: Performed experiments

AKT: Performed experiments

LM: Analyzed data co-wrote manuscript

**ABSTRACT**

One persistent challenge in membrane protein design is accomplishing extensive modifications of proteins without impairing their functionality. A truncation derivative of the ferric hydroxamate uptake component A (FhuA), which featured the deletion of the 160-residue cork domain and five large extracellular loops, produced the conversion of a non-conductive, monomeric, 22-stranded  $\beta$ -barrel protein into a large-conductance protein pore. Here, we show that this redesigned  $\beta$ -barrel protein tolerates an extensive alteration in the internal surface charge, encompassing 25 negative charge neutralizations. By using single-molecule electrophysiology, we noted that a commonality of various truncation FhuA protein pores was the occurrence of 33% blockades of the unitary current at very high transmembrane potentials. We determined that these current transitions were stimulated by their interaction with an external cationic polypeptide, which occurred in a fashion dependent on the surface charge of the pore interior as well as the polypeptide characteristics. This study shows promise for extensive engineering of a large monomeric  $\beta$ -barrel protein pore in molecular biomedical diagnosis, therapeutics, and biosensor technology.

## INTRODUCTION

In many situations, global engineering of membrane proteins impairs their functionality and folding state, sometimes leading to unfolded structures [1]. One class of relatively robust membrane proteins is that of transmembrane  $\beta$  barrels, which are primarily found in the outer membrane (OM) of chloroplasts, mitochondria, and Gram-negative bacteria [2]. Their stiffness is determined by the presence of a barrel scaffold consisted of anti-parallel, paired  $\beta$  strands. The network of many hydrogen bonds between different  $\beta$  strands is the basis for this unique structural robustness. This feature was at the heart of many investigations in the perpetually rich area of the engineering of  $\beta$ -barrel membrane proteins [3–8].

Monomeric  $\beta$ -barrels may be used as sensing elements, which rely upon single-molecule detection [9–12]. The main advantage of the monomeric  $\beta$  barrel is the ease of genetic engineering or chemical modification of single-polypeptide pores and channels, thus avoiding further complications of the purifications steps for separating the targeted engineered or modified oligomer from other byproducts of the oligomerization reaction. One challenging prerequisite for using these monomeric  $\beta$ -barrels in single-molecule detection is obtaining a quiet single-channel electrical signature that is freed of current gating fluctuations [13], otherwise interfering with the analyte-induced current blockades resulted from single-molecule detection. Spontaneous fluctuations in  $\beta$ -barrel protein channels, pores, and porins have been extensively explored [7, 14–21]. In general, these fluctuations are produced by conformational alterations of the large extracellular loops, which many times permanently or transiently fold back into the pore interior [7, 16].

An example of a versatile monomeric  $\beta$ -barrel model for extensive engineering and structure-function relationship studies is the outer membrane protein G (OmpG) from *E. coli* [22, 23], a 14-stranded  $\beta$ -barrel containing seven extracellular loops. It was identified that the motions of loop L6 determined the gating fluctuations observed with the wild-type OmpG protein [9]. Later, other groups independently confirmed that indeed L6 is responsible for the intense gating activity of OmpG [7, 24]. Recently, OmpG was successfully used for the single-molecule detection of bulky proteins by employing chemically modified flexible tethers [11, 12].

In this paper, we present a detailed examination of the global engineering of ferric hydroxamate uptake component A (FhuA) [25, 26], a monomeric  $\beta$ -barrel OM protein of *E. coli*. This 714-residue protein includes a large, 22-stranded barrel filled by an N-terminal, 160-residue cork domain located within the pore interior (Fig. 1A and Fig. 1B). The  $\beta$  strands are connected each other by 10 short  $\beta$  turns and 11 long extracellular loops (Supplementary Materials, Table S1, Fig. S1, Fig. S2). The internal cross-sectional surface of the barrel is elliptical with axis lengths of 26 and 39 Å, including the average length of the side chains. FhuA primarily functions as a transporter, facilitating the navigation of Fe<sup>3+</sup>, complexed by the siderophore ferrichrome, from the extracellular into periplasmic side [27]. In addition, it was determined that FhuA functions as a transporter for antibiotics, such as albomycin [28, 29] and rifamycin [30]. Remarkably, the transporter function of FhuA extends to receptor for colicin M and a number of bacteriophages, including T1, T5, and  $\phi$ 80 [29].

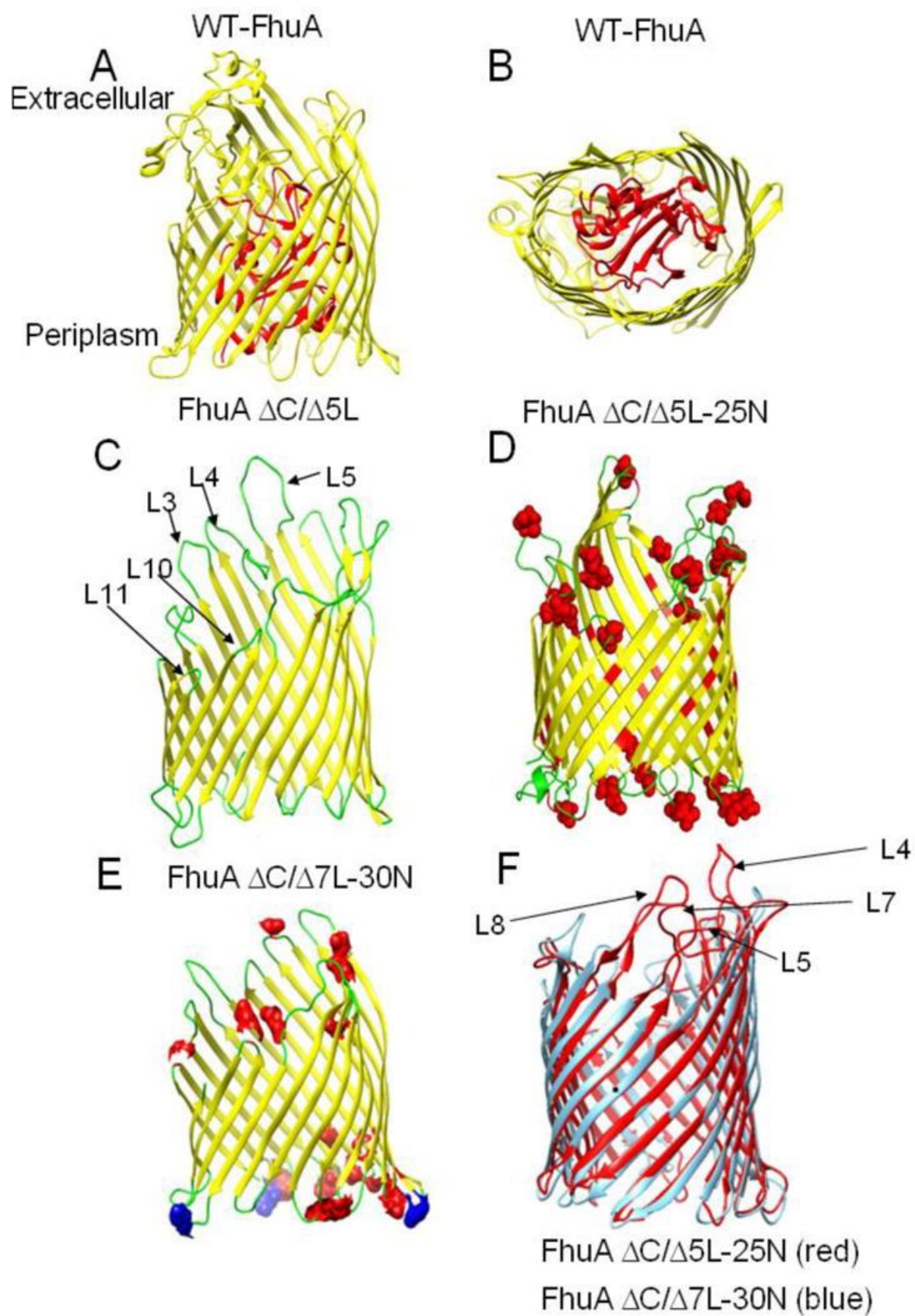


**Figure 1. Homology molecular structures created by Swiss-model [60, 61] to visually compare the global mutational alterations of the  $\beta$ -barrel scaffold of FhuA with respect to wild-type FhuA (WT-FhuA).**

(A) Side view of the ribbon structure of the WT-FhuA protein [25, 26]; (B) Top view, from the extracellular side, of the ribbon structure of the WT-FhuA protein. In (A) and (B), the 160-residue cork domain is illustrated in red; (C) FhuA  $\Delta C/\Delta 5L$  encompassing complete deletion of the cork domain ( $\Delta C$ ) and the major deletions of five extracellular loops, L3, L4, L5, L10, and L11, which are marked by arrows; (D) The FhuA  $\Delta C/\Delta 5L$ -25N derivative highlighting the location of 25 negative charge neutralizations, marked in red, with respect to FhuA  $\Delta C/\Delta 5L$ ; (E) FhuA  $\Delta C/\Delta 7L$ -30N that has been obtained by additional four extracellular loop deletions with respect to the FhuA  $\Delta C/\Delta 5L$  scaffold. This mutant contains 30 new positive charges with respect to FhuA  $\Delta C/\Delta 5L$ . Additional negative charge neutralizations with respect to FhuA  $\Delta C/\Delta 5L$  are marked in red, along with three additional lysine mutations in the  $\beta$  turns, out of which two are negative-to-positive charge reversals [62], which are marked in blue; (F) The superposition of the FhuA  $\Delta C/\Delta 5L$ -25N scaffold, marked in red, and FhuA  $\Delta C/\Delta 7L$ -30N, marked in blue, aligned and visualized by Chimera software package [63], highlighting the additional extracellular loop truncations of L4, L5, L7, and L8. All panels show the global FhuA derivatives from various angles for the sake of the clarity of specific details. Based on the X-ray crystal structure of FhuA [25, 26], the average luminal dimensions of FhuA  $\Delta C/\Delta 5L$  were determined to be  $\sim 3.1 \times 4.4$  nm, as measured from  $C\alpha$  to  $C\alpha$ . All homology structures of the globally mutated FhuA proteins were accomplished using FhuA PDB ID: 1FI1 [26].

Here, we show that deletion of the entire cork domain ( $\Delta C$ ) and part of five extracellular loops, L3, L4, L5, L10, and L11 ( $\Delta L5$ ) of FhuA results in a protein pore that is amenable to modular global engineering (Fig. 1C; Supplementary Materials, Tables S2–S4, Fig. S3). FhuA  $\Delta C/\Delta 5L$  was further redesigned by neutralizing 25 negative charges throughout the  $\beta$  turns,  $\beta$  strands, and extracellular loops (FhuA  $\Delta C/\Delta 5L$ -25N; Fig. 1D). A common trait of both truncation FhuA-based protein pores was the occurrence of uniform current transitions, whose amplitude was about 33% of the unitary current, among four long-lived sub-states at very high positive and negative transmembrane potentials of 180 mV. Subsequent deletion of extracellular loops, encompassing part of the already deleted loops L4 and L5, as well as additional two loop deletions L7 and L8 (FhuA  $\Delta C/\Delta 7L$ -30N; Fig. 1E and Fig. 1F), produced a quiet electrical signature at positive potentials, but frequent, large-amplitude, and short-lived current blockades at negative potentials that were never observed with the other truncation FhuA mutants.

Interestingly, we found that the 33% current blockades observed with FhuA  $\Delta C/\Delta 7L$ -30N were stimulated by its interaction with a short, 23-residue cationic polypeptide at lower positive transmembrane potentials of  $\sim 120$  mV. This phenomenon was also replicated with the more acidic FhuA  $\Delta C/\Delta 5L$  protein pore interacting with other cationic polypeptides. Therefore, we concluded that not only a high transmembrane potential, but also the presence of a “polypeptide collider” within the pore interior “stimulates” the occurrence of the 33% current transitions. We postulated that not only an external polypeptide, but also an internal, fluctuating polypeptide loop activates these transitions at lower transmembrane potentials. In accord with this hypothesis, under these conditions we noted standard 33% current blockades with a redesigned  $\beta$ -barrel, FhuA  $\Delta C/\Delta 5L$ -25N\_ELP, featuring an extended elastin-like-polypeptide (ELP) loop

engineered within the central part of the barrel. This extensive engineering of truncated FhuA-based protein pores demonstrates their modularity, allowing for further adaptations intended for the use in medical biotechnology, therapeutics, and biosensor arenas.

## **MATERIALS AND METHODS**

### **2.1. Protein overexpression and purification under denaturing condition**

Details on cloning of various multi-site mutants, which were derived from *fhua*  $\Delta c/\Delta 51$ , are provided in Supplementary Materials. All proteins were expressed in *E. coli* BL21 (DE3). Cells, transformed with pPR-IBA1-*fhua*  $\Delta c/\Delta 51$ -6 $\times$ His<sup>+</sup>, pPR-IBA1-*fhua*  $\Delta c/\Delta 51$ -25n-6 $\times$ His<sup>+</sup>, pPR-IBA1-*fhua*  $\Delta c/\Delta 51$ -25n\_elp-6 $\times$ His<sup>+</sup>, and pPR-IBA1-*fhua*  $\Delta c/\Delta 71$ -30n-6 $\times$ His<sup>+</sup> plasmids, were grown in 2X TY media at 37°C until OD<sub>600</sub> ~0.7–0.8, at which time the protein expression was induced with 0.5 mM isopropyl  $\beta$ -D-1-thiogalactopyranoside (IPTG) and allowed to continue until the cell growth plateaued, as measured by OD<sub>600</sub>. Cells were harvested by centrifugation and the pellet was resuspended in the resuspension buffer (1X PBS, pH 8.0). The resuspended cells were lysed using a Microfluidizer, model 110L (Microfluidics, Newton, MA). The homogenate was centrifuged for 20 min at 4,000 $\times$ g and 4°C. Inclusion bodies-containing pellets were resuspended in the inclusion body-cleaning buffer (1X PBS, 1% Triton X100, pH 8.0), homogenized using Potter-Elvehjem homogenizer (VWR, Bridgeport, NJ), and recentrifuged for 30 min at 30,000 $\times$ g and 4°C. This step was repeated three times. The final pellet was resuspended in denaturing buffer (10 mM potassium phosphate, 8 M urea, pH 8.0). The solution was subject to an additional 30 min-duration centrifugation at 30,000 $\times$ g and 4°C to remove the insoluble materials. The final protein-containing solutions were filtered using 0.2  $\mu$ M filters



(Thermo Fisher Scientific, Rochester, NY). The solubilized proteins were loaded onto a column packed with 2 ml of Ni<sup>2+</sup>-NTA resin (Bio-Rad, Hercules, CA), which was equilibrated in 200 mM NaCl, 10 mM potassium phosphate, 8 M urea, pH 8.0. The column was washed in two steps with 5 and 25 mM imidazole, respectively, in the same equilibrating buffer. The proteins were eluted with equilibrating buffer containing 350 mM imidazole in 5 ml fractions. SDS-PAGE was used to monitor the elution profile of pure proteins.

The tag-free FhuA  $\Delta C/5L$  protein, lacking the N-terminal, 33-residue signal polypeptide and the C-terminal, 6 $\times$ His<sup>+</sup> tag, named TL-FhuA  $\Delta C/5L$ , was also transformed into the *E. coli* BL21 (DE3) cells, which were grown and harvested as describe above. Cell lysates were centrifuged at 1,800 $\times$ g for approximately 15 min to separate the insoluble from the soluble proteins. The pellet was washed twice by resuspending it in washing buffer 1 (150 mM NaCl, 50 mM Tris, 1 mM EDTA, 2 M urea, pH 8.0) and centrifuging it for 20 min at 1,800 $\times$ g and 4°C. Then, the resulting pellet was washed twice by resuspending it in washing buffer 2 (150 mM NaCl, 50 mM Tris, 1 mM EDTA, 1% Triton X-100, pH 8.0) and centrifuging it for 20 min at 1,800 $\times$ g and 4°C. This procedure was followed by additional two washes of the pellet with ddH<sub>2</sub>O and its centrifugation for 20 min at 1,800 $\times$ g and 4°C. Finally, the pellet was denatured in the denaturing buffer (20 mM Tris, 6 M urea, pH 8.0) and loaded onto the ion exchange column (Bio-Rad) equilibrated with the same denaturing buffer. Protein was eluted using a linear gradient of elution buffer (20 mM Tris, 6 M urea, 1 M NaCl, pH 8.0). Collected fractions were analyzed on the SDS-PAGE gel for purity tests. Pure fractions were dialyzed against water. The final protein samples were lyophilized and stored at -80°C.

## **2.2. Refolding of FhuA $\Delta$ C/ $\Delta$ 5L, FhuA $\Delta$ C/ $\Delta$ 5L-25N, and FhuA $\Delta$ C/ $\Delta$ 7L-30N**

The modifications of the protocol for obtaining FhuA  $\Delta$ C/ $\Delta$ 5L through rapid-dilution refolding has been previously described [10]. Briefly, the method of refolding for these proteins was adopted from the protocol developed by Arora and colleagues [31]. 40  $\mu$ l of 6 $\times$ His<sup>+</sup>-tag purified denatured protein was 50-fold diluted into a 1.5% n-Dodecyl- $\beta$ -D-maltopyranoside (DDM) solution containing 200 mM NaCl, 10 mM sodium phosphate, pH 8.0. The diluted protein samples were left overnight at 23°C to complete the refolding process of proteins. Aggregated or misfolded proteins were removed by centrifugation at 16,000 $\times$ g for 15 minutes. Samples were stored at -80°C in 50  $\mu$ l aliquots.

## **2.3. Refolding of FhuA $\Delta$ C/ $\Delta$ 5L-25N\_ELP and TL-FhuA $\Delta$ C/ $\Delta$ 5L**

These particular constructs did not fare well with the rapid-dilution method, so that a slow-dialysis method was employed to increase the yield and channel activity. 1 ml of urea-denatured protein FhuA  $\Delta$ C/ $\Delta$ 5L-25N\_ELP or TL-FhuA  $\Delta$ C/ $\Delta$ 5L at a final concentration of  $\sim$ 50  $\mu$ M was added to cellulose dialysis tubing (Sigma, St. Louis, MO) containing 1.5% DDM. The tubing was placed in a 5-liter beaker containing a buffer solution of 200 mM NaCl, 10 mM sodium phosphate, pH 8.0. The dialysis was carried out for 48 hours at 4°C changing the solution once at 24 hours. The resulting protein-containing solution was spun at 16,000 $\times$ g and 4°C to remove large insoluble aggregates. To further separate the monomeric protein from potentially misfolded or aggregated species, the supernatant was applied to a Superdex 200 size-exclusion chromatography column (GE Healthcare, Piscataway, NJ) equilibrated with 0.5% DDM in 200

mM NaCl, 10 mM sodium phosphate, pH 8.0. The proteins were eluted at the flow rate of 0.25 ml/min and their elution was monitored by the absorbance at 280 nm.

#### **2.4. Single-channel electrical recordings on planar lipid bilayers**

Electrical recordings were carried out with planar bilayer lipid membranes (BLMs) [32, 33]. The two sides of the chamber, cis and trans (1.5 ml each), were separated by a 25  $\mu\text{m}$ -thick Teflon septum (Goodfellow Corporation, Malvern, PA). An aperture in the septum,  $\sim 80$   $\mu\text{m}$  in diameter, was pretreated with hexadecane (Sigma-Aldrich, St. Louis, MO), which was dissolved in highly purified pentane (Fisher HPLC grade, Fair Lawn, NJ) at a concentration of 10% (v/v). A 1,2-diphytanoyl-sn-glycero-phosphatidylcholine (Avanti Polar Lipids, Alabaster, AL) bilayer was formed across the aperture. For acquiring electrical recordings at single-channel resolution, the refolded engineered proteins were added to the cis chamber to a final concentration of  $\sim 0.1$ – $0.3$  ng/ $\mu\text{l}$ . Current recordings were obtained by using a patch-clamp amplifier (Axopatch 200B, Axon Instruments, Foster City, CA), which was connected to Ag/AgCl electrodes through agar bridges. The cis chamber was grounded, so that a positive current (upward deflection) represents positive charge moving from the trans to cis side. A Precision T3500 Tower Workstation Desktop PC (Dell Computers, Austin, TX) was equipped with a DigiData 1322A A/D converter (Axon) for data acquisition. The signal was low-pass filtered with an 8-pole Bessel filter (Model 900; Frequency Devices, Ottawa, IL) at a frequency of 10 kHz and sampled at 50 kHz, unless otherwise stated. For data acquisition and analysis, we used the pClamp9.2 and pClamp10.3 software packages (Axon). Details on ion selectivity measurements with asymmetric buffer conditions [34, 35] are provided in Supplementary experimental methods.

## RESULTS

### 3.1. Rationale for global engineering of the FhuA scaffold

A primary goal of this work was the conversion of the 714-residue, cork-filled FhuA protein into an open transmembrane pore that can maintain its functionality in a tractable mode upon global engineering (e.g. additional loop deletions, functional loop implementation, large modification of the protein surface charge). To achieve this goal, we have inspected the structural features of this protein [25, 26]. The extracellular loops L3, L4, L5, L10, and L11 are large and potentially flexible due to their random-coil structure. We determined that that extensive single-channel explorations of a multiple-truncation FhuA mutant encompassing the complete removal of the cork domain (C) as well as large deletions of the five above-mentioned extracellular loops, also called FhuA  $\Delta C/\Delta 5L$ , revealed a quiet electrical signature over a broad range of conditions, including salt concentration (20 mM–4M), pH (2.8–11.0), and applied transmembrane potential (–160 to +160 mV) (Supplementary Materials, Table S4, Figs. S4–S7) [10]. As compared with our prior membrane protein redesign studies [5, 10], here we pursued the following three distinct goals: (i) to examine the impact of an extensive alteration in the surface charge of the pore interior on its biophysical traits. For this purpose, we redesigned and created FhuA  $\Delta C/\Delta 5L$ -25N, which encompassed 25 neutralizations of negatively charged residues located within the  $\beta$ -turns,  $\beta$ -barrel part and extracellular loops. This truncation FhuA mutant features a much less acidic pore; (ii) to explore the effect of further truncation of the remaining large extracellular loops on the unitary conductance. In this way, we questioned whether the presence of remaining large extracellular loops contributes to the pore constriction. To accomplish this task, we redesigned and developed FhuA  $\Delta C/\Delta 7L$ -30N, featuring the truncation of seven extracellular

loops and the implementation of 30 new positive charges. This truncation FhuA mutant included 25 neutralizations of negatively charged residues, two negative-to-positive charge reversals, and one positive charge mutation of a neutral side chain. In this way, the pore interior of FhuA  $\Delta C/\Delta 7L-30N$  was even less acidic than that of FhuA  $\Delta C/\Delta 5L-25N$ ; (iii) to investigate the effect of an engineered neutral polypeptide loop within the central part of the  $\beta$ -barrel on the stability of the open-state current. To conduct these measurements, we created the FhuA  $\Delta C/\Delta 5L-25N\_ELP$  protein pore, which included an elastin-like-polypeptide loop engineered within the central part of the  $\beta$ -barrel of the FhuA  $\Delta C/\Delta 5L-25N$  scaffold. In addition, we redesigned and created a control truncation mutant, TL-FhuA  $\Delta C/\Delta 5L$ , whose polypeptide tags at the N and C termini, namely the 33-residue signal polypeptide and 6-His<sup>+</sup> tag, respectively, were deleted. In this way, we wanted to test whether the N- and C-terminal polypeptide tags do alter the occurrence of the 33% current blockades observed with the other truncations FhuA mutants.

### **3.2. Major charge neutralization of a $\beta$ -barrel scaffold maintains the electrical quietness of the pore**

Here, we were interested in examining whether this  $\beta$ -barrel scaffold of FhuA can tolerate a large alteration in the surface charge within the pore interior. Remarkably, despite numerous charge neutralizations of FhuA  $\Delta C/\Delta 5L-25N$ , this engineered protein pore exhibited closely similar single-channel electrical signature as compared to that of FhuA  $\Delta C/\Delta 5L$  (Fig. 1D; Supplementary Materials, Table S5, Figs. S8–S10). This drastic change in the number of negative charges facing the pore interior produced a significant change in ionic selectivity, from

a permeability ratio (PK/PCl) of ~5.5 recorded with FhuA  $\Delta C/\Delta 5L$  to ~0.60 observed with FhuA  $\Delta C/\Delta 5L-25N$  under asymmetric conditions (Supplementary Materials).

### **3.3. Voltage-induced gating of the engineered pores occurs in the form of uniform, 33% current transitions among four sub-states**

One striking commonality between FhuA  $\Delta C/\Delta 5L$  and FhuA  $\Delta C/\Delta 5L-25N$  is the display of voltage-induced current blockades at very high transmembrane potentials of 180 mV or greater and in 1 M KCl, 10 mM potassium phosphate, pH 7.4. The occurrence of fairly uniform, ~33% current blockades at highly elevated positive potentials for the two proteins is illustrated in Fig. 2A and Fig. 2B. They were also noted at highly elevated negative potentials (SUPPLEMENTARY MATERIALS, Figs. S11–S12). In addition, such transitions occurring among the four long-lived sub-states were reversible. It should be noted that O1 is a fully open current sub-state, reflecting the unitary conductance, whereas O4 is a closed current sub-state, exhibiting a very small residual current in the range of 0–20 pA at a potential of +180 mV. Therefore, the O2 and O3 current sub-states are intermediate states connecting the fully open and closed sub-states. It is worth mentioning that all transitions only occurred among consecutive sub-states, i.e., between O1 and O2, between O2 and O3, and between O3 and O4. They exhibited durations in a broad time range, from tens of milliseconds to hundreds of seconds, spanning a timescale up to six orders of magnitude.

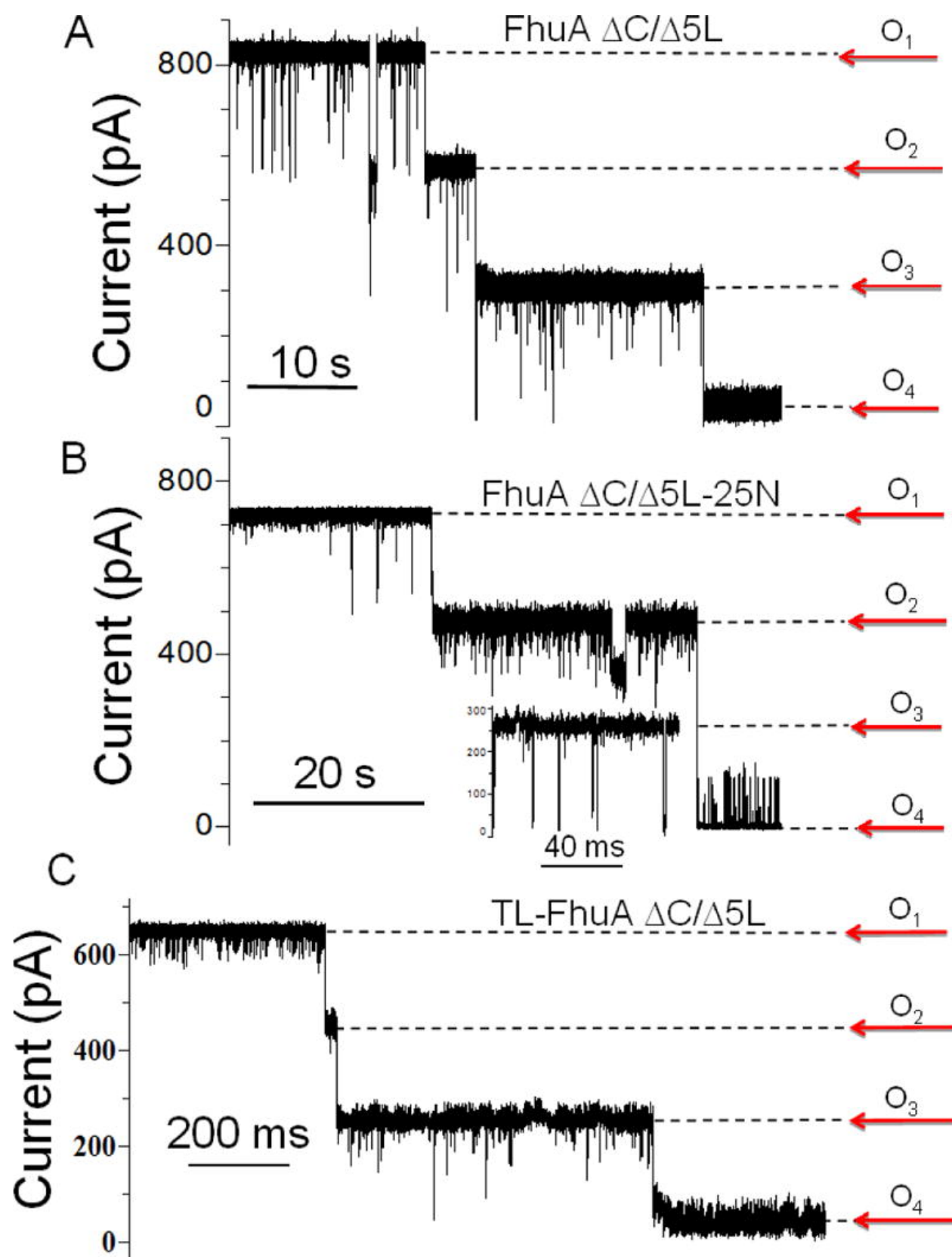


**Figure 2. Representative current blockades observed with globally mutated FhuA derivatives at very high positive potentials.**

These discrete blockades show each ~33% reduction in the unitary conductance. (A) FhuA  $\Delta C/\Delta 5L$  at +180 mV (n=10 distinct single-channel electrical recordings); (B) FhuA  $\Delta C/\Delta 5L-25N$  at +180 mV (n=2). The inset shows the O3 level by expanding the trace; (C) TL-FhuA  $\Delta C/\Delta 5L$  at +160 mV (n=3). All single-channel electrical recordings were achieved in 1M KCl, 10 mM potassium phosphate, pH 7.4. Single-channel electrical traces were low-pass Bessel filtered at 1.4 kHz.



One immediate question is whether the gating mechanism is impacted by the N- or C-terminus located near the periplasmic  $\beta$  turns of the protein (Fig. 1). This is especially reasoned by the additional polypeptides engineered at these termini. For example, FhuA  $\Delta C/\Delta 5L$  was fused with the 33-residue signal polypeptide at the N-terminus and the 6 $\times$ His<sup>+</sup> tag at the C-terminus. FhuA  $\Delta C/\Delta 5L$ -25N had only the 6 $\times$ His<sup>+</sup> tag at the C-terminus. Therefore, we redesigned and constructed an FhuA  $\Delta C/\Delta 5L$  mutant lacking both terminal polypeptides, which was named TL-FhuA  $\Delta C/\Delta 5L$ . Interestingly, Fig. 2C demonstrates that TL-FhuA  $\Delta C/\Delta 5L$  exhibited 33% current transitions among the four long-lived sub-states at an applied transmembrane potential of +160 mV. Such transitions were readily detectable among O1  $\leftrightarrow$  O2  $\leftrightarrow$  O3 at high negative potentials (Supplementary Materials, Fig. S13). Therefore, the polypeptides engineered at the N- and C-termini were not major perturbation factors on the stability of the open-state current of the FhuA  $\Delta C/\Delta 5L$  protein pores.

### **3.4. Extensive deletions of large extracellular loops impact the four sub-state dynamics of the pore at negative potential**

We wondered whether the remaining parts of extracellular loops might affect the four sub-state dynamics of the engineered FhuA  $\Delta C/\Delta 5L$  derivatives. Therefore, we designed and constructed a multiple loop deletion mutant derived from FhuA  $\Delta C/\Delta 5L$ -25N and characterized by further truncation of large loops L4, L5, L7, and L8, also named FhuA  $\Delta C/\Delta 7L$ -30N (Fig. 1E, Fig. 1F; Supplementary Materials, Tables S6–S8, Figs. S14–S16). Interestingly, FhuA  $\Delta C/\Delta 7L$ -30N exhibited a quiet single-channel electrical signature up to +120 mV (Fig. 3A). In contrast to FhuA  $\Delta C/\Delta 5L$  and FhuA  $\Delta C/\Delta 5L$ -25N, FhuA  $\Delta C/\Delta 7L$ -30N showed a distinctive single-channel

electrical signature at negative transmembrane potentials, which was decorated by frequent, large-amplitude transient current blockades (Fig. 3B). Remarkably, at  $-100$  mV the amplitude of some of these current transitions (OL) was greater than 50% of that of the unitary current. These experiments also reveal the asymmetry of voltage-induced current gating of FhuA  $\Delta C/\Delta 7L-30N$  with respect to the polarity of the applied transmembrane potential. This single-channel electrical signature consisted of small- (OS) and large- (OL) current amplitude blockades ( $n=3$ ; Fig. 3C). The amplitude of these current transitions was clearly distinct from those typically displayed as 33% current blockades observed with FhuA  $\Delta C/\Delta 5L$  and FhuA  $\Delta C/\Delta 5L-25N$  at positive and negative transmembrane potentials (Fig. 4). At very high negative potentials, greater than  $-120$  mV, the FhuA  $\Delta C/\Delta 7L-30N$  protein pore became fairly unstable and noisy.

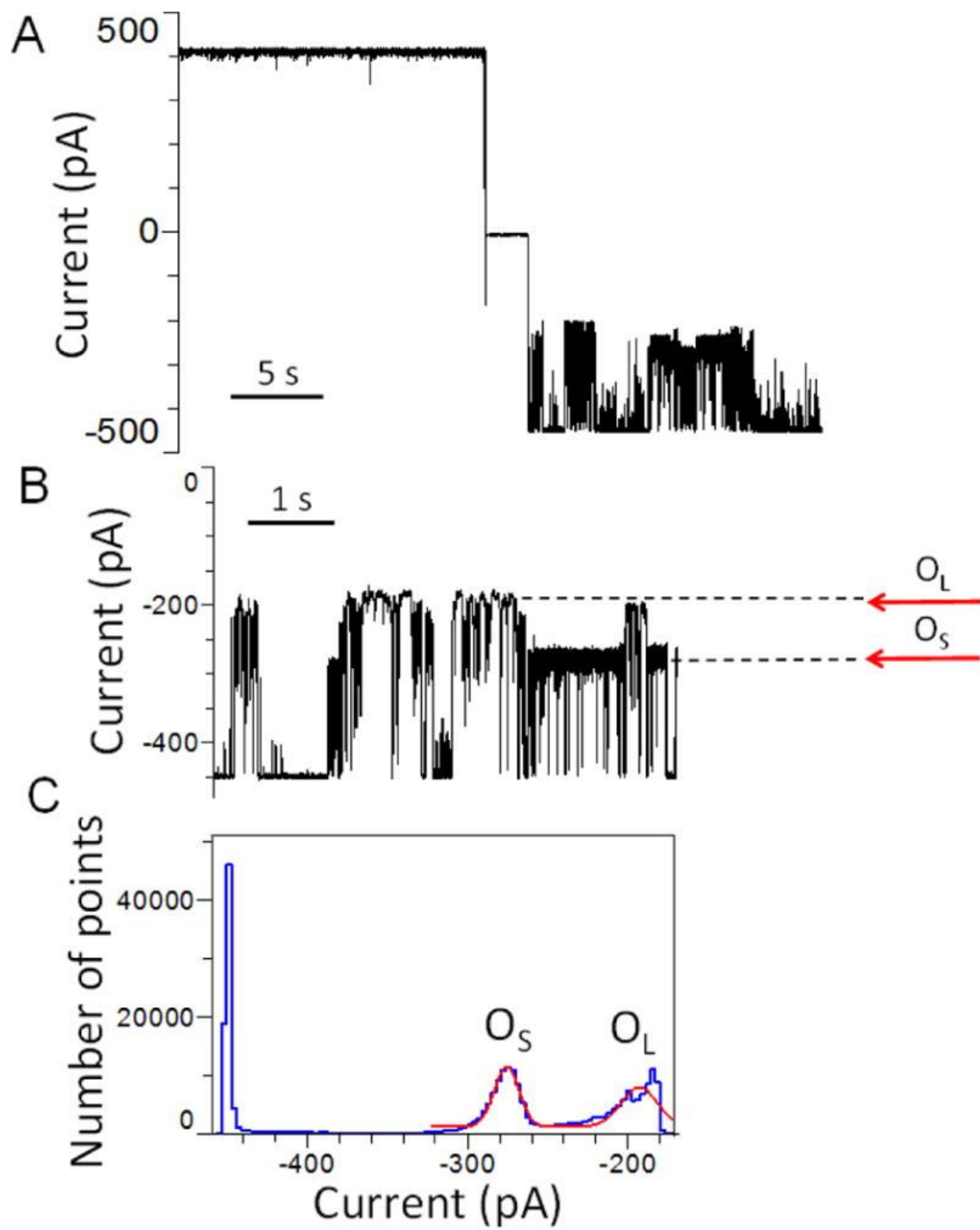


**Figure 3. Representative single-channel electrical signature of FhuA  $\Delta C/\Delta 7L$ -30N at a medium applied potential.**

(A) A representative single-channel electrical trace acquired with FhuA  $\Delta C/\Delta 7L$ -30N at applied transmembrane potentials of +100 and -100 mV. Transient, large-amplitude current fluctuations were observed at negative potentials; (B) A snapshot of a single-channel channel electrical recording obtained at a negative potential of -100 mV. The 33% closures were absent at either positive or negative potentials; (C) All-point current amplitude histogram of the electrical trace acquired in (B). These traces are representative over a number of at least four distinct single-channel electrical recordings. All single-channel electrical recordings were achieved in 1M KCl, 10 mM potassium phosphate, pH 7.4. The other experimental conditions were similar to those reported in Fig. 2.

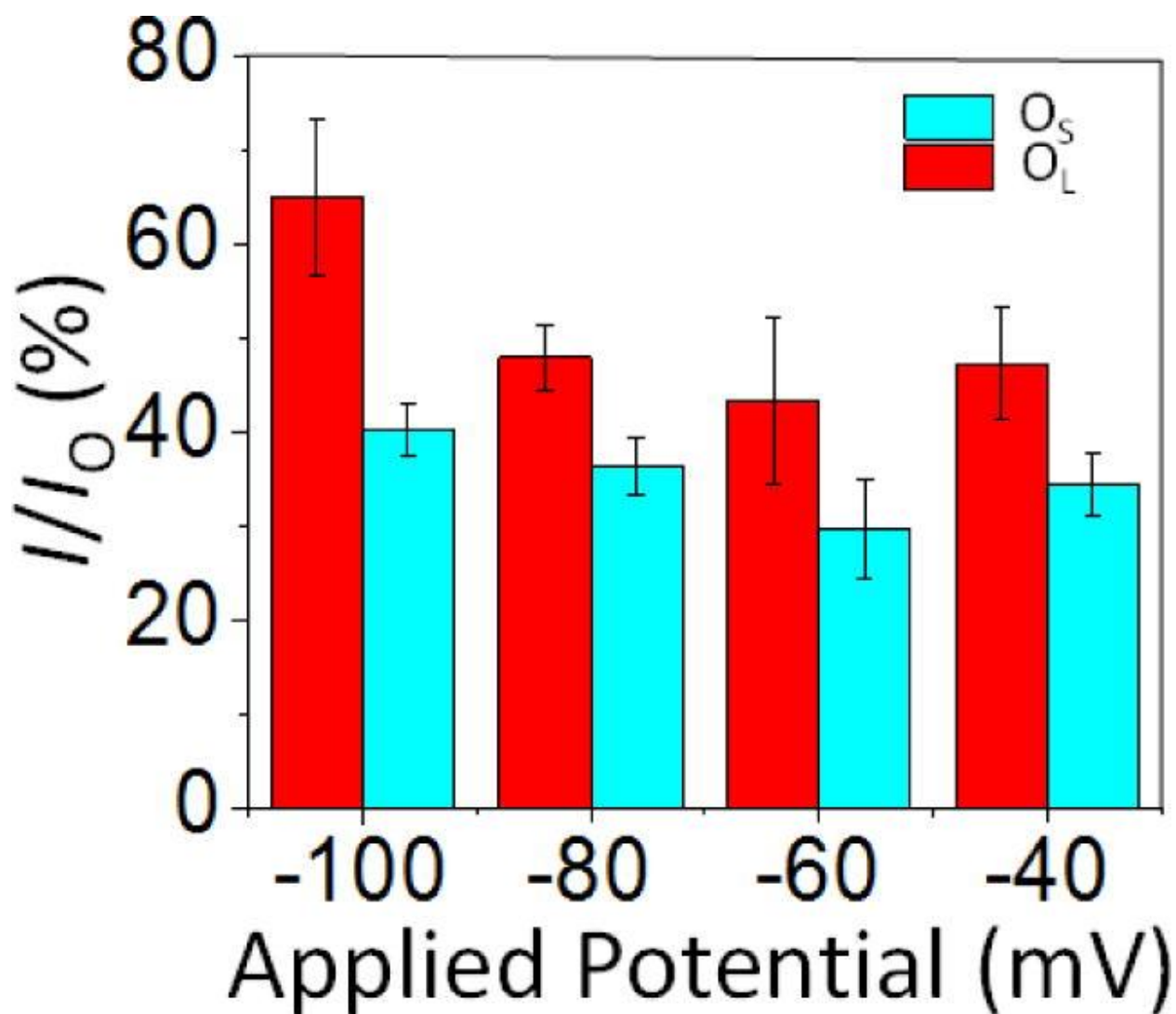


**Figure 4. FhuA  $\Delta C/\Delta 7L-30N$  shows a distinctive signature from the other truncation FhuA mutants.**

Current-amplitude histogram of the highly frequent current blockades observed with FhuA  $\Delta C/\Delta 7L-30N$  at negative potentials. The current amplitudes were normalized to that value corresponding to the unitary current. All single-channel electrical recordings were achieved in 1M KCl, 10 mM potassium phosphate, pH 7.4. The other experimental conditions were similar to those reported in Fig. 2.

### **3.5. The 33% current transitions are stimulated by the presence of an external polypeptide collider**

Remarkably, the dynamics of 33% current transitions was not only impacted by the value of applied transmembrane potential, but also by the interaction of FhuA  $\Delta C/\Delta 7L-30N$  with a positively charged polypeptide. Fig. 5 illustrates the interaction of Syn B2, a 23-residue polypeptide carrying five Arg residues [36] with FhuA  $\Delta C/\Delta 7L-30N$  at an applied potential of +120 mV. Fig. 5A shows a quiet signature of FhuA  $\Delta C/\Delta 7L-30N$ . When 10  $\mu$  M Syn B2 was added to the trans side, brief transient current blockades, with dwell times  $\tau_1 = 0.2$  ms and  $\tau_2 = 2.45$  ms, were recorded, indicating partitioning of Syn B2 into the pore interior (Fig. 5B; Supplementary Materials, Fig. S16). No  $O_2 \rightarrow O_3$  current transitions were observed under these experimental conditions ( $n= 3$ ). Interestingly, increasing the Syn B2 concentration at 20  $\mu$ M in the trans chamber determined an additional transition,  $O_2 \rightarrow O_3$ , and also brief Syn B2-induced current transitions reaching the  $O_4$  sub-state (Fig. 5C).

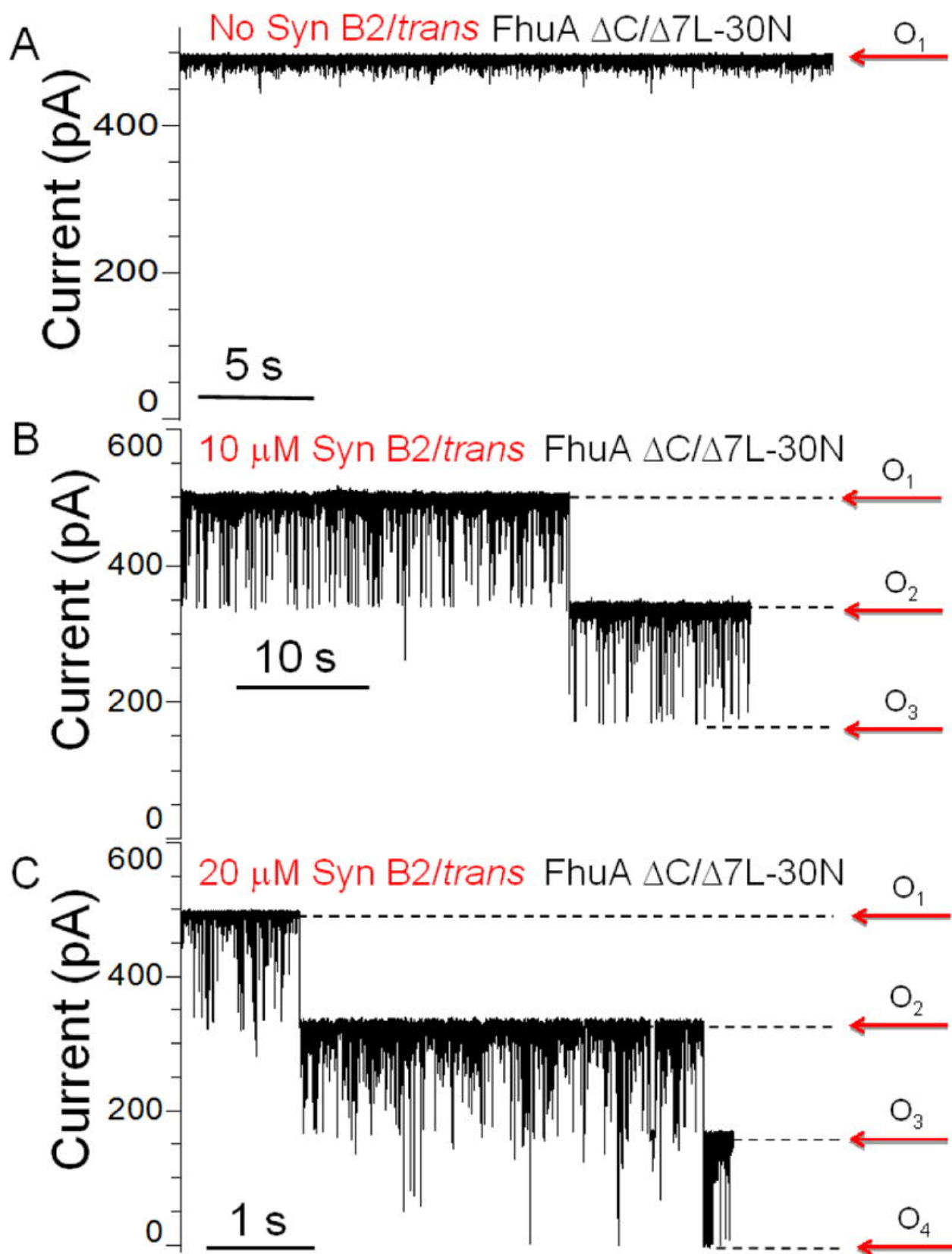


**Figure 5. Discrete current blockades observed with FhuA  $\Delta C/\Delta 7L$ -30N in the presence of Syn B2.**

(A) A representative single-channel electrical trace acquired with FhuA  $\Delta C/\Delta 7L$ -30N; (B) Application of low concentrations of the Syn B2 polypeptide to the trans side caused a 33% current blockade; (C) Application of increased concentrations of the Syn B2 polypeptide produced an additional 33% current blockade over that noted with FhuA  $\Delta C/\Delta 7L$ -30N alone. All single-channel electrical recordings were achieved in 1M KCl, 10 mM potassium phosphate, pH 7.4. The other experimental conditions were similar to those reported in Fig. 2.



We questioned whether this Syn B2-induced current transition between the O2 and O3 sub-states is only specific to its complex interactions with FhuA  $\Delta C/\Delta 7L$ -30N. Therefore, we executed single-channel electrical recordings with FhuA  $\Delta C/\Delta 5L$ , which can readily undergo 33% current transitions at very high transmembrane potentials. It should be noted that a much stronger interaction between positively charged Syn B2 and the more acidic  $\beta$ -barrel scaffold of FhuA  $\Delta C/\Delta 5L$  was expected, as compared to the Syn B2 - FhuA  $\Delta C/\Delta 7L$ -30N binding interactions. In accord with this anticipation, Syn B2 produced brief and transient current blockades at even lower transmembrane potentials (Supplementary Materials, Fig. S17). For example, in a range of transmembrane potentials between +20 and +80 mV, the dwell time of Syn B2 within the pore interior of FhuA  $\Delta C/\Delta 5L$  was between 0.08 and 0.18 ms. A biphasic voltage dependence of the dwell time or rate constant indirectly suggests that the relatively short Syn B2 polypeptide rapidly navigates across the pore interior of FhuA  $\Delta C/\Delta 5L$  at potentials greater than a critical value [36–38]. The conspicuous lack of the 33% blockades might likely be determined by the rapid Syn B2 translocation.

Therefore, we examined the interaction of larger cationic polypeptides with FhuA  $\Delta C/\Delta 5L$ , which would exhibit an even stronger binding interaction. First, we conducted single-channel recordings involving a 55-residue nucleocapsid protein 7 (NCp7) [39], a protein biomarker of the HIV-1 virus. The formal charge of NCp7 is +9 [32, 40, 41]. The addition of 20  $\mu$ M NCp7 to the trans side at a transmembrane potential of only +80 mV resulted in not only frequent, transient and brief current blockades with a duration of < 1 ms ( $n=3$ ), but also 33% current transitions among long-lived sub-states, such as O1  $\rightarrow$  O2, O2  $\rightarrow$  O3, and O3  $\rightarrow$  O4 (Supplementary Materials, Fig. S18). It is worth noting that the amplitude of the brief transient current blockades

was closely similar to the 33% normalized amplitude of the current transitions between the above-mentioned sub-states. Similarly with that situation of the interactions between Syn B2 and FhuA  $\Delta C/\Delta 7L-30N$ , we found that the probability of the NCp7-induced 33% current transitions in FhuA  $\Delta C/\Delta 5L$  was strongly dependent on the concentration of the external polypeptide. For example, at +80 mV, the first O1  $\rightarrow$  O2 transition occurred after a period of  $253 \pm 1$  s (n=2),  $103 \pm 2$  s (n=3), and  $9 \pm 13$  s (n=5) when 200 nM, 5  $\mu$ M, and 20  $\mu$ M were added to the trans chamber, respectively.

Moreover, we also inspected the interaction of the much larger pb2-Ba proteins [42] with FhuA  $\Delta C/\Delta 5L$ . pb2-Ba consists of the N terminal region of the pre-cytochrome b2 (pb2) of varying length (indicated as number of residues in parenthesis) fused to the N-terminus of the small ribonuclease barnase (Ba). They feature a high positive charge located on the leading sequence pb2 [36]. Under experimental conditions similar to those involving NCp7, we were able to detect the 33% current blockades O1  $\rightarrow$  O2, O2  $\rightarrow$  O3, and O3  $\rightarrow$  O4 at a transmembrane potential of +80 mV when only 200 nM of pb2-Ba was added to the trans side (Supplementary Materials, Fig. S18).

### **3.6. The 33% current transitions are stimulated by the presence of an engineered polypeptide loop within the pore interior.**

Based on findings pertinent to the impact of an external polypeptide collider on the dynamics of the 33% current transitions in FhuA  $\Delta C/\Delta 5L$  and FhuA  $\Delta C/\Delta 7L-30N$  protein pores, we hypothesized that discrete 33% current transitions among long-lived “metastable” sub-states can also be stimulated by the presence of an endogenously engineered polypeptide within the pore interior. Therefore, we engineered an elastin-like-polypeptide (ELP) loop by replacing Arg115 in the 6th  $\beta$ -strand, which is near the central part of the native  $\beta$ -barrel scaffold. The sequence of the ELP was (VPGGG)<sub>10</sub>, and was supplemented by two flexible Gly-Ser-based linkers, thus totaling 65 residues for the entire engineered polypeptide. The newly made construct, named FhuA  $\Delta C/\Delta 5L-25N\_ELP$ , was extensively examined under similar conditions with the other truncation FhuA mutants. This polypeptide lacks charge, avoiding some strong electrostatic interactions with the barrel walls. In addition, ELP is expected to be in expanded conformation [43, 44], perhaps reaching the extracellular region of the pore. In excellent accord with our above-mentioned postulation, Fig. 6A presents typical 33% current blockades of FhuA  $\Delta C/\Delta 5L-25N\_ELP$  occurring among all four long-lived sub-states at an applied transmembrane potential of  $-100$  mV, a condition at which we have never noted such events with the FhuA  $\Delta C/\Delta 5L-25N$  protein alone or with other truncation FhuA mutant. These 33% current transitions among long-lived sub-states were fully reversible (Fig. 6B; Supplementary Materials, Fig. S19).

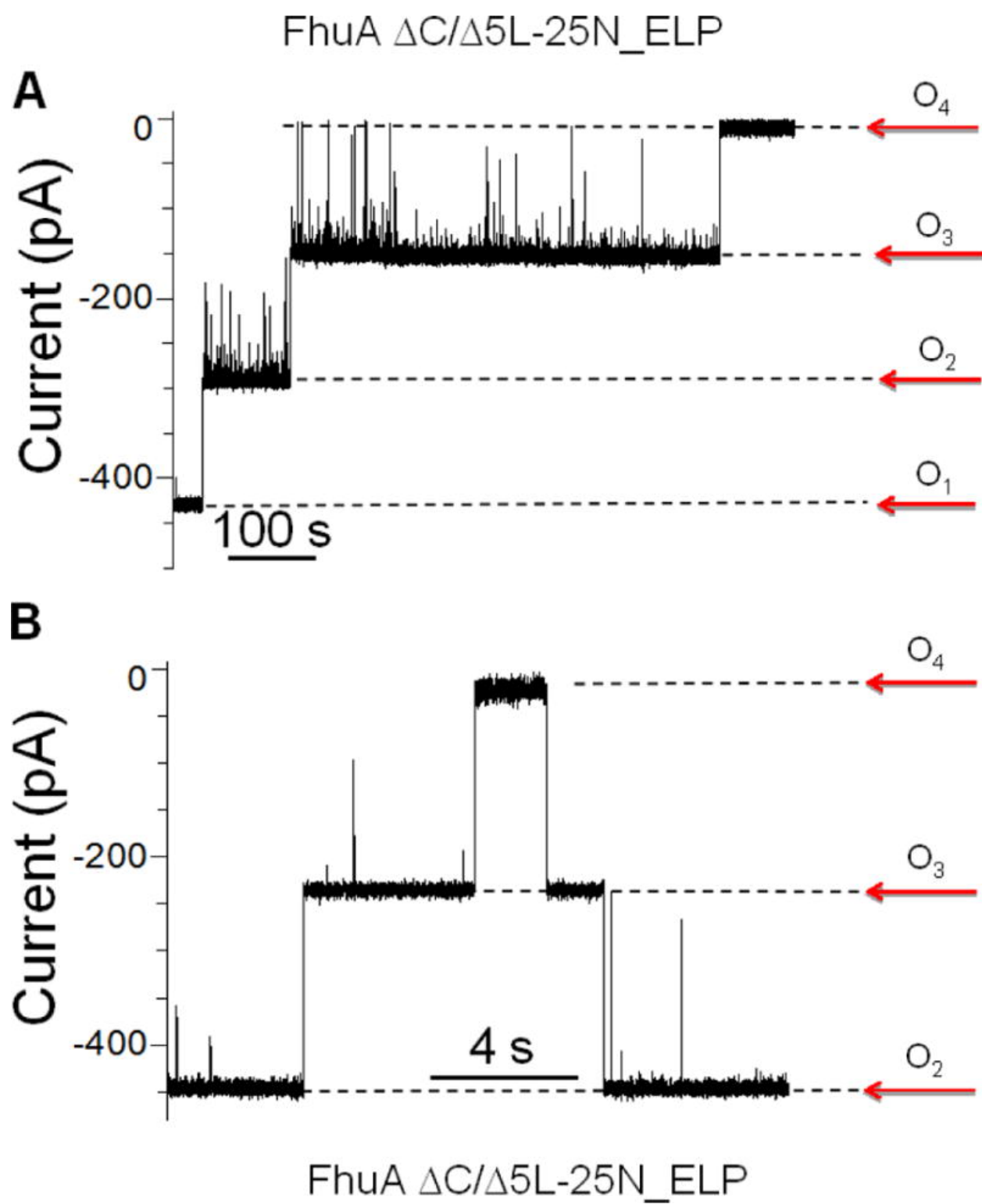


**Figure 6. Representative 33% current blockades observed with FhuA  $\Delta C/\Delta 5L$ -25N\_ELP.**

(A) The transmembrane potential was  $-100$  mV; (B) A short section of a typical single-channel electrical trace showing that the 33% current transitions observed with FhuA  $\Delta C/\Delta 5L$ -N25\_ELP were reversible. The transmembrane potential was  $-155$  mV. These electrical traces are representative over a number of seven independent experiments. All single-channel electrical recordings were achieved in 1M KCl, 10 mM potassium phosphate, pH 7.4. The other experimental conditions were similar to those reported in Fig. 2.

### 3.7. Conserved single-channel signatures of the globally engineered FhuA protein pores.

In this work, all globally mutated FhuA protein pores showed 33% current transitions, except FhuA  $\Delta C/\Delta 7L-30N$  at negative transmembrane potentials. Another conserved property of these proteins is their close similarity in unitary conductance. In Fig. 7A, the current-voltage plot illustrates an almost linear profile with little deviations in single-channel current. Interestingly, although the probability of occurrence of discrete current transitions among the four long-lived sub-states depended on various factors, including the applied transmembrane potential, the concentration of the external polypeptide collider or the presence of an internally fluctuating polypeptide, their conductance amplitude,  $\sim 1.3$  nS, was independent of the applied transmembrane potential (Fig. 7B). This finding suggests that these particular transitions observed with all explored globally engineered FhuA protein pores are produced by the same gating mechanism.

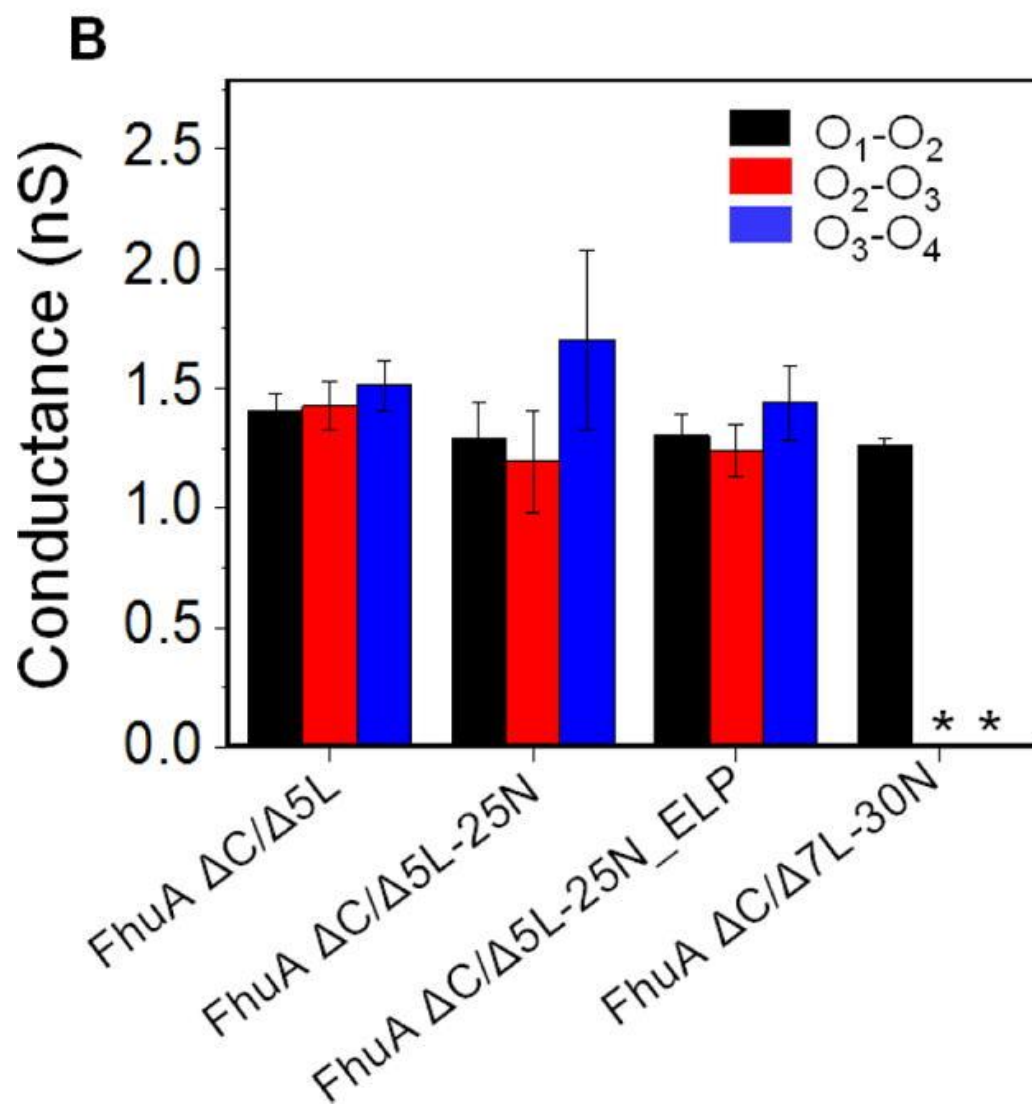
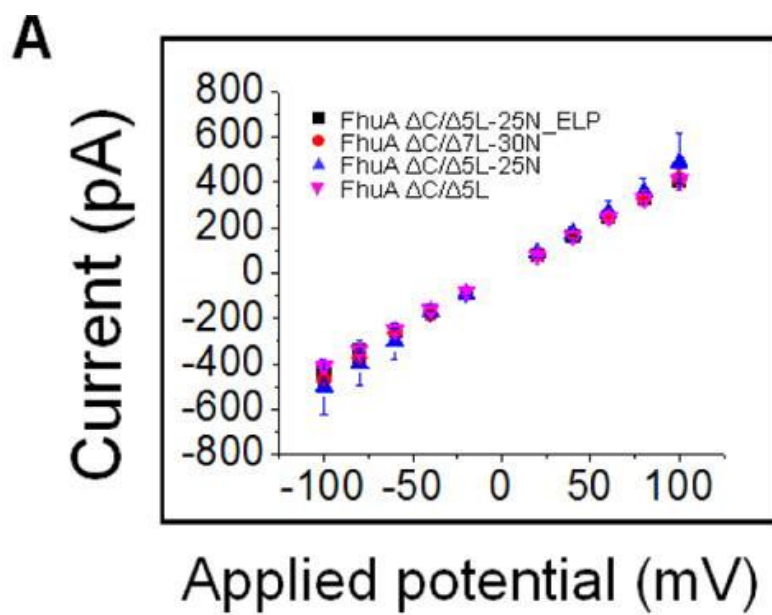


**Figure 7. Conserved single-channel features of the truncation FhuA mutants.**

(A) The current-voltage relationship represented as average  $\pm$  SD over at least three independent experimental determinations; (B) Voltage-induced current blockades with a normalized current amplitude of 33% are ubiquitous among all globally mutated FhuA proteins. Data represent normalized amplitude of the conductance of the current blockades from one discrete open sub-state to the other with respect to open sub-state (O1) unitary conductance. All current blockades were  $\sim 1.3$  nS in conductance or  $\sim 33\%$  of the open sub-state (O1) unitary conductance. “\*” stand for unavailable data, because we were not able to note such transitions in FhuA  $\Delta C/7L-30N$  alone. All single-channel electrical recordings were achieved in 1M KCl, 10 mM potassium phosphate, pH 7.4. The other experimental conditions were similar to those reported in Fig. 2.



## DISCUSSION

In this work, we extensively investigated truncation FhuA mutants lacking the cork domain and significant parts of several large extracellular loops. The large negative charge neutralization demonstrated the ability to modulate ion selectivity of a 22-stranded  $\beta$ -barrel protein in a predictive manner, from a strongly cation-selective to a weakly anion-selective pore. More importantly, this ion selectivity change was accomplished without a significant perturbation of primary biophysical traits, such as the unitary conductance of the protein pore, the quietness of its single-channel electrical signature under a broad range of experimental conditions, as well as the occurrence of the symmetrical 33% current blockades at very high transmembrane potentials.

The amplitudes of these 33% current blockades were not voltage dependent. Their occurrence was symmetric with respect to the polarity of the applied voltage, except those noted with FhuA  $\Delta C/\Delta 7L-30N$ . Ample changes in extracellular loops encompassing additional five positive charges perturbed the energetic landscape of the protein pore at negative potentials. The O1  $\rightarrow$  O2 transitions were still detectable with FhuA  $\Delta C/\Delta 7L-30N$  at lower positive potentials than those observed with FhuA  $\Delta C/\Delta 5L-25N$ , indicating that this gating mechanism is independent of the absence of large extracellular loops L3, L4, L5, L7, L8, L10, and L11. These current transitions were independent of the protein alterations at the N and C termini, as demonstrated with a TL-FhuA truncation mutant, as well as extensive charge modifications within the pore interior and major deletions of the extracellular loops. We speculate that these current transitions resulted from potential breathing deformations of the overall architecture of the  $\beta$ -barrel embedded into the bilayer, such as stretching and compression. The phenomenon of breathing fluctuations [45, 46] underlying the gating process was recently proposed in the case of outer

membrane protein G (OmpG) of *Escherichia coli*, a monomeric, 14-stranded  $\beta$ -barrel [7] and voltage-dependent anion channel (VDAC) [46]. Interestingly, Geng and colleagues reported voltage-induced 33% gating blockades among long-lived sub-states occurring in the phi29 connector protein channel [47]. A lack of crystallographic data of these truncation FhuA mutants precluded the obtaining of the molecular origin of the 3-fold nature of these current transitions among the four long-lived sub-states. One possibility would be that the surface molecular charge distribution throughout the pore interior features an almost 3-fold symmetry, so these current transitions in a 3-fold fashion are governed by strong electrostatic forces that span across the inner surface of the  $\beta$  barrel. We extensively examined the residue charge distribution within the  $\beta$  turns,  $\beta$  barrel, and undeleted extracellular loops and found a heterogeneous charge density throughout these regions of the protein, but without a 3-fold symmetry (Supplementary Materials, Fig. S20). The fact that FhuA  $\Delta C/\Delta 5L_{-25N}$ , which is characterized by 25 neutralizations of negative charges within the pore interior, underwent 33% current blockades in a closely similar fashion with FhuA  $\Delta C/\Delta 5L$ , strongly indicates that the charge density and distribution of  $\beta$  barrel is not a key player in such current transitions. It is also true that flexibility of the barrel depends on other factors, such as the hydrophobic interactions with the phospholipids of the bilayer as well as the side chains of the hydrophilic residues facing the pore interior. Therefore, it is unclear what are the dominant forces driving the pore structure in a “sub-trimeric” conformation.

It is conceivable that the duration of these “metastable” sub-states is modulated by transient pushing-pulling forces on the barrel wall. For example, an external polypeptide collider partitioning within the pore interior perturbed the system by transiently pushing the pore walls.

In contrast, an engineered polypeptide loop within the  $\beta$  barrel acted as an elastic spring pulling the walls through its conformational fluctuations [48]. At very high transmembrane potentials of  $\sim 180$  mV, these pushing-pulling forces are amplified by the thickness, bending and stretching fluctuations of the lipid bilayer [49, 50].

To our knowledge, these extensive truncations and global modifications of FhuA are the largest ever of a 22-stranded  $\beta$ -barrel examined by single-channel electrical recordings. In contrast to large-truncation FhuA protein pores encompassing several loop deletions as well as cork removal, shorter deletion mutants of FhuA exhibited complex voltage-induced current gating even at low applied transmembrane potentials. For example, the truncation of the cork domain resulted in highly noisy FhuA  $\Delta C$  single-channels [5, 51], which included frequent openings to a  $\sim 2.5$ -nS conductance state. Interestingly, a truncation mutant of FhuA that featured the deletion of the cork domain, gating loop L4 and strand  $\beta 7$ , showed a uniform 3.2-nS conductance open state decorated by brief 33% current blockades [5]. Currently, it is not clear whether these brief current transitions are generated by the same gating mechanism driving the 33% current blockades in the case of large-truncation FhuA pores.

Surprisingly, the ELP loop-containing FhuA  $\Delta C/\Delta 5L-25N$  showed insignificant change in the unitary conductance, but a voltage-induced gating activity at transmembrane potentials at which 33% current blockades were never observed in either FhuA  $\Delta C/\Delta 5L$  or FhuA  $\Delta C/\Delta 5L-25N$ . These experiments also demonstrate the opportunity for engineering a functional polypeptide plug at a different location than that in FhuA  $\Delta C/\Delta 5L-25N$ \_ELP. Therefore, we postulate that there is no technical difficulty in permanently placing other stimuli-responsive polypeptide plugs

[52] in various locations, such as the N and C termini as well as within the extracellular side of the protein. That would create of new class of proteinaceous nanodevices for controlling the transport of various compounds through lipid membranes of capsules as a result of a change in an environmental, physical or chemical parameter, such as temperature, pH, local osmotic gradient, redox potential, or light.

The relatively large size of the barrel, encompassing 22 anti-parallel  $\beta$  strands, provides prospects for the creation of protein nanovalves with relatively bulky polypeptide occlusions featuring different architectures [53]. If these developments would be coupled with extensive alterations of the surface charge of the  $\beta$  barrel, whose feasibility is demonstrated in this work, then such a generic protein nanovalve with controllable occlusions might be used in a broad range of arenas in medical biotechnology and therapeutics. As a matter of fact, not only FhuA [27, 54, 55], but also other outer membrane proteins, such as the PapC usher, a dimeric 24-stranded  $\beta$ -barrel of *E. coli* [15, 20, 56, 57], has a gating cork domain that undergoes conformational transitions upon an external chemical stimulus. Thus, the functionality of globally engineered FhuA-based protein pores would rely on a closely related mechanism inspired by those existent in nature. Overall, with  $\beta$ -barrel adaptations and further development, such engineered polypeptide plugs can be explored as a controllable delivery mechanism.

The 33% current transitions were also observed by interactions of cationic polypeptides with the interior of the globally engineered FhuA proteins when added to the trans side of the chamber. The frequency of these transitions was certainly dependent not only on the nature of the polypeptide, such as its length and charge, but also its concentration. If we take into account the

dimensions of the elliptical  $\beta$  barrel of FhuA excluding the cork domain, but including the side chains of the residues, such as the axis lengths  $a=26 \text{ \AA}$  and  $b=39 \text{ \AA}$ , as well as a minimum height,  $h_{\min}=20 \text{ \AA}$ , and a maximum height,  $h_{\max}=40 \text{ \AA}$ , then the calculated volume would have a value between 16,000 and 32,000  $\text{\AA}^3$ . The molecular weight of the engineered ELP loop, including the flexible Gly-Ser linkers was 4.8 kDa. The effective concentration within the pore interior is  $[\text{ELP}] = 1/(\text{NA}V_{\text{barrel}})$  [58], where NA is Avogadro's number and  $V_{\text{barrel}}$  is the internal volume of the  $\beta$  barrel. Under these conditions, the effective ELP concentration within the  $\beta$  barrel would be between 5.3 and 10.6 mM. This ELP concentration level is  $\sim 267$  and  $\sim 533$  times greater than the free concentration of Syn B2 producing the  $\text{O}_2 \rightarrow \text{O}_3$  transition in FhuA  $\Delta\text{C}/\Delta 7\text{L}-30\text{N}$ , respectively. The fact that these current transitions also occurred within FhuA  $\Delta\text{C}/\Delta 5\text{L}-25\text{N}_{\text{ELP}}$  at lower applied potentials, indicated that the cationic nature of the interacting polypeptide was just a requirement for its electrophoretic capture into the pore interior. This finding is consistent with a charge-independent pushing-pulling mechanism on the pore walls, as postulated above.

Given the observed long-lived sub-states, O1, O2, O3, and O4, it is difficult to infer the quantitative nature of the activation free energies for the transitions from one sub-state to another. For events lasting tens of seconds or minutes, the acquisition time of such single-channel electrical recordings would have to be in the order of several days. One possibility to address this challenge is to conduct these experiments at elevated temperatures [17, 59]. In this way, the activation free energies will decrease, shortening the duration of the time constants that correspond to all sub-states. This approach will reveal the most frequent transitions as well as the enthalpic and entropic contributions to all transition-rate constants governing these globally

engineered FhuA protein pores [33]. Drastic architectural modifications in the form of extensive deletions of extracellular loops and major modulation of the surface charge resulted in insignificant alterations of the single-channel conductance of these globally engineered FhuA protein pores, suggesting tractability and modularity features of this  $\beta$ -barrel scaffold, and in turn the feasibility to utilize this large redesigned protein pore in a wide range of applications. These characteristics will allow in the future obtaining conclusive and informative data pertinent to the perturbations of this  $\beta$ -barrel protein system. An absence of a significant change in the unitary conductance following extensive deletions in the extracellular loops implies that the constriction of these mutants does not seem to be created by the large extracellular loops folding back into the pore interior.

In summary, we demonstrated the versatility of the native  $\beta$ -barrel scaffold of FhuA to global engineering, showing modularity to  $\beta$  turn,  $\beta$  barrel and extracellular loop engineering. New aspects of this work included the extensive truncation of a large, 22-stranded  $\beta$  barrel up to seven extracellular loops, drastic alteration in the surface negative charge neutralization, up to 30 new positive charges, and engineering of a neutral polypeptide loop within the pore interior. Heavily redesigned FhuA  $\Delta C/\Delta 7L-30N$  exhibited a great disparity of the single-channel electrical signature between positive and negative transmembrane potentials. In this case, brief current blockades noted at negative potentials do not seem to fit within the confines of the gating mechanism responsible for 33% current fluctuations between the fourth long-lived and discrete current sub-states. With further development of such a truncation FhuA-based mutant, one can design and create a polarity-induced molecular switch, in which the redesigned FhuA protein is fully conductive at a positive potential, but closed at a negative potential. This study represents a

platform for future extensive engineering of FhuA for targeted applications in therapeutics and molecular biomedical technology.

## References

- [1] K.G. Fleming, Energetics of membrane protein folding, *Annu.Rev.Biophys.*, 43 (2014) 233-255.
- [2] W.C. Wimley, The versatile beta-barrel membrane protein, *Curr.Opin.Struct.Biol.*, 13 (2003) 404-411.
- [3] H. Bayley, L. Jayasinghe, Functional engineered channels and pores (Review), *Mol.Membr.Biol.*, 21 (2004) 209-220.
- [4] H. Hong, G. Szabo, L.K. Tamm, Electrostatic couplings in OmpA ion-channel gating suggest a mechanism for pore opening, *Nat.Chem.Biol.*, 2 (2006) 627-635.
- [5] M.M. Mohammad, K.R. Howard, L. Movileanu, Redesign of a plugged beta-barrel membrane protein, *J.Biol.Chem.*, 286 (2011) 8000-8013.
- [6] M. Pavlenok, I.M. Derrington, J.H. Gundlach, M. Niederweis, MspA Nanopores from Subunit Dimers, *PLoS.One.*, 7 (2012) e38726.
- [7] W. Grosse, G. Psakis, B. Mertins, P. Reiss, D. Windisch, F. Brademann, J. Burck, A.S. Ulrich, U. Koert, L.O. Essen, Structure-based engineering of a minimal porin reveals loop-independent channel closure, *Biochemistry*, 53 (2014) 4826-4838.
- [8] D. Stoddart, M. Ayub, L. Hofler, P. Raychaudhuri, J.W. Klingelhoefer, G. Maglia, A. Heron, H. Bayley, Functional truncated membrane pores, *Proc.Natl.Acad.Sci.U.S.A.*, 111 (2014) 2425-2430.
- [9] M. Chen, S. Khalid, M.S. Sansom, H. Bayley, Outer membrane protein G: Engineering a quiet pore for biosensing, *Proc.Natl.Acad.Sci.U.S.A.*, 105 (2008) 6272-6277.
- [10] M.M. Mohammad, R. Iyer, K.R. Howard, M.P. McPike, P.N. Borer, L. Movileanu, Engineering a Rigid Protein Tunnel for Biomolecular Detection, *J.Am.Chem.Soc.*, 134 (2012) 9521-9531.
- [11] M. Fahie, C. Chisholm, M. Chen, Resolved single-molecule detection of individual species within a mixture of anti-biotin antibodies using an engineered monomeric nanopore, *ACS Nano.*, 9 (2015) 1089-1098.
- [12] M.A. Fahie, M. Chen, Electrostatic Interactions between OmpG Nanopore and Analyte Protein Surface Can Distinguish between Glycosylated Isoforms, *The journal of physical chemistry. B*, 119 (2015) 10198-10206.
- [13] B. Sackmann, E. Neher, *Single-Channel Recording*, Second Edition ed., Kluwer Academic/Plenum Publishers, New York, 1995.
- [14] L. Kullman, P.A. Gunnev, M. Winterhalter, S.M. Bezrukov, Functional subconformations in protein folding: evidence from single-channel experiments, *Phys.Rev.Lett.*, 96 (2006) 038101.



- [15] O.S. Mapingire, N.S. Henderson, G. Duret, D.G. Thanassi, A.H. Delcour, Modulating effects of the plug, helix, and N- and C-terminal domains on channel properties of the PapC usher, *J.Biol.Chem.*, 284 (2009) 36324-36333.
- [16] B.R. Cheneke, B. van den Berg, L. Movileanu, Analysis of gating transitions among the three major open states of the OmpK channel, *Biochemistry*, 50 (2011) 4987-4997.
- [17] B.R. Cheneke, M. Indic, B. van den Berg, L. Movileanu, An Outer Membrane Protein undergoes Enthalpy- and Entropy-driven Transitions, *Biochemistry*, 51 (2012) 5348-5358.
- [18] E. Eren, J. Vijayaraghavan, J. Liu, B.R. Cheneke, D.S. Touw, B.W. Lepore, M. Indic, L. Movileanu, B. van den Berg, Substrate specificity within a family of outer membrane carboxylate channels, *PLoS Biology*, 10 (2012) e1001242.
- [19] E. Eren, J. Parkin, A. Adelanwa, B.R. Cheneke, L. Movileanu, S. Khalid, B. van den Berg, Towards understanding the outer membrane uptake of small molecules by *Pseudomonas aeruginosa*, *J.Biol.Chem*, 288 (2013) 12042-12053.
- [20] E. Volkan, V. Kalas, J.S. Pinkner, K.W. Dodson, N.S. Henderson, T. Pham, G. Waksman, A.H. Delcour, D.G. Thanassi, S.J. Hultgren, Molecular basis of usher pore gating in *Escherichia coli* pilus biogenesis, *Proc.Natl.Acad.Sci.U.S.A*, 110 (2013) 20741-20746.
- [21] K.R. Pothula, U. Kleinekathofer, Theoretical analysis of ion conductance and gating transitions in the OmpK (OccK1) channel, *Analyst*, 140 (2015) 4855-4864.
- [22] O. Yildiz, K.R. Vinothkumar, P. Goswami, W. Kuhlbrandt, Structure of the monomeric outer-membrane porin OmpG in the open and closed conformation, *EMBO J.*, 25 (2006) 3702-3713.
- [23] G.V. Subbarao, B. van den Berg, Crystal structure of the monomeric porin OmpG, *J.Mol.Biol*, 360 (2006) 750-759.
- [24] T. Zhuang, L.K. Tamm, Control of the Conductance of Engineered Protein Nanopores through Concerted Loop Motions, *Angew.Chem.Int.Ed Engl.*, 53 (2014) 5897-5902.
- [25] K.P. Locher, B. Rees, R. Koebnik, A. Mitschler, L. Moulinier, J.P. Rosenbusch, D. Moras, Transmembrane signaling across the ligand-gated FhuA receptor: crystal structures of free and ferrichrome-bound states reveal allosteric changes, *Cell*, 95 (1998) 771-778.
- [26] A.D. Ferguson, E. Hofmann, J.W. Coulton, K. Diederichs, W. Welte, Siderophore-mediated iron transport: crystal structure of FhuA with bound lipopolysaccharide, *Science*, 282 (1998) 2215-2220.
- [27] P.D. Pawelek, N. Croteau, C. Ng-Thow-Hing, C.M. Khursigara, N. Moiseeva, M. Allaire, J.W. Coulton, Structure of TonB in complex with FhuA, *E. coli* outer membrane receptor, *Science*, 312 (2006) 1399-1402.

- [28] A.D. Ferguson, V. Braun, H.P. Fiedler, J.W. Coulton, K. Diederichs, W. Welte, Crystal structure of the antibiotic albomycin in complex with the outer membrane transporter FhuA, *Protein Sci.*, 9 (2000) 956-963.
- [29] V. Braun, FhuA (TonA), the career of a protein, *J.Bacteriol.*, 191 (2009) 3431-3436.
- [30] A.D. Ferguson, J. Koding, G. Walker, C. Bos, J.W. Coulton, K. Diederichs, V. Braun, W. Welte, Active transport of an antibiotic rifamycin derivative by the outer-membrane protein FhuA, *Structure.*, 9 (2001) 707-716.
- [31] A. Arora, D. Rinehart, G. Szabo, L.K. Tamm, Refolded outer membrane protein A of *Escherichia coli* forms ion channels with two conductance states in planar lipid bilayers, *J.Biol.Chem.*, 275 (2000) 1594-1600.
- [32] D.J. Niedzwiecki, R. Iyer, P.N. Borer, L. Movileanu, Sampling a Biomarker of the Human Immunodeficiency Virus across a Synthetic Nanopore, *ACS Nano.*, 7 (2013) 3341-3350.
- [33] B.R. Cheneke, B. van den Berg, L. Movileanu, Quasithermodynamic contributions to the fluctuations of a protein nanopore, *ACS Chem.Biol.*, 10 (2015) 784-794.
- [34] J. Liu, E. Eren, J. Vijayaraghavan, B.R. Cheneke, M. Indic, B. van den Berg, L. Movileanu, OccK Channels from *Pseudomonas aeruginosa* Exhibit Diverse Single-channel Electrical Signatures, but Conserved Anion Selectivity, *Biochemistry*, 51 (2012) 2319-2330.
- [35] J. Liu, A.J. Wolfe, E. Eren, J. Vijayaraghavan, M. Indic, B. van den Berg, L. Movileanu, Cation Selectivity is a Conserved Feature in the OccD Subfamily of *Pseudomonas aeruginosa*, *Biochim.Biophys.Acta.-Biomembr.*, 1818 (2012) 2908-2916.
- [36] M.M. Mohammad, S. Prakash, A. Matouschek, L. Movileanu, Controlling a single protein in a nanopore through electrostatic traps, *J.Am.Chem.Soc.*, 130 (2008) 4081-4088.
- [37] A.J. Wolfe, M.M. Mohammad, S. Cheley, H. Bayley, L. Movileanu, Catalyzing the translocation of polypeptides through attractive interactions, *J.Am.Chem.Soc.*, 129 (2007) 14034-14041.
- [38] R. Bikwemu, A.J. Wolfe, X. Xing, L. Movileanu, Facilitated translocation of polypeptides through a single nanopore, *J.Phys.:Condens.Matter*, 22 (2010) 454117.
- [39] R.N. De Guzman, Z.R. Wu, C.C. Stalling, L. Pappalardo, P.N. Borer, M.F. Summers, Structure of the HIV-1 nucleocapsid protein bound to the SL3 psi-RNA recognition element, *Science*, 279 (1998) 384-388.
- [40] A.C. Paoletti, M.F. Shubsda, B.S. Hudson, P.N. Borer, Affinities of the nucleocapsid protein for variants of SL3 RNA in HIV-1, *Biochemistry*, 41 (2002) 15423-15428.
- [41] M.F. Shubsda, A.C. Paoletti, B.S. Hudson, P.N. Borer, Affinities of packaging domain loops in HIV-1 RNA for the nucleocapsid protein, *Biochemistry*, 41 (2002) 5276-5282.

- [42] S. Huang, K.S. Ratliff, A. Matouschek, Protein unfolding by the mitochondrial membrane potential, *Nat.Struct.Biol.*, 9 (2002) 301-307.
- [43] B. Li, D.O.V. Alonso, B.J. Bennion, V. Daggett, Hydrophobic hydration is an important source of elasticity in elastin-based biopolymers, *J.Am.Chem.Soc.*, 123 (2001) 11991-11998.
- [44] B. Li, D.O.V. Alonso, V. Daggett, The molecular basis for the inverse temperature transition of elastin, *J.Mol.Biol.*, 305 (2001) 581-592.
- [45] S. Villinger, R. Briones, K. Giller, U. Zachariae, A. Lange, B.L. de Groot, C. Griesinger, S. Becker, M. Zweckstetter, Functional dynamics in the voltage-dependent anion channel, *Proc.Natl.Acad.Sci.U.S.A.*, 107 (2010) 22546-22551.
- [46] U. Zachariae, R. Schneider, R. Briones, Z. Gattin, J.P. Demers, K. Giller, E. Maier, M. Zweckstetter, C. Griesinger, S. Becker, R. Benz, B.L. de Groot, A. Lange, beta-Barrel mobility underlies closure of the voltage-dependent anion channel, *Structure.*, 20 (2012) 1540-1549.
- [47] J. Geng, H. Fang, F. Haque, L. Zhang, P. Guo, Three reversible and controllable discrete steps of channel gating of a viral DNA packaging motor, *Biomaterials*, 32 (2011) 8234-8242.
- [48] O.V. Krasilnikov, C.G. Rodrigues, S.M. Bezrukov, Single polymer molecules in a protein nanopore in the limit of a strong polymer-pore attraction, *Phys.Rev.Lett.*, 97 (2006) 018301.
- [49] L. Movileanu, D. Popescu, S. Ion, A.I. Popescu, Transbilayer pores induced by thickness fluctuations, *Bull Math Biol*, 68 (2006) 1231-1255.
- [50] A.C. Woodka, P.D. Butler, L. Porcar, B. Farago, M. Nagao, Lipid bilayers and membrane dynamics: insight into thickness fluctuations, *Phys.Rev.Lett.*, 109 (2012) 058102.
- [51] M. Braun, H. Killmann, E. Maier, R. Benz, V. Braun, Diffusion through channel derivatives of the *Escherichia coli* FhuA transport protein, *Eur.J.Biochem.*, 269 (2002) 4948-4959.
- [52] Y. Jung, H. Bayley, L. Movileanu, Temperature-responsive protein pores, *J.Am.Chem.Soc.*, 128 (2006) 15332-15340.
- [53] L.M. Yang, P. Blount, Manipulating the permeation of charged compounds through the MscL nanovalve, *Faseb J.*, 25 (2011) 428-434.
- [54] E. Udho, K.S. Jakes, S.K. Buchanan, K.J. James, X. Jiang, P.E. Klebba, A. Finkelstein, Reconstitution of bacterial outer membrane TonB-dependent transporters in planar lipid bilayer membranes, *Proc.Natl.Acad.Sci.U.S.A.*, 106 (2009) 21990-21995.
- [55] J. Thoma, P. Bosshart, M. Pfreundschuh, D.J. Muller, Out but not in: the large transmembrane beta-barrel protein FhuA unfolds but cannot refold via beta-hairpins, *Structure.*, 20 (2012) 2185-2190.

- [56] Y. Huang, B.S. Smith, L.X. Chen, R.H. Baxter, J. Deisenhofer, Insights into pilus assembly and secretion from the structure and functional characterization of usher PapC, *Proc.Natl.Acad.Sci.U.S.A.*, 106 (2009) 7403-7407.
- [57] E. Volkan, B.A. Ford, J.S. Pinkner, K.W. Dodson, N.S. Henderson, D.G. Thanassi, G. Waksman, S.J. Hultgren, Domain activities of PapC usher reveal the mechanism of action of an *Escherichia coli* molecular machine, *Proc.Natl.Acad.Sci.U.S.A.*, 109 (2012) 9563-9568.
- [58] L. Movileanu, S. Cheley, H. Bayley, Partitioning of individual flexible polymers into a nanoscopic protein pore, *Biophys.J.*, 85 (2003) 897-910.
- [59] C. Chimere, L. Movileanu, S. Pezeshki, M. Winterhalter, U. Kleinekathofer, Transport at the nanoscale: Temperature dependence of ion conductance, *Eur.Biophys.J.*, 38 (2008) 121-125.
- [60] N. Guex, M.C. Peitsch, T. Schwede, Automated comparative protein structure modeling with SWISS-MODEL and Swiss-PdbViewer: a historical perspective, *Electrophoresis*, 30 Suppl 1 (2009) S162-S173.
- [61] F. Kiefer, K. Arnold, M. Kunzli, L. Bordoli, T. Schwede, The SWISS-MODEL Repository and associated resources, *Nucleic Acids Res.*, 37 (2009) D387-D392.
- [62] M.M. Mohammad, L. Movileanu, Impact of distant charge reversals within a robust beta-barrel protein pore, *J.Phys.Chem.B*, 114 (2010) 8750-8759.
- [63] E.F. Pettersen, T.D. Goddard, C.C. Huang, G.S. Couch, D.M. Greenblatt, E.C. Meng, T.E. Ferrin, UCSF Chimera--a visualization system for exploratory research and analysis, *J.Comput.Chem.*, 25 (2004) 1605-1612.

## Chapter 2.1 Supplement for Global Redesign of a Native $\beta$ -barrel Scaffold Continued

Aaron J. Wolfe,<sup>1,2</sup> Mohammad M. Mohammad,<sup>1</sup> Avinash K. Thakur,<sup>1,2</sup> and Liviu Movileanu<sup>1,2,3</sup>

<sup>1</sup>Department of Physics, Syracuse University, 201 Physics Building, Syracuse, New York 13244-1130, USA

<sup>2</sup>Structural Biology, Biochemistry, and Biophysics Program, Syracuse University, 111 College Place, Syracuse, New York 13244-4100, USA

<sup>3</sup>The Syracuse Biomaterials Institute, Syracuse University, 121 Link Hall, Syracuse, New York 13244, USA

This section was originally published as: **Aaron J. Wolfe**, M.M. Mohammad, A.K. Thakur, and L. Movileanu. Global Redesign of a Native Beta-barrel Scaffold, 2016, *Biochim. Biophys. Acta Biomembranes* 1858(1), 19-29. <https://doi.org/10.1016/j.bbamem.2015.10.006> © 2015 Elsevier B.V.

Author contributions:

AJW: Designed experiments, performed experiments, analyzed data, co-wrote manuscript.

MMM: Performed experiments

AKT: Performed experiments

LM: Analyzed data co-wrote manuscript

## SUPPLEMENTAL EXPERIMENTAL METHODS

### 1. Cloning of multi-site mutants.

The *fhua*  $\Delta c/\Delta 5l$  gene, lacking loops 3, 4, 5, 10, and 11, was constructed by GENEART (Regensburg, Germany) in the pMK-RQ plasmid flanked by EcoRI and XhoI restriction sites, but was previously mislabeled as *fhua*  $\Delta c/\Delta 4l$  [1, 2]. The *fhua*  $\Delta c/\Delta 5l$ -25n and *fhua*  $\Delta c/\Delta 7l$ -30n genes were synthesized by Integrated DNA Technologies (IDT, Coralville, IA) in pIDTSmart Amp vector. All genes contain a 3' thrombin site and 6×His<sup>+</sup> tag. The gene containing vector was transformed into Dh5 $\alpha$  chemically-competent cells from Invitrogen (Grand Island, NY). The transformed cells were grown in 5 ml of LB + amp and plasmid was extracted by Miniprep kit (Qiagen, Germantown, MD). The resulting DNA construct was subject to PCR using phosphorylated primers: 5'-ATC TCA GGT CTC TGC GCT TTA TTA GT-3' and 5'-CAA GGT GGT CTC CAA TGC TGA AAG AA-3' to add BsaI restriction sites and remove the 5' signal peptide which directs the protein to the outer membrane. The PCR product was gel-purified using the MinElute gel purification kit (Qiagen). Restriction digest with BsaI (New England Biolabs, Ipswich, MA) of the purified PCR product and the expression vector pPR-IBA1 were performed for one hour at 37°C. Expression vector restriction digest product was gel-purified using the MinElute gel purification kit (Qiagen), while the restriction digest product of the gene was purified using the QiaQuick PCR purification kit (Qiagen). The resulting purified restriction products were ligated together in a 1:1 ration using T4 DNA ligase at 16°C overnight. Ligation products were then transformed into DH5 $\alpha$  and selected for on AMP plates grown in LB + AMP Miniprep, as described above and verified by DNA sequencing. The *fhua*  $\Delta c/\Delta 5l$ -25n-elp gene was constructed by taking the *fhua*  $\Delta c/\Delta 5l$ -25n gene in the pPR-IBA1 expression vector and adding SpeI and NheI restriction sites via inverse PCR [3] using phosphorylated primers 5'-ACC GTT CGT CAG AAT CTGACT AGT GCT GCC-3' and 5'-GGT GGC GCT AGC TTT GCC GAA AAT AAA ACC-3'. This resulted in the removal of arginine at position 116. The PCR product was gel purified, ligated, transformed, isolated, and then sent to the DNA sequencing test, as described above. The ELP

insert was synthesized by IDT in pIDTSmart Amp vector. The insert was flanked by SpeI and NheI restriction sites. The ELP-encoding insert was the following: ACT AGT GGT GGT GGG TCT GGT GTA CCC GGG GGA GGG GTT CCT GGT GGC GGA GTC CCC GGA GGG GGC GTA CCC GGT GGA GGC GTA CCA GGT GGC GGA GTT CCT GGT GGC GGA GTC CCC GGA GGG GGC GTA CCA GGT GGC GGA GTG CCG GGT GGT GGA GTA CCC GGT GGA GGG GTC GGA GGT TCA TCT GGG GCT AGC. This insert and the previously made *fhuA*  $\Delta c/\Delta 5l$ -25n gene were cut using SpeI and NheI restriction enzymes for one hour at 37°C (New England Biolabs, Ipswich, MA). The resulting DNA construct was gel purified as described above. The cut and purified insert, as well as *fhuA*  $\Delta c/\Delta 5l$ -25n gene were ligated and transformed into the DH5 $\alpha$  cells. Colonies were isolated and miniprepes were performed. The resulting genes were verified by standard DNA sequencing.

## 2. Determination of the ionic selectivity.

The ionic selectivity of FhuA  $\Delta C/\Delta 5L$  and FhuA  $\Delta C/\Delta 5L$ -25N was measured by the following steps [4, 5]. The proteins were reconstituted into a planar lipid bilayer in symmetrical solutions of 0.2 M KCl, 10 mM potassium phosphate, pH 7.4. Then, the trans chamber was adjusted to 1 M KCl in the same buffer, after which the single-channel current (I) was then recorded versus the transmembrane potential (V) to determine the reverse potential ( $V_r$ ). Here, the reversed potential is defined as the transmembrane potential that corresponds to a zero single-channel current recorded under the above asymmetrical conditions. Finally, the ion permeability ratio  $P_K/P_{Cl}$  was calculated from the reverse potential ( $V_r$ ) by employing the Goldman-Hodgkin-Katz equation [6]:

$$\frac{P_K}{P_{Cl}} = \frac{[a_{Cl}]_t - [a_{Cl}]_c \exp\left(\frac{V_r F}{RT}\right)}{[a_K]_t \exp\left(\frac{V_r F}{RT}\right) - [a_K]_c}$$

where  $a$ ,  $F$ ,  $R$  and  $T$  are the activity coefficient, the Faraday constant, the gas constant and the absolute temperature, respectively.



## SUPPLEMENTAL DATA

## 3. Sequence alignment of the globally mutated FhuA protein pores.

## CLUSTAL 2.1 multiple sequence alignment.

```

FhuA ΔC/Δ5L-25N      LKEVQFKAGTNSLFQTFGDFSDSLDDGGVYSYRLTGLARSANAQQKGSEQQRYAIAPAFT 60
FhuA ΔC/Δ7L-30N     LKEVQFKAGTNSLFQTFGDFSDSLNKGGVYSYRLTGLARSAGSQQKGSEFQRYAIAPAFT 60
FhuA ΔC/Δ5L         LKEVQFKAGTNSLFQTFGDFSDSLDDGGVYSYRLTGLARSANAQQKGSEEQRYAIAPAFT 60
FhuA ΔC              LKEVQFKAGTNSLFQTFGDFSDSLDDGGVYSYRLTGLARSANAQQKGSEEQRYAIAPAFT 60
*****:*****:..*****:***** *****

FhuA ΔC/Δ5L-25N     WRPNKTNFTFLSYFQNEPQTG-----NSGGS--TYSRNEK 94
FhuA ΔC/Δ7L-30N     WRPNKTNFTFLSYFQNEPQTG-----NSGGS--TYSRNEK 94
FhuA ΔC/Δ5L         WRPDDKTNFTFLSYFQNEPETG-----NSEGS--TYSRNEK 94
FhuA ΔC              WRPDDKTNFTFLSYFQNEPETGYGWLPEKGTVEPLPNGKRLPTDFNEGAKNNIYSRNEK 120
*****:*****:*****:*****:*****

L3 →

FhuA ΔC/Δ5L-25N     MVGYSFNHQFNDTFTVRQNLRFENKTSQNSVYGNSEGSR----- 134
FhuA ΔC/Δ7L-30N     MVGYSFNHQFNGTFTVRQNLRFENKTSQ-----GS----- 125
FhuA ΔC/Δ5L         MVGYSDHEFNDTFTVRQNLRFENKTSQNSVYGNSEGSR----- 134
FhuA ΔC              MVGYSDHEFNDTFTVRQNLRFENKTSQNSVYGYGVCSDFANAYSKQCAALAPADKGHY 180
*****:*:*:*****:*****

L4 →

FhuA ΔC/Δ5L-25N     ---KYVVNDQKLQNFSDVTQLQSKFATGGINHTLLTGVD FMRMRNDINAWFGYNS---- 186
FhuA ΔC/Δ7L-30N     -----DQKLQNFSDVTQLQSKFATGKINHTLLTGVD FMRMRND-----GYNS---- 167
FhuA ΔC/Δ5L         ---KYVVNDEKLQNFSDVTQLQSKFATGDIDHTLLTGVD FMRMRNDINAWFGYNS---- 186
FhuA ΔC              LARKYVVNDEKLQNFSDVTQLQSKFATGDIDHTLLTGVD FMRMRNDINAWFGYDSDVPLLI 240
*****:*****:*****:*****:*****

L4 → L5 →

FhuA ΔC/Δ5L-25N     -----GGSSGPYRIILNKQKQTGVYVQDQAQWDKVLVTLGGRYDWDQES 230
FhuA ΔC/Δ7L-30N     -----GGS-----ILNKQKQTGVYVQDQAQWNKVLVTLGGRYDWDQES 206
FhuA ΔC/Δ5L         -----EGSSGPYRIILNKQKQTGVYVQDQAQWDKVLVTLGGRYDWDQES 230
FhuA ΔC              NLYNPVNTDFDFNAKDPANSGPYRIILNKQKQTGVYVQDQAQWDKVLVTLGGRYDWDQES 300
*****:*****:*****:*****

L5 →

FhuA ΔC/Δ5L-25N     LNRVAGTTNKRDDKQFTWRGGVNYLFDNGVTPYFSYSESFQSSQVGKDGNI FAPSKGKQ 290
FhuA ΔC/Δ7L-30N     LNRVAGTTNKRDDKQFTWRGGVNYLFDNGVTPYFSYSESFQSGQ-----SKGKQ 255
FhuA ΔC/Δ5L         LNRVAGTTDKRDDKQFTWRGGVNYLFDNGVTPYFSYSESFEPSSQVGKDGNI FAPSKGKQ 290
FhuA ΔC              LNRVAGTTDKRDDKQFTWRGGVNYLFDNGVTPYFSYSESFEPSSQVGKDGNI FAPSKGKQ 360
*****:*****:*****:*****

L7 →

```

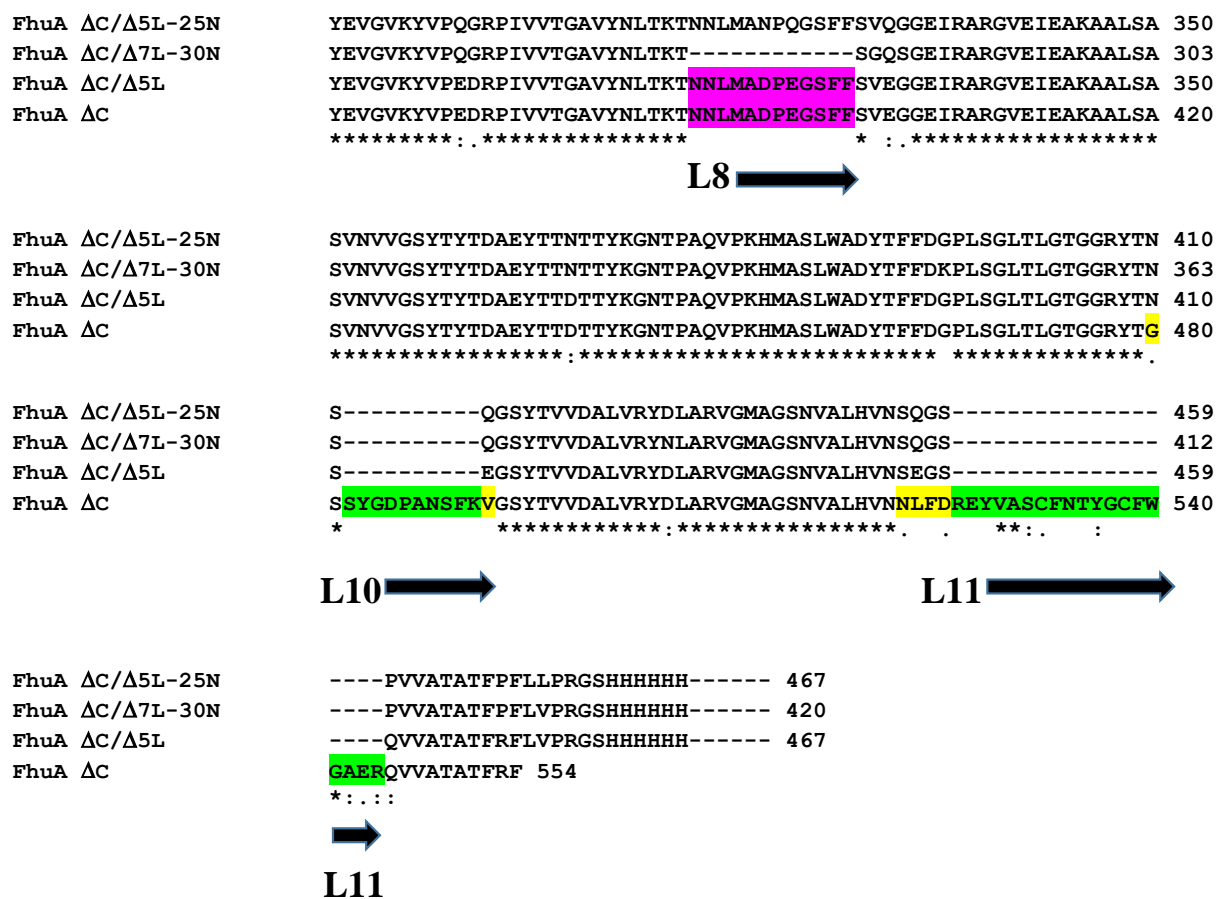


**Figure S1.** This amino acid alignment involves a cork-deletion mutant of the native FhuA (FhuA ΔC) as well as three globally-mutated polypeptides FhuAC/5L, FhuA ΔC/5L-25N, and FhuA ΔC/7L-30N.

The figure was generated using Clustal W 2.1. [7]. Conserved sites are marked with '\*', ':', or '.' at the bottom of the sequences. An asterisk (\*) shows locations which have a single, invariant residue. A colon (:) indicates conservation between groups of strongly similar properties (scoring > 0.5 in the Gonnet PAM 250 matrix). A period (.) points out conservation between groups of weakly similar properties (scoring ≤ 0.5 in the Gonnet PAM 250 matrix). The amino acid numbering does not include the first 160 residues in the sequence of the WT-FhuA protein, as they are part of the cork domain (ΔC) and removed in all FhuA derivatives explored in this work.

All amino acid identifications are done with respect to the presented alignment shown here. The methionine created from the start codon is intentionally left out of this alignment and the subsequent numbering schemes presented in the Tables S2, S5, S6, and S7. This is done for clarity as the methionine is either before the first leucine in the above sequences or it is in the N-terminal, 33-amino acid signal polypeptide. Its residue sequence is the following:

MARSKTAQPKHSLRKIAVVVATAVSGMSVYAQA

Residues marked in green indicate loop deletions in FhuA  $\Delta C/5L$  and FhuA  $\Delta C/5L-25N$ . FhuA  $\Delta C/\Delta 5L$  was constructed by deleting the cork domain ( $\Delta C$ ) as well as the large loops L3, L4, L5, L10 and L11. The amino acid sequence of the cork domain is the following:

AVEPKEDTITVTAAPAPQESAWGPAATIAARQSATGTKTDTPIQKVPQSSISVVTAEEMAL  
HQP KSVKE

ALS YTPGVSVGTRGASNTYDHLIIRGFAAEGQSQNNYLNGLKLQGNFYNDAVIDPYMLE  
RAEIMRGP VSVLYGKSSPGLLNMVSKRPTTEP These loops were replaced by the peptide linker sequence NSEGS. FhuA  $\Delta C/\Delta 6L-25N$  was made by neutralizing 25 negative charges of amino acids from FhuA  $\Delta C/\Delta 5L$  protein (EXPERIMENTAL PROCEDURES, Table S5, Fig. S6). Those residues marked in magenta show additional loop deletions in FhuA  $\Delta C/7L-30N$ . Loop deletions are also marked beneath all sequences by arrows in bold. Residues shown in yellow point out positions at which sequence alterations of FhuA  $\Delta C/5L$ , FhuA  $\Delta C/5L-25N$ , and FhuA  $\Delta C/7L-30N$ , were produced with respect to that of FhuA  $\Delta C$  (or WT-FhuA).

## WT-FhuA

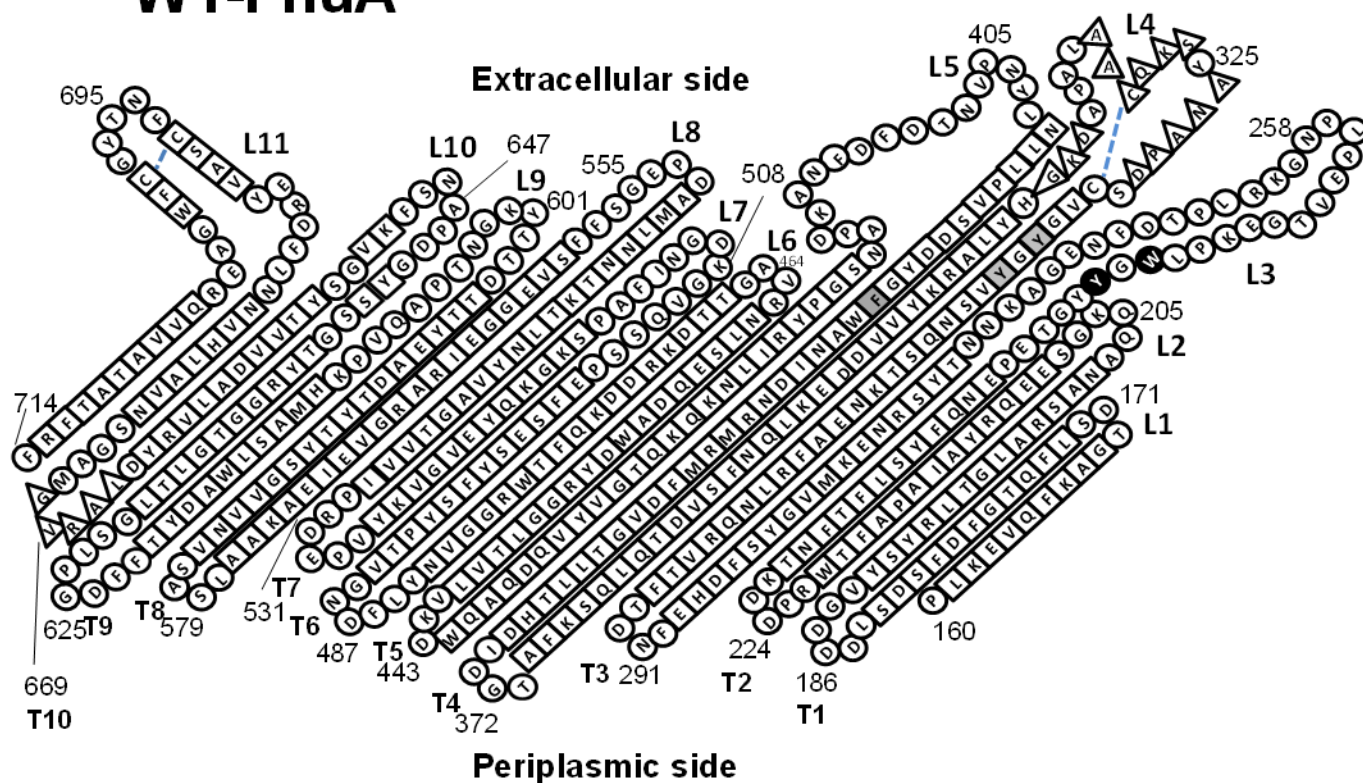


**Figure S2. Topology of the cork-free, wild-type FhuA protein (WT-FhuA  $\Delta$ C).**

Residues marked by squares are  $\beta$  stranded, whereas those marked by circles are not structured (e.g., present in loops and  $\beta$ -turns). Amino acids marked by triangles are part of the  $\alpha$ -helical structure [8, 9]. Extracellular loops (L) and  $\beta$  turns (T) are numbered from 1 to 11 and from 1 to 10, respectively. The first ( $\beta$  1) and last ( $\beta$  22)  $\beta$  sheets are shown in the figure.

**Table S1. Features of the extracellular loops of the WT-FhuA protein.**

Loop	Residues	Loop length <sup>1</sup> (Å)	Brief description
L1	T170-S172	7	Very short loop
L2	A203-S208	18	Relatively short loop
L3	Y243-N273	105	Large flexible and random coil loop that folds into the pore lumen.
L4	C318-H339	74	Large loop that contains three helices and a $\beta$ -strand. The loop features a stabilizing disulfide bridge C318-C329. It is likely that L4 along with part of the $\beta$ -strands block to the pore lumen.
L5	D394-N419	88	Large loop that contains a $\beta$ strand that likely occludes the lumen.
L6	R463-G466	11	Very short loop
L7	P502-P515	46	Flexible medium-sized loop that does block the pore lumen.
L8	D552-F559	25	Relatively short loop
L9	D598-K611	46	Medium-sized flexible loop. This is a rather rigid loop due to its positioning between two uneven $\beta$ strands.
L10	G640-S654	49	Medium-sized flexible loop that might block the pore lumen.
L11	N682-R704	77	Large loop that contains an anti-parallel $\beta$ -sheet, protruding into the pore lumen.

<sup>1</sup>The total length of the loop, which was determined under stretched out conformation.

**Table S2. Details of the truncation FhuA  $\Delta$ C/ $\Delta$ 5L mutant.**

Loop	Deletion	Deleted Residues	Point mutations	Purpose
$\Delta$ L3 (NSEGS)	$\Delta$ 243-266, $\Delta$ 272-273	YYGWLPKEGTVEPLPNGKRLPTDF, NN	E268S, G269E, A270G, K271S	NSEGS linker
$\Delta$ L4 (NSEGS)	$\Delta$ 321-343	PANAYSKQCAALAPADKGYHLAR	Y315N, G316S, V317E, C318G, D320R	NSEGS linker & reverse negative charge
$\Delta$ L5 (NSEGS)	$\Delta$ 396-416	SVPLLNLVNPVNTDFDFNAKD	D394N, D395S, P417E, A418G, N419S	NSEGS linker
$\Delta$ L10 (NSEGS)	$\Delta$ 642-651	SYGDPANSFK	G640N, V652E	NSEGS linker
$\Delta$ L11 (NSEGS)	$\Delta$ 685-703	REYVASCFNLYGCFWGAER	N681S, L682E, F683G, D684S	NSEGS linker

The truncation FhuA  $\Delta C/\Delta 5L$  mutant features both deleted residues and point mutations of the cork-free FhuA  $\Delta C$ . The resulting mutant has truncated loops L3, L4, L5, L10 and L11 as well as the addition of NSEGS-containing flexible loops. Here, we number all residues with respect to the WT-FhuA starting at position 161, which is due to the deletion of the 160-residue cork domain ( $\Delta C$ ). It should also be noted that the 33-residue signal polypeptide (see above) will be omitted in the numbering of amino acids with respect to WT-FhuA within this table (and Table S5). It should be clear to the reader that the first amino acid for the sequences not containing the N-terminal, 33-residue signal polypeptide is a methionine. This methionine is also omitted from numbering with respect to FhuA  $\square C$ , as its start codon is within the signal polypeptide. FhuA  $\Delta C/\Delta 5L-25N$  has the same loop deletions as FhuA  $\Delta C/\Delta 5L$ , except the linkers were point mutated in  $\Delta L3$ ,  $\Delta L5$ ,  $\Delta L10$ ,  $\Delta L11$  to NSGGS, NSGGS, NSQGS, NSQGS respectively.

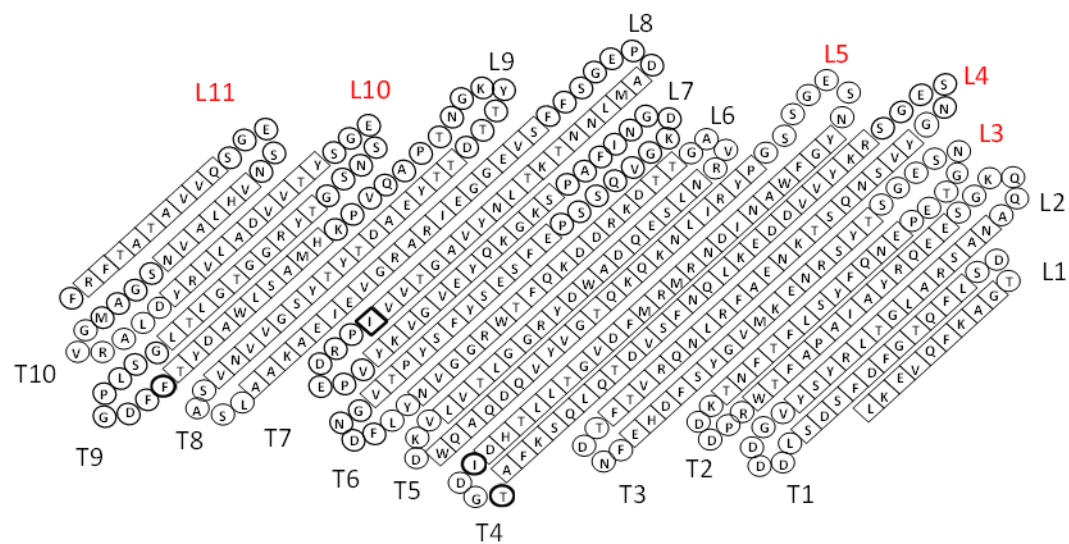


**Figure S3. Topology map of FhuA  $\Delta C/\Delta 5L$  showing in red the loops that have been altered from the WT-FhuA structure [8, 9].**

Squares represent amino acids assumed to be in  $\beta$  strands, while circles represent residues in the loops and  $\beta$  turns.

**Table S3. Comparison of the unitary conductance and oligomeric state of FhuA  $\Delta C/\Delta 5L$  pore with those of other protein nanopores.**

Protein pore	Constriction (nm) <sup>c</sup>	Conductance (nS) <sup>d</sup>	Oligomeric state <sup>f</sup>	Reference
$\alpha$ HL	1.4	1	7	[10, 11]
Phi29 connector	3.6	4.8	12	[12, 13]
M1MspA	1	~2 <sup>e</sup>	8	[14, 15]
ClyA <sup>a</sup>	3.8	1.8	12	[16, 17]
OmpG	1.4	1.2	1	[18-20]
FhuA $\Delta C/\Delta 5L$ <sup>b</sup>	2.6 X 3.9	3.9	1	This work

<sup>a</sup>This protein is from *S. typhi* bacterium and its dimensions were obtained using *E. coli* ClyA crystal structure [17].

<sup>b</sup>The dimensions of this protein were obtained using WT FhuA crystal structure as a template.

<sup>c</sup>The internal dimensions were determined including the side chains of the residues which form the constrictions in the respective crystal structures, or from modeled structures in case of ClyA and FhuA  $\Delta C/\Delta 5L$ .

<sup>d</sup>Conductances for other pores and all inner dimensions were obtained from respected references. All pores were engineered to give the reported conductance values with buffers containing 1 M KCl, except for ClyA, 150 mM NaCl.

<sup>e</sup>The unitary conductance value of M1MspA is 2-3 fold less than that of the WT MspA value (4.9 ns) [15].

<sup>f</sup>Represents how many subunits make up the pore.



**Table S4. Comparison of the unitary conductance of globally engineered FhuA-based protein pores under various experimental conditions.**

Unless otherwise indicated, the unitary conductance was obtained from single channel electrical recordings formed by n-dodecyl- $\beta$ -D-maltopyranoside (DDM)-refolded nanopores.

Protein	Conditions			Conductance (nS) <sup>a, b</sup>	Buffer conductivity (mS/cm)	Independent experiments
	Buffer	Salt concentration	pH			
FhuA $\Delta$ C/ $\Delta$ 5L	Phosphate	.02 M KCl	7.4	0.40 $\pm$ 0.07 (n=40)	4.5	4
		0.2 M KCl	7.4	1.2 $\pm$ 0.2 (n=15)	24.5	4
		1 M KCl	7.4	3.9 $\pm$ 0.6 (n=127)	99.5	7
		3 M KCl	7.4	10.2 $\pm$ 0.7 (n=4)	242.3	2
		1 M KCl	7.4	3.8 $\pm$ 0.8 (n=33) <sup>c</sup>	99.5	8
		1 M KCl	7.4	3.9 $\pm$ 0.4 (n=44) <sup>d</sup>	99.5	6
	Phosphate-citrate	1 M NaCl	2.8	2.7 $\pm$ 0.7 (n=39)	73.7	5
		1 M NaCl	4.3	2.4 $\pm$ 0.6 (n=47)	75.4	4
		1 M NaCl	7.4	2.5 $\pm$ 0.8 (n=15)	75.3	4
		1 M NaCl	11.6	2.5 $\pm$ 0.3 (n=10)	77.6	3
FhuA $\Delta$ C/ $\Delta$ 5L-25N	Phosphate	1 M KCl	7.4	3.4 $\pm$ 0.2 (n=3)	99.5	3
		0.2 M KCl	7.4	1.0 $\pm$ 0.2 (n=3)	24.5	3
	Phosphate-acetate	1 M KCl	3.4	4.1 $\pm$ 0.1 (n=3)	130	3
		0.2 M KCl	3.4	1.1 $\pm$ 0.1 (n=3)	30.5	3

<sup>a</sup>The conductance was obtained from the ratio of the measured current jumps (induced by discrete steps or single-channel insertions) to the applied voltage of +40 mV in the indicated buffer conditions. All channels were included in the conductance calculations.

<sup>b</sup>“n” represents the total number of discrete single-channel insertions from the indicated number of independent experiments.

<sup>c</sup>FhuA  $\Delta$ C/ $\Delta$ 5L protein was refolded using the n-octyl- $\beta$ -D-glucopyranoside (OG) detergent.

<sup>d</sup>FhuA  $\Delta$ C/ $\Delta$ 5L protein was refolded using the 1-lauroyl-2-hydroxy-*sn*-glycero-3-phosphocholine (LPhC) detergent.

#### 4. FhuA $\Delta C/\Delta 5L$ channel is stable under an unusually broad range of ion concentration conditions.

In 1 M KCl, 10 mM potassium phosphate, pH 7.4, the refolded proteins were stable up to  $\pm 140$  mV. We were able to reliably obtain single-channel step-wise insertions of FhuA  $\Delta C/\Delta 5L$  protein in the extreme symmetric ionic conditions between 20 mM and 4 M KCl (**Fig. S4**). For example, the conductance of FhuA  $\Delta C/\Delta 5L$  in 0.02 M KCl, 0.2 M KCl, and 3 M KCl, was  $0.4 \pm 0.07$  (n=40),  $1.2 \pm 0.2$  (n=15) and  $10.2 \pm 0.7$  (n=4), respectively, showing an expectation of the increase in unitary conductance with increasing conductivity of the bathing solution at greater salt concentration (**Table S4**). In **Fig. S5A**, we show the stability of the FhuA  $\Delta C/\Delta 5L$  protein in a symmetric condition of 20 mM KCl, 10 mM potassium phosphate, pH 7.4. This channel is stable at  $\pm 120$  mV in symmetric and very low ionic salt condition (20 mM *cis/trans*), displaying infrequent current spikes ( $\sim 0.4$  s<sup>-1</sup>; **Fig. S5A**). It is also stable at  $\pm 140$  mV in asymmetric ionic conditions (20 mM in *cis*, 200 mM in *trans*) (**Fig. S5B**). Finally, FhuA  $\Delta C/\Delta 5L$  is stable at +140 mV in symmetric and physiological salt condition of 200 mM KCl, showing short-lived, infrequent and low-amplitude current spikes (**Fig. S5C**). **Fig. S5D** shows a voltage ramp with FhuA  $\Delta C/\Delta 5L$ , from -140 to +140, and with a speed of 1.4 mVs<sup>-1</sup>, under symmetric ion concentration conditions of either 20 mM or 200 mM KCl. This plot indicates that this pore exhibits a nonlinear current-voltage, so it is ion selective. We determined that the FhuA  $\Delta C/\Delta 5L$  protein pore is cation selective with an ionic permeability ratio  $P_K/P_{Cl}$  of  $\sim 5.5$ . Further investigations on FhuA  $\Delta C/\Delta 5L$  showed a uniform single-channel conductance of  $\sim 0.4$  nS in 20 mM KCl-containing buffer solution (**Fig. S5E**).

## 5. FhuA $\Delta C/\Delta 5L$ protein is stable under acidic and basic pHs.

The FhuA  $\Delta C/\Delta 5L$  protein readily inserts and forms channels into a lipid bilayer at pH 2.8, 4.3, 7.4 and 11.6 (Fig. S6A). Electrical traces that show stepwise insertions were recorded under a similar symmetric ion concentration of 1 M NaCl. We determined that the unitary conductance of FhuA  $\Delta C/\Delta 5L$  is  $2.7 \pm 0.7$  (n=39),  $2.4 \pm 0.6$  (n=47),  $2.5 \pm 0.8$  (n=15) and  $2.5 \pm 0.3$  (n=10) at pH 2.8, 4.3, 7.4 and 11.6, respectively (Table S4). The unitary conductance values obtained here are lower than those values obtained in 1 M KCl-containing buffers owing to the decrease in the solution conductivity of 1 M NaCl-containing buffers (Table S4). Fig. S6B shows a voltage ramp with FhuA  $\Delta C/\Delta 5L$ , from -140 to +140 mV, with a speed of 1.4 mVs<sup>-1</sup>, under 1 M KCl-containing buffer conditions, and at pH 2.8, pH 4.3 and pH 11.6. Remarkably, the channels formed at various pHs remained open for long periods (Fig. S6C-E). This protein channel is very stable up to +140 mV and -100 mV at pH 2.8 (Fig. S6C). FhuA  $\Delta C/\Delta 5L$  maintained its stable, open-current state up to  $\pm 140$  mV in pH 7.4 under the same buffering condition (Fig. S6D), except that it underwent reversible closures at -140 mV, which were preceded by frequent millisecond-lived current fluctuations ( $\sim 3$  s<sup>-1</sup>) (Fig. S6D, the right panel). FhuA  $\Delta C/\Delta 5L$  was also stable at pH 11.6 (Fig. S6E). Under this condition, the single-channel electrical trace was accompanied by current spikes. We also examined the spectral density of the noise in the single-channel electrical recordings with FhuA  $\Delta C/\Delta 5L$  at different pH values (Fig. S7). The single-channel current of the FhuA  $\Delta C/\Delta 5L$  nanopore exhibits the highest noise at extreme pH values of 2.8 and 11.6. However, at pH 2.8, the noise frequency is highest in the range of 30 Hz to 10 KHz. At an applied potential of +140 mV, the noise of the nanopore increased significantly at pH 7.4.

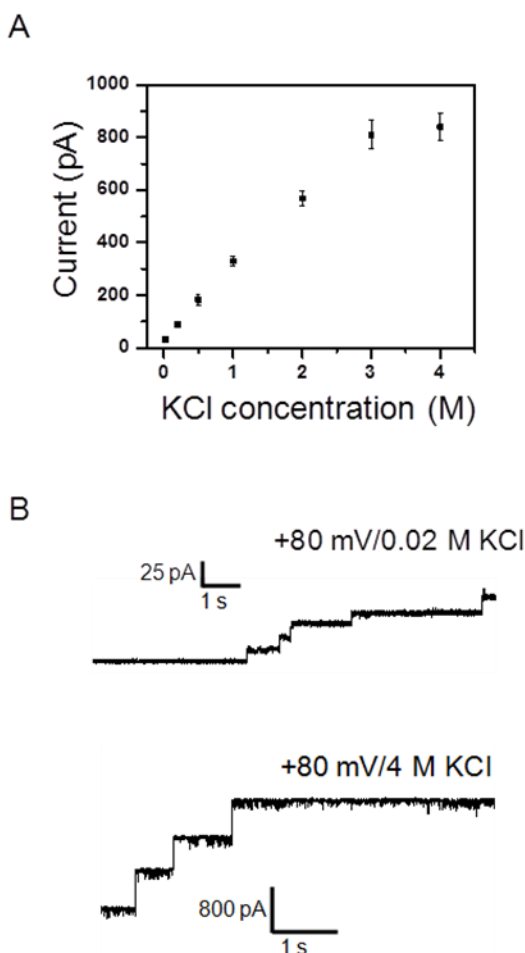


**Figure S4. (A) Single-channel current of FhuA  $\Delta$ C/ $\Delta$ 5L as a function of the KCl concentration.**

At each salt concentration, single-channel insertions from at least two different experiments were obtained (single channel  $\geq 6$  at different salt concentrations) at an applied potential of +80 mV and in 10 mM potassium phosphate, pH 7.4. The KCl concentration is indicated on the horizontal axis; (B) FhuA  $\Delta$ C/ $\Delta$ 5L pore inserts into lipid bilayer at low and high ionic salt conditions. This panel indicates stepwise single-channel insertions at low salt (20 mM KCl, upper panel) and high salt (4 M KCl, lower panel) concentrations. The KCl concentration is indicated on the top of each electrical trace.

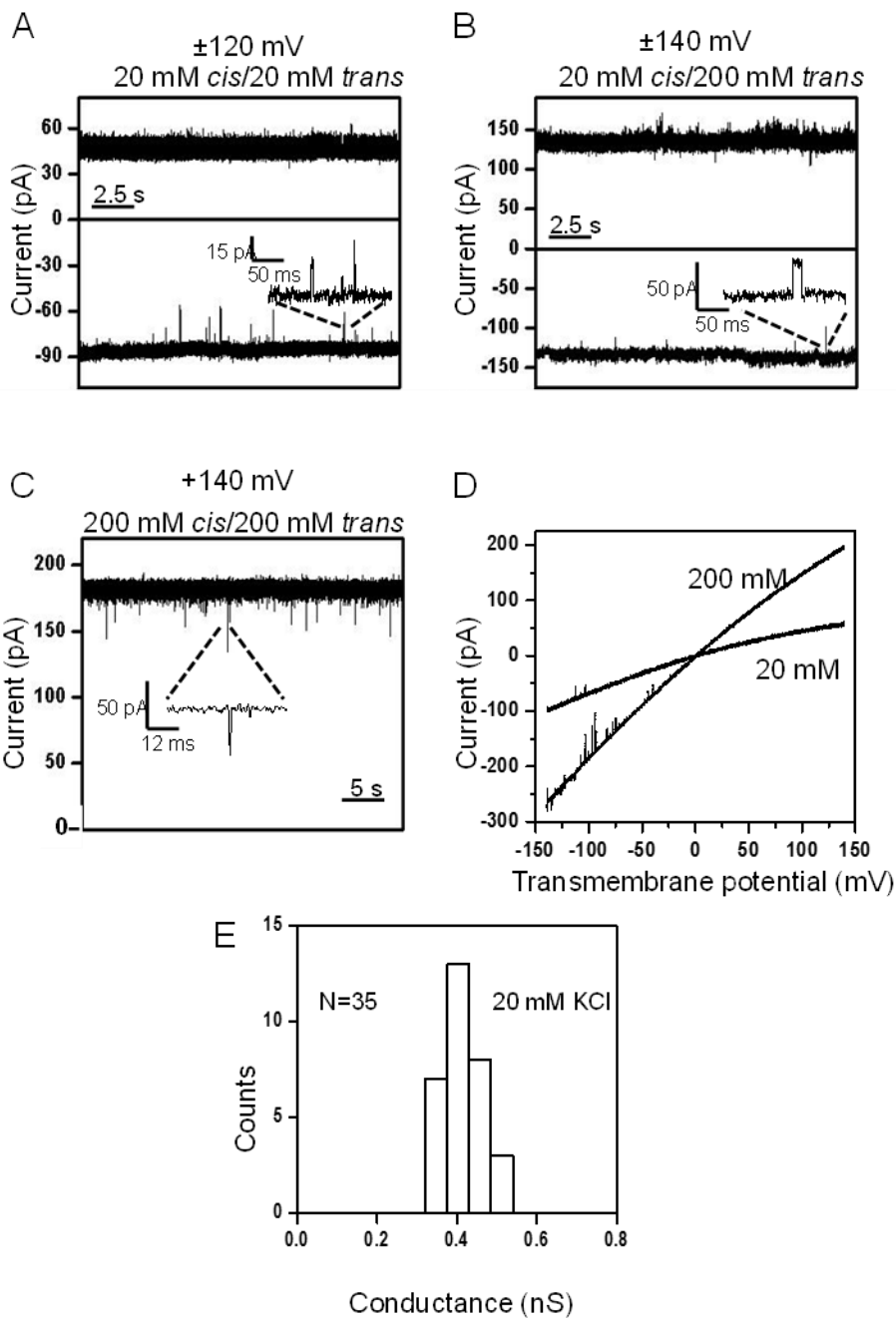


**Figure S5. Engineered FhuA  $\Delta C/\Delta 5L$  nanopores are stable under low-salt concentration conditions.**

Representative single-channel electrical recordings with FhuA  $\Delta C/\Delta 5L$  under symmetrical buffer solutions on both sides of the chamber, containing 20 mM KCl (A), under asymmetrical buffer

solutions, 20 mM KCl in cis side of the chamber and 200 mM KCl in trans side of the chamber (B), and under symmetrical buffer solutions on both sides of the chamber containing 200 mM KCl (C). The expanded traces in A, B and C illustrate the signature of the nanopore at a greater time resolution, In (D), current traces from single channels in symmetrical buffer solutions containing either 20 mM or 200 mM KCl, under a voltage ramp from -140 mV to +140 mV, are shown. The speed of the voltage ramping was 1.4 mV s<sup>-1</sup>. In (E), we present a histogram of the distribution of the single-channel conductance values of the FhuA  $\Delta C/\Delta 5L$  protein at an applied transmembrane potential of +40 mV and in 20 mM KCl. The buffer used in all experiments contained 10 mM potassium phosphate, pH 7.4. The single-channel electrical traces were low-pass Bessel filtered at 2 kHz.

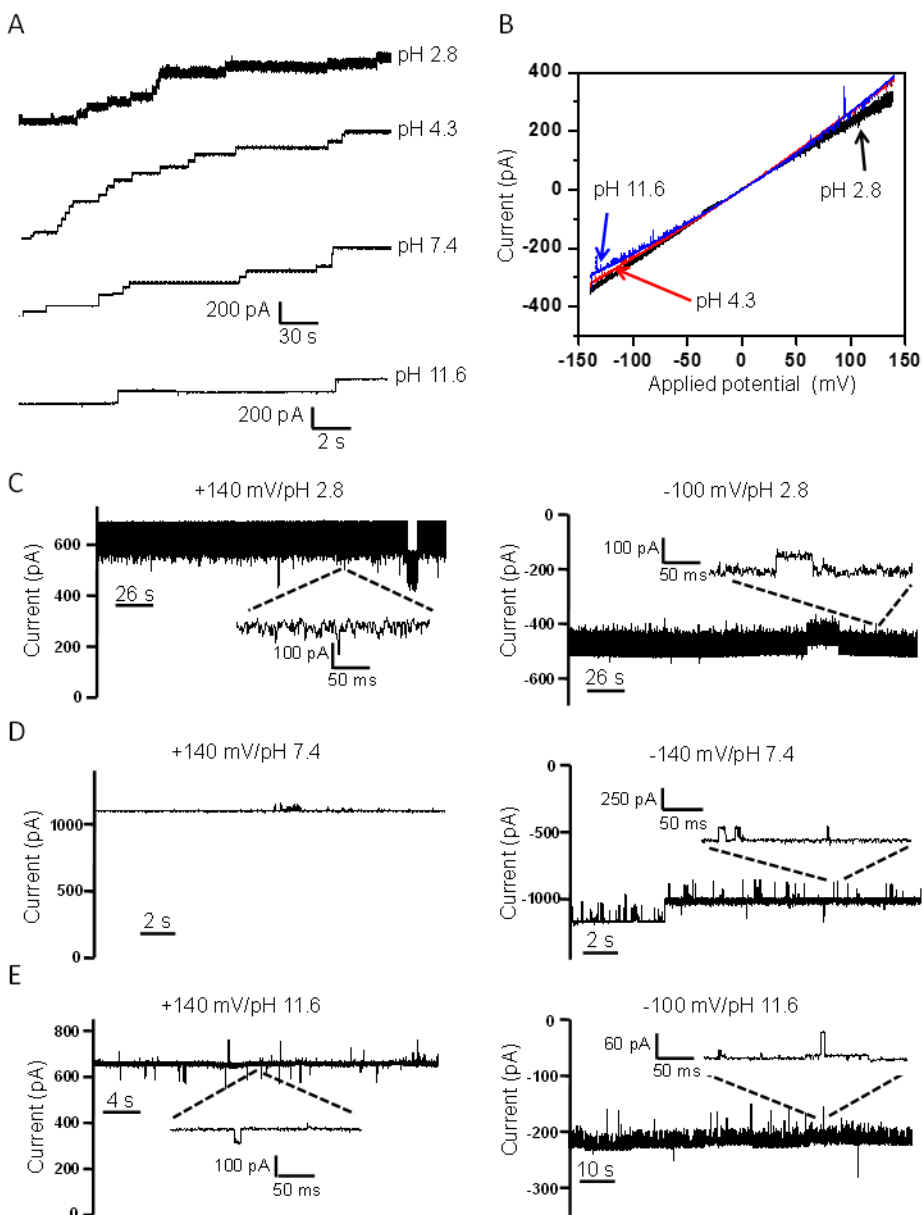


**Figure S6. Engineered FhuA  $\Delta C/\Delta 5L$  pores are stable under extreme pH and greater transmembrane potential conditions.**

(A) Stepwise insertions of single channels after the addition of the FhuA  $\Delta C/\Delta 5L$  protein and at an applied transmembrane potential of +40 mV. The buffer solution in the chamber contained 10 mM phosphate-citrate, 1 M NaCl buffer at indicated pH's, except for pH 11.6, at which

condition the buffer solution was 10 mM Na<sub>2</sub>HPO<sub>4</sub>·7H<sub>2</sub>O, 1 M NaCl. This type of stepwise insertions was reproduced in 5, 4, 4, and 3 different experiments for pH 2.8, pH 4.3, 7.4 and pH 11.6, respectively. For acquiring macroscopic current recordings with tens of channels inserted into a single lipid bilayer, 250 ng FhuA  $\Delta C/\Delta 5L$  was added to the cis chamber. The upper current/time scale is shown for stepwise channel insertions at pH values of 2.8, 4.3 and 7.4. The lower current/time scale is shown for stepwise channel insertions at a pH value of 11.6;

(B) Single-channel current traces recorded with FhuA  $\Delta C/\Delta 5L$  at pH 2.8 (black), 4.3 (red) and 11.6 (blue) under a voltage ramp from -140 mV to +140 mV. The speed of the voltage ramping was 1.4 mV s<sup>-1</sup>. The buffer conditions are the same as in A;

(C) Two-channel electrical recordings acquired with FhuA  $\Delta C/\Delta 5L$  at pH 2.8. The left and right panels indicate single-channel electrical traces at an applied transmembrane potential of +140 and -100 mV, respectively. The buffer solution in the chamber contained 1 M NaCl, 10 mM phosphate-citrate, pH 2.8; (D) Two-channel electrical recordings acquired with FhuA  $\Delta C/\Delta 5L$  pore at pH 7.4 and at an applied voltage of +140 (the left panel) and -140 mV (the right panel). The buffer solution in the chamber contained 1 M NaCl, 10 mM phosphate-citrate, pH 7.4;

(E) Electrical recordings acquired with FhuA  $\Delta C/\Delta 5L$  at pH 11.6 with an applied transmembrane potential of +140 (left panel) and -100 mV (right panel). The left and right traces in (E) represent currents through two channels and a single channel, respectively. The buffer solution in the chamber contained 1 M NaCl, 10 mM Na<sub>2</sub>HPO<sub>4</sub>·7H<sub>2</sub>O, pH 11.6. The expanded traces in C, D and E illustrate the signature of these traces at a greater time resolution. DDM-refolded FhuA  $\Delta C/\Delta 5L$  protein was used. The single-channel electrical traces were low-pass Bessel filtered at 2 kHz, except for B, the trace was filtered at 0.1 kHz to eliminate the noise from the amplifier during the application of the voltage ramp.



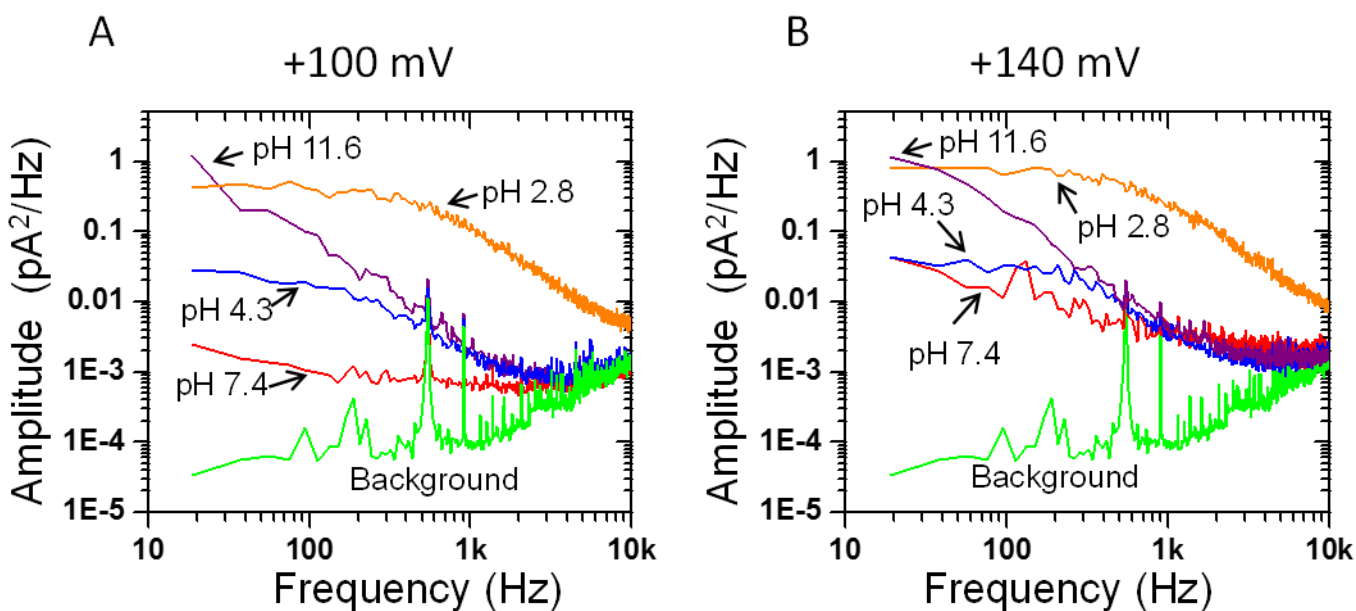


**Figure S7. Spectral density of the current noise of single FhuA  $\Delta C/\Delta 5L$  nanopores under different pH conditions.**

Data are collected at +100 mV (A) and +140 mV (B) and at pH values of 2.8 (orange), 4.3 (blue), 7.4 (red) and 11.6 (purple). The buffer solutions were the same as in Fig. S6A. Noise spectral density taken at 0 mV is the background signal (green). 5-s durations of the single-channel electrical traces were used for this current noise analysis. All current measurements were performed at a sampling rate of 50 kHz with an internal low-pass Bessel filter set at 10 kHz. No additional filtering was used prior to this analysis.



**Table S5. This table lists all of the point mutations in FhuA  $\Delta C/\Delta 5L-25N$  with respect to the sequence of FhuA  $\Delta C/\Delta 5L$ .**

Mutation	Region	Purpose	Mutation	Region	Purpose
D11N	loop 1	Neutralization	E187G	loop 5	Neutralization
D27G	turn 1	Neutralization	D239N	$\beta$ strand 12	Neutralization
E50Q	$\beta$ strand 4	Neutralization	D257G	turn 6	Neutralization
D64N	turn 2	Neutralization	E271Q	loop 7	Neutralization
D65N	turn 2	Neutralization	E300Q	turn 7	Neutralization
E80Q	loop 3	Neutralization	D301G	turn 7	Neutralization
E85G	loop 3	Neutralization	D322N	loop 8	Neutralization
D101N	$\beta$ strand 6	Neutralization	E324Q	loop 8	Neutralization
E103Q	$\beta$ strand 6	Neutralization	E331Q	loop 8	Neutralization
D139N	$\beta$ strand 8	Neutralization	D368N	loop 9	Neutralization
E141Q	$\beta$ strand 8	Neutralization	E412Q	loop 10	Neutralization
D160G	turn 4	Neutralization	E443Q	loop 11	Neutralization
D162N	turn 4	Neutralization			

## **6. The FhuA $\Delta C/\Delta 5L-25N$ nanopore is stable and displays a uniform single-channel conductance.**

For FhuA  $\Delta C/\Delta 5L-25N$ , we neutralized 25 negative charges (Fig. 1; Table S4). The aim of these modifications was to reduce the cationic selectivity of the FhuA  $\Delta C/\Delta 5L$  protein, allowing for future studies of anionic analytes. The new DDM-refolded nanopores formed channels in the lipid bilayer with no prior requirement for preparative reconstitution steps or osmotic gradients (Table S4). DDM-refolded FhuA  $\Delta C/\Delta 5L-25N$  protein formed stable and open nanopores with a unitary current of  $137 \pm 10$  pA, which corresponds to a single channel conductance of  $3.4 \pm 0.2$ , in 1 M KCl, 10 mM potassium phosphate, pH 7.4, and at an applied potential of +40 mV (n=3) (Table S4; Fig. S9A). The distribution of the unitary conductance values showed a single peak

centered at  $\sim 3.6$  nS (Fig. S9B). Further, we measured the conductance of the FhuA  $\Delta C/\Delta 5L-25N$  nanopores using a current-voltage curve (Fig. S9C). The single channel conductance was  $\sim 3.3$  nS (Table S4). As we expected, the permeability ratio  $P_{K^+}/P_{Cl^-}$  of FhuA  $\Delta C/\Delta 5L-25N$  has substantially dropped to  $0.60 \pm 0.09$  ( $n=3$ ) under asymmetric conditions of 200 mM KCl (cis)/1 M KCl (trans) in 10 mM potassium phosphate, pH 7.4. Similar to FhuA  $\Delta C/\Delta 5L$  nanopore, we were able to obtain stable, open-state channels with the FhuA  $\Delta C/\Delta 5L-25N$  protein in low ion concentration, low pH, and the combination of low ion concentration and low pH conditions (Table S4, Fig. S10). The unitary conductance of FhuA  $\Delta C/\Delta 5L-25N$  in 0.2 M KCl/pH 7.4, 0.2 M KCl/pH 3.4, and 1 M KCl/pH 3.4 was  $1.1 \pm 0.2$  ( $n=3$ ),  $1.1 \pm 0.1$  ( $n=3$ ), and  $4.1 \pm 0.1$  ( $n=3$ ), respectively (Table S4). In 0.2 M KCl, the protein channel was very stable at  $\pm 100$  mV (Fig. S10). This protein exhibited irresolvable and infrequent current spikes ( $0.2$  s $^{-1}$ ) with a low amplitude (5 -10% current reduction) at a positive transmembrane potential (Fig. S10A, the upper panel), and ms-duration, infrequent current spikes ( $0.3$  s $^{-1}$ ) with low amplitudes (8 -16% current reduction) at negative voltage (Fig. S10A, lower panel). FhuA  $\Delta C/\Delta 5L-25N$  maintained the same stability of the open state up to  $\pm 100$  mV in 200 mM KCl, pH 3.4 (Fig. S10B). At +100 mV, FhuA  $\Delta C/\Delta 5L-25N$  displayed infrequent millisecond-timescale duration events ( $0.1$  s $^{-1}$ ), with low current amplitudes ( $\sim 15\%$  current reduction) (Fig. S10B, the upper panel). Under 1 M KCl/pH 3.4 buffering condition, FhuA  $\Delta C/\Delta 5L-25N$  showed two types of current fluctuations (Fig. S10C). These fluctuations are quite distinct in their current amplitudes, dwell times, and frequencies. At +100 mV, the first type featured a low amplitude ( $\sim 9\%$  current reduction), a microsecond- to millisecond-timescale duration, and a high event frequency ( $\sim 110$  s $^{-1}$ ). The second type showed a larger amplitude ( $\sim 35\%$  current reduction), a microsecond-timescale duration, and a low event frequency ( $\sim 0.5$  s $^{-1}$ ).

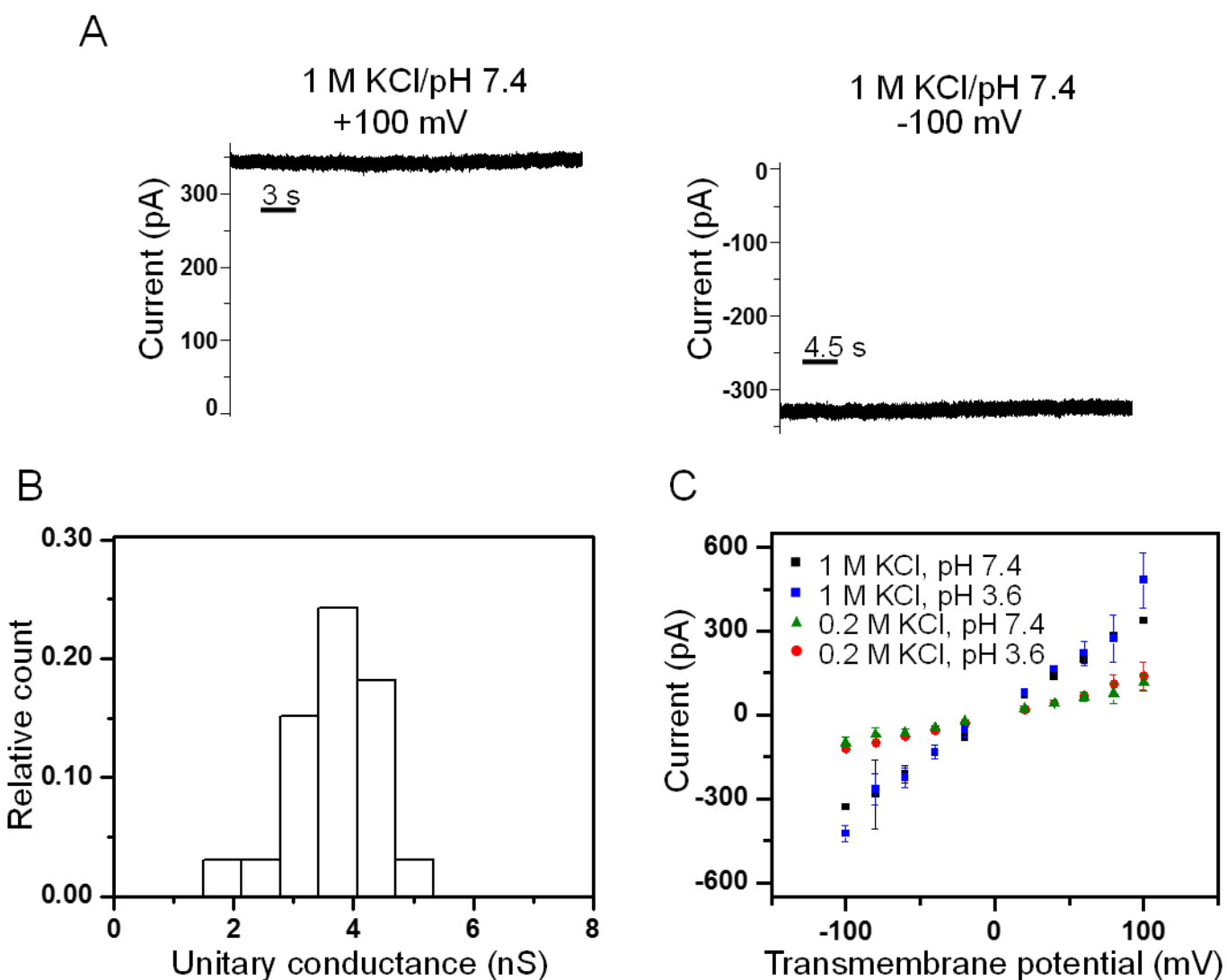


**Figure S9. FhuA  $\Delta C/\Delta 5L-25N$  shows a closely similar single-channel electrical signature to FhuA  $\Delta C/\Delta 5L$ .**

(A) Representative single-channel electrical recordings with FhuA  $\Delta C/\Delta 5L-25N$  in 1 M KCl, 10 mM potassium phosphate, pH 7.4, and at an applied transmembrane potential of +100 (the left panel) and -100 mV (the right panel). The single-channel electrical traces were low-pass Bessel

filtered at 2 kHz; (B) The histograms of the distribution of the single-channel conductance values of DDM-refolded FhuA  $\Delta C/\Delta 5L-25N$  at an applied transmembrane potential of +60 mV under the buffer conditions from A. The bin size was 0.64 nS; (C) The relationships between currents and voltages (I/V curves) of single protein channel insertions from -100 mV to +100 mV under different salt concentration and pH conditions, as indicated in the panel.

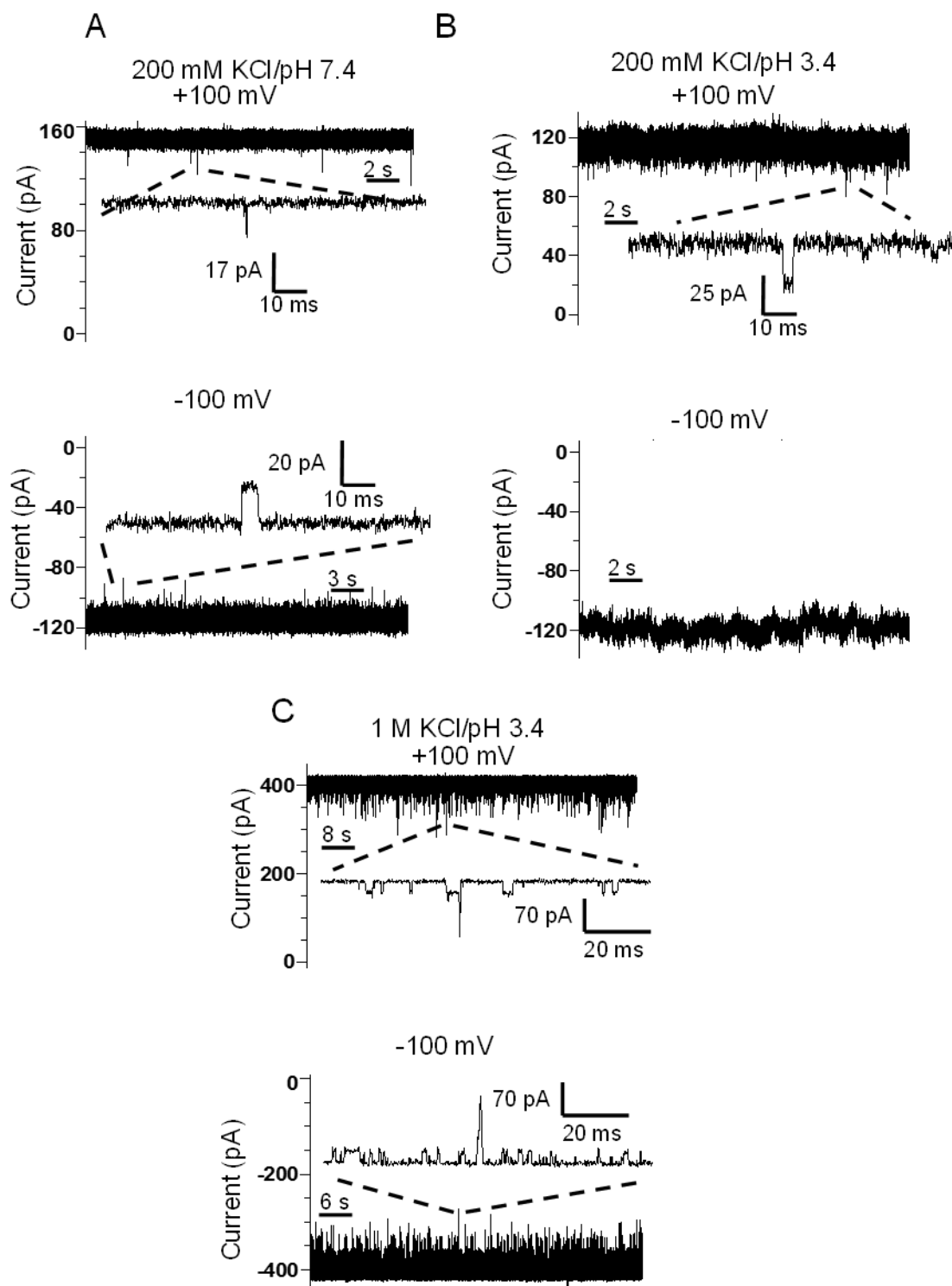


**Figure S10. Engineered FhuA  $\Delta C/\Delta 5L-25N$  pores are stable under a broad range of conditions.**

Representative single-channel electrical recordings acquired with FhuA  $\Delta C/\Delta 5L-25N$  at an applied transmembrane potential of +100 mV (the upper panels) and -100 mV (the lower panels). The buffer conditions were the following: (A) 0.2 M KCl, 10 mM potassium phosphate, pH 7.4, (B) 0.2 M KCl, 10 mM phosphate acetate, pH 3.4, and (C) 1 M KCl, 10 mM potassium acetate, pH 3.4. The expanded traces illustrate the signature of the channels at a greater time resolution. The single-channel electrical traces were low-pass Bessel filtered at 2 kHz.

**7. Discrete 33% current transitions noted with different truncation FhuA mutants at high transmembrane potentials.**



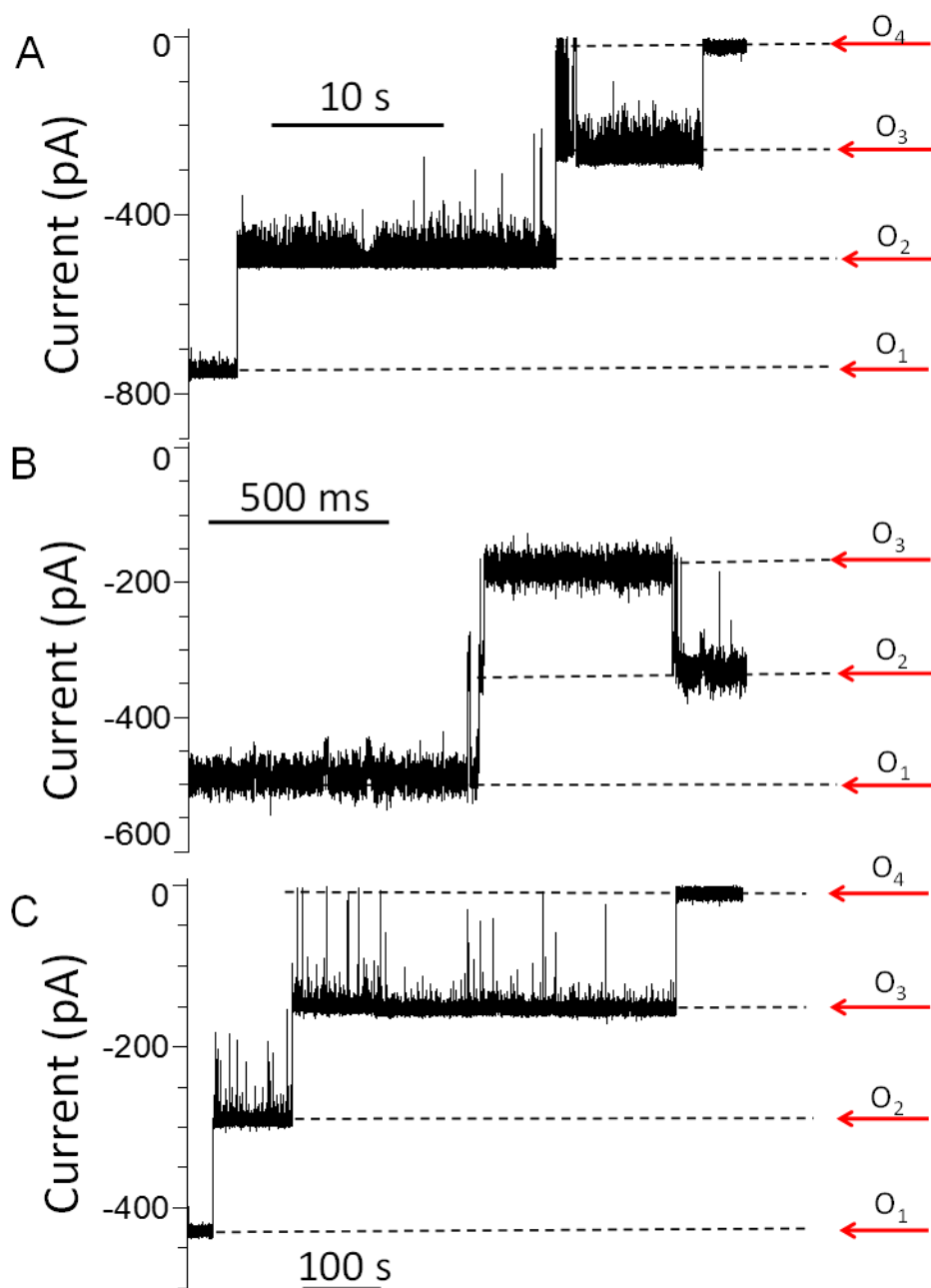


**Figure S11. Representative long-lived current blockades observed with globally mutated FhuA derivatives at greater negative applied transmembrane potentials.**

These discrete blockades show each ~33% reduction in the unitary conductance. (A) FhuA  $\Delta C/\Delta 5L$  at -180 mV (n=10 distinct single-channel electrical recordings); (B) FhuA  $\Delta C/\Delta 5L-25N$

at -180 mV (n=3); (C) FhuA  $\Delta C/\Delta 5L-25N\_ELP$  at -100 mV (n=3). All single-channel electrical recordings were achieved in 1M KCl, 10 mM potassium phosphate, pH 7.4. Single-channel electrical traces were low-pass Bessel filtered at 1.4 kHz.

**8. The 33% current blockades between various sub-states are reversible at high transmembrane potentials.**

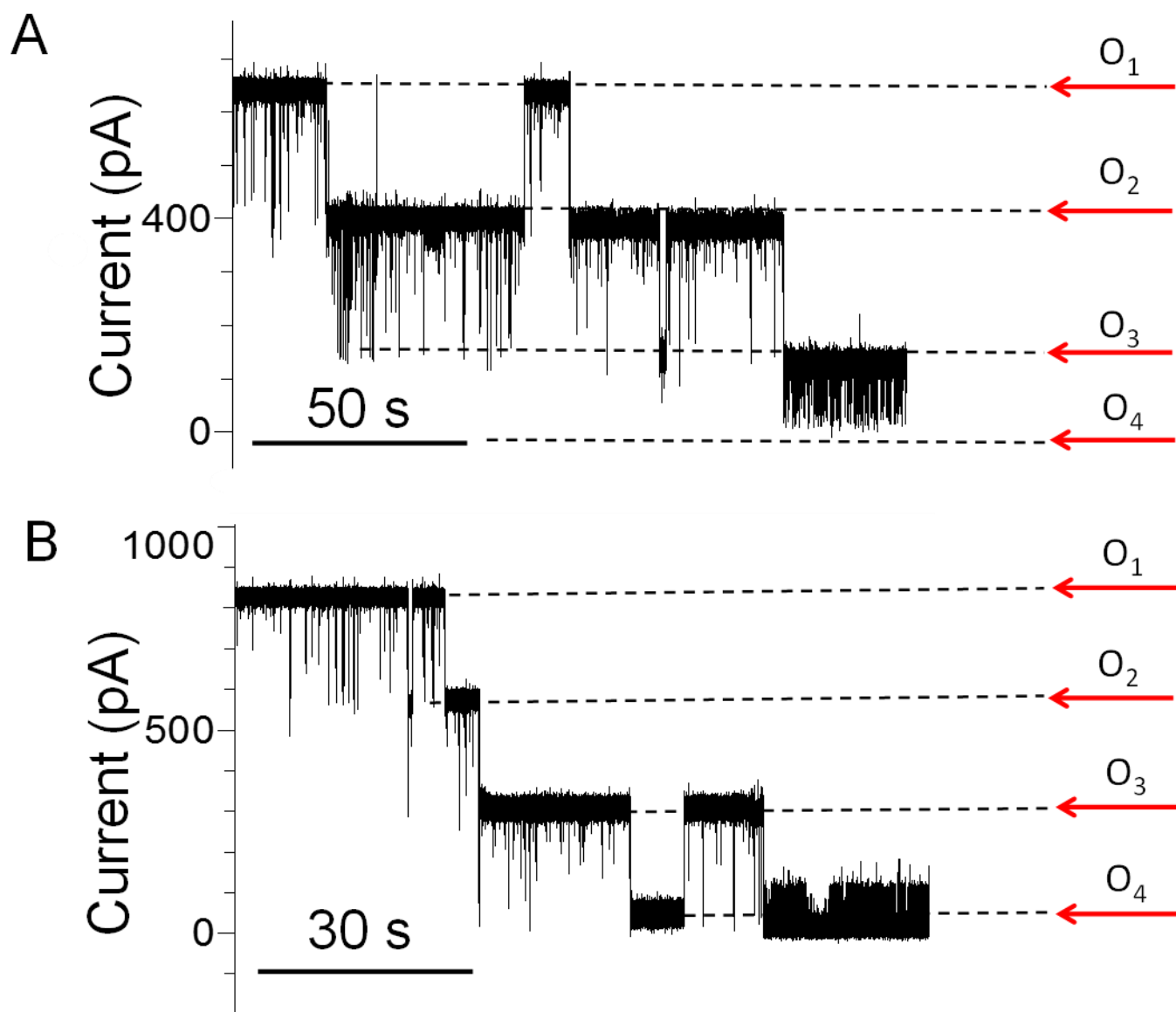


**Figure S12. The current transitions between the long-lived and discrete sub-states of FhuA  $\Delta C/\Delta 5L$  are reversible under extreme applied transmembrane potentials.**

In (A) and (B), we illustrate traces from two distinct single-channel electrical recordings showing reversibility of current transitions among various sub-states at a transmembrane potential of +180

mV. These recordings were conducted in 1M KCl, 10 mM potassium phosphate, pH 7.4. Single-channel electrical traces were low-pass Bessel filtered at 1.4 kHz.

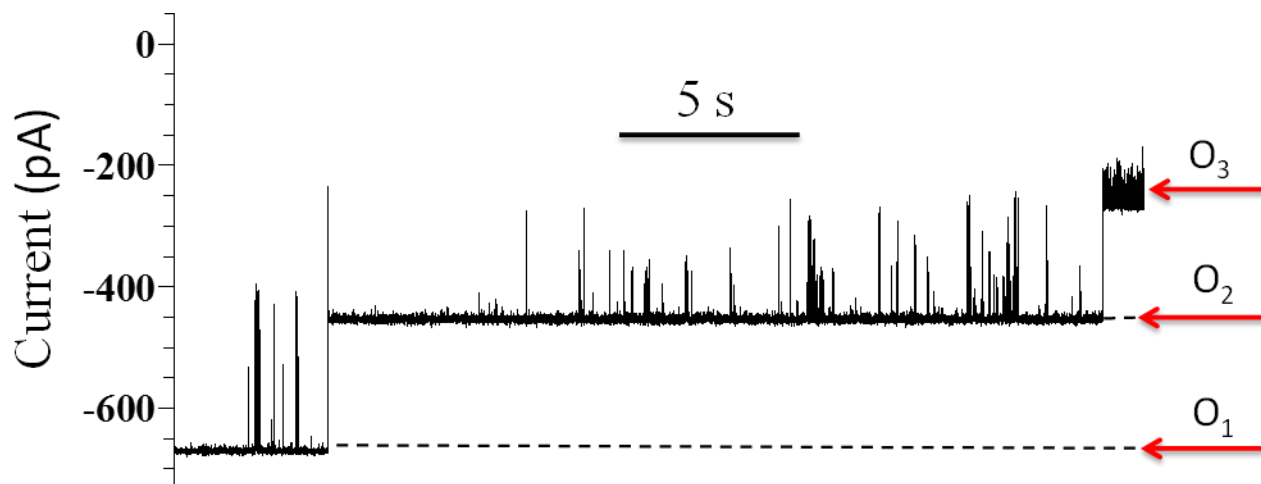


**Figure S13. Representative single-channel electrical recordings of TL-FhuA  $\Delta$ C/ 5L in 1M KCl, 10 mM potassium phosphate, pH 7.4.**

The applied transmembrane potential was -150 mV. The single-channel electrical trace was sampled at 100 kHz and low-pass Bessel filtered at 1 kHz. The acquired data are representative over three distinct single-channel electrical recordings.

**9. FhuA  $\Delta C/\Delta 7L-30N$  has an asymmetric single-channel electrical signature with respect to the voltage polarity.**

**Table S6. Details of the truncation FhuA  $\Delta C/\Delta 7L-30N$  mutant.**

<b>Mutation</b>	<b>Deletions</b>	<b>Deleted Residues</b>	<b>Point mutations</b>	<b>Purpose</b>
$\Delta L3$ (NSGGS)	$\Delta 243-266, \Delta 272-273$	YYGWLPKEGTVEPLPNGKRLPTDF, NN	E268S, G269G, A270G, K271S	NSGGS linker
$\Delta L4$ (GS)	$\Delta 310-317$ $\Delta 320-348$	NSVYGYGV, DPANAYSKQCAALAPADKGHYLA RKYVVD	C318G	GS linker
$\Delta L5$ (GYNSGGS)	$\Delta 387-391$ $\Delta 396-416,$ $\Delta 420-424$	INAWF, SVPLLNLNPNVNTDFDFNAKD, SGPYR	D394N, D395S, P417G, A418G, N419S	GYNSGGS linker
$\Delta L7$ (QSGQ)	$\Delta 505-515$	QVGKDGNI FAP	E501Q, P502S, S503G, S504Q	QSGS linker
$\Delta L8$ (SGQS)	$\Delta 547-558$	NNLMADPEGSFF	V560Q, E561Q ,G562S	(SGQS) linker
$\Delta L10$ (NSQGS)	$\Delta 642-651$	SYGDPANSFK	G640N, V652Q	NSEGS linker
$\Delta L11$ (NSQGS)	$\Delta 685-703$	REYVASCFN TYGCFWGAER	N681S, L682Q, F683G, D684S	NSEGS linker

This table shows all of the loop truncations and consequent linkers of FhuA  $\Delta C/\Delta 7L-30N$ . Here,

all numbering and mutations are with respect to the WT-FhuA. L4 and L5 were further truncated

from the FhuA  $\Delta C/\Delta 5L-25N$  deletions, whereas L7 and L8 were deleted in FhuA  $\Delta C/\Delta 7L-30N$ .

A direct comparison of the loop deletions between FhuA  $\Delta C/\Delta 5L$  and that of FhuA  $\Delta C/\Delta 7L-$

30N can be seen in **Fig. 1**, panel F.

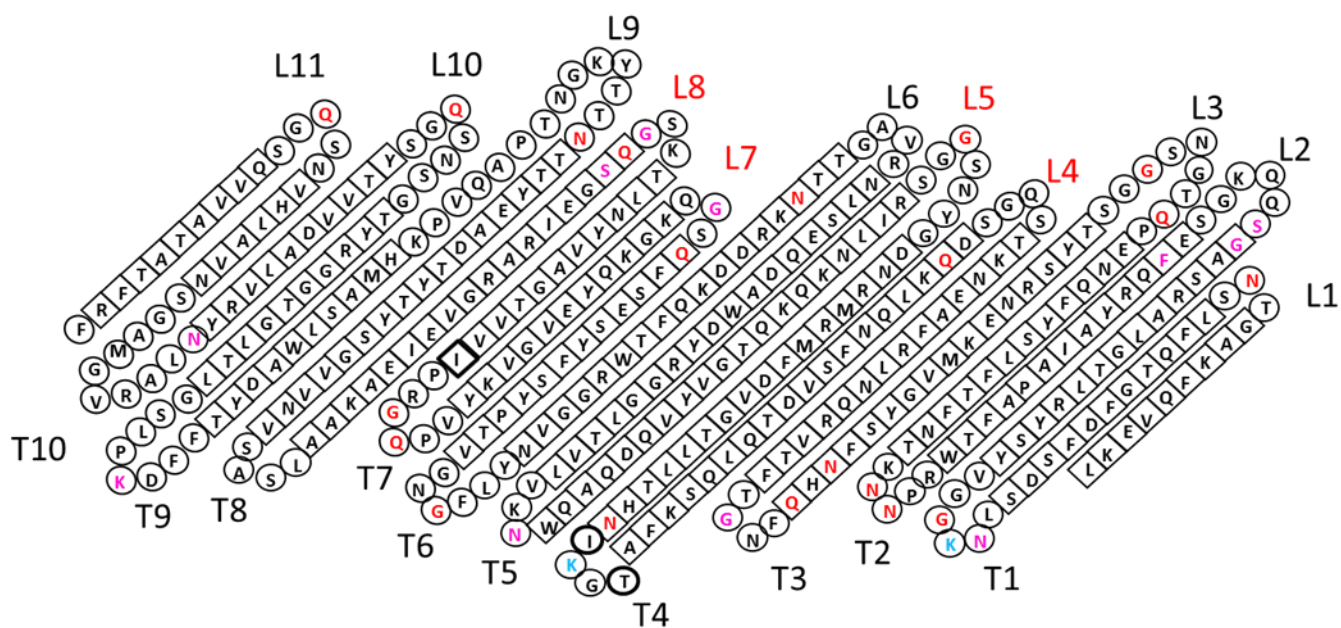


**Figure S14. Topology map of FhuA  $\Delta C/\Delta 7L-30N$ .** The four extracellular loops, which were reduced with respect  $\Delta C/\Delta 5L$  FhuA scaffold (L4, L5, L7, L8), are highlighted in red. The residues making up the total point mutations in this construct are labeled as follows: red are mutations still present from the FhuA  $\Delta C/\Delta 5L-25N$  protein, blue are additional charge reversals, and purple are other new mutations of the FhuA  $\Delta C/\Delta 7L-30N$  protein (see Tables S6 and S7).

**Table S7. The point mutations table highlights all of the point mutations that differentiate the FhuA  $\Delta C/\Delta 7L$ -N30 polypeptide from the FhuA  $\Delta C/\Delta 5L$ . All numbering is with respect to FhuA  $\Delta C/\Delta 5L$ .**

Mutation	Structure	Purpose	Mutation	Structure	Purpose
D11N	Loop 1	Neutralization	D162N	Turn 4	Neutralization
D25N	Turn 1	Neutralization	E187G	Loop 5	Neutralization
D26K	Turn 1	Charge reversal	D213N	Turn 5	Neutralization
D27G	Turn 1	Neutralization	D239N	$\beta$ strand 12	Neutralization
N42G	Loop2	Addition of Bam HI site	D257G	Turn 6	Neutralization
A43S	Loop2	Addition of Bam HI site	E271Q	Loop 7	Neutralization
E50F	Loop2	Neutralization & Addition of ECOR I site	S274G	Loop 7	Loop linker
D64N	Turn 2	Neutralization	E300Q	Turn 7	Neutralization
D65N	Turn 2	Neutralization	D301G	Turn 7	Neutralization
E80Q	Loop 3	Neutralization	V330G	Loop 8	Loop linker
E85G	Loop 3	Neutralization	E331Q	Loop 8	Neutralization
D101N	$\beta$ strand 6	Neutralization	G332S	Loop 8	Loop linker
E103Q	$\beta$ strand 6	Neutralization	D368N	Loop 9	Neutralization
D106G	Turn 3	Neutralization	G395K	Turn 9	+ charge
E141Q	$\beta$ strand 8	Neutralization	E412Q	Loop 10	Neutralization
			D425N	Turn 10	Neutralization
D160K	Turn 4	Charge reversal	E443Q	Loop 11	Neutralization



**Table S8. Loop modifications table highlighting the deletions and point modifications which make up the reduction of the specified loops in FhuA  $\Delta$ C/ $\Delta$ 7L-N30.** The amino acids in the parenthesis are the native amino acids that were left in-between deletion mutations to make up the loops. **Tables S7** and **S8** elucidate the total mutational landscape of FhuA  $\Delta$ C/ $\Delta$ 7L-N30 with respect to FhuA  $\Delta$ C/ $\Delta$ 5L.

<b>Mutation</b>	<b>Region</b>	<b>Purpose</b>
<b><math>\Delta</math>124-131 (GS) <math>\Delta</math>134-139</b>	Loop4	Reduction of large loop
<b><math>\Delta</math>178-182 (GYSNSGGS), <math>\Delta</math>189-194</b>	Loop5	Reduction of large loop
<b><math>\Delta</math>P272, S274G, <math>\Delta</math>276-285</b>	Loop7	Reduction of large loop
<b><math>\Delta</math>316-328, V330G, G332S</b>	Loop8	Reduction of large loop

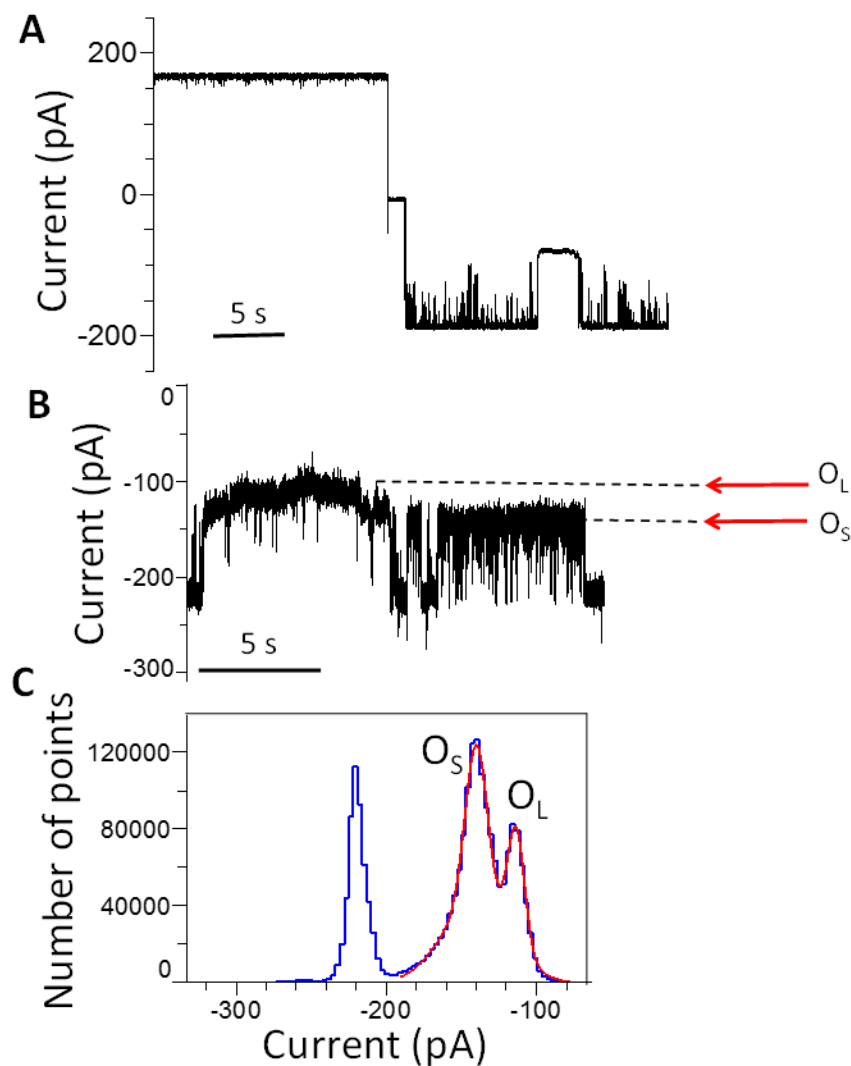


**Figure S15. Single-channel electrical signature of FhuA  $\Delta C/\Delta 7L-30N$  at lower applied potentials.**

(A) A representative single-channel electrical trace acquired with FhuA  $\Delta C/\Delta 7L-30N$  at applied transmembrane potentials of +40 and -40 mV. Transient current fluctuations are observed at negative potential;

(B) A snapshot of a single-channel channel electrical recording obtained at a negative potential of -40 mV. The 33% closures were absent at either positive or negative potentials; (C) All-point current amplitude histogram of the electrical trace acquired in (B). All single-channel electrical

recordings were accomplished in 1M KCl, 10 mM potassium phosphate, pH 7.4. The electrical traces were low-pass Bessel filtered at 1.4 kHz. These traces are representative over at least a number of four distinct single-channel electrical recordings.

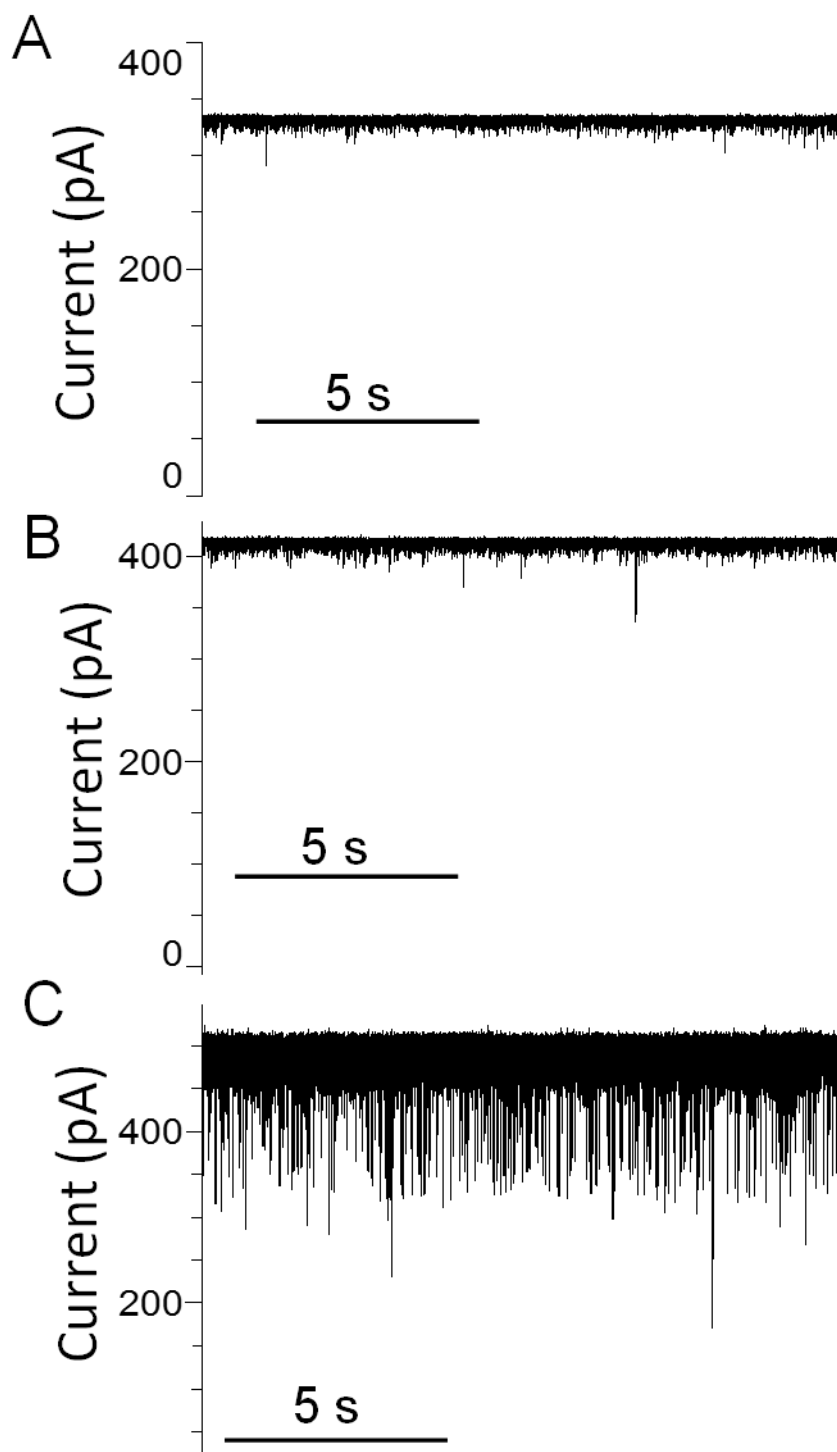


**Figure S16. FhuA  $\Delta C/\Delta 7L$ -30N showed brief current fluctuations when Syn B2, a cationic, 23-residue polypeptide, was added to the trans side at +120 mV.**

(A) The transmembrane potential was +80 mV. No current blockades were observed; (B) The transmembrane potential was +100 mV. Rare brief current blockades were noted; (C) The transmembrane potential was +120mV. Highly frequent Syn B2-induced current blockades were detected. In all cases, 10  $\mu$ M Syn B2 was added to the trans side of the bilayer. All single-channel measurements were conducted in 1 M KCl, 10 mM potassium phosphate, pH 7.4. The electrical traces were low-pass Bessel filtered at 1.4 kHz.

#### **10. Interaction of the Syn B2 polypeptide with FhuA $\Delta C/\Delta 5L$ .**

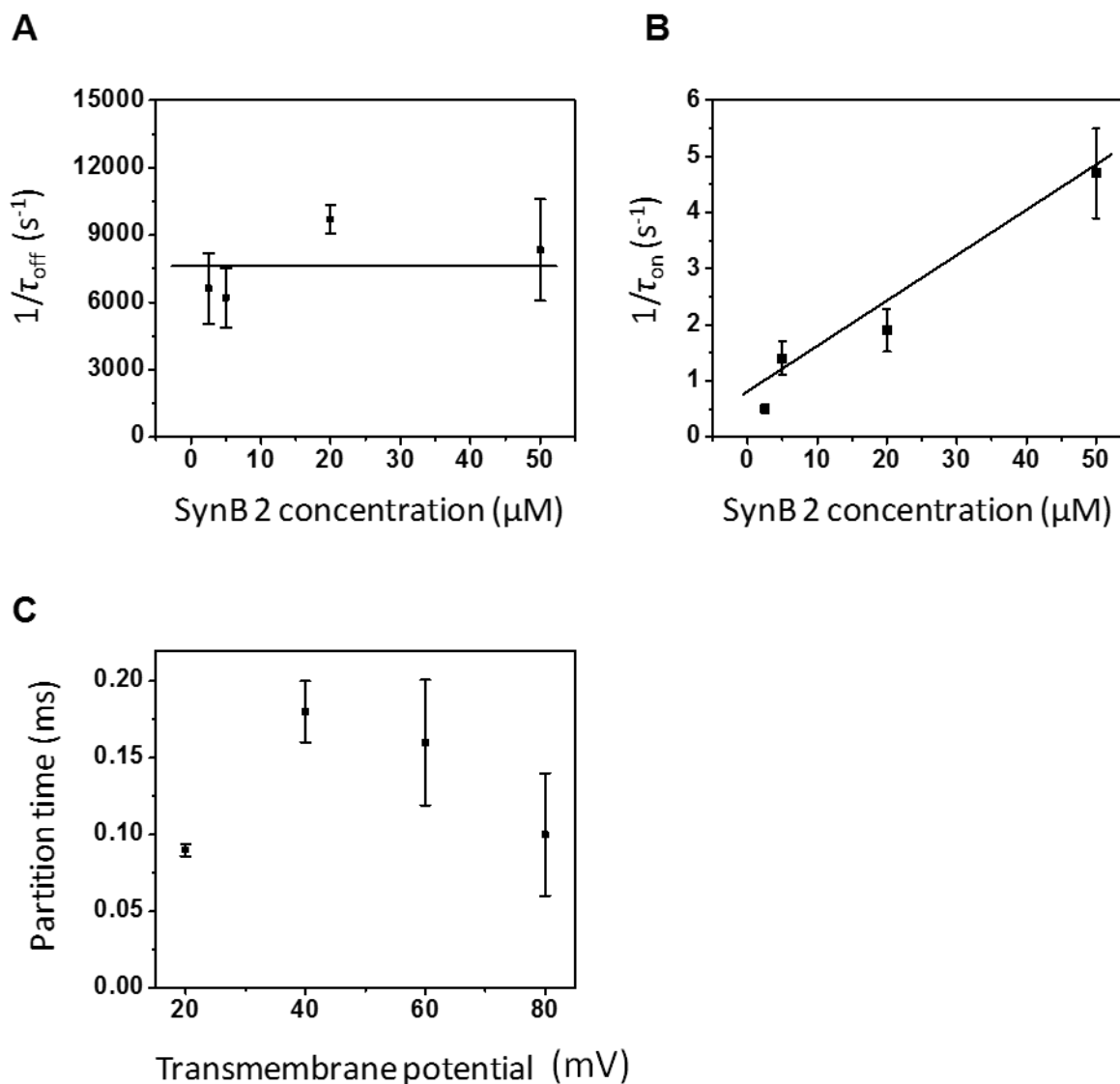


**Figure S17. Demonstration that engineered FhuA  $\Delta\text{C}/\Delta\text{5L}$  pore has a bimolecular interaction with the Syn B2 polypeptide.**

(A) The dose-response dependence of the  $1/\tau_{\text{off}}$  values; (B) The dose-response dependence of the  $1/\tau_{\text{on}}$  values; (C) The voltage-dependence of the time constants of dissociation ( $\tau_{\text{off}}$ ). The concentration of the polypeptide was 50  $\mu\text{M}$ . All measurements were carried out at room temperature in 1 M KCl, 10 mM potassium phosphate, pH 7.4. The transmembrane potential in

(A) and (B) was +80 mV. The plot from (C) reveals a biphasic dependence of the time constant on the applied transmembrane potential [21-23], suggesting that most of peptides are fully translocated from one side of the bilayer to the other at a potential greater than +60 mV.

**11. Interaction between the 55-residue nucleocapsid protein 7 (NCp7) with FhuA  $\Delta$  C/  $\Delta$  5L and between pb2-Ba proteins and FhuA  $\Delta$  C/ $\Delta$ 5L.**

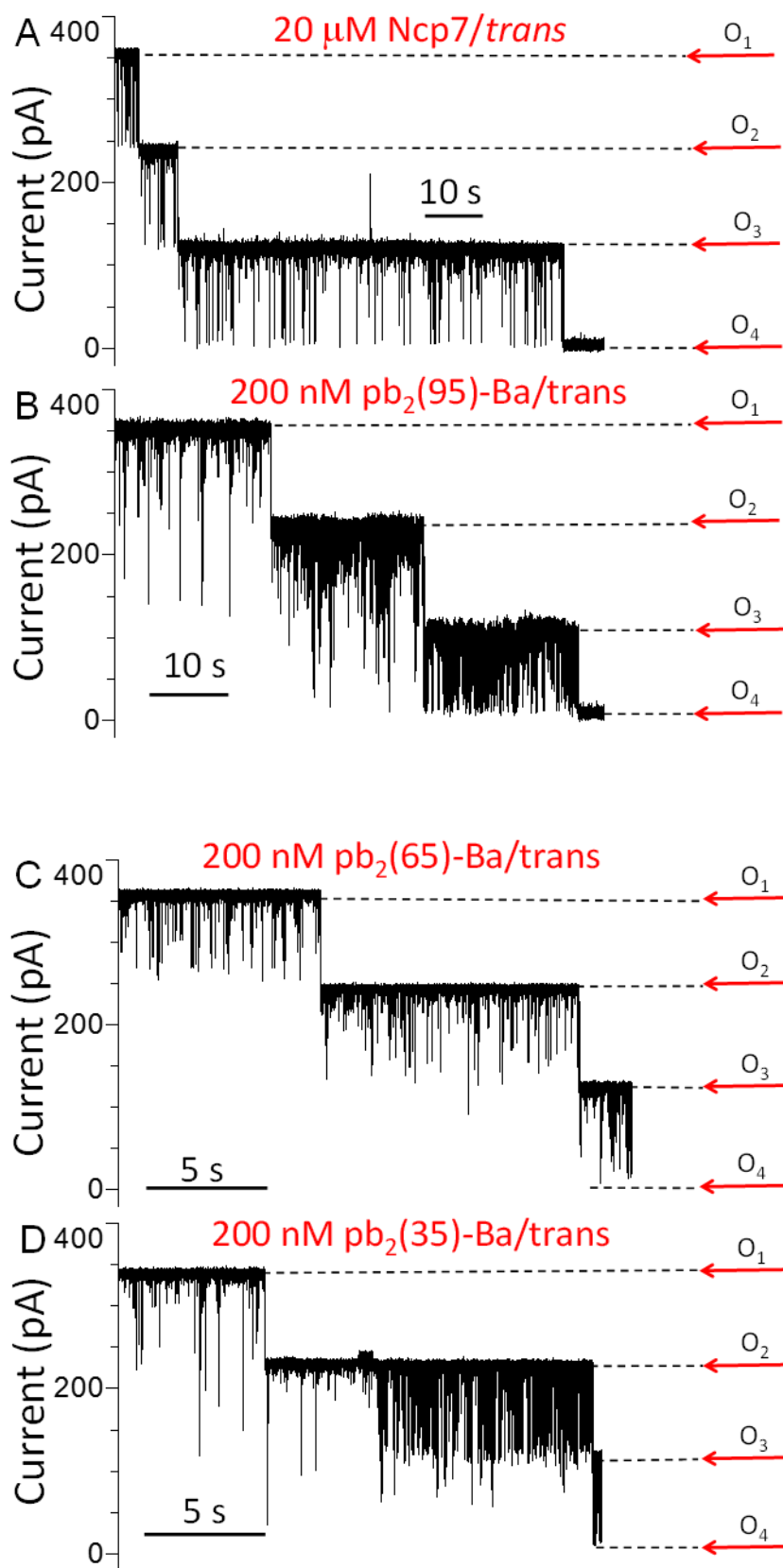




**Figure S18. Discrete long-lived current blockades were observed with FhuA  $\Delta$ C/ $\Delta$ 5L in the presence of 55-residue nucleocapsid protein 7 (NCp7) (A) [24, 25] as well as pb2(95)-Ba (B), pb2(65)-Ba (C), and pb2(35)-Ba (D) at a much lower applied transmembrane potential of +80 mV.**

pb2-Ba consists of the N terminal region of the pre-cytochrome b2 (pb2) of varying length (indicated as number of residues in parenthesis) fused to the N terminus of the small ribonuclease barnase (Ba) [23, 26]. All single-channel electrical recordings were accomplished in 1M KCl, 10 mM potassium phosphate, pH 7.4. Electrical traces were low-pass Bessel filtered at 1.4 kHz.

**12. The 33% current blockades observed with FhuA  $\Delta$ C/ $\Delta$ 5L-N25\_ELP are reversible.**

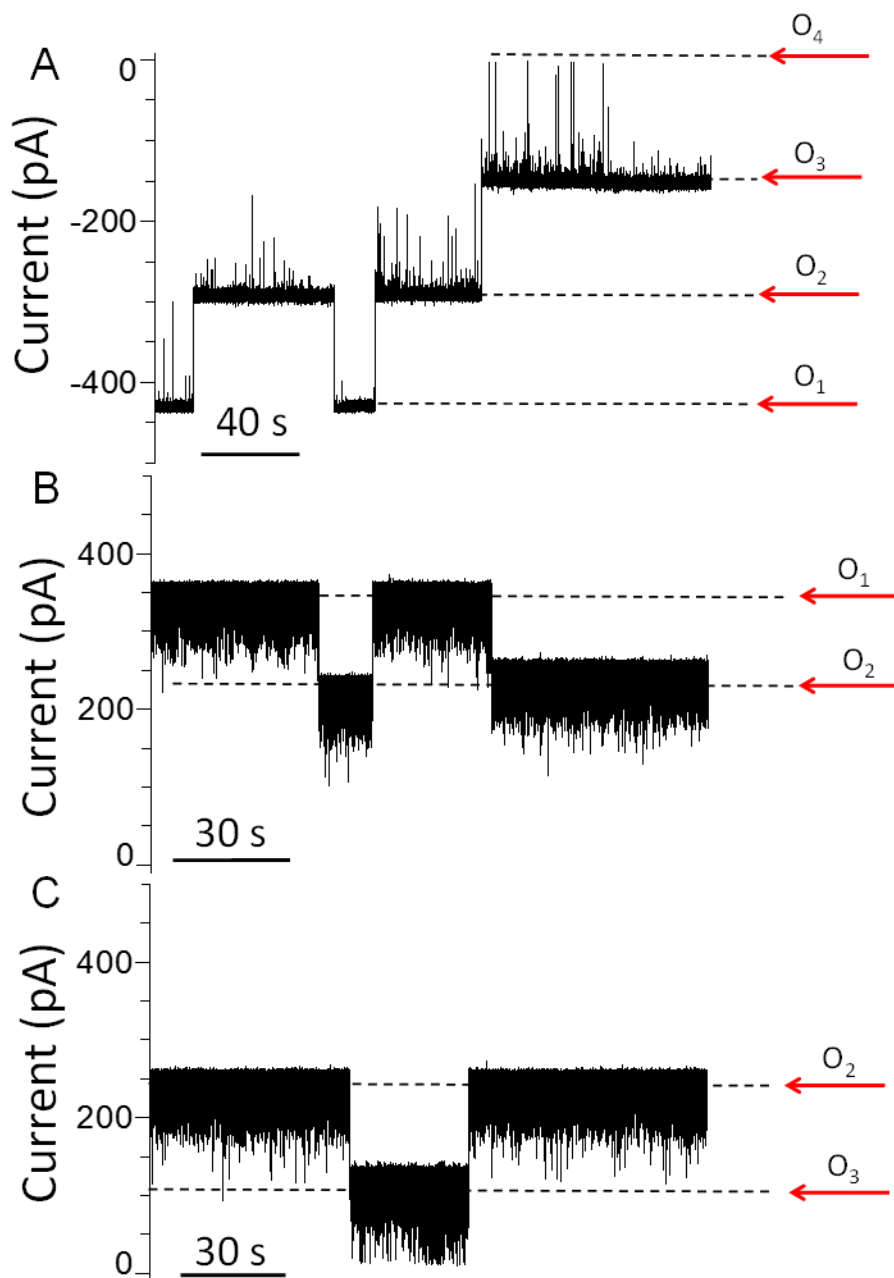


**Figure S19. The demonstration of the reversibility of the long-lived current blockades among long-lived sub-states observed with FhuA  $\Delta C/\Delta 5L-N25\_ELP$ .**

In this figure, we illustrate reversibility of 33% current transitions noted with FhuA  $\Delta C/\Delta 5L-N25\_ELP$ . The “on” and “off” rates of the transitions of this protein pore are greater than those observed with other globally mutated FhuA protein pores, suggesting lower energetic barriers among all open sub-states. (A) -100 mV; (B) +100 mV; (C) +100 mV. All single-channel

electrical recordings were accomplished in 1M KCl, 10 mM potassium phosphate, pH 7.4. Electrical traces were low-pass Bessel filtered at 1.4 kHz.

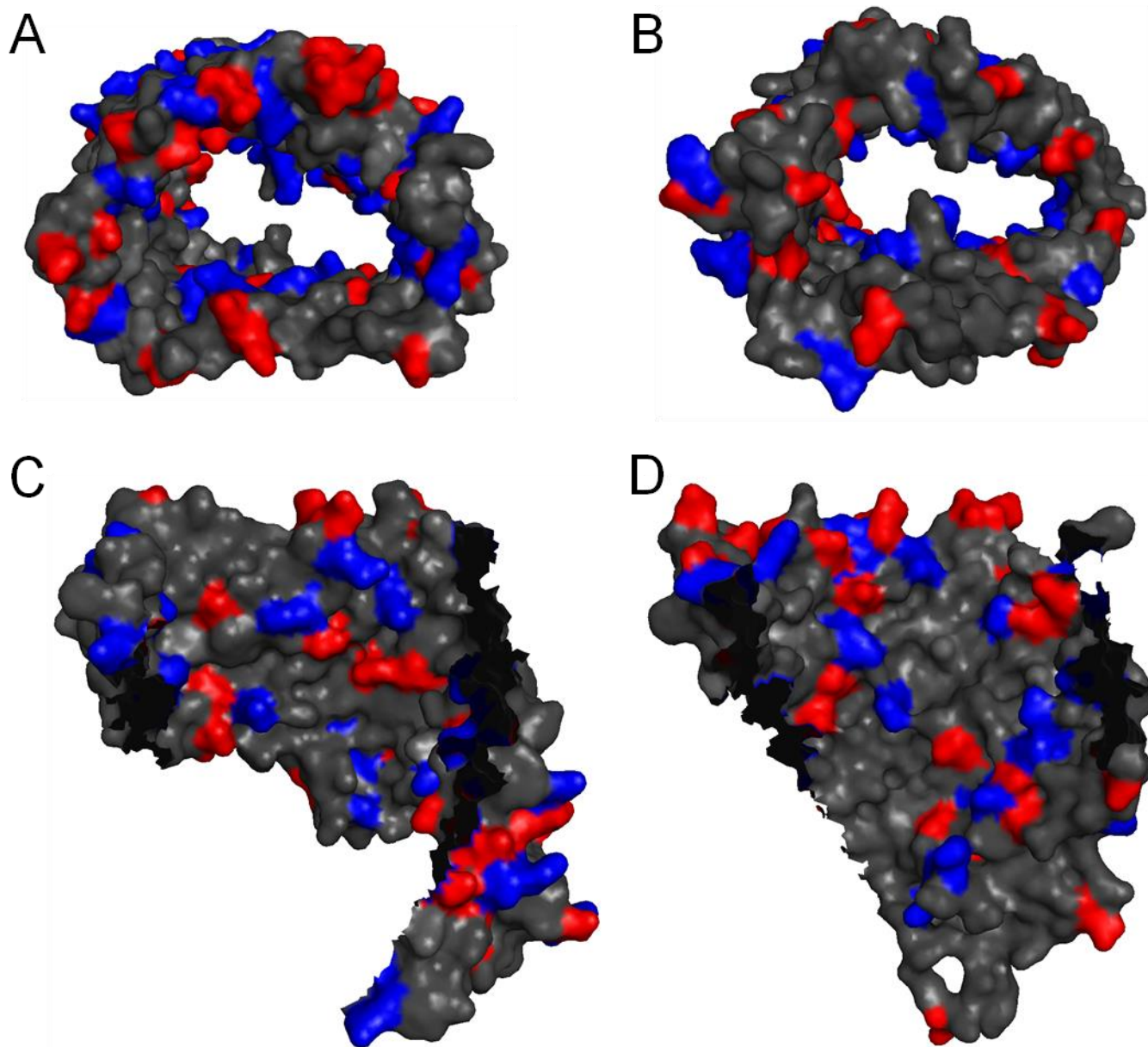


**Figure S20. FhuA  $\Delta C/\Delta 5L$  is characterized by heterogeneous positive and negative charge distribution throughout the  $\beta$  turns,  $\beta$  barrel, and extracellular loops.**

(A) Cross-sectional image from the periplasmic side, indicating charge heterogeneity of the  $\beta$  turns; (B) Cross-sectional image from the extracellular side, illustrating surface change

distribution within the remaining loops; **(C)** Longitudinal slice image of the protein showing the periplasmic turns on the top and presenting surface charge distribution within the pore interior between residues 1 and 218; **(D)** Longitudinal slice image of the protein showing the periplasmic turns on the top and presenting surface charge distribution within the pore lumen between residues 218 and 455. In all panels, negative charges are marked in red, whereas positive charges are marked in blue.

## References

- [1] M.M. Mohammad, K.R. Howard, L. Movileanu, Redesign of a plugged beta-barrel membrane protein, *J.Biol.Chem.*, 286 (2011) 8000-8013.
- [2] M.M. Mohammad, R. Iyer, K.R. Howard, M.P. McPike, P.N. Borer, L. Movileanu, Engineering a Rigid Protein Tunnel for Biomolecular Detection, *J.Am.Chem.Soc.*, 134 (2012) 9521-9531.
- [3] K. Akiyama, H. Watanabe, S. Tsukada, H. Sasai, A novel method for constructing gene-targeting vectors, *Nucleic Acids Res.*, 28 (2000) E77.
- [4] J. Liu, E. Eren, J. Vijayaraghavan, B.R. Cheneke, M. Indic, B. van den Berg, L. Movileanu, OccK Channels from *Pseudomonas aeruginosa* Exhibit Diverse Single-channel Electrical Signatures, but Conserved Anion Selectivity, *Biochemistry*, 51 (2012) 2319-2330.
- [5] J. Liu, A.J. Wolfe, E. Eren, J. Vijayaraghavan, M. Indic, B. van den Berg, L. Movileanu, Cation Selectivity is a Conserved Feature in the OccD Subfamily of *Pseudomonas aeruginosa*, *Biochim.Biophys.Acta.-Biomembr.*, 1818 (2012) 2908-2916.
- [6] B. Hille, *Ion Channels of Excitable Membranes*, Third Edition ed., Sinauer Associates, Inc., Sunderland, Massachusetts, USA, 2001.
- [7] J.D. Thompson, D.G. Higgins, T.J. Gibson, CLUSTAL W: improving the sensitivity of progressive multiple sequence alignment through sequence weighting, position-specific gap penalties and weight matrix choice, *Nucleic Acids Res.*, 22 (1994) 4673-4680.
- [8] A.D. Ferguson, E. Hofmann, J.W. Coulton, K. Diederichs, W. Welte, Siderophore-mediated iron transport: crystal structure of FhuA with bound lipopolysaccharide, *Science*, 282 (1998) 2215-2220.
- [9] K.P. Locher, B. Rees, R. Koebnik, A. Mitschler, L. Moulinier, J.P. Rosenbusch, D. Moras, Transmembrane signaling across the ligand-gated FhuA receptor: crystal structures of free and ferrichrome-bound states reveal allosteric changes, *Cell*, 95 (1998) 771-778.
- [10] L.Z. Song, M.R. Hobaugh, C. Shustak, S. Cheley, H. Bayley, J.E. Gouaux, Structure of staphylococcal alpha-hemolysin, a heptameric transmembrane pore, *Science*, 274 (1996) 1859-1866.
- [11] H. Bayley, P.S. Cremer, Stochastic sensors inspired by biology, *Nature*, 413 (2001) 226-230.
- [12] A.A. Simpson, Y. Tao, P.G. Leiman, M.O. Badasso, Y. He, P.J. Jardine, N.H. Olson, M.C. Morais, S. Grimes, D.L. Anderson, T.S. Baker, M.G. Rossmann, Structure of the bacteriophage phi29 DNA packaging motor, *Nature*, 408 (2000) 745-750.

- [13] D. Wendell, P. Jing, J. Geng, V. Subramaniam, T.J. Lee, C. Montemagno, P. Guo, Translocation of double-stranded DNA through membrane-adapted phi29 motor protein nanopores, *Nat.Nanotechnol.*, 4 (2009) 765-772.
- [14] M. Faller, M. Niederweis, G.E. Schulz, The structure of a mycobacterial outer-membrane channel, *Science*, 303 (2004) 1189-1192.
- [15] T.Z. Butler, M. Pavlenok, I. Derrington, M. Niederweis, J.H. Gundlach, Single-molecule DNA detection with an engineered MspA protein nanopore, *Proc.Natl.Acad.Sci.U.S.A.*, 105 (2008) 20647-20652.
- [16] M. Mueller, U. Grauschopf, T. Maier, R. Glockshuber, N. Ban, The structure of a cytolytic alpha-helical toxin pore reveals its assembly mechanism, *Nature*, 459 (2009) 726-730.
- [17] M. Soskine, A. Biesemans, B. Moeyaert, S. Cheley, H. Bayley, G. Maglia, An engineered ClyA nanopore detects folded target proteins by selective external association and pore entry, *Nano.Lett.*, 12 (2012) 4895-4900.
- [18] G.V. Subbarao, B. van den Berg, Crystal structure of the monomeric porin OmpG, *J.Mol.Biol.*, 360 (2006) 750-759.
- [19] O. Yildiz, K.R. Vinothkumar, P. Goswami, W. Kuhlbrandt, Structure of the monomeric outer-membrane porin OmpG in the open and closed conformation, *EMBO J.*, 25 (2006) 3702-3713.
- [20] M. Chen, S. Khalid, M.S. Sansom, H. Bayley, Outer membrane protein G: Engineering a quiet pore for biosensing, *Proc.Natl.Acad.Sci.U.S.A.*, 105 (2008) 6272-6277.
- [21] C.P. Goodrich, S. Kirmizialtin, B.M. Huyghues-Despointes, A.P. Zhu, Scholtz, J.M., D.E. Makarov, L. Movileanu, Single-molecule electrophoresis of beta-hairpin peptides by electrical recordings and Langevin dynamics simulations, *J.Phys.Chem.B.*, 111 (2007) 3332-3335.
- [22] A.J. Wolfe, M.M. Mohammad, S. Cheley, H. Bayley, L. Movileanu, Catalyzing the translocation of polypeptides through attractive interactions, *J.Am.Chem.Soc.*, 129 (2007) 14034-14041.
- [23] M.M. Mohammad, S. Prakash, A. Matouschek, L. Movileanu, Controlling a single protein in a nanopore through electrostatic traps, *J.Am.Chem.Soc.*, 130 (2008) 4081-4088.
- [24] L.M. Jenkins, J.C. Byrd, T. Hara, P. Srivastava, S.J. Mazur, S.J. Stahl, J.K. Inman, E. Appella, J.G. Omichinski, P. Legault, Studies on the mechanism of inactivation of the HIV-1 nucleocapsid protein NCp7 with 2-mercaptobenzamide thioesters, *J.Med.Chem.*, 48 (2005) 2847-2858.
- [25] D.J. Niedzwiecki, R. Iyer, P.N. Borer, L. Movileanu, Sampling a Biomarker of the Human Immunodeficiency Virus across a Synthetic Nanopore, *ACS Nano.*, 7 (2013) 3341-3350.

[26] M.M. Mohammad, L. Movileanu, Excursion of a single polypeptide into a protein pore: simple physics, but complicated biology, *Eur.Biophys.J.*, 37 (2008) 913-925.



# Chapter 3. Interrogating Detergent Desolvation of Nanopore-Forming Proteins by Fluorescence Polarization Spectroscopy

**Aaron J. Wolfe**,<sup>1,2</sup> Yi-Ching Hsueh,<sup>1</sup> Adam R. Blanden,<sup>3</sup> Mohammad M. Mohammad,<sup>1</sup> Bach Pham,<sup>4</sup> Avinash K. Thakur,<sup>1,2</sup> Min Chen,<sup>4</sup> Stewart N. Loh,<sup>3</sup> and Liviu Movileanu<sup>1,2,5</sup>

<sup>1</sup>Department of Physics, Syracuse University, 201 Physics Building, Syracuse, New York 13244-1130, USA

<sup>2</sup>Structural Biology, Biochemistry, and Biophysics Program, Syracuse University, 111 College Place, Syracuse, New York 13244-4100, USA

<sup>3</sup>Department of Chemistry, University of Massachusetts, 710 North Pleasant Street, Amherst, Massachusetts 01003-9336, USA

<sup>4</sup>Department of Biochemistry and Molecular Biology, State University of New York Upstate Medical University, 4249 Weiskotten Hall, 766 Irving Av., Syracuse, New York 13210, USA

<sup>5</sup>Department of Biomedical and Chemical Engineering, Syracuse University, Syracuse University, 223 Link Hall, Syracuse, New York 13244, USA

Reprinted with permission from **Aaron J Wolfe**, Y.C. Hsueh, A.R. Blanden, M.M. Mohammad, B. Pham, A.K. Thakur, S.N. Loh, M. Chen, and L. Movileanu, 2017, Interrogating Detergent Desolvation of Nanopore-forming Proteins by Fluorescence Polarization Spectroscopy, *Anal. Chem.* 89(15), 8013-8020. DOI: 10.1021/acs.analchem.7b01339 Copyright 2017 American Chemical Society.

Author contributions:

AJW: Designed experiments, performed experiments, analyzed data, co-wrote manuscript.

YCH: Performed experiments

ARB: Performed experiments

MMM: Performed experiments

BP: Performed experiments

AKT: Performed experiments

MC: helped manage her student

SNL: Helped managed his student

LM: Analyzed data, co-wrote manuscript

## ABSTRACT

Understanding how membrane proteins interact with detergents is of fundamental and practical significance in structural and chemical biology as well as in nanobiotechnology. Current methods for inspecting protein–detergent complex (PDC) interfaces require high concentrations of protein and are of low throughput. Here, we describe a scalable, spectroscopic approach that uses nanomolar protein concentrations in native solutions. This approach, which is based on steady-state fluorescence polarization (FP) spectroscopy, kinetically resolves the dissociation of detergents from membrane proteins and protein unfolding. For satisfactorily solubilizing detergents, at concentrations much greater than the critical micelle concentration (CMC), the fluorescence anisotropy was independent of detergent concentration. In contrast, at detergent concentrations comparable with or below the CMC, the anisotropy readout underwent a time-dependent decrease, showing a specific and sensitive protein unfolding signature. Functionally reconstituted membrane proteins into a bilayer membrane confirmed predictions made by these FP-based determinations with respect to varying refolding conditions. From a practical point of view, this 96-well analytical approach will facilitate a massively parallel assessment of the PDC interfacial interactions under a fairly broad range of micellar and environmental conditions. We expect that these studies will potentially accelerate research in membrane proteins pertaining to their extraction, solubilization, stabilization, and crystallization, as well as reconstitution into bilayer membranes.

## INTRODUCTION

Understanding the protein–detergent complex (PDC)(1) interface remains a ubiquitous problem in the extraction, solubilization, stabilization, and crystallization of membrane proteins. The PDCs were traditionally examined by numerous techniques, including small-angle X-ray

scattering (SAXS),(2) circular dichroism (CD) spectroscopy,(3) size-exclusion chromatography,(4) and tryptophan fluorescence quenching.(5) These approaches were used to determine a variety of physical properties of the proteomicelles, such as their size, shape, and distributions. In the past few years, there has been an increased interest in examining the details of the interfacial forces that govern the PDC formation as well as their effects on the protein structure, stability, and dynamics. CD spectroscopy was frequently used to determine the secondary structure and thermostability of membrane proteins under a variety of detergent solubilization conditions.(5, 6) Recently, the Brouillette group has developed differential scanning calorimetry (DSC) approaches for the inspection of the interactions between detergents and extramembranous water-soluble domains of the human cystic fibrosis transmembrane conductance regulator (hCFTR).(7, 8) Isothermal titration calorimetry (ITC) was also employed for the determination of thermodynamic phase diagrams of ternary lipid–detergent–protein systems and their deviation from data obtained in protein-free lipid–detergent mixtures.(9) Moreover, nuclear magnetic resonance (NMR) spectroscopy was extensively used for the examination of the interactions of membrane proteins with detergent micelles.(10, 11) In particular, solid-state NMR is a versatile approach for the investigation of membrane proteins in various detergent and lipid environments, including cell membranes.(12) For example, Frey and colleagues (2017) were able to characterize the internal backbone and side chain flexibility of the outer membrane protein X (OmpX) in micelles, bicelles, and nanodiscs using NMR relaxation in a broad range of time scales, from picoseconds to milliseconds.(13) Such a versatility and time resolution of NMR spectroscopy often facilitates direct correlations of the collected data with membrane protein folding(14) and function.(12)

However, current approaches require high concentrations of proteins. Such a problem is especially critical to membrane proteins, because the yield is unpredictable due to limited expression levels and unproductive aggregation. In addition, the signal-to-noise ratio of the most spectroscopic and calorimetric techniques is severely deteriorated by protein aggregation. As a result, these approaches cannot be readily expanded to a high-throughput format for the concurrent inspection of a broad array of environmental conditions and interacting partners. These problems restrain opportunities for acquiring a better quantitative and mechanistic information on the PDC interactions.

Here, we developed a single-fluorophore, 96-well plate-reader approach for obtaining a fast and scalable readout of the PDC interactions at low nanomolar concentrations of the protein. This assay relied on the use of fluorescence polarization (FP) spectroscopy.(15-18) In the past, FP spectroscopy was employed for inspecting the PDC interactions with either mild(19) or harsh detergents(20-22) and water-soluble proteins. In contrast to this work, prior sodium dodecyl sulfate (SDS)–protein interaction studies were focused on the mechanistic understanding of harsh detergent-induced protein unfolding(22) and resistance of proteins to denaturation(21) under diverse environmental conditions.

The steady-state FP spectroscopy facilitates the examination of the rotational mobility of a labeled protein. This analysis can be conducted by exciting a chemically attached fluorophore with plane-polarized light. If the labeled protein binds to a detergent micelle, then a slowed rotational diffusion of the PDC will be accompanied by an increased emission in the plane parallel to the polarized light and a decreased emission in the plane perpendicular to the polarized light. This emission change is measured and analyzed by a ratio between the numbers of free and bound proteins.(16) We postulated that the dynamics of the dissociation of the PDC

at detergent concentrations below the critical micelle concentration (CMC) can be examined by the steady-state fluorescence anisotropy and kinetic readouts. As a test case, we explored the detergent desolvation-induced unfolding of protein nanopores using ferric hydroxamate uptake component A (FhuA),(23) a monomeric outer membrane  $\beta$ -barrel protein of *Escherichia coli*. We employed FhuA  $\Delta C/\Delta 5L$ , an extensive truncation mutant (Figure 1),(24) so that FhuA was converted from a non-ion conducting transmembrane protein(25) to a large-conductance nanopore. Therefore, this redesigned protein nanopore enabled parallel inspections of the anisotropy readout of detergent-refolded FhuA in solution and its ion transport activity, as judged by single-molecule electrophysiology in planar lipid membranes.

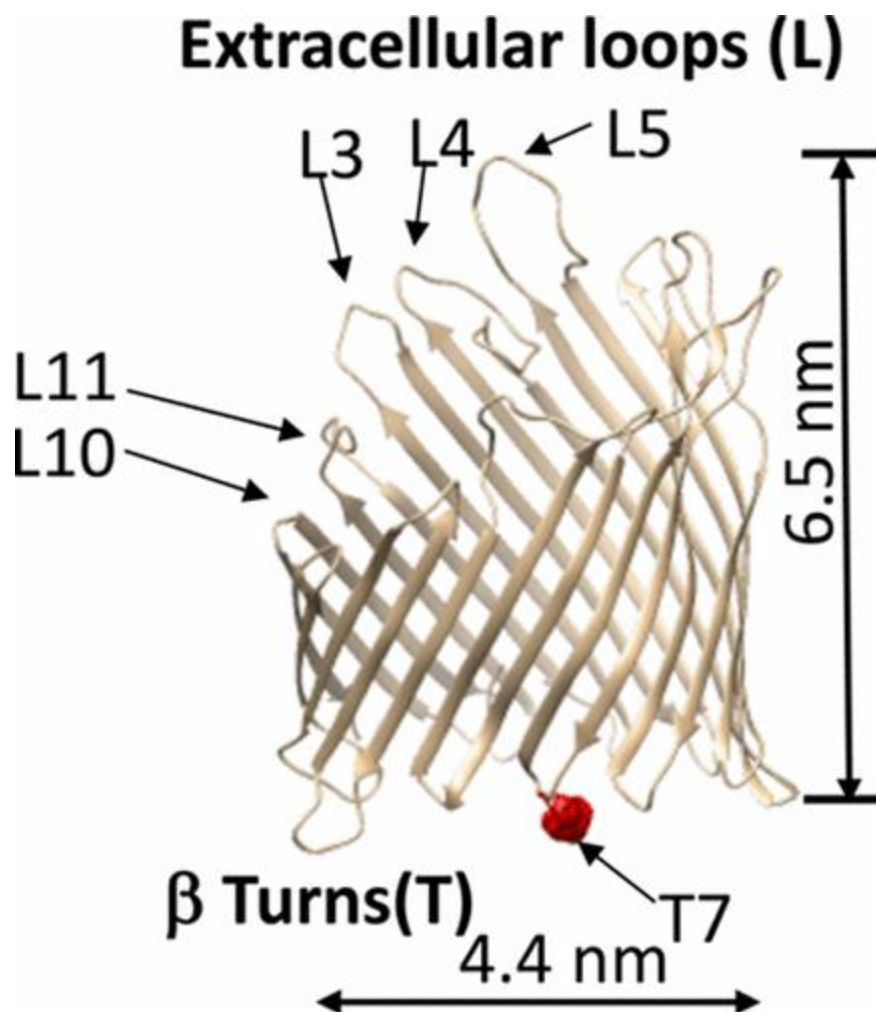


**Figure 1. Side view of the FhuA  $\Delta C/\Delta 5L$  protein,(24) illustrating five truncated extracellular loops, L3, L4, L5, L10, and L11 of FhuA by top arrows.(23) The bottom arrow indicates the T7  $\beta$  turn and site for protein labeling with Texas Red, which is marked by a red sphere.**

We examined the interactions of this redesigned  $\beta$ -barrel protein nanopore with 12 detergents of diverse hydrophilic head groups and hydrophobic tails. This FP-based analytical approach enabled the determination of the apparent dissociation constants of the PDC,  $K_d$ , over a 4 orders of magnitude range. It should be noted that the detergent desolvation of a protein nanopore is intimately related to its unfolding owing to detergent depletion in its proximity. From a practical point of view, this approach facilitates the detection of low-affinity PDC interfacial interactions, whereas the signal-to-noise ratio is not significantly impaired by the extent of protein aggregation. Moreover, the ability to obtain quantitative information about specific detergent–membrane protein interactions in a high-throughput format will be valuable by identifying satisfactory solvation and crystallization conditions for structural studies of membrane proteins.(26)

## **EXPERIMENTAL SECTION**

### **Refolding of FhuA $\Delta C/\Delta 5L$**

We employed a rapid-dilution refolding protocol(27) to obtain FhuA  $\Delta C/\Delta 5L$ . 40  $\mu$ L of  $6 \times$  His<sup>+</sup>-tag purified denatured protein was 50-fold diluted into 200 mM NaCl, 50 mM HEPES, pH 7.4 solutions at 4 °C, which contained various detergents at concentrations above the CMC (Table S1). Different starting detergent concentrations were as follows (when multiple concentrations are given, the lower concentrations were needed to get dilutions with a low enough detergent concentration to cover the required range): (i) for n-decyl- $\beta$ -d-maltopyranoside (DM), n-undecyl- $\beta$ -d-maltopyranoside (UM), and n-dodecyl- $\beta$ -d-maltopyranoside (DDM), we used 5 and 20 mM starting detergent concentration; (ii) 50 mM 4-cyclohexyl-1-butyl- $\beta$ -d-maltoside (CYMAL-4); (iii) 5 and 20 mM n-dodecyl-N,N-dimethylglycine (LD); (iv) 20 mM 1-

lauroyl-2-hydroxy-sn-glycero-3-phosphocholine (LysoFos); (v) 0.2, 0.5, 1, and 25 mM 1-palmitoyl-2-hydroxy-sn-glycero-3-[phospho-rac-(1-glycerol)] (LPPG); (vi) 50 mM 3-[(3-cholamidopropyl)-dimethylammonio]-1-propanesulfonate] (CHAPS); (vii) 100 mM N,N'-bis(3-d-gluconamidopropyl)cholamide (Big CHAP); (viii) 50 mM n-octyl- $\beta$ -d-glucoside (OG); and (ix) 50, 100, and 250 mM n-octyl- $\beta$ -d-thioglucoside (OTG). All detergents were obtained from Anatrace (Maumee, OH), except LPPG, which was purchased from Avanti Polar Lipids (Alabaster, AL). All detergent solutions were freshly prepared to avoid hydrolysis and oxidation.(28)

### **Anisotropy Measurements**

We employed a SpectraMax I3 plate reader (Molecular Devices, Sunnyvale, CA) equipped with the Paradigm detection cartridge for Rhodamine FP spectroscopy, which features the excitation and emission wavelengths of 535 and 595 nm, respectively. We covalently attached a hydrophilic Texas Red fluorophore(29) to a reactive cysteine sulfhydryl using an engineered flexible Gly/Ser-rich peptide loop within the T7  $\beta$  turn (Figure 1; Supporting Information, Figure S1). A similar fluorophore labeling approach was conducted using an engineered cysteine sulfhydryl on loop L6 of outer membrane protein G (OmpG D224C; Supporting Information, Figure S2).(30) We chose the labeling site on the aqueous phase-exposed regions of the proteins, because Texas Red is a hydrophilic compound. The primary advantage of Texas Red is its optical stability over a broad range of conditions.(31) Measurements were taken on black flat bottom 96-well Costar assay plates (Corning Incorporated Kennebunk, ME). The fluorescence anisotropy was calculated using the parallel,  $I_p(t)$ , and orthogonal,  $I_o(t)$ , time-dependent components of the emission intensity:(31, 32)



$$r(t) = \frac{I_p(t) - GI_o(t)}{I_p(t) + 2GI_o(t)} \quad (1) \quad G = \frac{I_{IHV}}{I_{IHH}} \quad (2)$$

where  $G$  is a sensitivity correction factor for the detection modes when emission polarizers are oriented vertically and horizontally. Thus where  $I_{HV}$  is the intensity with the excitation and emission polarizers in a horizontal and vertical orientation, respectively, whereas  $I_{HH}$  is the intensity with both the excitation and emission polarizers in a horizontal orientation. Because this study was conducted on a single instrument,  $G$  was assumed to be 1, and the numbers reported are uncalibrated anisotropy. The anisotropy measurements were conducted by taking the refolded protein sample and diluting it within individual wells with buffer containing various detergent concentrations. In this way, we gradually decreased the detergent concentration in individual wells, while keeping the final protein concentration constant at 28 nM. The anisotropy was determined for time periods in the range 30–60 min. Then samples were covered and placed at 4 °C, and end points of the PDC reaction were collected 24 h later for equilibrium determinations (Supporting Information, Figure S3). Anisotropy traces presented throughout this article represent averages  $\pm$  SD over a number of at least three independent data acquisitions.

## RESULTS

### Experimental Rationale

We found that bringing the protein from a Gdm-HCl-denaturing condition to a detergent concentration above the CMC, via a fast-dilution refolding protocol,<sup>(27)</sup> was accompanied by a maximum fluorescence anisotropy,  $r_{max}$  (Table S2). When the detergent concentration was brought to a value below the CMC, a reproducible and gradual time-dependent decrease in the fluorescence anisotropy was detected (Figure 2A–C). We interpret this decrease in the anisotropy

as the dissociation of the detergent from the nanopore. This detergent desolvation-induced unfolding resulted in a decrease in the hydrodynamic radius of the protein nanopore, thereby leading to an increase in its local mobility. Such an interpretation was also supported by a decrease in the anisotropy end point ( $r_{\min}$ ) due to a gradually reduced final detergent concentration ( $c$ ) within the well (Figure 2D). Moreover, the equilibrium anisotropy end points showed a clear two-state transition between  $r_{\min}$  and  $r_{\max}$ . In conclusion, detergent-solubilized proteins were characterized by a maximum anisotropy,  $r_{\max}$ , whereas detergent-desolvated proteins were featured by an absolute minimum anisotropy,  $r_{\min}$  (Table S2).

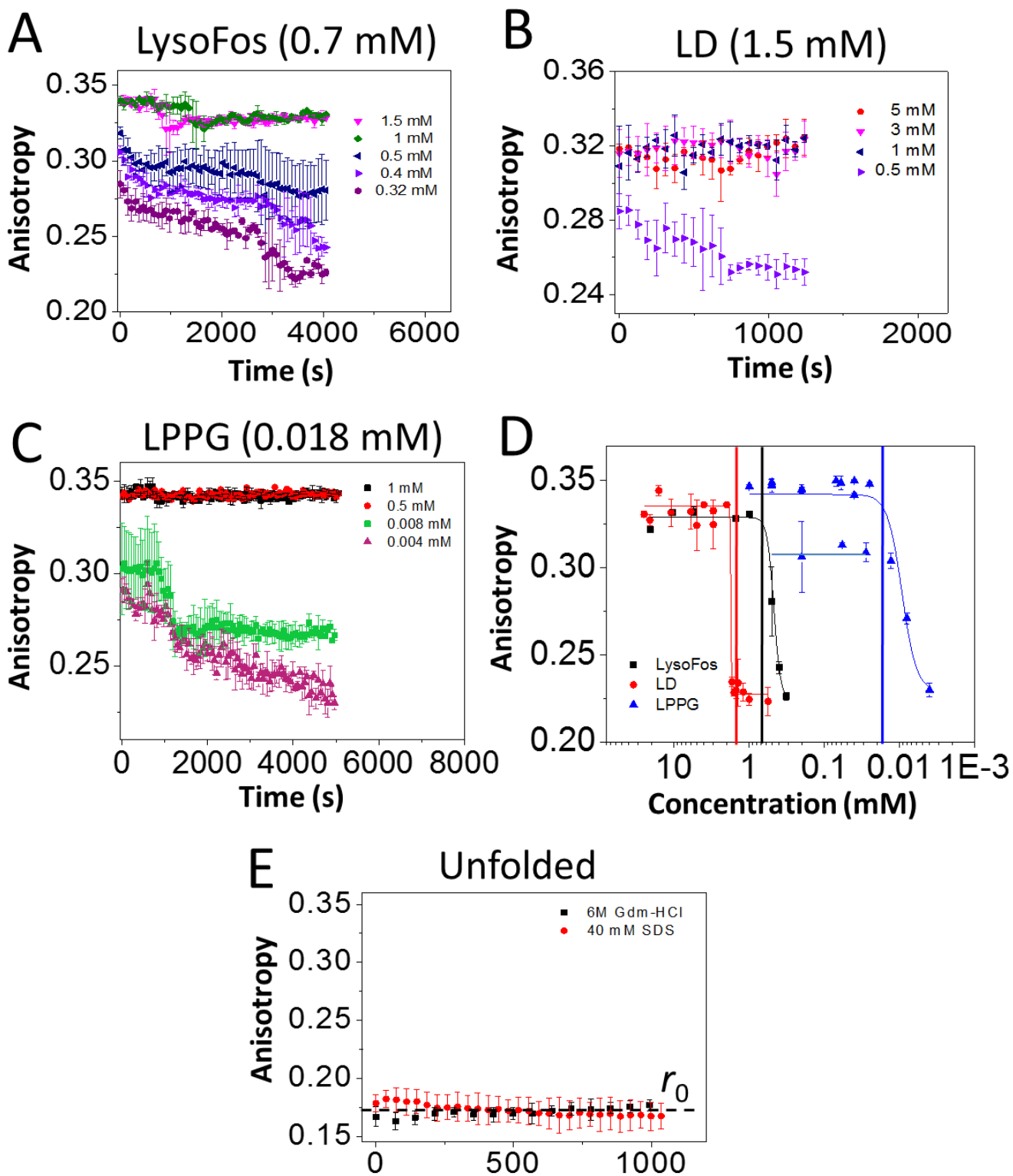


**Figure 2. Time-dependent anisotropy showing the protein–detergent complex (PDC) interfacial dynamics of FhuA  $\Delta C/\Delta 5L$ . The anisotropy data were acquired by adding overnight refolded protein to a bath of varying detergent concentration. All anisotropy measurements were carried out at room temperature in 200 mM NaCl, 50 mM HEPES, pH 7.4. The starting detergent concentrations were as follows: (A) 20 mM LysoFos; (B) 5 and 25 mM LD; and (C) 0.2, 0.5, and 1 mM LPPG. In (D), concentration–response anisotropy changes as a result of the PDC dissociation are shown. The horizontal axis indicates individual dilutions of detergent concentrations, while keeping the final protein concentration constant at 28 nM (see the Experimental Section). The anisotropy values on the vertical axis were collected 24 h later for equilibrium determinations. The LPPG data points belonging to the maximum state ( $r_{\max} = \sim 0.342$ ) were obtained when the protein was refolded in either 0.5 or 1 mM LPPG. The orange horizontal line on the LPPG data points corresponds to a secondary maximum anisotropy value,  $r_{\max} = 0.31$ , when the protein was refolded in 200  $\mu$ M LPPG. (E) This panel shows a low anisotropy value,  $r_1$ , which was recorded either in the presence of 40 mM SDS or 6 M Gdm-HCl. The top of each panel or vertical bars indicate the CMC (Table S1).**

### **Specificity and Sensitivity of the Time-Dependent Anisotropy on Detergent Properties**

#### **LPPG Exhibited a Strong Binding Affinity to FhuA $\Delta C/\Delta 5L$**

Here, we show a clear distinction among the time-dependent anisotropy signatures acquired with anionic and zwitterionic detergents, such as LysoFos (Figure 2A), LD (Figure 2B), and LPPG (Figure 2C). LPPG was able to maintain a uniform  $r_{\max}$ -based PDC population when the protein was solubilized into a detergent concentration of 1 mM (Figure 2C and Supporting Information,

Figure S4). To probe the LPPG-desolvation process of the protein, we solubilized FhuA  $\Delta C/\Delta 5L$  in 0.5 and 0.2 mM LPPG. Indeed, an anisotropy decrease was noticed at very low final LPPG concentrations of 4 and 8  $\mu\text{M}$ . For the sake of plot simplicity in Figure 2C, we illustrated only a few time-dependent anisotropy traces (others are in the Supporting Information, Figure S5). The presence of an excess of denaturing agent (6 M Gdm-HCl) revealed a low anisotropy of  $\sim 0.17$ , most likely due to a drastic increase in mobility of the protein in the denatured state (Figure 2E). Moreover, the observation of the absolute recorded minimum anisotropy,  $r_1$  (the dashed horizontal line), under denaturing conditions in the presence of 40 mM SDS, a harsh anionic surfactant, indicates that  $r_1$  corresponded to the highest tumbling rate of the protein nanopore. The concentration–response curves of the detergent-desolvation phases are Langmuir–Hill isothermal dissociation plots (Figure 2D).<sup>(33)</sup> These equilibrium concentration–response curves were fitted by a symmetrical four-parameter Hill equation, as previously conducted in other receptor–ligand binding assays:<sup>(34)</sup>

$$r(c) = \frac{r_{\min} + r_{\max} \left( \frac{c}{c_0} \right)^p}{1 + \left( \frac{c}{c_0} \right)^p} \quad (3)$$

Such a fitting procedure implied the assumption that the solvent-accessible surface of the protein exhibits individual binding sites for specific detergents. Here,  $r_{\min}$  and  $r_{\max}$  indicate the above-mentioned minima and maxima of anisotropy, respectively (Supporting Information, Table S2). We also assumed that  $r_{\max}$  corresponds to conditions in which all proteins ( $P_{\text{tot}}$ ) are fully solvated (e.g., all binding sites are occupied), whereas  $r_{\min}$  corresponds to conditions in which all proteins are desolvated (e.g., all detergent monomers are released; Supporting Information).  $p$  denotes the Hill coefficient. Assuming that all detergent molecules bind to the protein surface

with a similar binding affinity,  $p$  unambiguously indicates whether this binding occurs with a positive ( $p > 0$ ) or a negative cooperativity ( $p < 0$ ). It does not mean that  $p$  is equal to the exact number of binding sites of the protein surface for a certain detergent.<sup>(33)</sup> All  $p$  values were greater than 1 (Supporting Information, Table S3), suggesting that several to many detergent monomers bind to the protein surface with positive cooperativity. The Hill coefficients are nonintegers, because they are likely affected by intermediate state(s) of detergent–protein bindings, which are weighted by their distribution fractions. The midpoint of the protein unfolding transition corresponds to a concentration  $c_0$ , which is the apparent dissociation constant ( $K_d$ ; Table S3). The slope factor,  $q$ , is the slope of the unfolding transition at half saturation and is expressed in  $\text{mM}^{-1}$ .  $q$  is also the steepness of the protein unfolding transition at half detergent saturation. When the protein was solubilized in 200  $\mu\text{M}$  LPPG, we recorded data points corresponding to a substantially decreased  $r_{\text{max}}$  (the orange horizontal line, Figure 2D). This was likely caused by the inability to completely solubilize a large fraction of the proteins present in solution, otherwise achievable in 1 and 25 mM LPPG. We expanded our FP measurements to the steroidal group-based detergents, which included the zwitterionic CHAPS and Big CHAP (Supporting Information, Figure S6). CHAPS dissociated quickly from FhuA  $\Delta\text{C}/\Delta\text{5L}$  at a concentration of 2.1 mM, which is approximately 4-fold lower than the CMC. The long-lived fluctuations in the anisotropy signal were noticed when Big CHAP-solubilized FhuA  $\Delta\text{C}/\Delta\text{5L}$  was inspected, suggesting very weak PDC interactions (Table S3).

$$q = \frac{p(r_{\text{max}} - r_{\text{min}})}{4c_0} = \frac{p(r_{\text{max}} - r_{\text{min}})}{4K_d} \quad (4)$$

### **Neutral, Maltoside-Containing Detergents**

The same experimental approach was conducted in the case of four maltoside-containing detergents: DDM, UM, DM, and CYMAL-4 (Supporting Information, Figure S7). The first three detergents have 12, 11, and 10 alkyl carbons, respectively, whereas CYMAL-4 is also a maltoside-containing detergent with a very short hydrophobic tail, which includes only 4 alkyl carbons as well as a cyclohexyl group. It is worth mentioning that these time-dependent kinetic reads reveal the time scale of the detergent desolvation-induced protein unfolding. For example, at a DM concentration of 0.45 mM, the dissociation of detergent from FhuA  $\Delta C/\Delta 5L$  underwent three phases with lifetimes from a few minutes to tens of minutes.

### **Dependence of the Detergent Desolvation on the Nanopore Electrostatics**

To further examine the specificity of the anisotropy readout on nanopore properties, we analyzed four proteins of closely similar structure but of varying isoelectric point. These were wild-type OmpG(35) and three FhuA derivatives, FhuA  $\Delta C/\Delta 5L$ , FhuA  $\Delta C/\Delta 5L_{25N}$ , and FhuA  $\Delta C/\Delta 7L_{30N}$  (Figure 3A).<sup>(24)</sup> FhuA  $\Delta C/\Delta 5L_{25N}$  is a FhuA  $\Delta C/\Delta 5L$ -based nanopore, whose 25 negative residues were neutralized, whereas FhuA  $\Delta C/\Delta 7L_{30N}$  features 30 such negative neutralizations and further truncation of four major extracellular loops (L4, L5, L7, and L8). For all FhuA-based nanopores, Texas Red was attached on T7  $\beta$  turn. The isoelectric points of OmpG, FhuA  $\Delta C/\Delta 5L$ , FhuA  $\Delta C/\Delta 5L_{25N}$ , and FhuA  $\Delta C/\Delta 7L_{30N}$  are 4.4, 5.7, 9.3, and 9.6, respectively; thereby, at physiological pH, the first two nanopores are acidic, whereas the other two are basic. Figure 3B,C shows the dose–response anisotropy following LysoFos and OG depletion in the chamber, respectively. We were able to refold both acidic nanopores in OG and

noted the two-state protein unfolding transition. In contrast, experiments with basic nanopores showed low anisotropy end point values of  $\sim 0.17$ , because of very weak PDC interfacial interactions (Supporting Information, Figure S8). Therefore, the anisotropy values continue to decrease even at concentrations well above the CMC. A similar trait, but with a different anisotropy signature, was observed with the solubilization of FhuA  $\Delta C/\Delta 5L$  in OTG, another neutral, glucoside-containing detergent. Remarkably, distinctive anisotropy signatures of OG and OTG were noted, although the only molecular difference between the two detergents is the replacement of an oxygen with a sulfur atom (Supporting Information, Figure S9).



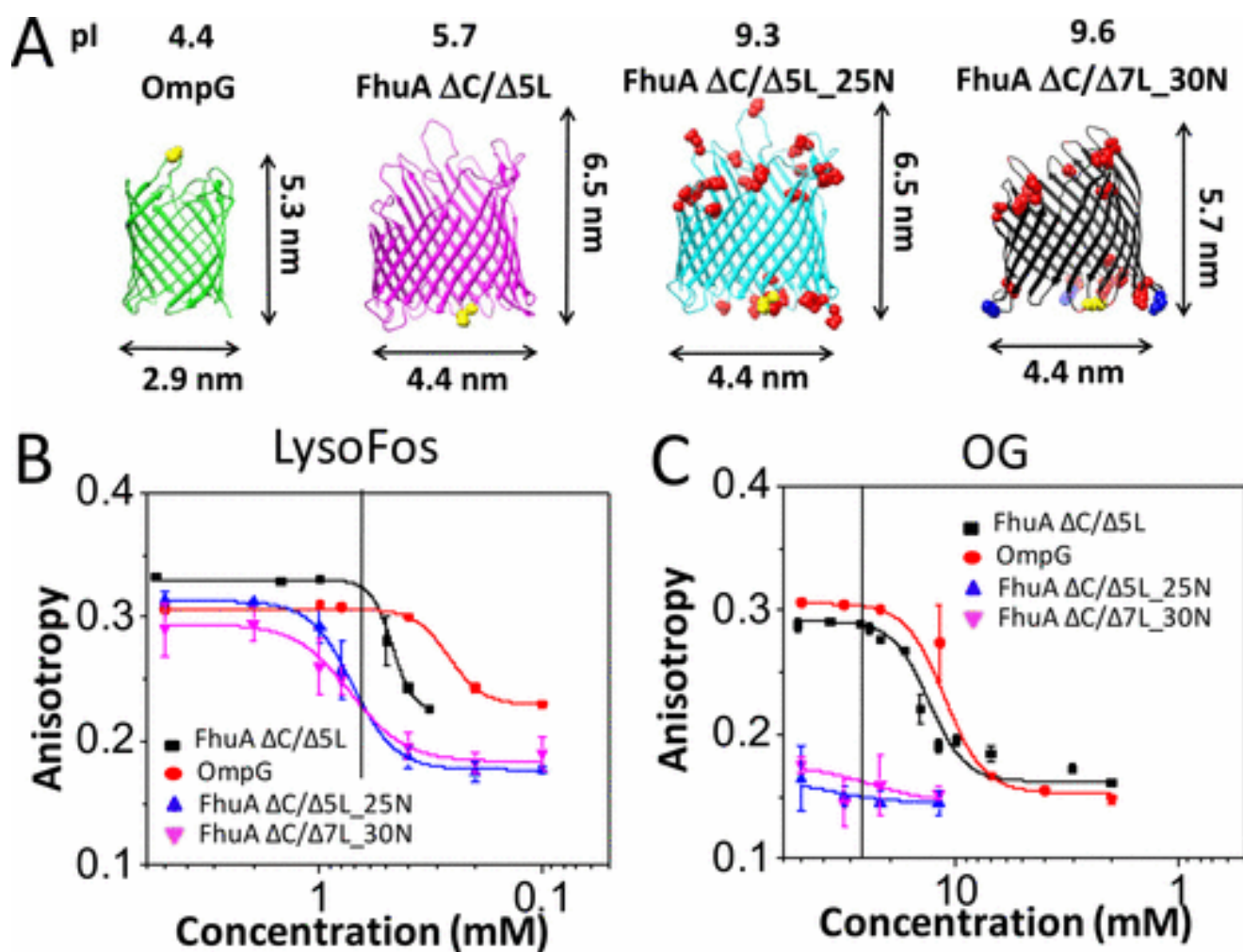


**Figure 3.** Concentration–response anisotropy changes recorded with protein nanopores of varying isoelectric point pI. (A) Side views of the four protein nanopores inspected in this work, OmpG, FhuA  $\Delta C/\Delta 5L$ , FhuA  $\Delta C/\Delta 5L_{25N}$ , and FhuA  $\Delta C/\Delta 7L_{30N}$ . Locations of fluorophore attachment are marked in yellow. Negative charge neutralizations with respect to FhuA  $\Delta C/\Delta 5L$  are marked in red. For FhuA  $\Delta C/\Delta 7L_{30N}$ , there are three additional lysine mutations in the  $\beta$  turns (marked in blue), out of which two are negative-to-positive charge reversals.(44) The top of each cartoon indicates the nanopore abbreviated name and its respective isoelectric point. (B) Dose–response of the LysoFos depletion in the well; (C) Dose–response of OG depletion in the well. Vertical bars indicate the CMC (Table S1). The

**horizontal axis indicates individual dilutions of detergent concentrations, while keeping the final protein concentration constant at 28 nM (see the Experimental Section). The anisotropy values on the vertical axis were collected 24 h later for equilibrium determinations. All of the other experimental conditions were the same as in Figure 2.**

### **Predictive Power of This Analytical Approach**

We validated this FP-based analytical assay using two independent approaches. First, the unusually strong binding interactions between LPPG and FhuA  $\Delta C/\Delta 5L$  (Figure 2C,D and the Supporting Information, Table S3) would normally result in a highly thermostable LPPG-solubilized membrane protein. This expectation was tested using temperature-dependent circular dichroism (CD) spectroscopy for identifying the presence of the  $\beta$ -structure in solution. Second, we examined whether the zwitterionic and neutral detergents that solubilized well FhuA  $\Delta C/\Delta 5L$  can be used for the reconstitution of uniform and stable protein nanopores into planar lipid membranes.

Figure 4A confirmed that solubilizing detergents LPPG, LysoFos, UM, DM, and DDM facilitate the formation of the  $\beta$  structure in solution (the method details are provided in the Supporting Information).<sup>(36)</sup> Protein samples solubilized with the other detergents did not exhibit a satisfactory CD signal under similar conditions. In Figure 4B, we show a clear distinction in the temperature-dependent profile between LPPG and LysoFos. Protein refolded in LysoFos began losing CD signal by  $\sim 50$  °C, with measurements beyond 67 °C rendered impossible by irreversible protein aggregation and visible precipitation in the cuvette. On the contrary, the CD signal recorded with LPPG-refolded FhuA  $\Delta C/\Delta 5L$  continued to decrease slowly, while no visible precipitation was noted, suggesting a much more thermodynamically stable protein

structure. These results are in excellent accord with the FP data, which indicated unusually strong binding interactions between LPPG and FhuA  $\Delta C/\Delta 5L$ . To validate the functional pore-forming properties of proteins solubilized with satisfactory detergents, we conducted single-molecule electrophysiology experiments (the method details are provided in the Supporting Information).<sup>(37, 38)</sup> In these experiments, we used representative detergents of three different classes, in which a detergent desolvation-induced protein unfolding transition was noted (LysoFos, Figure 3B; OG, Figure 3C; DDM, Supporting Information, Figure S7E). Indeed, we were able to confirm uniform single-channel insertions of LysoFos-, OG-, and DDM-refolded FhuA  $\Delta C/\Delta 5L$  nanopores (Figure 4C). The distributions of single-channel conductance values obtained with FhuA  $\Delta C/\Delta 5L$  refolded in each detergent provided a similar average unitary conductance of  $\sim 4$  nS (Figure 4D). Relatively uniform-conductance channels were observed with the LysoFos-refolded protein, but  $\sim 15\%$  and  $\sim 25\%$  outliers of the average conductance were detected with DDM- and OG-refolded proteins, respectively. This finding indicates that the uniformity of the histogram peak of the single-channel conductance was impaired by the refolding detergent (Supporting Information, Figures S10 and S11).

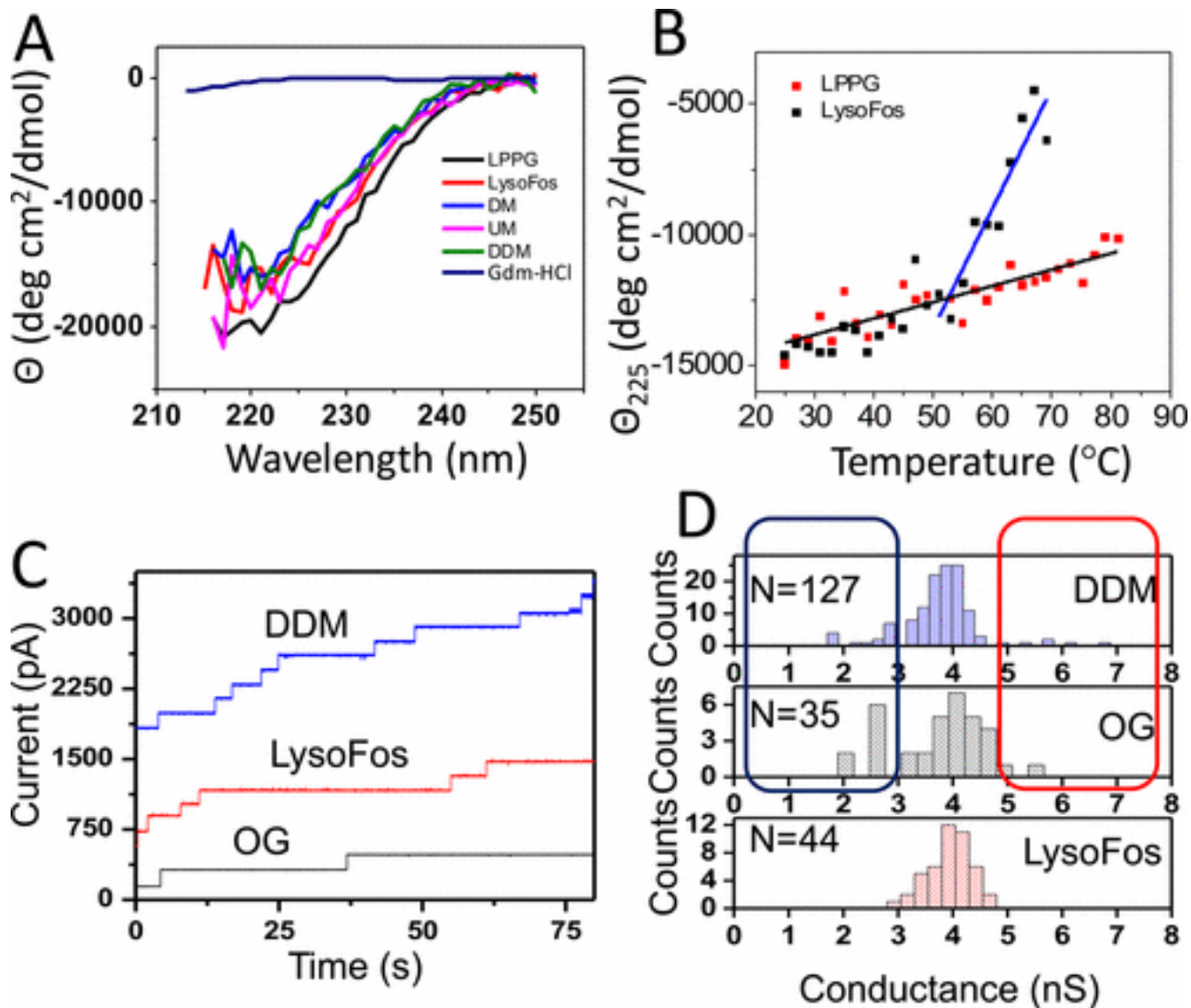


**Figure 4. Unusual thermostability of LPPG-refolded protein nanopores and functional reconstitution of LysoFos-, DDM-, and OG-refolded protein nanopores. (A) Wavelength circular dichroism scans of  $\sim 1 \mu\text{M}$  FhuA  $\Delta\text{C}/\Delta\text{5L}$  in 200 mM NaCl, 50 mM potassium phosphate, pH 7.4 with 20 mM of the specified detergent. In the negative control experiment, we used a buffer solution containing 6 M Gdm-HCl. (B) Temperature-dependent ellipticity  $\Theta_{225}$  of FhuA  $\Delta\text{C}/\Delta\text{5L}$  in either 20 mM LPPG or in 20 mM LysoFos.**

**For DDM, UM, and DM, we could not achieve a sufficiently high aggregation-free protein concentration. (C) Representative stepwise insertions of single nanopores, over at least six distinct experiments, after the addition of DDM- (blue), OG- (black), or LysoFos-refolded (red) FhuA  $\Delta C/\Delta 5L$  at an applied transmembrane potential of +40 mV. 40  $\mu L$  of pure and denatured  $6 \times His^+$ -tagged FhuA  $\Delta C/\Delta 5L$  was 50-fold diluted into 29 mM DDM, 85 mM OG, or 16 mM LysoFos, containing 200 mM NaCl, 50 mM Tris.HCl, 1 mM EDTA, pH 8.0. The dilution ratio of the refolded protein within the bilayer chamber was  $\sim 1:1000$ . Therefore, the presence of detergent within the bilayer chamber did not affect the stability of the membrane.(45) (D) The unitary-conductance histograms of DDM-, OG-, and LysoFos-refolded FhuA  $\Delta C/\Delta 5L$ . The electrical recordings were collected using 1 M KCl, 10 mM potassium phosphate, pH 7.4.**

## **DISCUSSION**

In this work, we show that the FP spectroscopy can be used as a molecular reporter of the detergent desolvation-induced unfolding of a membrane protein. While the local flexibility of the fluorophore can indeed contribute to the steady-state anisotropy value, the unfolding transition only occurs at detergent concentrations comparable with or lower than the CMC. That supports the most likely possibility that the tumbling rate (e.g., rotational correlation time) of the protein nanopore is indeed affected by the detergent coat. On the contrary, at concentrations of satisfactorily solubilizing detergents much greater than the CMC, no significant change in fluorescence anisotropy was noticed. Therefore, the detergent-induced aggregation of several proteins in one large proteomicelle, further declining the rotameric mobility of the protein, is unlikely under these conditions. In some cases, especially at detergent concentrations below their

corresponding CMC, we found either some small discrete changes in anisotropy or increased error bars (e.g., Figure 2A, 0.5, 1, and 1.5 mM LysoFos). This variability resulted, most likely, from the coexistence of multiple substates of the protein nanopores during the desolvation process. These physicochemical alterations are perhaps induced by changes in the internal pressure created by the detergent layer around the protein, leading sometimes to more discrete changes in anisotropy (e.g., Figure 2C, 0.008 mM LPPG).

We interpret that the two-state detergent desolvation-induced protein unfolding plots acquired in this work resulted from the average alterations in the overall cross-sectional size of the PDC due to detergent depletion within the well. Under conditions in which the detergent concentration is below the CMC, stochastic dissociation events of the detergent monomers from the proteomicelle are very likely,<sup>(39)</sup> leading to ruptured proteomicelles containing misfolded or unfolded proteins (Supporting Information, Figure S12 and Table S2). The rotational diffusion coefficients of fully solvated nanopores,  $D_{\text{slow}}$ , for various inspected detergents, were in a broad range,  $0.05\text{--}1.8 \times 10^7 \text{ s}^{-1}$ , revealing greatly distinctive tumbling rates of diverse proteomicelles (details are provided in the Supporting Information). In contrast, the rotational diffusion coefficients of unfolded proteins,  $D_{\text{fast}}$ , spanned a narrow range, between 2.9 and  $6.8 \times 10^7 \text{ s}^{-1}$ . At room temperature, a  $D_{\text{r}} = 3.0 \times 10^7 \text{ s}^{-1}$  corresponds to a rotational correlation time of 5.5 ns for an unfolded FhuA  $\Delta C/\Delta 5L$ , which features a molecular weight of  $\sim 55 \text{ kDa}$ . This is in good accord with the calculated rotational correlation time of 15.4 ns for a 50 kDa-protein at 20 °C.<sup>(40)</sup> Detergent desolvation-induced protein unfolding produced a change in the PDC hydrodynamic radius,  $\Delta R_{\text{h}}$ , within a broad range of 0.6–5.1 nm.

We were able to refold acidic nanopores in OG, and the two-state unfolding transitions of these nanopores were noted under physiological conditions. In contrast, we acquired low anisotropy

signals with the OG-refolded basic nanopores. Therefore, it is very unlikely that we can get functional membrane-inserted FhuA  $\Delta C/\Delta 5L_{25N}$  and FhuA  $\Delta C/\Delta 7L_{30N}$  nanopores under these denaturing conditions. This finding substantiates that the anisotropy readout is not primarily driven by the interaction of the fluorophore with a proteomicelle but the protein–micelle interactions. In other words, even if there is some mobility restraint of the fluorophore dynamics by the detergent coat, the anisotropy readout pertaining to the desolvation kinetics and energetics is strongly dependent on the properties of the PDC interactions. Figure 3C can be considered as a positive control experiment, in which all four anisotropy traces were collected under identical conditions but of strongly varying PDC interfacial interactions.(41)

It is worth mentioning that FhuA  $\Delta C/\Delta 5L$  interacted weakly with OG, as compared with LysoFos and DDM (Supporting Information, Table S3). A large number of unitary conductance outliers were noted with OG. This suggests that the insertion of many misfolded OG-solubilized proteins into bilayer were due to their residual detergent desolvation in aqueous phase (Figure 4D). Although the  $K_d$  values for DDM and LysoFos were closely similar, some unitary conductance outliers observed with DDM, but not LysoFos, imply that a highly uniform conductance peak might be determined by other physicochemical factors as well (e.g., size and packing of the proteomicelles), as the protein insertion is preceded by demicellization. It is also true that the functional activity of membrane proteins is sometimes compromised in part by their reduced internal flexibility within detergent micelles, which is another reason for the appearance of some unitary conductance outliers.(13)

One consequence of the detergent dissociation from membrane proteins is their aggregation. This process is accompanied by changes in the interactions of waters with the protein surface. In the absence of detergent, the waters lose their capacity to form hydrogen bonds with the protein

surface. Therefore, this unusual interaction is entropically unfavorable, leading to minimized interaction interfaces between water molecules and hydrophobic regions of the membrane protein. In this case, the waters are confined in small clusters surrounded by hydrophobically collapsed parts of the protein.

Our FP-based approach can be extended to other applications. For example, the inability to completely extract some lipids from membrane proteins during crystallographic studies is phenomenally interesting, indicating that the lipids have a required structural role for these proteins. With further developments, this FP method may be used to determine changes in the tumbling rate of membrane proteins under native (e.g., in lipid-bound detergent micelles) and denaturing (e.g., in the presence of Gdm-HCl) conditions. FP experiments with specific detergent–lipid solubilization mixtures(9) might potentially generate an understanding of the structural role of these lipids in the stabilization of membrane proteins.

Despite obvious advantages of this FP-based analytical assay, there are a number of limitations. First, this approach is restrained to a low-molecular size fluorophore. Large-molecular size fluorophores (e.g., genetically engineered green fluorescence protein (GFP) and its derivatives) are prone to distort the flexibility, dynamics, and structure of the inspected protein. Second, proteins with multiple native cysteines cannot be used if the approach is extended to time-resolved anisotropy and time-dependent, steady-state FP studies, because individual fluorophore anisotropy spectra can complicate data interpretations due to their diverse residue and solvent environments during the desolvation process. Moreover, a hydrophilic fluorophore needs to be attached within the aqueous phase-exposed domains of the protein for a satisfactory anisotropy signal-to-noise ratio.



In summary, we examined the time-dependent detergent-desolvation of protein nanopores. To our knowledge, this is the first study on the kinetic read of desolvation of water-insoluble proteins at detergent concentrations well below the CMC. This approach can be readily expanded to a broad range of situations for identifying optimized interfacial interactions. These include ionic strength, temperature, osmotic pressure, viscosity, pH, binary and ternary mixtures of detergents, as well as other nonclassical detergent-like compounds, such as lipopeptides(42) and amphipols.(43) Future developments of this analytical approach will likely impact advancements in the synthetic chemistry of newly designed detergent-like molecules and membrane proteins.

**REFERENCES**

1. Vergis, J. M.; Purdy, M. D.; Wiener, M. C. *Anal. Biochem.* 2010, 407, 1– 11, DOI: 10.1016/j.ab.2010.07.019
2. Pollock, N. L.; Satriano, L.; Zegarra-Moran, O.; Ford, R. C.; Moran, O. J. *Struct. Biol.* 2016, 194, 102– 111, DOI: 10.1016/j.jsb.2016.02.004
3. Grosse, W.; Psakis, G.; Mertins, B.; Reiss, P.; Windisch, D.; Brademann, F.; Burck, J.; Ulrich, A.; Koert, U.; Essen, L. O. *Biochemistry* 2014, 53, 4826– 4838, DOI: 10.1021/bi500660q [ACS Full Text ACS Full Text],
4. Ehsan, M.; Du, Y.; Scull, N. J.; Tikhonova, E.; Tarrasch, J.; Mortensen, J. S.; Loland, C. J.; Skiniotis, G.; Guan, L.; Byrne, B.; Kobilka, B. K.; Chae, P. S. *J. Am. Chem. Soc.* 2016, 138, 3789– 3796, DOI: 10.1021/jacs.5b13233
5. Tulumello, D. V.; Deber, C. M. *Biochemistry* 2009, 48, 12096– 12103, DOI: 10.1021/bi9013819
6. Miles, A. J.; Wallace, B. A. *Chem. Soc. Rev.* 2016, 45, 4859– 4872, DOI: 10.1039/C5CS00084J
7. Yang, Z.; Wang, C.; Zhou, Q.; An, J.; Hildebrandt, E.; Aleksandrov, L. A.; Kappes, J. C.; DeLucas, L. J.; Riordan, J. R.; Urbatsch, I. L.; Hunt, J. F.; Brouillette, C. G. *Protein Sci.* 2014, 23, 769– 789, DOI: 10.1002/pro.2460
8. Yang, Z.; Brouillette, C. G. *Methods Enzymol.* 2016, 567, 319– 358, DOI: 10.1016/bs.mie.2015.08.014
9. Jahnke, N.; Krylova, O. O.; Hoomann, T.; Vargas, C.; Fiedler, S.; Pohl, P.; Keller, S. *Anal. Chem.* 2014, 86, 920– 927, DOI: 10.1021/ac403723t
10. Columbus, L.; Lipfert, J.; Jambunathan, K.; Fox, D. A.; Sim, A. Y.; Doniach, S.; Lesley, S. A. *J. Am. Chem. Soc.* 2009, 131, 7320– 7326, DOI: 10.1021/ja808776j
11. Stanczak, P.; Horst, R.; Serrano, P.; Wuthrich, K. *J. Am. Chem. Soc.* 2009, 131, 18450– 18456, DOI: 10.1021/ja907842u
12. Baker, L. A.; Folkers, G. E.; Sinnige, T.; Houben, K.; Kaplan, M.; van der Crujisen, E. A.; Baldus, M. *Methods Enzymol.* 2015, 557, 307– 328, DOI: 10.1016/bs.mie.2014.12.023
13. Frey, L.; Lakomek, N. A.; Riek, R.; Bibow, S. *Angew. Chem., Int. Ed.* 2017, 56, 380– 383, DOI: 10.1002/anie.201608246
14. Raschle, T.; Rios Flores, P.; Opitz, C.; Muller, D. J.; Hiller, S. *Angew. Chem., Int. Ed.* 2016, 55, 5952– 5955, DOI: 10.1002/anie.201509910
15. Kwok, K. C.; Cheung, N. H. *Anal. Chem.* 2010, 82, 3819– 3825, DOI: 10.1021/ac1002245

16. Rossi, A. M.; Taylor, C. W. *Nat. Protoc.* 2011, 6, 365– 387, DOI: 10.1038/nprot.2011.305
17. Turman, D. L.; Nathanson, J. T.; Stockbridge, R. B.; Street, T. O.; Miller, C. *Proc. Natl. Acad. Sci. U. S. A.* 2015, 112, 5697– 5701, DOI: 10.1073/pnas.1505301112
18. Stoddart, L. A.; White, C. W.; Nguyen, K.; Hill, S. J.; Pflieger, K. D. *Br. J. Pharmacol.* 2016, 173, 3028– 3037, DOI: 10.1111/bph.13316
19. Jutila, A.; Zhu, K.; Patkar, S. A.; Vind, J.; Svendsen, A.; Kinnunen, P. K. *Biophys. J.* 2000, 78, 1634– 1642, DOI: 10.1016/S0006-3495(00)76715-4
20. Andersen, K. K.; Oliveira, C. L.; Larsen, K. L.; Poulsen, F. M.; Callisen, T. H.; Westh, P.; Pedersen, J. S.; Otzen, D. J. *Mol. Biol.* 2009, 391, 207– 226, DOI: 10.1016/j.jmb.2009.06.019
21. Fano, M.; van de Weert, M.; Moeller, E. H.; Kruse, N. A.; Frokjaer, S. *Arch. Biochem. Biophys.* 2011, 506, 92– 98, DOI: 10.1016/j.abb.2010.11.012
22. Naidu, K. T.; Prabhu, N. P. *J. Phys. Chem. B* 2011, 115, 14760– 14767, DOI: 10.1021/jp2062496
23. Ferguson, A. D.; Hofmann, E.; Coulton, J. W.; Diederichs, K.; Welte, W. *Science* 1998, 282, 2215– 2220, DOI: 10.1126/science.282.5397.2215
24. Wolfe, A. J.; Mohammad, M. M.; Thakur, A. K.; Movileanu, L. *Biochim. Biophys. Acta, Biomembr.* 2016, 1858, 19– 29, DOI: 10.1016/j.bbamem.2015.10.006
25. Udho, E.; Jakes, K. S.; Buchanan, S. K.; James, K. J.; Jiang, X.; Klebba, P. E.; Finkelstein, A. *Proc. Natl. Acad. Sci. U. S. A.* 2009, 106, 21990– 21995, DOI: 10.1073/pnas.0910023106
26. Pusey, M. L. *Cryst. Growth Des.* 2011, 11, 1135– 1142, DOI: 10.1021/cg1013522
27. Mohammad, M. M.; Iyer, R.; Howard, K. R.; McPike, M. P.; Borer, P. N.; Movileanu, L. J. *Am. Chem. Soc.* 2012, 134, 9521– 9531, DOI: 10.1021/ja3043646
28. Linke, D. *Methods Enzymol.* 2009, 463, 603– 617, DOI: 10.1016/S0076-6879(09)63034-2
29. Titus, J. A.; Haugland, R.; Sharrow, S. O.; Segal, D. M. *J. Immunol. Methods* 1982, 50, 193– 204, DOI: 10.1016/0022-1759(82)90225-3
30. Fahie, M.; Chisholm, C.; Chen, M. *ACS Nano* 2015, 9, 1089– 1098, DOI: 10.1021/nn506606e [ACS Full Text ACS Full Text],
31. Gradinaru, C. C.; Marushchak, D. O.; Samim, M.; Krull, U. J. *Analyst* 2010, 135, 452– 459, DOI: 10.1039/b920242k [CrossRef], [PubMed], [CAS]
32. Jameson, D. M.; Ross, J. A. *Chem. Rev.* 2010, 110, 2685– 2708, DOI: 10.1021/cr900267p
33. Woodbury, C. P. *Introduction to macromolecular binding equilibria*; CRC Press, Taylor & Francis: Boca Raton, FL, 2008.

34. Prinz, H. J. *Chem. Biol.* 2010, 3, 37– 44, DOI: 10.1007/s12154-009-0029-3
35. Liang, B.; Tamm, L. K. *Proc. Natl. Acad. Sci. U. S. A.* 2007, 104, 16140– 16145, DOI: 10.1073/pnas.0705466104
36. Greenfield, N. J. *Nat. Protoc.* 2007, 1, 2527– 2535, DOI: 10.1038/nprot.2006.204
37. Cheneke, B. R.; van den Berg, B.; Movileanu, L. *ACS Chem. Biol.* 2015, 10, 784– 794, DOI: 10.1021/cb5008025
38. Couoh-Cardel, S.; Hsueh, Y. C.; Wilkens, S.; Movileanu, L. *Sci. Rep.* 2016, 6, 24774, DOI: 10.1038/srep24774
39. Borysik, A. J.; Robinson, C. V. *Langmuir* 2012, 28, 7160– 7167, DOI: 10.1021/la3002866
40. Lakowicz, J. R. *Principles of Fluorescence Microscopy*, 2nd ed.; Springer: New York, 2006.
41. Khao, J.; Arce-Lopera, J.; Sturgis, J. N.; Duneau, J. P. *Eur. Biophys. J.* 2011, 40, 1143– 1155, DOI: 10.1007/s00249-011-0745-9
42. Prive, G. G. *Curr. Opin. Struct. Biol.* 2009, 19, 379– 385, DOI: 10.1016/j.sbi.2009.07.008
43. Kleinschmidt, J. H.; Popot, J. L. *Arch. Biochem. Biophys.* 2014, 564, 327– 343, DOI: 10.1016/j.abb.2014.10.013
44. Mohammad, M. M.; Movileanu, L. *J. Phys. Chem. B* 2010, 114, 8750– 8759, DOI: 10.1021/jp101311s
45. Mohammad, M. M.; Tomita, N.; Ohta, M.; Movileanu, L. *ACS Chem. Biol.* 2016, 11, 2506– 2518, DOI: 10.1021/acscchembio.6b00383

# Chapter 3.1 Supplement for Interrogating Detergent Desolvation of Nanopore-Forming Proteins by Fluorescence Polarization Spectroscopy

Aaron J. Wolfe,<sup>1,2</sup> Yi-Ching Hsueh,<sup>1</sup> Adam R. Blanden,<sup>3</sup> Mohammad M. Mohammad,<sup>1</sup> Bach Pham,<sup>4</sup> Avinash K. Thakur,<sup>1,2</sup> Min Chen,<sup>4</sup> Stewart N. Loh,<sup>3</sup> and Liviu Movileanu<sup>1,2,5</sup>

<sup>1</sup>Department of Physics, Syracuse University, 201 Physics Building, Syracuse, New York 13244-1130, USA

<sup>2</sup>Structural Biology, Biochemistry, and Biophysics Program, Syracuse University, 111 College Place, Syracuse, New York 13244-4100, USA

<sup>3</sup>Department of Chemistry, University of Massachusetts, 710 North Pleasant Street, Amherst, Massachusetts 01003-9336, USA

<sup>4</sup>Department of Biochemistry and Molecular Biology, State University of New York Upstate Medical University, 4249 Weiskotten Hall, 766 Irving Av., Syracuse, New York 13210, USA

<sup>5</sup>Department of Biomedical and Chemical Engineering, Syracuse University, Syracuse University, 223 Link Hall, Syracuse, New York 13244, USA

Reprinted with permission from **Aaron J Wolfe**, Y.C. Hsueh, A.R. Blanden, M.M. Mohammad, B. Pham, A.K. Thakur, S.N. Loh, M. Chen, and L. Movileanu, 2017, Interrogating Detergent Desolvation of Nanopore-forming Proteins by Fluorescence Polarization Spectroscopy, *Anal. Chem.* 89(15), 8013-8020. DOI: 10.1021/acs.analchem.7b01339 Copyright 2017 American Chemical Society.

Author contributions:

AJW: Designed experiments, performed experiments, analyzed data, co-wrote manuscript.

YCH: Performed experiments

ARB: Performed experiments

MMM: Performed experiments

BP: Performed experiments

AKT: Performed experiments

MC: helped manage her student

SNL: Helped managed his student

LM: Analyzed data, co-wrote manuscript

## SUPPLEMENTAL EXPERIMENTAL METHODS

**1. Protein overexpression and purification of FhuA-based nanopores under denaturing condition.** Through *de novo* synthesis (Genart, Regensburg, Germany),<sup>1</sup> the *fhuA*  $\Delta c/\Delta 5l$  gene lacked the regions coding for the cork domain and extracellular loops 3, 4, 5, 10, and 11, as compared to the wild-type *fhuA*. *fhuA*  $\Delta c/\Delta 5l\_t7$  was created by inverse PCR<sup>2</sup> using the forward primer 5'-/Phos/TGC GGG TCG TCC GGA GGT ATT GTG GTT ACC GGT GCC GTT T -3' and the reverse primer 5'-/Phos/GCC AGA TGA ACC TCC ATA TTT AAC GCC CAC TTC ATA CTG-3', using pPR-IBA1-*fhuA*  $\Delta c/\Delta 5l$ -6 $\times$ His<sup>+</sup> plasmid as a template. The PCR product was self-ligated to create pPR-IBA1-*fhuA*  $\Delta c/\Delta 5l\_t7$ -6 $\times$ His<sup>+</sup>. This replaced  $\beta$  turn T7 (V<sup>331</sup>PEDRP<sup>336</sup>) with a single cysteine-containing, flexible, GS-rich peptide loop (GGSSGCGSSGGS). Proteins were expressed in *E. coli* BL21 (DE3). Cells, transformed with pPR-IBA1-*fhuA*  $\Delta c/\Delta 5l\_t7$ -6 $\times$ His<sup>+</sup> plasmid, were grown in *LB* media at 37°C until OD<sub>600</sub> ~0.6-0.7, at which time the protein expression was induced with 0.5 mM isopropyl  $\beta$ -D-1-thiogalactopyranoside (IPTG) and allowed to continue until the cell growth plateaued, as measured by OD<sub>600</sub>. Cells were harvested by centrifugation and the pellet was resuspended in 1X PBS, pH 8.0. The cell lysis was conducted using a microfluidizer, model 110L (Microfluidics, Newton, MA). The homogenate was centrifuged for 20 min at 4,000 $\times$ g and 4°C. Inclusion bodies were resuspended and washed 3 times in 1X PBS, 1% Triton X-100, pH 8.0, followed by centrifugation for 30 min at 30,000 $\times$ g and 4°C. Resulting washed inclusion bodies were resuspended in 50 mM HEPES, 1 mM Tris(2-carboxyethyl)phosphine (TCEP), 6 M guanidinium hydrochloride (Gdm-HCl), pH 8.0, which was followed by centrifugation at 30,000 $\times$ g and 4°C to

remove the insoluble materials. The final protein-containing solutions were filtered using 0.2  $\mu\text{M}$  filters (Thermo Fisher Scientific, Rochester, NY). The solubilized proteins were loaded onto a column packed with 2 ml of  $\text{Ni}^{2+}$ -NTA resin (Bio-Rad, Hercules, CA), which was equilibrated in 200 mM NaCl, 50 mM HEPES, 6 M Gdm-HCl, 1 mM TCEP, pH 8.0. The column was washed in two steps with same equilibrating buffer, but containing 5 and 25 mM imidazole, respectively. The proteins were eluted with equilibrating buffer containing 250 mM imidazole in 5 ml fractions. SDS-PAGE was used to monitor the elution profile of pure proteins (**Supporting Information, Fig. S1**). For the sake of simplicity of mutant abbreviations, "T7" is omitted in the case of all FhuA-based nanopores examined in this study.

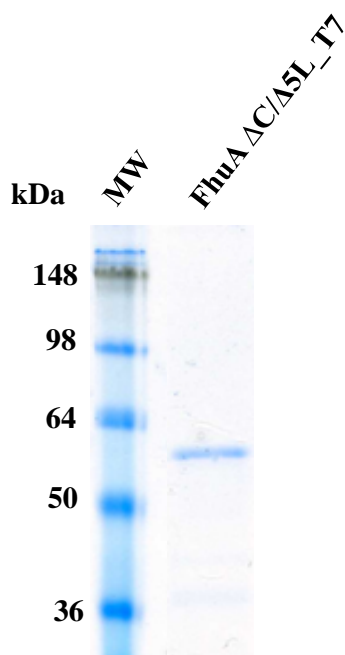


**Figure S1: SDS-PAGE gel of purified FhuA  $\Delta\text{C}/\Delta\text{5L}$ .** In this engineered FhuA protein, the  $\beta$  turn 7 ( $\text{V}^{331}\text{PEDRP}^{336}$ ) was replaced by a single cysteine-containing flexible peptide loop (GGSSGCGSSGGS). Proteins were visualized using GelCode Blue Stain Reagent (Thermo Scientific, Rockford, IL). MW stands for molecular-weight standards. For the sake of simplicity of the abbreviations, "T7" was omitted in the case

of all FhuA-based protein nanopores examined in this study.

## 2. Protein labeling of the FhuA derivatives.

10  $\mu\text{M}$  6 $\times$ His<sup>+</sup>-tagged FhuA  $\Delta\text{C}/\Delta\text{5L}$ , FhuA  $\Delta\text{C}/\Delta\text{5L}_{25\text{N}}$ , and FhuA  $\Delta\text{C}/\Delta\text{7L}_{30\text{N}}$  proteins were incubated with 200  $\mu\text{M}$  Texas Red C2 maleimide (Thermo Fisher Scientific) overnight at room temperature in 200 mM NaCl, 50 mM Tris, 1 mM TCEP, pH 8.0, and 6 M Gdm-HCl. Proteins were separated from free dye by Ni<sup>2+</sup>-NTA column chromatography in the same buffer, but with a 10-200 mM imidazole step gradient. Labeling stoichiometry was between 0.3-0.8 labels/protein using  $\epsilon_{595} = 104,000 \text{ M}^{-1}\text{cm}^{-1}$  for Texas Red and a correction factor of  $0.26 \times \epsilon_{595}$  to account for the dye absorbance at 280 nm.



**3. Expression, purification, and labeling of OmpG D224C proteins.** OmpG D224C (loop L6) was constructed and expressed in *E. coli*, as previously described.<sup>3</sup> Briefly, a single cysteine was introduced to replace the aspartic acid 224 by mutagenesis PCR. BL21 (pLys) *E. coli* cells were transformed with the plasmid pT7-OmpG D224C. Cells were grown in LB medium at 37°C until the OD<sub>600</sub> reached 0.6 and induced with IPTG (0.5 mM, final concentration). Cells were harvested 3 hours later and lysed in lysis buffer (50 mM Tris·HCl, pH 8.0, 150 mM NaCl, 200 µg/ml lysozyme, 1 mM EDTA, 3 mM TCEP) by sonication. The lysate was centrifuged at 19,000 *g* for 30 min before washing once with 30 ml 50 mM Tris·HCl, pH 8.0, 1.5 M Urea, 3 mM TCEP. Then the OmpG-containing inclusion body was dissolved in 30 ml 50 mM Tris·HCl, pH 8.0, 8 M Urea, 3 mM TCEP and passed through a 0.45 µm filter before FPLC purification. All OmpG proteins were purified using a 5ml Q-ionic exchange column (GE Healthcare) and eluted in buffer 50 mM Tris·HCl, pH 8.0, 8 M Urea, 3 mM TCEP, 500 mM NaCl by applying a gradient. The purified protein was incubated with 10 mM freshly prepared TCEP for 30 min on ice to reduce the thiols. The TCEP was then removed using a desalting column equilibrated with buffer 50 mM HEPES, pH 7.0, 150 mM NaCl, 8M Urea. Next, the protein was incubated with Texas Red® C<sub>2</sub> Maleimide (Life Technologies Corp) in a molar ratio 1:20 (protein to dye) at room temperature (~23°C) for 2 hours (or at 4 °C overnight). The reaction mixture was passed through the desalting column once again to remove the unreacted chemicals. The sample was snap-frozen in liquid nitrogen and stored at -80°C. To test the foldability of the labeled protein, an aliquot of the sample was then diluted with the refolding buffer 50 mM Tris·HCl, pH 9.0, 3.25% OG until the final concentration of urea reached 3.0 M. Samples were then incubated at 37 °C for 3 days. The refolding efficiency was determined by SDS-PAGE (**Supporting Information, Fig. S2**).

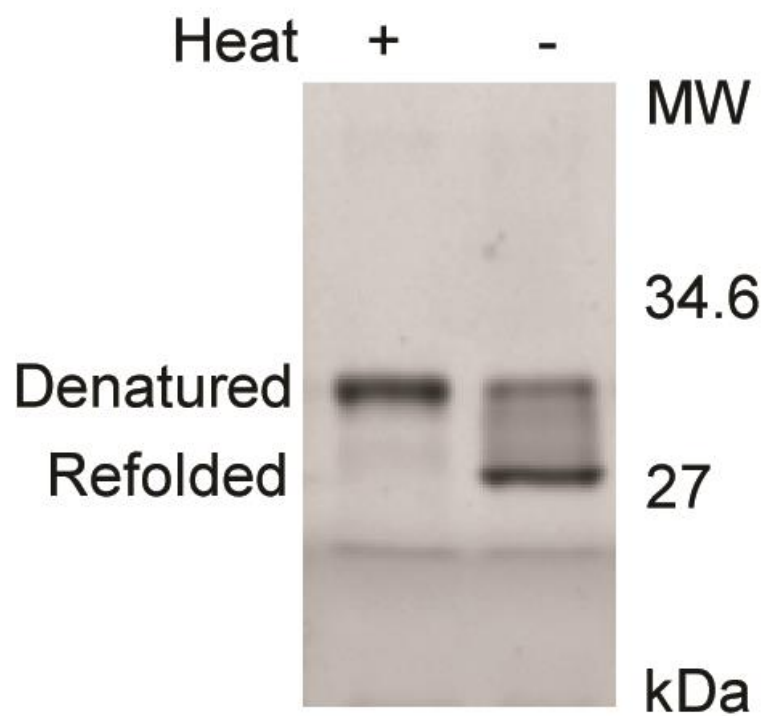


**Figure S2:** SDS-PAGE analysis of Texas Red labeled OmpG. The refolded OmpG construct was either pre-heated at 95°C for 15 min or directly loaded on a 12.5% SDS-PAGE.<sup>3</sup>

**Table S1: Physical features of the detergents used in this study.**

Detergent	FW (Da) <sup>a</sup>	Head group	Aggregation number	CMC (mM) <sup>b</sup>	Micellar weight (kDa)	References
1-lauroyl-2-hydroxy- <i>sn</i> -glycero-3-phosphocholine (LysoFos)	440	Zwitterionic <sup>c</sup>	NA <sup>c</sup>	~0.7 <sup>d</sup>	NA	4
<i>n</i> -dodecyl-N,N-dimethylglycine (LD)	271	Zwitterionic <sup>c</sup>	NA	~1.5 <sup>e</sup>	NA	5
sodium dodecanoyl sarcosine (Sarkosyl)	293	Anionic	2	~14.4 <sup>f</sup>	0.6	6
1-palmitoyl-2-hydroxy- <i>sn</i> -glycero-3-[phospho-rac-(1-glycerol)] (LPPG)	507	Anionic	125	~0.018 <sup>g</sup>	63	4,7
3-[(3-cholamidopropyl)-dimethylammonio]-1-propane sulfonate] (CHAPS)	615	Zwitterionic <sup>c</sup>	~10	~5.9 <sup>h</sup>	6	6
N,N'-bis-(3-D-gluconamidopropyl)cholamide (Big CHAP)	878	Non-ionic	~10	~2.9 <sup>b</sup>	9	6
<i>n</i> -octyl- $\beta$ -D-glucoside (OG)	292	Non-ionic	~27-100	~25 <sup>b</sup>	25	6
<i>n</i> -octyl- $\beta$ -D-thioglucoside (OTG)	308	Non-ionic	~189	~9 <sup>b</sup>	58	6
<i>n</i> -dodecyl- $\beta$ -D-maltoside (DDM)	511	Non-ionic	~78-149	~0.17 <sup>b</sup>	70	6
<i>n</i> -undecyl- $\beta$ -D-maltoside (UM)	497	Non-ionic	~71	~0.59 <sup>b</sup>	35	8
<i>n</i> -decyl- $\beta$ -D-maltoside (DM)	483	Non-ionic	~69	~1.8 <sup>b</sup>	33	6
4-cyclohexyl-1-Butyl- $\beta$ -D-maltoside (CYMAL-4)	481	Non-ionic	~25	~7.6 <sup>b</sup>	12	9

<sup>a</sup>Formula weights of the detergent monomers (FW) were reported by Anatrace (<https://www.anatrace.com/>).

<sup>b</sup>CMC values or aggregation numbers in water were reported by Anatrace (<https://www.anatrace.com/>).

<sup>c</sup>NA stands for not available.

<sup>d</sup>CMC value of LysoFos in 140 mM NaCl, 20 mM Tris-HCl, pH 7.2.<sup>4</sup>

<sup>e</sup>Detergent monomers are neutral at pH > 6.<sup>10</sup>

<sup>f</sup>CMC value in ionic solutions is not available.

<sup>g</sup>CMC value of LPPG in 100 mM Tris.HCl, pH 8.0.<sup>4</sup>

<sup>h</sup>CMC value of CHAPS in 200 mM NaCl.

#### 4. Contributions of anisotropy values to the Langmuir-Hill isothermal binding curves.

Our primary assumption is that during the desolvation process the proteins can be found in either bound or unbound state. A single fluorescent protein nanopore produces two distinct values of anisotropy, either bound,  $r_b$ , or unbound,  $r_u$ . Because anisotropy is an additive property, the overall anisotropy readout is a variable value given by the fraction-weighted sum of the two possible anisotropy values.

If the concentrations of the detergent desolvated and solvated proteins are  $[P]$  and  $[PD_n]$ , respectively, then the total protein concentration,  $P_{tot}$ , is given by

$$P_{tot} = [P] + [PD_n] \quad (\text{S1})$$

Therefore, the equilibrium isothermal binding curves undergo changes in  $r(c)$ , where  $c$  is the detergent concentration, as follows,

$$r(c) = \frac{[P]}{P_{tot}} r_u + \frac{[PD_n]}{P_{tot}} r_b \quad (\text{S2})$$

Using equation (S1), we rearrange (S2), as follows:

$$r(c) = \frac{P_{tot} - [PD_n]}{P_{tot}} r_u + \frac{[PD_n]}{P_{tot}} r_b \quad (\text{S3a})$$

$$r(c) = \left(1 - \frac{[PD_n]}{P_{tot}}\right) r_u + \frac{[PD_n]}{P_{tot}} r_b \quad (\text{S3b})$$

Under extremely low detergent concentration conditions, we assume that most of the proteins will be desolvated (e.g., unbound).

Thereby,

$$P_{\text{tot}} = [P]; [PD_n] = 0 \quad (\text{S4})$$

$$r(c) = r_u = r_{\text{min}} \quad (\text{S5})$$

Equation (S5) indicates that the unbound value of anisotropy is exactly the minimum value of anisotropy,

$r_{\text{min}}$ .

At detergent concentration much greater than the CMC, we assume that all available proteins are solvated. Therefore,

$$P_{\text{tot}} = [PD_n]; [P] = 0 \quad (\text{S6})$$

$$r(c) = r_b = r_{\text{max}} \quad (\text{S7})$$

**5. Secondary structure determination of the refolded FhuA  $\Delta C/\Delta 5L$  protein in solution using circular dichroism.** Circular dichroism (CD) spectra were collected using a Spectropolarimeter (Model 420; Aviv Biomedical, Lakewood, NJ) in a 1 cm x 1 cm quartz cuvette. The cuvette contained protein samples at a concentration of  $\sim 1 \mu\text{M}$ . For temperature melts, samples were heated at  $2^\circ\text{C}/\text{min}$ , with a 30 s equilibration prior to each 20 s data read at every  $1^\circ\text{C}$  with constant magnetic stirring.

## **6. Single-channel and macroscopic electrical recordings using planar lipid bilayers.**

Electrical recordings were conducted using planar bilayer lipid membranes (BLMs) were

published previously.<sup>11</sup> For macroscopic current recordings, FhuA  $\Delta C/\Delta 5L$  was added to the *cis* chamber to a final concentration of  $\sim 100$  ng/ $\mu$ l. 40  $\mu$ l pure and denatured 6 $\times$ His<sup>+</sup>-tagged FhuA  $\Delta C/\Delta 5L$  was 50-fold diluted into 29 mM DDM, 85 mM OG, or 16 mM LysoFos, containing 200 mM NaCl, 50 mM Tris-HCl, 1 mM EDTA, pH 8.0. The diluted protein samples were left overnight at 23°. Aggregated or misfolded proteins were removed by centrifugation for 15 minutes at 16,000 $\times g$ . Current recordings were obtained by using a patch-clamp amplifier (Axopatch 200B, Axon Instruments, Foster City, CA), which was connected to Ag/AgCl electrodes. The *cis* chamber was grounded, so that a positive current represents positive charge moving from the *trans* to *cis* side.

**7. Acquiring equilibrium steady-state endpoints of the FP anisotropy at different concentrations of detergents of varying chemistry.**

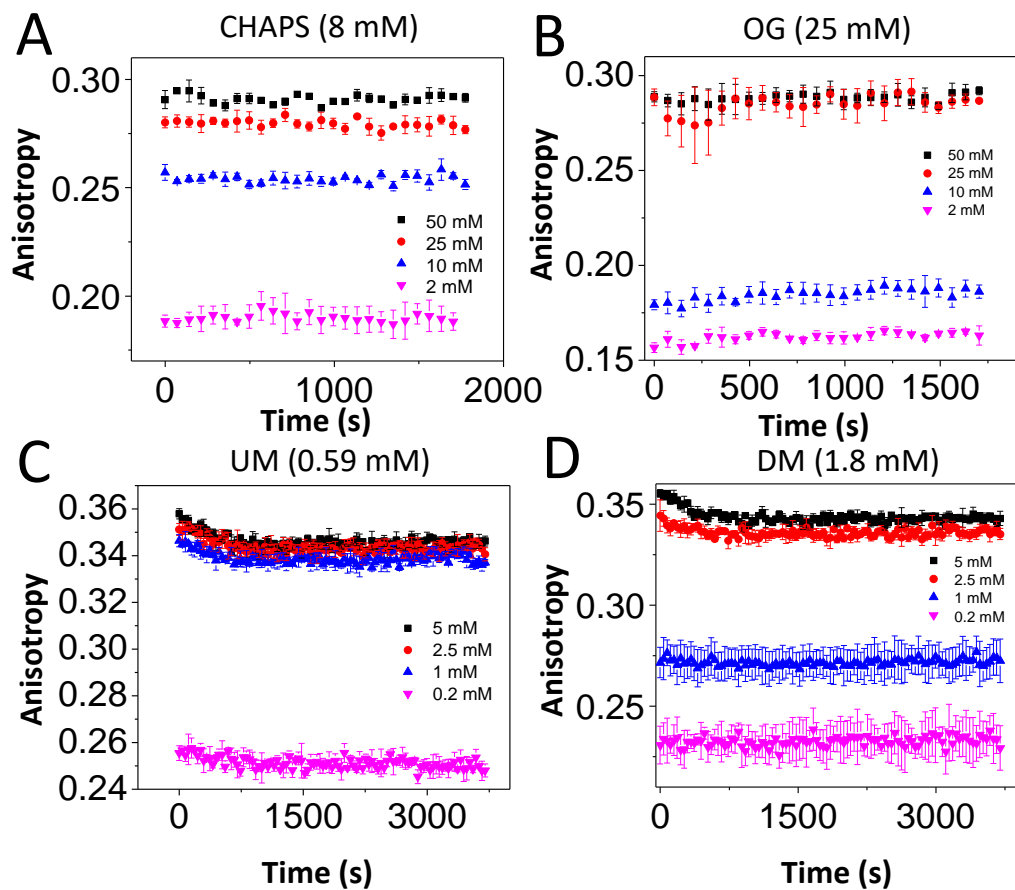


**Figure S3:** Some examples of concentration-dependent anisotropy endpoints of FhuA

$\Delta C/\Delta 5L$  determined after 24 hours incubation at 4°C. (A) CHAPS; (B) OG; (C) UM; (D)

DM. The other experimental conditions were the same as in Fig. 2.

**8. Rotational motions of the protein nanopores under detergent solvation and desolvation conditions.** The steady-state anisotropy measurements can be used to determine the changes in the hydrodynamic radius of the proteins under detergent solvation and desolvation conditions. Specifically, the Perrin equation relates the acquired steady-state fluorescence anisotropy,  $r$ , to the rotational diffusion coefficient of the labeled protein,  $D_r$ , as follows:<sup>12,13</sup>

$$\frac{r_0}{r} = 1 + 6D_r\tau_F \quad (\text{S8})$$

where  $r_0$  is the fundamental anisotropy or the theoretical intrinsic maximum anisotropy value.  $\tau_F$ , the fluorescence lifetime of Texas Red, has a value of 4.2 ns,<sup>14</sup> whereas  $r_0$  is 0.4.<sup>15</sup> On the other hand, the Perrin equation enables the determination of the rotational correlation time,  $\theta$ , as well as the apparent hydrodynamic volume of the labeled molecule,  $V_h$ , according to the following expressions:

$$\theta = \frac{1}{6D_r} \quad (\text{S9})$$

$$V_h = \frac{\theta k_B T}{\eta} = \frac{k_B T}{6\eta D_r} \quad (\text{S10})$$

Here,  $\eta$  denotes the dynamic viscosity of the solution, whereas  $k_B$  and  $T$  indicate the Boltzmann constant and absolute temperature, respectively. Therefore, we were able to determine the rotational diffusion coefficients of the fully solvated proteins,  $D_r^{\text{slow}}$ , and detergent desolvation-induced unfolded proteins,  $D_r^{\text{fast}}$ . Substantial changes in the rotational diffusion coefficients were conceivably determined by alterations in the apparent hydrodynamic radii varying solvation condition. At room temperature,  $k_B T = 4.11 \times 10^{-21}$  J. In order to determine the hydrodynamic radii (eq. (5)), we employed a dynamic viscosity,  $\eta = 1.028$  mPa s.<sup>16</sup> The average maximum hydrodynamic radii,  $R_h^{\text{max}}$ , which corresponded to the fully detergent solvated conditions as well



as changes in the average hydrodynamic radii between the solvation and desolvation conditions,  $\Delta R_h$ , were listed in **Table S2**.

**Table S2.** Table showing the acquired minima and maxima of anisotropy and rotational diffusion coefficients.<sup>a</sup>

Detergent <sup>b</sup>	$r_{\min}^c$	$r_{\max}^c$	$D_r^{\text{slow}} (10^7 \text{ s}^{-1})^d$	$D_r^{\text{fast}} (10^7 \text{ s}^{-1})^d$	$R_h^{\text{max}} (\text{nm})^e$	$\Delta R_h (\text{nm})^f$
LysoFos	0.224 ± 0.012	0.329 ± 0.002	0.86 ± 0.03	3.1 ± 0.4	2.7	0.93 ± 0.09
LD	0.228 ± 0.003	0.335 ± 0.001	0.77 ± 0.01	3.0 ± 0.1	2.7	1.0 ± 0.1
Sarkosyl	0.147 ± 0.139	0.337 ± 0.002	0.74 ± 0.03	6.8 ± 0.5	2.8	1.5 ± 0.3
LPPG	0.229 ± 0.037	0.342 ± 0.004	0.67 ± 0.05	3.0 ± 0.9	2.9	1.1 ± 0.2
CHAPS	0.172 ± 0.048	0.292 ± 0.005	1.5 ± 0.1	5.3 ± 2.0	2.2	0.77 ± 0.20
Big CHAP	0.227 ± 0.002	0.315 ± 0.012	1.1 ± 0.2	3.0 ± 0.1	2.5	0.72 ± 0.14
OG	0.162 ± 0.002	0.291 ± 0.002	1.5 ± 0.1	5.8 ± 0.1	2.2	0.81 ± 0.03
OTG	0.185 ± 0.010	0.277 ± 0.001	1.8 ± 0.1	4.6 ± 0.4	2.1	0.57 ± 0.05
DDM	0.196 ± 0.054	0.336 ± 0.003	0.76 ± 0.04	4.1 ± 1.7	2.8	1.2 ± 0.2
UM	0.230 ± 0.015	0.357 ± 0.003	0.48 ± 0.03	2.9 ± 0.4	3.2	1.5 ± 0.2
DM	0.190 ± 0.033	0.373 ± 0.002	0.29 ± 0.02	4.4 ± 1.2	3.8	2.3 ± 0.2
CYMAL-4	0.231 ± 0.019	0.395 ± 0.001	0.05 ± 0.01	2.9 ± 0.5	6.8	5.1 ± 0.5
SDS <sup>g</sup>	~0.16	~0.16	~0.057	~0.057	NA <sup>i</sup>	NA <sup>i</sup>
Gdm-HCl <sup>h</sup>	~0.16	~0.16	~0.057	~0.057	NA <sup>i</sup>	NA <sup>i</sup>

<sup>a</sup>To reach low detergent concentrations below CMC, the Gdm-HCl-solubilized FhuA  $\Delta C/\Delta 5L$  protein was refolded at various detergent concentrations above CMC. These values were stated in **Experimental Methods**.

<sup>b</sup>Full names of the detergents are provided in **Experimental Methods**.

<sup>c</sup>Experimentally determined anisotropy minima ( $r_{\min}$ ) and maxima ( $r_{\max}$ ) for various detergents.  $r_{\min}$  was extrapolated for the lowest detergent concentration in the well.  $r_{\max}$  was determined for detergent concentrations above the CMC.

<sup>d</sup> $D_r^{\text{slow}}$  and  $D_r^{\text{fast}}$  indicate the rotational diffusion coefficients of the FhuA  $\Delta C/\Delta 5L$  protein under solvation and desolvation conditions, respectively. Rotational diffusion coefficients were calculated using Perrin's equation (3)<sup>12-14</sup> for steady-state FP spectroscopy using the theoretical limiting anisotropy,  $r_0 = 0.4$ ,<sup>15</sup> and the fluorescence lifetime for the Texas Red fluorophore,  $\tau_F = 4.2$  ns.<sup>14</sup>

<sup>e</sup> $R_h^{\text{max}}$  are the maximum hydrodynamic radii of the FhuA  $\Delta C/\Delta 5L$  proteomicelle with various solubilizing detergents.

<sup>f</sup> $\Delta R_h$  is the decrease in the hydrodynamic radius,  $R_h$ , as a result of the detergent desolvation-induced unfolding transition of the protein.

<sup>g</sup>The lowest anisotropy,  $r_1$ , which was determined at a denaturing detergent concentration of 40 mM sodium dodecyl sulfate (SDS) (**Fig. 2E**). CMC of SDS is in the range  $1.2-7.1 \times 10^{-3}$  M depending on the ionic concentration of the buffer solution.<sup>9</sup>

<sup>h</sup>The lowest anisotropy,  $r_1$ , which was determined in 6 M Gdm-HCl.

<sup>i</sup>NA stands for not applicable.

**Table S3. Table showing the fitting parameters derived from dose-response dissociation phases of detergent tori from FhuA  $\Delta C/\Delta 5L$ .** The FP measurements were conducted using a buffer that contained 200 mM NaCl, 50 mM HEPES, pH 7.4 and at a temperature of 24°C. All data are derived as averages  $\pm$  SDs of three independent data acquisitions.

Detergent	$p$	Adj. R-squared <sup>a</sup>	$q^b$ (mM <sup>-1</sup> )	$K_d^c$ (mM)
LysoFos	~9.6	0.980	0.538	0.47 $\pm$ 0.07
LD	~81	0.994	1.241	1.8 $\pm$ 0.9
Sarkosyl	1.5 $\pm$ 0.4	0.971	0.139	~0.51
LPPG	~4.5	ND <sup>i</sup>	13.8	0.009 $\pm$ 0.003
CHAPS	1.7 $\pm$ 0.6	0.966	0.015	3.4 $\pm$ 1.8
Big CHAP	1.4 $\pm$ 0.6	0.997	0.001	25 $\pm$ 4
OG	5.3 $\pm$ 0.9	0.995	0.013	13 $\pm$ 1
OTG	2.5 $\pm$ 1.1	0.927	0.009	6.2 $\pm$ 2.4
DDM	1.1 $\pm$ 0.3	0.974	0.073	0.52 $\pm$ 0.36
UM	3.5 $\pm$ 0.9	0.935	0.381	0.29 $\pm$ 0.05
DM	1.6 $\pm$ 0.3	0.982	0.007	1.3 $\pm$ 0.4
CYMAL-4	4.4 $\pm$ 1.1	0.997	0.026	6.8 $\pm$ 0.9

<sup>a</sup>This column indicates the adjusted R-squared, which is a modified R-squared that has been adjusted by the number of predictors in the fitting model.

<sup>b</sup>The slope factor or transition steepness was calculated at the midpoint of the dissociation phase. See equations (3)-(5).

<sup>c</sup>The apparent dissociation constant,  $K_d$ , was determined as the midpoint of the dose-dependent dissociation phase (e.g.,  $c_0$ ).<sup>17</sup>

**9. Fluorescence anisotropy readout acquired with LPPG-refolded FhuA  $\Delta C/\Delta 5L$  at a final refolding detergent concentration of 25 mM.**

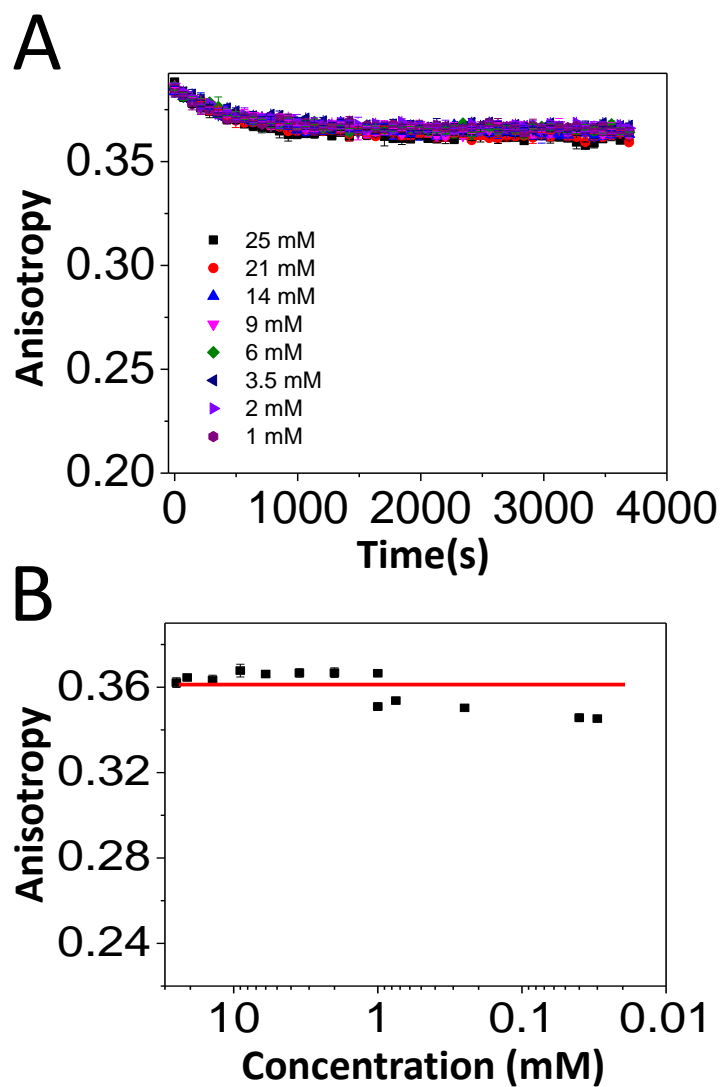


**Figure S4:** Specific fluorescence anisotropy signature of LPPG-refolded FhuA  $\Delta C/\Delta 5L$  at higher detergent concentrations. (A) Time-dependent fluorescence anisotropy of LPPG-refolded FhuA  $\Delta C/\Delta 5L$  at a detergent concentration of 25 mM; (B) Dose-response of the

endpoints of the PDC interfacial reaction after 24 hours at LPPG concentrations in the range 20  $\mu\text{M}$  – 25 mM. All the other experimental conditions were the same as in **Fig. 2**.

**10. Detailed time- and concentration-dependent anisotropy traces acquired with anionic and zwitterionic detergents.**

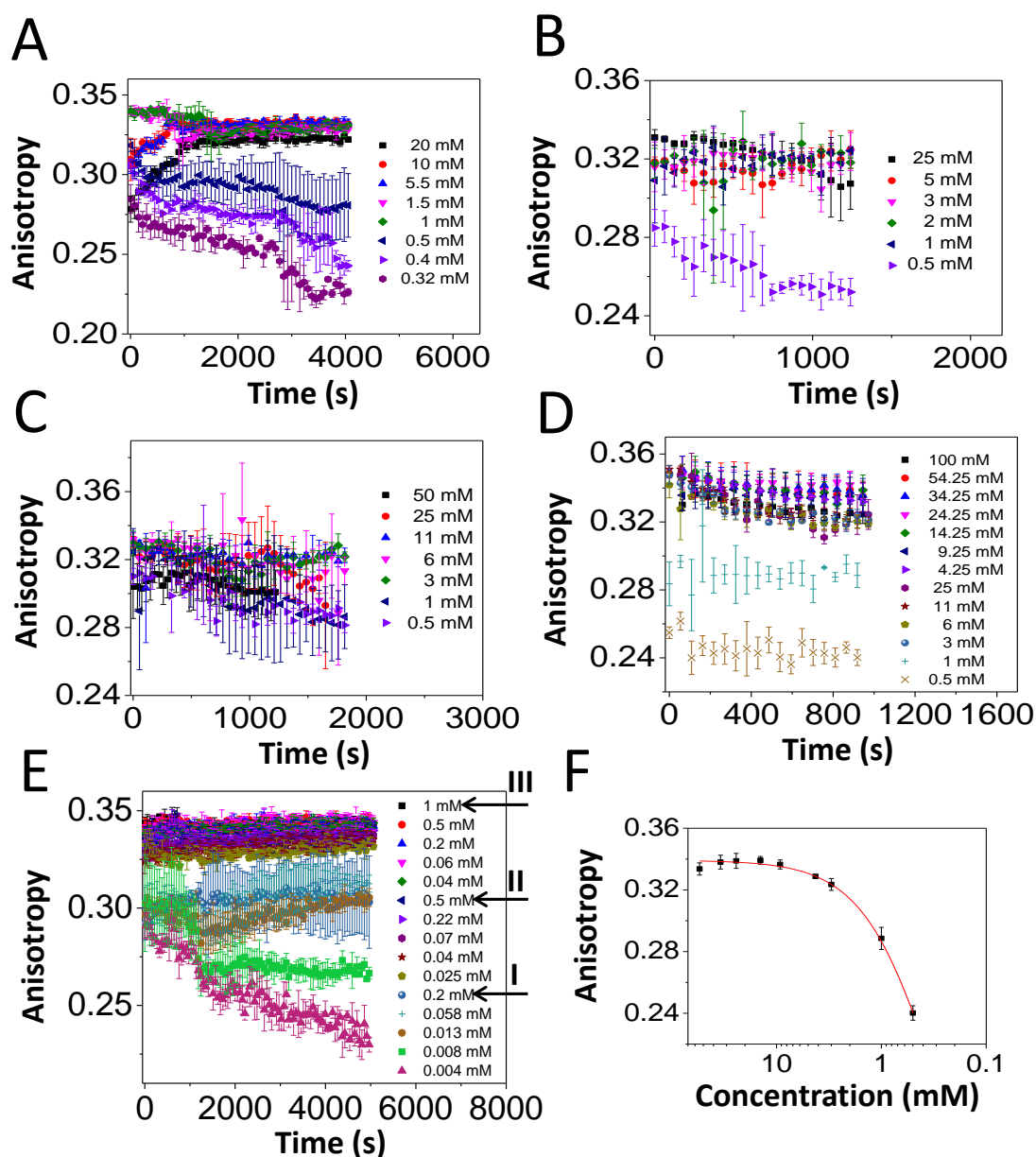


**Figure S5: Time- and concentration-dependent anisotropy traces acquired with anionic and zwitterionic detergents.** The anisotropy data was acquired by adding overnight refolded

protein to a bath of varying detergent concentration. All anisotropy measurements were carried out in 200 mM NaCl, 50 mM HEPES, pH 7.4, and at various detergent concentrations.

Detergents started at concentrations above the CMC and were diluted to concentrations below the CMC (**Experimental Methods**). Time-dependent anisotropy measurements were conducted directly after dilution of the refolded protein sample in respective detergent concentration. Final protein concentration was always maintained at 28 nM. The starting detergent concentrations were as follows: **(A)** 20 mM 1-Lauroyl-2-hydroxy-*sn*-glycero-3-phosphocholine (LysoFos); **(B)** 5 and 25 mM n-Dodecyl-N, N-Dimethylglycine (LD); **(C)** 50 mM Sodium dodecanoyl sarcosine (Sarkosyl); **(D)** 50 mM Sarkosyl read after additional 24 hour incubation at 4°C. This is shown, because first read **(C)** did not show clearly defined groups. Here, Sarkosyl refolding starting conditions were 25 mM and 100 mM; **(E)** 0.2, 0.5, and 1 mM 1-palmitoyl-2-hydroxy-*sn*-glycero-3-[phospho-*rac*-(1-glycerol)] (LPPG). The horizontal arrows indicate the three distinct families of curves that correspond to refolding detergent concentrations of 0.2 **(I)**, 0.5 **(II)**, and 1 mM **(III)**; **(F)** The concentration-response anisotropy data of Sarkosyl, which was fitted by a four-parameter Hill equation. At concentrations near CMC, there are long-lived anisotropy fluctuations, encompassing time-dependent increasing and decreasing phases. We interpret that these phases reflect different populations of detergent-associating (e.g., anisotropy increasing) and detergent-dissociating proteins (e.g., anisotropy decreasing).

**11. Steroidal group-containing detergents are weakly binding to the FhuA  $\Delta C/\Delta 5L$  nanopore.**

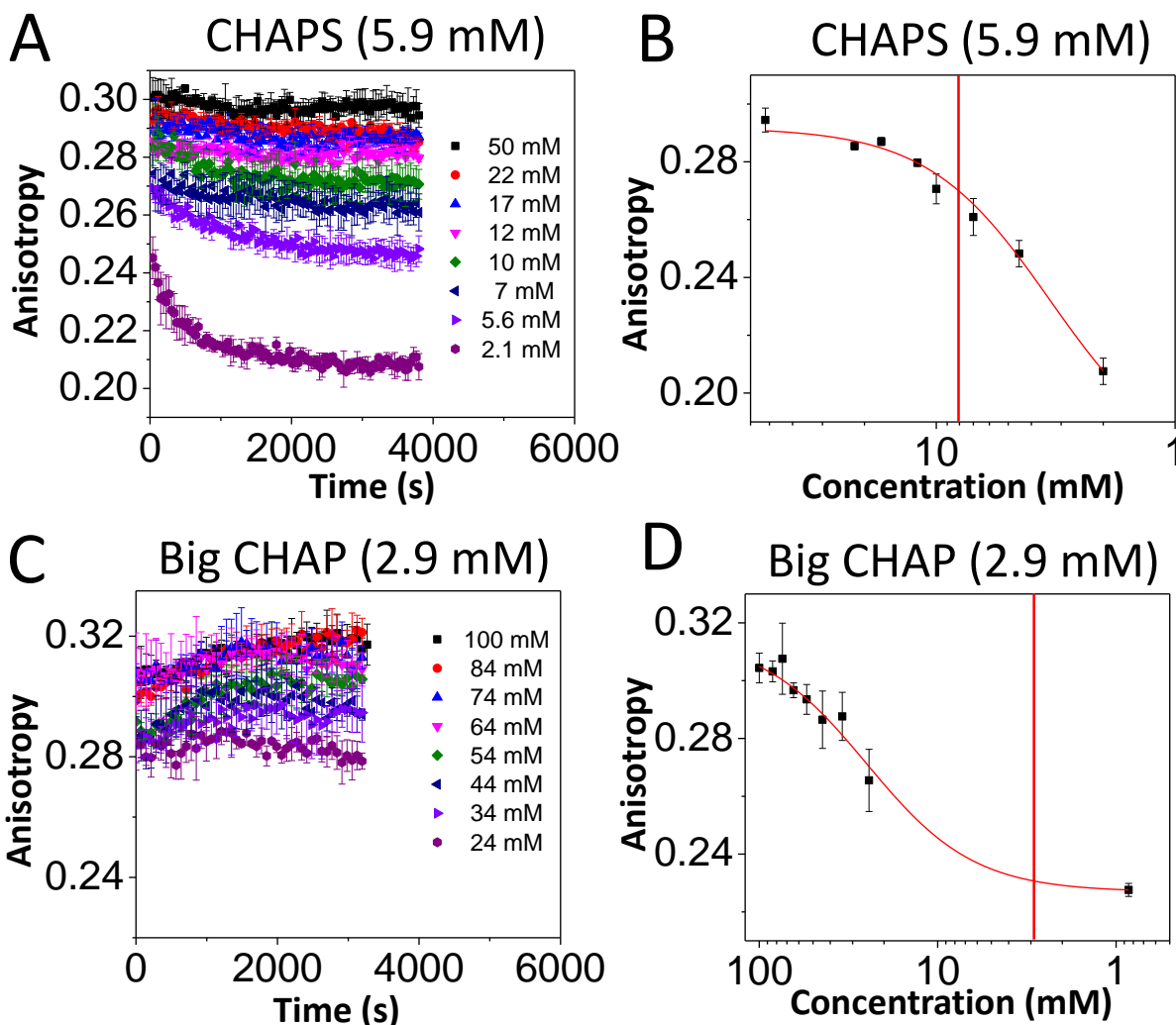


**Figure S6: Time-dependent changes in anisotropy produced by the dissociation of steroidal group-containing detergents from FhuA  $\Delta C/\Delta 5L$ .** (A) Time-dependent anisotropy for a starting concentration of 50 mM CHAPS; (B) Concentration-response anisotropy changes observed with CHAPS, whose data points were collected after 24 hours of the dissociation phase; (C) Time-dependent anisotropy for a starting concentration of 100 mM Big CHAP; (D) Concentration-response anisotropy changes observed with Big CHAP. The top of each panel or

vertical bars indicate the CMC (Table S1). All the other experimental conditions were the same as in Fig. 2.

## 12. Dissociation of maltoside-containing detergents from FhuA $\Delta C/\Delta 5L$ .

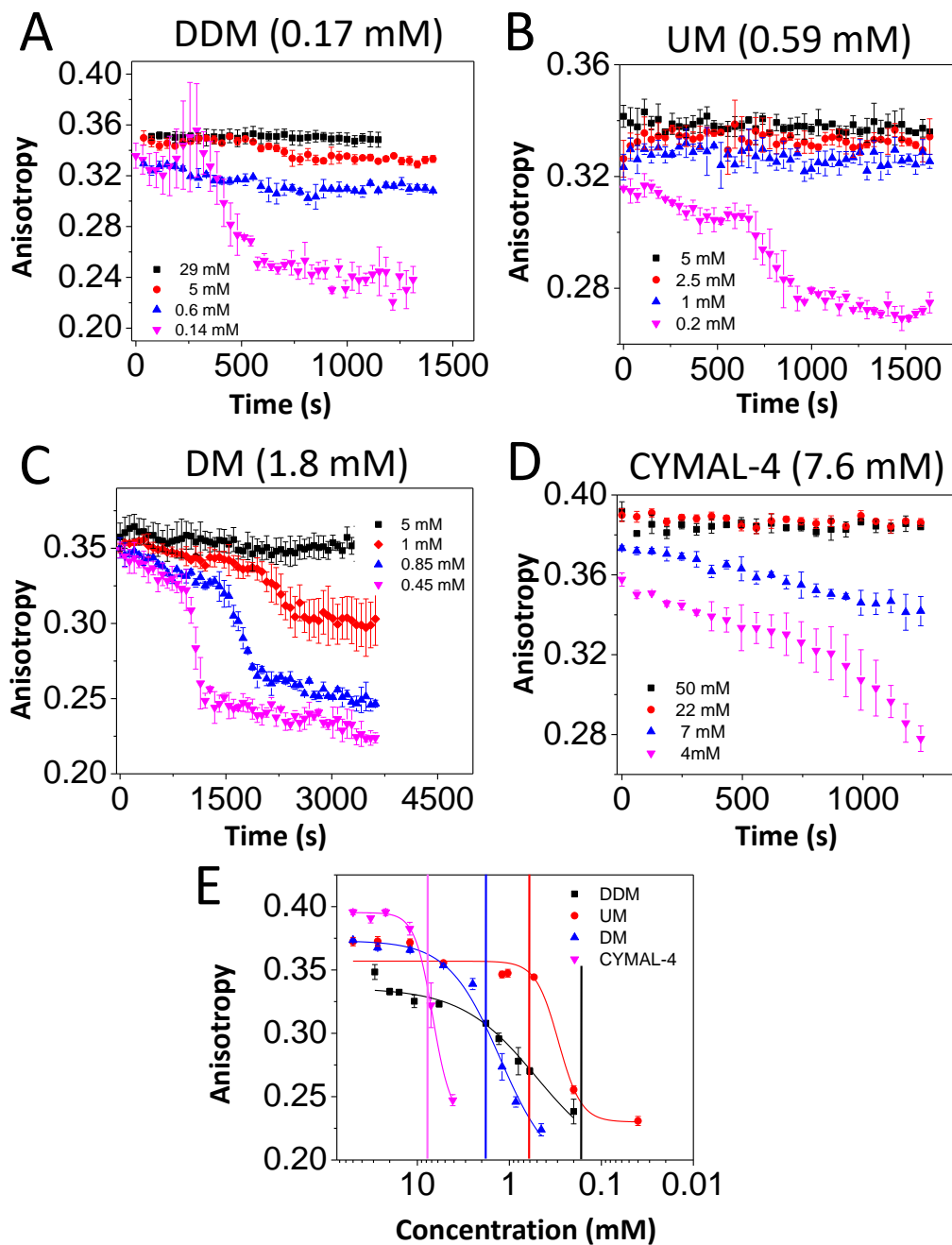




**Figure S7: Time-dependent changes in anisotropy produced by the dissociation of neutral, maltoside-containing detergents of varying tail from FhuA  $\Delta C/\Delta 5L$ .** The starting detergent concentrations were, as follows: (A) 5, 20, and 50 mM DDM, (B) 5, 20, and 50 mM UM, (C) 5, 20, and 50 mM DM, and (D) 50 mM CYMAL-4. (E) Concentration-response anisotropy changes observed for maltoside-containing detergents. The top of each panel or vertical bars indicate the CMC (**Table 1**). All the other experimental conditions were the same as in **Fig. 2**. For DM, we were not able to use the four-parameter Hill equation to obtain a statistically significant fit. Instead, we fitted the experimental data points with an asymmetrical five-parameter Hill curve:

$$r(c) = \frac{r_{max} + r_{min} \left\{ \left[ 1 + \left( \frac{c_0}{c} \right)^p \right]^s - 1 \right\}}{\left[ 1 + \left( \frac{c_0}{c} \right)^p \right]^s} \quad (\text{S11})$$

where  $s=0.071$  is an exponential constant accounting for the asymmetry of the sigmoidal curve. The other parameters in eq. (S11) were the same as those defined above for eqs. (3)-(4) in the text.

**13. Dependence of time-dependent, steady-state fluorescence anisotropy on proteins of closely similar structure, but varying isoelectric point.**

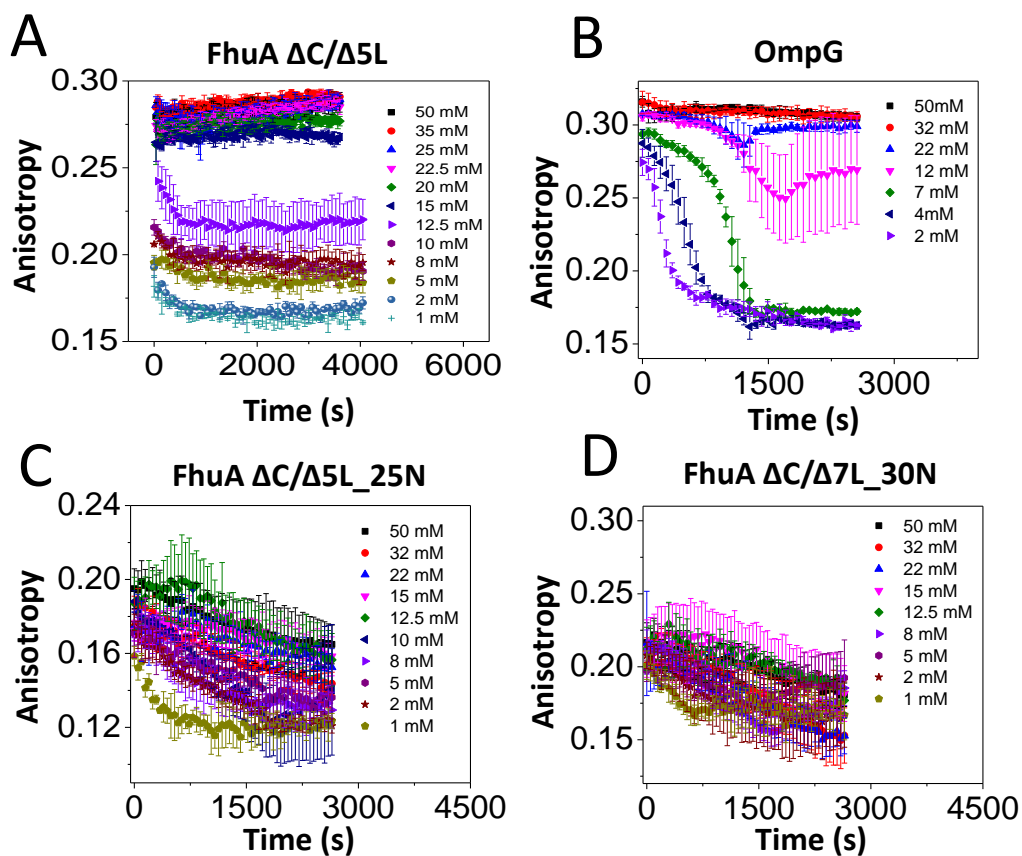


**Figure S8:** Time- and concentration-dependent anisotropy traces acquired with OG using four protein nanopores: FhuA  $\Delta C/\Delta 5L$ , OmpG, FhuA  $\Delta C/\Delta 5L_{25N}$ , and FhuA  $\Delta C/\Delta 7L_{30N}$ . The other experimental conditions were the same as in **Fig. 2**.

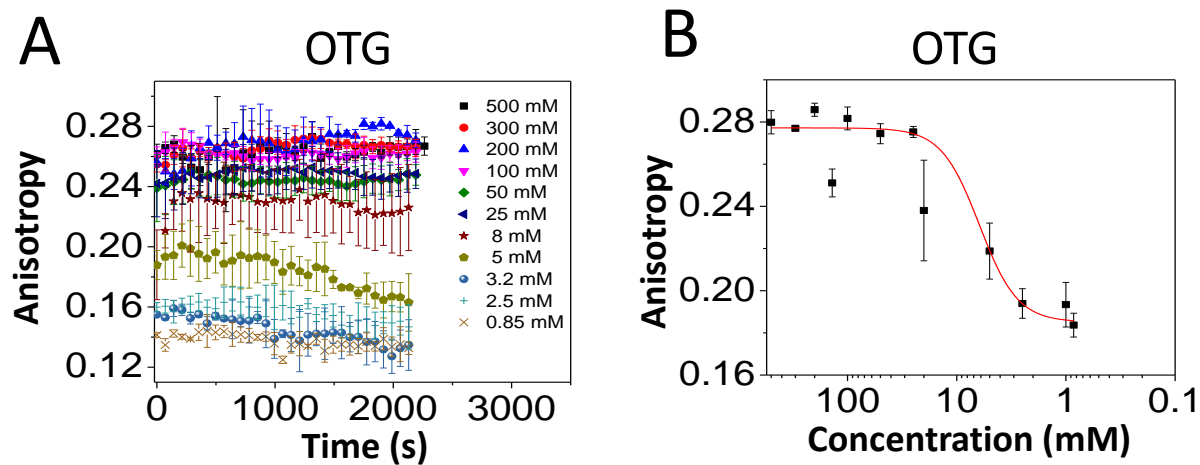


**Figure S9: Time- and concentration-dependent anisotropy traces acquired with FhuA**

$\Delta C/\Delta 5L$  in OTG. The other experimental conditions were the same as in Fig. 2.

**14. Current-voltage relationship of FhuA  $\Delta C/\Delta 5L$  refolded in detergents of varying**

**chemistry.** We also noticed unitary conductance values of DDM-refolded FhuA  $\Delta C/\Delta 5L$  proteins that were lower than 3 nS or greater than 5 nS (~11% and 4%, respectively). These histograms also revealed that 20% OG-refolded FhuA  $\Delta C/\Delta 5L$  proteins showed a single-channel conductance smaller than 3 nS, whereas only 3% displayed a single-channel conductance greater than 5 nS. Channels under these categories were excluded from further data analysis. The slopes of the current-voltage (I/V) plots recorded with DDM-, OG- and LysoFos-refolded proteins provided values of ~3.9 nS, ~4.4 nS, and ~4.3 nS, respectively (**Fig. S10A**). Similar I/V plots were also obtained from a voltage ramping, between -140 and +140 mV. The slopes gave the unitary conductance values of ~3.9 nS, ~4.4 nS, and ~4.2 nS for DDM-, OG- and LysoFos-refolded proteins, respectively (**Fig. S10B**).

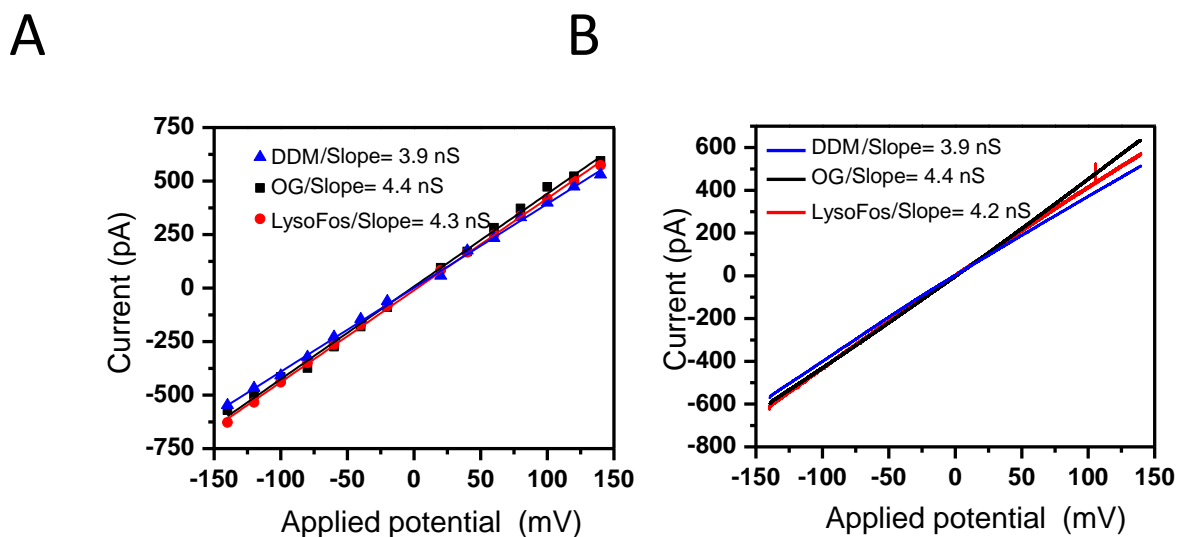


**Figure S10: Single-channel electrical signature of the engineered FhuA  $\Delta C/\Delta 5L$  protein pores refolded in different detergents.** (A) The relationship between current and voltage (I/V) of single protein pore insertions from -140 mV to +140 mV for the three proteins. The single-channel conductance values were derived using the I/V slopes. Error bars were omitted for the sake of clarity; (B) Single-channel currents from single channels of the three proteins under a voltage ramp from -140 to +140 mV. The speed of the voltage ramping was  $1.4 \text{ mV s}^{-1}$ . The single-channel conductance values were derived using the I/V slopes. In A, the single-channel electrical traces were low-pass Bessel filtered at 2 kHz. In B, the single-channel electrical traces were low-pass Bessel filtered at 0.1 kHz to eliminate the current noise generated by the patch-clamp amplifier during the application of the voltage ramp. The single-channel electrical recordings were collected under symmetrical buffer solutions on both sides of the chamber containing 1M KCl, 10 mM potassium phosphate, pH 7.4. For single-channel recordings, 40  $\mu\text{l}$  pure and denatured  $6\times\text{His}^+$ -tagged FhuA  $\Delta C/\Delta 5L$  was 50-fold diluted into 29 mM DDM, 85 mM OG, or 16 mM LysoFos, containing 200 mM NaCl, 50 mM Tris-HCl, 1 mM EDTA, pH 8.0. The

dilution ratio of the sample of refolded protein within lipid bilayer chamber was  $\sim 1/1000$ .

Therefore, the final detergent concentration in the bilayer chamber did not affect the stability of the membrane.<sup>18</sup>

### **15. Stability of the open-state current of the refolded FhuA $\Delta C/\Delta 5L$ proteins at higher**

**applied transmembrane potentials.** We examined the refolded FhuA  $\Delta C/\Delta 5L$  proteins at

transmembrane potentials in the ranges -140 to -80 mV and +80 to +140 mV. In 1 M KCl, 10

mM potassium phosphate, pH 7.4, the refolded proteins were stable up to  $\pm 140$  mV (**Fig. S11I-**

**III**). These refolded FhuA  $\Delta C/\Delta 5L$  proteins showed some reversible short-lived current

fluctuations (**Fig. S11**). In the case of the OG-refolded proteins, the single-channel current trace

was accompanied by highly infrequent millisecond-time scale, voltage-independent current

fluctuations ( $\sim 0.01$  s<sup>-1</sup>) (**Fig. S11II**). In this work, single-channel electrical recordings

performed on the DDM-, OG- or LysoFos-refolded FhuA  $\Delta C/\Delta 5L$  produced uniform channels

with high conductance  $\sim 4.0$  nS in 1 M KCl (**Fig. 4C and Fig. 4D**). Refolded FhuA  $\Delta C/\Delta 5L$

proteins showed very stable channel properties at higher voltages, displaying no major current

fluctuations or channel closures (**Fig. S11**). DDM-refolded FhuA  $\Delta C/\Delta 5L$  protein was stable up

to -120 mV and +140 mV (**Fig. S11CI, DI**), OG-refolded FhuA  $\Delta C/\Delta 5L$  protein was stable up to

$\pm 140$  mV (**Fig. S11DII**), and LysoFos-refolded FhuA  $\Delta C/\Delta 5L$  protein was stable up to -100 and

+140 mV (**Fig. S11BIII, DIII**). The stability and uniformity of channels produced by refolded

proteins in different detergents are an advantage. This means that we have options in choosing

detergents to refold modified or engineered FhuA proteins in the future. In addition, a uniform

conductance may indicate that protein pores, at least for the ones inserted into the bilayer, have

one major folded state.<sup>19,20</sup>

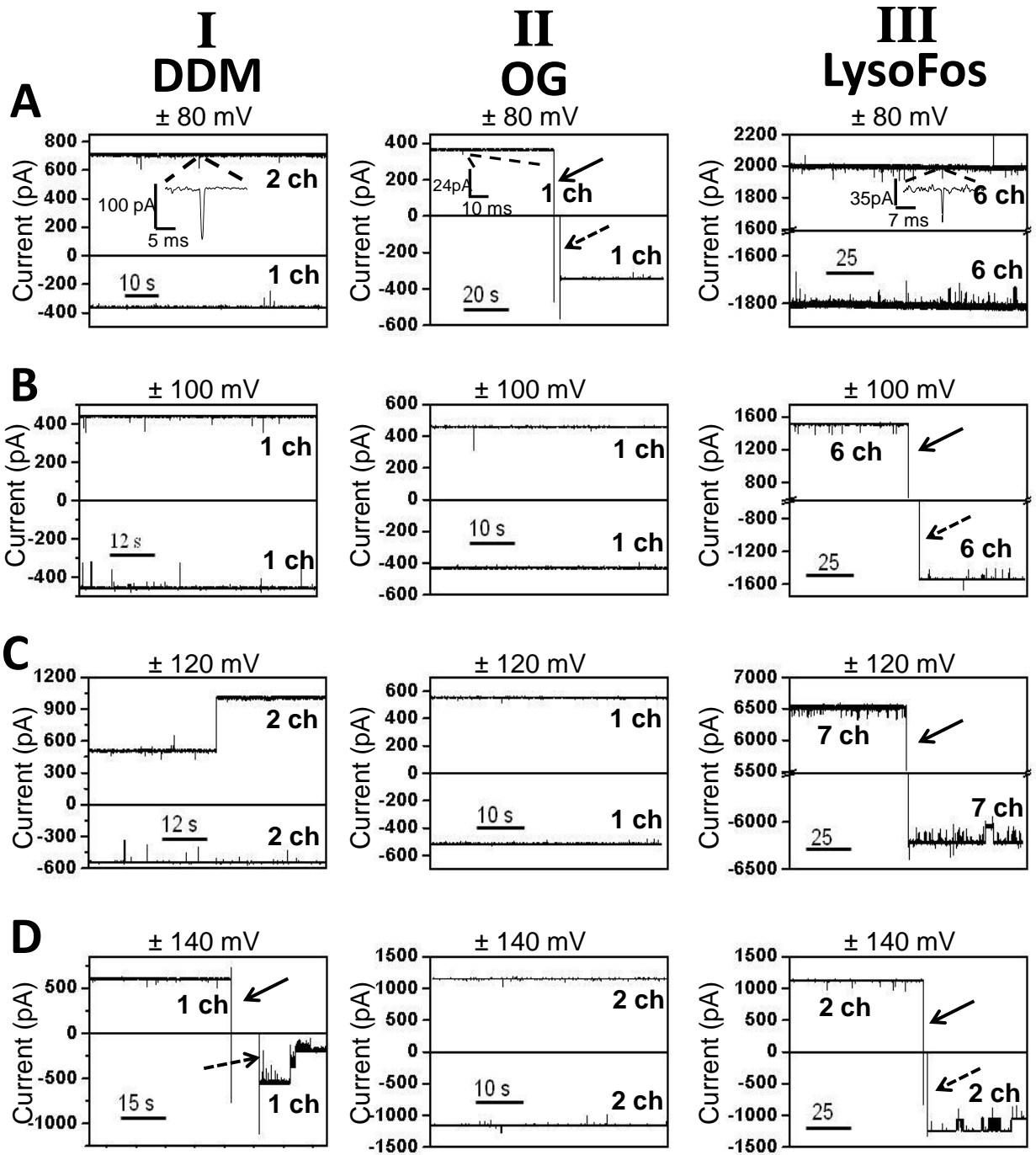
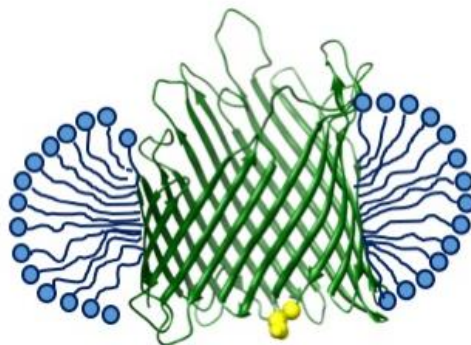


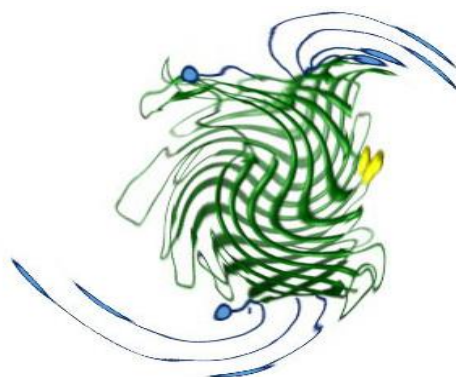
**Figure S11: Comparison of the single- and multi-channel electrical traces produced by the FhuA  $\Delta C/\Delta 5L$  proteins under various voltages.** DDM- (I), OG- (II) and LysoFos-refolded (III) FhuA  $\Delta C/\Delta 5L$  protein were reconstituted into planar lipid membranes. The single-channel electrical recordings were collected under symmetrical buffer solutions on both sides of the chamber containing 1M KCl, 10 mM potassium phosphate, pH 7.4. The number of reconstituted nanopores (e.g., 2 channels is denoted by 2 ch in bold) is indicated near the trace for positive and negative voltages, respectively. Solid and dashed arrows denote the end of the positive voltage and the start of the negative voltage in the same electrical trace, respectively. All electrical traces were low-pass Bessel filtered at 2 kHz. The expanded traces in IA and IIIA indicate representative current spikes recorded at a greater time resolution. The refolding conditions of FhuA  $\Delta C/\Delta 5L$  were the same as those mentioned in the caption of **Fig. S10**.



**A** Detergent-refolded protein  
in a prolate proteomicelle



**B** Desolvation-induced misfolded protein



**C** Desolvation-induced unfolded protein



**Figure S12:** Schematic model of the detergent desolvation-induced protein unfolding.

This example is for a prolate proteomicelle. **(A)** A nanopore-containing proteomicelle; **(B)** Loss of detergent molecules produces protein misfolding; **(C)** Complete detergent desolvation accelerates protein unfolding as well as reduction in the average hydrodynamic radius,  $\Delta R_h$  (**Table S2**).

**REFERENCES**

- (1) Wolfe, A. J.; Mohammad, M. M.; Thakur, A. K.; Movileanu, L. *Biochim. Biophys. Acta* **2016**, *1858*, 19-29.
- (2) Mohammad, M. M.; Howard, K. R.; Movileanu, L. *J.Biol.Chem.* **2011**, *286*, 8000-8013.
- (3) Fahie, M.; Chisholm, C.; Chen, M. *ACS Nano*. **2015**, *9*, 1089-1098.
- (4) Stafford, R. E.; Fanni, T.; Dennis, E. A. *Biochemistry* **1989**, *28*, 5113-5120.
- (5) Parker, J. L.; Newstead, S. *Protein Sci* **2012**, *21*, 1358-1365.
- (6) Linke, D. *Methods Enzymol.* **2009**, *463*, 603-617.
- (7) Lipfert, J.; Columbus, L.; Chu, V. B.; Lesley, S. A.; Doniach, S. *The journal of physical chemistry. B* **2007**, *111*, 12427-12438.
- (8) Oliver, R. C.; Lipfert, J.; Fox, D. A.; Lo, R. H.; Kim, J. J.; Doniach, S.; Columbus, L. *Langmuir* **2014**, *30*, 13353-13361.
- (9) le Maire, M.; Champeil, P.; Moller, J. V. *Biochimica et biophysica acta* **2000**, *1508*, 86-111.
- (10) Neugebauer, J. M. *Methods in enzymology* **1990**, *182*, 239-253.
- (11) Cheneke, B. R.; van den Berg, B.; Movileanu, L. *ACS Chem.Biol.* **2015**, *10*, 784-794.
- (12) Jameson, D. M.; Ross, J. A. *Chemical reviews* **2010**, *110*, 2685-2708.
- (13) Gradinaru, C. C.; Marushchak, D. O.; Samim, M.; Krull, U. J. *Analyst* **2010**, *135*, 452-459.
- (14) Lakowicz, J. R. *Principles of Fluorescence Microscopy*, 2nd ed.; Springer: New York, 2006.
- (15) Prazeres, T. J. V.; Fedorov, A.; Barbosa, S. P.; Martinho, J. M. G.; Berberan-Santos, M. N. *Journal of Physical Chemistry A* **2008**, *112*, 5034-5039.
- (16) Lide, D. R. E. *CRC Handbook of Chemistry and Physics - A Ready Reference Book of Chemical and Physical Data*, The 88th ed.; CRC Press - Taylor and Francis Group: Boca Raton 2008.
- (17) Rossi, A. M.; Taylor, C. W. *Nature protocols* **2011**, *6*, 365-387.
- (18) Mohammad, M. M.; Tomita, N.; Ohta, M.; Movileanu, L. *ACS chemical biology* **2016**, *11*, 2508-2518.
- (19) Arora, A.; Rinehart, D.; Szabo, G.; Tamm, L. K. *J.Biol.Chem.* **2000**, *275*, 1594-1600.

(20) Tamm, L. K.; Hong, H.; Liang, B. *Biochim.Biophys.Acta* **2004**, *1666*, 250-263.

# Chapter 4. Quantification of Membrane Protein-Detergent Complex Interactions

Aaron J. Wolfe,<sup>1,2</sup> Wei Si,<sup>3,4</sup> Zhengqi Zhang,<sup>5</sup> Adam R. Blanden,<sup>6</sup> Yi-Ching Hsueh,<sup>1</sup> Jack F. Gugel,<sup>1</sup> Bach Pham,<sup>7</sup> Min Chen,<sup>7</sup> Stewart N. Loh,<sup>6</sup> Sharon Rozovsky,<sup>5</sup> Aleksei Aksimentiev,<sup>\*4</sup> and Liviu Movileanu<sup>\*1,2,8</sup>

<sup>1</sup>Department of Physics, Syracuse University, 201 Physics Building, Syracuse, New York 13244-1130, USA

<sup>2</sup>Structural Biology, Biochemistry, and Biophysics Program, Syracuse University, 111 College Place, Syracuse, New York 13244-4100, USA

<sup>3</sup>Jiangsu Key Laboratory for Design and Manufacture of Micro-Nano Biomedical Instruments and School of Mechanical Engineering, Southeast University, Nanjing, 210096, China

<sup>4</sup>Department of Physics, University of Illinois at Urbana-Champaign, Urbana, Illinois 61801, USA

<sup>5</sup>Department of Chemistry and Biochemistry, University of Delaware, 136 Brown Laboratory, Newark, Delaware 19716, USA

<sup>6</sup>Department of Biochemistry and Molecular Biology, State University of New York Upstate Medical University, 4249 Weiskotten Hall, 766 Irving Av., Syracuse, New York 13210, USA

<sup>7</sup>Department of Chemistry, University of Massachusetts, 820 LGRT, 710 North Pleasant Street, Amherst, Massachusetts 01003-9336, USA

<sup>8</sup>Department of Biomedical and Chemical Engineering, Syracuse University, 329 Link Hall, Syracuse, New York 13244, USA

Reprinted with permission from **Quantification of Membrane Protein-Detergent Complex Interactions** Aaron J. Wolfe, Wei Si, Zhengqi Zhang, Adam R. Blanden, Yi-Ching Hsueh, Jack F. Gugel, Bach Pham, Min Chen, Stewart N. Loh, Sharon Rozovsky, Aleksei Aksimentiev, and Liviu Movileanu

The Journal of Physical Chemistry B **2017** *121* (44), 10228-10241

DOI: 10.1021/acs.jpcc.7b08045. Copyright 2017 American Chemical Society.

## Author contributions:

AJW: Designed experiments, performed experiments, analyzed data, interpreted data.

WS: Performed experiments

ZZ: Performed experiments

ARB: Performed experiments

YCH: Performed experiments

JFG: Analyzed data

BP: Performed experiments

MC: Managed her student

SNL: Managed his student

SR: Managed her student

AA: Performed experiments

LM: Analyzed data, wrote manuscript

**ABSTRACT**

Although fundamentally significant in structural, chemical, and membrane biology, the interfacial protein-detergent complex (PDC) interactions have been modestly examined because of the complicated behavior of both detergents and membrane proteins in aqueous phase. Membrane proteins are prone to unproductive aggregation resulting from poor detergent solvation, but the participating forces in this phenomenon remain ambiguous. Here, we show that using rational membrane protein design, targeted chemical modification, and steady-state fluorescence polarization spectroscopy, the detergent desolvation of membrane proteins can be quantitatively evaluated. We demonstrate that depleting the detergent in the sample well produced a two-state transition of membrane proteins between a fully detergent-solvated state and a detergent-desolvated state, the nature of which depended on the interfacial PDC interactions. Using a panel of six membrane proteins of varying hydrophobic topography, structural fingerprint, and charge distribution on the solvent-accessible surface, we provide direct experimental evidence for the contributions of the electrostatic and hydrophobic interactions to the protein solvation properties. Moreover, all-atom molecular dynamics simulations report the major contribution of the hydrophobic forces exerted at the PDC interface. This semi-quantitative approach might be extended in the future to include studies of the interfacial PDC interactions of other challenging membrane protein systems of unknown structure. This would have practical importance in protein extraction, solubilization, stabilization, and crystallization.

## INTRODUCTION

The protein-detergent complex (PDC) interactions play a pivotal role in extraction, solubilization, and stabilization of water-insoluble membrane proteins.<sup>1-5</sup> Therefore, they were studied by various approaches. For example, circular dichroism (CD) spectroscopy was employed to probe alterations in the secondary structure and stability of membrane proteins under diverse detergent-solubilization contexts.<sup>6</sup> Using hydrogen-deuterium exchange, along with NMR spectroscopy and mass spectrometry, Raschle and colleagues (2016) have recently examined the time-dependent protein folding of the outer membrane protein X in proteomicelles.<sup>7</sup> The nature of the interfacial PDC interactions was also inspected in the gas phase using ion-mobility mass spectrometry.<sup>8</sup> Moreover, isothermal titration calorimetry (ITC) was used for the real-time probing of phase diagrams between bilayer-forming lipids and micelle-forming detergents.<sup>9-10</sup> Differential scanning calorimetry (DSC) was adapted for the investigation of the impact of detergents on the water-soluble domains of membrane proteins.<sup>2, 5</sup> However, the detergent-mediated solubilization and refolding of membrane proteins often lead to aggregation,<sup>11</sup> a ubiquitous process caused by the inability of detergents to fully solvate them. There are at least three reasons for a modest progress in this research area. First, the protein aggregation substantially deteriorates the signal-to-noise ratio of most spectroscopic and calorimetric approaches. Second, the protein-free detergent micelles without an accurately determined concentration coexist with the proteomicelles in aqueous phase, adding an uncontrolled signal. Third, the quantitative assessment of the interfacial PDC interactions is impractical in the absence of a high-throughput screening (HTS) approach that utilizes a low concentration of membrane proteins.

Here, we show that we can overcome these challenges using rational membrane protein design, along with targeted chemical modification and steady-state fluorescence polarization (FP) spectroscopy,<sup>12-13</sup> to probe the detergent desolvation transitions of membrane proteins. The FP spectroscopy was previously used to inspect: (i) the interactions of mild<sup>14</sup> and harsh<sup>15</sup> detergents with water-soluble proteins, (ii) the harsh detergent-induced unfolding<sup>16</sup> and resistance of soluble proteins to denaturation,<sup>17</sup> (iii) the detergent-mediated oligomerization of hydrophobic proteins into proteomicelles,<sup>18</sup> and (iv) the impact of detergent on conformational changes<sup>14</sup> and enzymatic activity<sup>19</sup> of soluble proteins.

In this article, we place an emphasis on the transition of detergent desolvation of hydrophobic membrane proteins. Such a process undergoes a two-state transition, whose apparent dissociation constant,  $K_d$ , is usually within the same order of magnitude with the critical micelle concentration (CMC).<sup>2, 5, 20</sup> The adhesive interactions occur at the specific interface between the detergent tails and hydrophobic residues on the detergent-accessible surface of the membrane protein. In addition, these interactions occur at the specific interface between the polar head groups of the detergents and water-soluble parts of the membrane protein. In contrast, the cohesive interactions are mediated by detergents, maintaining the integrity of the proteomicelle. The aberrant imbalance between these interactions produces a significant departure of the proteomicelle dissociation from the demicellization transition.

For exploring the PDC interactions exposing  $\beta$ -barrel surfaces, we chose the outer membrane protein G (OmpG)<sup>21</sup> and three extensive truncation derivatives of ferric hydroxamate uptake

component A (FhuA)<sup>22</sup> of *E. coli* (**Fig. 1**). We demonstrate that robust  $\beta$ -barrel proteins, which tolerate extensive changes in charge distribution across the solvent-accessible surface, exhibit drastic alterations in the interfacial PDC interactions. In some instances, these major modifications culminated with the transition from excellent to poor solubilization properties due to variations from strong to very weak adhesive interactions. For example, the zwitterionic detergents solubilized well the acidic  $\beta$  barrels, but exhibited weak adhesive contacts with the basic  $\beta$  barrels, performing poorly in solubilizing the latter proteins. Moreover, hydrophobic interactions played a major role in the PDC. This was clearly supported by the full-atomistic molecular dynamics (MD) simulations with an uncharged maltoside-containing detergent. Finally, we show that such a semi-quantitative experimental approach might be extended to other challenging membrane protein systems of different subunit stoichiometry or unknown structure, suggesting its potentiality to produce impactful transformations in the areas of membrane chemical biology.



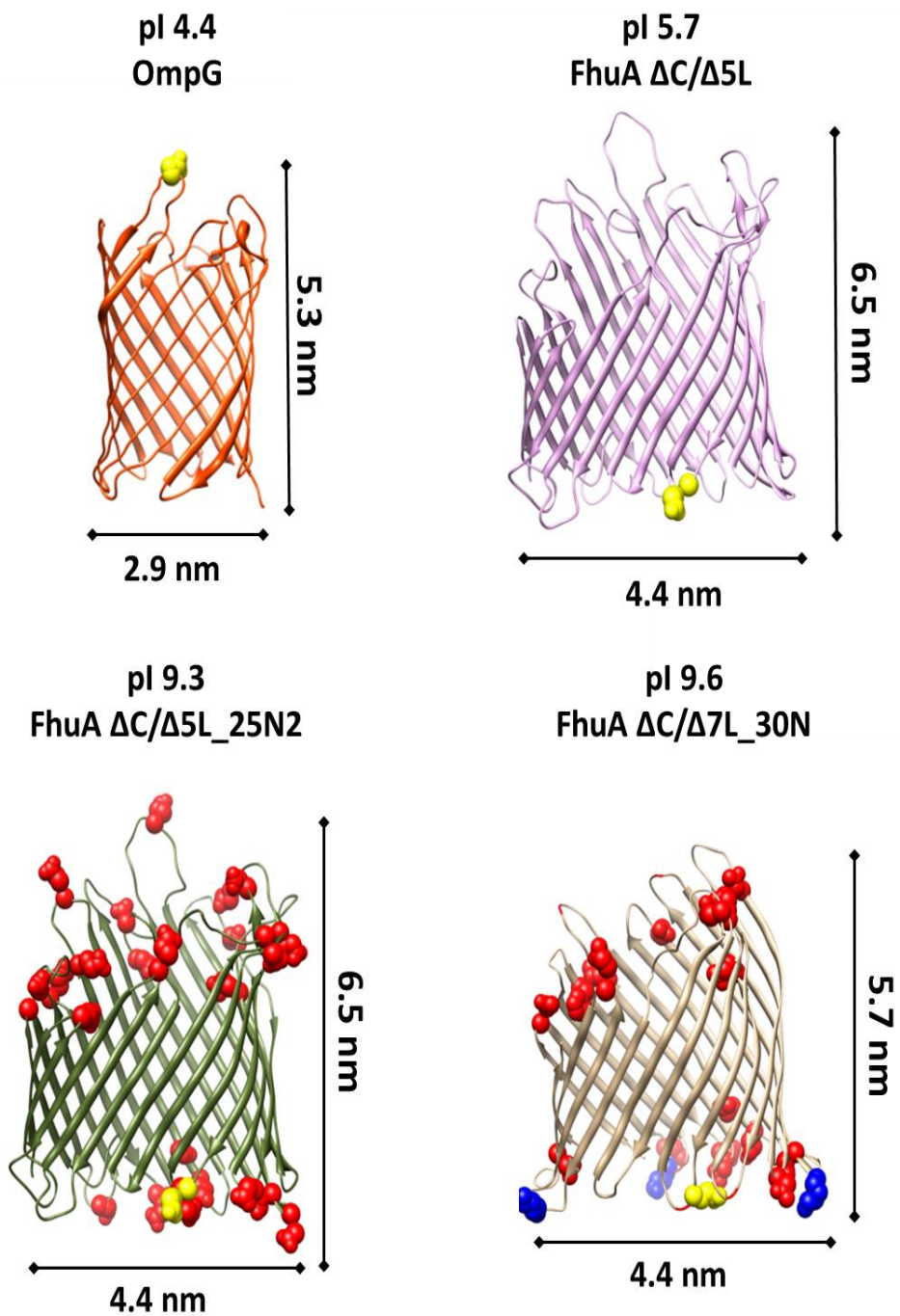


FIGURE 1.

**Figure 1:** Cartoons showing the backbone homology structures of the four  $\beta$ -barrel proteins inspected in this work. (A) OmpG; (B) FhuA  $\Delta C/\Delta 5L$ ; (C) FhuA  $\Delta C/\Delta 5L_{25N}$ ; and (D) FhuA  $\Delta C/\Delta 7L_{30N}$ . Positions of the fluorophore attachment are marked by yellow. All negative charge neutralizations with respect to FhuA  $\Delta C/\Delta 5L$  are indicated in red. Moreover, there are there are three additional lysine mutations in the  $\beta$  turns of FhuA  $\Delta C/\Delta 7L_{30N}$  that marked in blue, out of which two are negative-to-positive charge reversals. The top of each cartoon shows the protein abbreviated name and its respective isoelectric point.

## METHODS

**Cloning, expression, and purification of FhuA  $\Delta C/\Delta 5L$ .** The *fhuA  $\Delta c/\Delta 5l$*  gene lacking the regions coding for the cork domain (C) and five extracellular loops L3, L4, L5, L10, and L11, was produced through *de novo* synthesis (Geneart, Regensburg, Germany).<sup>23-24</sup> *fhuA  $\Delta c/\Delta 5l\_t7$*  was created by inverse PCR using pPR-IBA1-*fhuA  $\Delta c/\Delta 5l$ -6 $\times$ His<sup>+</sup>* plasmid as a template. The PCR product was self-ligated to create pPR-IBA1-*fhuA  $\Delta c/\Delta 5l\_t7$ -6 $\times$ His<sup>+</sup>*. The  $\beta$  turn T7 (V<sup>331</sup> PEDRP<sup>336</sup>) was replaced with a single cysteine-containing, flexible, GS-rich peptide loop (GGSSGCGSSGGS) for the fluorophore attachment. Protein expression was conducted, as previously published.<sup>25-26</sup>

**Table 1: Physical properties of the detergents examined in this work.**

Detergent	FW (Da) <sup>a</sup>	Head group	Aggregation number, $N_{agg}$ <sup>b</sup>	CMC (mM) <sup>b</sup>	Micellar Weight, $MW_m$ (kDa)	References
n-dodecyl- $\beta$ -D-maltoside (DDM)	511	Non-ionic	~78-149	~0.17	70	<sup>29</sup>
n-undecyl- $\beta$ -D-maltoside (UM)	497	Non-ionic	~71	~0.59	35	<sup>29</sup>
n-decyl- $\beta$ -D-maltoside (DM)	483	Non-ionic	~69	~1.8	33	<sup>29</sup>
4-cyclohexyl-1-Butyl- $\beta$ -D-maltoside (CYMAL-4)	481	Non-ionic	~25	~7.6	12	<sup>63</sup>
n-octyl- $\beta$ -D-glucoside (OG)	292	Non-ionic	~27-100	~25	25	<sup>29</sup>
3-[(3-cholamidopropyl)-dimethylammonio]-1-propane sulfonate] (CHAPS) <sup>c</sup>	615	Zwitterionic	~10	~5.9 <sup>c</sup>	6	<sup>29</sup>
1-lauroyl-2-hydroxy- <i>sn</i> -glycero-3-phosphocholine (LysoFos) <sup>d</sup>	440	Zwitterionic	80 <sup>d</sup>	~0.7 <sup>e</sup>	35	<sup>1, 64</sup>
n-dodecyl-N,N'-dimethylglycine (LD) <sup>d</sup>	271	Zwitterionic	NA <sup>f</sup>	~1.5 <sup>g</sup>	NA <sup>f</sup>	<sup>65</sup>

<sup>a</sup>Formula weights of the detergent monomers (FW) were reported by Anatrace (<https://www.anatrace.com/>).

<sup>b</sup>CMC values or aggregation numbers,  $N_{agg}$ , in water were reported by Anatrace (<https://www.anatrace.com/>).

<sup>c</sup>CMC value of CHAPS in 200 mM NaCl is 5.9 mM.<sup>66</sup>

<sup>d</sup>The  $N_{agg}$  for LysoFos used in this work is ~80.<sup>1</sup>

<sup>e</sup>CMC value of LysoFos in 140 mM NaCl, 20 mM Tris-HCl, pH 7.2 is 0.7 mM.<sup>64</sup>

<sup>f</sup>NA stands for not available.

<sup>g</sup>Detergent monomers are neutral at pH > 6.<sup>65</sup>

**Table 2: Biophysical properties of the  $\beta$ -barrel proteins used in this study.<sup>67</sup>**

<b>Protein<sup>a</sup></b>	<b>pI/Charge state</b>	<b>GRAVY<sup>c</sup></b>	<b>Aliphatic index<sup>d</sup></b>	<b>Negative residues</b>	<b>Positive residues</b>	<b>Total number of residues<sup>e</sup></b>
WT-OmpG	4.4/acidic	-0.798	55.87	55	22	281
FhuA $\Delta C/\Delta 5L^b$	5.7/acidic	-0.550	60.42	57	48	505
FhuA $\Delta C/\Delta 5L_{25}N$	9.3/basic	-0.563	58.31	34	43	473
FhuA $\Delta C/\Delta 7L_{30}N$	9.6/basic	-0.574	57.42	27	42	426

<sup>a</sup>All proteins have a 6His<sup>+</sup> tag at the C terminus.

<sup>b</sup>This engineered FhuA includes a 33-residue signal peptide at the N terminus.

<sup>c</sup>The GRAVY hydrophobicity parameter was calculated by adding individual hydropathy indexes<sup>68</sup> of each residue and dividing by the total number of residues. Increasing positive GRAVY number shows a more hydrophobic protein.

<sup>d</sup>The aliphatic index is given by the relative volume of aliphatic chain-containing residues.<sup>69</sup>

<sup>e</sup>The total number of residues includes those amino acids from the Gly/Ser-rich containing polypeptide loop and 6 $\times$ His<sup>+</sup> tag.

**Refolding of FhuA  $\Delta C/\Delta 5L$ .** We employed a rapid-dilution refolding protocol.<sup>27-28</sup> Briefly, 40  $\mu$ l of 6 $\times$ His<sup>+</sup>-tag purified and guanidinium hydrochloride (Gdm-HCl)-denatured FhuA protein was 50-fold diluted into 200 mM NaCl, 50 mM HEPES, pH 7.4 solutions at 4°C, which included detergents at concentrations above their CMC (**Table 1**). Different starting detergent concentrations were used, as follows (when multiple concentrations are given, the lower concentrations were needed to get dilutions with a low enough detergent concentration to cover the required range): (i) 5 and 20 mM starting detergent concentration for n-decyl- $\beta$ -D-maltopyranoside (DM), n-undecyl- $\beta$ -D-maltopyranoside (UM), and n-dodecyl- $\beta$ -D-maltopyranoside (DDM); (ii) 50 mM 4-cyclohexyl-1-butyl- $\beta$ -D-maltoside (CYMAL-4); (iii) 50 mM n-octyl- $\beta$ -D-glucoside (OG); (iv) 50 mM 3-[(3-cholamidopropyl)-dimethylammonio]-1-propane sulfonate] (CHAPS); and (v) 20 mM 1-lauroyl-2-hydroxy-*sn*-glycero-3-phosphocholine (LysoFos). All detergents were purchased from Anatrace (Maumee, OH). To avoid hydrolysis and oxidation,<sup>29</sup> detergent solutions were freshly prepared.

**Fluorescent labeling of the FhuA derivatives.** 10  $\mu$ M FhuA derivatives (**Table 2**) were each incubated with 200  $\mu$ M Texas Red C2 maleimide (Thermo Fisher Scientific) overnight at room temperature. The incubation buffer contained 200 mM NaCl, 50 mM Tris, 1 mM TCEP, pH 8.0, and 6 M Gdm-HCl. Proteins were separated from the unreacted fluorophore by Ni<sup>2+</sup>-NTA column chromatography in the same buffer, but with a 10-200 mM imidazole step gradient. Using  $\epsilon_{595} = 104,000 \text{ M}^{-1}\text{cm}^{-1}$  for Texas Red C2 and a correction factor of 0.26  $\times \epsilon_{595}$  to account for the fluorophore absorbance at 280 nm, labeling stoichiometry was determined as ~0.3-0.8 labels/protein.

**Expression and purification of OmpG D224C.** A cysteine was engineered on extracellular loop L6 of OmpG using single-site mutagenesis PCR. OmpG D224C was expressed, purified, and refolded as previously described.<sup>30</sup> Proteins were expressed in *E. coli* BL21 (pLys) cells, which were transformed with the plasmid pT7-OmpG D224C. Cells were grown in *LB* media at 37°C until the OD<sub>600</sub> reached a value of 0.6, at which time they were induced by 0.5 mM IPTG. Cells were harvested three hours later and lysed in lysis buffer (50 mM Tris·HCl, pH 8.0, 150 mM NaCl, 200 µg/ml lysozyme, 1 mM EDTA, 3 mM TCEP) via sonication. The lysate was centrifuged at 19,000 g for 30 min before washing once with 30 ml of a buffer containing 50 mM Tris·HCl, pH 8.0, 1.5 M urea, 3 mM TCEP. Then, the OmpG D224C-containing inclusion bodies were dissolved in 30 ml of buffer containing 50 mM Tris·HCl, pH 8.0, 8 M urea, 3 mM TCEP and passed through a 0.45 µm filter before FPLC purification. Protein purification was accomplished using a 5ml Q-ionic exchange column (GE Healthcare Life Sciences, Pittsburg, PA) and eluted in a buffer containing 50 mM Tris·HCl, pH 8.0, 8 M Urea, 3 mM TCEP, 500 mM NaCl by applying a salt gradient.

**Fluorescent labeling of the OmpG D224C.** After purification, OmpG D224C was incubated in 10 mM TCEP for 30 min on ice. Then, TCEP was removed using a desalting column, which was equilibrated with buffer containing 50 mM HEPES, pH 7.0, 150 mM NaCl, 8 M urea. The reduced protein was incubated in Texas Red C2-maleimide (Thermo Fisher Scientific), in a molar protein:fluorophore ratio 1:20 either at room temperature for 2 hours or at 4°C overnight. The reaction mixture was passed through the desalting column to eliminate all unreacted reagents. The chemically modified OmpG D224C sample was snap-frozen in liquid nitrogen and stored at -80°C. To test the folding properties of the labeled protein, an aliquot of

the protein sample was diluted with the refolding buffer containing 50 mM Tris·HCl, pH 9.0, 3.25% OG until the final urea concentration reached 3.0 M. Samples were then incubated at 37 °C for 3 days. The refolding efficiency of Texas Red-labeled OmpG D224C was determined using the heat-modifiability assay through the SDS-PAGE analysis.<sup>27,31</sup>

**Expression and purification of SELENOK U92C and SELENOS U188S.** The cloning, expression, and purification of *Homo sapiens* SELENOK U92C (UniProtKB Q9Y6D0) and SELENOS U188S (UniProtKB Q9BQE4) used in this study were described previously.<sup>32</sup> In short, SELENOK U92C was cloned into a pMAL-C5X vector (New England Biolabs, Ipswich, MA) and fused to maltose-binding protein (MBP). A 6×His<sup>+</sup> tag was introduced between residues I3 and E4 of MBP to facilitate purification. A short linker NSSS with a tobacco etch virus (TEV) protease cleavage site (ENLYFQG) was used to connect the two proteins. In addition, an eight-amino acid-StrepII tag (WSHPQFEK) was inserted between the TEV protease cleavage site and SELENOK U92C to assist the purification. Following cleavage of the fusion protein by TEV protease, SELENOK U92C retained in its N-terminus the sequence GWSHPQFEK. MBP-SELENOK U92C was purified by amylose affinity chromatography. Then the fusion partner MBP was cleaved off by TEV protease. SELENOK U92C was further purified by Strep-Tactin affinity column (GE Healthcare Life Sciences). All purification steps were carried out in buffers supplemented with 1.3 mM DDM, which represented the starting detergent concentration for the follow-up dilutions. Protein purity, as assessed by 16% TRICINE-SDS-PAGE, was greater than 95% (**Supporting Information, Fig. S1**). Similarly, SELENOS U188S, with the native selenocysteine at position 188 mutated to serine, was cloned in the same way into the pMAL-C5X vector and fused with MBP.<sup>33</sup> A short linker NSSS and a TEV cleavage site,



ENLYFQS, was used to connect the two proteins. Following cleavage with TEV protease, only a serine was present before the first native amino acid. Expression and purification of SELENOS U188S was similar to the procedure above with the only difference that instead of the Strep-Tactin affinity chromatography SELENOS U188S was purified by a HisTrap FF column (GE Healthcare Life Sciences) to remove the 6×His<sup>+</sup> tagged-MBP and TEV protease.<sup>34</sup> The flow through containing the purified SELENOS U188S was collected. The protein purity, as determined by SDS-PAGE, was greater than 95%.

**Fluorescent Labeling of SELENOK U92C and SELENOS U188S.** 40 μM SELENOK U92C or SELENOS U188S were reduced by addition of 5 mM dithiothreitol (DTT) and incubated at room temperature for 20 min. DTT was then removed using a desalting column (5 mL HiTrap desalting column, GE Healthcare Life Sciences). Labeling reactions were carried out using 50 μM SELENOK U92C or SELENOS U188S in the reaction buffer (50 mM sodium phosphate, 200 mM NaCl, 0.067% DDM, 1 mM EDTA, pH 7.5) supplemented with 1 mM Texas Red C2- maleimide (Setareh Biotech, Eugene, OR) and incubated at room temperature for 1 h. Excess Texas Red C2 maleimide was removed by dialysis in the dark against the reaction buffer. SELENOK U92C was specifically labeled on the C92 position, as this is the only cysteine in the protein. SELENOS U188S was only labeled on the C174 position since the other cysteine is located in the trans-membrane helix and was proven to be inaccessible for fluorescent labeling.

**Anisotropy measurements.** For FP measurements, we used a SpectraMax I3 plate reader (Molecular Devices, Sunnyvale, CA) equipped with the Paradigm detection cartridge for

Rhodamine FP spectroscopy.<sup>35</sup> The excitation and emission wavelengths were 535 and 595 nm, respectively. A Texas Red fluorophore was covalently attached to an engineered cysteine sulfhydryl, because of its optical stability over a broad range of experimental circumstances.<sup>36</sup> The attachment site was chosen on the water-soluble domains of the membrane proteins, because of the hydrophilic nature of this bright fluorophore.<sup>37</sup> The FP recordings were carried out using 96-well Costar assay plates (Corning Incorporated, Kennebunk, ME). The fluorescence anisotropy depends on the time-dependent orthogonal,  $I_o(t)$ , and parallel,  $I_p(t)$ , emission intensities, as follows:<sup>36, 38</sup>

$$r(t) = \frac{I_p(t) - GI_o(t)}{I_p(t) + 2GI_o(t)} \quad (1)$$

Here,  $G$  is a sensitivity correction factor for the detection modes when emission polarizers are oriented vertically and horizontally.

$$G = \frac{I_{HV}}{I_{HH}} \quad (2)$$

$I_{HH}$  denotes the intensity with both the excitation and emission polarizers in a horizontal orientation.  $I_{HV}$  indicates the intensity with the excitation and emission polarizers oriented horizontally and vertically, respectively. The FP data were processed as average  $\pm$  SD over a number of at least three independent acquisitions. The robustness of the acquired data was illustrated in figures through vertical SD bars.

We executed steady-state anisotropy recordings with diluted refolded protein samples within individual wells, while keeping the final protein concentration constant at either 28 nM ( $\beta$ -barrel proteins) or at 200 nM ( $\alpha$ -helical proteins). For all proteins, this was accomplished by diluting the refolded protein sample within individual wells with buffer containing detergents at various

concentrations. The final detergent concentration in the protein samples for anisotropy measurements was derived using the following equation:

$$C_f V = C_s V_s + C_d V_d = (C_s f_s + C_d f_d) V \quad (3)$$

where  $V$  and  $C_f$  denote the well volume and the final detergent concentration of the protein sample for anisotropy measurements, respectively.  $C_s$  and  $C_d$  indicate the detergent concentrations of the refolded protein (starting concentrations) and diluting buffer, respectively.  $V_s$  and  $f_s$  are the volume and fractional volume ( $V_s/V$ ) of the refolded protein sample at a starting detergent concentration, respectively.  $V_d$  and  $f_d$  are the volume and fractional volume ( $V_d/V$ ) of the diluting buffer containing detergents at different concentrations, respectively. In this way, we were able to prepare samples containing detergents in a broad range of concentrations below and above their CMC.

We verified that potential self-quenching of Texas Red does not produce a time-dependent reduction in the FP output of the protein-Texas Red conjugate. Therefore, we performed control time-dependent anisotropy experiments, as follows: (i) at the beginning of the measurements at detergent concentrations much greater than their CMCs (**Supporting Information, Fig. S2**); and (ii) after 24 hours, reaching the endpoints of the detergent desolvation reaction (**Supporting Information, Fig. S3**). In both cases, we found no time-dependent alterations of the anisotropy readout. The FP anisotropy measurements were conducted under equilibrium conditions. The incubation time for the equilibration of protein samples after detergent dilution was 15 min. Then, a time-dependent kinetic read of the fluorescence anisotropy was acquired at the beginning of the detergent desolvation reaction. To assure uniform recording conditions, we collected the endpoints after 24 h, a period in which the protein samples, incubated at different detergent

concentrations, were covered and placed at 4°C. These endpoints were used to achieve the detergent dissociation isotherms. Protein aggregation increased over time upon drastic detergent depletion, but without affecting the signal-to-noise ratio of the anisotropy endpoints. The Hill-Langmuir dissociation-isotherm curves were fitted by:<sup>39</sup>

$$r(c) = \frac{r_{\min} + r_{\max} \left(\frac{c}{K_d}\right)^p}{1 + \left(\frac{c}{K_d}\right)^p} \quad (4)$$

$r_{\min}$  and  $r_{\max}$  denote the minimum and maximum values of anisotropy, respectively.<sup>10</sup>  $p$  and  $K_d$  indicate the Hill coefficient and the apparent dissociation constant, respectively. The major assumption of this fitting procedure is that the protein surface shows specific binding sites for detergent monomers. The steepness of the two-state transition of detergent desolvation at half detergent saturation,  $q$ , was calculated by the following equation:

$$q = \frac{p(r_{\max} - r_{\min})}{4K_d} \quad (5)$$

**MD simulations of the interactions of DDM with  $\beta$ -barrel proteins.** All simulations were performed using the molecular dynamics program NAMD2,<sup>40</sup> periodic boundary conditions, and a 2-fs timestep. The CHARMM36 force field<sup>41</sup> was used to describe proteins, detergents, TIP3P water, and ions. The CUFIX corrections were applied to improve description of charge-charge interactions.<sup>42-43</sup> RATTLE<sup>44</sup> and SETTLE<sup>45</sup> algorithms were applied to describe covalent bonds that involved hydrogen atoms in proteins, detergents and water molecules. Particle-Mesh-Ewald (PME)<sup>46</sup> algorithm was used to evaluate the long-range electrostatic interaction on a 1 Å-spaced grid; the full electrostatics calculation was performed every three timesteps. Van der Waals interactions were evaluated using a smooth 10-12 Å cutoff. Atomic coordinates of the four  $\beta$ -barrel proteins, OmpG (PDB entry 2IWV<sup>21</sup>), FhuA  $\Delta C/\Delta 5L$  (PDB entry 1BY5<sup>22</sup>), FhuA

$\Delta C/\Delta 5L_{25N}$ , and FhuA  $\Delta C/\Delta 7L_{30N}$ , were obtained from the Protein Data Bank. Structures containing deletions and mutations were built by modifying the wild-type structure. For each  $\beta$ -barrel protein, two systems were constructed differing by the initial placement of the DDM molecules. The cubic arrangement of DDM was realized by placing 21 DDM molecules around the protein with the average protein-to-DDM distance of 5.7 nm, whereas in the planar arrangement, the DDM molecules were placed within a plane passing through the geometrical center of the protein. The systems were solvated using the VMD's Solvate plugin. Waters overlapping with the proteins and DDM molecules were removed. Sodium and chloride ions were added to neutralize the system and bring the ion concentration to 200 mM. The final systems contained approximately 172,000 atoms. The initial DDM concentration was 20 mM. One additional FhuA  $\Delta C/\Delta 5L$  system was built to containing 105 DDM molecules in the same electrolyte volume, which corresponded to a concentration of 100 mM DDM with cubic arrangement. Each system was minimized for 9600 steps using the conjugate gradient method, then equilibrated for  $\sim 230$  ns in the constant number of atoms, pressure and temperature ensemble. The Nose-Hoover Langevin piston pressure control<sup>47-48</sup> was used to maintain the pressure of the system at 1 atm by adjusting the system's dimension. Langevin thermostat<sup>49</sup> was applied to all the heavy atoms of the system with a damping coefficient of  $0.1 \text{ ps}^{-1}$ . All the trajectories were analyzed by using VMD.<sup>50</sup>

## RESULTS

**Rationale for data acquisition, analysis, and interpretation.** For a satisfactorily solubilizing detergent, we determined that at concentrations much greater than the CMC (**Table 1**) the FP anisotropy reached a concentration-independent maximum value,  $r_{\max}$  (**Fig. 2**). In contrast, at detergent concentrations comparable with or below the CMC, the FP anisotropy followed a decrease to a concentration-dependent value,  $r(c) < r_{\max}$ . Moreover, at detergent concentrations much lower than the CMC the FP anisotropy decreased to a concentration-independent minimum value,  $r_{\min}$ . OmpG<sup>51</sup> and FhuA<sup>23, 35</sup> proteins exhibit an overwhelming preponderance of anti-parallel  $\beta$ -sheet structure in solution under detergent-refolding conditions. At detergent concentrations well below their CMC, a decrease in the FP anisotropy was produced by the dissociation of the detergent monomers from the protein, resulting in a reduction in the hydrodynamic radius,  $R_h$ , of the PDC, and a corresponding increase in its tumbling rate. This interpretation was also supported by the observation that at detergent concentrations well above their CMC, no significant change in the FP anisotropy readout was noted (**Supporting Information, Fig. S2**).

Therefore, the detergent-solubilized membrane proteins featured a maximum anisotropy,  $r_{\max}$ , whereas the detergent-desolvated proteins exhibited a minimum anisotropy,  $r_{\min}$  (**Fig. 2**). Of course, deviations from this rule occurred under poor detergent solubilization conditions, even if the detergent concentration was much greater than the CMC. For each case, the mid-point of the transition of detergent desolvation,  $K_d$ , was compared with CMC. If  $K_d > \text{CMC}$ , then the cohesive interactions were greater than the adhesive interactions (**Fig. 2A**), and vice-versa, if  $K_d$

< CMC (**Fig. 2B**). The adhesive and cohesive interactions were comparable to each other when  $K_d \cong \text{CMC}$  (**Fig. 2C**).

FIGURE 2.

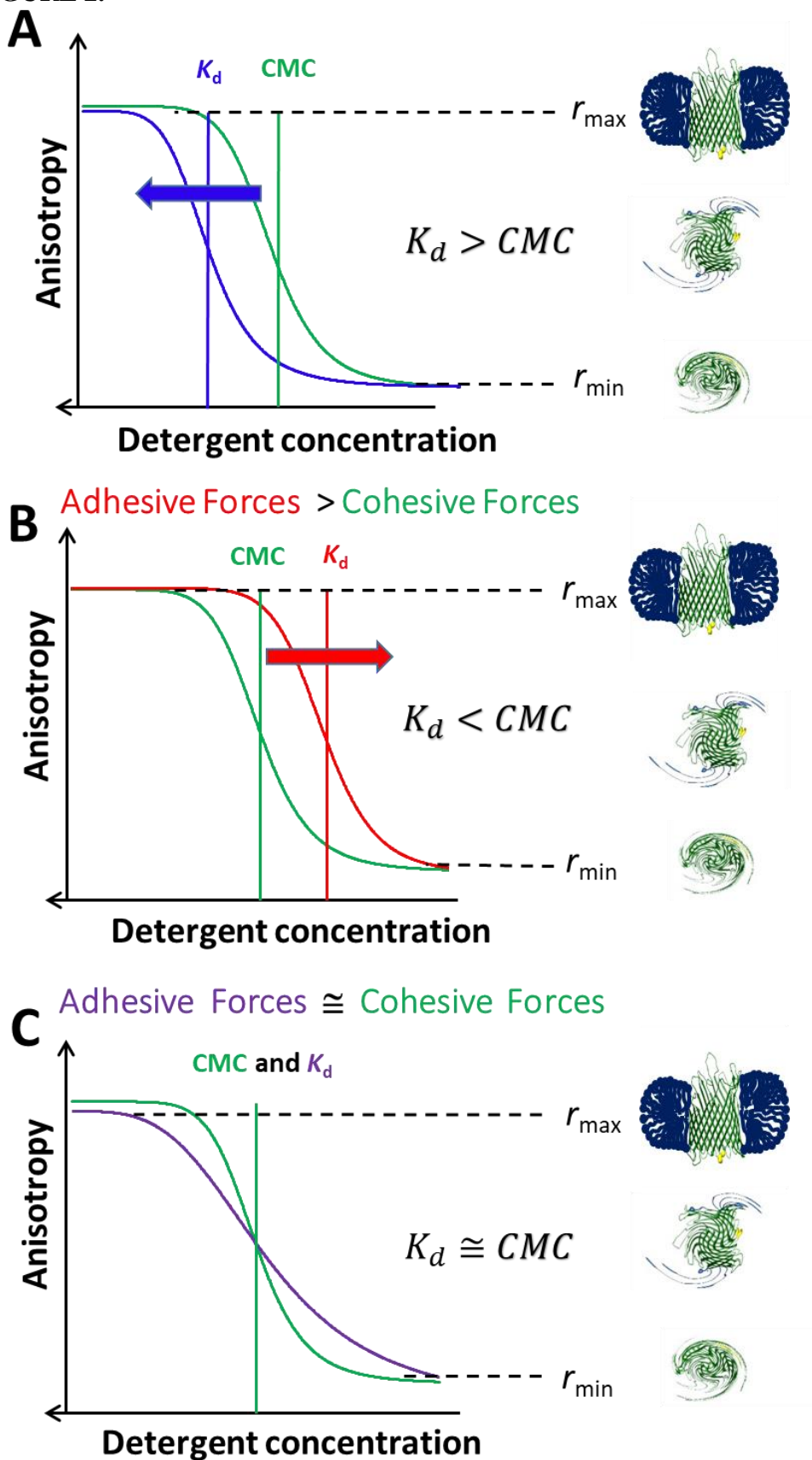




**Figure 2: Graphic illustrating the three hypothetical scenarios of the balance between adhesive and cohesive interactions of PDCs. (A)** The detergent-protein interactions are weaker than the detergent-detergent interactions that keep the proteomicelle molecules together; **(B)** The detergent-protein interactions are stronger than the detergent-detergent interactions; **(C)** The two types of interactions are of similar magnitude.

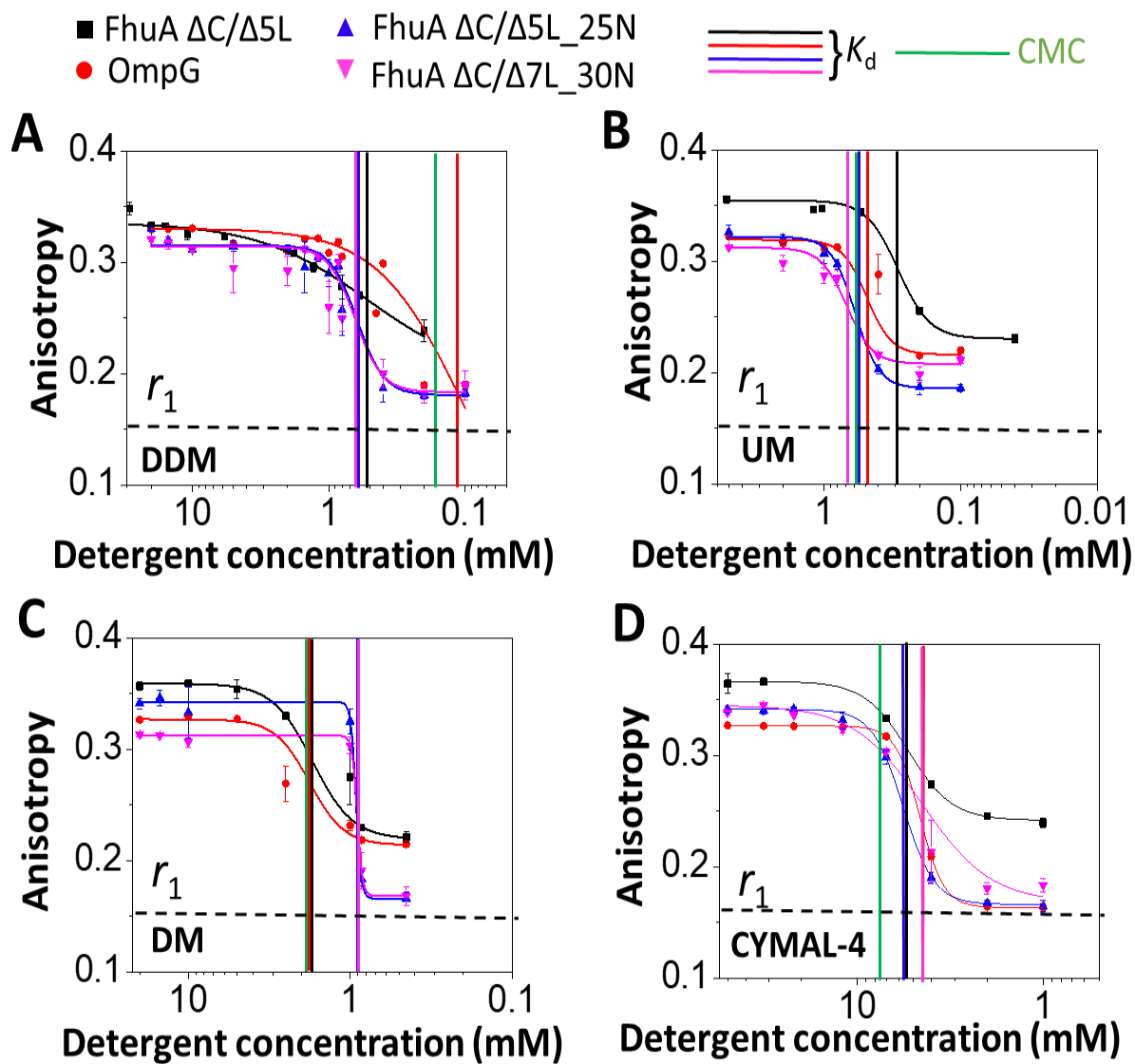


FIGURE 3.

**Figure 3: Dose-response changes in fluorescence anisotropy for neutral maltoside-containing detergents.** (A) n-dodecyl- $\beta$ -D-maltoside (DDM); (B) n-undecyl- $\beta$ -D-maltoside (UM); (C) n-Decyl- $\beta$ -D-maltoside (DM); (D) 4-Cyclohexyl-1-butyl- $\beta$ -D-maltoside (CYMAL-4). All anisotropy measurements were conducted out in 200 mM NaCl, 50 mM HEPES, pH 7.4, and at room temperature. The anisotropy data were recorded by adding overnight detergent-refolded protein to a bath of varying detergent concentration, but keeping the final protein concentration at 28 nM. Starting detergent concentrations were above the CMC. Thereafter, they were reduced at concentrations below the CMC (**Experimental Methods**). Time-dependent anisotropy measurements were conducted directly after dilution of the refolded protein sample at respective detergent concentration. Vertical bars represent the magnitudes of the CMC and  $K_d$  of the PDCs of varying isoelectric point of the proteins. The horizontal dashed bar represents the minimum anisotropy value,  $r_1 = \sim 0.16$ , obtained with FhuA  $\Delta C/\Delta 5L$  in 6 M Gdm-HCl (**Table 3**). This anisotropy value corresponds to the most rotationally diffusive FhuA  $\Delta C/\Delta 5L$ .

**Table 3: The recorded minima and maxima of the anisotropy with neutral and zwitterionic detergents and  $\beta$ -barrel proteins.**<sup>a</sup> This table also illustrates the rotational diffusion coefficients as well as alterations in hydrodynamic radii of the proteomicelles during the detergent desolvation transitions.

DM <sup>b</sup>	$r_{\min}^c$	$r_{\max}^c$	$D_r^{\text{slow}} (10^7 \text{ s}^{-1})^d$	$D_r^{\text{fast}} (10^7 \text{ s}^{-1})^d$	$R_h^{\text{max}} (\text{nm})^e$	$\Delta R_h (\text{nm})^f$
OmpG	$0.214 \pm 0.005$	$0.327 \pm 0.001$	$0.89 \pm 0.02$	$3.5 \pm 0.2$	2.6	$0.95 \pm 0.04$
FhuA $\Delta C/\Delta 5L$	$0.219 \pm 0.005$	$0.360 \pm 0.001$	$0.44 \pm 0.01$	$3.3 \pm 0.2$	3.3	$1.6 \pm 0.1$
FhuA $\Delta C/\Delta 5L_{25N}$	$0.166 \pm 0.003$	$0.343 \pm 0.002$	$0.66 \pm 0.03$	$5.6 \pm 0.2$	3.0	$1.5 \pm 0.1$
FhuA $\Delta C/\Delta 7L_{30N}$	$0.168 \pm 0.007$	$0.312 \pm 0.001$	$1.1 \pm 0.1$	$5.5 \pm 0.4$	2.4	$1.0 \pm 0.1$
CYMAL-4 <sup>b</sup>	$r_{\min}^c$	$r_{\max}^c$	$D_r^{\text{slow}} (10^7 \text{ s}^{-1})^d$	$D_r^{\text{fast}} (10^7 \text{ s}^{-1})^d$	$R_h^{\text{max}} (\text{nm})^e$	$\Delta R_h (\text{nm})^f$
OmpG	$0.163 \pm 0.001$	$0.326 \pm 0.001$	$0.90 \pm 0.01$	$5.8 \pm 0.1$	2.6	$1.2 \pm 0.1$
FhuA $\Delta C/\Delta 5L$	$0.242 \pm 0.001$	$0.367 \pm 0.001$	$0.36 \pm 0.01$	$2.6 \pm 0.1$	3.6	$1.7 \pm 0.1$
FhuA $\Delta C/\Delta 5L_{25N}$	$0.166 \pm 0.001$	$0.341 \pm 0.001$	$0.69 \pm 0.01$	$5.6 \pm 0.1$	2.9	$1.4 \pm 0.1$
FhuA $\Delta C/\Delta 7L_{30N}$	$0.168 \pm 0.025$	$0.345 \pm 0.004$	$0.63 \pm 0.05$	$5.5 \pm 1.2$	2.9	$1.5 \pm 0.2$
OG <sup>b</sup>	$r_{\min}^c$	$r_{\max}^c$	$D_r^{\text{slow}} (10^7 \text{ s}^{-1})^d$	$D_r^{\text{fast}} (10^7 \text{ s}^{-1})^d$	$R_h^{\text{max}} (\text{nm})^e$	$\Delta R_h (\text{nm})^f$
OmpG	$0.153 \pm 0.002$	$0.306 \pm 0.001$	$1.2 \pm 0.1$	$6.4 \pm 0.1$	2.4	$1.0 \pm 0.1$
FhuA $\Delta C/\Delta 5L$	$0.162 \pm 0.002$	$0.291 \pm 0.002$	$1.5 \pm 0.1$	$5.8 \pm 0.1$	2.2	$0.80 \pm 0.02$
FhuA $\Delta C/\Delta 5L_{25N}$	$\sim 0.15$	$\sim 0.17$	$\sim 5.2$	$\sim 6.6$	ND <sup>h</sup>	ND <sup>h</sup>
FhuA $\Delta C/\Delta 7L_{30N}$	$\sim 0.15$	$\sim 0.17$	$\sim 5.2$	$\sim 6.6$	ND <sup>h</sup>	ND <sup>h</sup>
CHAPS <sup>b</sup>	$r_{\min}^c$	$r_{\max}^c$	$D_r^{\text{slow}} (10^7 \text{ s}^{-1})^d$	$D_r^{\text{fast}} (10^7 \text{ s}^{-1})^d$	$R_h^{\text{max}} (\text{nm})^e$	$\Delta R_h (\text{nm})^f$
OmpG	ND <sup>h</sup>	$0.318 \pm 0.002$	$1.0 \pm 0.1$	ND <sup>h</sup>	2.5	ND <sup>h</sup>
FhuA $\Delta C/\Delta 5L$	$0.172 \pm 0.048$	$0.292 \pm 0.004$	$0.53 \pm 0.2$	$1.5 \pm 0.1$	2.2	$0.77 \pm 0.18$
FhuA $\Delta C/\Delta 5L_{25N}$	$\sim 0.15$	$\sim 0.17$	$\sim 5.2$	$\sim 6.6$	ND <sup>h</sup>	ND <sup>h</sup>
FhuA $\Delta C/\Delta 7L_{30N}$	$\sim 0.16$	$\sim 0.17$	$\sim 5.2$	$\sim 6.0$	ND <sup>h</sup>	ND <sup>h</sup>
LysoFos <sup>b</sup>	$r_{\min}^c$	$r_{\max}^c$	$D_r^{\text{slow}} (10^7 \text{ s}^{-1})^d$	$D_r^{\text{fast}} (10^7 \text{ s}^{-1})^d$	$R_h^{\text{max}} (\text{nm})^e$	$\Delta R_h (\text{nm})^f$
OmpG	$0.229 \pm 0.006$	$0.307 \pm 0.001$	$1.2 \pm 0.1$	$3.0 \pm 0.2$	2.4	$0.61 \pm 0.04$
FhuA $\Delta C/\Delta 5L$	$0.223 \pm 0.007$	$0.330 \pm 0.001$	$0.84 \pm 0.01$	$3.1 \pm 0.2$	2.7	$0.95 \pm 0.05$
FhuA $\Delta C/\Delta 5L_{25N}$	$0.177 \pm 0.001$	$0.313 \pm 0.001$	$1.1 \pm 0.02$	$5.0 \pm 0.1$	2.4	$0.96 \pm 0.02$
FhuA $\Delta C/\Delta 7L_{30N}$	$0.184 \pm 0.003$	$0.294 \pm 0.005$	$1.4 \pm 0.1$	$4.7 \pm 0.1$	2.2	$0.73 \pm 0.06$
FhuA $\Delta C/\Delta 5L$ in Gdm-HCl <sup>g</sup>	$\sim 0.16$	$\sim 0.16$	$\sim 6.0$	$\sim 6.0$	1.4	NA <sup>i</sup>

<sup>a</sup>To reach low detergent concentrations below CMC, the Gdm-HCl-solubilized protein was refolded at various detergent concentrations above the CMC.

<sup>b</sup>Full names of the detergents are provided in **Experimental and computational methods**.

<sup>c</sup> $r_{\min}$  was extrapolated for the lowest detergent concentration in the well.  $r_{\max}$  was determined at detergent concentrations above the CMC.

<sup>d</sup> $D_r^{\text{slow}}$  and  $D_r^{\text{fast}}$  indicate the rotational diffusion coefficients under solvation and desolvation conditions, respectively.

<sup>e</sup> $R_h^{\text{max}}$  is the maximum hydrodynamic radius of the proteomicelle.

<sup>f</sup> $\Delta R_h$  is the decrease in the hydrodynamic radius,  $R_h$ , as a result of the detergent desolvation.

<sup>g</sup>Anisotropy was determined in 6 M Gdm-HCl.

<sup>h</sup>Not determined.

<sup>i</sup>Not applicable.

**Alterations in the charge distribution of the solvent-accessible surface of  $\beta$ -barrels.** To further examine the impact of electrostatic adhesive interactions on  $K_d$ , we examined four  $\beta$ -barrel proteins of varying charge distribution on the solvent-accessible surface (**Table 2**). These were OmpG<sup>21</sup> and three derivatives of FhuA<sup>22</sup> of *E.coli*, FhuA  $\Delta C/\Delta 5L$ , FhuA  $\Delta C/\Delta 5L_{25N}$ , and FhuA  $\Delta C/\Delta 7L_{30N}$  (**Fig. 1**).<sup>24</sup> FhuA  $\Delta C/\Delta 5L$  is a truncation FhuA mutant lacking the 160-residue, N-terminal cork domain (C) and extensive parts of the extracellular loops L3, L4, L5, L10, and L11. FhuA  $\Delta C/\Delta 5L_{25N}$  features 25 negative charge neutralizations on the extracellular loops and periplasmic  $\beta$  turns with respect to FhuA  $\Delta C/\Delta 5L$ . FhuA  $\Delta C/\Delta 7L_{30N}$  was derived by additional four loop truncations, L4, L5, L7, and L8, with respect to the FhuA  $\Delta C/\Delta 5L$  scaffold, and with a total of 30 negative charge neutralizations with respect to FhuA  $\Delta C/\Delta 5L$ . These charge neutralizations were conducted by replacing D and E with N and Q, respectively. In this way, we accomplished an extensive change in the balance between positive and negative residues on the solvent-accessible surface. Therefore, at physiological pH negative residues were dominant in OmpG and FhuA  $\Delta C/\Delta 5L$ , making these proteins acidic ( $pI < 7.0$ ), whereas positive side chains are prevalent in FhuA  $\Delta C/\Delta 5L_{25N}$  and FhuA  $\Delta C/\Delta 7L_{30N}$ , making these proteins basic ( $pI > 7.0$ ) (**Table 2**).

### **The balance of adhesive and cohesive interactions of the $\beta$ barrel-containing proteomicelles**

**Neutral detergents.** **Fig. 3** shows the transitions of detergent desolvation with four maltoside-containing neutral detergents, as follows: DDM (**Fig. 3A**), UM (**Fig. 3B**), DM (**Fig. 3C**), CYMAL-4 (**Fig. 3D**) (**Supporting Information, Table S1**). In these panels, we showed the basal anisotropy readout,  $r_1 = 0.16$ , recorded with FhuA  $\Delta C/\Delta 5L$  when fully unfolded (e.g., in

most rotationally diffusive state) using 6 M Gdm-HCl (**Table 3**). The only distinction among DDM, UM, and DM is the length of their hydrophobic tail, with 12, 11, and 10 alkyl carbons, respectively. CYMAL-4 is also a maltoside-containing detergent, but containing a very short hydrophobic tail (e.g., 4 alkyl carbons) and a cyclohexyl group. When all four proteins were incubated in DDM, we noted that the three FhuA protein mutants exhibited  $K_d$  values greater than the CMC, suggesting that the cohesive forces outperformed the adhesive forces, a finding that was not encountered with OmpG (**Supporting Information, Table S2**). The FhuA mutants showed a shift in the UM desolvation-induced transition towards stronger adhesive interactions (**Fig. 3B**). Interestingly, the DM desolvation-induced transition recoded with the basic FhuA proteins was very sharp and featured the largest positive Hill cooperativity  $p$  values of  $\sim 27$  (**Fig. 3C and Table 4**), contrasting to those noted with weakly adhesive acidic  $\beta$  barrels. Moreover, all four  $\beta$ -barrel proteins exhibited stronger adhesive than cohesive interactions with CYMAL-4 (**Fig. 3D and Table 4**). Therefore, at physiological pH conditions, we found that for basic  $\beta$  barrels the adhesive interactions increased with respect to cohesive interactions in the order DDM  $\rightarrow$  UM  $\rightarrow$  CYMAL-4  $\rightarrow$  DM (**Supporting Information, Table S2**; last column).

We were able to refold the acidic  $\beta$ -barrel proteins in glucoside-containing neutral detergent (OG) and noted a detergent desolvation-induced transition with maximum and minimum anisotropy values of  $\sim 0.30$  and  $\sim 0.16$ , respectively (**Table 3, Table 4**). In contrast, the experiments with the basic  $\beta$ -barrel proteins revealed very low anisotropy values of  $\sim 0.17$ , near  $r_1$ , which corresponded to the most rotationally diffusive FhuA  $\Delta C/\Delta 5L$ , indicating poor solubility features under these experimental conditions. Because the two-state detergent desolvation-induced transition was only observed with acidic, but not basic  $\beta$  barrels, it is

conceivable that the anisotropy value,  $r$ , is strongly dependent on the characteristics of the PDC, even if there is some mobility restriction of the fluorophore by the detergent coat. Therefore, these examples illustrate how extensive changes in the charge distribution across the solvent-accessible surface of the  $\beta$  barrel proteins produced dramatic alterations in the magnitude of adhesive interactions.

**Zwitterionic detergents.** We extended these studies to zwitterionic detergents. Interestingly, we were able to refold the acidic  $\beta$  barrels in CHAPS, but not the basic  $\beta$  barrels (**Fig. 4**). This situation resembles that found with OG. Indeed, the time-dependent changes in the FP anisotropy revealed a fast dissociation of CHAPS from FhuA  $\Delta C/\Delta 5L$  at a detergent concentration of 2 mM, which is  $\sim 3$ -fold lower than its CMC (**Table 1, Supporting Information, Fig. S4**). In contrast, we found a strong binding interaction between CHAPS and OmpG, with a  $K_d < 0.6$  mM (**Table 4**). n-dodecyl-N,N-dimethylglycine (LD), another zwitterionic detergent, showed a closely similar signature, encompassing adhesive interactions with the acidic  $\beta$  barrels, but weak interactions with the basic  $\beta$  barrels (**Supporting Information, Fig. S5**). In excellent accord with the outcomes pertaining to the above-mentioned zwitterionic detergents, LysoFos exhibited stronger adhesive interactions with the acidic  $\beta$ -barrels than those interactions with the basic  $\beta$  barrels (**Table 3 and Table 4**). On the other hand, the  $K_d$  values noted with the interaction of LysoFos with the basic  $\beta$  barrels matched the CMC under similar experimental conditions, indicating no significant difference between adhesive and cohesive interactions (**Table 1 and Table 4**). Therefore, LysoFos was found as a satisfactorily solubilizing detergent for both the acidic and basic  $\beta$  barrels.



- FhuA  $\Delta C/\Delta 5L$     ▲ FhuA  $\Delta C/\Delta 5L_{25N}$   
 ● OmpG                      ▼ FhuA  $\Delta C/\Delta 7L_{30N}$



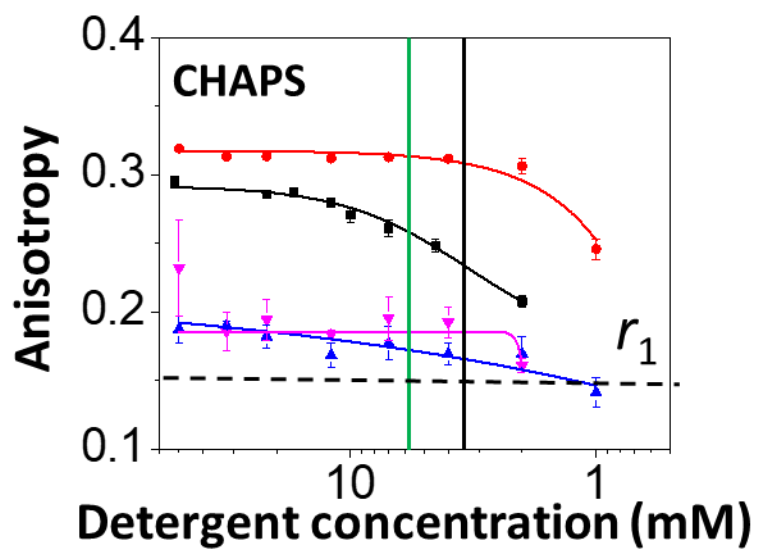


FIGURE 4.

**Figure 4: Dose-response changes in fluorescence anisotropy recorded with zwitterionic detergents and proteins of varying isoelectric point pI.** This panel shows a desorption isotherms recorded with 3-[(3-Cholamidopropyl) dimethylammonio]-1-Propanesulfonate (CHAPS). Vertical bars represent the magnitudes of the CMC and  $K_d$  of the PDCs of the proteins of varying isoelectric point. The horizontal dashed bar represents the minimum anisotropy value,  $r_0 = \sim 0.16$ , obtained with FhuA  $\Delta C/5L$  in 6 M Gdm-HCl (**Table 3**). All the other experimental conditions were the same as in **Fig. 3**.

**Table 4: Summary of the fitting results of the two-state, concentration-dependent anisotropy curves of the endpoints of the detergent desolvation phase with neutral**

**detergents.**<sup>a,b</sup> This was determined with three FhuA derivatives and OmpG as well as a panel of five neutral detergents of varying hydrophobic chain and hydrophilic head group. The FP measurements were carried in 200 mM NaCl, 50 mM HEPES, pH 7.4 and at a temperature of 24°C. All data were derived as averages  $\pm$  SDs of three independent data acquisitions.

DM <sup>c</sup>	$p^d$	$K_d^e$ (mM)	$q^f$ (mM <sup>-1</sup> )	$\Delta G^g$ (kcal/mol)	Balance <sup>h</sup>
OmpG	4.1 ± 1.2	1.8 ± 0.4	0.064	-3.7 ± 0.1	$F_{adh} \cong F_{coh}$
FhuA $\Delta C/\Delta 5L$	3.5 ± 0.5	1.7 ± 0.1	0.072	-3.8 ± 0.1	$F_{adh} \cong F_{coh}$
FhuA $\Delta C/\Delta 5L_{25N}$	27 ± 3	0.9 ± 0.1	1.30	-4.1 ± 0.1	$F_{adh} \gg F_{coh}$
FhuA $\Delta C/\Delta 7L_{30N}$	27 ± 6	0.9 ± 0.1	1.07	-4.1 ± 0.1	$F_{adh} \gg F_{coh}$
CYMAL-4 <sup>c</sup>	$p^d$	$K_d^e$ (mM)	$q^f$ (mM <sup>-1</sup> )	$\Delta G^g$ (kcal/mol)	Balance <sup>h</sup>
OmpG	6.7 ± 0.1	4.6 ± 0.1	0.25	-3.2 ± 0.1	$F_{adh} > F_{coh}$
FhuA $\Delta C/\Delta 5L$	3.7 ± 0.1	5.3 ± 0.1	0.38	-3.1 ± 0.1	$F_{adh} > F_{coh}$
FhuA $\Delta C/\Delta 5L_{25N}$	5.2 ± 0.3	5.7 ± 0.1	0.28	-3.1 ± 0.1	$F_{adh} > F_{coh}$
FhuA $\Delta C/\Delta 7L_{30N}$	2.3 ± 0.9	4.5 ± 1.1	0.17	-3.2 ± 0.1	$F_{adh} > F_{coh}$
OG <sup>c</sup>	$p^d$	$K_d^e$ (mM)	$q^f$ (mM <sup>-1</sup> )	$\Delta G^g$ (kcal/mol)	Balance <sup>h</sup>
OmpG	4.9 ± 0.5	11 ± 1	0.017	-2.7 ± 0.1	$F_{adh} > F_{coh}$
FhuA $\Delta C/\Delta 5L$	5.3 ± 0.9	13 ± 1	0.013	-2.5 ± 0.1	$F_{adh} > F_{coh}$
FhuA $\Delta C/\Delta 5L_{25N}$	ND <sup>i</sup>	ND <sup>i</sup>	ND <sup>i</sup>	ND <sup>i</sup>	$F_{adh} \ll F_{coh}$
FhuA $\Delta C/\Delta 7L_{30N}$	ND <sup>i</sup>	ND <sup>i</sup>	ND <sup>i</sup>	ND <sup>i</sup>	$F_{adh} \ll F_{coh}$
CHAPS <sup>c</sup>	$p^d$	$K_d^e$ (mM)	$q^f$ (mM <sup>-1</sup> )	$\Delta G^g$ (kcal/mol)	Balance <sup>h</sup>
OmpG	~1.6	< 0.6	ND <sup>i</sup>	~-7.0	$F_{adh} \gg F_{coh}$
FhuA $\Delta C/\Delta 5L$	1.7 ± 0.6	3.3 ± 1.8	0.015	-3.4 ± 0.5	$F_{adh} > F_{coh}$
FhuA $\Delta C/\Delta 5L_{25N}$	ND <sup>i</sup>	ND <sup>i</sup>	ND <sup>i</sup>	ND <sup>i</sup>	$F_{adh} \ll F_{coh}$
FhuA $\Delta C/\Delta 7L_{30N}$	ND <sup>i</sup>	ND <sup>i</sup>	ND <sup>i</sup>	ND <sup>i</sup>	$F_{adh} \ll F_{coh}$
LysoFos <sup>c</sup>	$p^d$	$K_d^e$ (mM)	$q^f$ (mM <sup>-1</sup> )	$\Delta G^g$ (kcal/mol)	Balance <sup>h</sup>
OmpG	5.6 ± 1.5	0.26 ± 0.03	0.41	-4.9 ± 0.1	$F_{adh} > F_{coh}$
FhuA $\Delta C/\Delta 5L$	9.1 ± 6.2	0.47 ± 0.04	0.51	-4.5 ± 0.1	$F_{adh} > F_{coh}$
FhuA $\Delta C/\Delta 5L_{25N}$	4.5 ± 0.5	0.71 ± 0.03	0.22	-4.3 ± 0.1	$F_{adh} \cong F_{coh}$
FhuA $\Delta C/\Delta 7L_{30N}$	3.5 ± 0.7	0.73 ± 0.04	0.13	-4.3 ± 0.1	$F_{adh} \cong F_{coh}$

<sup>a</sup>To reach low detergent concentrations below the CMC, the Gdm-HCl-solubilized (FhuA derivatives) or urea-solubilized (OmpG) proteins were refolded at various detergent concentrations above the CMC.

<sup>b</sup>The dose-response equilibrium curves were fitted by the four-parameter Hill equation.

<sup>c</sup>This column indicates the names of the detergents and proteins used in this work.

<sup>d</sup> $p$  is the Hill coefficient.

<sup>e</sup>The apparent dissociation constant,  $K_d$ , was determined as the midpoint of the dose-dependent dissociation phase.<sup>13</sup>

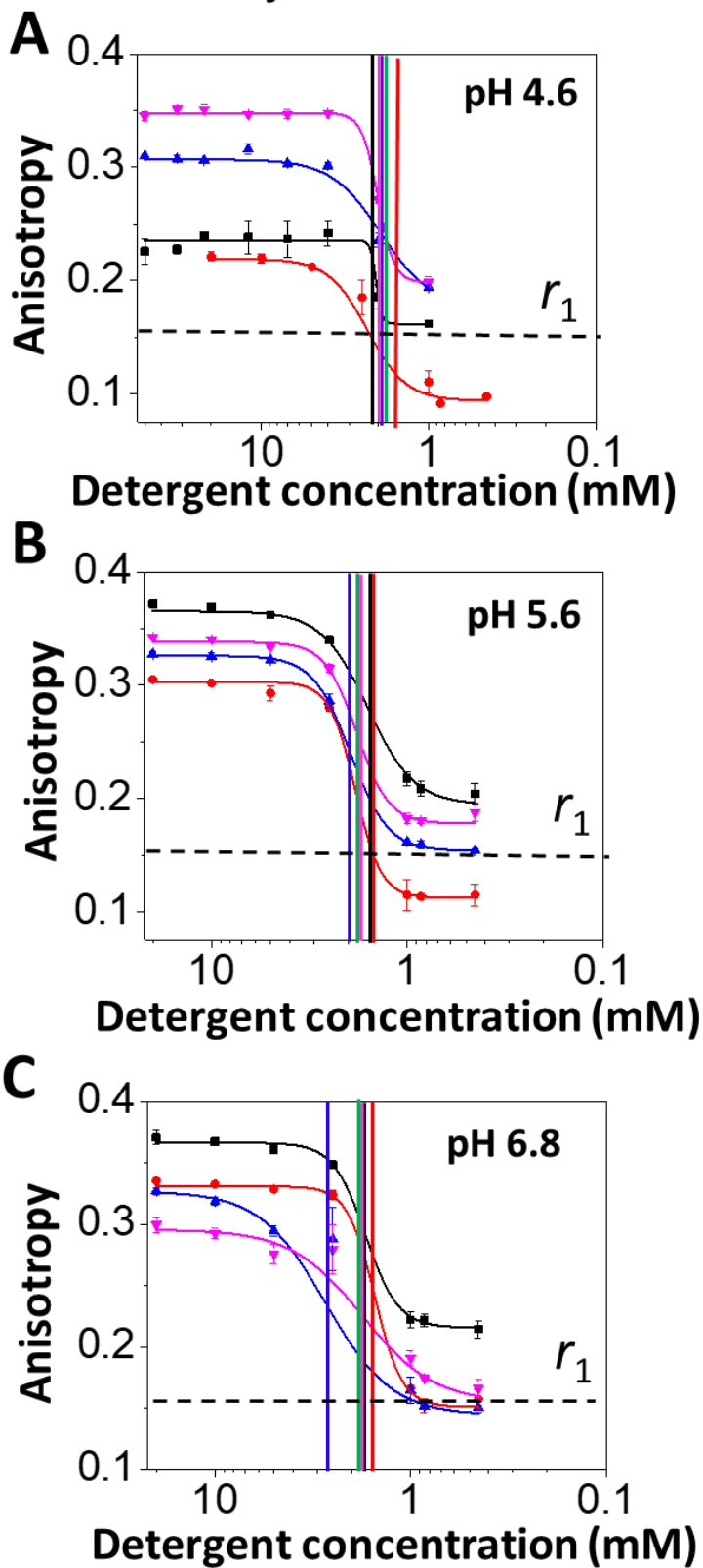
<sup>f</sup>The slope factor or transition steepness was calculated at the midpoint of the dissociation phase.

<sup>g</sup>Free energies were determined using the standard thermodynamic relationship  $\Delta G = RT \ln K_d$ .

<sup>h</sup>The quantitative balance between the adhesive protein-detergent ( $F_{adh}$ ) and cohesive detergent-detergent interactions ( $F_{coh}$ ) of the proteomicelles.

<sup>i</sup>Not determined.

**Does pH alter the interfacial interactions of the PDC with neutral detergents?** Here, we asked whether pH alters the balance between the adhesive and cohesive interactions. It is worth mentioning that Texas Red is a pH insensitive fluorophore.<sup>52</sup> Because pH modifications affect the protein electrostatics, but not the cohesive interactions within proteomicelles formed by a neutral detergent, we examined the PDC interfacial interactions mediated by DM (**Fig. 5; Supporting Information, Table S3 and Table S4**). The rationale of this choice resided in the fact that at physiological pH DM showed substantially increased adhesive interactions with the basic  $\beta$  barrels ( $K_d \sim 0.9$  mM), as compared with the acidic  $\beta$  barrels ( $K_d \sim 1.8$  mM), although it is a neutral detergent (**Fig. 3C**). At acidic pH values, no significant distinctions between  $K_d$  and CMC were observed, despite a broad pI range among the four  $\beta$  barrels. In contrast to all FhuA derivatives, DM-refolded OmpG showed no significant pH-dependent alterations in the balance between adhesive and cohesive interactions when examined in the pH range 4.6 – 8.2 (**Supporting Information, Table S4**; last column), likely due to very strong hydrophobic interactions at the PDC interface.



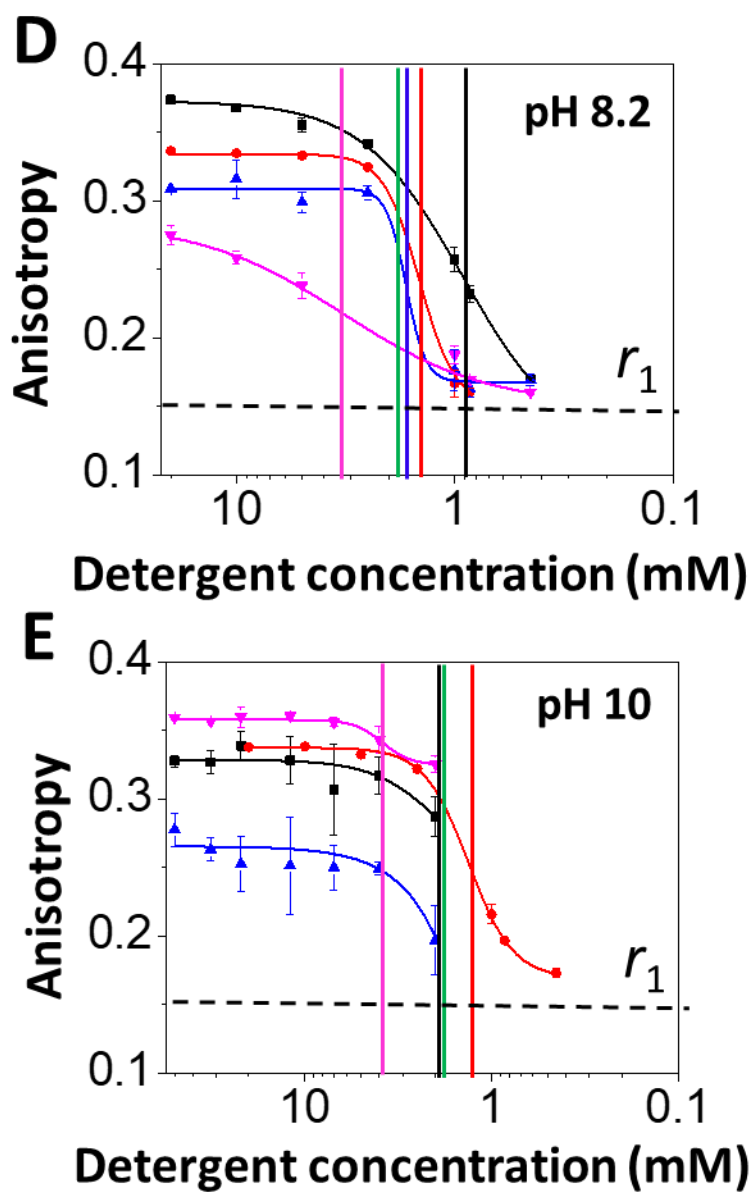


FIGURE 5.



**Figure 5: Dose-response changes in fluorescence anisotropy acquired with DM under acidic conditions.** (A) pH 4.6; (B) pH 5.6; (C) pH 6.8; (D) pH 8.2; and (E) pH 10.0. The buffer was either 50 mM HEPES (pH 6.8), or 50 mM NaOAc (pH 4.6, pH 5.6). The salt concentration was 200 mM NaCl. Vertical bars represent the magnitudes of the CMC and  $K_d$  of the PDCs of varying isoelectric point of the proteins. The horizontal dashed bar represents the minimum anisotropy value,  $r_0 = \sim 0.16$ , obtained with FhuA  $\Delta C/5L$  in either 40 mM SDS or 6 M Gdm-HCl (Table 3). All the other experimental conditions were the same as in Fig. 3.

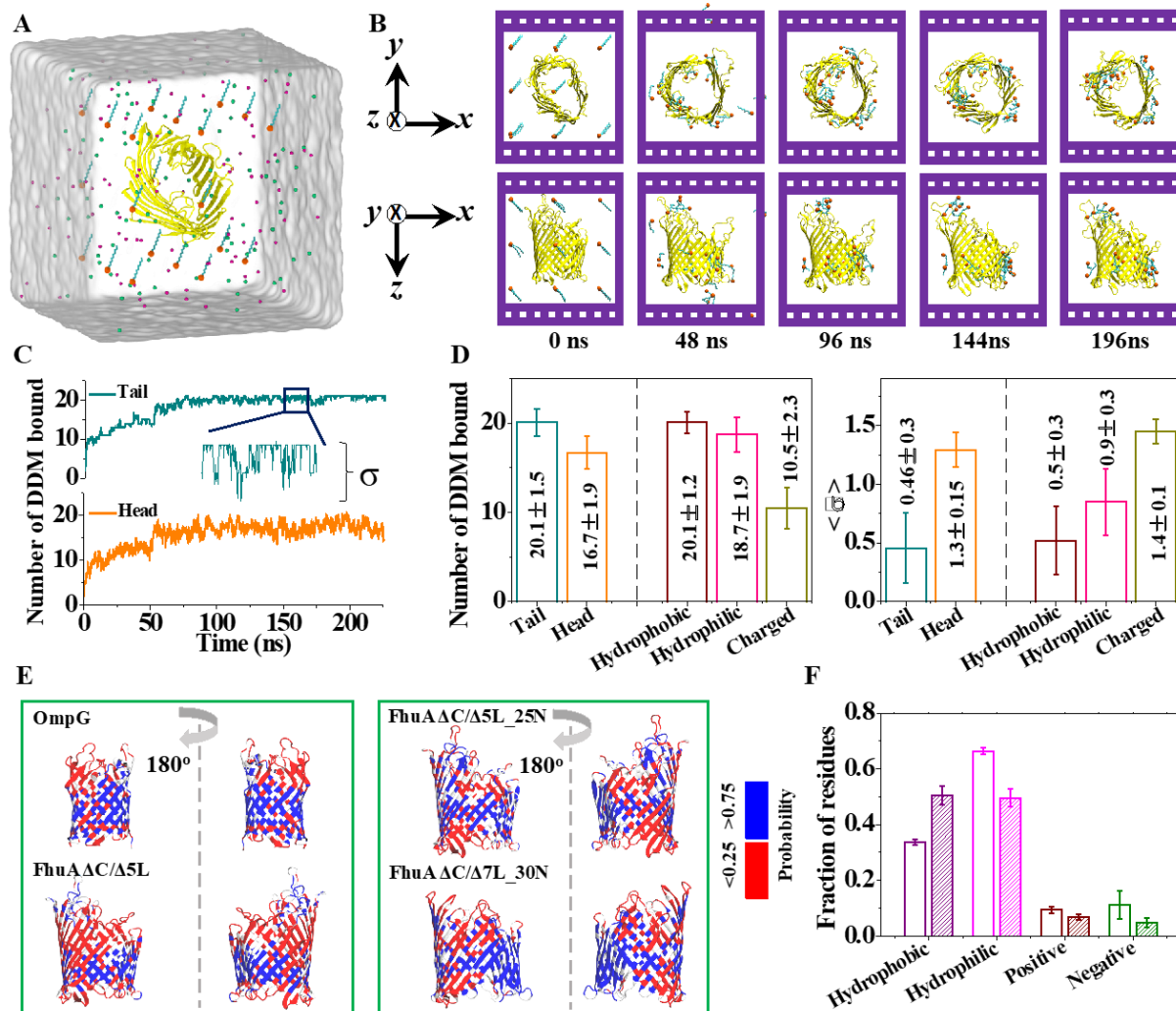


FIGURE 6.

**Figure 6: MD simulations of DDM binding to the  $\beta$ -barrel proteins.** (A) Initial setup of a typical MD simulation. FhuA  $\Delta C/\Delta 5L$  is shown using a cartoon representation (yellow); the head and the tail regions of the DDM molecules are shown as orange spheres and cyan lines, respectively. The magenta and green spheres indicate the sodium and chloride ions, respectively; the semitransparent surface indicate the volume occupied by the electrolyte; (B) A sequence of microscopic configurations realized in a typical MD simulation. Images in the top and bottom rows depict the same system from two different viewpoints; (C) The number of the DDM molecules bound to FhuA  $\Delta C/\Delta 5L$  with their tail (top) or head (bottom) parts *versus* simulation time. The simulation system contained 20 mM DDM initially placed on a cubic lattice around the protein. To count as a binding event, any atom of a DDM must reside within 4 Å of any atom of the protein. The traces show 0.48 ns block average of 2.4 ps-sampled data. The inset image shows a zoomed-in view of a 10-ns fragment of the binding trace. The standard deviation of the number of bound DDM molecules,  $\sigma$ , is used as an effective measure of the molecules' binding affinity: smaller deviation indicates stronger binding; (D) The mean equilibrium number of DDM molecules bound to the proteins (left) and the mean equilibrium standard deviation (right) of the number of DDM molecules bound to the proteins. In each figure, the left two columns characterize binding of the tail or head groups of DDM to the proteins; the right three columns characterize binding of entire DDM molecules to the hydrophobic, hydrophilic and charged residues of the proteins. The data were averaged over the steady-state (last ~70 ns) parts of two independent MD trajectories for each protein and then over the four protein systems; (E) Four  $\beta$ -barrel proteins colored according to their local propensity for forming an interface with DDM molecules. For each residue, the contact probability was calculated as the fraction of the time it

was bound to a DDM molecule within the last ~70 ns of the equilibration simulation; **(F)** The average fraction of the hydrophobic, hydrophilic, positively and negatively charged residues in the four  $\beta$ -barrel proteins (open bars) and the fraction of those residues that bind DDM (filled bars) during the steady-state (last ~70 ns) parts of the MD trajectories. The data were averaged over the two independent MD trajectories for each protein and then over the four protein systems. In panels **D** and **F**, error bars represent standard deviations among the eight simulations.

**MD simulations of the interactions between DDM and the  $\beta$ -barrel proteins.** To gain insights into the PDC interactions at the submicroscopic level, we simulated spontaneous aggregation of DDM detergents around OmpG, FhuA  $\Delta C/\Delta 5L$ , FhuA  $\Delta C/\Delta 5L_{25N}$ , and FhuA  $\Delta C/\Delta 7L_{30N}$ , using the MD method of Bond and colleagues (2004).<sup>53</sup> Each simulation system contained one copy of the protein, 21 or 105 DDM molecules, which translates into 20 or 100 mM DDM concentration, respectively, and 200 mM NaCl electrolyte (**Fig. 6A**). Two independent simulations were performed for each system differing by the initial arrangements of the DDM molecules (**Methods**). Starting from a disperse configuration, DDM molecules were seen to aggregate at the surface of the proteins, reaching a dynamic equilibrium after ~100 ns (**Fig. 6B**; **Supporting Information, Fig. S6A**). In all simulations, all DDM molecules were observed to eventually form a complex with the protein (**Supporting Information, Fig. S6B-D**). All proteins maintained their structural integrity at our simulation timescale. Reflecting the progress of the aggregation process, the radius of gyration of the DDM-protein complex,  $R_g$ , reached steady-state values of ~2.2, ~2.9, ~2.7, and ~2.6 nm for proteomicelles with OmpG, FhuA  $\Delta C/\Delta 5L$ , FhuA  $\Delta C/\Delta 5L_{25N}$ , and FhuA  $\Delta C/\Delta 7L_{30N}$ , respectively (**Supporting**

**Information, Fig. S6B,C**). Interestingly, increasing DDM concentration by 5-fold produced a rather modest ( $\sim 0.6$  nm) increase of  $R_g$  (**Supporting Information, Fig. S6D**).

The steady-state parts of the trajectories were used to extract information about DDM-protein interactions. **Fig. 6C** shows two typical traces characterizing binding of DDM's hydrophobic (tail) and hydrophilic (head) parts to FhuA  $\Delta C/\Delta 5L$ . The tail parts of all DDM molecules bind to the protein surface, which is not the case for the head groups of which only  $\sim 80\%$  have atoms that are in contact with the protein surface (**Fig. 6D**). The most dramatic difference, however, is seen in the magnitude of the steady-state fluctuations,  $\sigma$ , which we use as an effective measure of binding affinity. Indeed, assuming that the binding of a detergent to a protein can be described by a harmonic potential and that the conditions of the equipartition theorem are met, the spring constant of the harmonic potential should be inversely proportional to the square of the standard deviation. According to this argument, the head group of DDM binds to the protein  $\sim 8$  times less strongly than the tail part (**Fig. 6D**). Similarly, we find that the binding of DDM to hydrophobic residues to be  $\sim 2.6$  times stronger than to hydrophilic residues and  $\sim 8$  times stronger than to charged residues (**Fig. 6D; Supporting Information, Fig. S7A**). Here and anywhere else in the paper, hydrophilic residues include polar and charged residues. Analyzing the binding of head groups and tails of DDM separately, we find only the tail domain to exhibit considerable dependence of binding strength on the residue type (**Supporting Information, Fig. S7B-C**). Further analysis found no significant correlation between the DDM binding affinity and the sign of the charged residues (**Supporting Information, Fig. S7D-F**).

**Fig. 6E** shows the structure of the four proteins colored by the local probability of binding

DDM molecules. Interestingly, DDM molecules did not uniformly cover the hydrophobic belt of the protein and tended to form half-micelle like aggregates at the junction of the loops and the  $\beta$  barrel. One possible explanation for such an arrangement is that detergent molecules seek such configurations where both their hydrophobic and hydrophilic parts are placed in the most favorable environment. At the same time, the pattern of DDM binding (**Fig. 6E**) is very similar to the pattern of hydrophobic and hydrophilic residues in the protein structures (**Supporting Information, Fig. S8A**). Note that increasing the number of DDM molecules does not lead to formation of half-micelles at the hydrophobic belt of the protein (**Supporting Information, Fig. S6A**). Unfortunately, statistical sampling of binding events was not sufficient in our simulations to elucidate the effect of point mutations on DDM binding. Nevertheless, we could infer this information by evaluating the effect that a residue type has on its probability to bind DDM. **Fig. 6F** plots the fraction of hydrophobic, hydrophilic, as well as positively and negatively charged residues in the respective protein structures, which was averaged over the four proteins. **Fig. S8A (Supporting Information)** show the same data for individual proteins. If the binding of DDM molecules to a protein were completely random, the fraction of residues that would bind detergent would be the same as the fraction of the residues in the protein. Analysis of MD simulations, however, does not support this conjecture. DDM molecules are found to bind hydrophobic residues 50% more likely than suggested by their abundance in the structure whereas binding hydrophilic residues was 30% less likely (**Fig. 6F**). Interestingly, the hydrophobic residues of OmpG bind DDM considerably stronger than those of FhuA variants (**Supporting Information, Fig. S8B**), in agreement with the proteins' grand average of hydropathicity indices (**Table 2**). Substantial reduction of DDM binding is also observed in the case of positively and negatively charged residues.

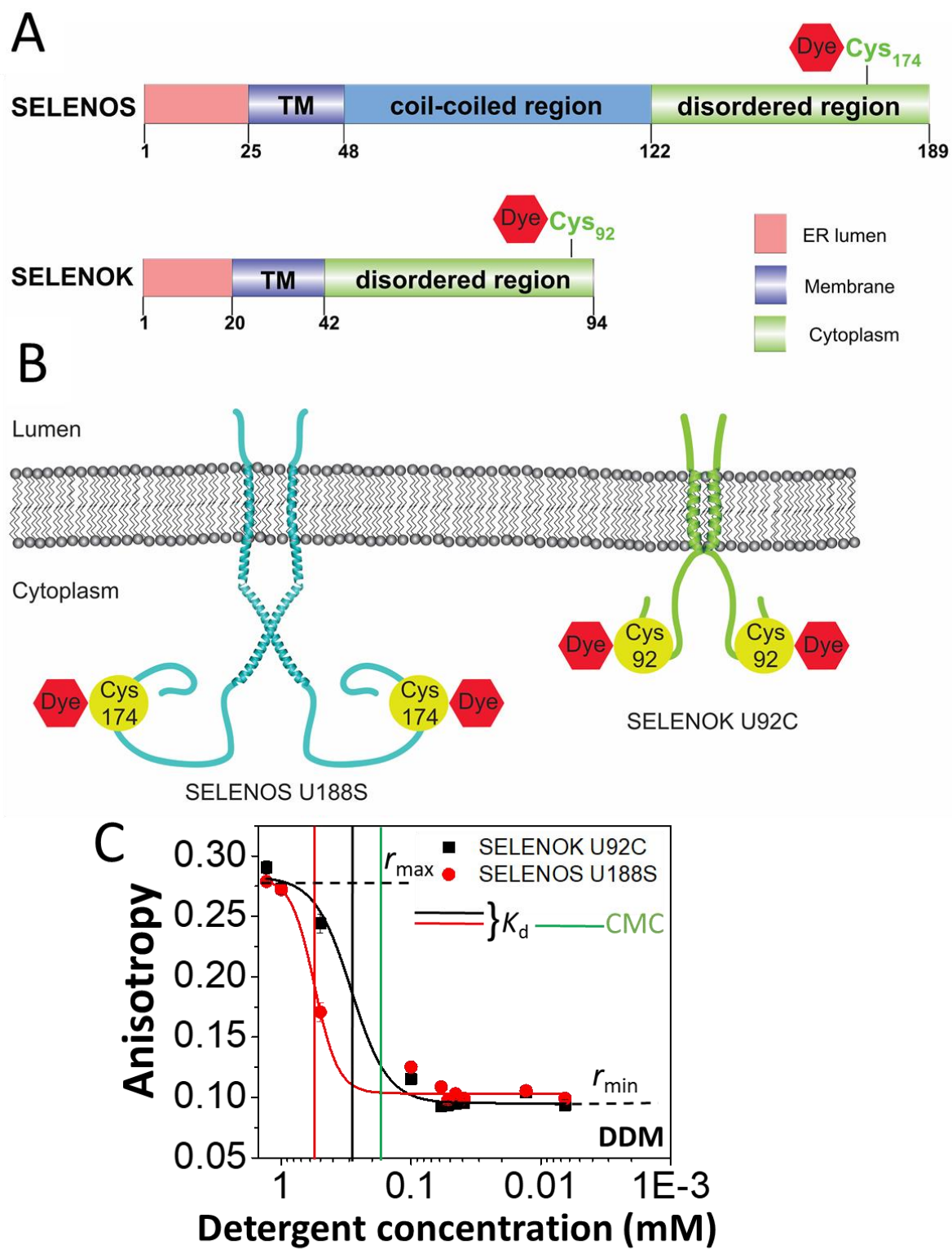


Figure 7

**Figure 7: Dose-response in fluorescence anisotropy acquired with SELENOK U92C and SELENOS U188S, two short single  $\alpha$ -helical transmembrane proteins solubilized in DDM.**

(A) Cartoon presenting the transmembrane topography of the SELENOK U92C and SELENOS U188S proteins; (B) Domain organization and the position of relevant Cys and Sec residues of SELENOS and SELENOK. TM stands for the transmembrane region of these proteins; (C) The protein concentration in the well was 200 nM. The initial DDM concentration was 1.3 mM. The FP measurements were carried out using a solution that contained 200 mM NaCl, 50 mM HEPES, pH 7.4 at a temperature of 24°C. Vertical bars represent the magnitudes of the CMC and  $K_d$ . All the other experimental conditions were the same as in **Fig. 3**.



**Do  $\alpha$ -helical transmembrane proteins undergo a two-state detergent desolvation-induced transition?** One question is whether we can extend this FP-based approach to other membrane proteins, which are different in structure from  $\beta$  barrels. Therefore, we inspected SELENOS and SELENOK, two small, human membrane proteins that are not related in structure and homology with either OmpG or FhuA. SELENOS and SELENOK are single-pass polypeptides with a short luminal segment, a single transmembrane helix, and a cytoplasmic domain housing a selenocysteine (Sec) residue.<sup>54</sup> The cytoplasmic regions contain an unstructured segment rich in glycine, proline, and polar residues (**Fig. 7A**). Both SELENOS<sup>34</sup> and SELENOK<sup>32</sup> are homodimers (**Fig 7B**). In this work, we explored SELENOK U92C and SELENOS U188S, in which the selenocysteine was mutated either to cysteine (SELENOK) or serine (SELENOS), leaving a sole cysteine in the protein for fluorescent labeling (**Supporting Information, Table S5**). We also noted that these proteins underwent a two-state DDM desolvation transition in proteomicelles, but between significantly lower  $r_{\max}$  and  $r_{\min}$  values than those determined with the FhuA derivatives (**Supporting Information, Table S6**). For both  $\alpha$ -helical proteins, the apparent  $K_d$  values were greater than the CMC, suggesting that the cohesive interactions were greater than the adhesive interactions (**Fig. 7C; Supporting Information, Table S7**; last column).

## DISCUSSION

In this work, we inspected the interfacial interactions between detergents and water-insoluble membrane proteins. The detergent desolvation of insoluble membrane proteins is closely related to protein unfolding. Recently, using temperature-dependent circular dichroism (CD) spectroscopy and chemical denaturant-induced protein unfolding, we showed that  $r_{\max}$  and  $r_{\min}$  correspond to the folded and unfolded states, respectively.<sup>35</sup> This finding implies that the unfolding transition of these  $\beta$  barrel proteins in aqueous phase occurs in between these states. However, the observed changes in the FP anisotropy directly reflected adhesion-dissociation of detergent monomers from the protein, not protein folding-unfolding. The two-state transition of detergent desolvation was due to detergent depletion in the proximity of a hydrophobic membrane protein or weak adhesive PDC interactions. The steady-state FP anisotropy values on these plots represent the endpoints of the desolvation reaction; thereby, the signal resulting from more fluorophores has no impact on the endpoints of the desolvation reaction. For example, we show the ability of obtaining the two-state Langmuir-Hill dissociation curves using two dimeric selenoproteins of unknown structure. Moreover, three distinct protein instances (e.g., FhuA, OmpG, and selenoproteins) indicate the effective labeling of the membrane proteins within the aqueous phase-exposed domains for quantitative FP studies.

In general, the very acidic OmpG exhibited stronger adhesive interactions with both neutral and zwitterionic detergents than the other FhuA protein mutants, likely due to strong hydrophobic PDC contacts. The all-atom MD simulations confirmed a stronger binding interaction of DDM to OmpG than to other FhuA derivatives (**Fig. 3; Table S2; Supporting Information, Fig. S8B**). At physiological conditions, the adhesive interactions were greater than

the cohesive interactions in the case of acidic  $\beta$  barrels solubilized by neutral, short-hydrophobic tail detergents CYMAL-4 and OG, as well as by zwitterionic detergents CHAPS, LD, and LysoFos. In contrast, the basic  $\beta$  barrels could not be folded in OG, CHAPS and LD, but showed comparable adhesive and cohesive interactions when incubated in LysoFos. These findings imply that for the zwitterionic detergents the electrical dipoles of the monomers are attracted by the dominant negative charges of the acidic  $\beta$  barrels, but repelled by the dominant positive charges of the basic  $\beta$  proteins. Another clear distinction between acidic and basic barrels was noted with DM at physiological pH. Closely similar adhesive and cohesive interactions were apparent for the acidic  $\beta$  barrels, but strong adhesive interactions were found for the basic  $\beta$  barrels. These few examples illuminate the entanglement and importance of the hydrophobic and electrostatic interactions in mediating the PDC interface.

$r_{\min}$  and  $r_{\max}$ , defining the two sub-states of the desolvation transition, were significantly smaller for the shorter polypeptides, which is in accord with a greater rotational mobility of a lower-molecular mass proteomicelle. For example, the 102-residue SELENOK U92C and 190-residue SELENOS U188S showed  $r_{\min}$  values of  $0.095 \pm 0.002$  and  $0.103 \pm 0.002$ , respectively, when they were solubilized in 1.3 mM DDM. These values correspond to rotational diffusion coefficients,  $D_r^{\text{fast}}$ , of  $\sim 1.3 \times 10^8$  and  $\sim 1.1 \times 10^8 \text{ s}^{-1}$  (**Supporting Information, Table S6**), respectively, giving rotational correlation times,  $\theta$ , in the range 1.3 -1.5 ns. This time interval compares well with the rotational correlation time  $\theta = 14.2$  ns, as calculated for Stam2 VHS-domain (VHS), a 17.7 kDa protein, at 20°C.<sup>55</sup> Another interesting aspect of the hydrodynamics of DDM-containing proteomicelles is that the average radius,  $R_h$ , determined with  $\beta$  barrel proteins, ranged a narrow interval between 2.5 and 2.8 nm, whereas that calculated for the

shorter helical polypeptides was ~2.1 nm. The MD trajectories of the DDM-mediated proteomicellizations with all four  $\beta$  barrels indicated a gyration radius covering a range between 2.2 nm and 2.9 nm. Our full-atomistic MD computational studies also indicated that a substantial increase in the DDM concentration did not produce a significant change in the PDC gyration radius. This finding is in accord with the FP anisotropy measurements, which did not reveal alterations in the FP anisotropy at detergent concentrations much greater than the CMC (**Supporting Information, Fig. S2**).

In some cases (e.g., all desorption isotherms in **Fig. 3B**), the  $r_{\min}$  values acquired with the  $\beta$ -barrel proteins were greater than the value corresponding to most rotationally diffusive FhuA  $\Delta C/\Delta 5L$  protein ( $r_1 = \sim 0.16$ ), which was acquired under denaturing conditions by excess of Gdm-HCl. At least two possibilities can explain these slightly elevated  $r_{\min}$  values. First, there might be a small residual amount of yet-bound detergent monomers at the lowest detergent concentrations used in this work, thus contributing to a decreased rotational mobility of the desolvated protein. Second, there are effects of the *soluble* local aggregation, again decreasing the tumbling rate of the desolvated protein. It should be noted that *soluble* aggregates of proteins would increase the anisotropy due to the size increase from monomers. Because the proteins examined in this work are hydrophobic, we do also see, as expectedly, *insoluble* aggregation at detergent concentrations much smaller than the CMC, resulting in a decrease in raw polarization signal.

We used Texas Red, a bright fluorophore,<sup>36</sup> enabling a low concentration of the inspected protein. This is a very important asset of this approach, given the limited expression and

purification yields of water-insoluble membrane proteins. Previous FP methods also involved time-resolved anisotropy measurements that require a very fast detector.<sup>56</sup> This latter FP method facilitates the determination of anisotropy decays of proteins exposed to excitation light pulses shorter than the decay time constant of the sample. In this way, time-resolved anisotropy studies can reveal details lost in the averaging process, such as molecular shape, conformational sub-states, and local flexibility. Because of the need for sophisticated equipment, these time-resolved anisotropy measurements cannot be expanded to a multiplexed format for inspecting a large sample number, which is a critical requirement in the HTS area of the PDC interactions. One immediate question is whether this semi-quantitative FP-based approach can be expanded by employing intrinsic tryptophan fluorescence. This is because in general membrane proteins have multiple tryptophan residues exposed to their hydrophobic interface.<sup>24</sup> We judge that it is not very convenient to use intrinsic tryptophan fluorescence for the FP-based spectroscopy studies for a number of reasons. They include complex contributions of individual-residue tryptophan spectra to the overall FP spectrum of the protein as well as rapid tryptophan quenching, because the indole nucleus is prone to electron donation during the excitation state.<sup>57</sup> Moreover, the presence of multiple tryptophan residues in any given membrane protein requires their mutagenesis with non-fluorescent side chains.<sup>14</sup> Therefore, many applications of the FP spectroscopy rely on covalently attached intense fluorophores, such as Texas Red from this work. It should be mentioned that this approach cannot be coupled with large fluorophores, such as green fluorescence protein (GFP) and its derivatives, because they can potentially impact the local tumbling rate, flexibility, and even conformation of the inspected protein.

There are various ways to identify contributions (if any significant) of light scattering to the FP anisotropy signal. We think that the light scattering has negligible effects to our acquired fluorescence anisotropy signal for the following independent reasons: (i) the Spectramax i3 plate reader that we used is equipped with emission filters for rhodamine derivatives (Texas Red is one of them). These filters are designed for excitation at 535 nm and emission at 595 nm. This rather large separation between excitation and emission ( $\sim 60$  nm) ensures that scattering is minimal in our data; (ii) the large wavelength of emission was strategically used to avoid Raman and Rayleigh scattering effects. This is because the light intensities of both scattering contributions are proportional to  $\lambda^{-4}$ , where  $\lambda$  is the wavelength;<sup>58</sup> (iii) in our very preliminary stage of these studies, we have increased the concentration of labeled proteins up to a level, in which the signal was independent on protein concentration;<sup>59</sup> (iv) we conducted control experiments with proteins of closely similar molecular mass, but that exhibit a broad range of detergent solubilization properties under identical micellization conditions. The basal fluorescence anisotropy of the unfolded FhuA variants under excess of Gdm-HCl was  $\sim 0.16$ . We demonstrated that acidic FhuA proteins were refolded in OG, showing an anisotropy signal of  $\sim 0.3$ . On the contrary, the basic FhuA variants were not refolded in OG and aggregated in solution in the presence of OG-induced micelles, exhibiting a fluorescence anisotropy of  $\sim 0.16$ . This control experiment demonstrated that both the light scattering contributions and protein aggregation did not affect the FP anisotropy signal under OG-induced micellization conditions. Such a control experiment was also recapitulated with other detergent micelles (e.g., CHAPS in **Table 3, Fig. 4**). These experimental outcomes indicates that the fluorophore directly probed whether the protein is in a detergent solvated or desolvated state.<sup>35</sup> Overall, we think that the

light scattering of the incident excitation light into the emission pathway does not affect the anisotropy values reported here.

## CONCLUSIONS

In summary, we report a comparative study of the detergent desolvation-induced transitions of membrane proteins of varying biophysical and structural fingerprint. This approach for deriving the energetics of detergent desolvation was used for four robust  $\beta$ -barrels, but extended to two  $\alpha$ -helical ones, whose X-ray crystal structure is not yet available. These membrane proteins were expressed, solubilized, purified, and refolded under very distinctive protocols, reinforcing the impact of this approach on other membrane proteins to examine their interfacial PDC interactions. Therefore, this method may be applied to diverse mixtures of detergents with complementary interfacial features. For example, such measurements might be expanded to mechanistic studies of the PDC interactions of newly developed detergent-like compounds, such as steroid-based facial amphiphiles,<sup>60</sup> lipopeptides<sup>61</sup> and amphipols.<sup>62</sup>

**Supporting Information.** (i) Characterization of selenoproteins prior to and following labeling with Texas Red; (ii) Example of steady-state FP traces illustrating no time-dependent alterations in the anisotropy readout at detergent concentrations much greater than the CMC; (iii) Example of steady-state FP traces showing no time-dependent alterations in the anisotropy readout after 24 hours;

(iv) Hydrodynamic changes of the proteomicelles during the transition of detergent desolvation; (v) Table that summarizes the recorded minima and maxima of the anisotropy with maltoside-containing detergents; (vi) Summary of the fitting results of the two-state, concentration-dependent anisotropy curves acquired with maltoside-containing detergents; (vii) Time-dependent changes in the FP anisotropy acquired with CHAPS; (viii) Time-dependent FP anisotropy acquired with LD; (ix) Table that summarizes the recorded minima and maxima of the anisotropy readout with DM at various pH values; (x) Summary of the fitting results of the two-state desolvation curves acquired with DM at various pH values; (xi) MD simulations of DDM molecules binding to  $\beta$ -barrel proteins; (xii) Differential affinity of DDM molecules to residues of  $\beta$ -barrels; (xiii) DDM binding *versus* residue type; (xiv) Biophysical properties of the selenoproteins; (xv) Table that summarizes the recorded minima and maxima of the anisotropy readout with the  $\alpha$ -helical membrane proteins solubilized in DDM; (xvi) Summary of the fitting results of the two-state, concentration-dependent anisotropy curves acquired with  $\alpha$ -helical transmembrane proteins. These materials are available free of charge via the Internet at <http://pubs.acs.org>



**Acknowledgements.** We thank Motahareh Larimi and Avinash Thakur valuable feedback and stimulating discussions. This study was supported by the US National Institutes of Health grants GM113299 (A.R.B.), GM115442 (M.C.), GM115762 (S.N.L.), and GM088403 (L.M.), as well as National Science Foundation grant MCB-1616178 (S.R.). The Delaware COBRE program supported this research with the US National Institutes of Health grants P20 GM104316 and P30 GM110758-02. The computational studies in this article were supported by a grant from the National Institutes of Health P41-RR005969. The authors acknowledge supercomputer time provided through the XSEDE Allocation Grant MCA05S028 and the Blue Waters petascale supercomputer system at the University of Illinois at Urbana-Champaign. W.S. acknowledges financial support from the China Scholarship Council (CSC201506090040) and the National Natural Science Foundation of China (Grant No. 51435003).

## REFERENCES

1. Stangl, M.; Veerappan, A.; Kroeger, A.; Vogel, P.; Schneider, D., Detergent properties influence the stability of the glycoporphin A transmembrane helix dimer in lysophosphatidylcholine micelles. *Biophys. J.* **2012**, *103* (12), 2455-64.
2. Yang, Z.; Wang, C.; Zhou, Q.; An, J.; Hildebrandt, E.; Aleksandrov, L. A.; Kappes, J. C.; DeLucas, L. J.; Riordan, J. R.; Urbatsch, I. L.; et al., Membrane protein stability can be compromised by detergent interactions with the extramembranous soluble domains. *Protein Sci.* **2014**, *23* (6), 769-89.
3. Roy, A., Membrane preparation and solubilization. *Methods Enzymol.* **2015**, *557*, 45-56.
4. Sadaf, A.; Cho, K. H.; Byrne, B.; Chae, P. S., Amphipathic agents for membrane protein study. *Methods Enzymol.* **2015**, *557*, 57-94.
5. Yang, Z.; Brouillette, C. G., A guide to differential scanning calorimetry of membrane and soluble proteins in detergents. *Methods Enzymol.* **2016**, *567*, 319-58.
6. Miles, A. J.; Wallace, B. A., Circular dichroism spectroscopy of membrane proteins. *Chem. Soc. Rev.* **2016**, *45* (18), 4859-72.
7. Raschle, T.; Rios Flores, P.; Opitz, C.; Muller, D. J.; Hiller, S., Monitoring backbone hydrogen-bond formation in beta-barrel membrane protein folding. *Angew. Chem. Int. Ed. Engl.* **2016**, *55* (20), 5952-5.
8. Borysik, A. J.; Hewitt, D. J.; Robinson, C. V., Detergent release prolongs the lifetime of native-like membrane protein conformations in the gas-phase. *J. Am. Chem. Soc.* **2013**, *135* (16), 6078-83.
9. Jahnke, N.; Krylova, O. O.; Hoomann, T.; Vargas, C.; Fiedler, S.; Pohl, P.; Keller, S., Real-time monitoring of membrane-protein reconstitution by isothermal titration calorimetry. *Anal. Chem.* **2014**, *86* (1), 920-927.
10. Textor, M.; Keller, S., Automated analysis of calorimetric demicellization titrations. *Anal. Biochem.* **2015**, *485*, 119-21.
11. Qin, X.; Liu, M.; Yang, D.; Zhang, X., Concentration-dependent aggregation of CHAPS investigated by NMR spectroscopy. *J. Phys. Chem. B* **2010**, *114* (11), 3863-8.
12. Turman, D. L.; Nathanson, J. T.; Stockbridge, R. B.; Street, T. O.; Miller, C., Two-sided block of a dual-topology F- channel. *Proc. Natl. Acad. Sci. U.S.A.* **2015**, *112* (18), 5697-701.
13. Stoddart, L. A.; White, C. W.; Nguyen, K.; Hill, S. J.; Pflieger, K. D., Fluorescence- and bioluminescence-based approaches to study GPCR ligand binding. *Br. J. Pharmacol.* **2016**, *173* (20), 3028-3037.

14. Jutila, A.; Zhu, K.; Patkar, S. A.; Vind, J.; Svendsen, A.; Kinnunen, P. K., Detergent-induced conformational changes of *Humicola lanuginosa* lipase studied by fluorescence spectroscopy. *Biophys. J.* **2000**, *78* (3), 1634-42.
15. Andersen, K. K.; Oliveira, C. L.; Larsen, K. L.; Poulsen, F. M.; Callisen, T. H.; Westh, P.; Pedersen, J. S.; Otzen, D., The role of decorated SDS micelles in sub-CMC protein denaturation and association. *J. Mol. Biol.* **2009**, *391* (1), 207-26.
16. Naidu, K. T.; Prabhu, N. P., Protein-surfactant interaction: sodium dodecyl sulfate-induced unfolding of ribonuclease A. *J. Phys. Chem. B* **2011**, *115* (49), 14760-7.
17. Fano, M.; van de Weert, M.; Moeller, E. H.; Kruse, N. A.; Frokjaer, S., Ionic strength-dependent denaturation of *Thermomyces lanuginosus* lipase induced by SDS. *Arch. Biochem. Biophys.* **2011**, *506* (1), 92-8.
18. Li, J.; Qiu, X. J., Quantification of membrane protein self-association with a high-throughput compatible fluorescence assay. *Biochemistry* **2017**, *56* (14), 1951-1954.
19. Kubler, D.; Bergmann, A.; Weger, L.; Ingenbosch, K. N.; Hoffmann-Jacobsen, K., Kinetics of detergent-induced activation and inhibition of a minimal lipase. *J. Phys. Chem. B* **2017**, *121* (6), 1248-1257.
20. Khao, J.; Arce-Lopera, J.; Sturgis, J. N.; Duneau, J. P., Structure of a protein-detergent complex: the balance between detergent cohesion and binding. *Eur. Biophys. J.* **2011**, *40* (10), 1143-55.
21. Yildiz, O.; Vinothkumar, K. R.; Goswami, P.; Kuhlbrandt, W., Structure of the monomeric outer-membrane porin OmpG in the open and closed conformation. *EMBO J.* **2006**, *25* (15), 3702-3713.
22. Locher, K. P.; Rees, B.; Koebnik, R.; Mitschler, A.; Moulinier, L.; Rosenbusch, J. P.; Moras, D., Transmembrane signaling across the ligand-gated FhuA receptor: crystal structures of free and ferrichrome-bound states reveal allosteric changes. *Cell* **1998**, *95* (6), 771-778.
23. Mohammad, M. M.; Howard, K. R.; Movileanu, L., Redesign of a plugged beta-barrel membrane protein. *J. Biol. Chem.* **2011**, *286* (10), 8000-8013.
24. Wolfe, A. J.; Mohammad, M. M.; Thakur, A. K.; Movileanu, L., Global redesign of a native beta-barrel scaffold. *Biochim. Biophys. Acta* **2016**, *1858* (1), 19-29.
25. Niedzwiecki, D. J.; Mohammad, M. M.; Movileanu, L., Inspection of the engineered FhuA deltaC/delta4L protein nanopore by polymer exclusion. *Biophys. J.* **2012**, *103* (10), 2115-2124.
26. Thakur, A. K.; Larimi, M. G.; Gooden, K.; Movileanu, L., Aberrantly large single-channel conductance of polyhistidine arm-containing protein nanopores. *Biochemistry* **2017**, *56* (36), 4895-4905.

27. Mohammad, M. M.; Iyer, R.; Howard, K. R.; McPike, M. P.; Borer, P. N.; Movileanu, L., Engineering a rigid protein tunnel for biomolecular detection. *J. Am. Chem. Soc.* **2012**, *134* (22), 9521-9531.
28. Tomita, N.; Mohammad, M. M.; Niedzwiecki, D. J.; Ohta, M.; Movileanu, L., Does the lipid environment impact the open-state conductance of an engineered beta-barrel protein nanopore? *Biochim.Biophys.Acta.-Biomembr.* **2013**, *1828* (3), 1057-1065.
29. Linke, D., Detergents: an overview. *Methods Enzymol.* **2009**, *463*, 603-617.
30. Fahie, M.; Chisholm, C.; Chen, M., Resolved single-molecule detection of individual species within a mixture of anti-biotin antibodies using an engineered monomeric nanopore. *ACS nano* **2015**, *9* (2), 1089-1098.
31. Chen, M.; Khalid, S.; Sansom, M. S.; Bayley, H., Outer membrane protein G: engineering a quiet pore for biosensing. *Proc. Natl. Acad. Sci. U.S.A.* **2008**, *105* (17), 6272-6277.
32. Liu, J.; Zhang, Z.; Rozovsky, S., Selenoprotein K form an intermolecular diselenide bond with unusually high redox potential. *FEBS Lett.* **2014**, *588* (18), 3311-21.
33. Liu, J.; Srinivasan, P.; Pham, D. N.; Rozovsky, S., Expression and purification of the membrane enzyme selenoprotein K. *Protein Expr. Purif.* **2012**, *86* (1), 27-34.
34. Liu, J.; Li, F.; Rozovsky, S., The intrinsically disordered membrane protein selenoprotein S is a reductase in vitro. *Biochemistry* **2013**, *52* (18), 3051-61.
35. Wolfe, A. J.; Hsueh, Y. C.; Blanden, A. R.; Mohammad, M. M.; Pham, B.; Thakur, A. K.; Loh, S. N.; Chen, M.; Movileanu, L., Interrogating detergent desolvation of nanopore-forming proteins by fluorescence polarization spectroscopy. *Analytical chemistry* **2017**, *89* (15), 8013-8020.
36. Gradinaru, C. C.; Marushchak, D. O.; Samim, M.; Krull, U. J., Fluorescence anisotropy: from single molecules to live cells. *Analyst* **2010**, *135* (3), 452-9.
37. Titus, J. A.; Haugland, R.; Sharrow, S. O.; Segal, D. M., Texas Red, a hydrophilic, red-emitting fluorophore for use with fluorescein in dual parameter flow microfluorometric and fluorescence microscopic studies. *J. Immunol. Methods* **1982**, *50* (2), 193-204.
38. Jameson, D. M.; Ross, J. A., Fluorescence polarization/anisotropy in diagnostics and imaging. *Chem. Rev.* **2010**, *110* (5), 2685-708.
39. Prinz, H., Hill coefficients, dose-response curves and allosteric mechanisms. *J. Chem. Biol.* **2010**, *3* (1), 37-44.
40. Phillips, J. C.; Braun, R.; Wang, W.; Gumbart, J.; Tajkhorshid, E.; Villa, E.; Chipot, C.; Skeel, R. D.; Kale, L.; Schulten, K., Scalable molecular dynamics with NAMD. *J. Comput. Chem.* **2005**, *26* (16), 1781-802.

41. Vanommeslaeghe, K.; Hatcher, E.; Acharya, C.; Kundu, S.; Zhong, S.; Shim, J.; Darian, E.; Guvench, O.; Lopes, P.; Vorobyov, I.; et al., CHARMM general force field: A force field for drug-like molecules compatible with the CHARMM all-atom additive biological force fields. *J. Comput. Chem.* **2010**, *31* (4), 671-90.
42. Yoo, J. J.; Aksimentiev, A., Improved parametrization of Li<sup>+</sup>, Na<sup>+</sup>, K<sup>+</sup>, and Mg<sup>2+</sup> ions for all-atom molecular dynamics simulations of nucleic acid systems. *J. Phys. Chem. Lett.* **2012**, *3* (1), 45-50.
43. Yoo, J.; Aksimentiev, A., Improved parameterization of amine-carboxylate and amine-phosphate interactions for molecular dynamics simulations using the CHARMM and AMBER force fields. *J. Chem. Theory Comput.* **2016**, *12* (1), 430-43.
44. Andersen, H. C., RATTLE - A velocity version of the shake algorithm for molecular-dynamics calculations. *J. Comput. Phys.* **1983**, *52* (1), 24-34.
45. Miyamoto, S.; Kollman, P. A., SETTLE - An analytical version of the shake and rattle algorithm for rigid water models. *J. Comput. Chem.* **1992**, *13* (8), 952-962.
46. Darden, T.; York, D.; Pedersen, L., Particle mesh Ewald - An N.LOG(N) method for the Ewald sums in large systems. *J. Chem. Phys.* **1993**, *98* (12), 10089-10092.
47. Martyna, G. J.; Tobias, D. J.; Klein, M. L., Constant-pressure molecular dynamics algorithms. *J. Chem. Phys.* **1994**, *101* (5), 4177-4189.
48. Feller, S. E.; Zhang, Y. H.; Pastor, R. W.; Brooks, B. R., Constant-pressure molecular dynamics simulation - The langevin piston method. *J. Chem. Phys.* **1995**, *103* (11), 4613-4621.
49. Brunger, A. T., X-PLOR, Version 3.1: A System for X-ray Crystallography and NMR, The Howard Hughes Medical Institute and Department of Molecular Biophysics and Biochemistry, Yale University, New Haven, CT. **1992**.
50. Humphrey, W.; Dalke, A.; Schulten, K., VMD: Visual molecular dynamics. *J. Mol. Graph.* **1996**, *14* (1), 33-38.
51. Grosse, W.; Psakis, G.; Mertins, B.; Reiss, P.; Windisch, D.; Brademann, F.; Burck, J.; Ulrich, A.; Koert, U.; Essen, L. O., Structure-based engineering of a minimal porin reveals loop-independent channel closure. *Biochemistry* **2014**, *53* (29), 4826-38.
52. Sandoval, R. M.; Kennedy, M. D.; Low, P. S.; Molitoris, B. A., Uptake and trafficking of fluorescent conjugates of folic acid in intact kidney determined using intravital two-photon microscopy. *Am. J. Physiol. Cell Physiol.* **2004**, *287* (2), C517-26.
53. Bond, P. J.; Cuthbertson, J. M.; Deol, S. S.; Sansom, M. S., MD simulations of spontaneous membrane protein/detergent micelle formation. *J. Am. Chem. Soc.* **2004**, *126* (49), 15948-9.

54. Shchedrina, V. A.; Novoselov, S. V.; Malinouski, M. Y.; Gladyshev, V. N., Identification and characterization of a selenoprotein family containing a diselenide bond in a redox motif. *Proceedings of the National Academy of Sciences of the United States of America* **2007**, *104* (35), 13919-24.
55. Chen, P. C.; Hologne, M.; Walker, O., Computing the rotational diffusion of biomolecules via molecular dynamics simulation and quaternion orientations. *J. Phys. Chem. B* **2017**, *121* (8), 1812-1823.
56. Lakowicz, J. R., *Principles of fluorescence microscopy*. 2nd ed.; Springer: New York, 2006.
57. Mann, T. L.; Krull, U. J., Fluorescence polarization spectroscopy in protein analysis. *Analyst* **2003**, *128* (4), 313-7.
58. Splinter, R. H., B.A., *An introduction to biomedical optics*. Taylor & Francis, New York.: 2007; p 602.
59. Zhang, H.; Wu, Q.; Berezin, M. Y., Fluorescence anisotropy (polarization): from drug screening to precision medicine. *Expert Opin. Drug Discov.* **2015**, *10* (11), 1145-61.
60. Lee, S. C.; Bennett, B. C.; Hong, W. X.; Fu, Y.; Baker, K. A.; Marcoux, J.; Robinson, C. V.; Ward, A. B.; Halpert, J. R.; Stevens, R. C.; Stout, C. D.; Yeager, M. J.; Zhang, Q., Steroid-based facial amphiphiles for stabilization and crystallization of membrane proteins. *Proc Natl Acad Sci U S A* **2013**, *110* (13), E1203-11.
61. Prive, G. G., Lipopeptide detergents for membrane protein studies. *Curr. Opin. Struct. Biol.* **2009**, *19* (4), 379-85.
62. Kleinschmidt, J. H.; Popot, J. L., Folding and stability of integral membrane proteins in amphipols. *Arch. Biochem. Biophys.* **2014**, *564*, 327-43.
63. le Maire, M.; Champeil, P.; Moller, J. V., Interaction of membrane proteins and lipids with solubilizing detergents. *Biochim. Biophys. Acta* **2000**, *1508* (1-2), 86-111.
64. Stafford, R. E.; Fanni, T.; Dennis, E. A., Interfacial properties and critical micelle concentration of lysophospholipids. *Biochemistry* **1989**, *28* (12), 5113-20.
65. Neugebauer, J. M., Detergents: an overview. *Methods Enzymol.* **1990**, *182*, 239-53.
66. Chattopadhyay, A.; Harikumar, K. G., Dependence of critical micelle concentration of a zwitterionic detergent on ionic strength: implications in receptor solubilization. *FEBS letters* **1996**, *391* (1-2), 199-202.
67. Gasteiger, E.; Hoogland, C.; Gattiker, A.; Duvaud, S.; Wilkins, M. R.; Appel, R. D.; Bairoch, A., Protein identification and analysis tools on the ExPASy server. In *Proteomics Protocols Handbook*, J.M., W., Ed. Humana Press: 2005; pp 571-607.

68. Kyte, J.; Doolittle, R. F., A simple method for displaying the hydropathic character of a protein. *J. Mol. Biol* **1982**, *157* (1), 105-132.
69. Ikai, A., Thermostability and aliphatic index of globular proteins. *J. Biochem.* **1980**, *88* (6), 1895-1898.

## Chapter 4.1 Supplement for Quantification of Membrane Protein-Detergent Complex Interactions

Aaron J. Wolfe,<sup>1,2</sup> Wei Si,<sup>3,4</sup> Zhengqi Zhang,<sup>5</sup> Adam R. Blanden,<sup>6</sup> Yi-Ching Hsueh,<sup>1</sup> Jack F. Gugel,<sup>1</sup> Bach Pham,<sup>7</sup> Min Chen,<sup>7</sup> Stewart N. Loh,<sup>6</sup> Sharon Rozovsky,<sup>5</sup> Aleksei Aksimentiev,<sup>\*4</sup> and Liviu Movileanu<sup>\*1,2,8</sup>

<sup>1</sup>Department of Physics, Syracuse University, 201 Physics Building, Syracuse, New York 13244-1130, USA

<sup>2</sup>Structural Biology, Biochemistry, and Biophysics Program, Syracuse University, 111 College Place, Syracuse, New York 13244-4100, USA

<sup>3</sup>Jiangsu Key Laboratory for Design and Manufacture of Micro-Nano Biomedical Instruments and School of Mechanical Engineering, Southeast University, Nanjing, 210096, China

<sup>4</sup>Department of Physics, University of Illinois at Urbana-Champaign, Urbana, Illinois 61801, USA

<sup>5</sup>Department of Chemistry and Biochemistry, University of Delaware, 136 Brown Laboratory, Newark, Delaware 19716, USA

<sup>6</sup>Department of Biochemistry and Molecular Biology, State University of New York Upstate Medical University, 4249 Weiskotten Hall, 766 Irving Av., Syracuse, New York 13210, USA

<sup>7</sup>Department of Chemistry, University of Massachusetts, 820 LGRT, 710 North Pleasant Street, Amherst, Massachusetts 01003-9336, USA

<sup>8</sup>Department of Biomedical and Chemical Engineering, Syracuse University, 329 Link Hall, Syracuse, New York 13244, USA

Reprinted with permission from **Quantification of Membrane Protein-Detergent Complex Interactions** Aaron J. Wolfe, Wei Si, Zhengqi Zhang, Adam R. Blanden, Yi-Ching Hsueh, Jack F. Gugel, Bach Pham, Min Chen, Stewart N. Loh, Sharon Rozovsky, Aleksei Aksimentiev, and Liviu Movileanu

The Journal of Physical Chemistry B **2017** *121* (44), 10228-10241

DOI: 10.1021/acs.jpcc.7b08045. Copyright 2017 American Chemical Society.

### Author contributions:

AJW: Designed experiments, performed experiments, analyzed data, interpreted data.

WS: Performed experiments

ZZ: Performed experiments

ARB: Performed experiments

YCH: Performed experiments

JFG: Analyzed data

BP: Performed experiments

MC: Managed her student

SNL: Managed his student

SR: Managed her student

AA: Performed experiments

LM: Analyzed data, co-wrote manuscript



*1. Characterization of SELENOK U92C and SELENOS U188S proteins prior to and following labeling with Texas Red*

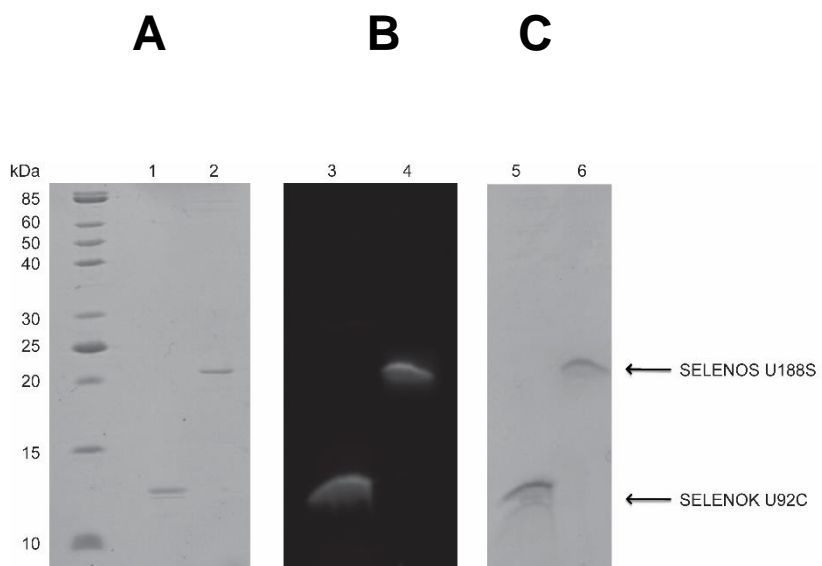


**Figure S1: Characterization of SELENOK U92C and SELENOS U188S prior to and following labeling with Texas Red.** (A) The purity of SELENOK U92C (lane 1) and SELENOS U188S (lane 2) prior to labeling was assessed from 16% Tris-Glycine SDS-PAGE. Electrophoresis was performed under reducing conditions. The molecular weights of SELENOK U92C and SELENOS U188S are 11.5 and 21.2 kDa, respectively. (B) The fluorescence of SELENOS U188S and SELENOK U92C labeled with Texas Red C2-maleimide was visualized using a FluorChem Q imaging system (Alpha Innotech, San Jose, CA) with a Cy5 filter (lanes 3 and 4). (C) The same gel from B was visualized by coomassie-blue staining (lanes 5 and 6).

*2. Example of steady-state FP traces illustrating no time-dependent alterations in the anisotropy readout at detergent concentrations much greater than their corresponding CMCs*

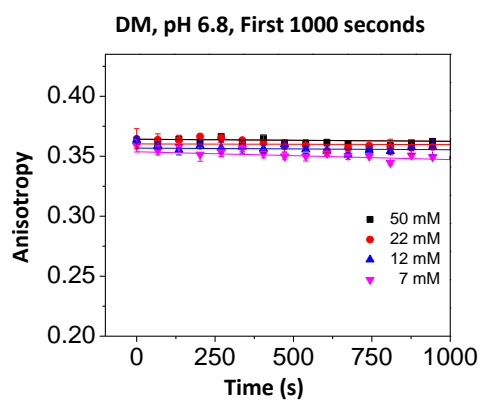


**Figure S2: Time-dependent fluorescence anisotropy traces acquired with n-Decyl- $\beta$ -D-maltoside (DM).** The anisotropy data were collected by adding overnight refolded protein to a bath of varying detergent concentration, as indicated in the legend. All anisotropy measurements were conducted at room temperature in 200 mM NaCl, 50 mM HEPES, pH 6.8. Time-dependent anisotropy measurements were executed directly after dilution of the refolded protein sample at respective detergent concentration. Final protein concentration was maintained at 28 nM.

3. Example of steady-state FP traces showing no time-dependent alterations in the anisotropy readout after 24 hours, regardless of the detergent concentration inspected in this work.

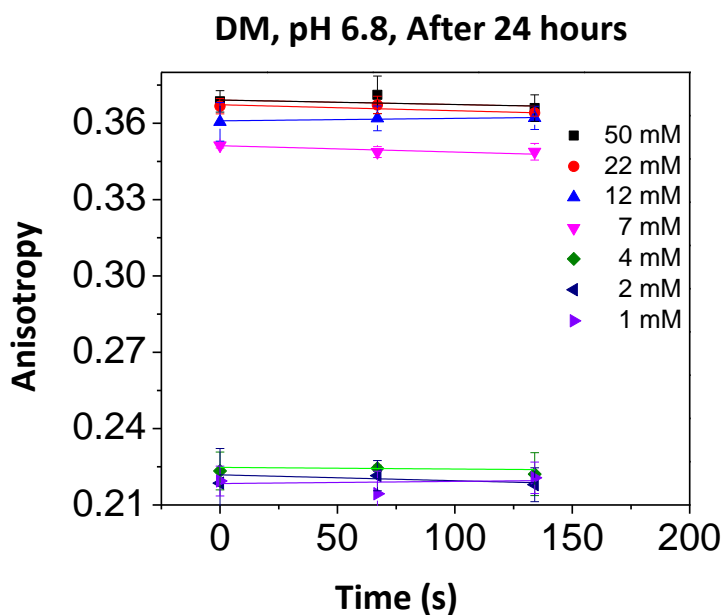


***Figure S3:*** Anisotropy readout was collected after 24 hours, but under similar experimental conditions with those mentioned in the caption of Fig. S2.

#### 4. Hydrodynamic changes of the proteomicelles during the transition of detergent

**desolvation.** Data resulting from steady-state FP measurements were used to derive the hydrodynamic radius of the proteins under detergent solvation and desolvation conditions.

Perrin's equation relates the rotational diffusion coefficient,  $D_r$ , to the steady-state fluorescence anisotropy,  $r$ ,<sup>1</sup>

$$\frac{r_0}{r} = 1 + 6D_r \tau_F \quad (\text{S1})$$

$r_0$  indicates the fundamental maximum anisotropy value. Here,  $\tau_F$  is the fluorescence lifetime of the fluorophore. In the case of Texas Red,  $r_0$  is 0.4,<sup>2</sup> whereas  $\tau_F$  is 4.2 ns.<sup>3</sup> The rotational correlation time,  $\theta$ , relates to the apparent hydrodynamic volume of the labeled molecule,  $V_h$ , as follows:<sup>3</sup>

$$\theta = \frac{1}{6D_r} \quad (\text{S2})$$

$$V_h = \frac{\theta k_B T}{\eta} = \frac{k_B T}{6\eta D_r} \quad (\text{S3})$$

Using (S1) and (S2):

$$\frac{r_0}{r} = 1 + \frac{\tau_F}{\theta} \quad (\text{S4})$$

Here, the dynamic viscosity of the buffer solution that corresponds to 200 mM NaCl,  $\eta$ , is 1.028 mPa s.<sup>4</sup>  $k_B$  and  $T$  denote the Boltzmann constant and absolute temperature, respectively.

Therefore, we determined the rotational diffusion coefficients of the fully solvated proteins,

$D_r^{\text{slow}}$ , and detergent-desolvated proteins,  $D_r^{\text{fast}}$ , as well as the average maximum hydrodynamic radii,  $R_h^{\text{max}}$  (**Table3**).

**Table S1: Table that summarizes the recorded minima and maxima of the anisotropy readout with neutral, maltoside-containing detergents and the four  $\beta$ -barrel proteins.<sup>a</sup> This table also illustrates the rotational diffusion coefficients as well as alterations in hydrodynamic radii of the proteomicelles during the detergent desolvation transitions.**

DDM <sup>b</sup>	$r_{\min}^c$	$r_{\max}^c$	$D_r^{\text{slow}} (10^7 \text{ s}^{-1})^d$	$D_r^{\text{fast}} (10^7 \text{ s}^{-1})^d$	$R_h^{\text{max}}$ (nm) <sup>e</sup>	$\Delta R_h$ (nm) <sup>f</sup>
OmpG	ND <sup>g</sup>	0.330 ± 0.004	0.84 ± 0.06	ND <sup>g</sup>	2.7	ND <sup>g</sup>
FhuA $\Delta C/\Delta 5L$	0.196 ± 0.054	0.336 ± 0.003	0.76 ± 0.04	4.1 ± 1.7	2.8	1.2 ± 0.2
FhuA $\Delta C/\Delta 5L_{25N}$	0.181 ± 0.008	0.315 ± 0.003	1.1 ± 0.1	4.8 ± 0.4	2.5	0.97 ± 0.07
FhuA $\Delta C/\Delta 7L_{30N}$	0.183 ± 0.012	0.314 ± 0.002	1.1 ± 0.1	4.7 ± 0.5	2.5	0.95 ± 0.08
UM <sup>b</sup>	$r_{\min}^c$	$r_{\max}^c$	$D_r^{\text{slow}} (10^7 \text{ s}^{-1})^d$	$D_r^{\text{fast}} (10^7 \text{ s}^{-1})^d$	$R_h^{\text{max}}$ (nm) <sup>e</sup>	$\Delta R_h$ (nm) <sup>f</sup>
OmpG	0.216 ± 0.006	0.319 ± 0.002	1.1 ± 0.1	3.4 ± 0.2	2.5	0.83 ± 0.06
FhuA $\Delta C/\Delta 5L$	0.230 ± 0.015	0.357 ± 0.003	0.48 ± 0.04	2.9 ± 0.4	3.2	1.5 ± 0.2
FhuA $\Delta C/\Delta 5L_{25N}$	0.186 ± 0.002	0.322 ± 0.002	0.96 ± 0.03	4.6 ± 0.01	2.6	1.0 ± 0.1
FhuA $\Delta C/\Delta 7L_{30N}$	0.208 ± 0.005	0.312 ± 0.002	1.1 ± 0.1	3.7 ± 0.2	2.4	0.79 ± 0.05
DM <sup>b</sup>	$r_{\min}^c$	$r_{\max}^c$	$D_r^{\text{slow}} (10^7 \text{ s}^{-1})^d$	$D_r^{\text{fast}} (10^7 \text{ s}^{-1})^d$	$R_h^{\text{max}}$ (nm) <sup>e</sup>	$\Delta R_h$ (nm) <sup>f</sup>

OmpG	0.214 ± 0.005	0.327 ± 0.001	0.89 ± 0.02	3.5 ± 0.2	2.6	0.95 ± 0.04
FhuA ΔC/Δ5L	0.219 ± 0.005	0.360 ± 0.001	0.44 ± 0.01	3.3 ± 0.2	3.3	1.6 ± 0.1
FhuA ΔC/Δ5L_25N	0.166 ± 0.003	0.343 ± 0.002	0.66 ± 0.03	5.6 ± 0.2	3.0	1.5 ± 0.1
FhuA ΔC/Δ7L_30N	0.168 ± 0.007	0.312 ± 0.001	1.1 ± 0.1	5.5 ± 0.4	2.4	1.0 ± 0.1
CYMAL-4 <sup>b</sup>	$r_{\min}^c$	$r_{\max}^c$	$D_r^{\text{slow}} (10^7 \text{ s}^{-1})^d$	$D_r^{\text{fast}} (10^7 \text{ s}^{-1})^d$	$R_h^{\text{max}}$ (nm) <sup>e</sup>	$\Delta R_h$ (nm) <sup>f</sup>
OmpG	0.163 ± 0.001	0.326 ± 0.001	0.90 ± 0.01	5.8 ± 0.1	2.6	1.2 ± 0.1
FhuA ΔC/Δ5L	0.242 ± 0.001	0.367 ± 0.001	0.36 ± 0.01	2.6 ± 0.1	3.6	1.7 ± 0.1
FhuA ΔC/Δ5L_25N	0.166 ± 0.001	0.341 ± 0.001	0.69 ± 0.01	5.6 ± 0.2	2.9	1.4 ± 0.1
FhuA ΔC/Δ7L_30N	0.168 ± 0.025	0.345 ± 0.004	0.63 ± 0.05	5.5 ± 1.2	2.9	1.5 ± 0.2

<sup>a</sup>To reach low detergent concentrations below CMC, the Gdm-HCl-solubilized proteins were refolded at various detergent concentrations above CMC.

<sup>b</sup>Full names of the detergents are provided in **Experimental Methods**.

<sup>c</sup>Experimentally determined anisotropy minima ( $r_{\min}$ ) and maxima ( $r_{\max}$ ) for various detergents.  $r_{\min}$  was extrapolated for the lowest detergent concentration in the well.  $r_{\max}$  was determined for detergent concentrations above the CMC.

<sup>d</sup> $D_r^{\text{slow}}$  and  $D_r^{\text{fast}}$  indicate the rotational diffusion coefficients of the protein under solvation and desolvation conditions, respectively.

<sup>e</sup> $R_h^{\text{max}}$  are the maximum hydrodynamic radii of the proteomicelle with various solubilizing detergents.

<sup>f</sup> $\Delta R_h$  is the decrease in the hydrodynamic radius,  $R_h$ , as a result of the detergent desolvation transition of the protein.

<sup>g</sup>Not determined.



**Table S2: Summary of the fitting results of the two-state, concentration-dependent anisotropy curves acquired with neutral, maltoside-containing detergents.<sup>a,b</sup>** This was determined with three FhuA derivatives and OmpG as well as a panel of five neutral detergents of varying hydrophobic chain and hydrophilic head group. The FP measurements were carried in 200 mM NaCl, 50 mM HEPES, pH 7.4 and at a temperature of 24°C. All data were derived as averages  $\pm$  SDs of three independent data acquisitions.

DDM <sup>c</sup>	$p^d$	$K_d^e$ (mM)	$q^f$ (mM <sup>-1</sup> )	$\Delta G^g$ (kcal/mol)	Balance <sup>h</sup>
OmpG	1.4 ± 0.9	~0.11	0.99	-5.4 ± 1.2	$F_{adh} \gg F_{coh}$
FhuA $\Delta C/\Delta 5L$	1.1 ± 0.3	0.52 ± 0.36	0.07	-4.5 ± 0.7	$F_{adh} \leq F_{coh}$
FhuA $\Delta C/\Delta 5L_{25N}$	4.4 ± 2.8	0.62 ± 0.17	0.24	-4.4 ± 0.1	$F_{adh} < F_{coh}$
FhuA $\Delta C/\Delta 7L_{30N}$	4.4 ± 1.6	0.64 ± 0.10	0.22	-4.3 ± 0.1	$F_{adh} < F_{coh}$
UM <sup>c</sup>	$p^d$	$K_d^e$ (mM)	$q^f$ (mM <sup>-1</sup> )	$\Delta G^g$ (kcal/mol)	Balance <sup>h</sup>
OmpG	4.8 ± 3.1	0.49 ± 0.17	0.25	-4.5 ± 0.3	$F_{adh} \leq F_{coh}$
FhuA $\Delta C/\Delta 5L$	3.5 ± 0.9	0.29 ± 0.05	0.38	-4.8 ± 0.1	$F_{adh} > F_{coh}$
FhuA $\Delta C/\Delta 5L_{25N}$	4.9 ± 0.3	0.59 ± 0.02	0.28	-4.4 ± 0.1	$F_{adh} \cong F_{coh}$
FhuA $\Delta C/\Delta 7L_{30N}$	4.6 ± 1.1	0.69 ± 0.07	0.17	-4.3 ± 0.1	$F_{adh} \cong F_{coh}$
DM <sup>c</sup>	$p^d$	$K_d^e$ (mM)	$q^f$ (mM <sup>-1</sup> )	$\Delta G^g$ (kcal/mol)	Balance <sup>h</sup>
OmpG	4.1 ± 1.2	1.8 ± 0.4	0.064	-3.7 ± 0.1	$F_{adh} \cong F_{coh}$
FhuA $\Delta C/\Delta 5L$	3.5 ± 0.5	1.7 ± 0.1	0.072	-3.8 ± 0.1	$F_{adh} \cong F_{coh}$
FhuA $\Delta C/\Delta 5L_{25N}$	27 ± 3	0.9 ± 0.1	1.30	-4.1 ± 0.1	$F_{adh} \gg F_{coh}$
FhuA $\Delta C/\Delta 7L_{30N}$	27 ± 6	0.9 ± 0.1	1.07	-4.1 ± 0.1	$F_{adh} \gg F_{coh}$
CYMAL-4 <sup>c</sup>	$p^d$	$K_d^e$ (mM)	$q^f$ (mM <sup>-1</sup> )	$\Delta G^g$ (kcal/mol)	Balance <sup>h</sup>
OmpG	6.7 ± 0.1	4.6 ± 0.1	0.25	-3.2 ± 0.1	$F_{adh} > F_{coh}$
FhuA $\Delta C/\Delta 5L$	3.7 ± 0.1	5.3 ± 0.1	0.38	-3.1 ± 0.1	$F_{adh} > F_{coh}$
FhuA $\Delta C/\Delta 5L_{25N}$	5.2 ± 0.3	5.7 ± 0.1	0.28	-3.1 ± 0.1	$F_{adh} > F_{coh}$
FhuA $\Delta C/\Delta 7L_{30N}$	2.3 ± 0.9	4.5 ± 1.1	0.17	-3.2 ± 0.1	$F_{adh} > F_{coh}$

<sup>a</sup>To reach low detergent concentrations below the CMC, the Gdm-HCl-solubilized proteins were refolded at detergent concentrations above the CMC.

<sup>b</sup>The dose-response equilibrium curves were fitted by the four-parameter Hill equation (eq. (3)).

<sup>c</sup>This column indicates the names of the detergents and proteins used in this work. Other details are provided in **Methods**.

<sup>d</sup> $p$  is the Hill coefficient.

<sup>e</sup>The apparent dissociation constant,  $K_d$ , was determined as the midpoint of the dose-dependent dissociation phase (e.g.,  $c_0$ ).<sup>5</sup>

<sup>f</sup>The slope factor or transition steepness was calculated at the midpoint of the dissociation phase.

<sup>g</sup>Free energies were determined using the standard thermodynamic relationship  $\Delta G = RT \ln K_d$ .

<sup>h</sup>The semi-quantitative balance between the adhesive protein-detergent ( $F_{adh}$ ) and cohesive detergent-detergent interactions ( $F_{coh}$ ) of the proteomicelles.

5. Time-dependent changes in the FP anisotropy when the four  $\beta$ -barrel proteins were incubated in CHAPS at detergent concentrations above and below the CMC

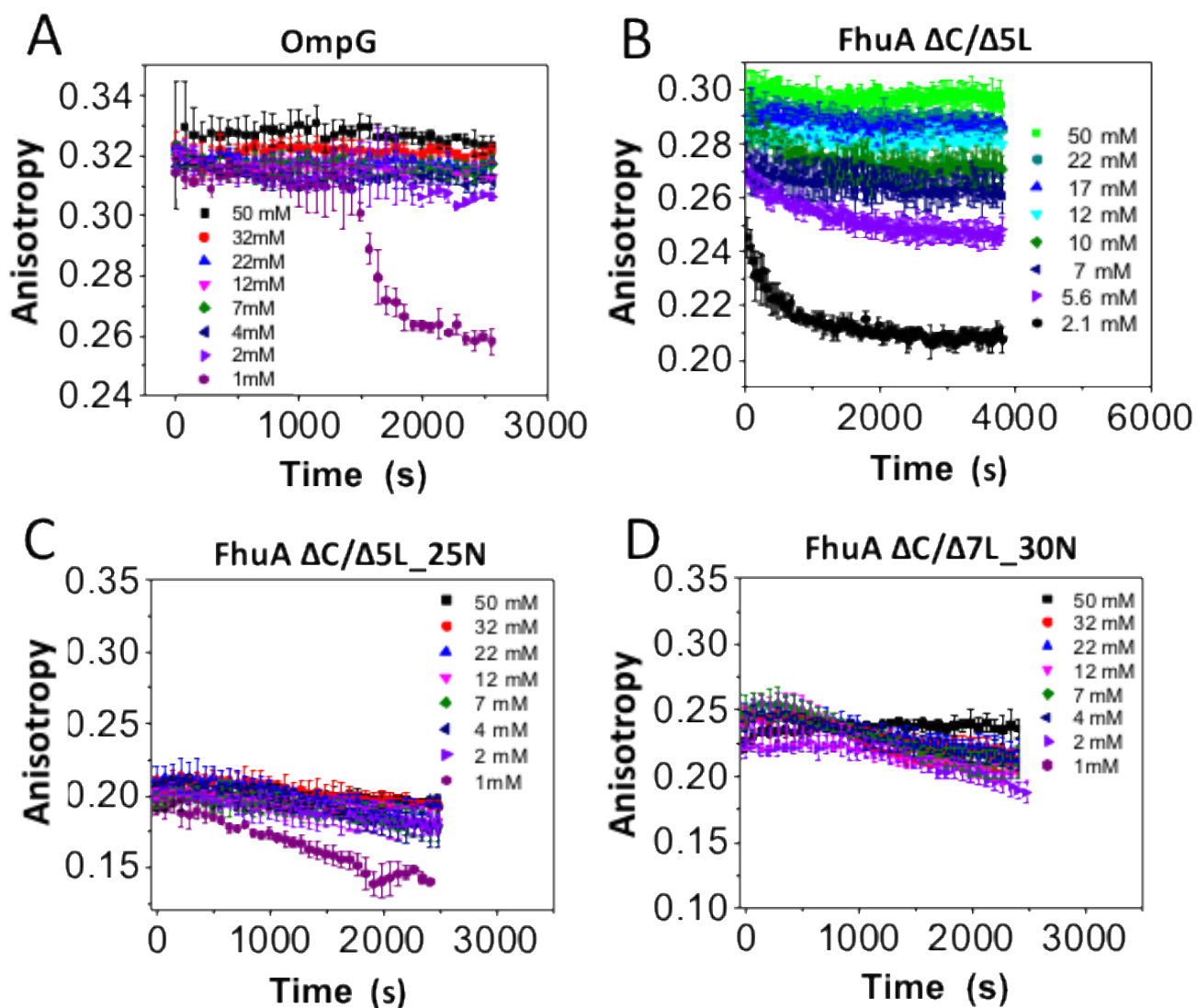


***Figure S4:*** Time-dependent changes in the FP anisotropy when the four  $\beta$ -barrel proteins were incubated in CHAPS at detergent concentrations above and below the CMC. (A) OmpG; (B) FhuA  $\Delta C/\Delta 5L$ ; (C) FhuA  $\Delta C/\Delta 5L_{25N}$ ; (D) FhuA  $\Delta C/\Delta 7L_{30N}$ . The other experimental conditions were similar to those presented in **Fig. 3** and **Table 4**.

6. Time-dependent changes in the FP anisotropy when the four  $\beta$ -barrel proteins were incubated in LD.

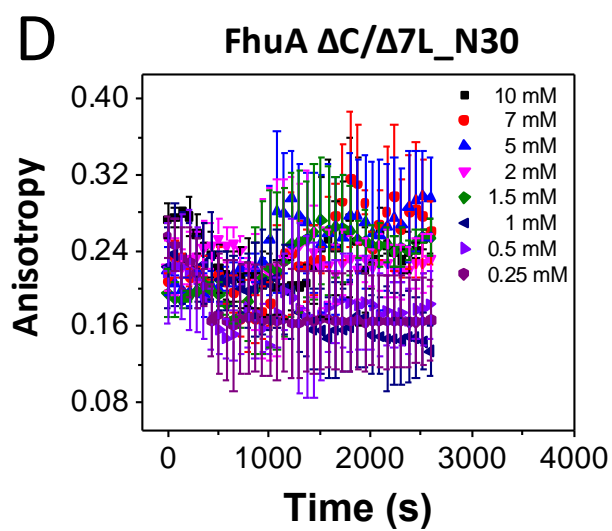
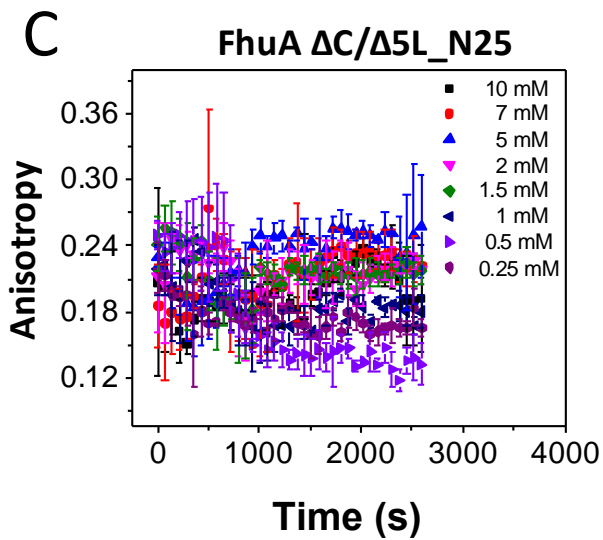
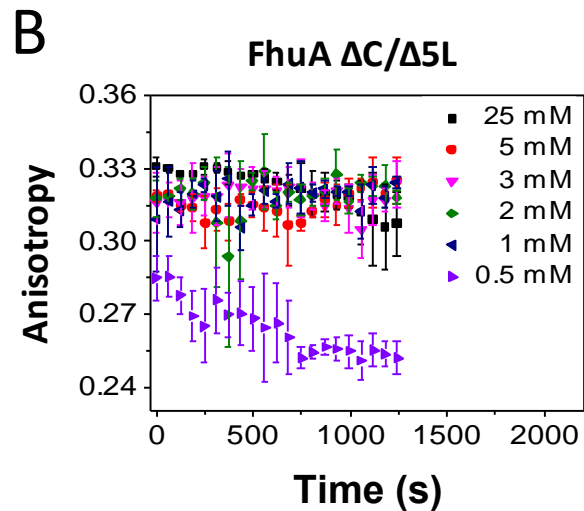
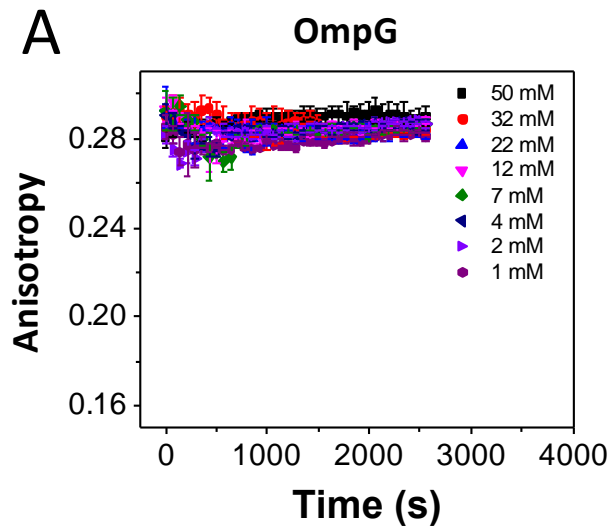


***Figure S5:*** Time-dependent changes in the FP anisotropy when the four  $\beta$ -barrel proteins were incubated in n-dodecyl-N,N-dimethylglycine (LD). (A) OmpG; (B) FhuA  $\Delta C/\Delta 5L$ ; (C) FhuA  $\Delta C/\Delta 5L_{25N}$ ; (D) FhuA  $\Delta C/\Delta 7L_{30N}$ . The other experimental conditions were similar to those presented in **Fig. 3** and **Table 4**.

**Table S3:** Table that summarizes the recorded minima and maxima of the anisotropy readout with DM and the four  $\beta$ -barrel proteins under conditions of varying pH.<sup>a</sup> This table also illustrates the rotational diffusion coefficients as well as alterations in the hydrodynamic radii of the proteomicelles during the two-state detergent desolvation transitions.

OmpG <sup>b</sup>	$r_{\min}^c$	$r_{\max}^c$	$D_r^{\text{slow}} (10^7 \text{ s}^{-1})^d$	$D_r^{\text{fast}} (10^7 \text{ s}^{-1})^d$	$R_h^{\text{max}} (\text{nm})^e$	$\Delta R_h (\text{nm})^f$
4.6	0.094 ± 0.004	0.219 ± 0.005	3.3 ± 0.2	13 ± 1	1.7	0.62 ± 0.05
5.6	0.112 ± 0.009	0.303 ± 0.001	1.3 ± 0.1	10 ± 1	2.3	1.2 ± 0.1
6.8	0.151 ± 0.019	0.331 ± 0.002	0.83 ± 0.02	6.5 ± 1.2	2.7	1.3 ± 0.1
7.4	0.214 ± 0.005	0.327 ± 0.001	0.89 ± 0.02	3.4 ± 0.2	2.6	0.95 ± 0.04
8.2	0.150 ± 0.027	0.334 ± 0.001	0.79 ± 0.01	6.6 ± 1.6	2.7	1.4 ± 0.1
10	0.169 ± 0.004	0.337 ± 0.001	0.74 ± 0.01	5.4 ± 0.2	2.8	1.3 ± 0.1
FhuA $\Delta C/\Delta 5L^b$	$r_{\min}^c$	$r_{\max}^c$	$D_r^{\text{slow}} (10^7 \text{ s}^{-1})^d$	$D_r^{\text{fast}} (10^7 \text{ s}^{-1})^d$	$R_h^{\text{max}} (\text{nm})^e$	$\Delta R_h (\text{nm})^f$
4.6	0.161 ± 0.005	0.235 ± 0.003	2.8 ± 0.1	5.8 ± 0.2	1.8	0.40 ± 0.04
5.6	0.195 ± 0.016	0.365 ± 0.002	0.38 ± 0.02	4.2 ± 0.6	3.5	1.9 ± 0.1
6.8	0.216 ± 0.005	0.366 ± 0.002	0.37 ± 0.02	3.4 ± 0.2	3.5	1.8 ± 0.1



7.4	0.219 ± 0.005	0.360 ± 0.001	0.44 ± 0.01	3.3 ± 0.2	3.3	1.6 ± 0.1
8.2	0.117 ± 0.024	0.373 ± 0.002	0.29 ± 0.02	9.6 ± 2.3	3.8	2.6 ± 0.2
10	~0.238	0.329 ± 0.003	~0.86	~2.7	2.6	~0.84
FhuA ΔC/Δ5L_25N <sup>b</sup>	$r_{\min}^c$	$r_{\max}^c$	$D_r^{\text{slow}} (10^7 \text{ s}^{-1})^d$	$D_r^{\text{fast}} (10^7 \text{ s}^{-1})^d$	$R_h^{\text{max}} (\text{nm})^e$	$\Delta R_h (\text{nm})^f$
4.6	0.176 ± 0.024	0.307 ± 0.002	1.2 ± 0.3	5.1 ± 1.1	2.4	0.89 ± 0.11
5.6	0.154 ± 0.002	0.326 ± 0.001	0.90 ± 0.01	6.3 ± 0.1	2.6	1.2 ± 0.1
6.8	0.144 ± 0.009	0.327 ± 0.005	0.89 ± 0.07	7.1 ± 0.7	2.6	1.3 ± 0.1
7.4	0.166 ± 0.003	0.343 ± 0.002	0.66 ± 0.03	5.6 ± 0.2	2.9	1.5 ± 0.1
8.2	0.168 ± 0.004	0.309 ± 0.001	1.2 ± 0.02	5.5 ± 0.2	2.4	0.96 ± 0.02
10	ND <sup>g</sup>	0.265 ± 0.007	2.0 ± 0.2	ND <sup>g</sup>	2.0	ND <sup>g</sup>
FhuA ΔC/Δ7L_30N <sup>b</sup>	$r_{\min}^c$	$r_{\max}^c$	$D_r^{\text{slow}} (10^7 \text{ s}^{-1})^d$	$D_r^{\text{fast}} (10^7 \text{ s}^{-1})^d$	$R_h^{\text{max}} (\text{nm})^e$	$\Delta R_h (\text{nm})^f$
4.6	0.198 ± 0.006	0.348 ± 0.001	0.59 ± 0.01	4.1 ± 0.2	3.0	1.4 ± 0.1
5.6	0.178 ± 0.010	0.338 ± 0.002	0.73 ± 0.03	5.0 ± 0.5	2.8	1.3 ± 0.1

6.8	0.155 ± 0.016	0.296 ± 0.006	1.4 ± 0.1	6.3 ± 1.0	2.3	0.89 ± 0.12
7.4	0.168 ± 0.007	0.312 ± 0.001	1.1 ± 0.1	5.5 ± 0.4	2.4	1.0 ± 0.1
8.2	0.151 ± 0.010	0.284 ± 0.026	1.6 ± 0.5	6.5 ± 0.7	2.1	0.80 ± 0.22
10	0.325 ± 0.009	0.358 ± 0.001	0.4 ± 0.1	0.9 ± 0.1	3.2	0.66 ± 0.14

<sup>a</sup>To reach low detergent concentrations below CMC, the Gdm-HCl-solubilized FhuA  $\Delta C/\Delta 5L$  protein was refolded at various detergent concentrations above CMC. These values were stated in **Methods**.

<sup>b</sup>Full names of the detergents are provided in **Methods**.

<sup>c</sup>Experimentally determined anisotropy minima ( $r_{\min}$ ) and maxima ( $r_{\max}$ ) for various detergents.  $r_{\min}$  was extrapolated for the lowest detergent concentration in the well.  $r_{\max}$  was determined for detergent concentrations above the CMC.

<sup>d</sup> $D_r^{\text{slow}}$  and  $D_r^{\text{fast}}$  indicate the rotational diffusion coefficients of the FhuA  $\Delta C/\Delta 5L$  protein under solvation and desolvation conditions, respectively.

<sup>e</sup> $R_h^{\text{max}}$  are the maximum hydrodynamic radii of the proteomicelle with various solubilizing detergents.

<sup>f</sup> $\Delta R_h$  is the decrease in the hydrodynamic radius,  $R_h$ , as a result of the detergent desolvation transition of the protein.

ND<sup>g</sup> Not determined.

**Table S4: Summary of the fitting results of the two-state, concentration-dependent anisotropy curves acquired with three FhuA derivatives and OmpG under conditions of varying pH.<sup>a,b</sup> DM was the detergent used in this case.** The solution contained 200 mM NaCl at room temperature. The buffer was either 50 mM HEPES (pH 6.8, pH 7.4, pH 8.2), 50 mM NaOAc (pH 4.6, pH 5.6) or 50 mM Sodium borate (pH 10.0). All data were derived as averages  $\pm$  SDs of three independent data acquisitions.

OmpG <sup>c</sup>	$p^d$	$K_d^e$ (mM)	$q^f$ (mM <sup>-1</sup> )	$\Delta G^g$ (kcal/mol)	Balance <sup>h</sup>
4.6	3.7 $\pm$ 1.2	1.6 $\pm$ 0.5	0.05	-3.8 $\pm$ 0.2	$F_{adh} \cong F_{coh}$
5.6	6.5 $\pm$ 6.8	1.8 $\pm$ 0.6	0.17	-3.7 $\pm$ 0.2	$F_{adh} \cong F_{coh}$
6.8	6.2 $\pm$ 3.4	1.5 $\pm$ 0.4	0.18	-3.8 $\pm$ 0.2	$F_{adh} \cong F_{coh}$
7.4	4.1 $\pm$ 1.2	1.8 $\pm$ 0.4	0.064	-3.7 $\pm$ 0.1	$F_{adh} \cong F_{coh}$
8.2	5.2 $\pm$ 2.1	1.5 $\pm$ 0.4	0.17	-3.9 $\pm$ 0.2	$F_{adh} \cong F_{coh}$
10	3.6 $\pm$ 0.2	1.3 $\pm$ 0.1	0.12	-3.9 $\pm$ 0.1	$F_{adh} > F_{coh}$
FhuA $\Delta C/\Delta 5L^c$	$p^d$	$K_d^e$ (mM)	$q^f$ (mM <sup>-1</sup> )	$\Delta G^g$ (kcal/mol)	Balance <sup>h</sup>
4.6	~25	~2.1	0.23	~-3.6	$F_{adh} < F_{coh}$
5.6	3.7 $\pm$ 0.8	1.6 $\pm$ 0.2	0.098	-3.8 $\pm$ 0.1	$F_{adh} \cong F_{coh}$
6.8	5.3 $\pm$ 1.0	1.7 $\pm$ 0.1	0.12	-3.8 $\pm$ 0.1	$F_{adh} \cong F_{coh}$
7.4	3.5 $\pm$ 0.5	1.7 $\pm$ 0.1	0.072	-3.8 $\pm$ 0.1	$F_{adh} \cong F_{coh}$
8.2	1.9 $\pm$ 0.3	0.9 $\pm$ 0.1	0.13	-4.1 $\pm$ 0.1	$F_{adh} > F_{coh}$
10	~2.4	~1.9	0.029	~-3.7	$F_{adh} \cong F_{coh}$
FhuA $\Delta C/\Delta 5L_{25N}^c$	$p^d$	$K_d^e$ (mM)	$q^f$ (mM <sup>-1</sup> )	$\Delta G^g$ (kcal/mol)	Balance <sup>h</sup>

4.6	$2.9 \pm 0.9$	$1.9 \pm 0.5$	0.049	$-3.7 \pm 0.2$	$F_{adh} \cong F_{coh}$
5.6	$4.5 \pm 0.3$	$2.0 \pm 0.1$	0.10	$-3.7 \pm 0.2$	$F_{adh} < F_{coh}$
6.8	$2.6 \pm 0.6$	$2.7 \pm 0.5$	0.043	$-3.5 \pm 0.1$	$F_{adh} < F_{coh}$
7.4	$27 \pm 2.9$	$0.9 \pm 0.1$	1.30	$-4.1 \pm 0.1$	$F_{adh} \gg F_{coh}$
8.2	$\sim 9.7$	$1.7 \pm 1.2$	0.20	$-3.8 \pm 0.7$	$F_{adh} \cong F_{coh}$
10	$2.0 \pm 6.7$	$< 2.0$	ND <sup>a</sup>	$\sim -5.6$	$F_{adh} \cong F_{coh}$
FhuA $\Delta C/\Delta 7L_{30N}^c$	$p^d$	$K_d^e$ (mM)	$q^f$ (mM <sup>-1</sup> )	$\Delta G^g$ (kcal/mol)	Balance <sup>h</sup>
4.6	$9.0 \pm 7.6$	$2.0 \pm 0.1$	0.17	$-3.7 \pm 0.1$	$F_{adh} < F_{coh}$
5.6	$5.3 \pm 2.7$	$1.8 \pm 0.3$	0.12	$-3.7 \pm 0.1$	$F_{adh} \cong F_{coh}$
6.8	$2.4 \pm 0.9$	$1.8 \pm 0.4$	0.048	$-3.7 \pm 0.1$	$F_{adh} \cong F_{coh}$
7.4	$27 \pm 6$	$0.9 \pm 0.1$	1.07	$-4.1 \pm 0.1$	$F_{adh} \gg F_{coh}$
8.2	$1.3 \pm 0.5$	$3.2 \pm 1.5$	0.014	$-3.4 \pm 0.5$	$F_{adh} < F_{coh}$
10	$5.6 \pm 7.4$	$3.9 \pm 1.2$	0.012	$-3.3 \pm 0.2$	$F_{adh} < F_{coh}$

<sup>a</sup>To reach low detergent concentrations below the CMC, the Gdm-HCl-solubilized proteins were refolded at detergent concentrations above the CMC. These values were stated in **Methods**.

<sup>b</sup>The dose-response equilibrium curves were fitted by the four-parameter Hill equation.

<sup>c</sup>This column indicates the names of the proteins and various pH values examined used in this work. Other details are provided in **Methods**.

<sup>d</sup> $p$  is the Hill coefficient.

<sup>e</sup>The apparent dissociation constant,  $K_d$ , was determined as the midpoint of the dose-dependent dissociation phase (e.g.,  $c_0$ ).<sup>5</sup>

<sup>f</sup>The slope factor or transition steepness was calculated at the midpoint of the dissociation phase.

<sup>g</sup>Free energies were determined using the standard thermodynamic relationship  $\Delta G = RT \ln K_d$ .

<sup>h</sup>The semi-quantitative balance between the adhesive protein-detergent ( $F_{adh}$ ) and cohesive detergent-detergent interactions ( $F_{coh}$ ) of the proteomicelles.

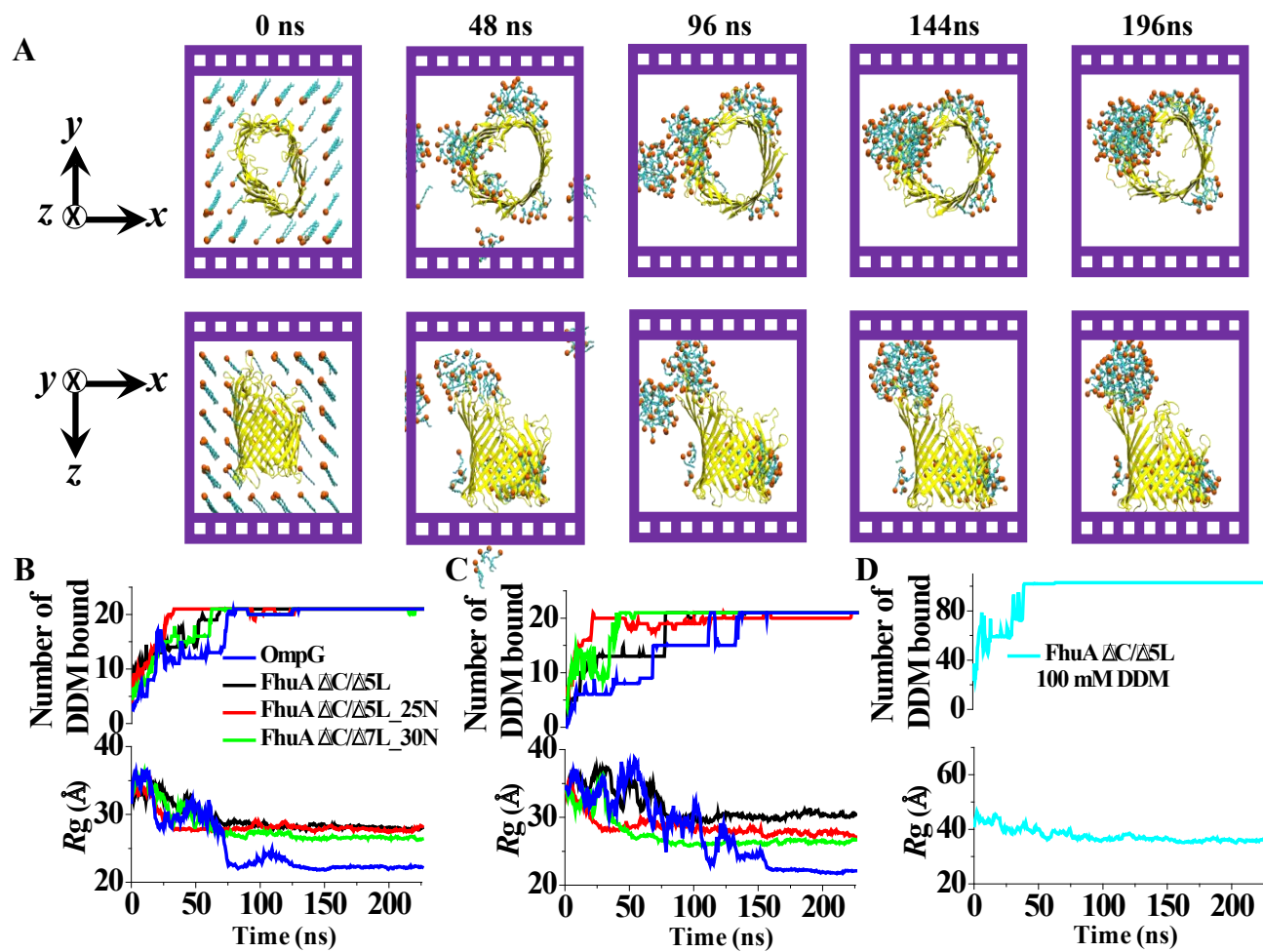


**Figure S6: MD simulations of DDM molecules binding to  $\beta$ -barrel proteins.** (A) A sequence of microscopic configurations realized in simulations of FhuA  $\Delta C/\Delta 5L$  with 100 mM DDM molecules around it. Images in the top and bottom rows depict the same system from two different viewpoints: top view (above) and side view (bottom); (B) The number of the DDM molecules bound to each of the four  $\beta$ -barrel proteins (top) and the radius of gyration of the protein-DDM complex (bottom) *versus* simulation time. The initial concentration of DDM was 20 mM; the DDM molecules were initially arranged on a cubic lattice around the proteins. The mean values of the  $R_g$  for the protein-DDM complexes during the last  $\sim 70$  ns equilibrated simulations are: 22.2 Å for OmpG, 28.1 Å for FhuA  $\Delta C/\Delta 5L$ , 27.8 Å for FhuA  $\Delta C/\Delta 5L_{25N}$  and 26.6 Å for FhuA  $\Delta C/\Delta 7L_{30N}$ . Each data point represents a 0.48 ns block average of 2.4 ps sampled values; (C) The same as in panel B, but for the initially planar arrangement of the DDM molecules around the proteins. The mean values of the  $R_g$  for the protein-DDM complexes during the last  $\sim 70$  ns equilibrated simulations are: 22.1 Å for OmpG, 30.3 Å for FhuA  $\Delta C/\Delta 5L$ , 27.7 Å for FhuA  $\Delta C/\Delta 5L_{25N}$  and 26.4 Å for FhuA  $\Delta C/\Delta 7L_{30N}$ ; (D) The same as in panel B, but for 100 mM DDM concentration. The mean values of the  $R_g$  for the protein-DDM complexes during the last  $\sim 70$  ns equilibrated simulation is 35.8 Å.

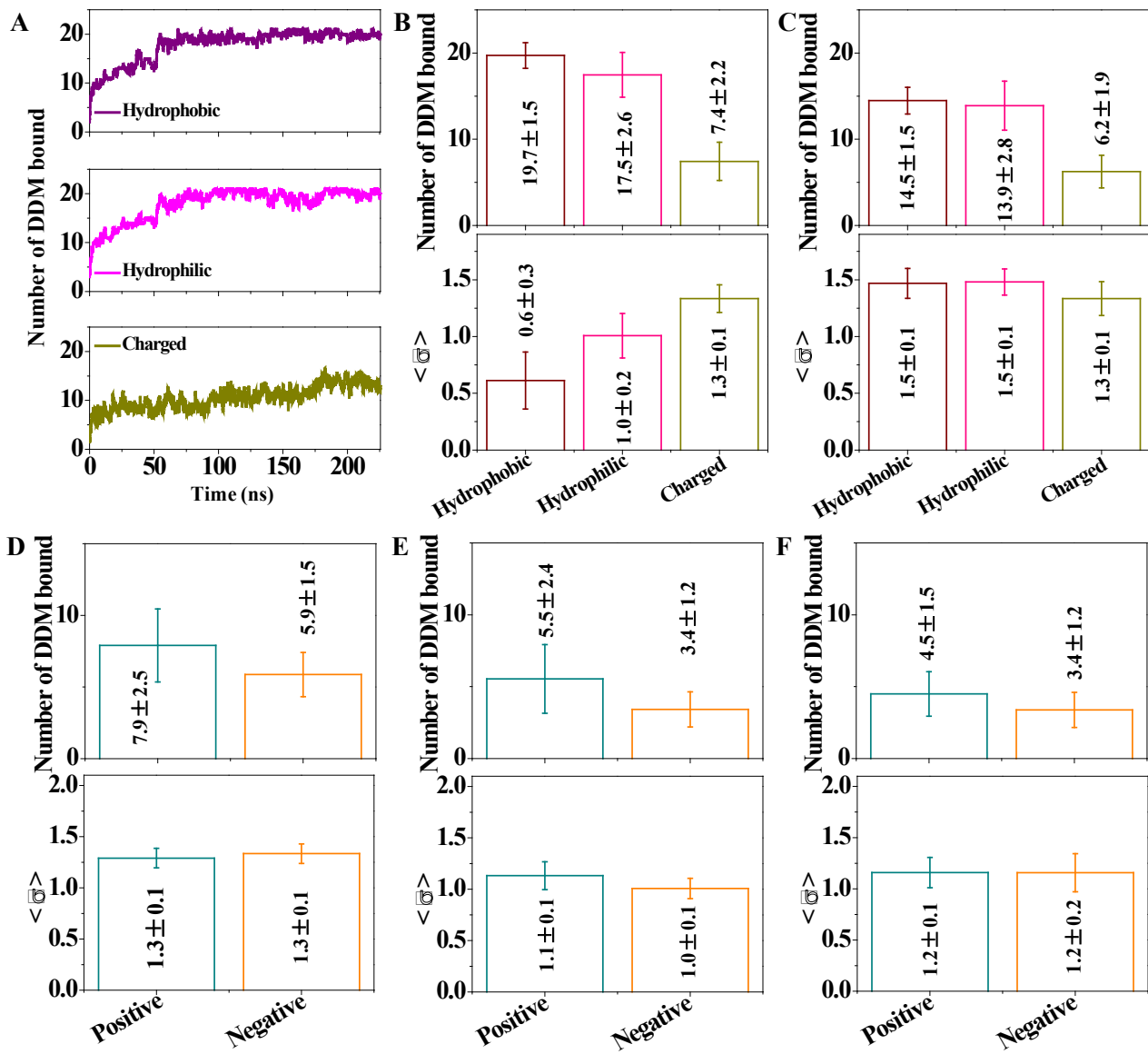




**Figure S7: Differential affinity of DDM molecules to residues of  $\beta$ -barrel proteins. (A)**

The number of DDM molecules bound to the hydrophobic (top), hydrophilic (middle) and charged (bottom) residues of FhuA  $\Delta C/\Delta 5L$  versus simulation time. The simulation system contained 20 mM DDM initially placed on a cubic lattice around the protein. The traces were sampled at 2.4 ps intervals and block-averaged in 0.12 ns blocks; **(B-C)** The mean equilibrium number (top) and the standard deviation (bottom) of the number of DDM molecules bound, with either their tail (panel **B**) and head (panel **C**) parts, to the hydrophobic, hydrophilic or charged residues of the four  $\beta$ -barrel proteins. To count as a binding event, any atom of the tail (or the head) part of the molecule must reside within 4 Å of any atom of the hydrophobic, hydrophilic or charged residue of the protein. To compute the mean equilibrium number of bound molecules and its standard deviation, the last ~70 ns of an equilibration trajectory was split into 10 ns fragments; the mean and the standard deviation was computed for each of the fragment and then averaged over all fragments. The final plotted values were obtained by averaging over the two independent MD simulations of each protein system and then over the four protein systems. Error bars represent standard deviations among the eight simulations; **(D-F)** Same as in panel **B** and **C** but for binding of the entire DDM molecules (panel **D**), and separately of their tail (panel **E**) and head (panel **F**) parts to all positively or negatively charged residues of the  $\beta$ -barrel proteins.

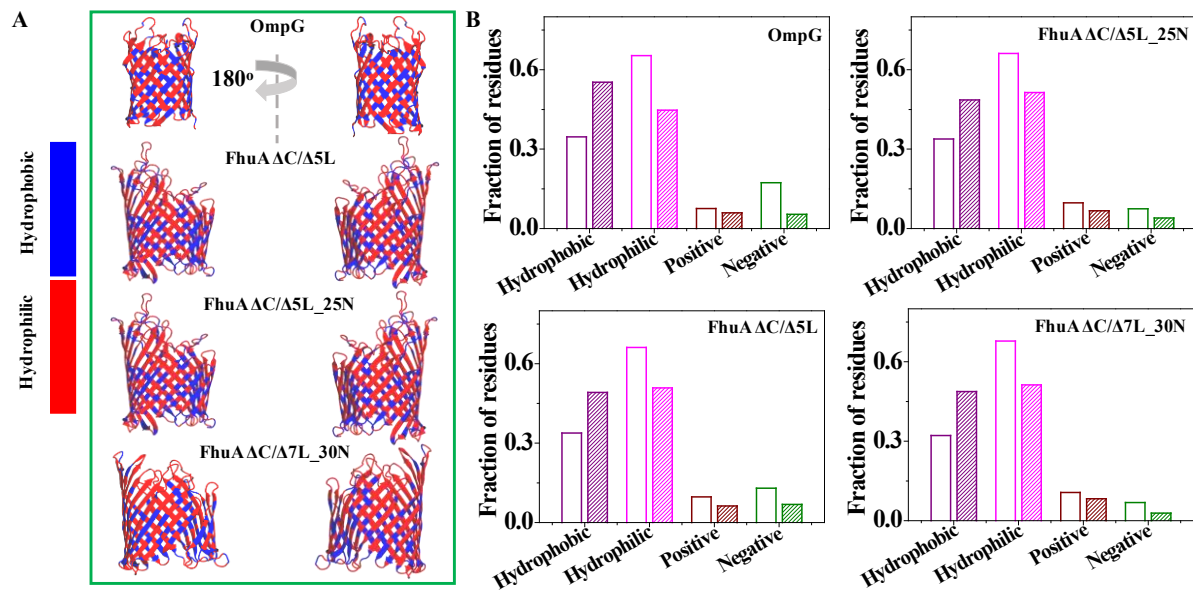


**Figure S8: DDM binding versus residue type.** (A) Molecular structures of the four  $\beta$ -barrel proteins colored to highlight the presence of the hydrophobic (blue) and hydrophilic (red) residues. The proteins are shown from the same viewpoints as in **Fig. 6E**; (B) The fraction of the hydrophobic, hydrophilic (polar or charged), as well as positively and negatively charged residues in the respective protein structures (open bars) and the fraction of those residues that bind to DDM (filled bars) during the steady-state (last ~70 ns) parts of the MD trajectories. For each protein, the data were averaged over the two independent MD trajectories, which were different by the initial arrangement of the DDM molecules. The hydrophobic residues of OmpG bind DDM 60% more likely than suggested by their abundance in the structure, whereas the hydrophobic residues of FhuA variants bind DDM 47% more likely than suggested by the structure.

**Table S5: Biophysical properties of the  $\alpha$ -helical proteins used in this study.<sup>6-7</sup>**

<b>Protein</b>	<b>pI</b>	<b>GRAVY<sup>1</sup></b>	<b>Aliphatic index<sup>2</sup></b>	<b>Negative residues</b>	<b>Positive residues</b>	<b>Total number of residues</b>
SELENOK U92C	10.34	-0.723	59.22	8	15	102
SELENOS U188S	9.72	-0.791	70.89	24	34	190

<sup>1</sup>The GRAVY hydrophobicity parameter was calculated by adding individual hydrophathy indexes<sup>8</sup> of each residue and dividing by the total number of the protein residues. Increasing positive GRAVY number shows a more hydrophobic protein.

<sup>2</sup>The aliphatic index is given by the relative volume of aliphatic chain-containing residues.<sup>9</sup>

**Table S6:** Table that summarizes the recorded minima and maxima of the anisotropy readout with the SELENOK U92C and SELENOS U188S  $\alpha$ -helical membrane proteins solubilized in DDM.<sup>a</sup> This table also illustrates the rotational diffusion coefficients as well as alterations in the hydrodynamic radii of the proteomicelles during the two-state detergent desolvation transitions.

Protein <sup>b</sup>	$r_{\min}^c$	$r_{\max}^c$	$D_r^{\text{slow}} (10^9 \text{ s}^{-1})^d$	$D_r^{\text{fast}} (10^9 \text{ s}^{-1})^d$	$R_h^{\text{max}} (\text{nm})^e$	$\Delta R_h (\text{nm})^f$
SELENOK U92C	$0.095 \pm 0.002$	$0.283 \pm 0.023$	$0.016 \pm 0.004$	$0.127 \pm 0.003$	2.1	$1.1 \pm 0.2$
SELENOS U188S	$0.103 \pm 0.002$	$0.282 \pm 0.029$	$0.017 \pm 0.005$	$0.114 \pm 0.003$	2.1	$1.0 \pm 0.2$

<sup>a</sup>To reach low detergent concentrations below the CMC, the Gdm-HCl-solubilized protein was refolded at detergent concentrations above the CMC.

<sup>b</sup>Details about these proteins are provided in **Methods**.

<sup>c</sup>Experimentally determined anisotropy minima ( $r_{\min}$ ) and maxima ( $r_{\max}$ ).  $r_{\min}$  was extrapolated for the lowest detergent concentration in the well.  $r_{\max}$  was determined for detergent concentrations above the CMC.

<sup>d</sup> $D_r^{\text{slow}}$  and  $D_r^{\text{fast}}$  indicate the rotational diffusion coefficients of the proteins under solvation and desolvation conditions, respectively.

<sup>e</sup> $R_h^{\text{max}}$  are the maximum hydrodynamic radii of the proteomicelle with various solubilizing detergents.

<sup>f</sup> $\Delta R_h$  is the decrease in the hydrodynamic radius,  $R_h$ , as a result of the detergent desolvation transition.

**Table S7: Summary of the fitting results of the two-state, concentration-dependent anisotropy curves acquired with SELENOK U92C and SELENOS U188S  $\alpha$ -helical transmembrane proteins.** DDM was the detergent used in this case. The protein concentration in the well was 200 nM. The initial detergent concentration was 1.3 mM. The FP measurements were carried out using a solution that contained 200 mM NaCl, 50 mM HEPES, pH 7.4 at a temperature of 24°C. All data were derived as averages  $\pm$  SDs of three independent data acquisitions.

Protein	$p^b$	$K_d^c$ (mM)	$q^d$ (mM <sup>-1</sup> )	$\Delta G^e$ (kcal/mol)	Balance <sup>f</sup>
SELENOK U92C	3.1 $\pm$ 1.6	0.29 $\pm$ 0.13	0.50	-4.8 $\pm$ 0.3	$F_{adh} \leq F_{coh}$
SELENOS U188S	4.8 $\pm$ 5.0	0.55 $\pm$ 0.12	0.39	-4.4 $\pm$ 0.1	$F_{adh} < F_{coh}$

<sup>a</sup>Experimentally determined anisotropy minima ( $r_{min}$ ) and maxima ( $r_{max}$ ) for various detergents and proteins.  $r_{min}$  was extrapolated for the lowest detergent concentration in the well.  $r_{max}$  was determined for detergent concentrations above the CMC.

<sup>b</sup> $p$  is the Hill coefficient

<sup>c</sup>The apparent dissociation constant,  $K_d$ , was determined as the midpoint of the dose-dependent dissociation phase (e.g.,  $c_0$ ).<sup>5</sup>

<sup>d</sup>The slope factor or transition steepness was calculated at the midpoint of the dissociation phase.

<sup>e</sup>Free energies were determined using the standard thermodynamic relationship  $\Delta G = RT \ln K_d$ .

<sup>f</sup>The quantitative balance between the adhesive protein-detergent ( $F_{adh}$ ) and cohesive detergent-detergent interactions ( $F_{coh}$ ) of the proteomicelles.

**REFERENCES**

1. Gradinaru, C. C.; Marushchak, D. O.; Samim, M.; Krull, U. J., Fluorescence anisotropy: from single molecules to live cells. *Analyst* **2010**, *135* (3), 452-9.
2. Prazeres, T. J. V.; Fedorov, A.; Barbosa, S. P.; Martinho, J. M. G.; Berberan-Santos, M. N., Accurate determination of the limiting anisotropy of rhodamine 101. Implications for its use as a fluorescence polarization standard. *J. Phys. Chem. A* **2008**, *112* (23), 5034-5039.
3. Lakowicz, J. R., *Principles of fluorescence microscopy*. 2nd ed.; Springer: New York, 2006.
4. Lide, D. R. E., *CRC Handbook of chemistry and physics - A ready reference book of chemical and physical data*. The 88th ed.; CRC Press - Taylor and Francis Group: Boca Raton 2008.
5. Rossi, A. M.; Taylor, C. W., Analysis of protein-ligand interactions by fluorescence polarization. *Nat. Protoc.* **2011**, *6* (3), 365-87.
6. Gasteiger, E.; Gattiker, A.; Hoogland, C.; Ivanyi, I.; Appel, R. D.; Bairoch, A., ExPASy: The proteomics server for in-depth protein knowledge and analysis. *Nucleic Acids Res.* **2003**, *31* (13), 3784-3788.
7. Gasteiger, E.; Hoogland, C.; Gattiker, A.; Duvaud, S.; Wilkins, M. R.; Appel, R. D.; Bairoch, A., Protein identification and analysis tools on the ExPASy server. In *Proteomics Protocols Handbook*, J.M., W., Ed. Humana Press: 2005; pp 571-607.
8. Kyte, J.; Doolittle, R. F., A simple method for displaying the hydropathic character of a protein. *J. Mol. Biol* **1982**, *157* (1), 105-132.
9. Ikai, A., Thermostability and aliphatic index of globular proteins. *J. Biochem.* **1980**, *88* (6), 1895-1898.

## Chapter 5. Detergent Desorption of Membrane Proteins Exhibits Two Kinetic Phases

Aaron J. Wolfe,<sup>1,2</sup> Jack F. Gugel,<sup>1</sup> Min Chen,<sup>3</sup> and Liviu Movileanu\*<sup>1,2,4</sup>

<sup>1</sup>*Department of Physics, Syracuse University, 201 Physics Building, Syracuse, New York 13244-1130, USA*

<sup>2</sup>*Structural Biology, Biochemistry, and Biophysics Program, Syracuse University, 111 College Place, Syracuse, New York 13244-4100, USA*

<sup>3</sup>*Department of Chemistry, University of Massachusetts, 820 LGRT, 710 North Pleasant Street, Amherst, Massachusetts 01003-9336, USA*

<sup>4</sup>*Department of Biomedical and Chemical Engineering, Syracuse University, Syracuse University, 223 Link Hall, Syracuse, New York 13244, USA*

Reprinted with permission from **Detergent Desorption of Membrane Proteins Exhibits Two Kinetic Phases** Aaron J. Wolfe, Jack F. Gugel, Min Chen, and Liviu Movileanu  
*The Journal of Physical Chemistry Letters* **2018** 9 (8), 1913-1919 DOI:  
10.1021/acs.jpcelett.8b00549 Copyright 20018 American Chemical Society.

Author contributions:

AJW: Designed experiments, performed experiments, analyzed data, interpreted data.

JFG: Analyzed data

MC: Performed experiments

LM: Analyzed data, interpreted data, wrote manuscript



**ABSTRACT**

Gradual dissociation of detergent molecules from water-insoluble membrane proteins culminates in protein aggregation. However, the time-dependent trajectory of this process remains ambiguous, because the signal-to-noise ratio of most spectroscopic and calorimetric techniques is declined by the presence of protein aggregates in solution. Here, we show that by using steady-state fluorescence polarization (FP) spectroscopy, the dissociation of the protein-detergent complex (PDC) can be inspected in real time at detergent concentrations below the critical micelle concentration (CMC). This article provides experimental evidence for the coexistence of two distinct phases of the dissociations of detergent monomers from membrane proteins. We first noted a slow detergent predesolvation process, which was accompanied by a relatively modest change in the FP anisotropy, suggesting a small number of dissociated detergent monomers from the proteomicelles. This predesolvation phase was followed by a fast detergent desolvation process, which was highlighted by a major alteration in the FP anisotropy. The durations and rates of these phases were dependent on both the detergent concentration and interfacial PDC interactions. Further development of this approach might lead to the creation of a new semi-quantitative method for the assessment of the kinetics of association and dissociation of proteomicelles.

## INTRODUCTION

Interactions of detergents with membrane proteins are ubiquitous in structural and chemical biology, as well as biotechnology.<sup>1-5</sup> These interactions are complex because of the diversity of architectural fingerprints of membrane proteins in various reconstitution systems, such as liposomes, nanodiscs, and planar lipid membranes.<sup>6</sup> The complicated behavior of membrane proteins in solution is driven by the subtle balance among their physicochemical features, which include the interfacial forces with detergent micelles.<sup>7-8</sup> In many instances, the inability of membrane proteins to optimally interact with detergents leads to their loss of activity,<sup>6,9</sup> stability,<sup>10-12</sup> and proper solubilization,<sup>2, 12-15</sup> preceding the protein aggregation.<sup>16-17</sup> The presence of aggregates in solution adds to the difficulty of many approaches to characterize the stability and interfacial dynamics of insoluble membrane proteins in aqueous phase.<sup>18</sup> This is especially a frequent problem at detergent concentrations comparable with or below the critical micelle concentration (CMC). Therefore, the interfacial protein-detergent complex (PDC) interactions are not normally assessed under these harsh, low-detergent concentration conditions.<sup>16, 19</sup>

Recently, we have shown that these challenges of measuring the interfacial PDC interactions can be overcome using steady-state fluorescence polarization (FP) spectroscopy.<sup>20</sup> Additional advantageous traits of this approach included its amenability for a high-throughput microplate reader-based setting, low-nanomolar concentration of protein sample, and an increased optical signal-to-noise ratio due to a bright and photostable fluorophore.<sup>21</sup> These attributes enabled us to determine the isothermal Hill-Langmuir desorption curves of the proteomicelles containing either  $\alpha$ -helical or  $\beta$ -barrel membrane proteins of varying size, charge, stability, and structure.<sup>22</sup>

Here, we show that this approach can be extended to infer the time-dependent detergent desorption curves of membrane proteins at detergent concentrations below the CMC. The primary attribute of this approach is the fact that the FP readout for a noninteracting fluorophore is not dependent on its effective concentration.<sup>4,23</sup> Therefore, the dissociation of detergent micelles from membrane proteins was observed as a relative change in the population of the fluorescent proteins between detergent solvated and desolvated states. The membrane proteins were first incubated in solubilizing mild detergents at concentrations much greater than the CMC. Under these circumstances, all proteins were detergent solvated, so that a high FP anisotropy was noted, reflecting a slow tumbling rate of the proteomicelles. Of course, this assumes that the detergent exhibited good solubilizing properties of a membrane protein. Interestingly, a time-dependent reduction in the FP anisotropy was noted when the proteins were diluted at a detergent concentration below the CMC, suggesting that there was a gradual detergent desolvation process. This finding was in good accord with an increased rotational diffusion coefficient of the dissociated membrane proteins.

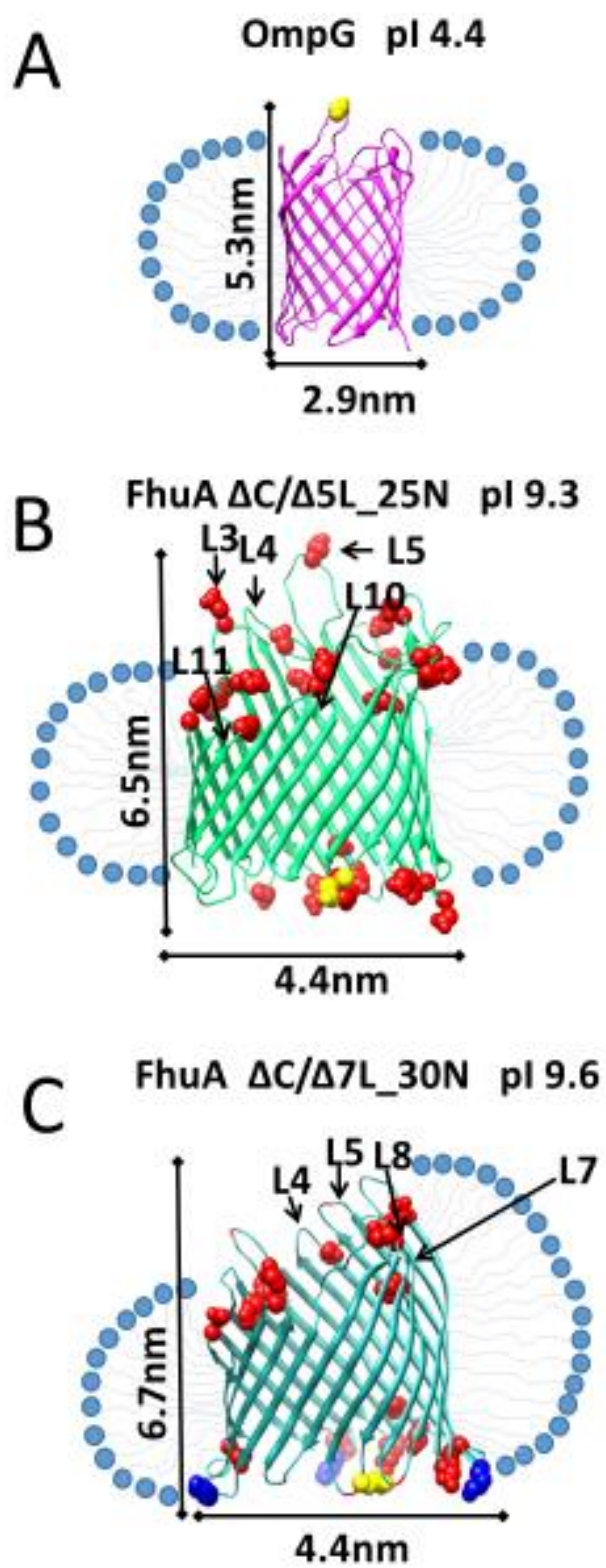


Figure 1

**Figure 1: Side-view of the molecular structures of OmpG and truncation FhuA mutants.**

(A) OmpG; (B) FhuA  $\Delta C/\Delta 5L_{-25N}$ ; (C)  $\Delta C/\Delta 7L_{-30N}$ . The positions of the fluorophore were marked in yellow. For OmpG, Texas Red<sup>21</sup> was tethered at position D224C on loop L6. For the two truncation FhuA derivatives, Texas Red was attached to an engineered GS-rich, cysteine-containing loop on the T7  $\beta$  turn. FhuA  $\Delta C/\Delta 5L_{-25N}$  and FhuA  $\Delta C/\Delta 7L_{-30N}$  show charge neutralizations, which are marked in red with respect to the native FhuA. For the latter FhuA mutant, there are three additional lysine mutations within the  $\beta$  turns, which are marked in blue, out of which two are negative-to-positive charge reversals.<sup>38-39</sup> The arrows indicate molecular dimensions, as inferred from  $C_{\alpha}$  to  $C_{\alpha}$ , which were obtained from the X-ray crystal structure of both proteins<sup>33-34</sup> Cartoons show proteomicelles in a prolate geometrical packing.<sup>40</sup> The homology structure of truncation FhuA derivatives was accomplished using Swiss-model<sup>41</sup> and FhuA PDB ID:1FI1.<sup>34</sup>

## EXPERIMENTAL METHODS

**Expression, extraction, and purification of the OmpG and FhuA proteins.** Expression, extraction, and purification of OmpG,<sup>22, 24</sup> as well as the truncation FhuA<sup>25-26</sup> proteins FhuA  $\Delta C/\Delta 5L\_25N$  and FhuA  $\Delta C/\Delta 7L\_30N$ , were previously reported. The deletion FhuA mutants lacked the internal cork domain (C) and either five (L3, L4, L5, L10, and L11) or seven (L3, L4, L5, L7, L8, L10, and L11) extracellular loops, respectively.<sup>27-28</sup> In addition, they featured either 25 or 30 negative charge neutralizations with respect to the wild-type FhuA barrel scaffold, making them basic proteins. For the fluorophore covalent attachment, the T7  $\beta$  turn (V<sup>331</sup>PEDRP<sup>336</sup>) of the truncation FhuA mutants was replaced with a cysteine-containing, GS-rich flexible loop (GGSSGCGSSGGS). In the case of OmpG, the cysteine sulfhydryl was engineered on extracellular loop L6 at position D224.

**Refolding of the  $\beta$ -barrel membrane proteins.** A rapid-dilution refolding protocol was employed for the refolding of all proteins.<sup>29</sup> 40  $\mu$ l of 6 $\times$ His tag-purified and guanidinium hydrochloride (Gdm-HCl)-denatured protein was 50-fold diluted into 200 mM NaCl, 50 mM HEPES, pH 7.4 solutions at 4°C, which contained detergents (Anatrace, Maumee, OH) at concentrations above their CMC. The starting detergent concentrations were the following: (i) 20 mM 1-lauroyl-2-hydroxy-*sn*-glycero-3-phosphocholine (LysoFos); (ii) 5 and 20 mM starting detergent concentration for n-decyl- $\beta$ -D-maltopyranoside (DM) and n-undecyl- $\beta$ -D-maltopyranoside (UM); (iii) 50 mM 4-cyclohexyl-1-butyl- $\beta$ -D-maltoside (CYMAL-4).

**Fluorescent labeling of the FhuA and OmpG proteins.** Texas Red C2-maleimide (Thermo Fisher Scientific) was used for fluorescent labeling of all membrane proteins, as previously reported.<sup>20, 22</sup>

**FP anisotropy determinations.** The time-dependent FP anisotropy traces were acquired using a SpectraMax I3 plate reader (Molecular Devices, Sunnyvale, CA), which was equipped with a Paradigm detection cartridge for rhodamine FP spectroscopy.<sup>20</sup> Texas Red fluorophore<sup>21, 30</sup> was covalently attached to an engineered cysteine sulfhydryl of the membrane proteins. The FP traces were collected using the excitation and emission wavelengths of 535 and 595 nm, respectively. The time-dependent, steady-state FP anisotropy traces were acquired with diluted detergents either above or below their CMC, while keeping the final protein concentration constant at 28 nM.<sup>20</sup> The buffer solution contained 200 mM NaCl, 50 mM HEPES, pH 7.4. This was achieved by titrating the same protein sample with buffer solutions of varying detergent concentration. The equilibration of the samples was conducted using an incubation time of ~15 min, which was followed by a time-dependent FP anisotropy read. Drastic detergent reduction within the well increased the protein aggregation over time, but without impacting the optical signal-to-noise ratio of the FP anisotropy. In addition, we checked that the self-quenching of Texas Red did not induce a time-dependent reduction in the FP anisotropy.<sup>22</sup>

**Determination of the predesolvation and desolvation rates.** The observed predesolvation rates ( $k_{\text{obs}}^{\text{pre}}$ ) were determined at various detergent concentrations below the CMC (**Supporting Information, Table S3**). This was accomplished using a linear fit of the time-dependent FP anisotropy (i.e.,  $k_{\text{obs}}^{\text{pre}}$  is  $\Delta r/\Delta t$ ),  $r(t)$ :

$$r(t) = -k_{\text{obs}}^{\text{pre}} \times t + r_{\text{max}} \quad (1)$$

Here,  $r_{\text{max}}$  is the maximum FP anisotropy at the initial recording time, whereas  $t$  shows the elapsed time during the predesolvation phase. The observed desolvation rates,  $k_{\text{obs}}^{\text{des}}$ , were also determined at various detergent concentrations below the CMC. This was accomplished using a single-exponential fit of the time-dependent FP anisotropy (i.e.,  $k_{\text{obs}}^{\text{des}}$  is  $1/\tau$ , where  $\tau$  is the time constant),  $r(t)$ , as follows:

$$r(t) = r_0 e^{-\frac{t}{\tau}} + r_{\text{min}} \quad (2)$$

Here,  $r_{\text{min}}$  denotes the minimum FP anisotropy at the infinite time of the desolvation reaction.  $t$  shows the elapsed time during the desolvation phase, including the total time of the predesolvation phase. In most cases, the observed desolvation rate,  $k_{\text{obs}}^{\text{des}}$ , was derived by fitting the single-exponential decay of the time-dependent FP anisotropy,  $r(t)$ , except in a number of cases that were approached with a linear dependence. In Eq. (2),  $r_0$  is an FP anisotropy constant, so that the initial FP anisotropy during desolvation phase,  $r_{\text{in}}$ , is given as follows ( $r_{\text{max}} > r_{\text{in}} > r_{\text{min}}$ ),

$$r_{\text{in}} = r(T_{\text{pre}}) = r_0 e^{-\frac{T_{\text{pre}}}{\tau}} + r_{\text{min}} \quad (3)$$

where  $T_{\text{pre}}$  is the total predesolvation time, which provides the following expression:

$$r_0 = \frac{r_{\text{in}} - r_{\text{min}}}{e^{-\frac{T_{\text{pre}}}{\tau}}} \quad (4)$$

Using eqns. (2) and (4), one obtains the final form of the time-dependent FP anisotropy function for the detergent desolvation phase of proteomicelles:

$$r(t) = (r_{\text{in}} - r_{\text{min}}) e^{-\frac{t - T_{\text{pre}}}{\tau}} + r_{\text{min}} \quad (5)$$



In general, the experimental uncertainty was greater at detergent concentrations below the CMC than that measured at concentrations above the CMC. We think that this alteration in the experimental uncertainty was primarily determined by the coexistence of complex sub-states of soluble and insoluble protein aggregates.

**The reduction in light scattering effects.** One obvious difficulty of these steady-state FP-based determinations was the presence of light scattering signals produced by the detergent micelles and proteomicelles in solution and at detergent concentrations either below or above the CMC. Therefore, their scattering effects must be minimized. Both Raman and Rayleigh scattering factors feature light intensity contributions, which are proportional to the power of  $\lambda^{-4}$ , where  $\lambda$  is the wavelength.<sup>31-32</sup> Therefore, we tactically employed a large wavelength of the emission to preclude these light scattering effects. During the preliminary stage of this work, we gradually amplified the concentrations of Texas Red-labeled proteins until a value, beyond which the emission was independent of the protein concentration. This value was in the low-nanomolar range. Moreover, the SpectraMax I3 plate reader (Molecular Devices) is equipped with excitation and emission filters that form a spectral gap of 60 nm, ensuring that scattering effect contributions are minimized. Finally, the light scattering effects are always significantly reduced when the FP anisotropy signals are independent of both protein concentration and emission wavelength.<sup>32</sup>

## RESULTS AND DISCUSSION

In this work, we explored this time-dependent detergent desorption process for three  $\beta$ -barrel membrane proteins of varying charge and size, which were solubilized using a panel of four detergents of diverse hydrophobic tails and polar head groups. These studies were conducted using a wild-type outer membrane protein G (OmpG),<sup>33</sup> a medium-size, 14-stranded  $\beta$ -barrel, and two extensive-truncation derivatives of *ferric hydroxamate uptake* component A (FhuA),<sup>34</sup> a large 22-stranded  $\beta$ -barrel (**Fig. 1; Supporting Information, Table S1**). The FhuA derivatives FhuA  $\Delta C/\Delta 5L_{25N}$  and FhuA  $\Delta C/\Delta 7L_{30N}$  featured a complete deletion of an internal cork domain (C) as well as the truncation of five (L3, L4, L5, L10, and L11) and seven (L3, L4, L5, L7, L8, L10, and L11) extracellular loops, respectively. OmpG is an acidic protein at physiological conditions (pI 4.4). On the contrary, these truncation FhuA variants encompass 25 and 30 negative charge neutralizations, respectively, producing a charge reversal of the wild-type FhuA from acidic to basic values under physiological circumstances.<sup>28</sup> The basic FhuA variants feature pI values of 9.3 and 9.6, respectively. Here, we were interested to examine whether the FP anisotropy is a robust readout of the time-dependent desorption process of these three  $\beta$ -barrel membrane proteins solubilized in detergents of varying physicochemical properties (**Supporting Information, Table S2**). These detergents included 1-lauroyl-2-hydroxy-*sn*-glycero-3-phosphocholine (LysoFos), a zwitterionic molecule, as well as *n*-undecyl- $\beta$ -D-maltopyranoside (UM), *n*-decyl- $\beta$ -D-maltopyranoside (DM), and 4-cyclohexyl-1-butyl- $\beta$ -D-maltoside (CYMAL-4), three neutral molecules of varying hydrophobic tails. These maltoside-containing detergents have 11, 10, and 4 alkyl groups, respectively. Furthermore, CYMAL-4 differs from UM and DM through the addition of a benzene ring.

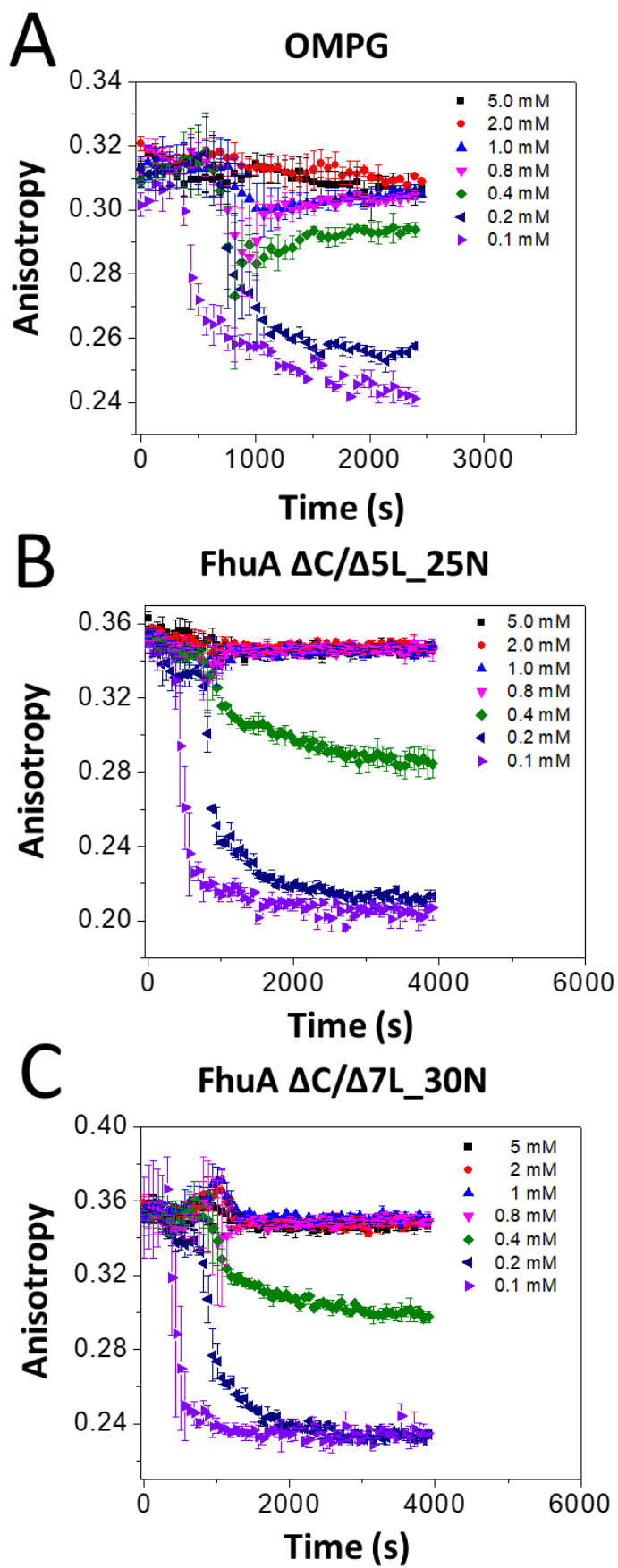


Figure 2

**Figure 2: Time-dependent alterations in the FP anisotropy when the membrane proteins were incubated at different concentrations of LysoFos, a zwitterionic detergent. (A) OmpG; (B) FhuA  $\Delta C/\Delta 5L_{25}N$ ; (C) FhuA  $\Delta C/\Delta 7L_{30}N$ .** The solubilized protein concentration was 28 nM. The buffer solution contained 200 mM NaCl, 50 mM HEPES, pH 7.4. The experimental FP data were presented as average  $\pm$  SD over a number of at least three distinct acquisitions.

## UM (0.59 mM)

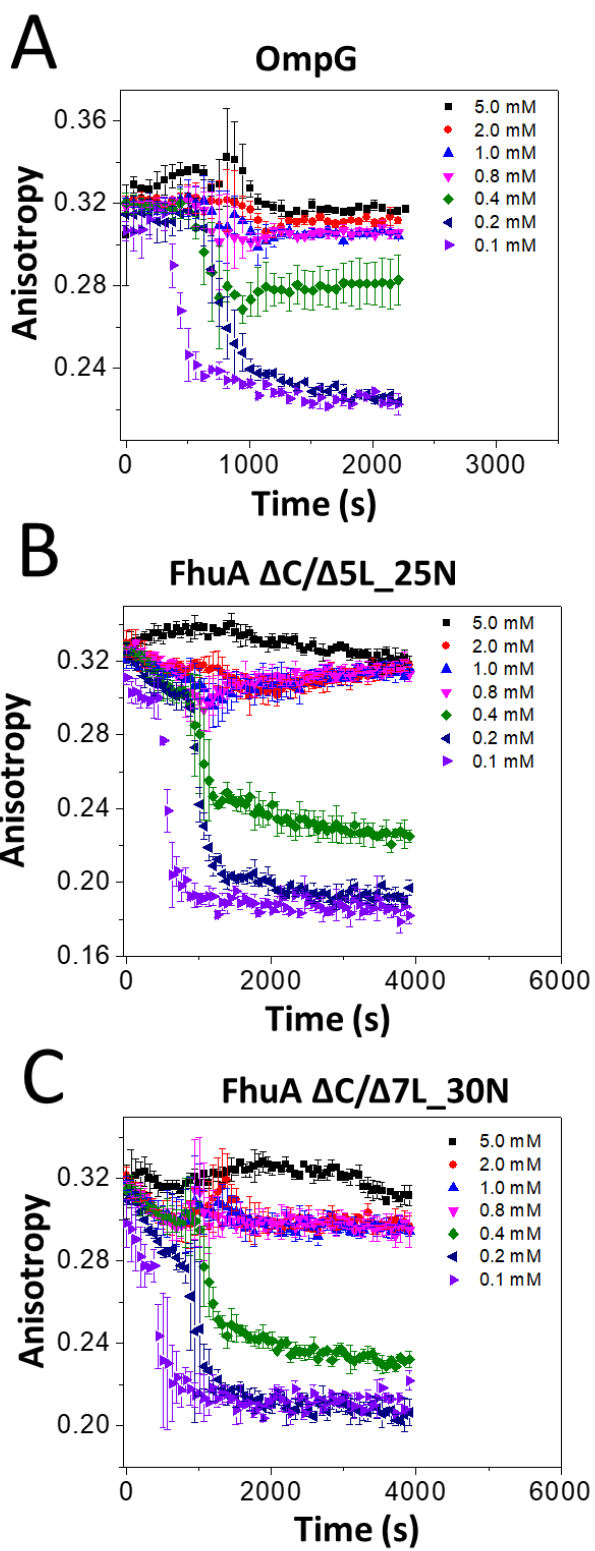


Figure 3

**Figure 3:** Time-dependent alterations in the FP anisotropy when the membrane proteins were incubated at different concentrations of UM, a neutral maltoside-containing detergent. (A) OmpG; (B) FhuA  $\Delta C/\Delta 5L_{25N}$ ; (C) FhuA  $\Delta C/\Delta 7L_{30N}$ . The other experimental conditions were the same as those in **Fig. 2**.

In **Fig. 2**, we illustrated the time-dependent change in the FP anisotropy when these  $\beta$ -barrel membrane proteins were incubated in LysoFos at concentrations either above or below the CMC value of this zwitterionic detergent (0.7 mM). As a common feature, at detergent concentrations much greater than the CMC, all proteins showed a fairly unchanged FP anisotropy for long periods, suggesting robust proteomicelles formed with LysoFos. In contrast, at detergent concentrations comparable with or less than the CMC, the FP anisotropy underwent a time-dependent significant modification. Moreover, the FP readout was also sensitive upon the dilution of detergent concentration within the well at values below the CMC. Another similar trait among all proteins was coexistence of a slow, low-FP amplitude change phase, which was followed by a fast, high-FP amplitude alteration phase. In this article, we will call these phases predesolvation and desolvation, respectively. Notably, the predesolvation phase, as the longer of the two phases, lasted for a few minutes (**Supporting Information, Table S3**). The desolvation phase followed an exponential decay (**Supporting Information, Figs. S1-S3, Table S4**). For the basic FhuA proteins, the observed desorption rate,  $k_{\text{obs}}^{\text{des}}$ , increased by decreasing the detergent concentration within the well. For example, at LysoFos concentrations of 0.4, 0.2, and 0.1 mM, the observed desorption rates,  $k_{\text{obs}}^{\text{des}}$ , for FhuA  $\Delta\text{C}/\Delta\text{5L}_{25\text{N}}$  were  $(140 \pm 9) \times 10^{-5} \text{ s}^{-1}$ ,  $(360 \pm 22) \times 10^{-5} \text{ s}^{-1}$ , and  $(510 \pm 27) \times 10^{-5} \text{ s}^{-1}$ , respectively. The corresponding  $k_{\text{obs}}^{\text{des}}$  rates for FhuA  $\Delta\text{C}/\Delta\text{7L}_{30\text{N}}$  were  $(182 \pm 9) \times 10^{-5} \text{ s}^{-1}$ ,  $(284 \pm 14) \times 10^{-5} \text{ s}^{-1}$ , and  $(719 \pm 20 \text{ s}^{-1}) \times 10^{-5} \text{ s}^{-1}$ , respectively.

In **Fig. 3**, we show the time-dependent alteration in the FP anisotropy when these  $\beta$ -barrel membrane proteins were incubated in UM. Again, at concentrations below the CMC for this detergent ( $\sim 0.59$  mM), we noted two distinct phases: a slow predesolvation phase, which was

followed by a fast desolvation phase. The duration of the predesolvation phase recorded with an UM concentration of 0.1 mM was shorter than those found by using higher detergent concentrations (**Supporting Information, Figs. S4-S6, Table S3**). In general, the desolvation of these membrane proteins from UM followed faster rates than those observed with LysoFos (**Supporting Information, Table S4**). This outcome indicates a specific, time-dependent FP-based signature of this detergent desorption process, despite closely similar CMC values and apparent dissociation constants of their proteomicelles,  $K_d$ . Moreover, this finding shows that in the case of UM, the adhesion forces between proteins and detergent monomers were weaker as compared to those in the case of LysoFos. For example, the CMC values of LysoFos and UM are  $\sim 0.7$  and  $\sim 0.6$  mM (**Supporting Information, Table S2**), respectively. On the other hand, their previously determined  $K_d$  are in the range 0.3-0.7 and 0.5-0.7 mM, respectively.<sup>22</sup>

When the proteins were incubated in DM at concentrations below the CMC ( $\sim 1.8$  mM), the predesolvation and desolvation were also dependent on the detergent concentration within the well (**Fig. 4; Supporting Information, Figs. S7-S9**). Specifically, at a lower detergent concentration, the predesolvation phase rates were shorter, whereas the observed desolvation rates were faster (**Supporting Information, Table S3, Table S4**). At DM concentrations of 0.45, 0.85, and 1 mM, the observed predesolvation rates,  $k_{\text{obs}}^{\text{pre}}$ , recorded for FhuA  $\Delta C/\Delta 5L_{25N}$  were  $(54.4 \pm 0.1) \times 10^{-6} \text{ s}^{-1}$ ,  $(29.7 \pm 0.1) \times 10^{-6} \text{ s}^{-1}$ , and  $(19.8 \pm 0.1) \times 10^{-6} \text{ s}^{-1}$ , respectively. On the other hand, the corresponding  $k_{\text{obs}}^{\text{des}}$  values for FhuA  $\Delta C/\Delta 5L_{25N}$  were  $(629 \pm 59) \times 10^{-5} \text{ s}^{-1}$ ,  $(353 \pm 36) \times 10^{-5} \text{ s}^{-1}$ , and  $(191 \pm 19) \times 10^{-5} \text{ s}^{-1}$ , respectively. At the same time, the  $k_{\text{obs}}^{\text{des}}$  values noted with FhuA  $\Delta C/\Delta 7L_{30N}$  were  $(599 \pm 50) \times 10^{-5} \text{ s}^{-1}$ ,  $(478 \pm 37) \times 10^{-5} \text{ s}^{-1}$ , and  $(369 \pm 44) \times 10^{-5} \text{ s}^{-1}$ , respectively. These rates indicate that at a lower detergent concentration there is a shift of



the association-dissociation equilibrium of the proteomicelles with the coexistent micelles towards dissociation.

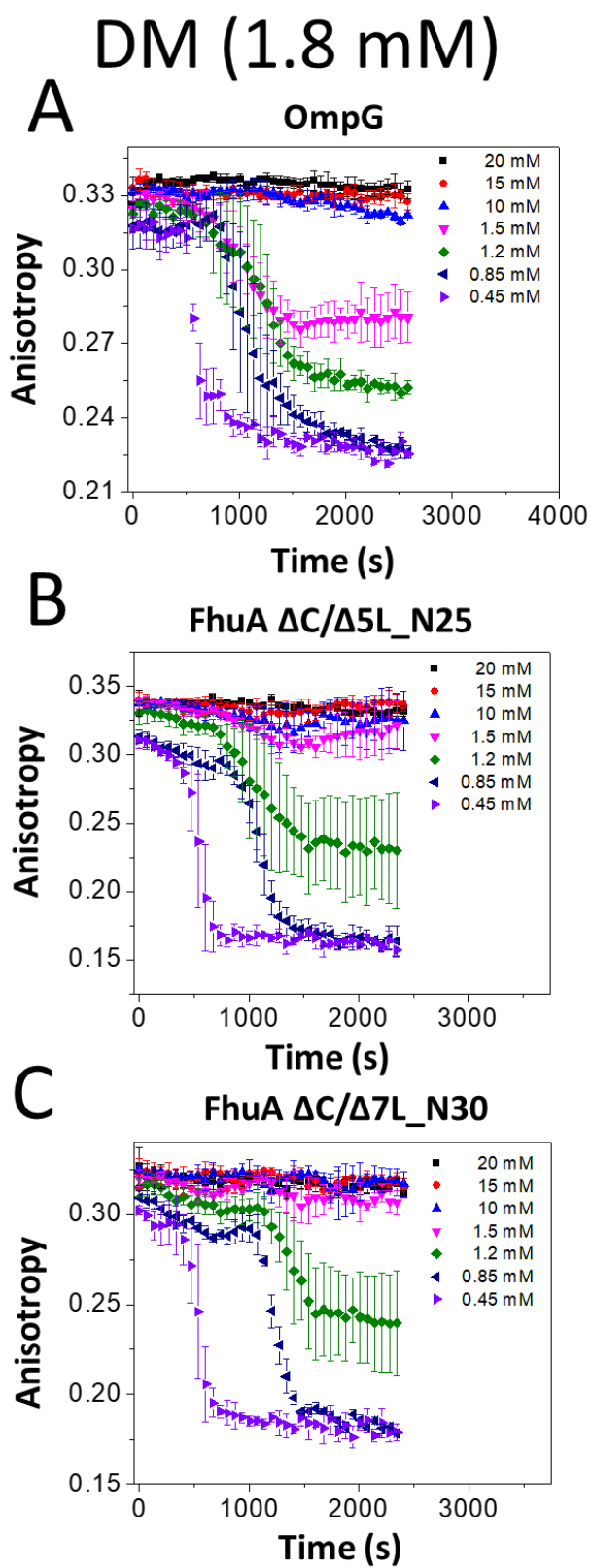


Figure 4

**Figure 4:** Time-dependent alterations in the FP anisotropy when the membrane proteins were incubated at different concentrations of DM, a neutral maltoside-containing detergent. (A) OmpG; (B) FhuA  $\Delta C/\Delta 5L_{25N}$ ; (C) FhuA  $\Delta C/\Delta 7L_{30N}$ . The other experimental conditions were the same as those in **Fig. 2**.

## CYMAL-4 (7.6 mM)

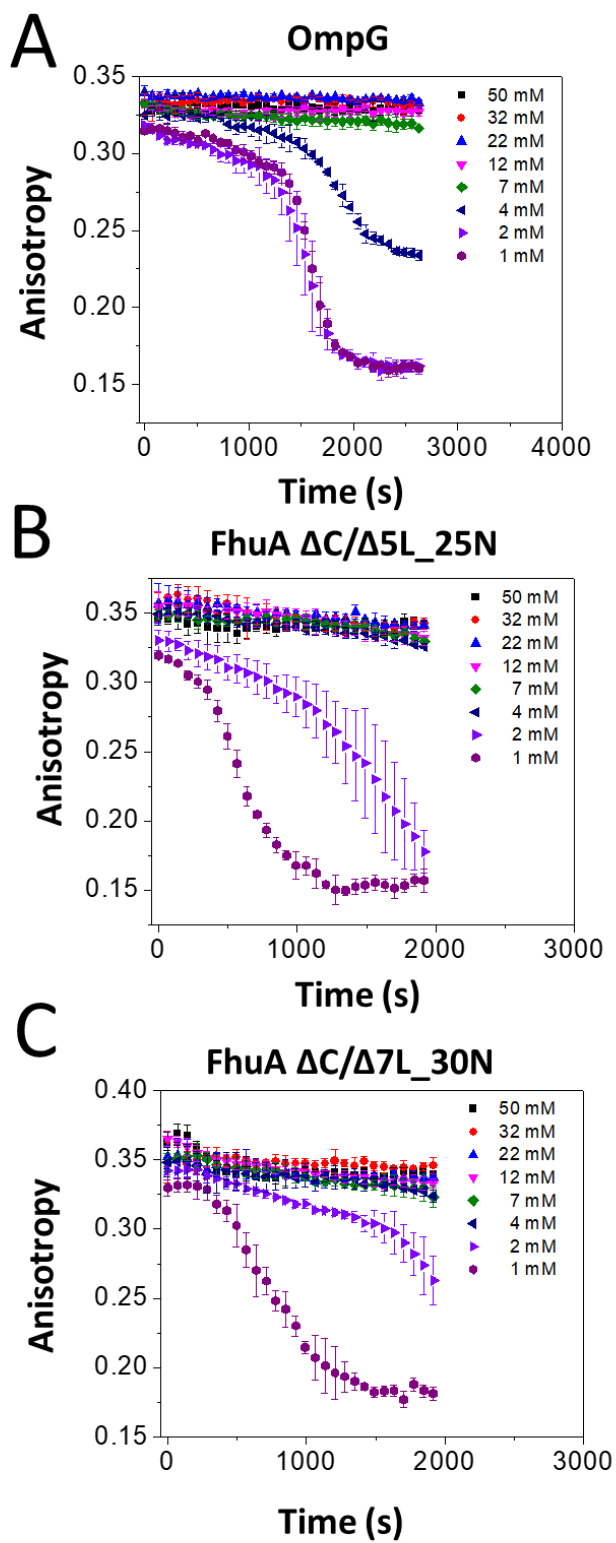
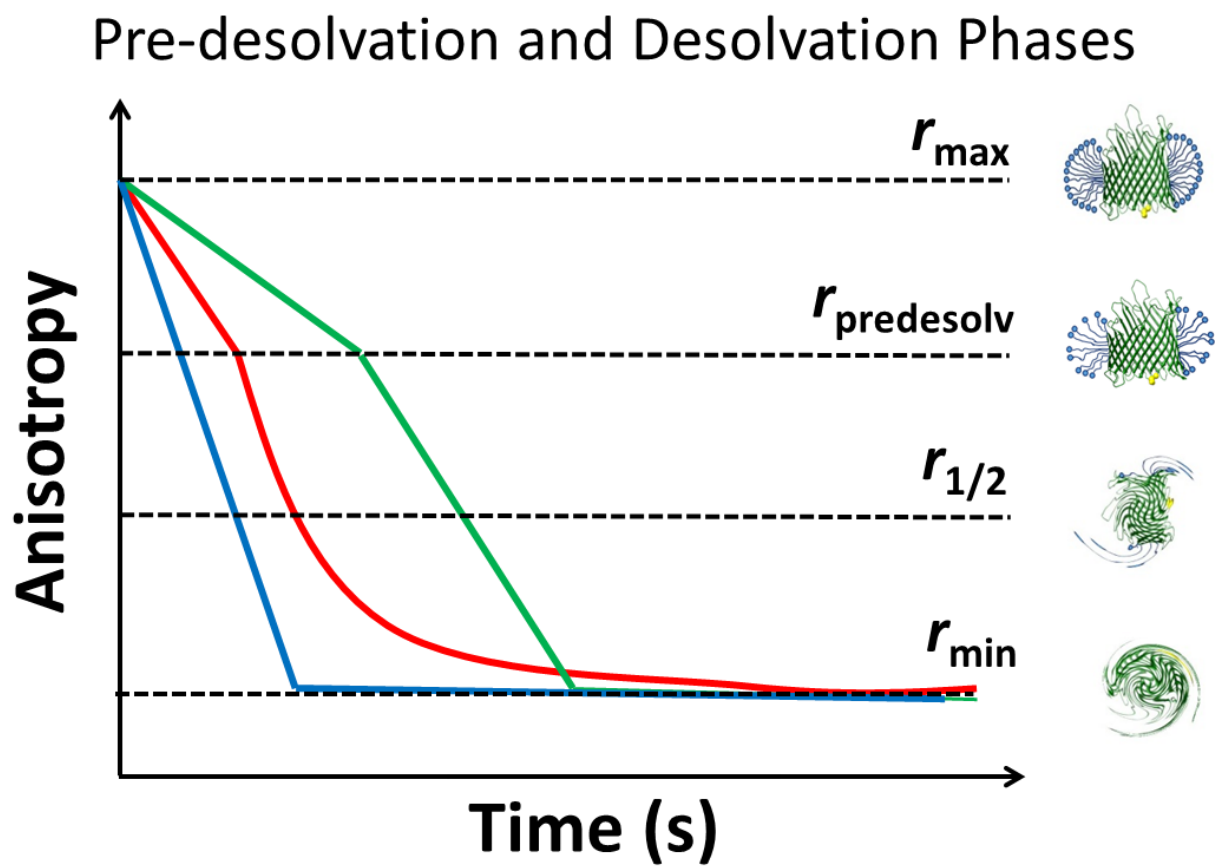


Figure 5

**Figure 5:** Time-dependent alterations in the FP anisotropy when the membrane proteins were incubated at different concentrations of CYMAL-4, a neutral maltoside-containing detergent.

(A) OmpG; (B) FhuA  $\Delta C/\Delta 5L_{25N}$ ; (C) FhuA  $\Delta C/\Delta 7L_{30N}$ . The other experimental conditions were the same as those in **Fig. 2**.

Finally, we show the time-dependent change in the FP anisotropy recorded when the proteins were incubated in CYMAL-4 (**Fig. 5; Supporting Information, Figs. S10-S12**). Remarkably, very long predesolvation durations were recorded at detergent concentrations below the  $\text{CMC}^{\text{CYMAL-4}}$  ( $\sim 7.6$  mM). For example, the predesolvation times recorded with all proteins at 2 mM CYMAL-4 were greater than 20 min, suggesting strong adhesive interactions between detergent monomers and these proteins. Moreover, no FP anisotropy changes were noted when the truncation FhuA proteins were incubated at 4 mM CYMAL-4, a concentration significantly smaller than the corresponding CMC. These results illuminate that the adhesive PDC interactions between proteins and CYMAL-4 are greater than the cohesive interactions among the detergent monomers. These time-dependent FP anisotropy reads are in good accord with the recently determined apparent equilibrium constants,  $K_d$ , for CYMAL-4 with  $\beta$ -barrel membrane proteins.<sup>22</sup> Specifically, these  $K_d$  values for the PDC formed by CYMAL-4 with OmpG, FhuA  $\Delta C/\Delta 5L_{25N}$ , and FhuA  $\Delta C/\Delta 7L_{30N}$  are 4.6, 5.7, and 4.5 mM, respectively.

**Figure 6**

**Figure 6: Cartoon showing different FP anisotropy-based trajectories of the proteodemicellization.** The predesolvation phase underwent a linear change in the FP anisotropy, whereas the desolvation phase followed either a linear regime, which was marked in green, or an exponential decay, which was marked in red. In the case of weak PDC interactions and low incubating detergent concentration, there is no a predesolvation phase, whereas the desolvation phase, which is marked in blue, is rapid.



It is now clear that satisfactory detergent-mediated solvation forces of  $\beta$ -barrel membrane proteins contribute to the existence of a predesolvation phase. We found that the characteristics of the predesolvation phase strongly depends not only on these adhesive PDC interactions, but also the available detergent concentration within the well. It is conceivable that a very weak interfacial PDC interaction of a certain detergent-membrane protein pair might impede the presence of a predesolvation phase, whereas the desolvation should normally occur within a matter of seconds. Therefore, we illustrated a cartoon in **Fig. 6**, which presents three distinct FP anisotropy-based trajectories of the time-dependent desolvation of a membrane protein. A predesolvation phase occurs when these adhesive PDC interactions between the detergent molecules and membrane proteins overcome the cohesive forces among the detergent monomers. Because of the low FP anisotropy alteration during this predesolvation phase, we think that the average proteomicelle still maintains most of the solubilizing detergent monomers under these conditions. It is more than likely that the predesolvation phase represents a relatively small loss of detergent monomers of the proteomicelle, inducing a reconfiguration of the internal packing forces of the proteomicelle. This proteomicelle rearrangement leads to fast desolvation phase.

The desolvation rate is always greater than the predesolvation rate and occurs in an exponential fashion. Assuming a simple bimolecular model of association of the  $\beta$ -barrel membrane protein to a detergent micelle and a high detergent concentration at values below the CMC, the observed desolvation rate,  $k_{\text{obs}}^{\text{des}}$ , is  $-k_{\text{on}}[\text{D}] + k_{\text{off}}$ .<sup>35</sup> Here, the detergent concentration,  $[\text{D}]$ , is in the micromolar to millimolar range, which is much greater than the protein concentration,  $[\text{P}]$ , in the nanomolar concentration. That means a linear dependence of  $k_{\text{obs}}^{\text{des}}$  on detergent concentration,  $[\text{D}]$ , with a slope of  $-k_{\text{on}}$  and an intercept with the vertical axis of  $k_{\text{off}}$ .

Among all cases examined in this work, we only found this behavior in the case of the desolvation process of the truncation FhuA derivatives from LysoFos (**Supporting Information, Fig. S13, Table S5**). For example,  $k_{\text{on}}$  and  $k_{\text{off}}$  of the PDC made with FhuA  $\Delta C/\Delta 5L_{-25N}$  were  $12.1 \pm 1 \text{ M}^{-1}\text{s}^{-1}$  and  $(6.2 \pm 0.3) \times 10^{-3} \text{ s}^{-1}$ , respectively, giving an apparent  $K_{\text{d}}$  of 0.51 mM. This value is in excellent agreement with the apparent  $K_{\text{d}}$  of 0.71 mM for the same PDC, which was determined from isothermal Hill-Langmuir desorption curves.<sup>22</sup> A certain numerical difference between the two equilibrium constants might also arise from the fact that the predesolvation phase was neglected in the determination of  $K_{\text{d}}$  via kinetic FP anisotropy-based measurements. The above kinetic rate constants illustrate a very slow association process and a relatively long  $\tau_{\text{off}}$  binding time. Taken together, the weak binding interactions leading to millimolar values of the apparent dissociation constant,  $K_{\text{d}}$ , are primarily determined by the very slow association process ( $k_{\text{on}}$ ) (**Supporting Information, Fig. S13, Table S5**). However, we determined other scaling functions of  $k_{\text{obs}}^{\text{des}}$  with the final detergent concentration in the well, [D], suggesting diverse kinetic models of varying order of the desolvation reaction (**Supporting Information, Figs. S14-S16, Table S6**). This finding shows that the desolvation kinetic scheme strongly depends on the architectural and biophysical fingerprints of the membrane proteins as well as the physicochemical characteristics of the solubilizing detergents.

## CONCLUSIONS

In summary, this study sheds light on the time-dependent detergent desorption of membrane proteins at detergent concentrations below the CMC. We were able to observe this process by employing a steady-state FP spectroscopy approach that featured a bright and photostable fluorophore, maintaining the optical signal-to-noise ratio within a satisfactory range. Notably, the approach that we present in this paper requires extremely small quantities of membrane proteins (e.g., tens of nanograms per trial). Moreover, these time-dependent FP anisotropy reads were conducted using a microplate format, potentially allowing for parallel assessment of hundreds-thousands of conditions in minutes-hours. We showed that the detergent desolvation of membrane proteins using both zwitterionic and uncharged detergents is preceded by a slow predesolvation phase that can be longer than 20 minutes. This predesolvation phase might either be slowed at detergent concentrations approaching the CMC value or accelerated at very low detergent concentrations within the well. Future developments of this steady-state FP spectroscopy-based approach might lead to the creation of a detailed kinetic analysis of the interfacial PDC interactions, involving challenging membrane protein systems and detergents of varying physicochemical properties. Finally, these semi-quantitative studies might stimulate novel discoveries in membrane protein solubilization, stabilization, and crystallization.<sup>17, 36-37</sup>

**ACKNOWLEDGEMENTS.** We thank Yi-Ching Hsueh, Adam Blanden, and Bach Pham for their assistance during the very early stages of these studies. This research project was supported by the US National Institutes of Health grants R01 GM115442 (M.C.) and R01 GM088403 (L.M.).

**Supporting Information.** (i) Properties of the membrane proteins used in this work; (ii) Properties of the detergents used in this work; (iii) Detailed graphical presentation of the fits of the predesolvation and desolvation phases; (iv) Results of the fits of the predesolvation phase; (v) Results of the fits of the desolvation phase; (vi) Dependence of the observed desolvation rates on the detergent concentration. These materials are available free of charge via the Internet at <http://pubs.acs.org>

## REFERENCES

1. Pocanschi, C. L.; Popot, J. L.; Kleinschmidt, J. H. Folding and stability of outer membrane protein A (OmpA) from *Escherichia coli* in an amphipathic polymer, amphipol A8-35. *Eur. Biophys. J.* **2013**, *42* (2-3), 103-118.
2. Sadaf, A.; Cho, K. H.; Byrne, B.; Chae, P. S. Amphipathic agents for membrane protein study. *Methods Enzymol.* **2015**, *557*, 57-94.
3. Pollock, N. L.; Satriano, L.; Zegarra-Moran, O.; Ford, R. C.; Moran, O. Structure of wild type and mutant F508del CFTR: A small-angle X-ray scattering study of the protein-detergent complexes. *J. Struct. Biol.* **2016**, *194* (1), 102-111.
4. Li, J.; Qiu, X. J. Quantification of membrane protein self-association with a high-throughput compatible fluorescence assay. *Biochemistry* **2017**, *56* (14), 1951-1954.
5. Ehsan, M.; Du, Y.; Scull, N. J.; Tikhonova, E.; Tarrasch, J.; Mortensen, J. S.; Loland, C. J.; Skiniotis, G.; Guan, L.; Byrne, B.; Kobilka, B. K.; Chae, P. S. Highly branched pentasaccharide-bearing amphiphiles for membrane protein studies. *J. Am. Chem. Soc.* **2016**, *138* (11), 3789-96.
6. Frey, L.; Lakomek, N. A.; Riek, R.; Bibow, S. Micelles, bicelles, and nanodiscs: comparing the impact of membrane mimetics on membrane protein backbone dynamics. *Angew. Chem. Int. Ed. Engl.* **2017**, *56* (1), 380-383.
7. Linke, D. Detergents: an overview. *Methods Enzymol.* **2009**, *463*, 603-617.
8. Khao, J.; Arce-Lopera, J.; Sturgis, J. N.; Duneau, J. P. Structure of a protein-detergent complex: the balance between detergent cohesion and binding. *Eur. Biophys. J.* **2011**, *40* (10), 1143-55.
9. Raschle, T.; Rios Flores, P.; Opitz, C.; Muller, D. J.; Hiller, S. Monitoring backbone hydrogen-bond formation in beta-barrel membrane protein folding. *Angew. Chem. Int. Ed. Engl.* **2016**, *55* (20), 5952-5.
10. Stangl, M.; Veerappan, A.; Kroeger, A.; Vogel, P.; Schneider, D. Detergent properties influence the stability of the glycophorin A transmembrane helix dimer in lysophosphatidylcholine micelles. *Biophys. J.* **2012**, *103* (12), 2455-64.
11. Yang, Z.; Wang, C.; Zhou, Q.; An, J.; Hildebrandt, E.; Aleksandrov, L. A.; Kappes, J. C.; DeLucas, L. J.; Riordan, J. R.; Urbatsch, I. L.; Hunt, J. F.; Brouillette, C. G. Membrane protein stability can be compromised by detergent interactions with the extramembranous soluble domains. *Protein Sci.* **2014**, *23* (6), 769-89.
12. Yang, Z.; Brouillette, C. G. A guide to differential scanning calorimetry of membrane and soluble proteins in detergents. *Methods Enzymol.* **2016**, *567*, 319-58.
13. Roy, A. Membrane preparation and solubilization. *Methods Enzymol.* **2015**, *557*, 45-56.

14. Le Roy, A.; Wang, K.; Schaack, B.; Schuck, P.; Breyton, C.; Ebel, C. AUC and small-angle scattering for membrane proteins. *Methods in enzymology* **2015**, *562*, 257-86.
15. Baker, L. A.; Folkers, G. E.; Sinnige, T.; Houben, K.; Kaplan, M.; van der Crujisen, E. A.; Baldus, M. Magic-angle-spinning solid-state NMR of membrane proteins. *Methods Enzymol.* **2015**, *557*, 307-28.
16. Jahnke, N.; Krylova, O. O.; Hoomann, T.; Vargas, C.; Fiedler, S.; Pohl, P.; Keller, S. Real-time monitoring of membrane-protein reconstitution by isothermal titration calorimetry. *Analytical chemistry* **2014**, *86* (1), 920-927.
17. Neale, C.; Ghanei, H.; Holyoake, J.; Bishop, R. E.; Prive, G. G.; Pomes, R. Detergent-mediated protein aggregation. *Chem. Phys. Lipids* **2013**, *169*, 72-84.
18. Miles, A. J.; Wallace, B. A. Circular dichroism spectroscopy of membrane proteins. *Chem. Soc. Rev.* **2016**, *45* (18), 4859-72.
19. Textor, M.; Keller, S. Automated analysis of calorimetric demicellization titrations. *Anal. Biochem.* **2015**, *485*, 119-21.
20. Wolfe, A. J.; Hsueh, Y. C.; Blanden, A. R.; Mohammad, M. M.; Pham, B.; Thakur, A. K.; Loh, S. N.; Chen, M.; Movileanu, L. Interrogating detergent desolvation of nanopore-forming proteins by fluorescence polarization spectroscopy. *Analytical chemistry* **2017**, *89* (15), 8013-8020.
21. Titus, J. A.; Haugland, R.; Sharrow, S. O.; Segal, D. M. Texas Red, a hydrophilic, red-emitting fluorophore for use with fluorescein in dual parameter flow microfluorometric and fluorescence microscopic studies. *J. Immunol. Methods* **1982**, *50* (2), 193-204.
22. Wolfe, A. J.; Si, W.; Zhang, Z.; Blanden, A. R.; Hsueh, Y. C.; Gugel, J. F.; Pham, B.; Chen, M.; Loh, S. N.; Rozovsky, S.; Aksimentiev, A.; Movileanu, L. Quantification of membrane protein-detergent complex interactions. *J. Phys. Chem. B* **2017**, *121* (44), 10228-10241.
23. Rossi, A. M.; Taylor, C. W. Analysis of protein-ligand interactions by fluorescence polarization. *Nat. Protoc.* **2011**, *6* (3), 365-87.
24. Fahie, M.; Chisholm, C.; Chen, M. Resolved single-molecule detection of individual species within a mixture of anti-biotin antibodies using an engineered monomeric nanopore. *ACS nano* **2015**, *9* (2), 1089-1098.
25. Niedzwiecki, D. J.; Mohammad, M. M.; Movileanu, L. Inspection of the engineered FhuA deltaC/delta4L protein nanopore by polymer exclusion. *Biophys. J.* **2012**, *103* (10), 2115-2124.
26. Thakur, A. K.; Larimi, M. G.; Gooden, K.; Movileanu, L. Aberrantly large single-channel conductance of polyhistidine arm-containing protein nanopores. *Biochemistry* **2017**, *56* (36), 4895-4905.

27. Mohammad, M. M.; Howard, K. R.; Movileanu, L. Redesign of a plugged beta-barrel membrane protein. *J. Biol. Chem.* **2011**, *286* (10), 8000-8013.
28. Wolfe, A. J.; Mohammad, M. M.; Thakur, A. K.; Movileanu, L. Global redesign of a native beta-barrel scaffold. *Biochim. Biophys. Acta* **2016**, *1858* (1), 19-29.
29. Mohammad, M. M.; Iyer, R.; Howard, K. R.; McPike, M. P.; Borer, P. N.; Movileanu, L. Engineering a rigid protein tunnel for biomolecular detection. *J. Am. Chem. Soc.* **2012**, *134* (22), 9521-9531.
30. Gradinaru, C. C.; Marushchak, D. O.; Samim, M.; Krull, U. J. Fluorescence anisotropy: from single molecules to live cells. *Analyst* **2010**, *135* (3), 452-9.
31. Splinter, R. H., B.A. *An introduction to biomedical optics*. Taylor & Francis, New York.: 2007; p 602.
32. Lea, W. A.; Simeonov, A. Fluorescence polarization assays in small molecule screening. *Expert opinion on drug discovery* **2011**, *6* (1), 17-32.
33. Yildiz, O.; Vinothkumar, K. R.; Goswami, P.; Kuhlbrandt, W. Structure of the monomeric outer-membrane porin OmpG in the open and closed conformation. *EMBO J.* **2006**, *25* (15), 3702-3713.
34. Ferguson, A. D.; Hofmann, E.; Coulton, J. W.; Diederichs, K.; Welte, W. Siderophore-mediated iron transport: crystal structure of FhuA with bound lipopolysaccharide. *Science* **1998**, *282* (5397), 2215-2220.
35. Kwok, K. C.; Cheung, N. H. Measuring binding kinetics of ligands with tethered receptors by fluorescence polarization and total internal reflection fluorescence. *Anal. Chem.* **2010**, *82* (9), 3819-3825.
36. Prive, G. G. Detergents for the stabilization and crystallization of membrane proteins. *Methods* **2007**, *41* (4), 388-397.
37. Prive, G. G. Lipopeptide detergents for membrane protein studies. *Curr. Opin. Struct. Biol.* **2009**, *19* (4), 379-85.
38. Mohammad, M. M.; Movileanu, L. Impact of distant charge reversals within a robust beta-barrel protein pore. *J. Phys. Chem. B* **2010**, *114* (26), 8750-8759.
39. Bikwemu, R.; Wolfe, A. J.; Xing, X.; Movileanu, L. Facilitated translocation of polypeptides through a single nanopore. *J. Phys.: Condens. Matter* **2010**, *22* (45), 454117.
40. le Maire, M.; Champeil, P.; Moller, J. V. Interaction of membrane proteins and lipids with solubilizing detergents. *Biochim. Biophys. Acta* **2000**, *1508* (1-2), 86-111.

41. Guex, N.; Peitsch, M. C.; Schwede, T. Automated comparative protein structure modeling with SWISS-MODEL and Swiss-PdbViewer: a historical perspective. *Electrophoresis* **2009**, *30 Suppl 1*, S162-S173.



# Chapter 5.1 Supplement for Detergent Desorption of Membrane Proteins Exhibits Two Kinetic Phases

Aaron J. Wolfe,<sup>1,2</sup> Jack F. Gugel,<sup>1</sup> Min Chen,<sup>3</sup> and Liviu Movileanu\*<sup>1,2,4</sup>

<sup>1</sup>*Department of Physics, Syracuse University, 201 Physics Building, Syracuse, New York 13244-1130, USA*

<sup>2</sup>*Structural Biology, Biochemistry, and Biophysics Program, Syracuse University, 111 College Place, Syracuse, New York 13244-4100, USA*

<sup>3</sup>*Department of Chemistry, University of Massachusetts, 820 LGRT, 710 North Pleasant Street, Amherst, Massachusetts 01003-9336, USA*

<sup>4</sup>*Department of Biomedical and Chemical Engineering, Syracuse University, Syracuse University, 223 Link Hall, Syracuse, New York 13244, USA*

Reprinted with permission from **Detergent Desorption of Membrane Proteins Exhibits Two Kinetic Phases** Aaron J. Wolfe, Jack F. Gugel, Min Chen, and Liviu Movileanu  
*The Journal of Physical Chemistry Letters* **2018** 9 (8), 1913-1919 DOI:  
10.1021/acs.jpcl.8b00549 Copyright 2018 American Chemical Society.

Author contributions:

AJW: Designed experiments, performed experiments, analyzed data, interpreted data.

JFG: Analyzed data

MC: Performed experiments

LM: Analyzed data, interpreted data, wrote manuscript

## **Contents of Supplementary Information**

1. Properties of the membrane proteins used in this work
2. Properties of the detergents used in this work
3. Detailed graphical presentation of the fits of the predesolvation and desolvation phases
4. Results of the fits of the predesolvation phase
5. Results of the fits of the desolvation phase
6. Dependence of the observed desolvation rates on the detergent concentration

**1. Properties of the membrane proteins used in this work**

**Table S1: Characteristics of the  $\beta$ -barrel proteins examined in this study.<sup>a</sup>**

$\beta$ -barrel <sup>b</sup>	Charge state	pI	GRAVY <sup>c</sup>	Positive residues	Negative residues	Total number of residues <sup>d</sup>
WT-OmpG	acidic	4.4	-0.8	22	55	281
FhuA $\Delta$ C/ $\Delta$ 5L_25N	basic	9.3	-0.6	43	34	473
FhuA $\Delta$ C/ $\Delta$ 7L_30N	basic	9.6	-0.6	42	27	426

<sup>a</sup>This table was adapted from Wolfe et al. (2017).<sup>1</sup>

<sup>b</sup>All proteins contain a 6 $\times$ His<sup>+</sup> tag at the C terminus.

<sup>c</sup>This hydrophobicity parameter was determined by summing the hydropathy indexes<sup>2</sup> of residues, then dividing it by the total residue number.<sup>3</sup>

<sup>d</sup>This number also includes the residues of the Gly/Ser-rich containing loop and 6 $\times$ His<sup>+</sup> tag.

## 2. Properties of the detergents used in this work

**Table S2: Physicochemical features of the detergents used in this article.<sup>a</sup>**

Detergent	Head group	CM C (mM) <sup>b</sup>	FW (Da) <sup>c</sup>	Aggregation number, $N_{agg}$ <sup>d</sup>	Micellar Weight, $MW_m$ (kDa)	References
1-lauroyl-2-hydroxy- <i>sn</i> -glycero-3-phosphocholine (LysoFos) <sup>e,f</sup>	Zwitterionic	~0.7 <sup>d</sup>	440	80 <sup>e</sup>	35	4-5
n-undecyl- $\beta$ -D-maltoside (UM)	Non-ionic	~0.59	497	~71	35	6
n-decyl- $\beta$ -D-maltoside (DM)	Non-ionic	~1.8	483	~69	33	6
4-cyclohexyl-1-Butyl- $\beta$ -D-maltoside (CYMAL-4)	Non-ionic	~7.6	481	~25	12	7

<sup>a</sup> This table was adapted from Wolfe et al. (2017).<sup>1</sup>

<sup>b</sup> CMC values in water were reported by Anatrace (<https://www.anatrace.com/>).

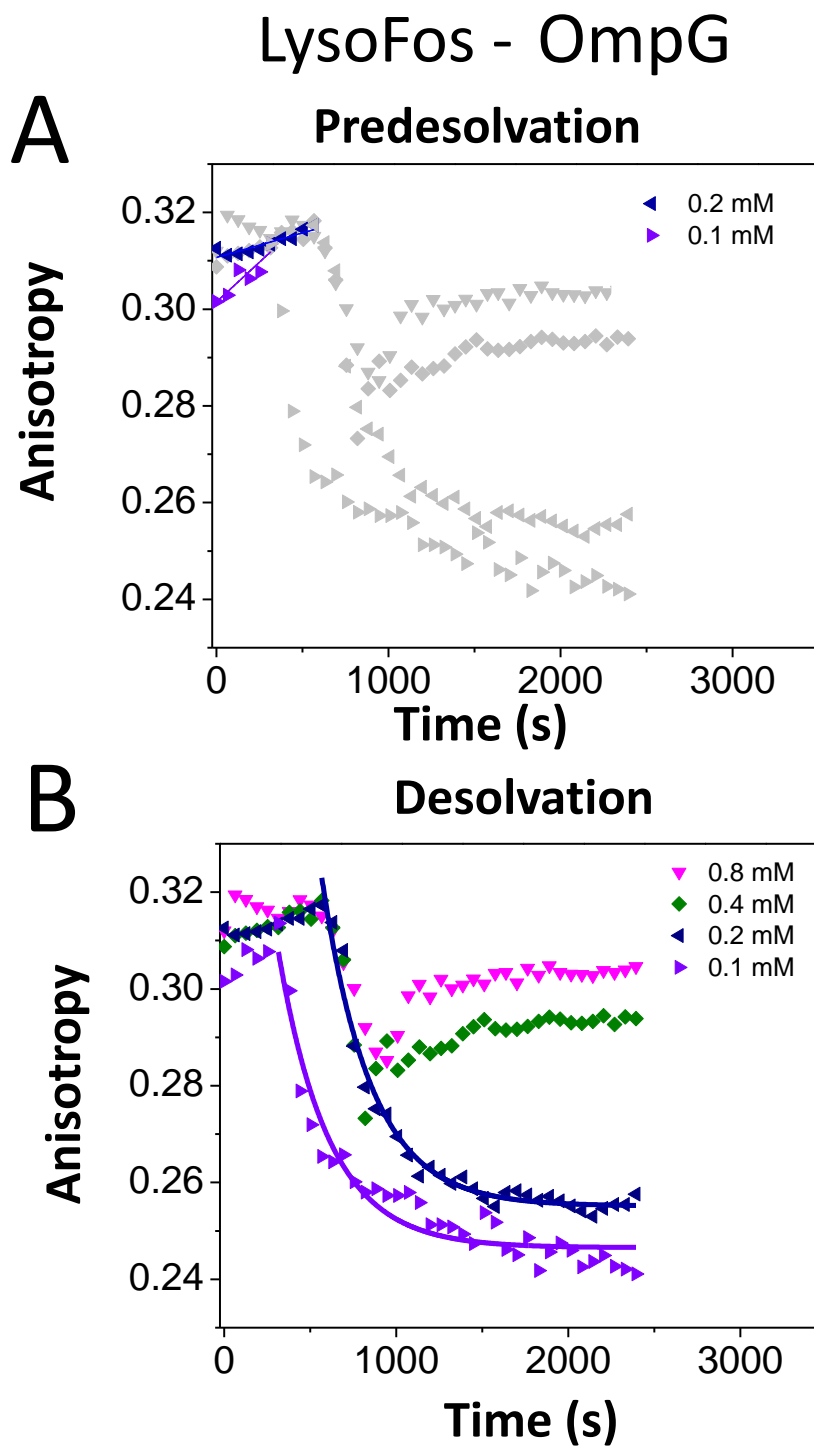
<sup>c</sup> Formula weights of the detergent monomers (FW) were reported by Anatrace (<https://www.anatrace.com/>).

<sup>d</sup> Aggregation numbers,  $N_{agg}$ , in water were reported by Anatrace (<https://www.anatrace.com/>).

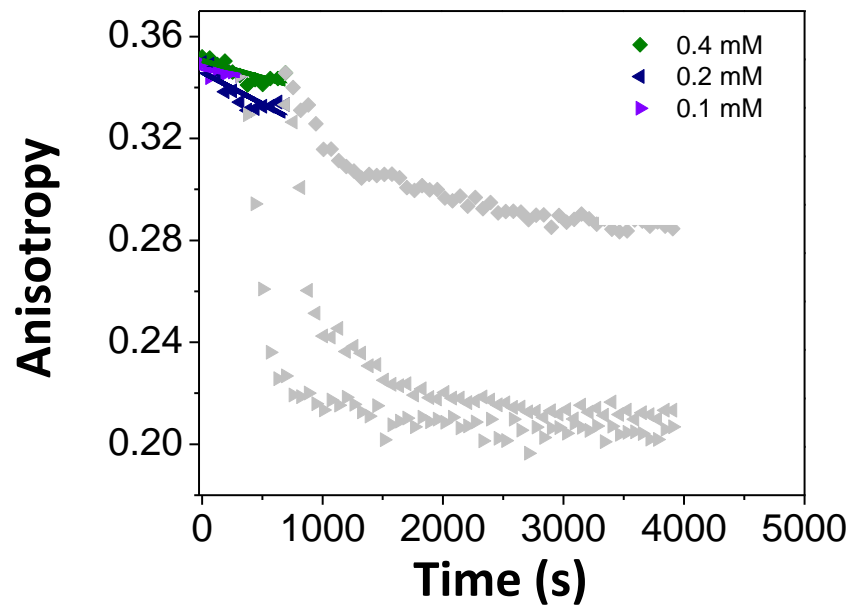
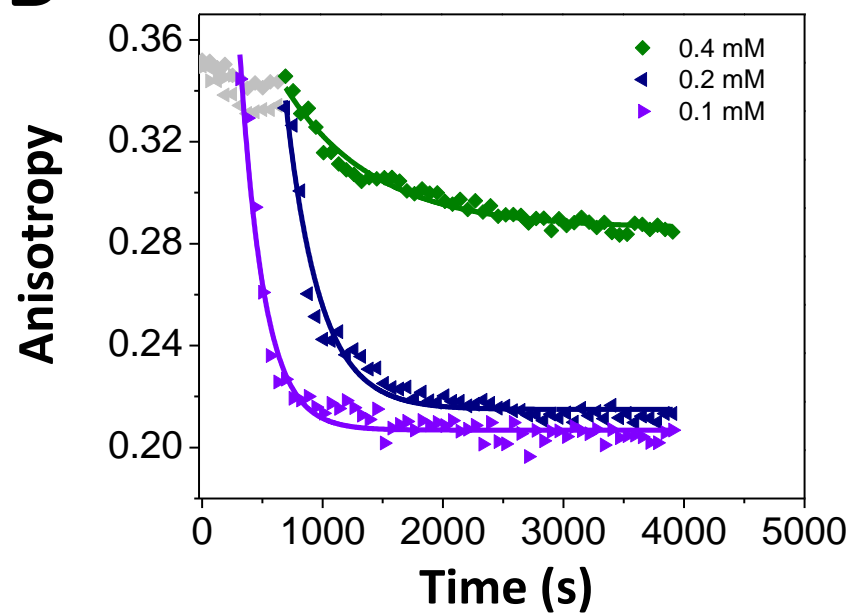
<sup>e</sup> CMC value of LysoFos in 140 mM NaCl, 20 mM Tris-HCl, pH 7.2 is 0.7 mM.<sup>4</sup>

<sup>f</sup> The  $N_{agg}$  for LysoFos used in this work is ~80.<sup>5</sup>

3. Detailed graphical presentation of the fits of the predesolvation and desolvation phases.

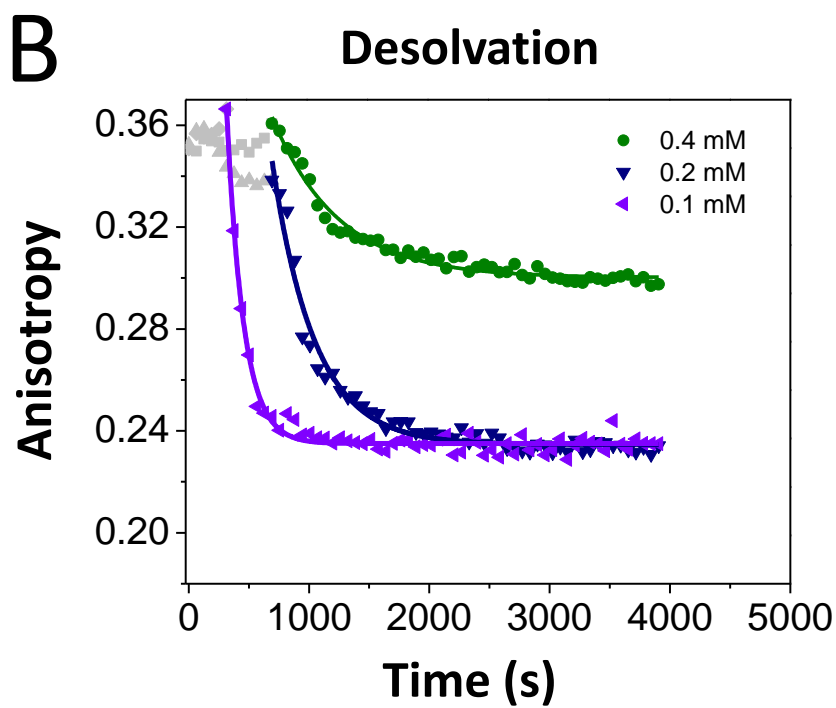
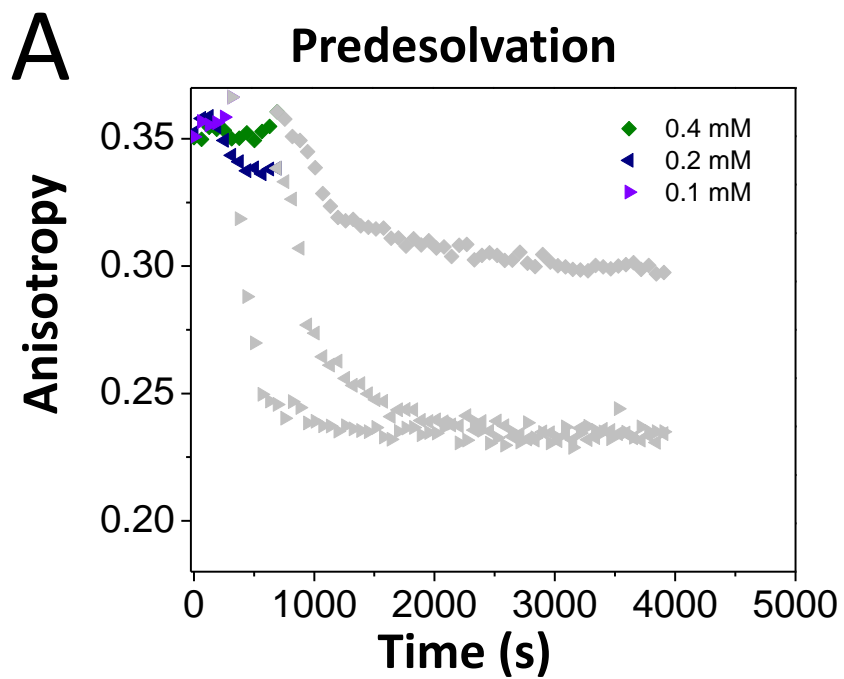


**Figure S1: Illustration of the time-dependent predesolvation and desolvation of OmpG solubilized with 20 mM LysoFos.** These phases were recorded using detergent concentrations below the  $\text{CMC}^{\text{LysoFos}} = 0.7 \text{ mM}$ . The solubilized protein concentration was 28 nM, whereas the buffer solution contained 200 mM NaCl, 50 mM HEPES, pH 7.4

LysoFos - FhuA  $\Delta C/\Delta 5L_{25N}$ **A****Predesolvation****B****Desolvation**

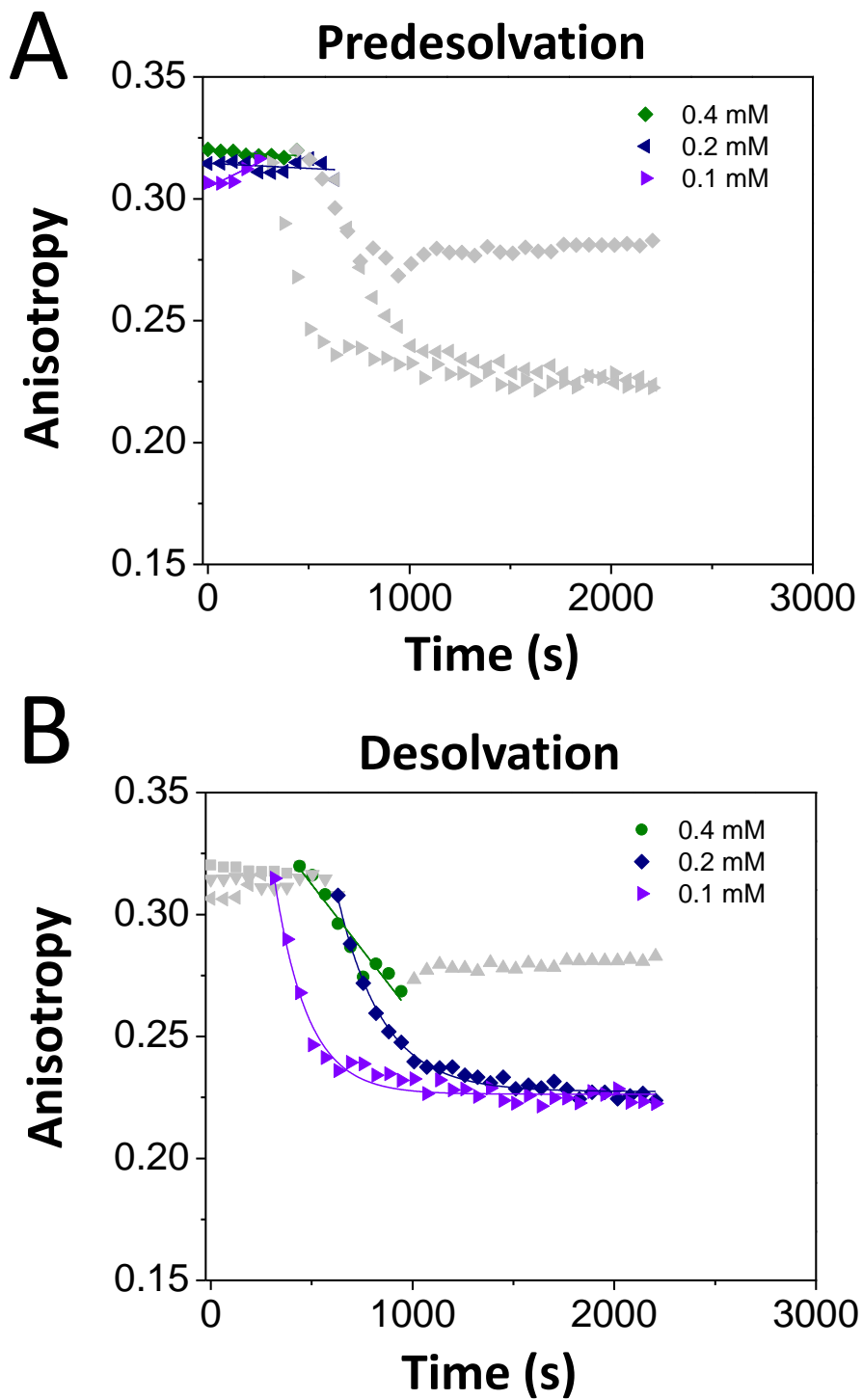
**Figure S2: Illustration of the time-dependent predesolvation and desolvation of FhuA  $\Delta C/\Delta 5L_{25N}$  solubilized with 20 mM LysoFos.** These phases were recorded using detergent concentrations below the  $CMC^{LysoFos} = 0.7$  mM. The other experimental conditions were the same as in **Fig. S1**.



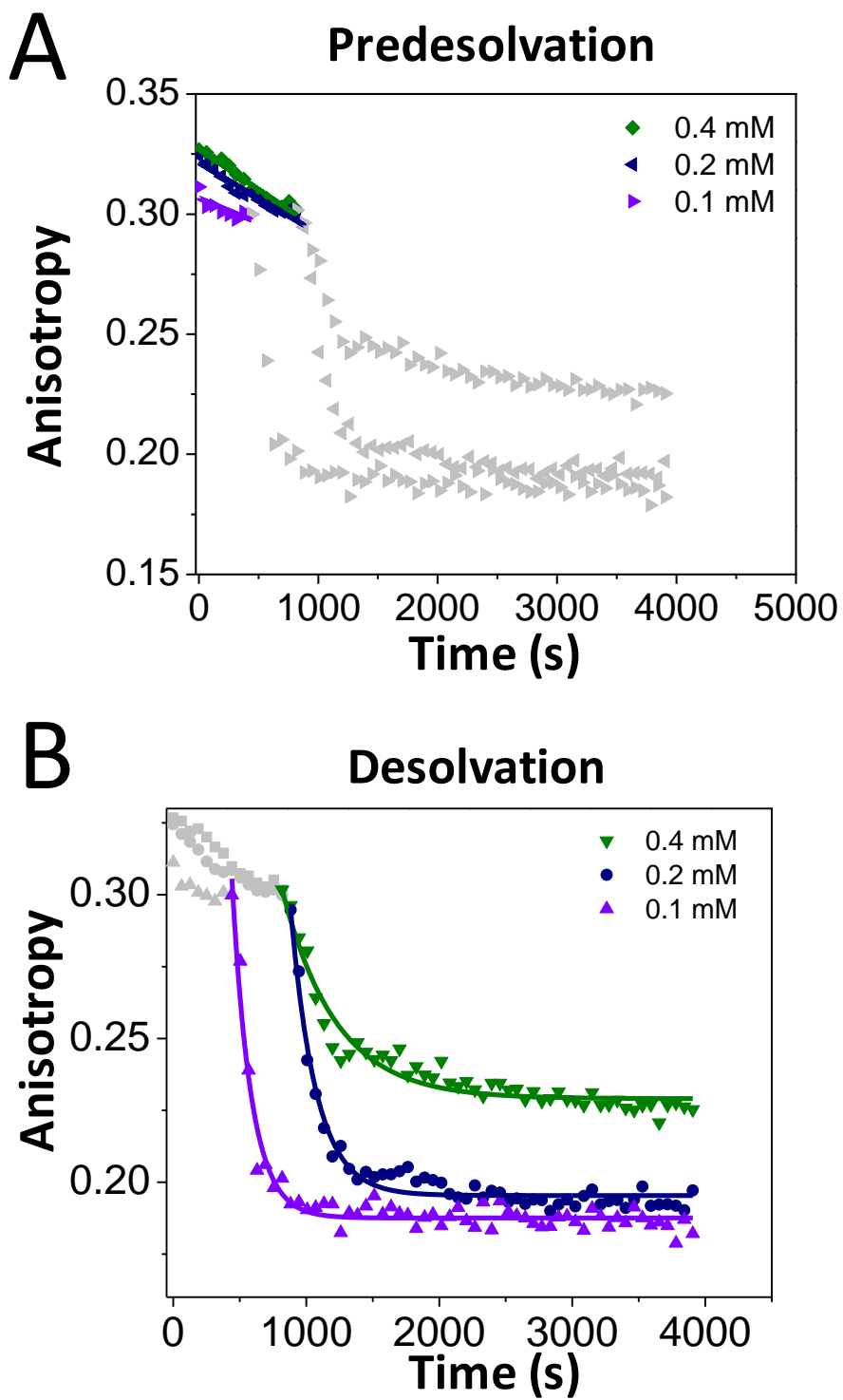
LysoFos – FhuA  $\Delta 5C/\Delta 7L_{30N}$ 

**Figure S3: Illustration of the time-dependent predesolvation and desolvation of FhuA  $\Delta C/\Delta 7L_{30N}$  solubilized with 20 mM LysoFos.** These phases were recorded using detergent concentrations below the  $CMC^{LysoFos} = 0.7$  mM. The other experimental conditions were the same as in **Fig. S1**.

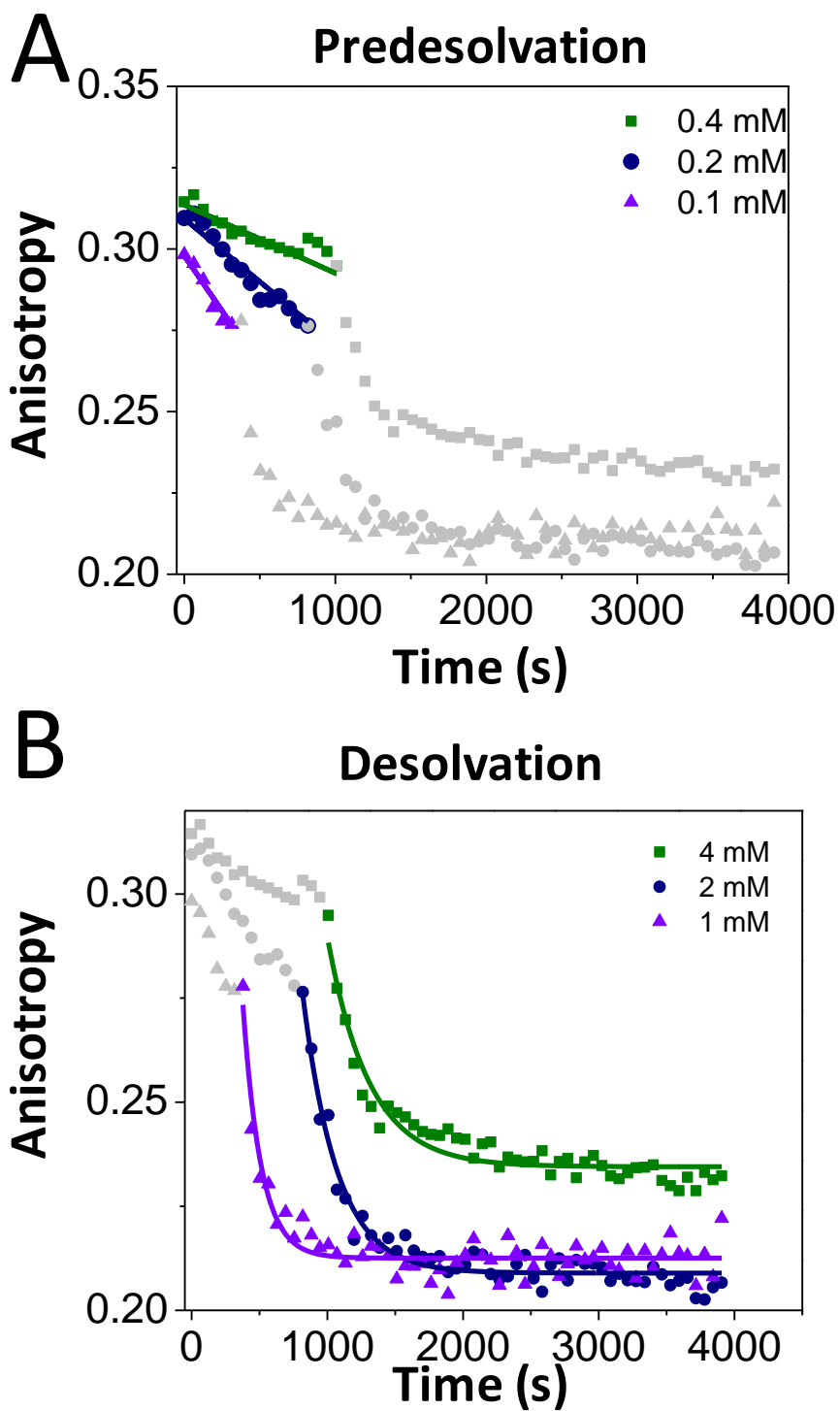
## UM - OMPG



**Figure S4: Illustration of the time-dependent predesolvation and desolvation of OmpG solubilized with 5 mM UM.** These phases were recorded using detergent concentrations below the  $\text{CMC}^{\text{UM}} = 0.59$  mM. The other experimental conditions were the same as in **Fig. S1**.

UM – FhuA  $\Delta C/\Delta 5L\_25N$ 

**Figure S5: Illustration of the time-dependent predesolvation and desolvation of FhuA  $\Delta C/\Delta 5L_{25N}$  solubilized with 5 mM UM.** These phases were recorded using detergent concentrations below the  $CMC^{UM} = 0.59$  mM. The other experimental conditions were the same as in **Fig. S1**.

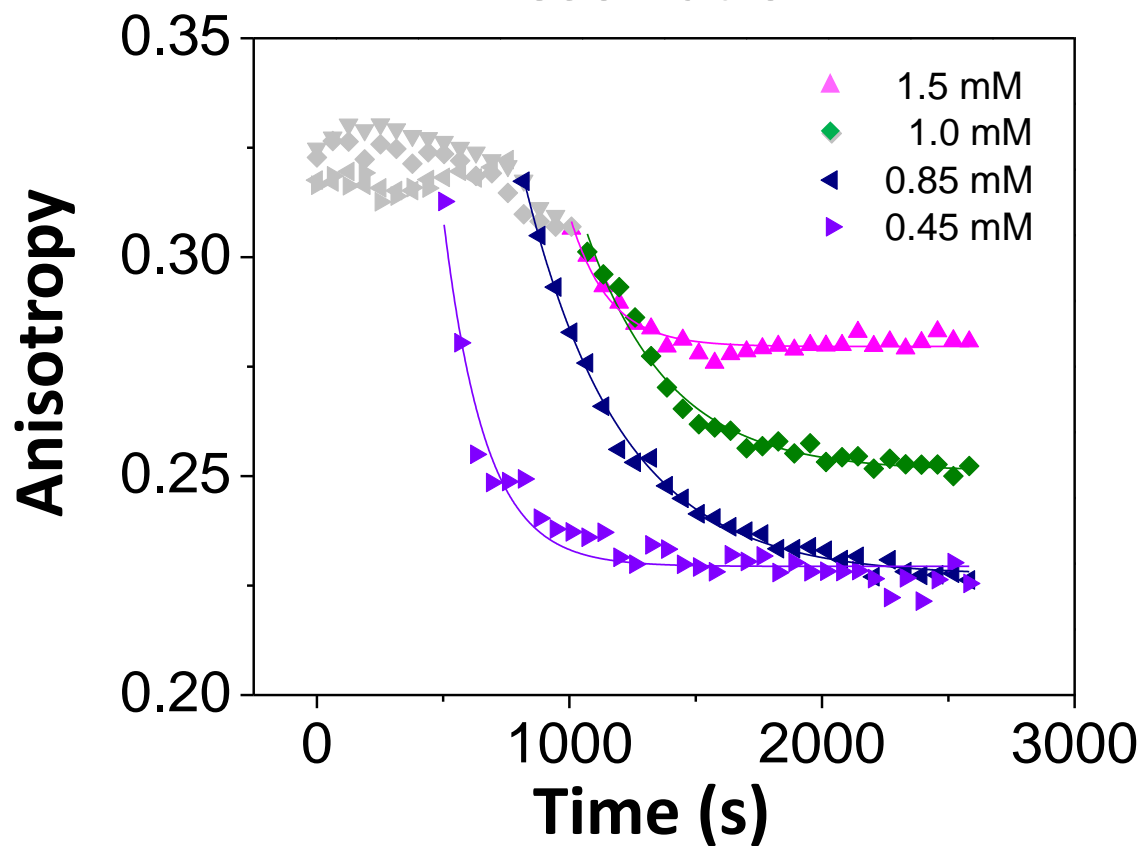
UM – FhuA  $\Delta C/\Delta 7L_{30N}$ 

**Figure S6: Illustration of the time-dependent predesolvation and desolvation of FhuA  $\Delta C/\Delta 7L_{30N}$  solubilized with 5 mM UM.** These phases were recorded using detergent concentrations below the  $CMC^{UM} = 0.59$  mM. The other experimental conditions were the same as in **Fig. S1**.

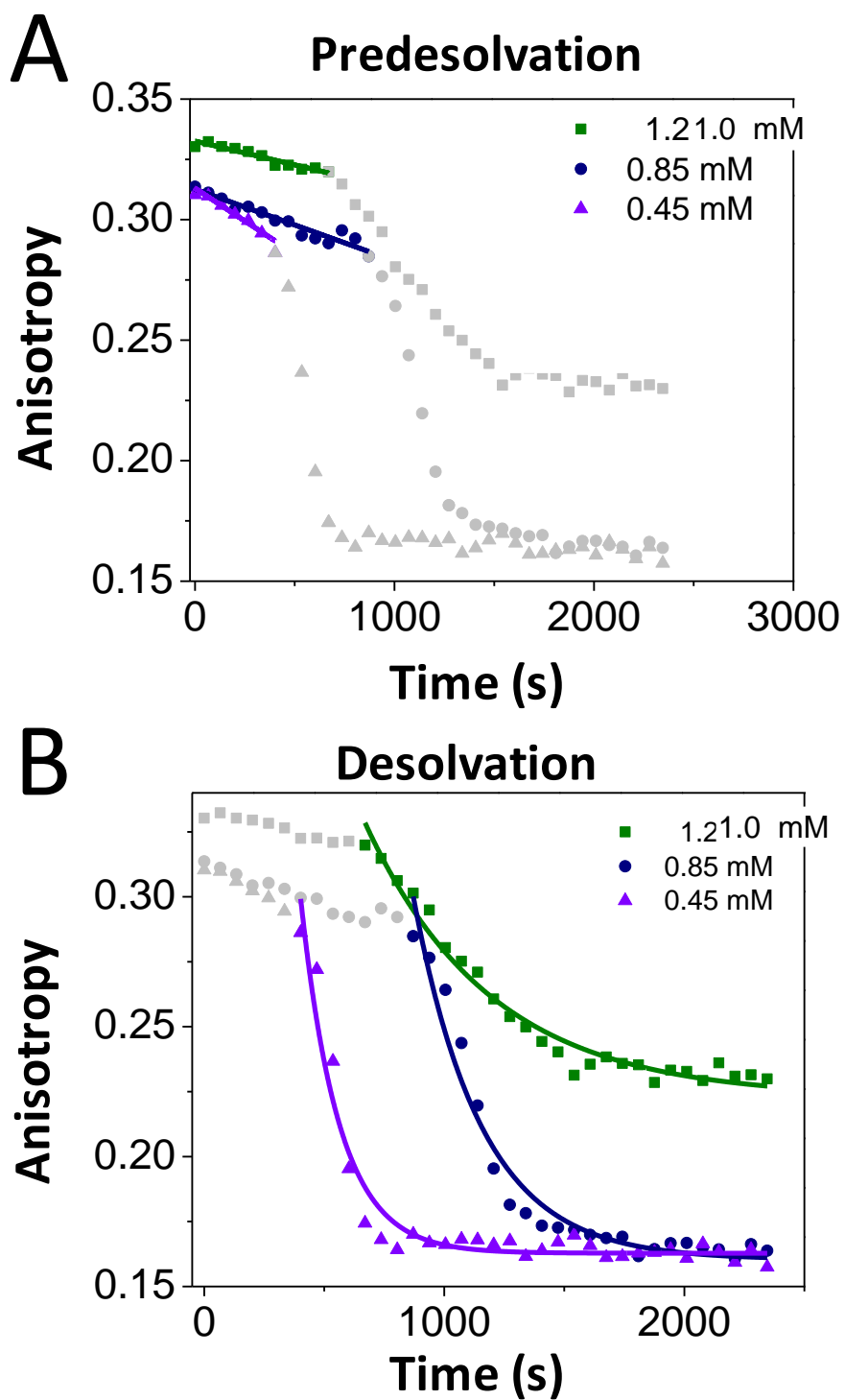


# DM - OmpG

## Desolvation

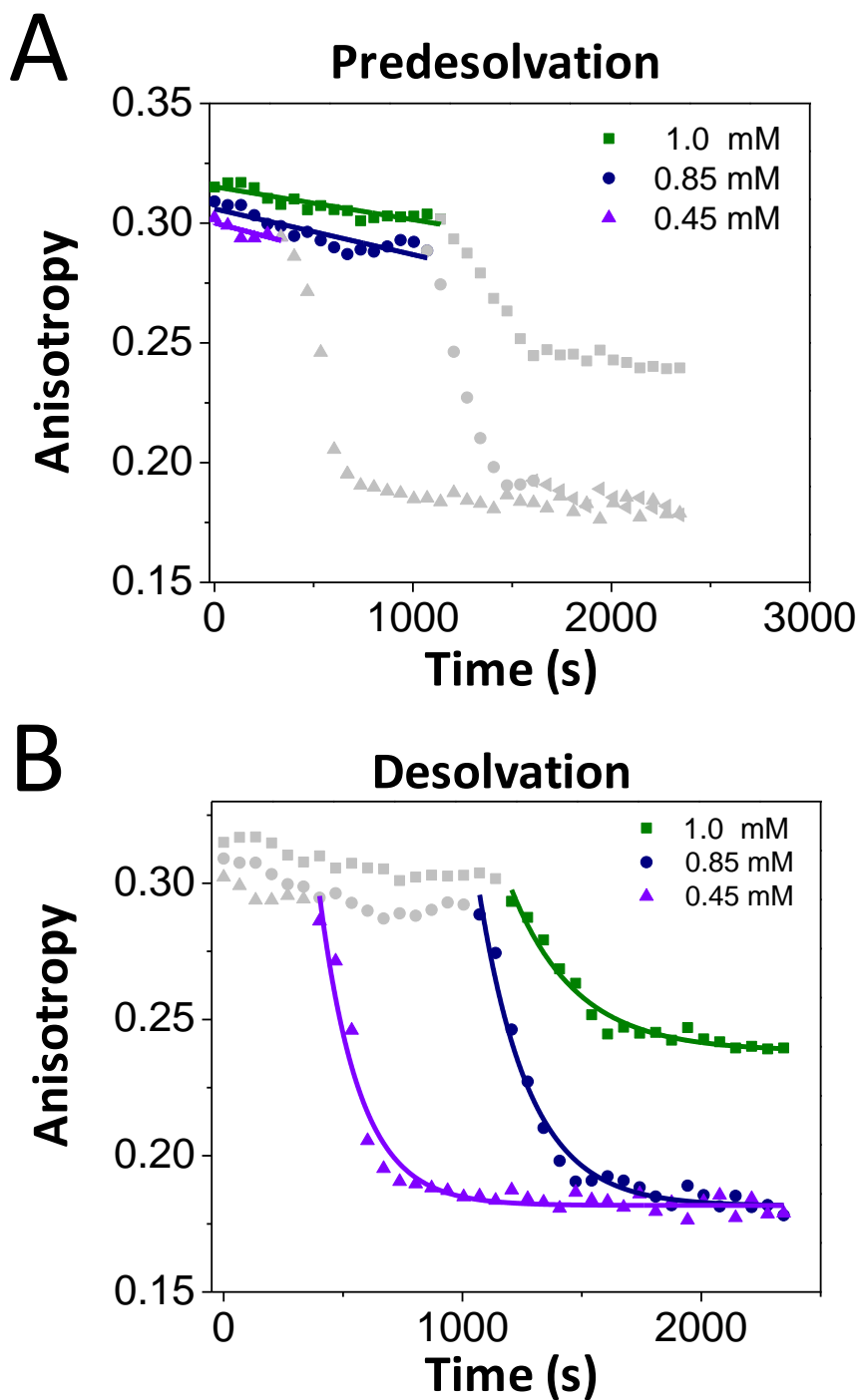


**Figure S7**: Illustration of the time-dependent desolvation of OmpG solubilized with 5 mM DM. These phases were recorded using detergent concentrations below the  $CMC^{DM} = 1.8$  mM. The other experimental conditions were the same as in **Fig. S1**.

DM – FhuA  $\Delta C/\Delta 5L\_25N$ 

**Figure S8: Illustration of the time-dependent predesolvation and desolvation of FhuA**

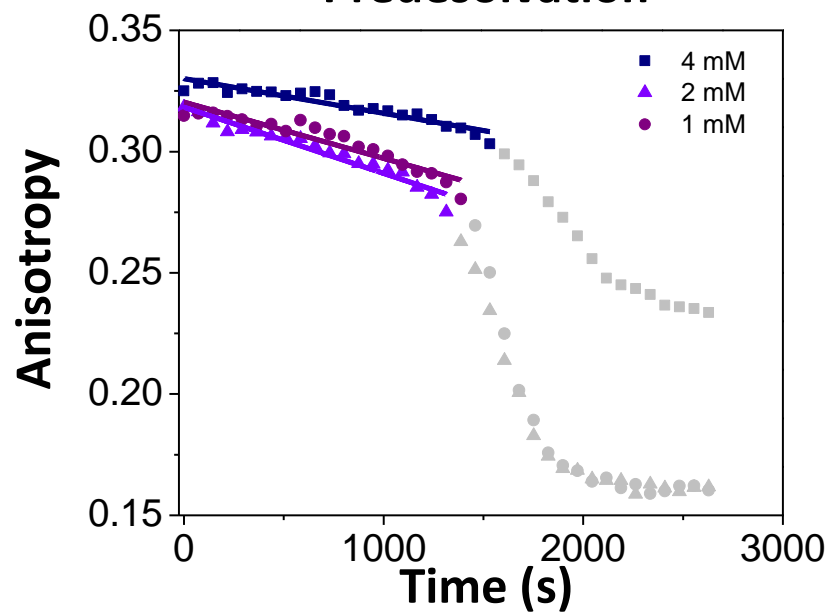
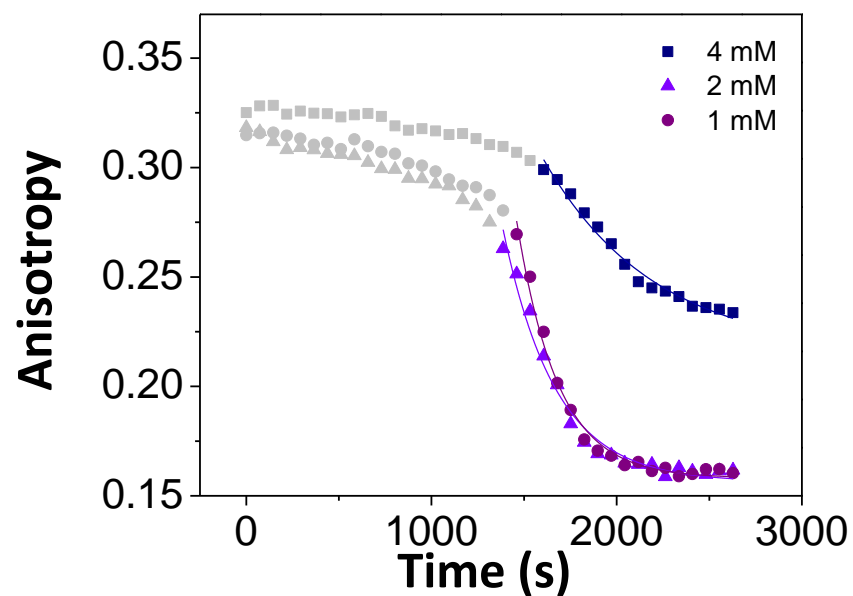
**$\Delta C/\Delta 5L_{25N}$  solubilized with 5 mM DM.** These phases were recorded using detergent concentrations below the  $CMC^{DM} = 1.8$  mM. The other experimental conditions were the same as in **Fig. S1**.

DM – FhuA  $\Delta C/\Delta 7L\_30N$ 

**Figure S9: Illustration of the time-dependent predesolvation and desolvation of FhuA**

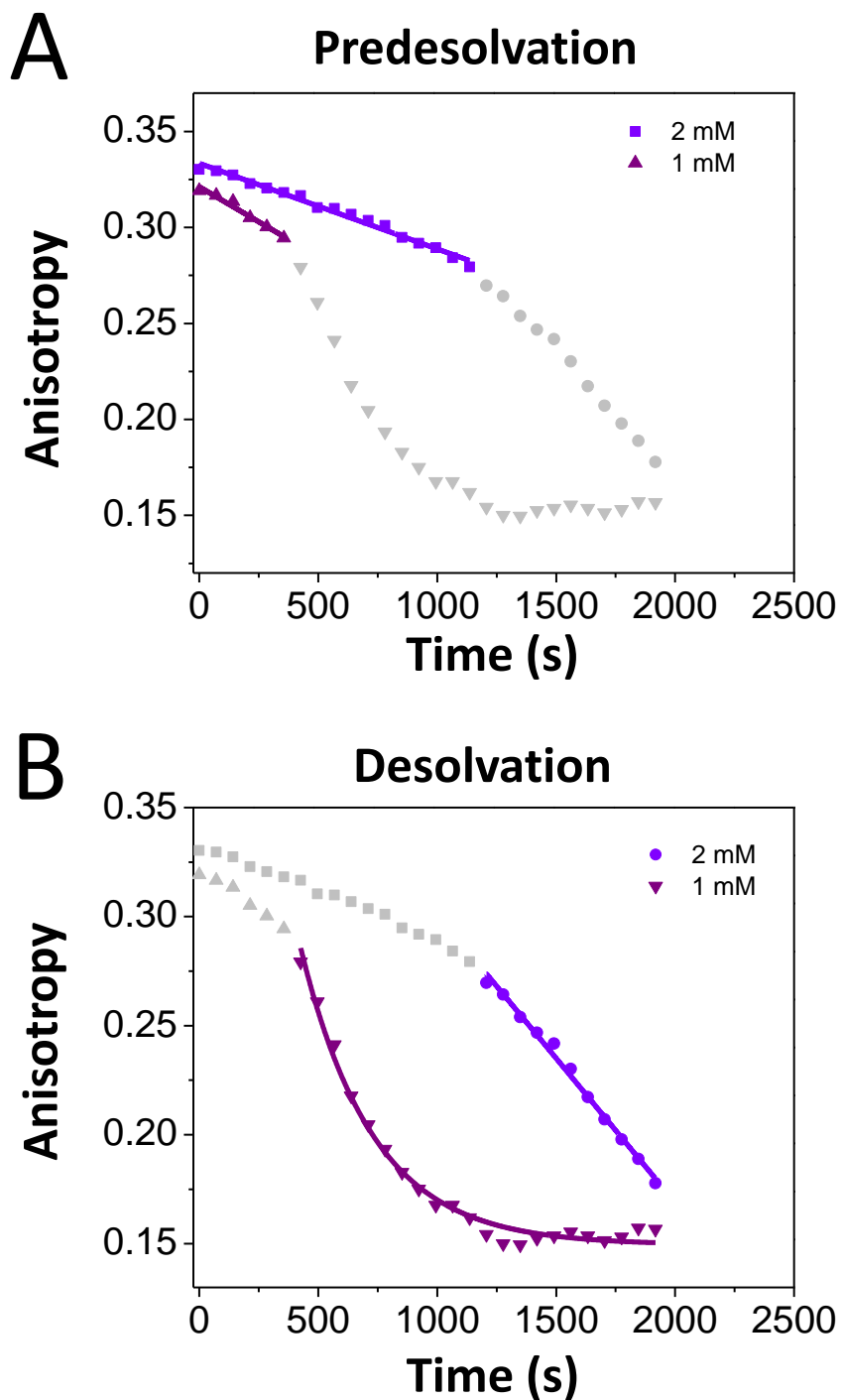
**$\Delta C/\Delta 7L_{30N}$  solubilized with 5 mM DM.** These phases were recorded using detergent concentrations below the  $CMC^{DM} = 1.8$  mM. The other experimental conditions were the same as in **Fig. S1**.

## CYMAL-4 - OmpG

**A****Predesolvation****B****Desolvation**

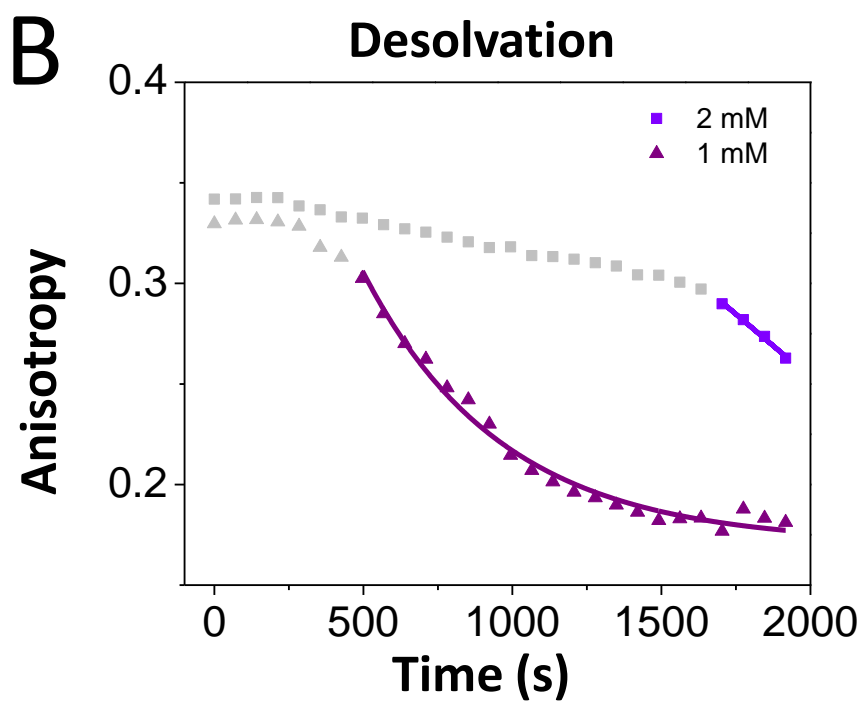
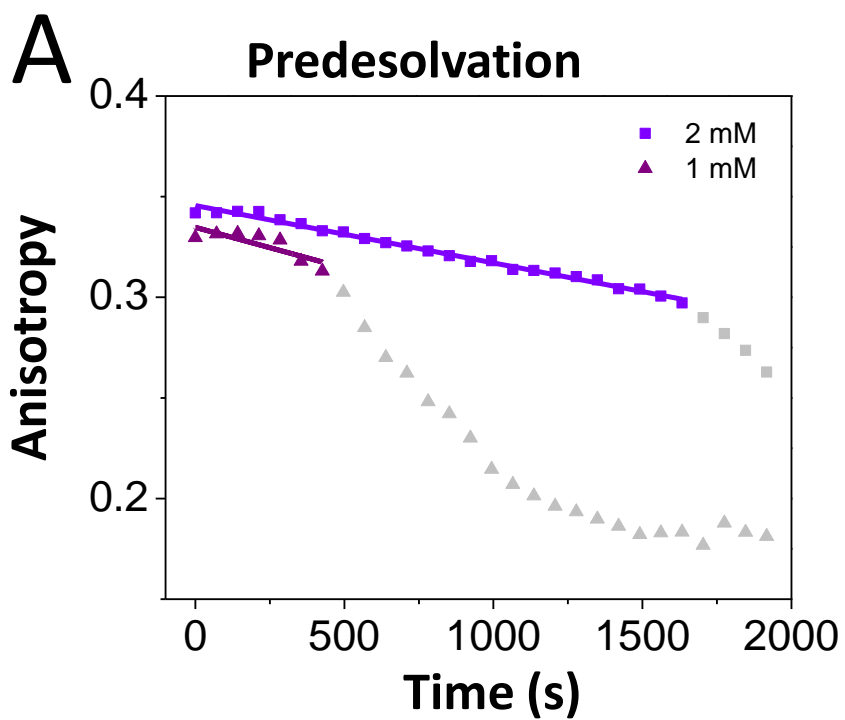
**Figure S10: Illustration of the time-dependent predesolvation and desolvation of OmpG solubilized with 50 mM CYMAL-4.** These phases were recorded using detergent concentrations below the  $\text{CMC}^{\text{CYMAL-4}} = 7.6 \text{ mM}$ . The other experimental conditions were the same as in **Fig. S1**.



CYMAL-4 - FhuA  $\Delta C/\Delta 5L_{25N}$ 

**Figure S11: Illustration of the time-dependent predesolvation and desolvation of FhuA**

**$\Delta C/\Delta 5L\_25N$  solubilized with 50 mM CYMAL-4.** These phases were recorded using detergent concentrations below the  $CMC^{CYMAL-4} = 7.6$  mM. The other experimental conditions were the same as in **Fig. S1**.

CYMAL-4 - FhuA  $\Delta C/\Delta 7L$  \_30N

**Figure S12: Illustration of the time-dependent predesolvation and desolvation of FhuA**

**$\Delta C/\Delta 7L\_30N$  solubilized with 50 mM CYMAL-4.** These phases were recorded using detergent concentrations below the  $CMC^{CYMAL-4} = 7.6$  mM. The other experimental conditions were the same as in **Fig. S1**

#### 4. Results of the fits of the predesolvation phase

**Table S3: Determination of the observed predesolvation rates ( $k_{\text{obs}}$ ).** The predesolvation rates were determined at various detergent concentrations below the CMC. The solubilized protein concentration was 28 nM. The buffer solution contained 200 mM NaCl, 50 mM HEPES, pH 7.4. In the below equation of **Table S3**,  $r(t)$  indicates the time-dependent FP anisotropy during the predesolvation phase. Here,  $r_{\text{max}}$  is the maximum FP anisotropy at the initial recording time and  $t$  is the elapsed time during the predesolvation phase.  $k_{\text{obs}}^{\text{pre}}$  denotes the observed predesolvation rate.

$r(t) = -k_{\text{obs}}^{\text{pre}} \times t + r_{\text{max}}$		
[Detergent] (mM)	$k_{\text{obs}}^{\text{pre}} \times 10^6$ (s <sup>-1</sup> )	Predesolvation duration, $T_{\text{pre}}$ (s)
<b>LysoFos – OmpG</b>		
0.2	10 ± 2	~567
0.1	33 ± 8	~315
<b>LysoFos – FhuA ΔC/Δ5L_25N</b>		
0.4	13 ± 3	~693
0.2	25 ± 5	~693
0.1	~8.7	~315
<b>Lysofos – FhuA ΔC/Δ7L_30N</b>		
0.4	~6.7	~693
0.2	34 ± 5	~693
0.1	38 ± 1	~315
<b>UM – OmpG</b>		
0.4	~4.1	~441
0.2	~4.2	~630
0.1	41 ± 11	~252
<b>UM – FhuA ΔC/Δ5L_25N</b>		
0.4	33 ± 2	~819
0.2	30 ± 2	~882
0.1	21 ± 7	~441
<b>UM – FhuA ΔC/Δ7L_30N</b>		
0.4	17 ± 2	~1010
0.2	44 ± 2	~819
0.1	77 ± 8	~315
<b>DM – OmpG</b>		
1	19 ± 3	~945
0.85	4.9 ± 2.1	~756
0.45	~7.7	~504
<b>DM – FhuA ΔC/Δ5L_25N</b>		
1	19.8 ± 0.1	~670
0.85	29.7 ± 0.1	~871
0.45	54.4 ± 0.1	~402
<b>DM – FhuA ΔC/Δ7L_30N</b>		
1	13.7 ± 1.6	~469
0.85	19.1 ± 2.7	~536
0.45	21.9 ± 8.6	~335
<b>CYMAL-4 – OmpG</b>		
4	16 ± 1	~1610
2	27 ± 2	~1390
1	21 ± 2	~1310
<b>CYMAL-4 – FhuA ΔC/Δ5L_25N</b>		

2	$45 \pm 1$	~1250
1	$73 \pm 6$	~355
<b>CYMAL-4 – FhuA <math>\Delta</math>C/<math>\Delta</math>7L_30N</b>		
2	$29 \pm 1$	~1633
1	$40 \pm 12$	~426

### **5. Results of the fits of the desolvation phase**

**Table S4: Determination of the observed desolvation rates,  $k_{\text{obs}}^{\text{des}}$ .** The desolvation rates were determined at various detergent concentrations below the CMC. The solubilized protein concentration was 28 nM. The buffer solution contained 200 mM NaCl, 50 mM HEPES, pH 7.4. NA is indicated for those cases that cannot be fitted with a single-exponential function, but a simple linear dependence. Below,  $r(t)$  indicates the time-dependent FP anisotropy during the detergent desolvation phase. Here,  $r_{\text{min}}$  denotes the minimum FP anisotropy at the infinite time of the desolvation reaction.  $t$  shows the elapsed time during the desolvation phase, including the total time of the predesolvation phase. The observed desolvation rate,  $k_{\text{obs}}^{\text{des}}$ , was derived by fitting the single-exponential decay of the time-dependent FP anisotropy,  $r(t)$ .  $r_0$  is an FP anisotropy constant.



$r(t) = r_0 \cdot \exp(-t/\tau) + r_{\min}$				
[Detergent] (mM)	$k_{\text{obs}}^{\text{des}} \times 10^5 \text{ (s}^{-1}\text{)}$	$r_{\min}$	$r_0$	$\tau$ (s)
<b>LysoFos – OmpG</b>				
0.2	350 ± 22	0.26 ± 0.01	0.49 ± 0.07	286 ± 18
0.1	340 ± 35	0.25 ± 0.01	0.18 ± 0.03	293 ± 30
<b>LysoFos – FhuA ΔC/Δ5L_25N</b>				
0.4	140 ± 9	0.29 ± 0.01	0.14 ± 0.01	735 ± 50
0.2	360 ± 22	0.21 ± 0.01	1.42 ± 0.24	281 ± 17
0.1	510 ± 27	0.21 ± 0.01	0.72 ± 0.08	198 ± 11
<b>LysoFos – FhuA ΔC/Δ7L_30N</b>				
0.4	182 ± 9	0.30 ± 0.01	0.22 ± 0.02	549 ± 28
0.2	284 ± 14	0.23 ± 0.01	0.80 ± 0.09	352 ± 17
0.1	719 ± 29	0.24 ± 0.01	1.26 ± 0.13	139 ± 6
<b>UM – OmpG</b>				
0.4	10.7 ± 1.1	NA	NA	NA
0.2	446 ± 21	0.23 ± 0.01	1.32 ± 0.19	224 ± 10
0.1	610 ± 43	0.23 ± 0.01	0.61 ± 0.09	164 ± 12
<b>UM – FhuA ΔC/Δ5L_25N</b>				
0.4	248 ± 19	0.23 ± 0.01	0.55 ± 0.10	404 ± 31
0.2	526 ± 30	0.20 ± 0.01	10.4 ± 2.9	190 ± 11
0.1	704 ± 45	0.19 ± 0.01	2.6 ± 0.5	142 ± 9
<b>UM – FhuA ΔC/Δ5L_30N</b>				
0.4	324 ± 28	0.23 ± 0.01	1.4 ± 0.4	309 ± 27
0.2	395 ± 27	0.21 ± 0.01	1.7 ± 0.4	253 ± 17
0.1	752 ± 85	0.21 ± 0.01	1.0 ± 0.4	133 ± 15
<b>DM – OmpG</b>				
1	272 ± 21	0.25 ± 0.01	0.95 ± 0.21	367 ± 29
0.85	262 ± 8	0.23 ± 0.01	0.77 ± 0.06	382 ± 12
0.45	610 ± 55	0.23 ± 0.01	1.67 ± 0.51	164 ± 15
<b>DM – FhuA ΔC/Δ5L_25N</b>				
1	191 ± 19	0.22 ± 0.01	0.38 ± 0.05	523 ± 51
0.85	353 ± 36	0.16 ± 0.01	3.0 ± 1.0	283 ± 29
0.45	629 ± 59	0.16 ± 0.01	1.7 ± 0.4	159 ± 15
<b>DM – FhuA ΔC/Δ7L_30N</b>				
1	369 ± 44	0.24 ± 0.01	5.1 ± 2.6	271 ± 32
0.85	478 ± 37	0.18 ± 0.01	19.2 ± 7.8	209 ± 16
0.45	599 ± 50	0.18 ± 0.01	1.3 ± 0.3	167 ± 14
<b>CYMAL-4 – OmpG</b>				
4	211 ± 27	0.22 ± 0.01	2.6 ± 1.1	473 ± 61
2	352 ± 33	0.16 ± 0.01	15 ± 7	284 ± 26
1	353 ± 36	0.15 ± 0.01	19 ± 9	283 ± 29
<b>CYMAL-4 – FhuA ΔC/Δ5L_25N</b>				

1	$328 \pm 19$	$0.15 \pm 0.01$	$0.55 \pm 0.05$	$305 \pm 18$
2	$13.2 \pm 0.01$	NA	NA	NA
<b>CYMAL-4 – FhuA <math>\Delta C/\Delta 7L</math> 30N</b>				
2	$12.6 \pm 0.69$	NA	NA	NA
1	~214	$0.17 \pm 0.01$	$0.393 \pm 0.03$	$467 \pm 0.0$

6. Dependence of the observed desolvation rates on the detergent concentration

## LysoFos - FhuA $\Delta C/\Delta 5L\_25N$

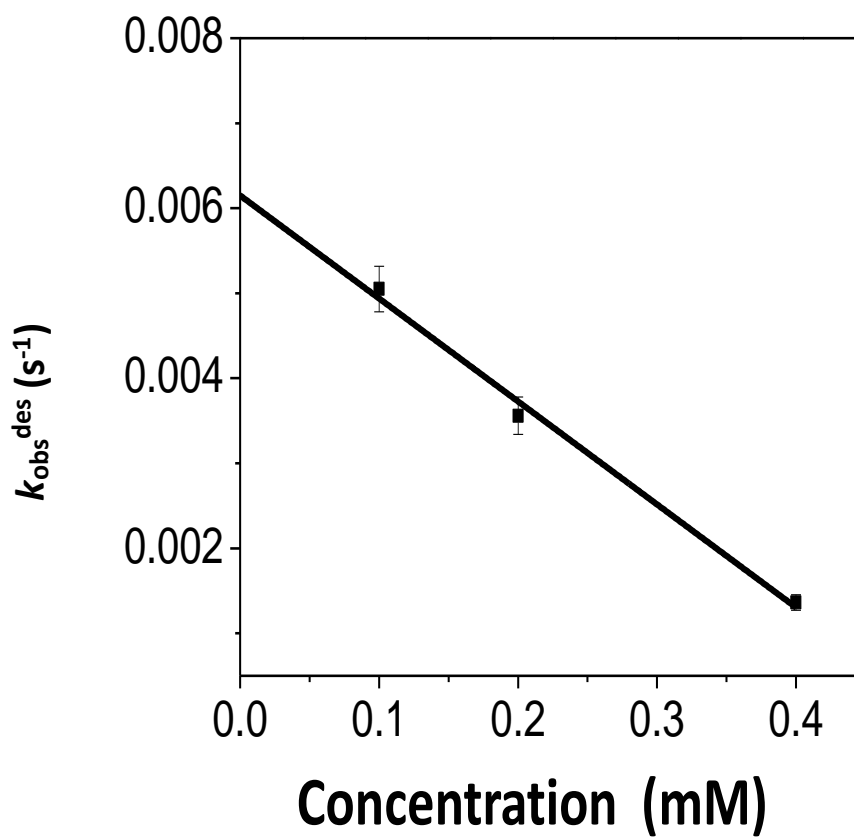
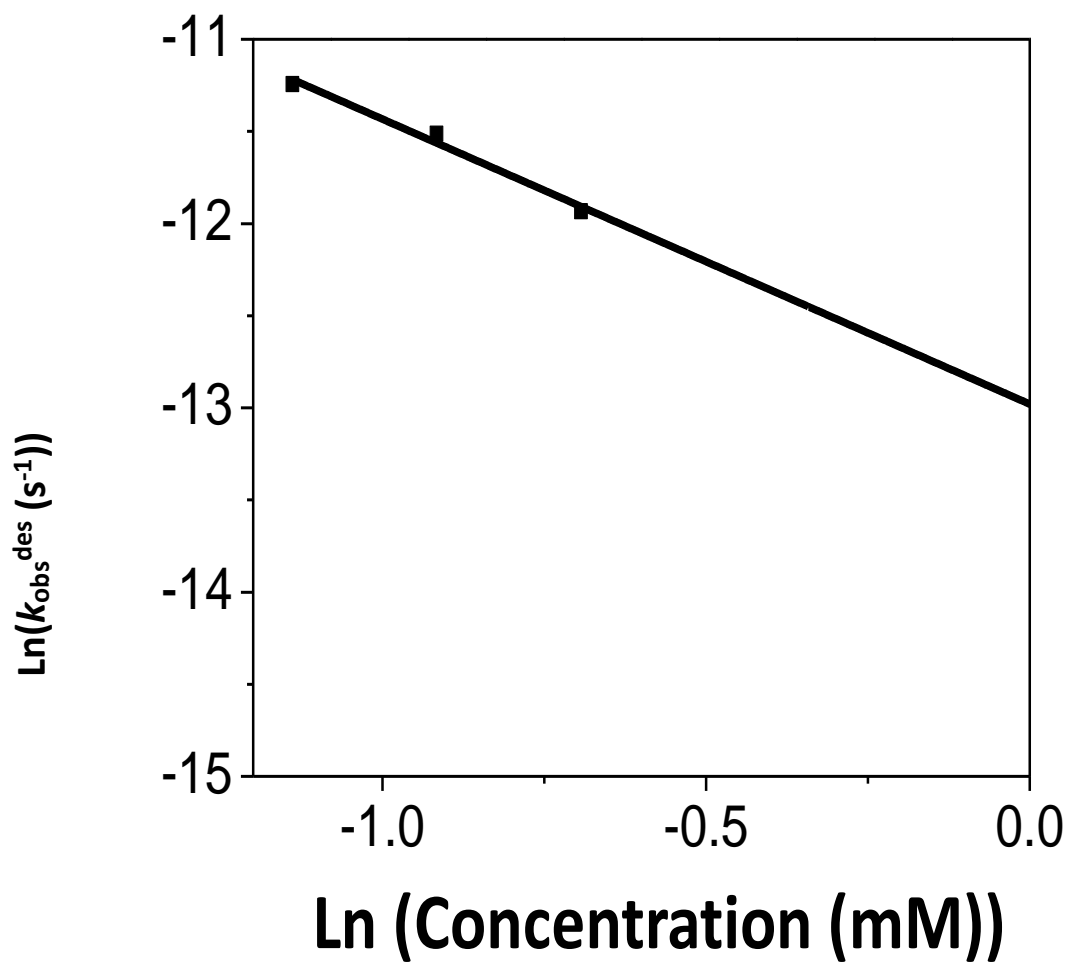


**Figure S13: Illustration of the dependence of the observable desolvation rate,  $k_{\text{obs}}^{\text{des}}$ , on the detergent concentrations at values below the CMC.** The cartoon show the rate data obtained FhuA  $\Delta C/\Delta 5L_{25N}$  solubilized in 20 mM LysoFos.  $k_{\text{obs}}^{\text{des}}$  data points were inferred from single-exponential decay fits of at least three independent FP traces.

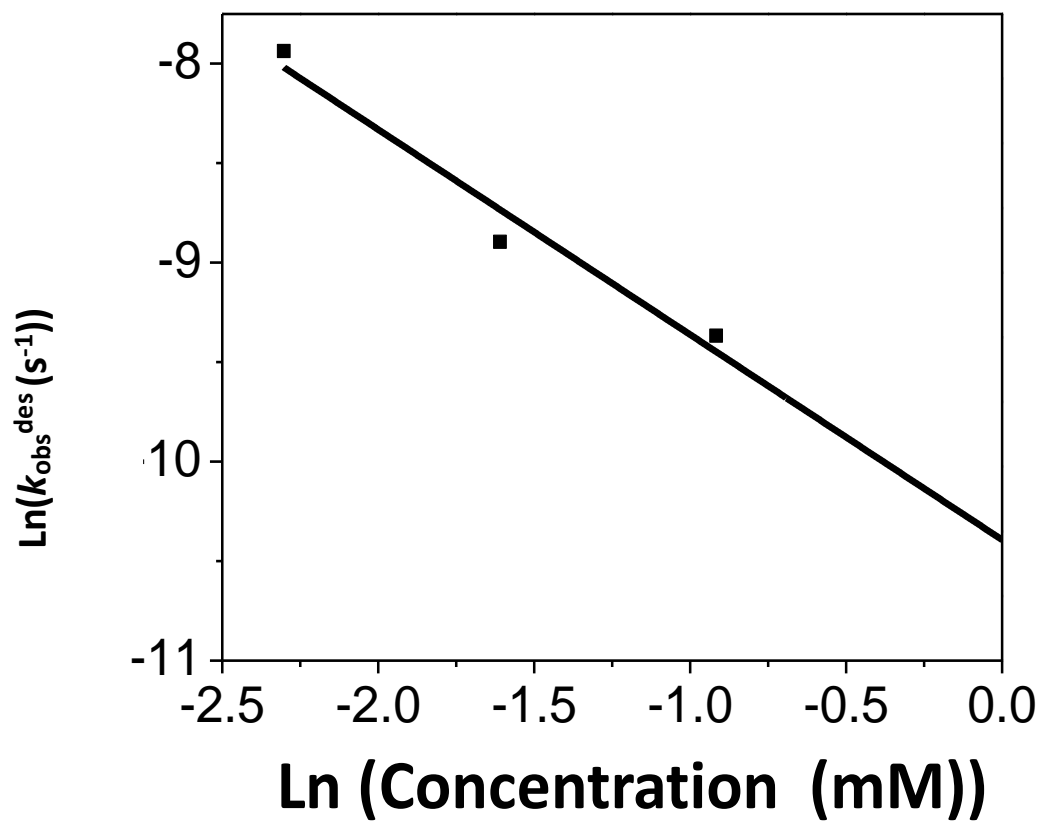
**Table S5:** Determination of the kinetic rate constants of association ( $k_{on}$ ) and dissociation ( $k_{off}$ ) of proteomicelles formed by LysoFos with truncation FhuA derivatives.

$k_{on}$ ( $M^{-1}s^{-1}$ )	$k_{off} \times 10^3$ ( $s^{-1}$ )	$K_d$ (mM)
<b>LysoFos – FhuA <math>\Delta C/\Delta 5L</math> 25N</b>		
$12 \pm 1$	$6.2 \pm 0.3$	$0.51 \pm 0.03$
<b>LysoFos – FhuA <math>\Delta C/\Delta 7L</math> 30N</b>		
~16	~7.8	~0.48

## LysoFos - FhuA $\Delta C/\Delta 5L$



**Figure S14:** Logarithmic plot showing that the observable desolvation rate,  $k_{\text{obs}}^{\text{des}}$ , recorded with FhuA  $\Delta\text{C}/\Delta\text{5L}$  scales with the detergent concentration of LysoFos at values below the  $\text{CMC}^{\text{LysoFos}} = 0.7 \text{ mM}$ . The truncation FhuA  $\Delta\text{C}/\Delta\text{5L}$  mutant features complete deletion of the internal cork domain C and removal of five extracellular loops (L3, L4, L5, L10, and L11), but without any charge neutralization with respect to the native FhuA protein. The protein was solubilized in 20 mM LysoFos. The other experimental conditions were the same as in **Fig. S1**.

DDM - FhuA  $\Delta C/\Delta 7L\_30N$ 



**Figure S15:** Logarithmic plot showing that the observable desolvation rate,  $k_{\text{obs}}^{\text{des}}$ , recorded with FhuA  $\Delta C/\Delta 7L\_30N$  scales with the detergent concentration of dodecyl- $\beta$ -D-maltoside (DDM) at values below the  $\text{CMC}^{\text{DDM}} = 0.17$  mM. The protein was solubilized in 5 mM DDM. The other experimental conditions were the same as in **Fig. S1**.

# UM -FhuA $\Delta C/\Delta 5L_{25N}$

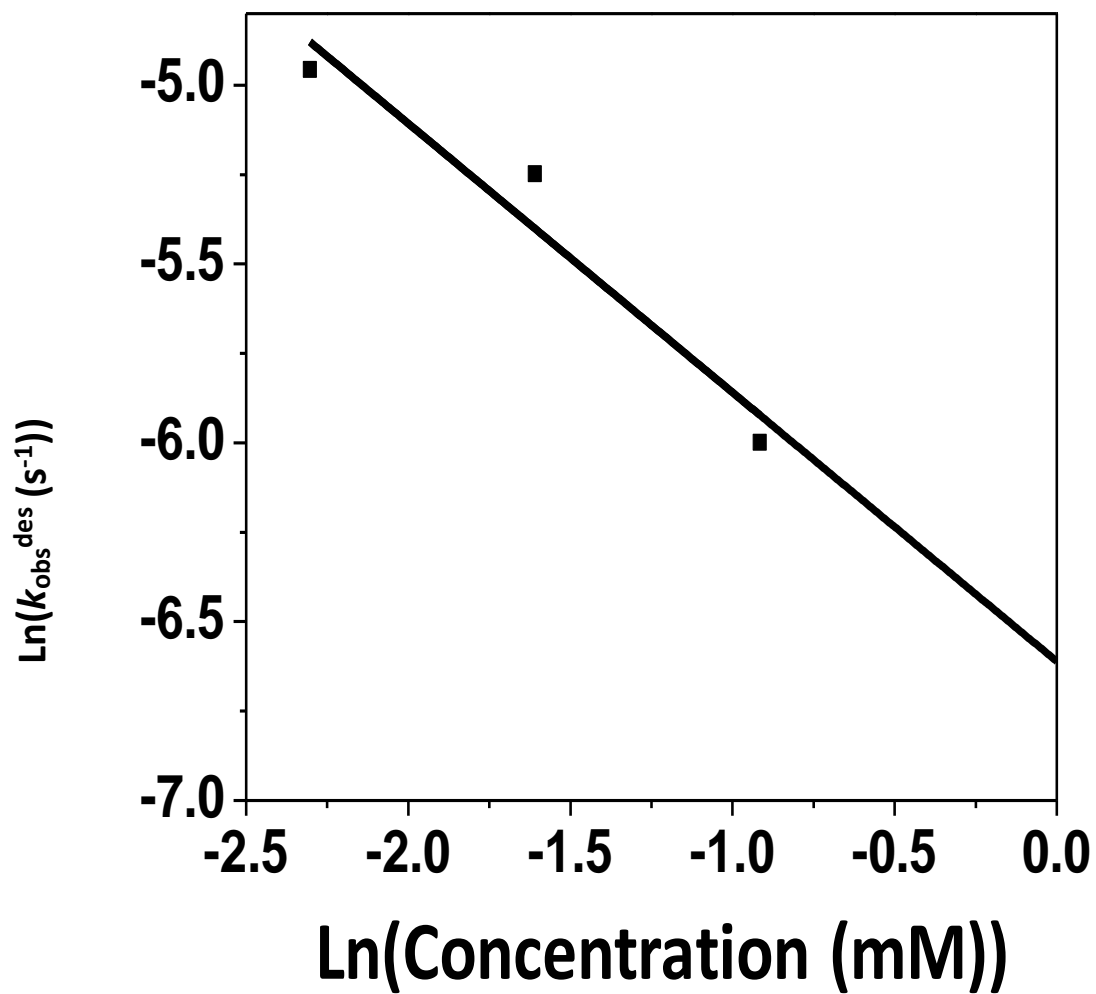


**Figure S16:** Logarithmic plot showing that the observable desolvation rate,  $k_{\text{obs}}^{\text{des}}$ , recorded with FhuA  $\Delta C/\Delta 7L_{-25N}$  scales with the detergent concentration of UM at values below the  $\text{CMC}^{\text{UM}} = 0.59 \text{ mM}$ . The protein was solubilized in 5 mM UM. The other experimental conditions were the same as in **Fig. S1**.

In **Figures S14-S16**, the observed desolvation constant,  $k_{obs}^{des}$ , is a function of the apparent first-order reaction rate constant,  $k'$ , and the order,  $r$ , of the reaction with respect to  $[D]$ , the detergent concentration:

$$k_{obs}^{des} = k[P]^s[D]^r = k'[D]^r \quad (S1)$$

where

$$k' = k[P]^s \quad (S2)$$

and

$$\ln k_{obs}^{des} = \ln k' + r \ln [D] \quad (S3)$$

Here,  $s$  is the order of the reaction with respect to  $[P]$ , the protein concentration, whereas  $k$  denotes the reaction rate constant of association. In **Table S6**, the negative values of  $r$  indicate that the analyzed process is a dissociation (detergent desolvation).

**Table S6:** The dissociation rate scaling with the final detergent concentration in the sample well.

<b>Detergent – Protein Pair</b>	<b><i>r</i></b>	<b><i>k</i>'×10<sup>5</sup> (s<sup>-1</sup>)</b>
LysoFos - FhuA ΔC/Δ5L	-1.54 ± 0.19	0.23
DDM - FhuA ΔC/Δ7L 30N	-1.00 ± 0.20	3.00
UM – FhuA ΔC/Δ5L_25N	-0.75 ± 0.19	135

**REFERENCES**

1. Wolfe, A. J.; Si, W.; Zhang, Z.; Blanden, A. R.; Hsueh, Y. C.; Gugel, J. F.; Pham, B.; Chen, M.; Loh, S. N.; Rozovsky, S.; Aksimentiev, A.; Movileanu, L. Quantification of membrane protein-detergent complex interactions. *J. Phys. Chem. B* **2017**, *121* (44), 10228-10241.
2. Kyte, J.; Doolittle, R. F. A simple method for displaying the hydropathic character of a protein. *J. Mol. Biol* **1982**, *157* (1), 105-132.
3. Gasteiger, E.; Hoogland, C.; Gattiker, A.; Duvaud, S.; Wilkins, M. R.; Appel, R. D.; Bairoch, A. Protein identification and analysis tools on the ExPASy server. In *Proteomics Protocols Handbook*, J.M., W., Ed. Humana Press: 2005; pp 571-607.
4. Stafford, R. E.; Fanni, T.; Dennis, E. A. Interfacial properties and critical micelle concentration of lysophospholipids. *Biochemistry* **1989**, *28* (12), 5113-20.
5. Stangl, M.; Veerappan, A.; Kroeger, A.; Vogel, P.; Schneider, D. Detergent properties influence the stability of the glycophorin A transmembrane helix dimer in lysophosphatidylcholine micelles. *Biophys. J.* **2012**, *103* (12), 2455-64.
6. Linke, D. Detergents: an overview. *Methods Enzymol.* **2009**, *463*, 603-617.
7. le Maire, M.; Champeil, P.; Moller, J. V. Interaction of membrane proteins and lipids with solubilizing detergents. *Biochim. Biophys. Acta* **2000**, *1508* (1-2), 86-111.

## Chapter 6. Kinetics of Membrane Protein-Detergent Interactions Depend on Protein Electrostatics

Aaron J. Wolfe,<sup>1,2</sup> Jack F. Gugel,<sup>1</sup> Min Chen,<sup>3</sup> and Liviu Movileanu<sup>1,2,4,\*</sup>

<sup>1</sup>Department of Physics, Syracuse University, 201 Physics Building, Syracuse, New York 13244-1130, USA

<sup>2</sup>Structural Biology, Biochemistry, and Biophysics Program, Syracuse University, 111 College Place, Syracuse, New York 13244-4100, USA

<sup>3</sup>Department of Chemistry, University of Massachusetts, 820 LGRT, 710 North Pleasant Street, Amherst, Massachusetts 01003-9336, USA

<sup>4</sup>Department of Biomedical and Chemical Engineering, Syracuse University, Syracuse University, 223 Link Hall, Syracuse, New York 13244, USA

Reprinted with permission from **Kinetics of Membrane Protein-Detergent Interactions Depend on Protein Electrostatics**, Aaron J. Wolfe, Jack F. Gugel, Min Chen, and Liviu Movileanu 2018 Sep 25. doi: 10.1021/acs.jpcc.8b07889. *J. Phys. Chem. B*, Copyright 2018 American Chemical Society.

Author contributions:

AJW: Designed experiments, performed experiments, analyzed data, interpreted data.

JFG: Analyzed data

MC: Performed experiments

LM: Analyzed data, interpreted data, wrote manuscript

**ABSTRACT**

Interactions of a membrane protein with a detergent micelle represent a fundamental process with practical implications in structural and chemical biology. Quantitative assessment of the kinetics of protein-detergent complex (PDC) interactions has always been challenged by complicated behavior of both membrane proteins and solubilizing detergents in aqueous phase. Here, we show the kinetic reads of the desorption of maltoside-containing detergents from  $\beta$ -barrel membrane proteins. Using steady-state fluorescence polarization (FP) anisotropy measurements, we recorded real-time, specific signatures of the PDC interactions. The results of these measurements were used to infer the model-dependent rate constants of association and dissociation of the proteomicelles. Remarkably, the kinetics of the PDC interactions depend on the overall protein charge despite the nonionic nature of the detergent monomers. In the future, this approach might be employed for high-throughput screening of kinetic fingerprints of different membrane proteins stabilized in micelles that contain mixtures of various detergents.



## INTRODUCTION

Understanding the specific interactions at the protein-detergent complex (PDC) interface has critical importance to membrane protein structure,<sup>1-2</sup> function,<sup>3-4</sup> stability,<sup>5-6</sup> and dynamics.<sup>7-8</sup> Current approaches for an assessment of the PDC kinetics have numerous limitations. Available techniques are not amenable to high-throughput settings, are too highly specialized for a widespread adoption, or require high amounts of membrane protein. Because both the detergents and membrane proteins exhibit complex phases in solution,<sup>9-11</sup> these challenges add up to a list of various difficulties for inferring a comprehensive determination of the forces that govern the kinetics of the PDC formation and dissociation. In many instances, the presence of protein aggregates,<sup>10, 12</sup> which coexist with both micelles and proteomicelles in solution, produces a significant deterioration in the signal-to-noise ratio of prevailing spectroscopic and calorimetric methods. These shortcomings are primarily determined by the direct relationship between the recorded readout and effective concentration of the detergent-solubilized membrane protein in solution.<sup>13</sup> In the absence of a robust membrane protein scaffold that features programmable functional and biophysical properties, obtaining the kinetic fingerprints at the PDC interface remains challenging. This gap of fundamental knowledge, which profoundly impacts structural biology and protein biotechnology, restrains the progress in the extensive screening of newly synthesized non-conventional detergents<sup>14-16</sup> for membrane protein research.

To address these intimidating barriers, we developed a scalable approach for determining the real-time kinetic reads of the PDC interactions. This method is based upon a widely accessible, single-fluorophore probe technique. The pivotal concept of this study is the specific and sensitive modulation in the steady-state fluorescence polarization (FP) anisotropy<sup>17-20</sup> of a membrane

protein by alterations in its interfacial interactions with solubilizing detergent monomers. Dissociation of a membrane protein from a detergent micelle is accompanied by a decreased emission in the plane parallel to the polarized light and an increased emission to the plane orthogonal to the polarized light.<sup>21</sup> In this way, the PDC dissociation is accompanied by a decrease in the FP anisotropy, so the opposite is true for the PDC formation. Thus, the time-dependent steady-state FP anisotropy is recorded and processed as a ratio between the numbers of detergent-free and detergent-solvated membrane proteins.

$\beta$ -barrel proteins are versatile to remodeling in various ways.<sup>22-23</sup> The targeted panel in this study included the outer membrane protein G (OmpG)<sup>24</sup>, a medium-sized, 14-stranded  $\beta$ -barrel (pI 4.4; **Fig. 1A**), and three homologous variants of the *ferric hydroxamate uptake component A* (FhuA) of *E. coli*, a large 22-stranded  $\beta$ -barrel (**Fig. 1B-D**).<sup>25</sup> The monomeric nature of these outer membrane proteins is advantageous for both the preparative steps<sup>26-28</sup> and further data analysis of the steady-state FP anisotropy recordings.<sup>21</sup> In order to explore the effect of the protein charge on the PDC kinetics, we conducted local and global protein engineering of FhuA. The 505-residue FhuA  $\Delta C/\Delta 5L$  protein is an extensive truncation mutant of the wild-type, 714-residue FhuA, lacking an N-terminal, 160-residue cork domain and five large extracellular loops (pI 5.7; **Fig. 1B**).<sup>29</sup> Furthermore, dramatic alterations in the charge of the acidic FhuA  $\Delta C/\Delta 5L$  protein were conducted by neutralizing its 25 and 30 negative charges, resulting in two basic  $\beta$ -barrels, FhuA  $\Delta C/\Delta 5L_{25N}$  (pI 9.3; **Fig. 1C**) and FhuA  $\Delta C/\Delta 7L_{30}$  (pI 9.6; **Fig. 1D**), respectively. In this way, the targeted panel in this work included two acidic and two basic proteins, out of which the 281-residue OmpG protein featured a relatively smaller size than that of the three homologous FhuA variants. This experimental design enabled us to observe whether

a change in the membrane protein size has a significant impact on the steady-state FP anisotropy. Notably, the truncation FhuA variants exhibit a fairly stable  $\beta$ -barrel scaffold under a very broad range of experimental conditions, including very acidic pH,<sup>30-31</sup> highly osmotic<sup>26, 32</sup> or electro-osmotic pressure,<sup>30</sup> and elevated temperatures.<sup>30</sup> In addition, the stability of FhuA is not impaired by local and global modifications even when accommodating newly functional polypeptides within the pore interior.<sup>31</sup>

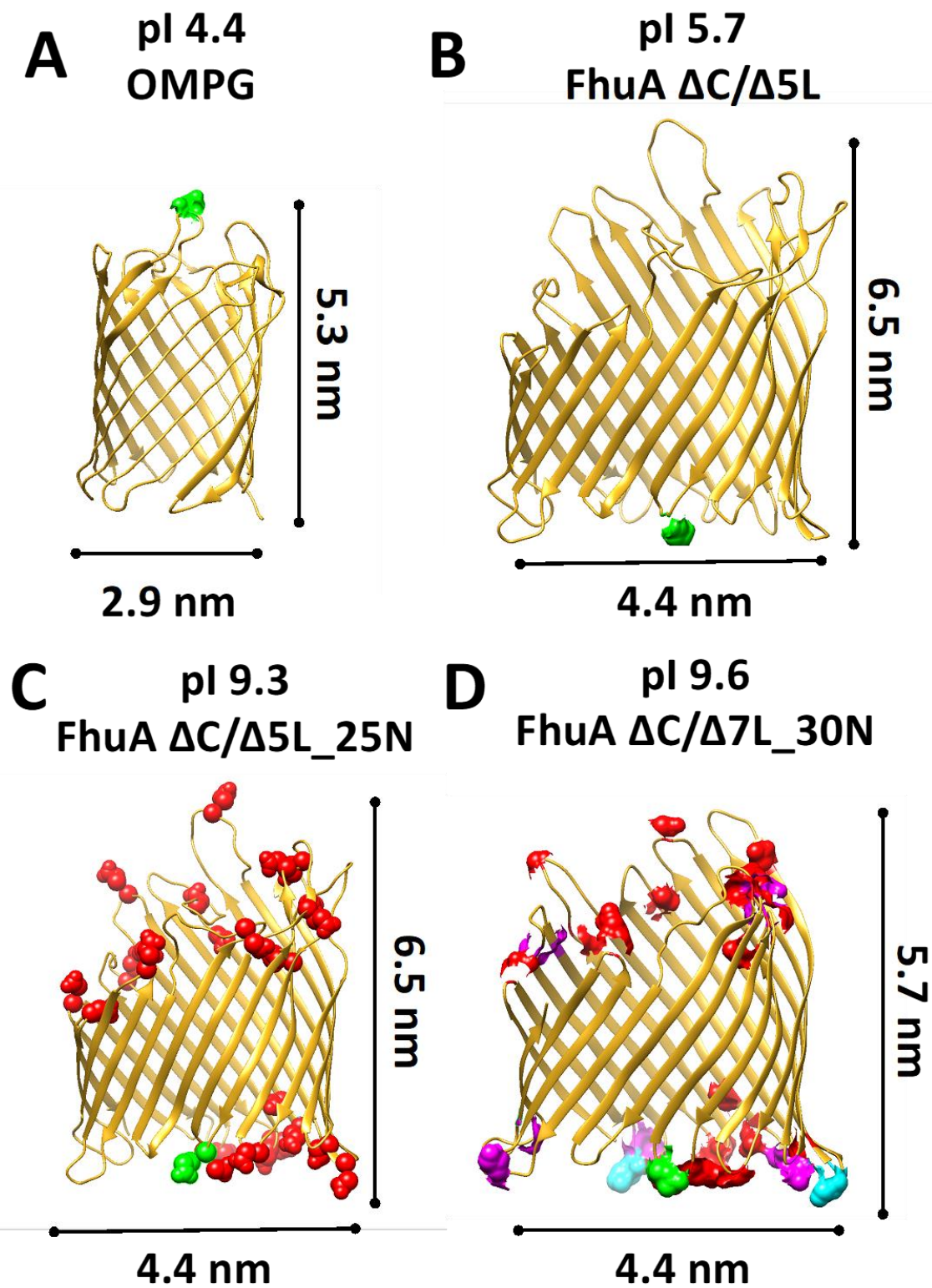


Figure 1

**Figure 1: Structural homology models of the four proteins explored in this work. (A)**

OmpG, **(B)** FhuA  $\Delta C/\Delta 5L$ , **(C)** FhuA  $\Delta C/5L_{25N}$ , **(D)** FhuA  $\Delta C/\Delta 7L_{30N}$ . The native residues are shown in gold. Charge neutralizations that occur in both FhuA  $\Delta C/\Delta 5L_{25N}$  and FhuA  $\Delta C/\Delta 7L_{30N}$  are shown in red. Additional charge reversals that occur only in FhuA  $\Delta C/\Delta 7L_{30N}$  are shown in cyan. Other non-charge altering mutations of FhuA  $\Delta C/\Delta 7L_{30N}$ , with respect to FhuA  $\Delta C/\Delta 5L_{25N}$ , are shown in magenta. For each protein, the position of Texas Red<sup>53</sup> is labeled in green. The corresponding isoelectric point (pI) of each protein is presented on the top of individual panels.

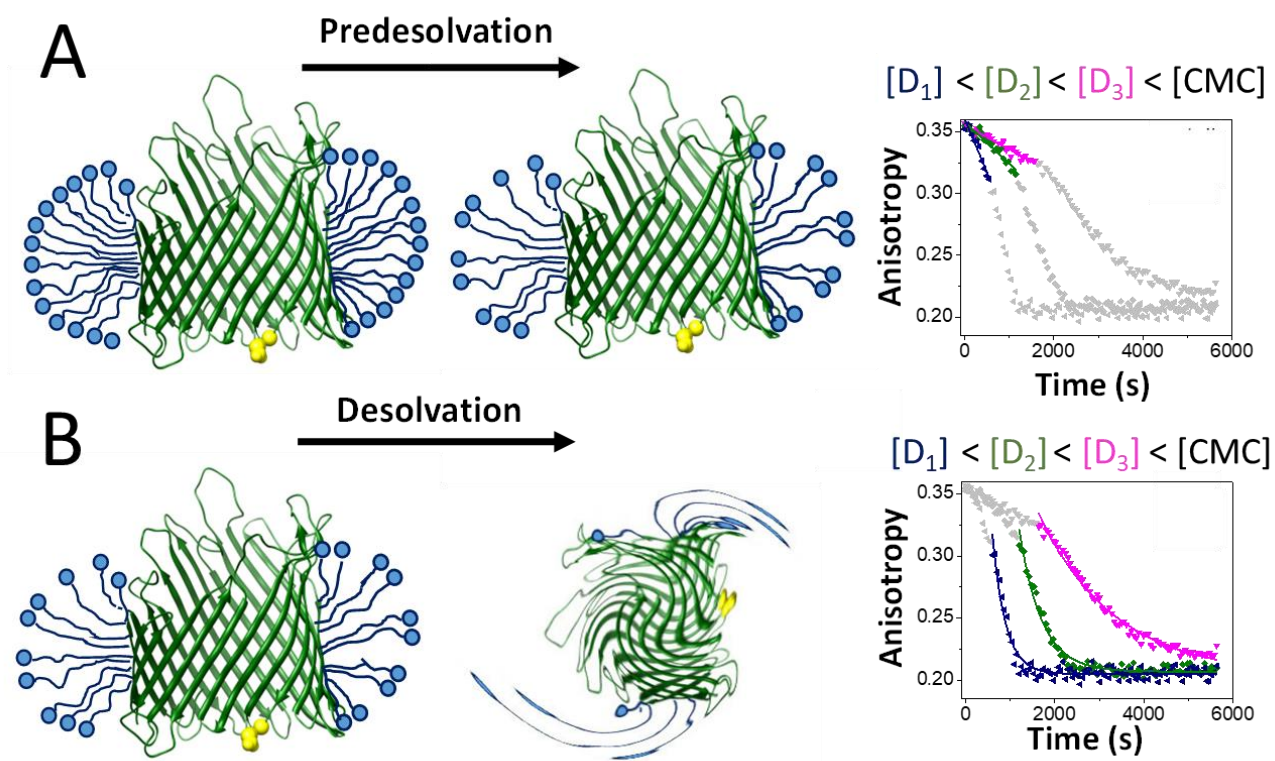


Figure 2

**Figure 2:** Cartoon illustrating the two phases noted as a result of detergent depletion within the sample well. (A) Predesolvation; (B) Detergent desolvation. Predesolvation phase is accompanied by the dissociation of a small number of detergent monomers from proteomicelles, contributing to a low modification of the FP anisotropy. Detergent desolvation is a rapid dissociation of numerous detergent monomers in single-exponential decay fashion. The right-hand panels show typical trajectories of the FP anisotropy of the predesolvation and desolvation phases for various detergent concentrations below the CMC.

Very recently, we showed that the desorption of detergent monomers from membrane proteins undergoes two distinct phases: a slow detergent predesolvation, which is highlighted by a minor and linear decrease in the FP anisotropy (**Fig. 2A**), and a fast detergent desolvation, which is characterized by a drastic, exponential-decay change in the FP anisotropy (**Fig. 2B**).<sup>33</sup> In this work, we systematically examined the kinetic reads of the PDC interactions for  $\beta$ -barrel membrane proteins of varying surface charge. Specifically, we were able to probe time-dependent FP anisotropy changes at detergent concentrations comparable with and below the critical micelle concentration (CMC), but keeping the protein concentration constant at a low-nanomolar level. Our method enables model-dependent determinations of the kinetic rate constants and equilibrium dissociation constants of the proteomicelles. These interfacial PDC interactions were inferred for two nonionic, maltoside-containing detergents, whose CMC values are in the millimolar range. In the future, this method might be employed for rapid screening of the kinetic reads of proteomicelles under a broad range of physical and chemical conditions.

## METHODS

**Cloning, expression, and purification of membrane proteins.** The *fhua*  $\Delta c/\Delta 5l$  gene, which lacked the regions coding for five extracellular loops L3, L4, L5, L10, and L11, as well as the cork domain (C), was produced through *de novo* synthesis (Geneart, Regensburg, Germany).<sup>27, 31</sup> The *fhua*  $\Delta c/\Delta 5l_{25n}$  and *fhua*  $\Delta c/\Delta 7l_{30n}$  genes were generated by Integrated DNA Technologies (IDT, Coralville, IA) in pIDTSmart Amp vector. All genes included a 3' thrombin site and 6 $\times$ His<sup>+</sup> tag. *fhua*  $\Delta c/\Delta 5l_{t7}$  was developed using inverse PCR and pPR-IBA1-*fhua*  $\Delta c/\Delta 5l$ -6 $\times$ His<sup>+</sup> as a template. The PCR product was self-ligated for the creation of pPR-IBA1-*fhua*  $\Delta c/\Delta 5l_{t7}$ -6 $\times$ His<sup>+</sup>. The T7  $\beta$  turn (V<sup>331</sup> PEDRP<sup>336</sup>) was replaced with a cysteine-



containing, GS-rich flexible loop (GGSSGCGSSGGS) for the fluorophore grafting. Similar approach was used for the mutagenesis within the *fhuA*  $\Delta c/\Delta 5l\_25n$  and *fhuA*  $\Delta c/\Delta 7l\_30n$  genes. Protein expression and extraction of truncation FhuA<sup>29, 32</sup> mutants and OmpG<sup>34-35</sup> proteins were previously reported. In the case of OmpG, the cysteine sulfhydryl was engineered at position D224, on extracellular loop L6, using single-site mutagenesis PCR.

**Refolding of proteins.** A rapid-dilution refolding protocol was used for the refolding of all proteins.<sup>30</sup> 40  $\mu$ l of purified and guanidinium hydrochloride (Gdm-HCl)-denatured protein was 50-fold diluted into 200 mM NaCl, 50 mM HEPES, pH 7.4 solutions at 4°C, which contained detergents (Anatrace, Maumee, OH) at concentrations above their CMC. Detergent solutions were freshly produced to avoid their oxidation and hydrolysis.<sup>36</sup> Different incubation detergent concentrations were prepared, as follows: (i) 5, 20, and 50 mM n-decyl- $\beta$ -D-maltopyranoside (DM); and (ii) 50 mM 4-cyclohexyl-1-butyl- $\beta$ -D-maltoside (CYMAL-4).

**Fluorescent labeling of the FhuA and OmpG proteins.** Texas Red C2-maleimide (Thermo Fisher Scientific) was used for fluorescent labeling of all membrane proteins, as previously reported.<sup>21</sup>

**Steady-state FP anisotropy recordings.** Time-dependent FP anisotropy traces were acquired using a SpectraMax I3 plate reader (Molecular Devices, Sunnyvale, CA) equipped with a Paradigm detection cartridge for rhodamine FP spectroscopy.<sup>21</sup> These measurements were conducted using 96-well Costar assay plates (Corning Incorporated, Kennebunk, ME). The wavelengths of excitation and emission were 535 and 595 nm, respectively. The attachment site of Texas Red was chosen on the water-soluble domains of the membrane proteins, because of the

hydrophilic nature of this fluorophore.<sup>37</sup> The FP anisotropy depended on the orthogonal,  $I_o(t)$ , and parallel,  $I_p(t)$ , emission intensities:<sup>38-39</sup>

$$r(t) = \frac{I_p(t) - GI_o(t)}{I_p(t) + 2GI_o(t)} \quad (1)$$

where,  $G$  is a sensitivity correction factor for the detection modes when emission polarizers are oriented vertically and horizontally, as follows:

$$G = \frac{I_{HV}}{I_{HH}} \quad (2)$$

Here,  $I_{HH}$  is the intensity with both the excitation and emission polarizers in a horizontal orientation, whereas  $I_{HV}$  shows the intensity with the excitation and emission polarizers oriented horizontally and vertically, respectively. The experimental FP data were presented as average  $\pm$  SD over a number of at least three distinct acquisitions. The time-dependent, steady-state FP anisotropy traces were acquired with diluted detergents, while keeping the final protein concentration constant at 28 nM. These detergent dilutions were conducted by titrating the refolded protein samples with buffer containing detergents at various concentrations. The final detergent concentration was inferred using the equation:

$$C_f V = C_s V_s + C_d V_d \quad (3)$$

$V$  and  $C_f$  indicate the well volume and final detergent concentration of the protein sample, respectively.  $C_s$  and  $C_d$  show the detergent concentrations of the refolded protein (starting concentrations) and diluting buffer, respectively.  $V_s$  and  $V_d$  denote the volume of the refolded protein sample at a starting detergent concentration and the volume of the diluting buffer containing detergent at a given concentration, respectively. For DM, we used three concentrations below the CMC (0.45, 0.85, and 1 mM) and four concentrations above the CMC (2.5, 5, 10, and 20 mM). For CYMAL-4, four concentrations below the CMC (1, 2, 4, and 7 mM) and two concentrations above the CMC (12 and 50 mM) were employed. It was noted that

in the case of DM-solvated FhuA variants the FP anisotropy curves were very noisy at extreme pH values (e.g., pH 4.6 and pH 10.0) and detergent concentrations lower than 1 mM. This outcome precluded the determination of statistically significant rate constants of association and dissociation. In addition, the FP anisotropy decayed even at detergent concentrations above the CMC, suggesting a slow increase in the tumbling rate of the proteomicelles under these experimental conditions. Therefore, we expanded the dilution spectrum of DM in the range of 1-50 mM for these specific cases. The self-quenching of Texas Red did not induce a time-dependent reduction in the FP anisotropy.<sup>35</sup> Radical detergent depletion within the wells increased protein aggregation, but without impacting the optical signal-to-noise ratio of the FP anisotropy. The experimental uncertainty was affected at detergent concentrations below the CMC as compared to that at concentrations above the CMC, most likely because of the coexistence of complex substates produced by soluble and insoluble protein aggregates.

**Minimizing the effects of light scattering.** These studies involved the presence of nanoscopic particles within the sample well, such as detergent micelles, proteomicelles and protein aggregates. Therefore, these steady-state FP anisotropy recordings were subject to light scattering signals produced by these particles in solution and at detergent concentrations either below or above the CMC. The major contributions to light scattering are the Rayleigh and Raman factors, which are characterized by light intensity functions proportional to the power of  $\lambda^{-4}$ , where  $\lambda$  is the emission wavelength.<sup>20, 40</sup> For that reason, our assay was conducted using a long emission wavelength. Moreover, the concentration of the Texas Red-labeled proteins was increased up to a critical value, beyond which the FP anisotropy readout was independent of the protein concentration.<sup>35</sup> In addition, SpectraMax I3 plate reader features excitation and emission

filters that form a spectral gap of 60 nm, contributing to a reduction in the light scattering signals. Finally, additional control experiments reinforced the minimized contributions of light scattering to the FP anisotropy readout. For example, at increased detergent concentrations above the CMC, the FP anisotropy readout reached a well-defined plateau with a maximum value,  $r_{max}$ . In the presence of significant light scattering contributions, enhanced concentrations of detergent micelles above the CMC would gradually increase the steady-state FP anisotropy, which was not found in our studies.

**Analysis of the predesolvation and desolvation rates.** The observed predesolvation rate constants ( $k_{obs}^{pre}$ ) were determined using a linear fit of the time-dependent FP anisotropy,  $r(t)$ , at detergent concentrations below the CMC (**Supporting Information, Tables S1-S8**):

$$r(t) = -k_{obs}^{pre}t + r_{max} \quad (4)$$

where,  $r_{max}$  is the maximum FP anisotropy recorded at time zero. Here,  $t$  is the recording time during the predesolvation phase. In fact,  $k_{obs}^{pre}$  is the apparent zero-order rate constant for the predesolvation reaction of the proteomicelles. On the other hand, the observed desolvation rate constants,  $k_{obs}^{des}$ , were determined at various detergent concentrations below the CMC using a single-exponential fit of the time-dependent FP anisotropy (i.e.,  $k_{obs}^{des}$  is  $1/\tau$ , where  $\tau$  is the desolvation time constant):

$$r(t) = r_d e^{-\frac{t}{\tau}} + r_{min} \quad (5)$$

where  $r_{min}$  is the minimum recorded FP anisotropy at time infinity of the desolvation phase.  $t$  indicates the recorded time during the desolvation phase. This time includes the total time of the predesolvation phase,  $T^{pre}$ . In general, the observed desolvation rate constant,  $k_{obs}^{des}$ , was determined by a single-exponential decay fit of the time-dependent FP anisotropy,  $r(t)$ . In fact,

$k_{obs}^{des}$  is the apparent first-order rate constant<sup>41</sup> for the desolvation reaction of the proteomicelles. This rate constant includes a composite mixture of the kinetic rate constants of association ( $k_{on}$ ) and dissociation ( $k_{off}$ ) (**Supporting Information**).<sup>42</sup> Deviations from this pattern occurred in a number of cases that were treated by a linear time-dependence fit. In Eq. (5),  $r_d$  is a constant, so that the initial FP anisotropy during the desolvation phase,  $r_{in}$ , is given by the following equation:

$$r_{in} = r(T^{pre}) = r_d e^{-\frac{T^{pre}}{\tau}} + r_{min} \quad (6)$$

which provides the  $r_d$  constant:

$$r_d = \frac{r_{in} - r_{min}}{e^{-\frac{T^{pre}}{\tau}}} \quad (7)$$

Using eqns. (5) and (7), one derives the time-dependent FP anisotropy for the detergent desolvation phase of proteomicelles:

$$r(t) = (r_{in} - r_{min}) e^{-\frac{t - T^{pre}}{\tau}} + r_{min} \quad (8)$$

The time-dependent protein concentration that is still detergent solvated,  $[P(t)]$ , is given by the following equation:

$$[P(t)] = [P_t] \left( \frac{r(t) - r_{min}}{r_{in} - r_{min}} \right) \quad (9)$$

Therefore, the time-dependent observed desolvation rate is:

$$R^{des}(t) = \left| \frac{d[P(t)]}{dt} \right| = [P_t] \frac{1}{\tau e^{-\frac{t - T^{pre}}{\tau}}} \quad (10)$$

where  $[P_t]$  is the total protein concentration at the beginning of the desolvation process. At the initial time of the desolvation process,  $t = T^{pre}$ . Consequently, the initial observed desolvation rate,  $R_{in}^{des}$ , is the following:

$$R_{in}^{des} = \frac{[P_t]}{\tau} = [P_t] k_{obs}^{des} \quad (11)$$

Here,  $\Delta r = r_{in} - r_{min}$  is the absolute FP anisotropy change during the desolvation phase.

Finally, the time-independent rate of the protein predesolvation is the following:

$$R^{pre} = \frac{[P_t]}{t^{pre}} \quad (12)$$

## RESULTS

### **Kinetics of the neutral detergent – membrane protein interactions are pH dependent.**

Prior steady-state FP anisotropy studies under equilibrium conditions demonstrated that the apparent dissociation constant,  $K_d$ , of proteomicelles with maltoside-containing detergents is not generally affected by the pH.<sup>35</sup> Here, we inspected whether this is also true for the kinetic reads of proteomicelles containing either n-decyl- $\beta$ -D-maltopyranoside (DM) or 4-cyclohexyl-1-butyl- $\beta$ -D-maltoside (CYMAL-4), two nonionic detergents. DM encompasses a medium-sized hydrophobic chain with 10 alkyl carbons. CYMAL-4 includes a short hydrophobic chain with four alkyl carbons and a cyclohexyl group. The CMC values of DM and CYMAL-4 are ~1.8 and 7.6 mM, respectively.<sup>21, 36</sup> We found that at detergent concentrations much greater than the CMC, there was no significant alteration in the FP anisotropy (**Figs. 3-7; Supporting Information, Figs. S1-S3**).<sup>21</sup> Under these conditions, both OmpG<sup>43</sup> and truncation FhuA<sup>21, 27</sup> variants were fully detergent-solvated and showed a preponderant  $\beta$ -sheet structure in solution. Thus, the proteomicelles reached the slowest rotational mobility, which corresponded to the highest FP anisotropy value,  $r_{\max}$ . However, at detergent concentrations comparable with or below the CMC, the FP anisotropy showed drastic changes as a result in the desorption of detergent monomers from proteomicelles. Therefore, for these conditions the FP anisotropy varied between  $r_{\max}$ , which corresponded to slowly tumbling proteomicelles, and  $r_{\min}$ , which was reached under detergent-desolvated conditions (**Supporting Information, Figs. S4-S21**).

## DM - OmpG

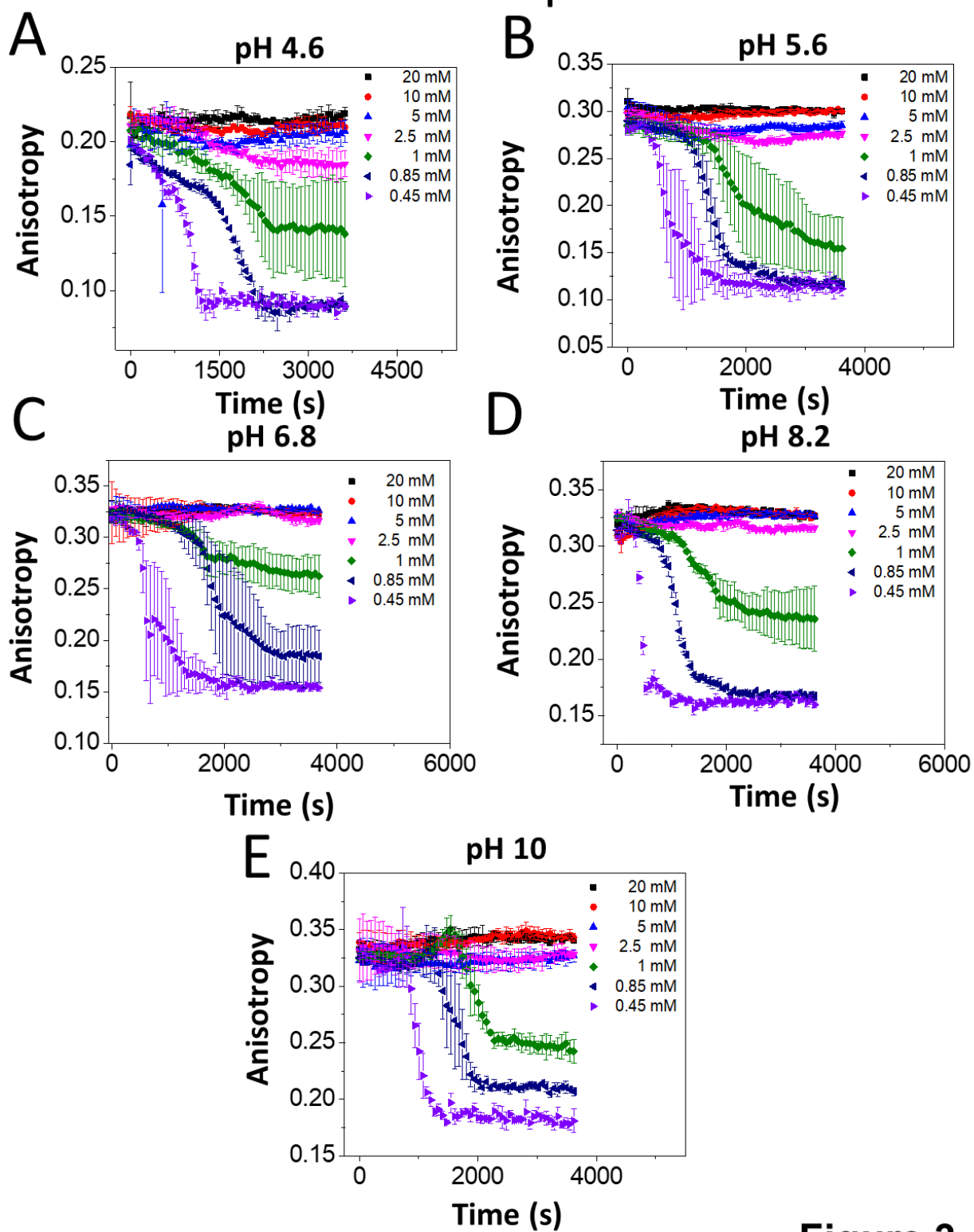


Figure 3



**Figure 3: Time-dependent anisotropy showing the DM desolvation of OmpG at various pH values.** The starting DM concentration was 20 mM. (A) pH 4.6; (B) pH 5.6; (C) pH 6.8; (D) pH 8.2; (E) pH 10.0. The FP measurements were carried out using a solution that contained 200 mM NaCl at room temperature. The buffer was either 50 mM HEPES (pH 6.8 and pH 8.2), 50 mM NaOAc (pH 4.6 and pH 5.6) or 50 mM sodium borate (pH 10.0). All data were derived as averages  $\pm$  SD of at least three independent data acquisitions.

## CYMAL-4 - OmpG

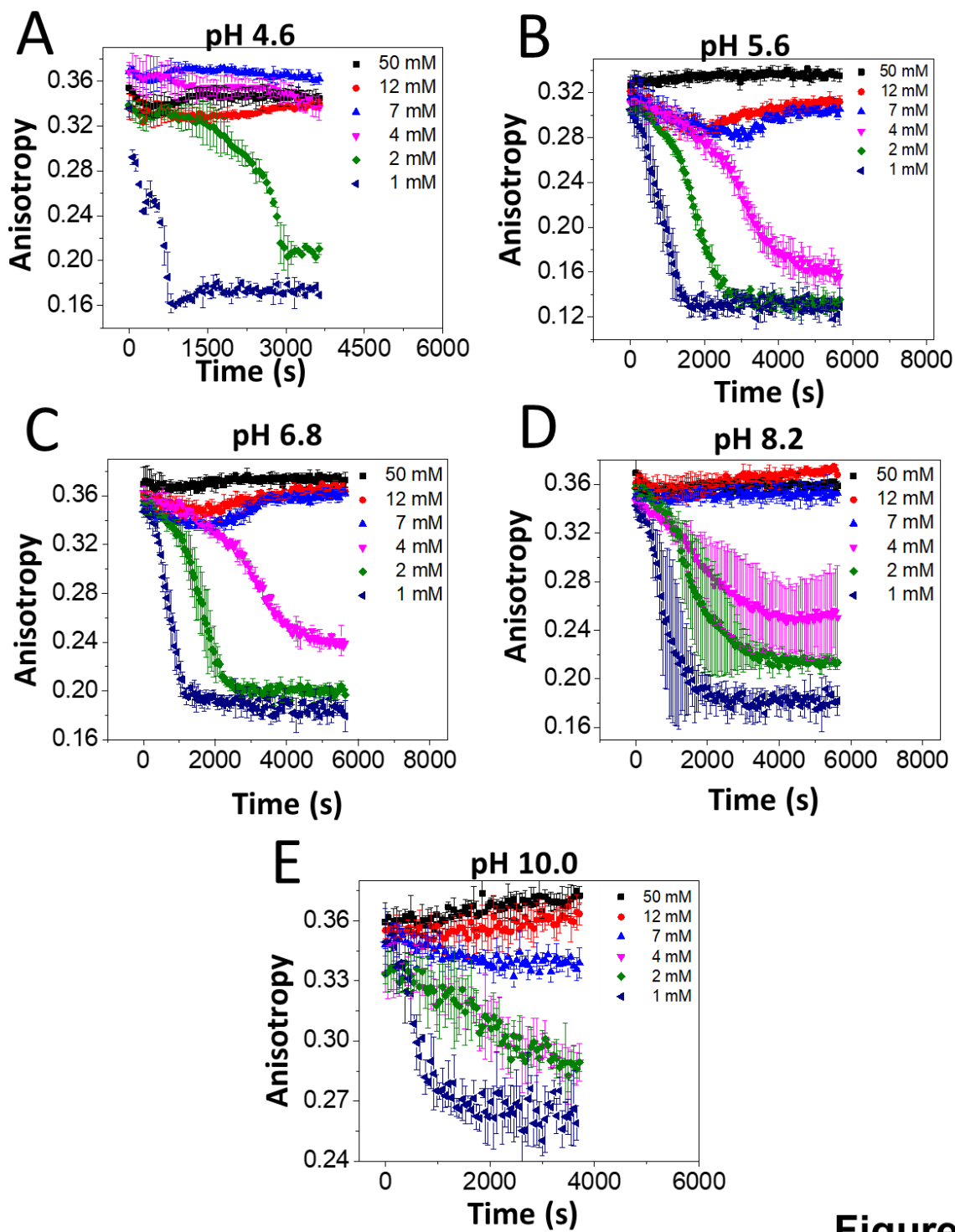


Figure 4

**Figure 4:** Time-dependent FP anisotropy showing the CYMAL-4 desolvation of OmpG at various pH values. The starting CYMAL-4 concentration was 50 mM. (A) pH 4.6; (B) pH 5.6; (C) pH 6.8; (D) pH 8.2; (E) pH 10.0. The other experimental conditions were the same as those stated in the caption of **Fig. 3**.

The linear and exponential phases of the time-dependent FP anisotropy decrease were employed to determine the apparent zero-order and first-order rate constants of the predesolvation and desolvation processes (**METHODS**), respectively. Usually, the observed predesolvation rate constants ( $k_{obs}^{pre}$ ) (**Supporting Information, Tables S1-S8**) and desolvation rate constants ( $k_{obs}^{des}$ ) (**Supporting Information, Tables S9-S16**) increased by reducing the detergent concentration within the sample well. By changing the pH, the overall protein charge of a membrane proteins is altered. Therefore, we first explored this effect using steady-state FP anisotropy measurements under detergent desolvation conditions. At pH 4.6, the  $k_{obs}^{pre}$  values for the DM-OmpG proteomicelles acquired at DM concentrations of 1, 0.85, and 0.45 mM were  $(1.9 \pm 0.1) \times 10^{-5}$ ,  $(2.0 \pm 0.1) \times 10^{-5}$ , and  $(5.2 \pm 0.4) \times 10^{-5} \text{ s}^{-1}$ , respectively (**Fig. 3; Supporting Information, Table S1**). On the other hand, the corresponding  $k_{obs}^{des}$  values for similar experimental conditions were  $(2.6 \pm 0.3) \times 10^{-3}$ ,  $(3.0 \pm 0.3) \times 10^{-3}$ , and  $(4.5 \pm 0.5) \times 10^{-3} \text{ s}^{-1}$ , respectively (**Supporting Information, Table S9**). At a slightly acidic pH of 6.8, the  $k_{obs}^{pre}$  values were  $(0.9 \pm 0.1) \times 10^{-5}$ ,  $(2.1 \pm 0.1) \times 10^{-5}$ , and  $(4.2 \pm 0.7) \times 10^{-5} \text{ s}^{-1}$ , respectively. Under identical experimental conditions, the corresponding  $k_{obs}^{des}$  values were lower than those noted at pH 4.6, as follows:  $(1.3 \pm 0.1) \times 10^{-3}$ ,  $(2.0 \pm 0.1) \times 10^{-3}$ , and  $(2.4 \pm 0.2) \times 10^{-3} \text{ s}^{-1}$ , respectively. On the contrary, higher  $k_{obs}^{des}$  values were recorded at pH 10:  $(2.4 \pm 0.2) \times 10^{-3}$ ,  $(2.7 \pm 0.2) \times 10^{-3}$ , and  $(5.1 \pm 0.2) \times 10^{-3} \text{ s}^{-1}$ , respectively. This non-monotonic pH-dependence of the  $k_{obs}^{des}$  values suggests compensatory effects of the numerous heterogeneously distributed electrostatic interactions at the PDC interface.  $k_{obs}^{pre}$  was less sensitive than  $k_{obs}^{des}$  upon pH changes. This is an intuitive finding, because it is conceivable that during the predesolvation phase only a limited number of nonionic detergent monomers detach from the proteomicelles.

On the other hand, an atypical desolvation pattern was noted with CYMAL-4-OmpG proteomicelles at pH 4.6 and at 1 and 2 mM CYMAL-4 (**Fig. 4**). For example, the FP anisotropy traces acquired at 1 mM showed a fast desolvation phase, whereas those recorded at 2 mM exhibited a long predesolvation phase. Interestingly, at a CYMAL-4 concentration of 4 mM or greater than this value,<sup>21</sup> no significant time-dependent FP anisotropy change was noted. At an acidic pH of 5.6, the  $k_{obs}^{pre}$  values for the CYMAL-4-OmpG proteomicelles at CYMAL-4 concentrations of 4, 2, and 1 mM were  $(2.0 \pm 0.1) \times 10^{-5}$ ,  $(3.4 \pm 0.2) \times 10^{-5}$ , and  $(5.8 \pm 0.3) \times 10^{-5}$  s<sup>-1</sup>, respectively (**Supporting Information, Table S5**). The corresponding  $k_{obs}^{des}$  values for identical conditions were  $(1.1 \pm 0.1) \times 10^{-3}$ ,  $(1.7 \pm 0.1) \times 10^{-3}$ , and  $(2.0 \pm 0.1) \times 10^{-3}$  s<sup>-1</sup>, respectively (**Supporting Information, Table S13**). Under a mildly acidic pH of 6.8, the  $k_{obs}^{pre}$  values for the CYMAL-4-OmpG proteomicelles at CYMAL-4 concentrations of 4, 2, and 1 mM were  $(1.7 \pm 0.1) \times 10^{-5}$ ,  $(2.7 \pm 0.1) \times 10^{-5}$ , and  $(3.0 \pm 0.6) \times 10^{-5}$  s<sup>-1</sup>, respectively. The corresponding  $k_{obs}^{des}$  values under similar conditions were close to those noted at pH 5.6, as follows:  $(1.0 \pm 0.1) \times 10^{-3}$ ,  $(2.0 \pm 0.1) \times 10^{-3}$ , and  $(2.4 \pm 0.1) \times 10^{-3}$  s<sup>-1</sup>, respectively. When these experiments were conducted at pH 10.0, a significant increase in the signal noise was recorded (**Fig. 4**), impeding an accurate determination of the observed rate constants of predesolvation and desolvation.

**The apparent first-order rate constants of detergent desolvation of the proteomicelles depend on the protein charge.** In the prior results section, we demonstrate that even if the detergent monomers are nonionic the interfacial PDC interactions might be affected by pH. Here, we asked whether these interactions with neutral detergents depend on the overall protein charge. The test case was conducted for radically altered FhuA  $\Delta C/\Delta 5L_{25N}$  and FhuA  $\Delta C/\Delta 7L_{30N}$ ,

two homologous FhuA variants whose 25 and 30 negative charges were neutralized with respect to FhuA  $\Delta C/\Delta 5L$  protein. The presence of slow predesolvation and fast desolvation phases were also noted for these proteins that encompassed radical alterations in the overall protein charge (**Figs. 5-7**). At 1 mM DM and pH 5.6, we acquired desolvation rate constants of  $(1.6 \pm 0.1) \times 10^{-3}$ ,  $(3.4 \pm 0.2) \times 10^{-3}$ , and  $(1.1 \pm 0.1) \times 10^{-3} \text{ s}^{-1}$  for FhuA  $\Delta C/\Delta 5L$ , FhuA  $\Delta C/\Delta 5L_{25N}$ , and FhuA  $\Delta C/\Delta 7L_{30N}$ , respectively (**Fig. 8A; Supporting Information, Tables S10-S12**). Under similar conditions, but at slightly alkaline pH 8.2, these values were  $(1.9 \pm 0.2) \times 10^{-3}$ ,  $(3.4 \pm 0.2) \times 10^{-3}$ , and  $(2.6 \pm 0.2) \times 10^{-3} \text{ s}^{-1}$ , respectively. If the DM concentration was reduced to 0.85 mM, then the  $k_{obs}^{des}$  values at an acidic pH of 5.6 were  $(3.2 \pm 0.1) \times 10^{-3}$ ,  $(3.4 \pm 0.2) \times 10^{-3}$ , and  $(2.2 \pm 0.1) \times 10^{-3} \text{ s}^{-1}$ , respectively (**Fig. 8B**). At the same time, at pH 8.2, a significant reduction in the  $k_{obs}^{des}$  values was noted for the acidic FhuA derivative, but substantially increased values were determined for the basic FhuA variants. This finding indicates stronger interfacial PDC interactions of the acidic FhuA protein as compared to those corresponding to basic FhuA variants.

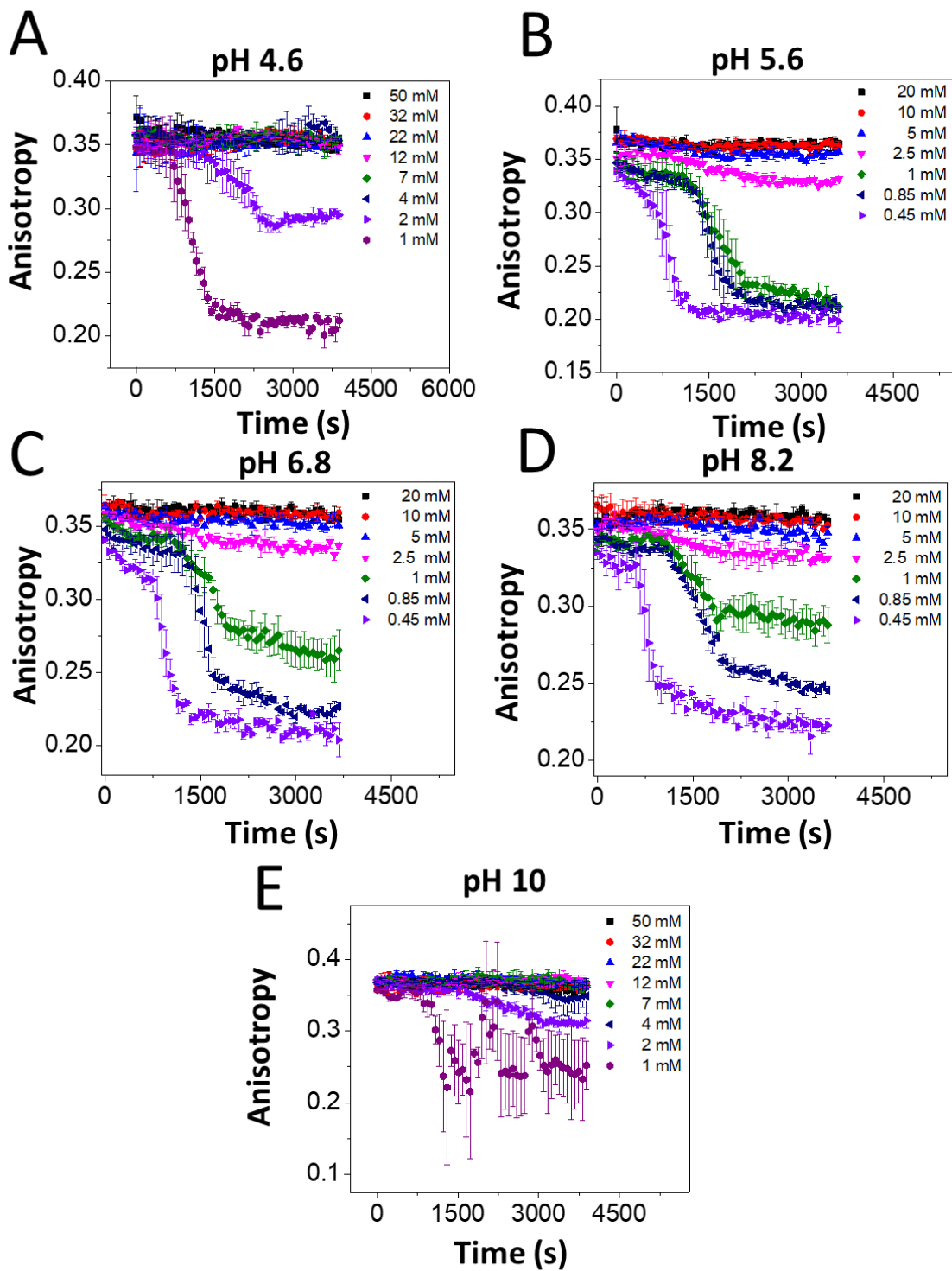
DM - FhuA  $\Delta C/\Delta 5L$ 

Figure 5

**Figure 5:** Time-dependent FP anisotropy showing the DM desolvation of FhuA  $\Delta C/5\Delta L$  at various pH values. (A) pH 4.6; (B) pH 5.6; (C) pH 6.8; (D) pH 8.2; (E) pH 10.0. The other experimental conditions were the same as those stated in the caption of **Fig. 3**.



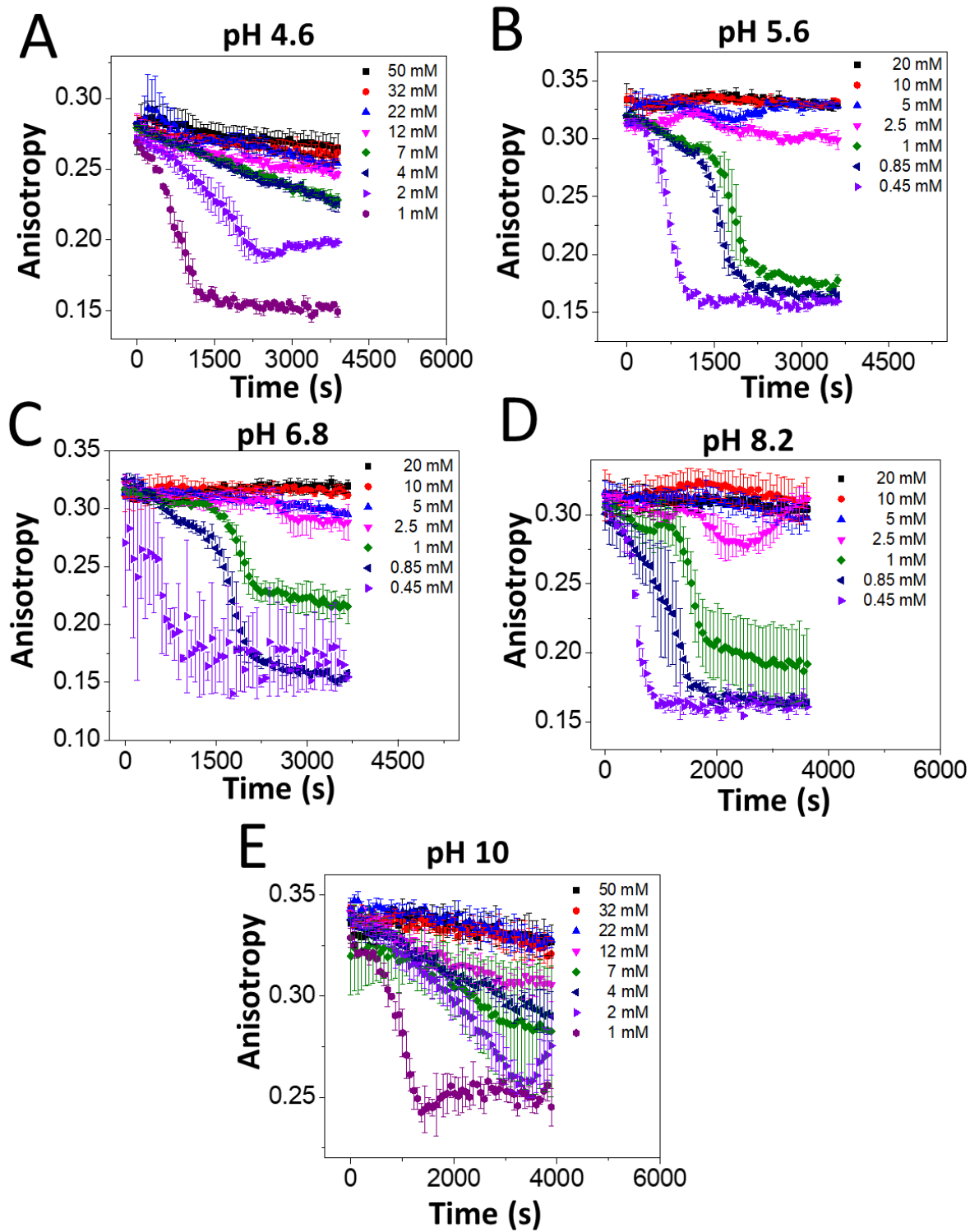
DM - FhuA  $\Delta C/\Delta 5L_{25N}$ 

Figure 6

**Figure 6: Time-dependent FP anisotropy showing the DM desolvation of FhuA**

$\Delta C/5\Delta L_{25N}$  at various pH values. (A) pH 4.6; (B) pH 5.6; (C) pH 6.8; (D) pH 8.2; (E) pH 10.0. The other experimental conditions were the same as those stated in the caption of **Fig. 3**.

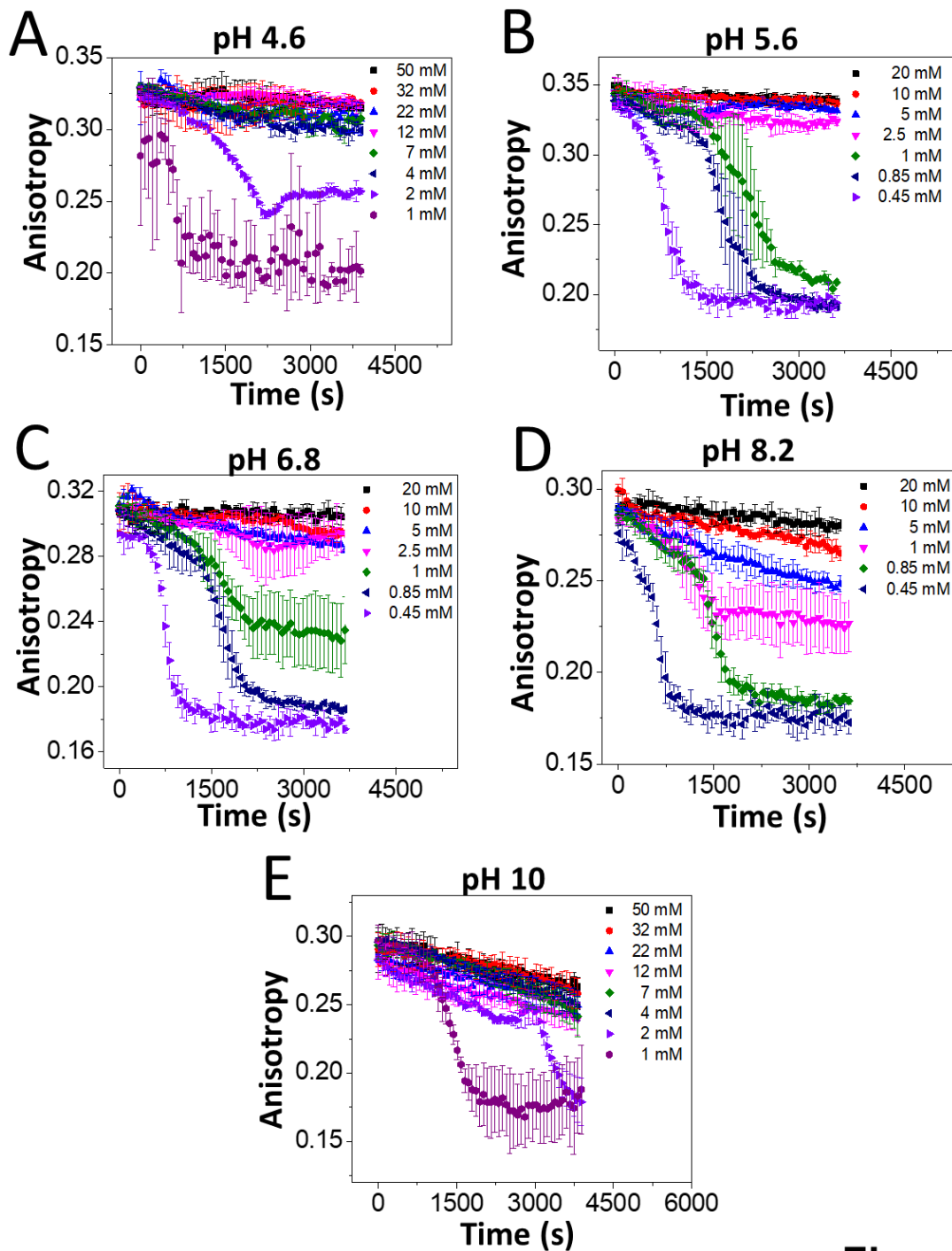
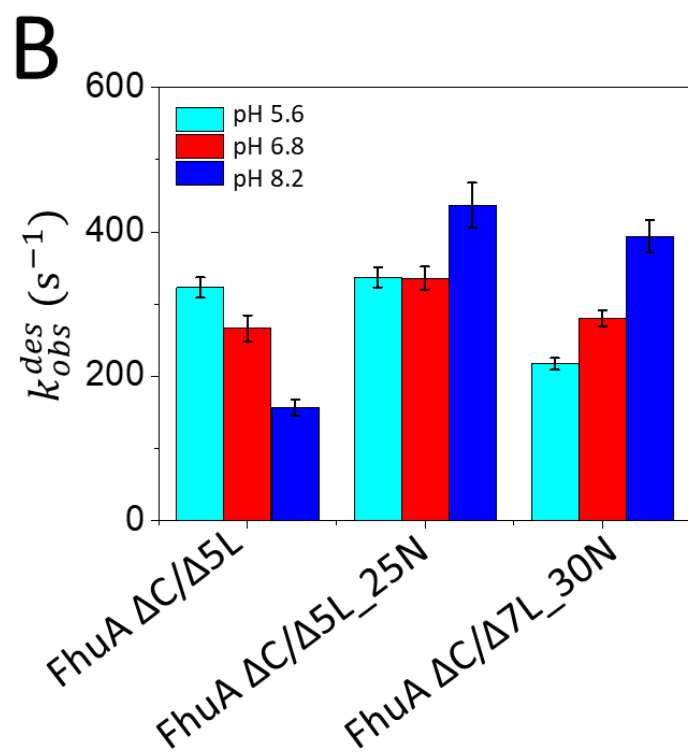
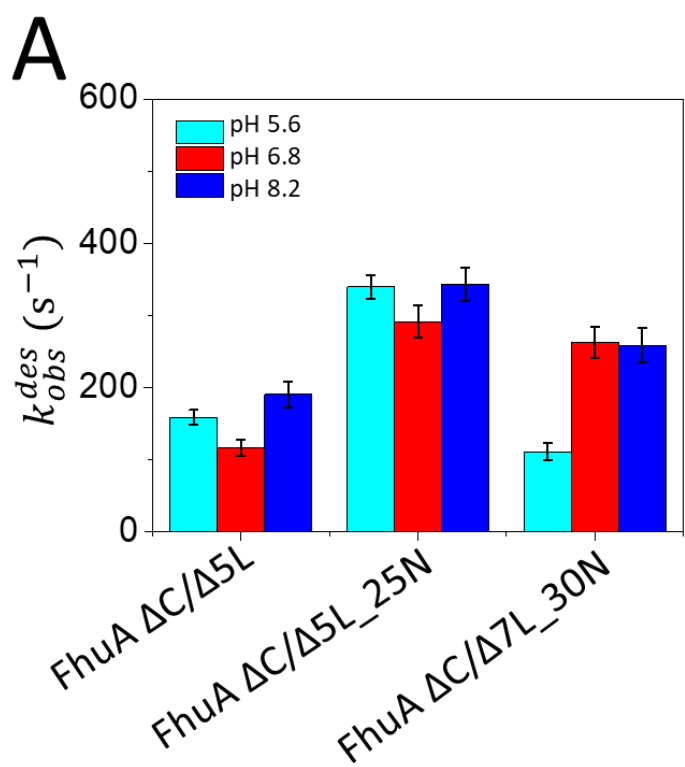
DM - FhuA  $\Delta C/\Delta 7L_{30N}$ 

Figure 7

**Figure 7: Time-dependent FP anisotropy showing the DM desolvation of FhuA**

**$\Delta C/7\Delta L_{N30}$  at various pH values. (A) pH 4.6; (B) pH 5.6; (C) pH 6.8; (D) pH 8.2; (E) pH 10.0.** The other experimental conditions were the same as those stated in the caption of **Fig. 3**.



**Figure 8**

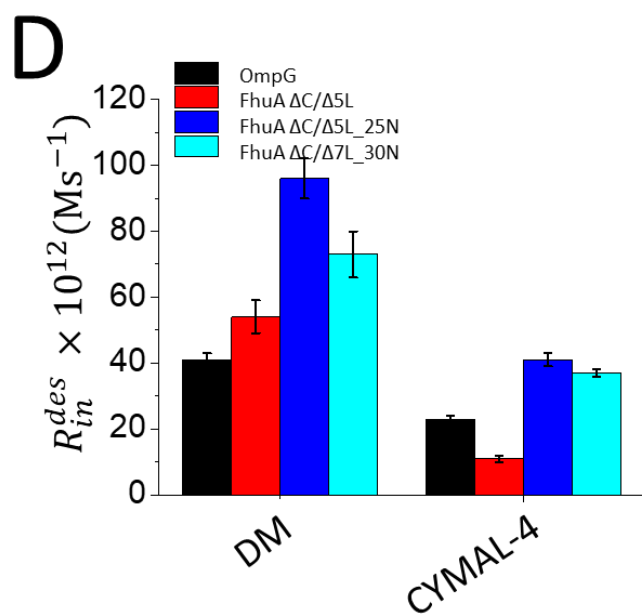
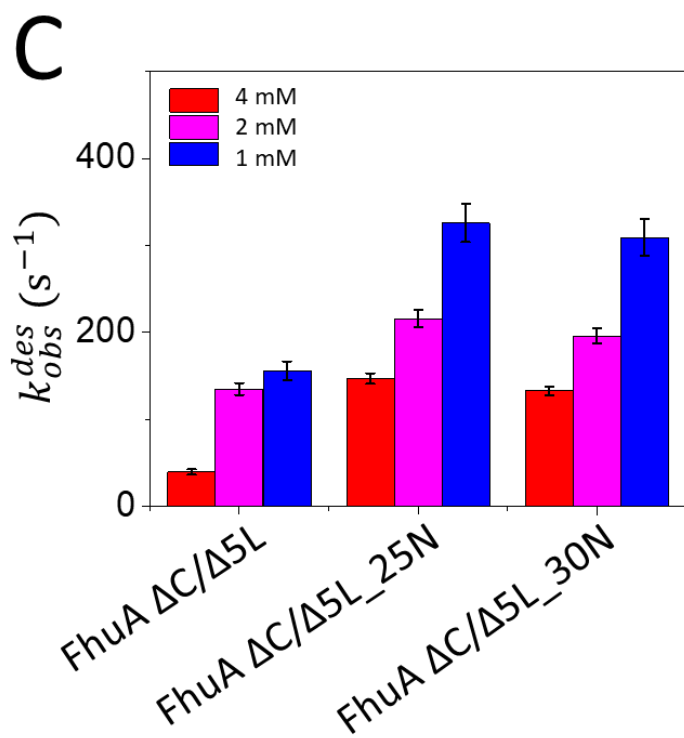


**Figure 8 - Continuation**

**Figure 8: Dependence of the observed desolvation rate constants,  $k_{obs}^{des}$ , on the protein charge.**

(A) The values were determined for the DM desolvation of FhuA  $\Delta C/\Delta 5L$ , FhuA  $\Delta C/\Delta 5L_{25N}$ , and FhuA  $\Delta C/\Delta 7L_{30N}$  at 1 mM DM; (B) The values were determined for the DM desolvation of FhuA  $\Delta C/\Delta 5L$ , FhuA  $\Delta C/\Delta 5L_{25N}$ , and FhuA  $\Delta C/\Delta 7L_{30N}$  at 0.85 mM DM; (C) The values were determined for the CYMAL-4 desolvation of FhuA  $\Delta C/\Delta 5L$ , FhuA  $\Delta C/\Delta 5L_{25N}$ , and FhuA  $\Delta C/\Delta 7L_{30N}$  at pH 8.2. Different vertical columns show data acquired at various CYMAL-4 concentrations; (D) Illustration of the initial desolvation rates,  $R_{in}^{des}$ , which were determined for proteins of varying overall charge at pH 8.2. The final detergent concentrations for DM and CYMAL-4 were 1 and 4 mM, respectively. The other experimental conditions were the same as those stated in the caption of **Fig. 3**.

**Kinetics but not energetics of the adhesive PDC interactions depend on the protein charge.**

These steady-state FP anisotropy measurements enabled the determination of the  $k_{obs}^{des}$  values at detergent concentrations below the CMC. In most cases examined in this study, the  $k_{obs}^{des}$  values scaled with the detergent concentration in a linear fashion (**Supporting Information, Figs. S22-S29**). Therefore, we formulated a simple kinetic model of proteomicelles, which includes the bimolecular association of a membrane protein with a detergent micelle and unimolecular dissociation of a membrane protein from a micelle (**Supporting Information**).<sup>37</sup> The two processes are quantitatively assessed by the apparent model-dependent rate constants of association,  $k_{on}$ , and dissociation,  $k_{off}$ . These data, which were determined for the four proteins, two maltoside-containing detergents, and three pH values, are illustrated in **Fig. 9A** and **Fig. 9B**, respectively.



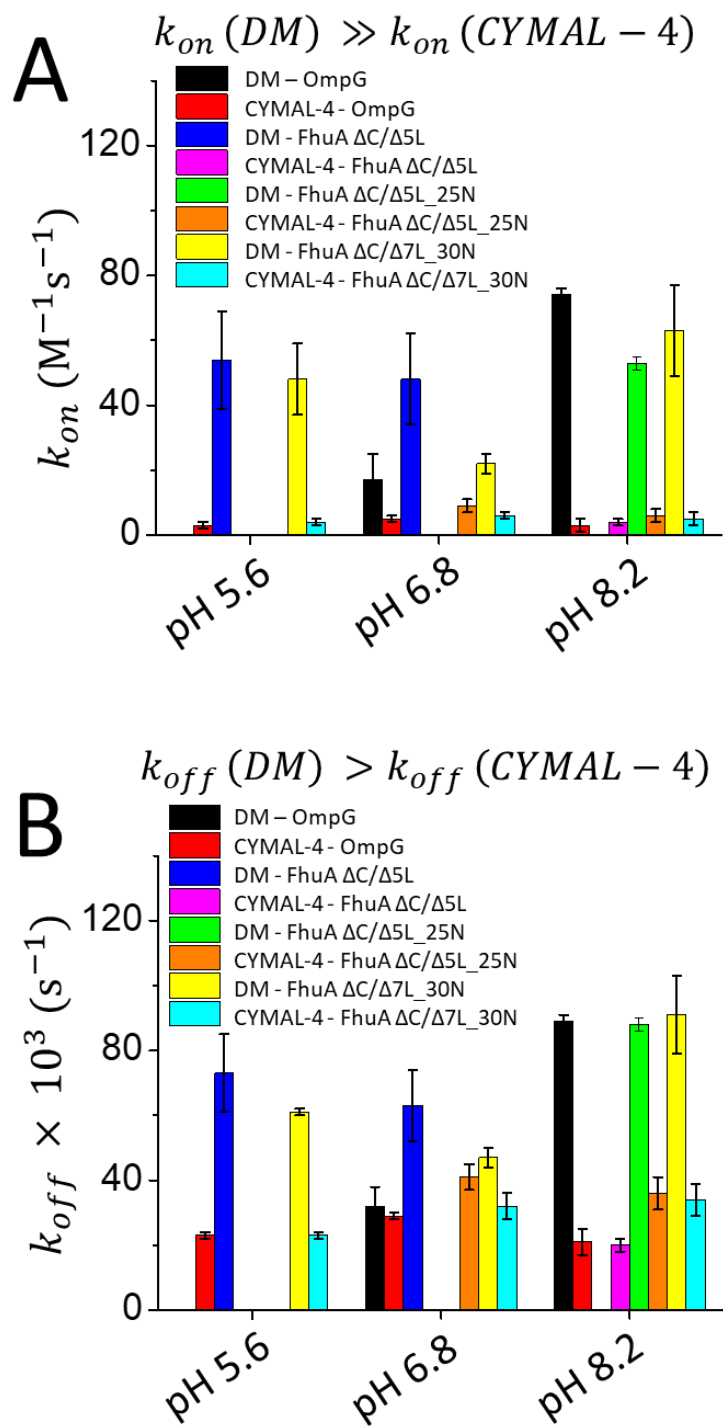


**Figure 9**

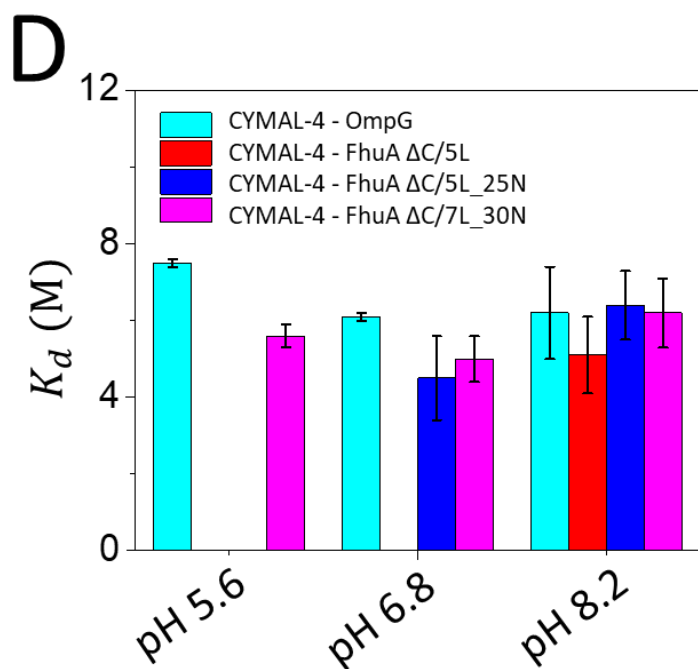
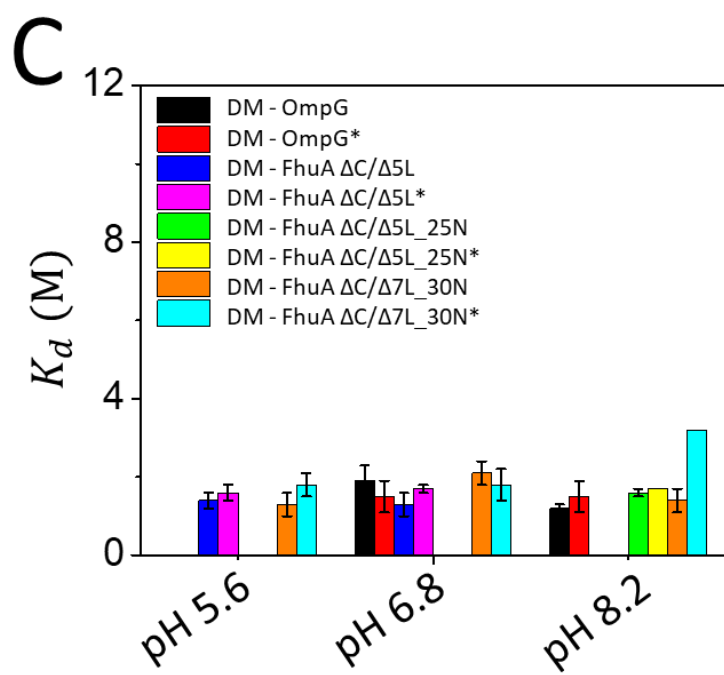


**Figure 9 - continuation**

**Figure 9: The apparent rate constants of the interfacial PDC interactions of proteomicelles.**

(A) The association rate constants of DM-containing proteomicelles are much greater than those of CYMAL-4-containing proteomicelles; (B) The dissociation rate constants of DM-containing proteomicelles are greater than those of CYMAL-4-containing proteomicelles; (C) The model-dependent (this work) and model-free<sup>34</sup> equilibrium dissociation constants,  $K_d$ , of the DM-containing proteomicelles; (D) The model-dependent apparent dissociation constants,  $K_d$ , of the CYMAL-4-containing proteomicelles. The other experimental conditions were the same as those stated in the caption of **Fig. 3**.

The impact of protein electrostatics on adhesive interactions was also noted in the case of CYMAL-4-FhuA proteomicelles. For example, at pH 8.2 the  $k_{obs}^{des}$  values acquired with the acidic FhuA mutant were significantly smaller than those obtained for the basic FhuA variants (**Fig. 8C**; **Supporting Information, Tables S14-S16**). **Fig. 8D** illustrates the initial desolvation rates,  $R_{in}^{des}$  (**METHODS**), which were inferred for various types of proteomicelles at detergent concentrations of 1 mM DM and 4 mM CYMAL-4. These concentrations are about ~55% and ~52% of their corresponding CMC values, respectively. For both cases DM- and CYMAL-4-containing proteomicelles, the initial desolvation rates of the acidic proteins OmpG and FhuA  $\Delta C/\Delta 5L$  were lower than those determined for the basic truncation FhuA mutants (**Fig. 8D**; **Supporting Information, Table S17**). This outcome suggests stronger adhesive forces of the acidic protein-containing proteomicelles than those interfacial interactions of the basic protein-containing proteomicelles at pH 8.2.

**Kinetics but not energetics of the adhesive PDC interactions depend on the protein charge.** In most cases examined in this study, the  $k_{obs}^{des}$  values scaled with the detergent concentration in a linear fashion (**Supporting Information, Figs. S22-S29**). Therefore, we formulated a simple kinetic model of proteomicelles, which includes the bimolecular association of a membrane protein with a detergent micelle and unimolecular dissociation of a membrane protein from a micelle (**Supporting Information**).<sup>42</sup> The two processes are quantitatively assessed by the apparent model-dependent rate constants of association,  $k_{on}$ , and dissociation,  $k_{off}$ . These data, which were determined for the four proteins, two maltoside-containing detergents, and three pH values, are illustrated in **Fig. 9A** and **Fig. 9B**, respectively.

An immediate observation is that the  $k_{\text{on}}$  values obtained for DM are from several fold to about one order of magnitude greater than those determinations acquired for CYMAL-4 (**Fig. 9A; Supporting Information, Tables S18-S19**). For example, these  $k_{\text{on}}$  values inferred for the most basic protein, FhuA  $\Delta\text{C}/\Delta\text{7L}_{30\text{N}}$ , and DM-containing proteomicelles were  $48 \pm 11$ ,  $22 \pm 3$ , and  $63 \pm 14 \text{ M}^{-1}\text{s}^{-1}$  at pH values of 5.6, 6.8, and 8.2, respectively. Under similar experimental conditions, the  $k_{\text{on}}$  values for CYMAL-4-containing proteomicelles were  $4 \pm 1$ ,  $6 \pm 1$ , and  $5 \pm 2 \text{ M}^{-1}\text{s}^{-1}$ , respectively. The fact of the  $k_{\text{on}}$  values obtained for DM-containing proteomicelles are substantially greater than those inferred for CYMAL-4-containing proteomicelles is in accord with a longer alkyl chain of DM. The dissociation rate constants,  $k_{\text{off}}$ , of the DM-containing proteomicelles were also greater than those inferred for the CYMAL-4-containing proteomicelles (**Fig. 9B**). Therefore, the alteration in the hydrophobic interactions at the PDC interface through the length of the alkyl chain has a significant effect on the association rate constants. We were able to calculate the apparent equilibrium dissociation constants of the PDC using the model-dependent  $k_{\text{on}}$  and  $k_{\text{off}}$  values (e.g.,  $K_{\text{d}} = k_{\text{off}}/k_{\text{on}}$ ). These determinations neglected the contributions of the predesolvation phases (**Fig. 9C** and **Fig. 9D**). Remarkably, the model-dependent apparent  $K_{\text{d}}$  values for DM-containing proteomicelles were comparable with the  $\text{CMC}^{\text{DM}}$  ( $\sim 1.8 \text{ mM}$ ) (**Supporting Information, Table S18**),<sup>35-36</sup> suggesting that the adhesion forces between the membrane proteins and DM detergent monomers are well balanced by the cohesive forces among the detergent monomers. Finally, these equilibrium constants were neither dependent on the overall protein charge nor sensitive to alterations in pH, contrasting the outcomes pertaining to observed desolvation constants as well as the rate constants of association and dissociation (**Fig. 9C, Fig. 9D**).

In this paper, we show a semiquantitative approach for the determination of model-dependent association and dissociation rate constants of proteomicelles. To the best of our knowledge, this is the first kinetic method of proteomicelles that has potential for high-throughput screening,<sup>19-20</sup> because of its amenability to a 1536-well, plate-reader format. The central player of this approach is a bright,<sup>39, 44</sup> optically stable,<sup>39, 44</sup> and pH insensitive<sup>45</sup> Texas Red fluorophore. In addition, the photophysics of Texas Red is not sensitive to its environmental changes,<sup>46</sup> permitting these extensive measurements in a fairly broad range of physical and chemical circumstances. Here, Texas Red was covalently attached either on a flexible loop (e.g., OmpG) or on a  $\beta$  turn (e.g., FhuA derivative) using maleimide chemistry. Because the fluorophore was not located within the core of the folded  $\beta$ -barrel protein, but at its periphery, the recorded FP anisotropy is not directly related to protein folding, contrasting an intrinsic, internal tryptophan probe.<sup>13</sup> A sharp decrease in the FP anisotropy is most likely directly determined by the reduction in the hydrodynamic radius of the proteomicelle,  $R_h$ , resulting from detergent desorption at the protein surface. Therefore, we think that FP anisotropy curves are not expectedly sensitive to changes in the site of fluorescent labeling on the protein surface.

Recently, we have used this approach for screening detergents of varying physicochemical properties in order to select those that exhibit satisfactory solubilizing features.<sup>21</sup> The value of the steady-state FP anisotropy followed a two-state transition when the protein sample was brought from a detergent concentration greater than the CMC to a detergent concentration below the CMC. The isothermal detergent desorption curves were used to infer the equilibrium dissociation constants of the proteomicelles containing  $\alpha$ -helical membrane proteins.<sup>35</sup> The

process of detergent desorption showed the existence of slow predesolvation and fast desolvation phases for detergents with excellent solubilizing characteristics.<sup>33</sup> The kinetic details of the interfacial PDC interactions represent a foundation for developing novel protocols employed in the functional reconstitution of membrane proteins. Previously, isothermal titration calorimetry (ITC)<sup>47</sup> has been successfully employed to unravel equilibrium phase diagrams of complex ternary mixtures of lipid-detergent-protein systems.<sup>11, 48</sup> This information has practical implications for the protein reconstitution into lipid vesicles.

Our FP anisotropy approach is also facilitated by the fact that the steady-state FP anisotropy is insensitive to changes in protein concentration.<sup>49</sup> Accordingly, a gradual decrease in the effective detergent-solubilized protein concentration, which potentially results from unproductive aggregation,<sup>10, 12</sup> does not impair the optical signal-to-noise ratio. Indeed, the truncation FhuA variants are highly prone to aggregation as a result of detergent depletion within the sample well at concentrations well below the CMC. Despite these environmentally harsh conditions for these  $\beta$ -barrel membrane proteins, we were still able to measure time-dependent changes in the FP anisotropy that reflect the decrease of the proteomicelle size in a reproducible fashion. Gradual protein aggregation might have various effects on the FP readout, including quenching. According to Perrin's equation,<sup>20</sup>  $r_o/r$  is an additive function of  $6D_r\tau_F$ , where  $r_o$ ,  $r$ ,  $D_r$ , and  $\tau_F$  denote the fundamental maximum FP anisotropy, recorded steady-state FP anisotropy, rotational diffusion coefficient of the proteomicelle, and fluorescence lifetime of the fluorophore, respectively. Therefore, quenching increases the FP anisotropy. Second, protein aggregation, even without quenching, decreases the tumbling rate of the detergent-desolvated proteins. Third, it is conceivable that a residual amount of bound detergent monomers still exists under detergent

depletion conditions. These effects likely increase the  $r_{\min}$  values depending on their relative impact on the raw FP signal at detergent concentrations much lower than the CMC. In accord with these expectations, we often observed elevated  $r_{\min}$  states in these FP anisotropy measurements. The truncation FhuA variants exhibit an  $r_{\min}$  of  $\sim 0.16$  under fully denaturing conditions in the presence of chaotropic agents,<sup>21</sup> but time-dependent FP anisotropy measurements during detergent desolvation phase at times showed the  $r_{\min}$  values even greater than 0.2.

On the other hand, at detergent concentrations much greater than the CMC, we recorded high FP anisotropy values with  $r_{\max}$  of  $\sim 0.3$  or even greater, approaching the fundamental maximum FP anisotropy,  $r_o$  ( $r_o = 0.4$ ).<sup>50</sup> This reason is primarily determined by probing relatively slow rotational diffusion mobilities of the membrane proteins. Under these conditions, the diffusional correlation times are slightly greater than the fluorescence lifetime of Texas Red ( $\tau_F = 4.2$  ns).<sup>44</sup> High anisotropy data points indicate that the majority of the emitted photons maintain their original polarization. The high FP anisotropy is related not only to the size of the membrane protein, but also to the overall size of micelles, so that these values are expected under detergent-mediated refolding conditions.

Different groups routinely recorded steady-state FP anisotropy values of  $\sim 0.3$  under equilibrium conditions.<sup>44, 49, 51-52</sup> For example, Qiao and coworkers (2011) found anisotropy changes between 0.1 and 0.3 when Texas Red was attached to short peptides forming complexes with antibodies.<sup>53</sup> Again, such a high FP anisotropy value of  $\sim 0.3$  is expected under conditions in which the tumbling rate of the peptide-protein complex is drastically slowed down. Here, we provide compelling evidence for the high sensitivity and specificity of our method, which in



many examples feature FP anisotropy changes of  $\sim 0.15$ , namely  $\sim 38\%$  out of the maximum anisotropy range. Interestingly, at final detergent concentrations much greater than the CMC, the steady-state FP anisotropy remains fairly unchanged at a value  $r_{\max}$ , suggesting that the proteomicelles reach the lowest rotational mobilities under this experimental circumstance. This situation corresponds to the highest hydrodynamic radius of proteomicelles. Such an outcome is somewhat counterintuitive, because of the gradually enhanced solution viscosity at increased detergent concentrations. However, our finding is in good accord with prior NMR studies performed by Stanczak and coworkers,<sup>54</sup> who also discovered that the hydrodynamic radius of the PDC containing n-decylphosphocholine (Fos-10) and outer membrane protein X (OmpX) is not affected by greatly increased Fos-10 concentrations above the CMC.

The observed predesolvation and desolvation rate constants depend on the alkyl chain of the detergent monomers, charge of the membrane protein, and pH of the interfacial PDC space. These variables modulate the adhesion forces of the proteomicelles between detergent monomers and membrane proteins. Notably, the observed desolvation rate constants,  $k_{obs}^{des}$ , are generally greater for the basic homologous FhuA variants than those acquired for the acidic proteins OmpG and FhuA  $\Delta C/\Delta 5L$ . A deviation from this trend occurred for DM-containing proteomicelles at pH 5.6 and 0.85 mM DM. It should be noted that changing the pH would also change the overall protein charge, explaining at least in part the non-monotonic nature of the pH dependence of  $k_{obs}^{des}$ . Furthermore, the initial desolvation rates,  $R_{in}^{des}$ , of the DM- and CYMAL-4-containing proteomicelles were also greater for the basic proteins than those obtained for the acidic  $\beta$ -barrels. This finding suggests that the adhesive interactions at the PDC interface<sup>55</sup> are generally stronger for the acidic proteins than those for the basic ones. These results agree well

with prior studies that indicated satisfactory solubilization traits of nonionic n-octyl- $\beta$ -D-glucoside (OG) for acidic but not basic  $\beta$ -barrels.<sup>21</sup>

## CONCLUSIONS

In summary, we show time-dependent kinetic determinations of proteomicelles containing  $\beta$ -barrel membrane proteins of varying isoelectric point. The model-dependent apparent  $K_d$  values are fairly independent of pH and protein charge, but they are comparable with or slightly lower than the CMC. Because the affinity constants of the PDC interactions are closely similar to the corresponding CMC, these inspected  $\beta$ -barrel membrane proteins are poor nucleators of the proteomicellization process. Therefore, the detergent monomers have little discrimination in associating either with the proteins or with themselves. The high equilibrium dissociation constants, in the millimolar range, are primarily caused by low association rate constants of the proteomicelles. Small  $k_{on}$  values, lower than  $10^2 \text{ M}^{-1}\text{s}^{-1}$ , provide a quantitative confirmation of fairly low diffusion coefficients of hydrophobic molecules, either detergent monomers or membrane proteins, in aqueous phase. Further adaptations of this approach will likely impact accelerated discoveries in the synthetic chemistry of non-conventional detergents<sup>56</sup> as well as in the structural, physical, and chemical biology of membrane proteins.

**SUPPORTING INFORMATION.** (i) Time-dependent FP anisotropy changes of membrane proteins of varying isoelectric point (pI) at detergent incubations above and below the CMC, and in buffers of varying pH; (ii) Curve fits of the predesolvation and desolvation phases at detergent concentrations below the CMC and in buffers of varying pH; (iii) Determination of the predesolvation rates of protein nanopores of varying pI, at detergent concentrations below the CMC, and in buffers of varying pH; (iv) Determination of the desolvation rate and time constants of protein nanopores of varying pI, and at detergent concentrations below the CMC, and in buffers of varying pH; (v) Initial desolvation rates determined for acidic and basic  $\beta$ -barrel membrane proteins; (vi) Calculation of the association ( $k_{\text{on}}$ ) and dissociation ( $k_{\text{off}}$ ) rate constants using detergent desolvation curves; (vii) Scaling of the observed desolvation rates of the protein nanopores with the detergent concentrations at values below the CMC; (viii) Kinetic rate constants of association and dissociation of proteomicelles using time-dependent FP anisotropy changes. These materials are available free of charge via the Internet at <http://pubs.acs.org>

**ACKNOWLEDGMENTS.** We thank Yi-Ching Hsueh, Adam Blanden, and Bach Pham for their assistance during the very early stage of these studies. The authors are also grateful to Motahareh Ghahari Larimi and Lauren Mayse for their comments and stimulating discussions. This research was supported by the US National Institutes of Health grants GM115442 (to M.C.), GM088403 (to L.M.), and GM129429 (to L.M.).

## REFERENCES

1. Reading, E.; Liko, I.; Allison, T. M.; Benesch, J. L.; Laganowsky, A.; Robinson, C. V. The role of the detergent micelle in preserving the structure of membrane proteins in the gas phase. *Angew. Chem. Int. Ed. Engl.* **2015**, *54*, 4577-81.
2. Kleinschmidt, J. H. Folding of beta-barrel membrane proteins in lipid bilayers - Unassisted and assisted folding and insertion. *Biochim. Biophys. Acta* **2015**, *1848*, 1927-43.
3. Nadeau, V. G.; Rath, A.; Deber, C. M. Sequence hydrophathy dominates membrane protein response to detergent solubilization. *Biochemistry* **2012**, *51*, 6228-37.
4. Pollock, N. L.; Satriano, L.; Zegarra-Moran, O.; Ford, R. C.; Moran, O. Structure of wild type and mutant F508del CFTR: A small-angle X-ray scattering study of the protein-detergent complexes. *J. Struct. Biol.* **2016**, *194*, 102-11.
5. Stangl, M.; Veerappan, A.; Kroeger, A.; Vogel, P.; Schneider, D. Detergent properties influence the stability of the glycophorin A transmembrane helix dimer in lysophosphatidylcholine micelles. *Biophys. J.* **2012**, *103*, 2455-64.
6. Yang, Z.; Wang, C.; Zhou, Q.; An, J.; Hildebrandt, E.; Aleksandrov, L. A.; Kappes, J. C.; DeLucas, L. J.; Riordan, J. R.; Urbatsch, I. L.; et al. Membrane protein stability can be compromised by detergent interactions with the extramembranous soluble domains. *Protein Sci.* **2014**, *23*, 769-89.
7. Rath, A.; Glibowicka, M.; Nadeau, V. G.; Chen, G.; Deber, C. M. Detergent binding explains anomalous SDS-PAGE migration of membrane proteins. *Proceedings of the National Academy of Sciences of the United States of America* **2009**, *106*, 1760-5.
8. Frey, L.; Lakomek, N. A.; Riek, R.; Bibow, S. Micelles, bicelles, and nanodiscs: comparing the impact of membrane mimetics on membrane protein backbone dynamics. *Angew. Chem. Int. Ed. Engl.* **2017**, *56*, 380-383.
9. Crichton, P. G.; Harding, M.; Ruprecht, J. J.; Lee, Y.; Kunji, E. R. Lipid, detergent, and Coomassie Blue G-250 affect the migration of small membrane proteins in blue native gels: mitochondrial carriers migrate as monomers not dimers. *J. Biol. Chem.* **2013**, *288*, 22163-73.
10. Neale, C.; Ghanei, H.; Holyoake, J.; Bishop, R. E.; Prive, G. G.; Pomes, R. Detergent-mediated protein aggregation. *Chem. Phys. Lipids* **2013**, *169*, 72-84.
11. Jahnke, N.; Krylova, O. O.; Hoomann, T.; Vargas, C.; Fiedler, S.; Pohl, P.; Keller, S. Real-time monitoring of membrane-protein reconstitution by isothermal titration calorimetry. *Analytical chemistry* **2014**, *86*, 920-927.

12. Khelashvili, G.; LeVine, M. V.; Shi, L.; Quick, M.; Javitch, J. A.; Weinstein, H. The membrane protein LeuT in micellar systems: aggregation dynamics and detergent binding to the S2 site. *J. Am. Chem. Soc.* **2013**, *135*, 14266-75.
13. Horne, J. E.; Radford, S. E. A growing toolbox of techniques for studying beta-barrel outer membrane protein folding and biogenesis. *Biochem. Soc. Trans.* **2016**, *44*, 802-9.
14. Sadaf, A.; Cho, K. H.; Byrne, B.; Chae, P. S. Amphipathic agents for membrane protein study. *Methods Enzymol.* **2015**, *557*, 57-94.
15. Ehsan, M.; Du, Y.; Scull, N. J.; Tikhonova, E.; Tarrasch, J.; Mortensen, J. S.; Loland, C. J.; Skiniotis, G.; Guan, L.; Byrne, B.; et al. Highly branched pentasaccharide-bearing amphiphiles for membrane protein studies. *J. Am. Chem. Soc.* **2016**, *138*, 3789-96.
16. Das, M.; Du, Y.; Ribeiro, O.; Hariharan, P.; Mortensen, J. S.; Patra, D.; Skiniotis, G.; Loland, C. J.; Guan, L.; Kobilka, B. K.; et al. Conformationally preorganized diastereomeric norbornane-based maltosides for membrane protein study: implications of detergent kink for micellar properties. *J. Am. Chem. Soc.* **2017**, *139*, 3072-3081.
17. Yengo, C. M.; Berger, C. L. Fluorescence anisotropy and resonance energy transfer: powerful tools for measuring real time protein dynamics in a physiological environment. *Curr. Opin. Pharmacol.* **2010**, *10*, 731-7.
18. Rossi, A. M.; Taylor, C. W. Analysis of protein-ligand interactions by fluorescence polarization. *Nat. Protoc.* **2011**, *6*, 365-87.
19. Lea, W. A.; Simeonov, A. Fluorescence polarization assays in small molecule screening. *Expert. Opin. Drug. Discov.* **2011**, *6*, 17-32.
20. Zhang, H.; Wu, Q.; Berezin, M. Y. Fluorescence anisotropy (polarization): from drug screening to precision medicine. *Expert. Opin. Drug. Discov.* **2015**, *10*, 1145-61.
21. Wolfe, A. J.; Hsueh, Y. C.; Blanden, A. R.; Mohammad, M. M.; Pham, B.; Thakur, A. K.; Loh, S. N.; Chen, M.; Movileanu, L. Interrogating detergent desolvation of nanopore-forming proteins by fluorescence polarization spectroscopy. *Analytical chemistry* **2017**, *89*, 8013-8020.
22. Ayub, M.; Bayley, H. Engineered transmembrane pores. *Curr. Opin. Chem. Biol.* **2016**, *34*, 117-126.
23. Slusky, J. S. Outer membrane protein design. *Curr. Opin. Struct. Biol.* **2016**, *45*, 45-52.
24. Yildiz, O.; Vinothkumar, K. R.; Goswami, P.; Kuhlbrandt, W. Structure of the monomeric outer-membrane porin OmpG in the open and closed conformation. *EMBO J.* **2006**, *25*, 3702-3713.

25. Locher, K. P.; Rees, B.; Koebnik, R.; Mitschler, A.; Moulinier, L.; Rosenbusch, J. P.; Moras, D. Transmembrane signaling across the ligand-gated FhuA receptor: crystal structures of free and ferrichrome-bound states reveal allosteric changes. *Cell* **1998**, *95*, 771-778.
26. Liu, Z.; Ghai, I.; Winterhalter, M.; Schwaneberg, U. Engineering Enhanced Pore Sizes Using FhuA Delta1-160 from E. coli Outer Membrane as Template. *ACS Sens.* **2017**, *2*, 1619-1626.
27. Mohammad, M. M.; Howard, K. R.; Movileanu, L. Redesign of a plugged beta-barrel membrane protein. *J. Biol. Chem.* **2011**, *286*, 8000-8013.
28. Chen, M.; Khalid, S.; Sansom, M. S.; Bayley, H. Outer membrane protein G: engineering a quiet pore for biosensing. *Proc. Natl. Acad. Sci. U.S.A.* **2008**, *105*, 6272-6277.
29. Thakur, A. K.; Larimi, M. G.; Gooden, K.; Movileanu, L. Aberrantly large single-channel conductance of polyhistidine arm-containing protein nanopores. *Biochemistry* **2017**, *56*, 4895-4905.
30. Mohammad, M. M.; Iyer, R.; Howard, K. R.; McPike, M. P.; Borer, P. N.; Movileanu, L. Engineering a rigid protein tunnel for biomolecular detection. *J. Am. Chem. Soc.* **2012**, *134*, 9521-9531.
31. Wolfe, A. J.; Mohammad, M. M.; Thakur, A. K.; Movileanu, L. Global redesign of a native beta-barrel scaffold. *Biochim. Biophys. Acta* **2016**, *1858*, 19-29.
32. Niedzwiecki, D. J.; Mohammad, M. M.; Movileanu, L. Inspection of the engineered FhuA deltaC/delta4L protein nanopore by polymer exclusion. *Biophys. J.* **2012**, *103*, 2115-2124.
33. Wolfe, A. J.; Gugel, J. F.; Chen, M.; Movileanu, L. Detergent Desorption of Membrane Proteins Exhibits Two Kinetic Phases. *J. Phys. Chem. Lett.* **2018**, *9*, 1913-1919.
34. Fahie, M.; Chisholm, C.; Chen, M. Resolved single-molecule detection of individual species within a mixture of anti-biotin antibodies using an engineered monomeric nanopore. *ACS nano* **2015**, *9*, 1089-1098.
35. Wolfe, A. J.; Si, W.; Zhang, Z.; Blanden, A. R.; Hsueh, Y. C.; Gugel, J. F.; Pham, B.; Chen, M.; Loh, S. N.; Rozovsky, S.; et al. Quantification of membrane protein-detergent complex interactions. *J. Phys. Chem. B* **2017**, *121*, 10228-10241.
36. Linke, D. Detergents: an overview. *Methods Enzymol.* **2009**, *463*, 603-617.
37. Titus, J. A.; Haugland, R.; Sharrow, S. O.; Segal, D. M. Texas Red, a hydrophilic, red-emitting fluorophore for use with fluorescein in dual parameter flow microfluorometric and fluorescence microscopic studies. *J. Immunol. Methods* **1982**, *50*, 193-204.
38. Jameson, D. M.; Ross, J. A. Fluorescence polarization/anisotropy in diagnostics and imaging. *Chem. Rev.* **2010**, *110*, 2685-708.

39. Gradinaru, C. C.; Marushchak, D. O.; Samim, M.; Krull, U. J. Fluorescence anisotropy: from single molecules to live cells. *Analyst* **2010**, *135*, 452-9.
40. Splinter, R. H., B.A. *An introduction to biomedical optics*. Taylor & Francis, New York.: 2007; p 602.
41. Movileanu, L.; Cheley, S.; Howorka, S.; Braha, O.; Bayley, H. Location of a constriction in the lumen of a transmembrane pore by targeted covalent attachment of polymer molecules. *J. Gen. Physiol.* **2001**, *117*, 239-251.
42. Stoddart, L. A.; White, C. W.; Nguyen, K.; Hill, S. J.; Pflieger, K. D. Fluorescence- and bioluminescence-based approaches to study GPCR ligand binding. *Br. J. Pharmacol.* **2016**, *173*, 3028-3037.
43. Grosse, W.; Psakis, G.; Mertins, B.; Reiss, P.; Windisch, D.; Brademann, F.; Burck, J.; Ulrich, A.; Koert, U.; Essen, L. O. Structure-based engineering of a minimal porin reveals loop-independent channel closure. *Biochemistry* **2014**, *53*, 4826-38.
44. Lakowicz, J. R. *Principles of fluorescence microscopy*. 2nd ed.; Springer: New York, 2006.
45. Ji, J.; Rosenzweig, N.; Griffin, C.; Rosenzweig, Z. Synthesis and application of submicrometer fluorescence sensing particles for lysosomal pH measurements in murine macrophages. *Analytical chemistry* **2000**, *72*, 3497-503.
46. Unruh, J. R.; Gokulrangan, G.; Wilson, G. S.; Johnson, C. K. Fluorescence properties of fluorescein, tetramethylrhodamine and Texas Red linked to a DNA aptamer. *Photochem. Photobiol.* **2005**, *81*, 682-90.
47. Heerklotz, H. H.; Binder, H.; Epand, R. M. A "release" protocol for isothermal titration calorimetry. *Biophys. J.* **1999**, *76*, 2606-13.
48. Heerklotz, H.; Tsamaloukas, A. D.; Keller, S. Monitoring detergent-mediated solubilization and reconstitution of lipid membranes by isothermal titration calorimetry. *Nature protocols* **2009**, *4*, 686-97.
49. Li, J.; Qiu, X. J. Quantification of membrane protein self-association with a high-throughput compatible fluorescence assay. *Biochemistry* **2017**, *56*, 1951-1954.
50. Prazeres, T. J. V.; Fedorov, A.; Barbosa, S. P.; Martinho, J. M. G.; Berberan-Santos, M. N. Accurate determination of the limiting anisotropy of rhodamine 101. Implications for its use as a fluorescence polarization standard. *J. Phys. Chem. A* **2008**, *112*, 5034-5039.
51. Neves, P.; Lopes, S. C.; Sousa, I.; Garcia, S.; Eaton, P.; Gameiro, P. Characterization of membrane protein reconstitution in LUVs of different lipid composition by fluorescence anisotropy. *J. Pharm. Biomed. Anal.* **2009**, *49*, 276-81.

52. Heidebrecht, T.; Fish, A.; von Castelmur, E.; Johnson, K. A.; Zaccari, G.; Borst, P.; Perrakis, A. Binding of the J-binding protein to DNA containing glucosylated hmU (base J) or 5-hmC: evidence for a rapid conformational change upon DNA binding. *J. Am. Chem. Soc.* **2012**, *134*, 13357-65.
53. Qiao, Y.; Tang, H.; Munske, G. R.; Dutta, P.; Ivory, C. F.; Dong, W. J. Enhanced fluorescence anisotropy assay for human cardiac troponin I and T detection. *J. Fluoresc.* **2011**, *21*, 2101-10.
54. Stanczak, P.; Horst, R.; Serrano, P.; Wuthrich, K. NMR characterization of membrane protein-detergent micelle solutions by use of microcoil equipment. *J. Am. Chem. Soc.* **2009**, *131*, 18450-6.
55. Khao, J.; Arce-Lopera, J.; Sturgis, J. N.; Duneau, J. P. Structure of a protein-detergent complex: the balance between detergent cohesion and binding. *Eur. Biophys. J.* **2011**, *40*, 1143-55.
56. Yang, Z.; Brouillette, C. G. A guide to differential scanning calorimetry of membrane and soluble proteins in detergents. *Methods Enzymol.* **2016**, *567*, 319-58.
57. Mohammad, M. M.; Movileanu, L. Impact of distant charge reversals within a robust beta-barrel protein pore. *J. Phys. Chem. B* **2010**, *114*, 8750-8759.



## Chapter 6.1 Kinetics of Membrane Protein-Detergent Interactions Depend on Protein Electrostatics

Aaron J. Wolfe,<sup>1,2</sup> Jack F. Gugel,<sup>1</sup> Min Chen,<sup>3</sup> and Liviu Movileanu<sup>1,2,4,\*</sup>

<sup>1</sup>Department of Physics, Syracuse University, 201 Physics Building, Syracuse, New York 13244-1130, USA

<sup>2</sup>Structural Biology, Biochemistry, and Biophysics Program, Syracuse University, 111 College Place, Syracuse, New York 13244-4100, USA

<sup>3</sup>Department of Chemistry, University of Massachusetts, 820 LGRT, 710 North Pleasant Street, Amherst, Massachusetts 01003-9336, USA

<sup>4</sup>Department of Biomedical and Chemical Engineering, Syracuse University, Syracuse University, 223 Link Hall, Syracuse, New York 13244, USA

Reprinted with permission from **Kinetics of Membrane Protein-Detergent Interactions Depend on Protein Electrostatics**, Aaron J. Wolfe, Jack F. Gugel, Min Chen, and Liviu Movileanu 2018 Sep 25. doi: 10.1021/acs.jpcc.8b07889. *J. Phys. Chem. B*, Copyright 2018 American Chemical Society.

Author contributions:

AJW: Designed experiments, performed experiments, analyzed data, interpreted data.

JFG: Analyzed data

MC: Performed experiments

LM: Analyzed data, interpreted data, wrote manuscript

## Contents of Supporting Information

(i) Time-dependent FP anisotropy changes of protein nanopores of varying isoelectric point (pI) at detergent incubations above and below the CMC, and in buffers of varying pH;

(ii) Curve fits of the predesolvation and desolvation phases at detergent concentrations below the CMC and in buffers of varying pH;

(iii) Determination of the predesolvation rates of protein nanopores of varying pI, at detergent concentrations below the CMC, and in buffers of varying pH;

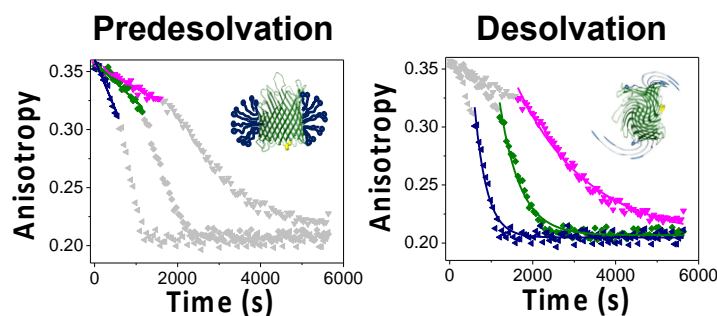
(iv) Determination of the desolvation rate and time constants of protein nanopores of varying pI, and at detergent concentrations below the CMC, and in buffers of varying pH;

(v) Initial desolvation rates determined for acidic and basic  $\beta$ -barrel membrane proteins;

(vi) Calculation of the association ( $k_{on}$ ) and dissociation ( $k_{off}$ ) rate constants using detergent-desolvation curves;

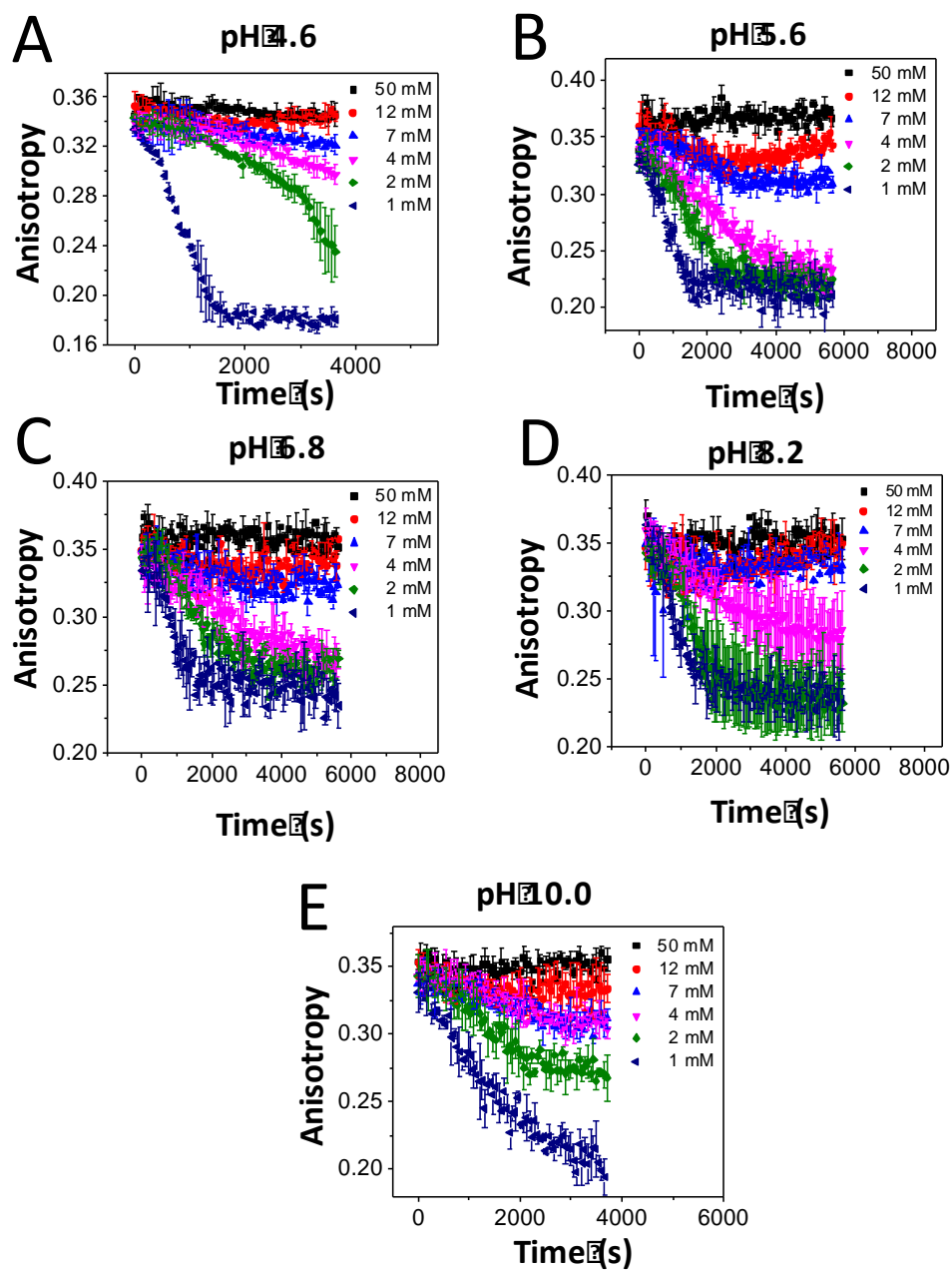
(vii) Scaling of the observed desolvation rates of the protein nanopores with the detergent concentrations at values below the CMC;

(viii) Kinetic rate constants of association and dissociation of proteomicelles using time-dependent FP anisotropy changes.



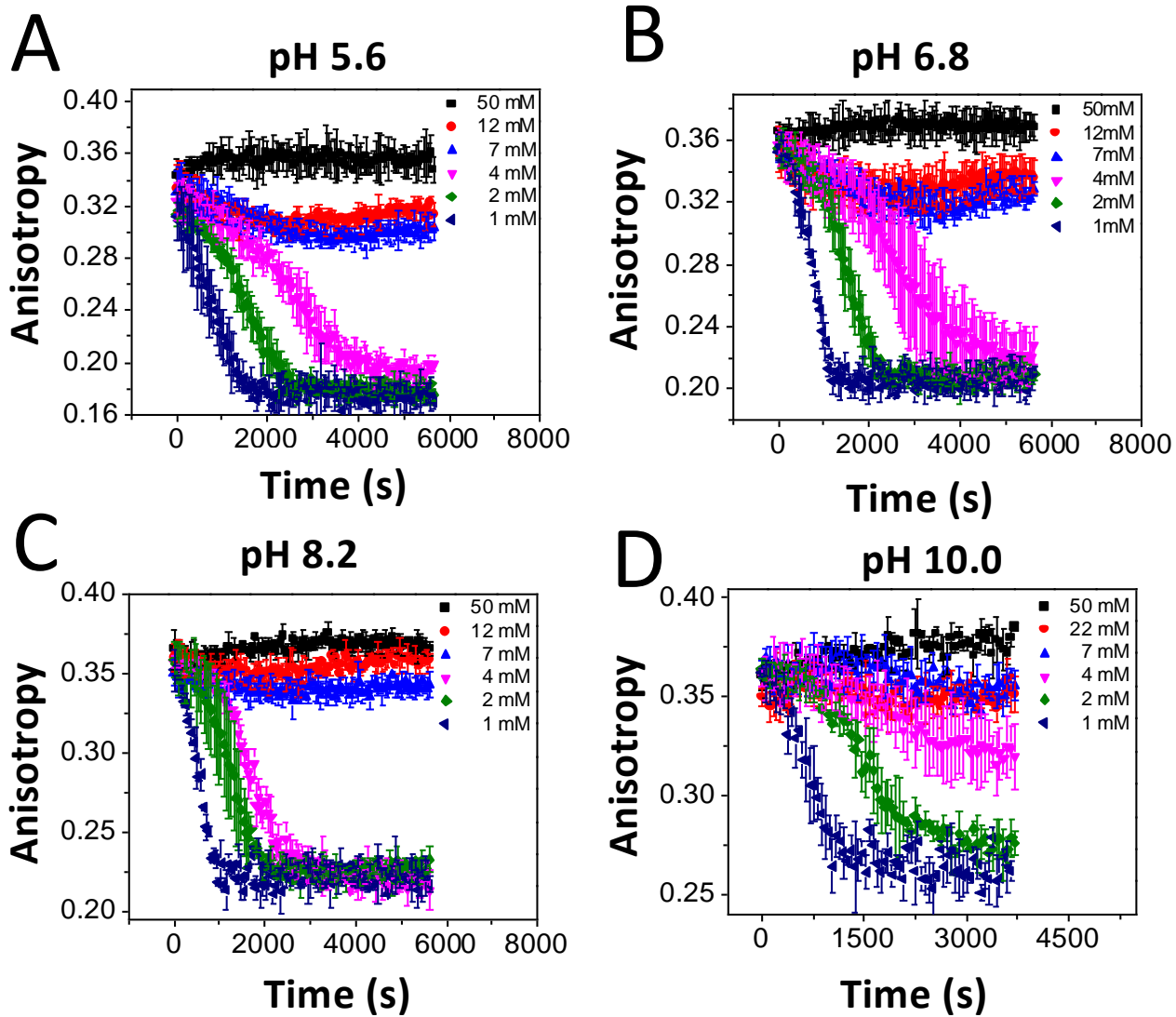
1. Time-dependent FP anisotropy changes of protein nanopores of varying isoelectric point (pI), at detergent concentrations above and below the CMC, and in buffers of varying pH.

## CYMAL-4 $\square$ FhuA $\Delta$ C/ $\Delta$ 5L



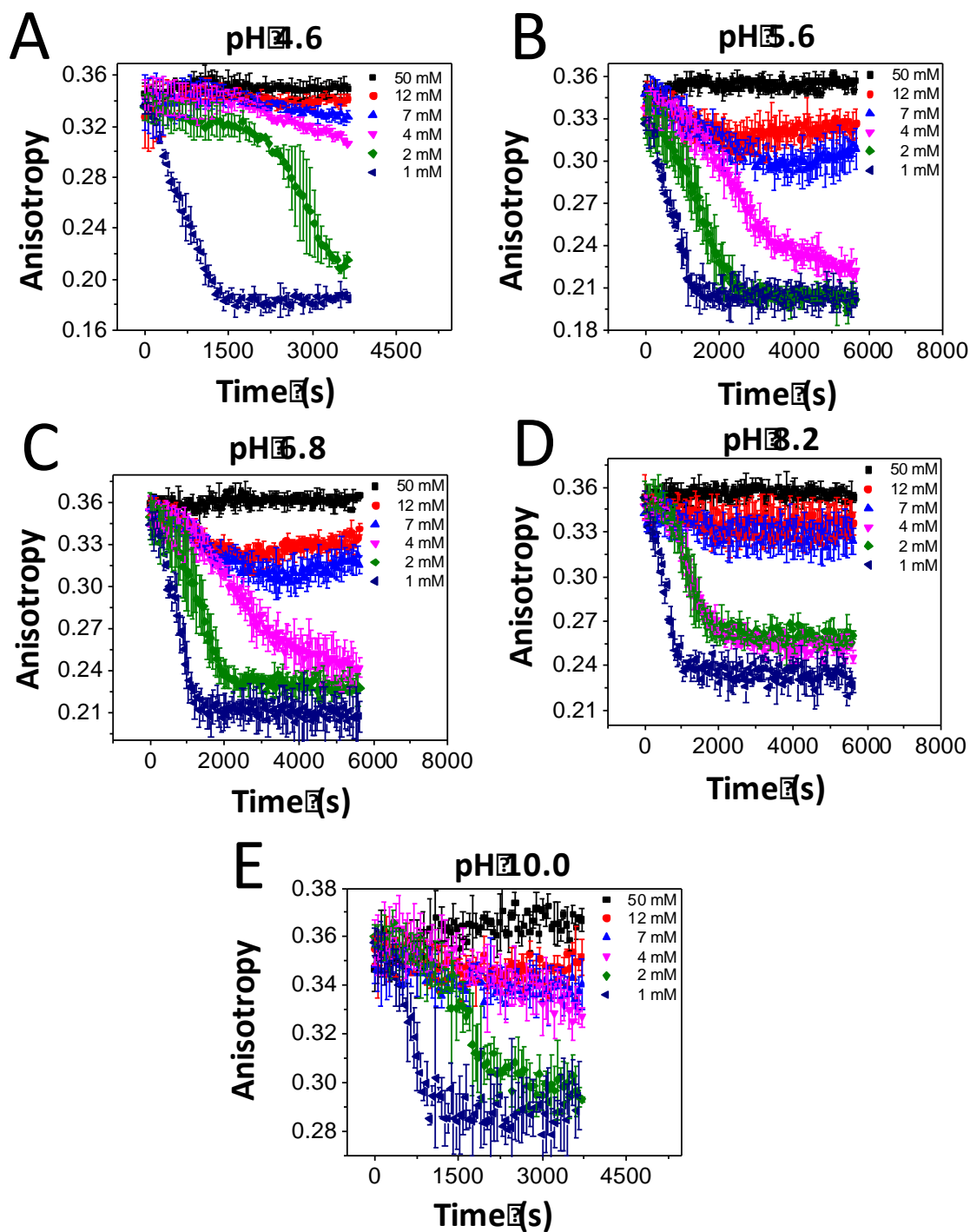
**Figure S1: Time-dependent desolvation of FhuA  $\Delta$ C/ $\Delta$ 5L incubated in CYMAL-4.**

(A) pH 4.6; (B) pH 5.6; (C) pH 6.8; (D) pH 8.2; (E) pH 10.0. The solubilized protein concentration was 28 nM. Detergent dilutions above the  $CMC^{CYMAL-4}$  (~7.6 mM) were conducted using an incubation concentration of 50 mM CYMAL-4. The FP measurements were carried out using a solution that contained 200 mM NaCl at room temperature. The buffer was either 50 mM HEPES (pH 6.8 and pH 8.2), 50 mM NaOAc (pH 4.6 and pH 5.6) or 50 mM sodium borate (pH 10.0). All data were derived as averages  $\pm$  SDs of three independent data acquisitions.

CYMAL-4 - FhuA  $\Delta$ C/ $\Delta$ 5L\_25N

**Figure S2: Time-dependent desolvation of FhuA  $\Delta C/\Delta 5L_{25N}$  incubated in CYMAL-4.**

(A) pH 5.6; (B) pH 6.8; (C) pH 8.2; (D) pH 10.0. The solubilized protein concentration was 28 nM. Detergent dilutions were conducted using an incubation concentration of 50 mM CYMAL-4. The other experimental conditions were the same as in **Fig. S1**.

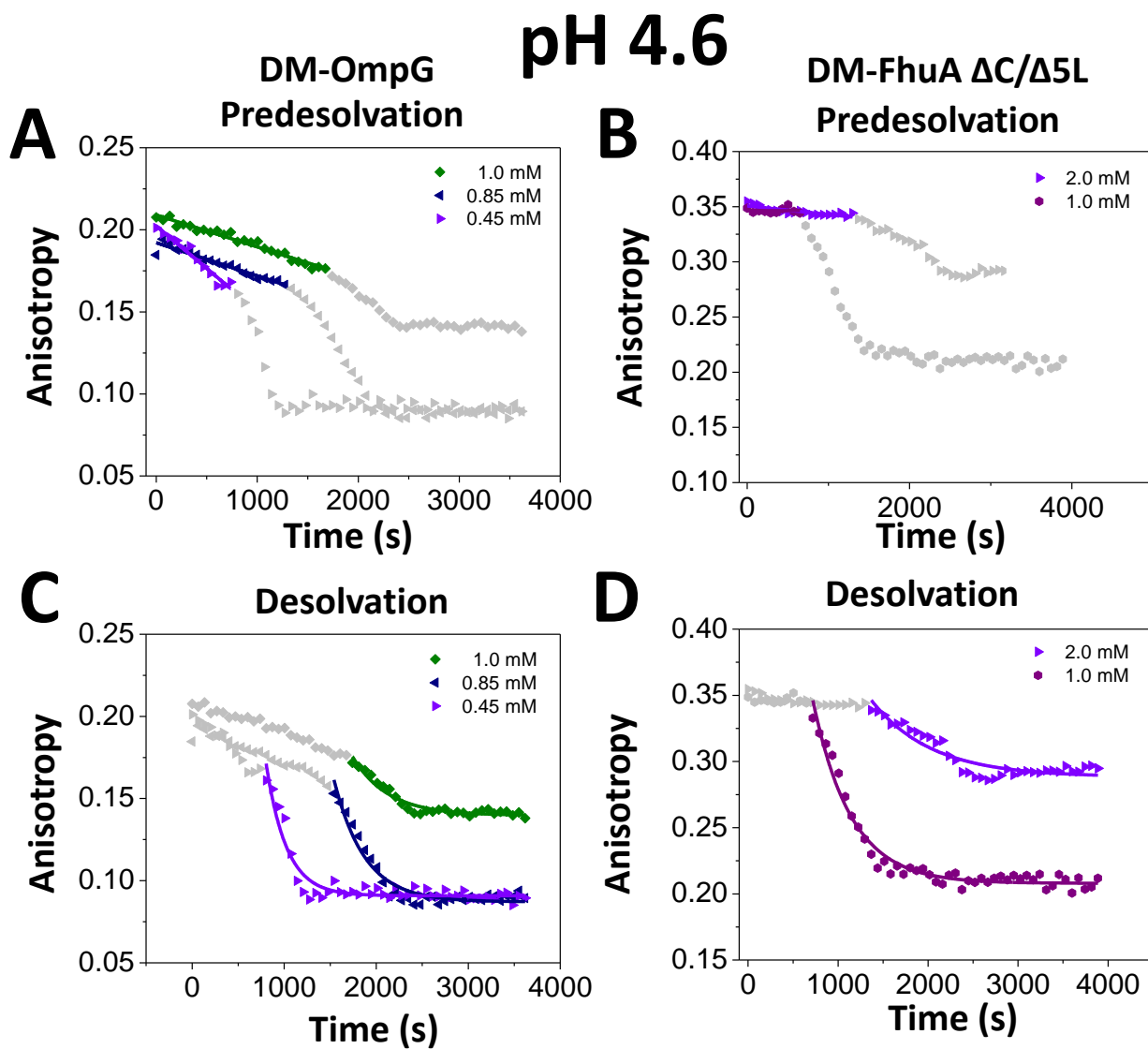
CYMAL-4<sup>+</sup> FhuA  $\Delta$ C/ $\Delta$ 7L<sub>30N</sub>

**Figure S3: Time-dependent desolvation of FhuA  $\Delta C/\Delta 5L_{25N}$  incubated in CYMAL-4.**

(A) pH 4.6; (B) pH 5.6; (C) pH 6.8; (D) pH 8.2; (E) pH 10.0. The solubilized protein concentration was 28 nM. Detergent dilutions were conducted using an incubation concentration of 50 mM CYMAL-4. The other experimental conditions were the same as in **Fig. S1**.

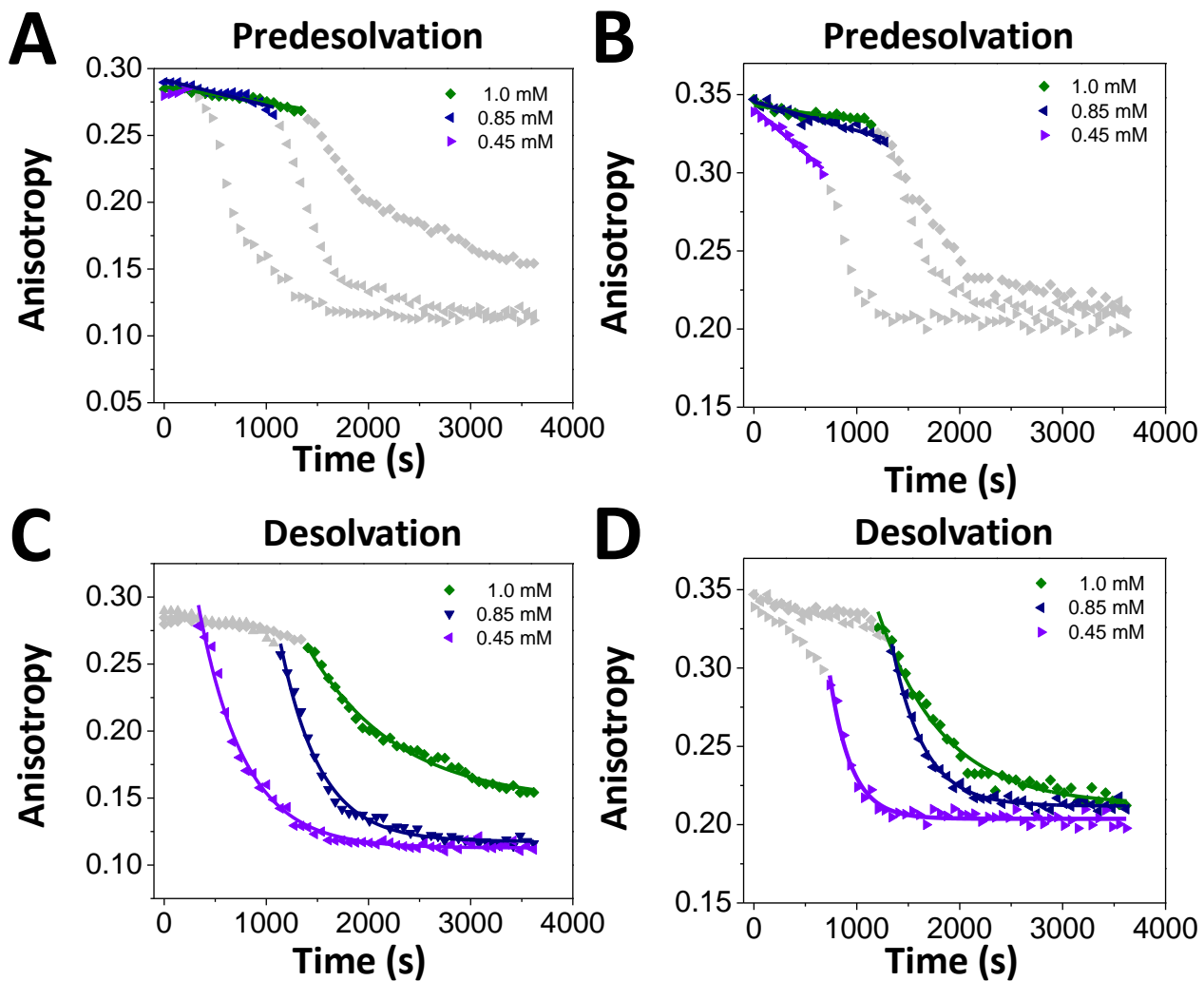


2. Curve fits of the predesolvation and desolvation phases at detergent concentrations below the CMC and in buffers of varying pH.

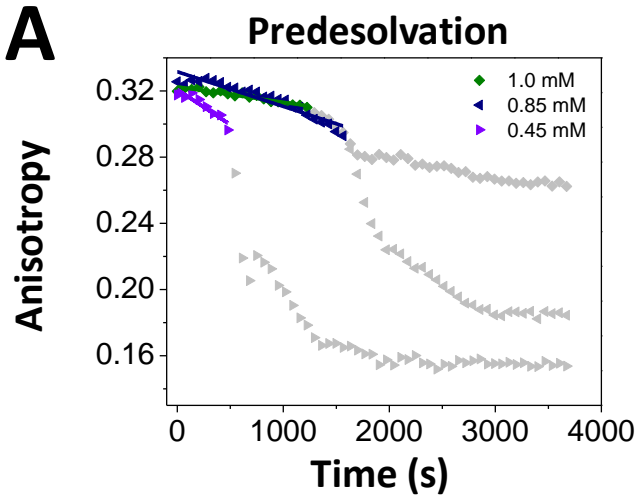
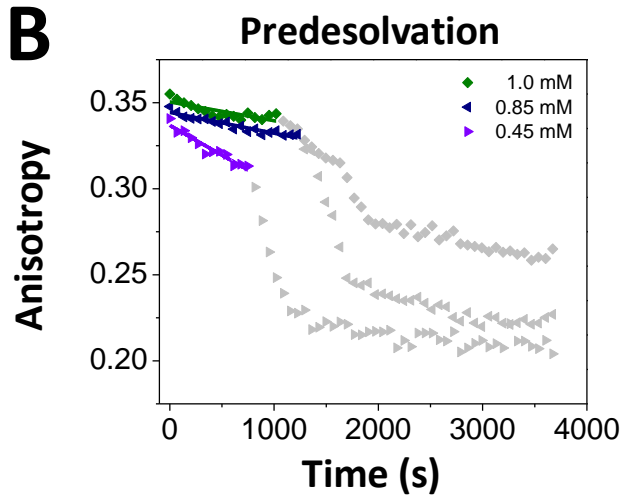
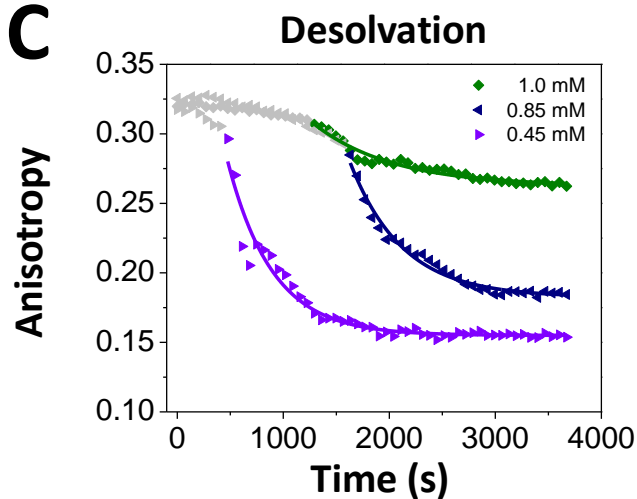
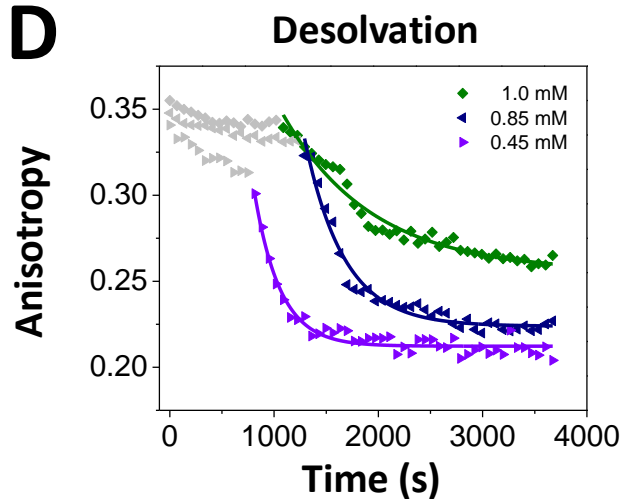


**Figure S4: Time-dependent predesolvation and desolvation of OmpG and FhuA  $\Delta C/\Delta 5L$  incubated with DM at pH 4.6.** (A) Predesolvation of OmpG from DM ; (B) Predesolvation of FhuA  $\Delta C/\Delta 5L$  from DM; (C) Desolvation of OmpG from DM; (D) Desolvation of FhuA  $\Delta C/\Delta 5L$  from DM. The solubilized protein concentration was 28 nM. Detergent dilutions were conducted using an incubation concentration of 5 mM DM. The other experimental conditions were the same as in **Fig. S1**.

DM-OmpG **pH 5.6** DM-FhuA  $\Delta C/\Delta 5L$



**Figure S5: Time-dependent predesolvation and desolvation of OmpG and FhuA  $\Delta C/\Delta 5L$  incubated with DM at pH 5.6.** (A) Predesolvation of OmpG from DM ; (B) Predesolvation of FhuA  $\Delta C/\Delta 5L$  from DM; (C) Desolvation of OmpG from DM; (D) Desolvation of FhuA  $\Delta C/\Delta 5L$  from DM. The solubilized protein concentration was 28 nM. Detergent dilutions were conducted using an incubation concentration of 5 mM DM. The other experimental conditions were the same as in **Fig. S1**.

DM-OmpG **pH 6.8**DM-FhuA  $\Delta C/\Delta 5L$ **A****B****C****D**

**Figure S6: Time-dependent predesolvation and desolvation of OmpG and FhuA  $\Delta C/\Delta 5L$  incubated with DM at pH 6.8.** (A) Predesolvation of OmpG from DM ; (B) Predesolvation of FhuA  $\Delta C/\Delta 5L$  from DM; (C) Desolvation of OmpG from DM; (D) Desolvation of FhuA  $\Delta C/\Delta 5L$  from DM. The solubilized protein concentration was 28 nM. Detergent dilutions were conducted using an incubation concentration of 5 mM DM. The other experimental conditions were the same as in **Fig. S1**.

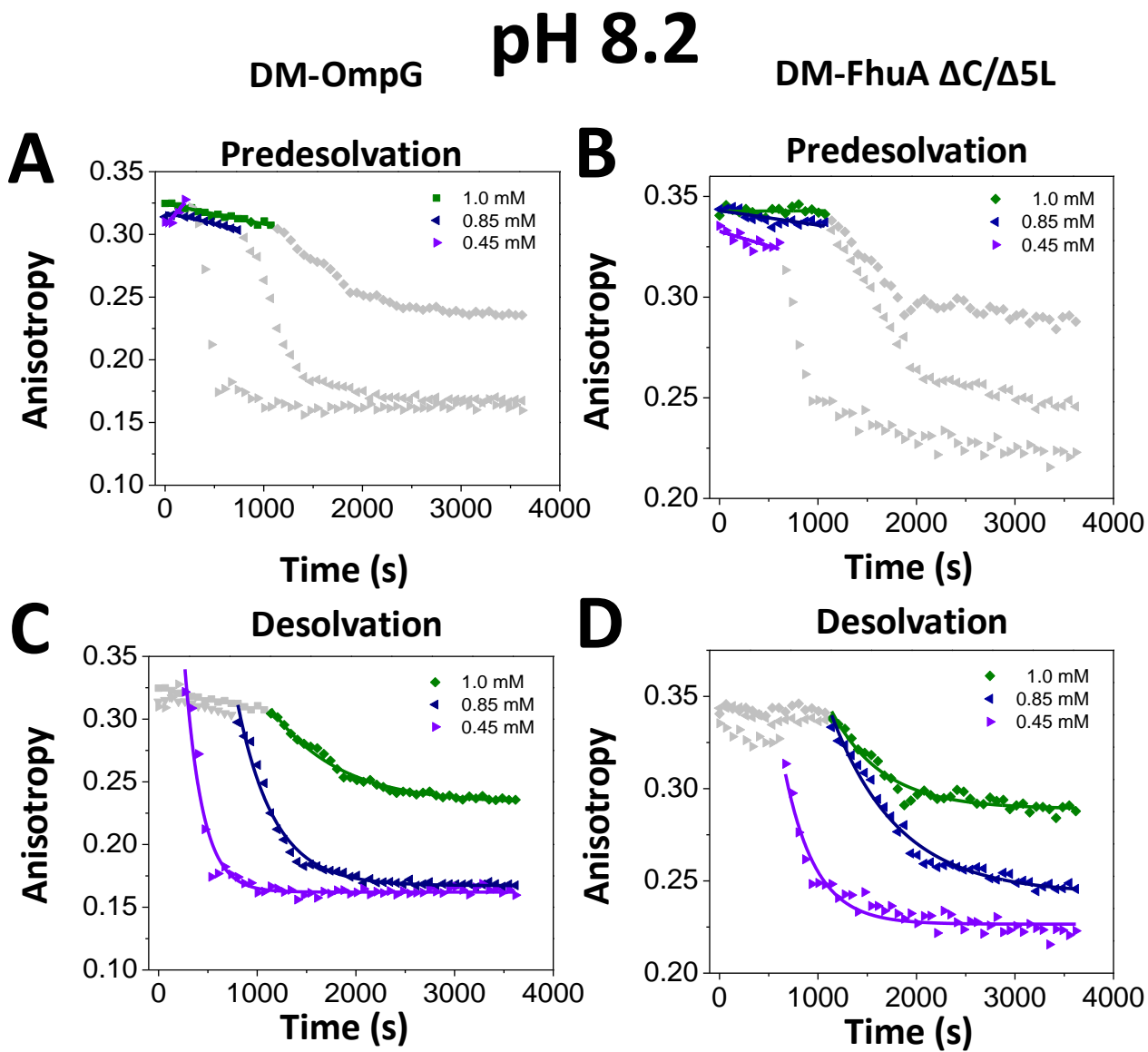


**Figure S7: Time-dependent predesolvation and desolvation of OmpG and FhuA  $\Delta C/\Delta 5L$  incubated with DM at pH 8.2.** (A) Predesolvation of OmpG from DM ; (B) Predesolvation of FhuA  $\Delta C/\Delta 5L$  from DM; (C) Desolvation of OmpG from DM; (D) Desolvation of FhuA  $\Delta C/\Delta 5L$  from DM. The solubilized protein concentration was 28 nM. Detergent dilutions were conducted using an incubation concentration of 5 mM DM. The other experimental conditions were the same as in **Fig. S1**.

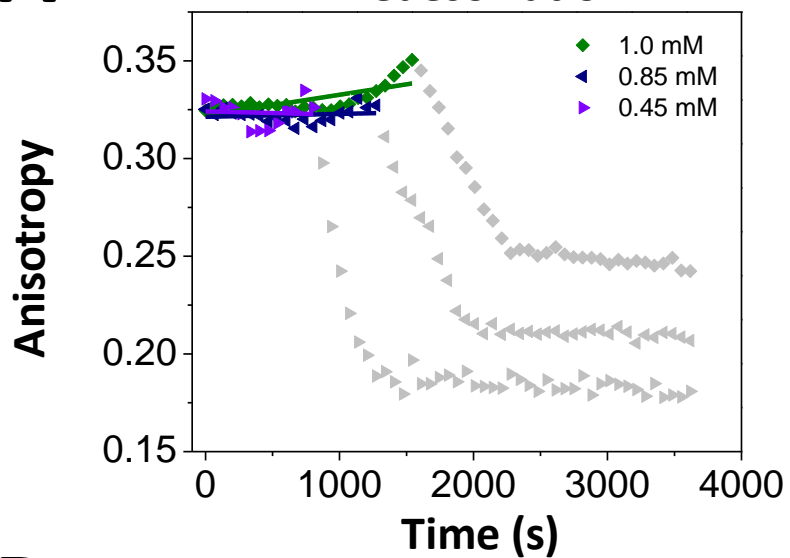


# pH 10.0

## DM-OmpG

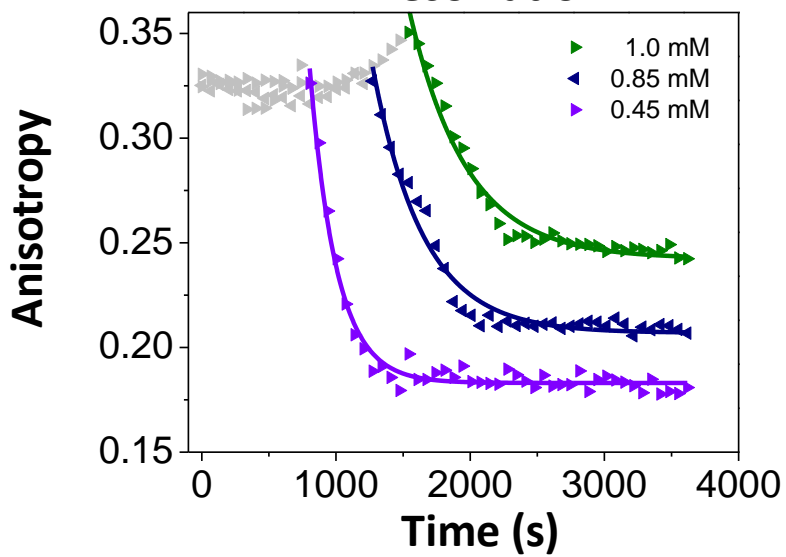
### A

#### Predesolvation



### B

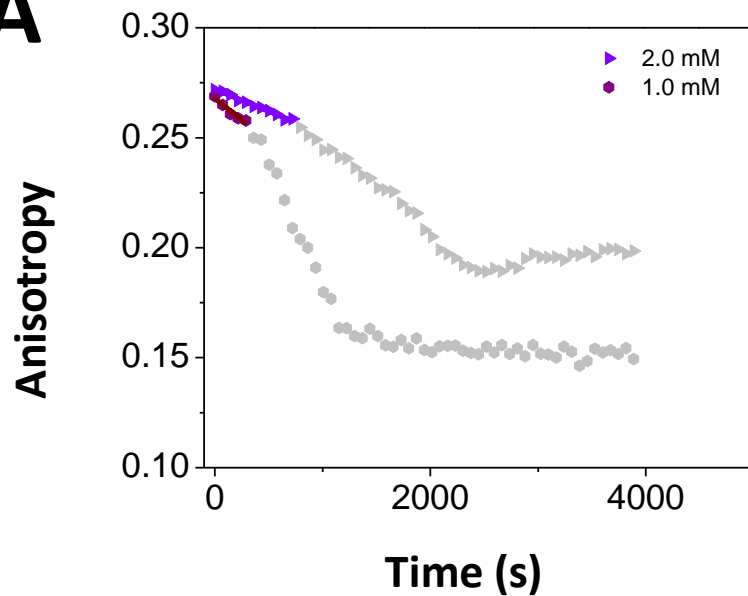
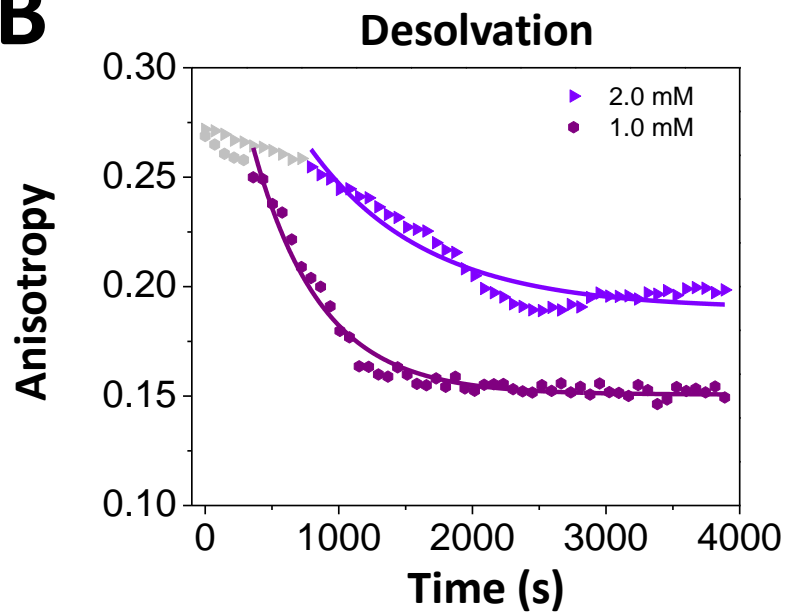
#### Desolvation



**Figure S8: Time-dependent predesolvation and desolvation of OmpG incubated with DM at pH 10.0.** (A) Predesolvation of OmpG from DM; (B) Desolvation of OmpG from DM. The solubilized protein concentration was 28 nM. Detergent dilutions were conducted using an incubation concentration of 5 mM DM. The other experimental conditions were the same as in **Fig. S1**.

# pH 4.6

## DM-FhuA $\Delta C/\Delta 5L_{25N}$

**A****B**

**Figure S9: Time-dependent predesolvation and desolvation of FhuA  $\Delta C/\Delta 5L_{25N}$**

**incubated with DM at pH 4.6. (A)** Predesolvation of FhuA  $\Delta C/\Delta 5L_{25N}$  from DM; **(B)**

Desolvation of FhuA  $\Delta C/\Delta 5L_{25N}$  from DM. The solubilized protein concentration was 28 nM.

Detergent dilutions were conducted using an incubation concentration of 5 mM DM. The other experimental conditions were the same as in **Fig. S1**.

# pH 5.6

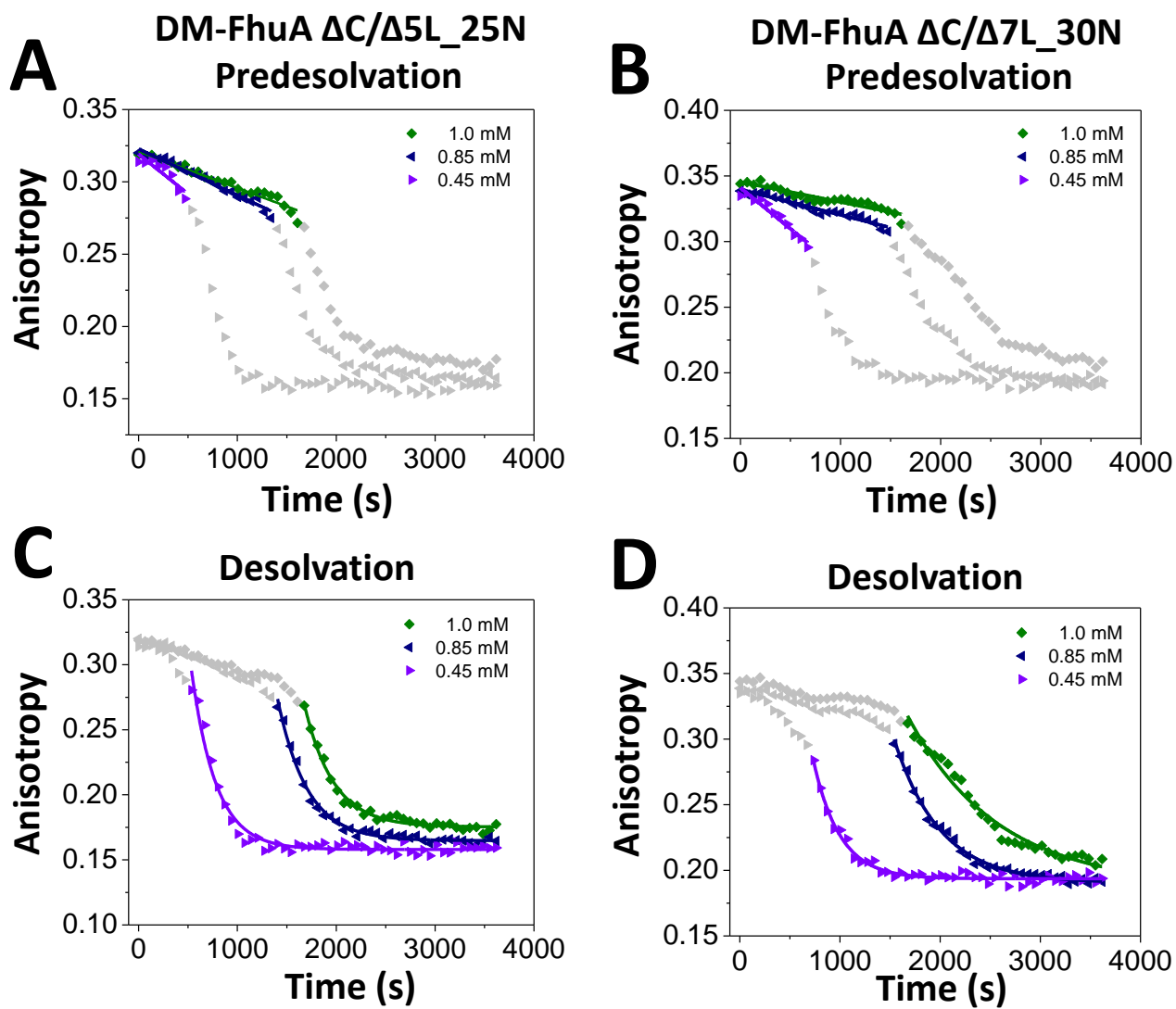


**Figure S10: Time-dependent predesolvation and desolvation of FhuA  $\Delta C/\Delta 5L_{25N}$  and FhuA  $\Delta C/\Delta 7L_{30N}$  incubated with DM at pH 5.6. (A) Predesolvation of FhuA  $\Delta C/\Delta 5L_{25N}$  from DM ; (B) Predesolvation of FhuA  $\Delta C/\Delta 7L_{30N}$  from DM; (C) Desolvation of FhuA  $\Delta C/\Delta 5L_{25N}$  from DM; (D) Desolvation of FhuA  $\Delta C/\Delta 7L_{30N}$  from DM. The solubilized protein concentration was 28 nM. Detergent dilutions were conducted using an incubation concentration of 5 mM DM. The other experimental conditions were the same as in **Fig. S1**.**

# pH 6.8

DM-FhuA  $\Delta C/\Delta 5L_{25N}$

DM-FhuA  $\Delta C/\Delta 7L_{30N}$

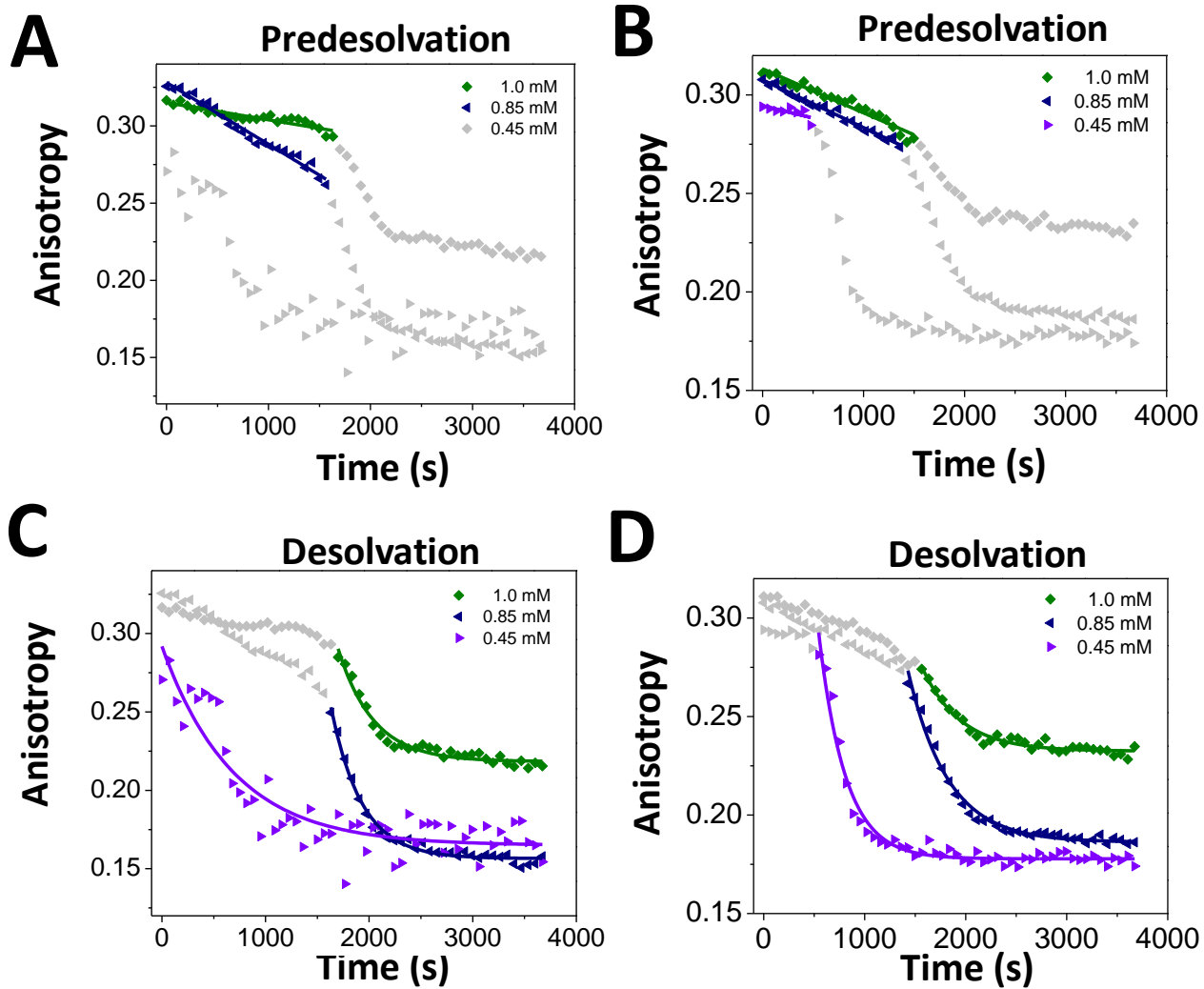


**Figure S11: Time-dependent predesolvation and desolvation of FhuA  $\Delta C/\Delta 5L_{25N}$  and FhuA  $\Delta C/\Delta 7L_{30N}$  incubated with DM at pH 6.8.** (A) Predesolvation of FhuA  $\Delta C/\Delta 5L_{25N}$  from DM ; (B) Predesolvation of FhuA  $\Delta C/\Delta 7L_{30N}$  from DM; (C) Desolvation of FhuA  $\Delta C/\Delta 5L_{25N}$  from DM; (D) Desolvation of FhuA  $\Delta C/\Delta 7L_{30N}$  from DM. The solubilized protein concentration was 28 nM. Detergent dilutions were conducted using an incubation concentration of 5 mM DM. The other experimental conditions were the same as in **Fig. S1**.

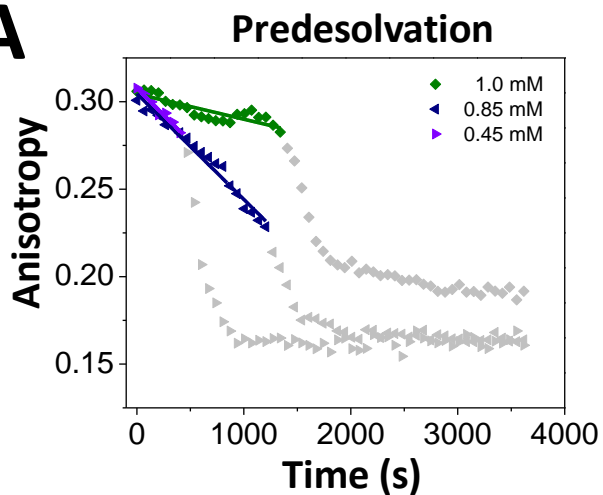


# pH 8.2

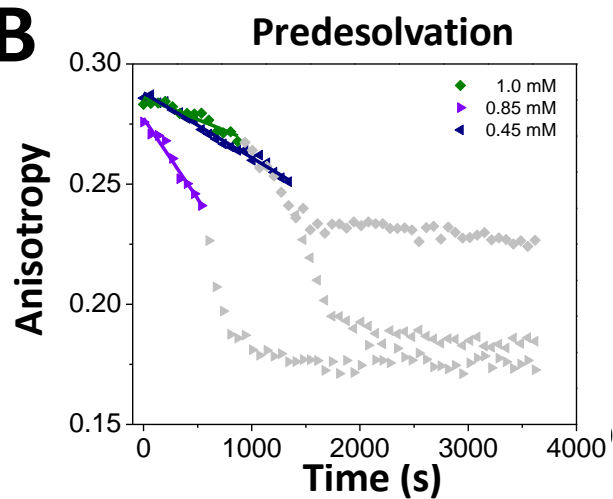
DM-FhuA  $\Delta C/\Delta 5L_{25N}$

DM-FhuA  $\Delta C/\Delta 7L_{30N}$

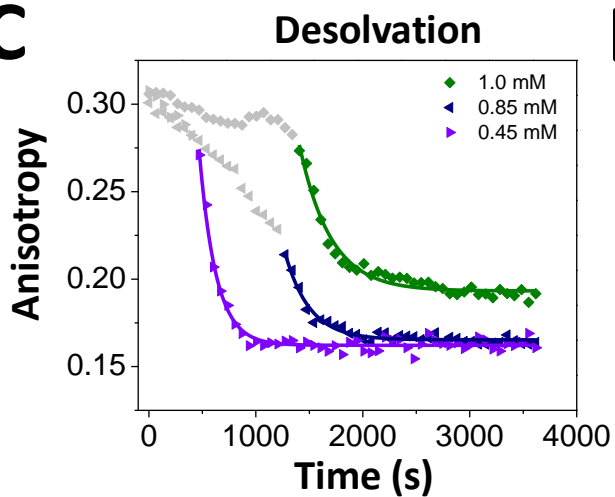
**A**



**B**



**C**



**D**

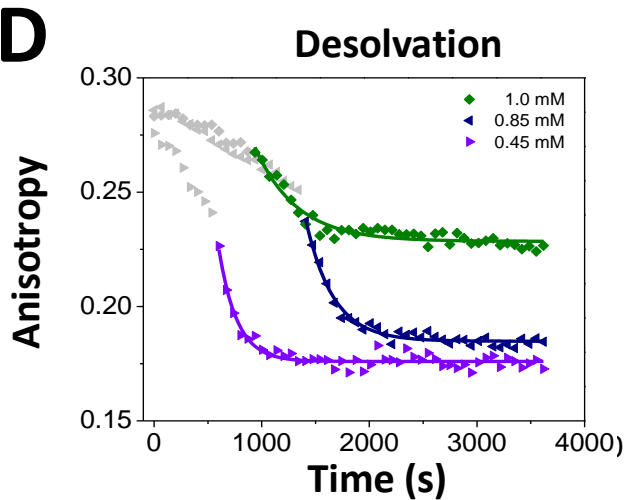


**Figure S12: Time-dependent predesolvation and desolvation of FhuA  $\Delta C/\Delta 5L$  and FhuA  $\Delta C/\Delta 7L_{30N}$  incubated with DM at pH 8.2.** (A) Predesolvation of FhuA  $\Delta C/\Delta 5L_{25N}$  from DM ;  
(B) Predesolvation of FhuA  $\Delta C/\Delta 7L_{30N}$  from DM; (C) Desolvation of FhuA  $\Delta C/\Delta 5L_{25N}$  from DM; (D) Desolvation of FhuA  $\Delta C/\Delta 7L_{30N}$  from DM. The solubilized protein concentration was 28 nM. Detergent dilutions were conducted using an incubation concentration of 5 mM DM. The other experimental conditions were the same as in **Fig. S1**.

# pH 4.6

## CYMAL-4 - FhuA DC/D5L

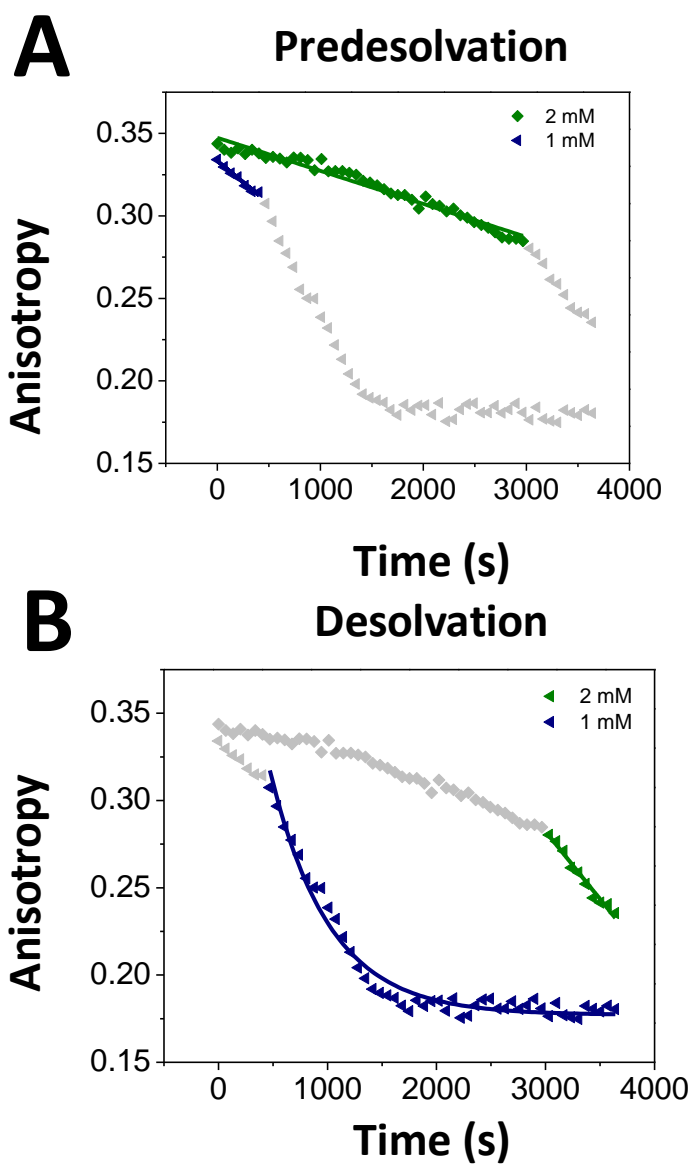


**Figure S13: Time-dependent predesolvation and desolvation of FhuA  $\Delta C/\Delta 5L$  incubated with CYMAL-4 at pH 4.6. (A) Predesolvation of FhuA  $\Delta C/\Delta 5L$  from CYMAL-4; (B) Desolvation of FhuA  $\Delta C/\Delta 5L$  from CYMAL-4. The solubilized protein concentration was 28 nM. Detergent dilutions were conducted using an incubation concentration of 50 mM CYMAL-4. The other experimental conditions were the same as in **Fig. S1**.**

# pH 5.6

## CYMAL-4 - OmpG

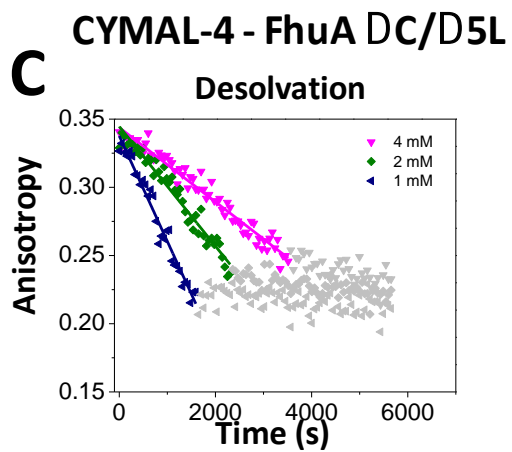
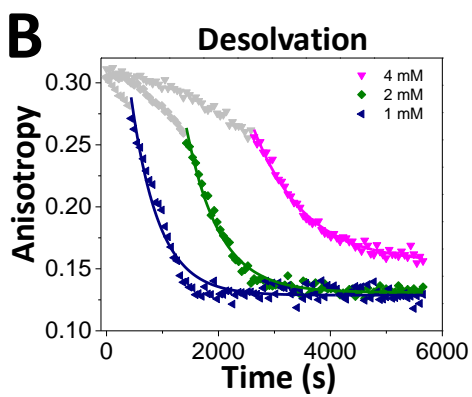
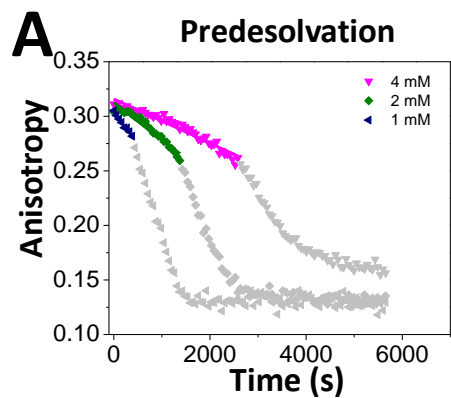
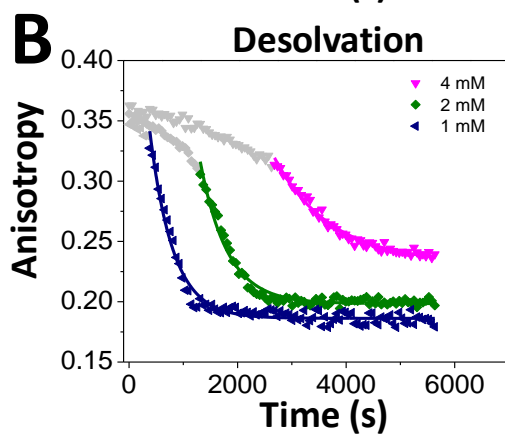
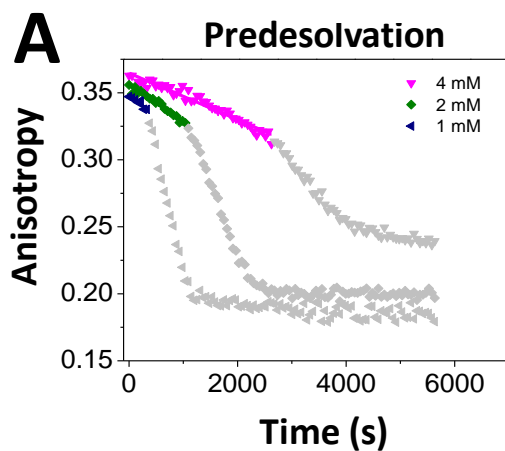


**Figure S14: Time-dependent predesolvation and desolvation of OmpG and FhuA  $\Delta C/\Delta 5L$  incubated with CYMAL-4 at pH 5.6.** (A) Predesolvation of OmpG from CYMAL-4; (B) Desolvation of OmpG from CYMAL-4; (C) Desolvation of FhuA  $\Delta C/\Delta 5L$  from CYMAL-4. The solubilized protein concentration was 28 nM. Detergent dilutions were conducted using an incubation concentration of 50 mM CYMAL-4. The other experimental conditions were the same as in **Fig. S1**.

# pH 6.8

## CYMAL-4 - OmpG



## CYMAL-4 - FhuA DC/D5L

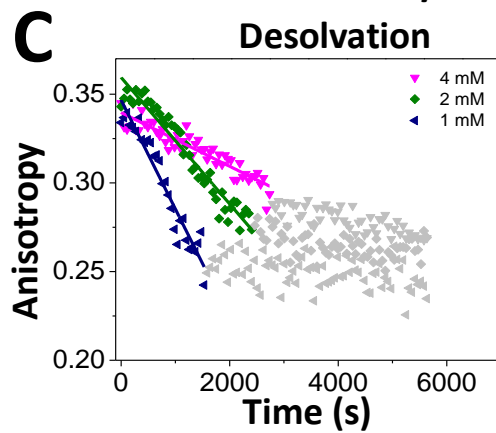


**Figure S15: Time-dependent predesolvation and desolvation of OmpG and FhuA  $\Delta C/\Delta 5L$  incubated with CYMAL-4 at pH 6.8.** (A) Predesolvation of OmpG from CYMAL-4; (B) Desolvation of OmpG from CYMAL-4; (C) Desolvation of FhuA  $\Delta C/\Delta 5L$  from CYMAL-4. The solubilized protein concentration was 28 nM. Detergent dilutions were conducted using an incubation concentration of 50 mM CYMAL-4. The other experimental conditions were the same as in **Fig. S1**.



CYMAL-4 - OmpG **pH 8.2** CYMAL-4 - FhuA DC/D5L

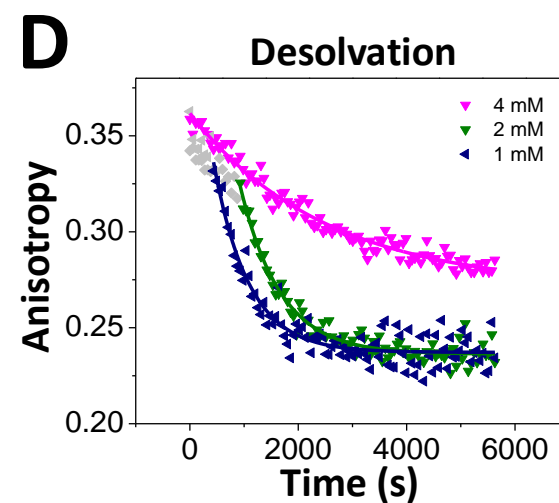
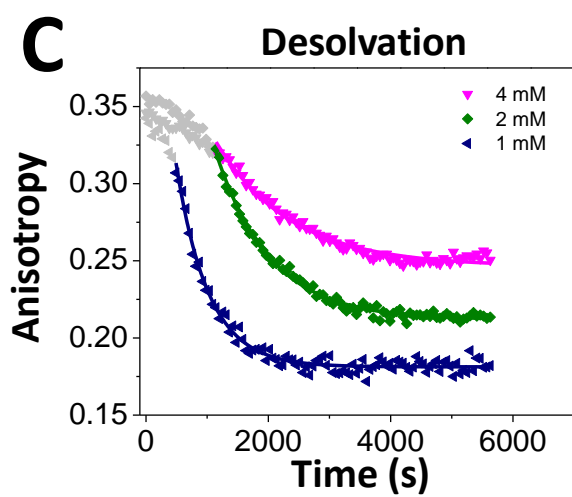
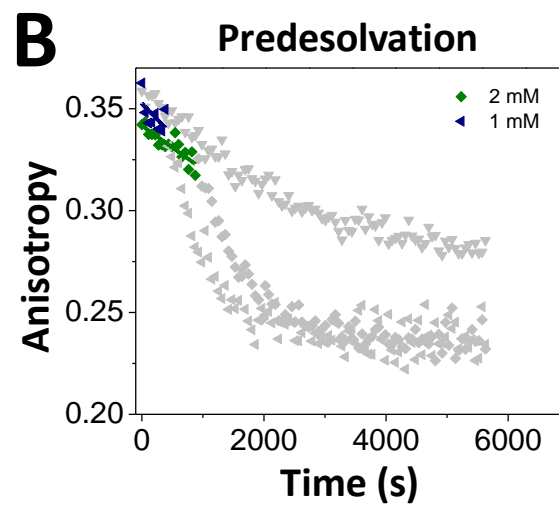
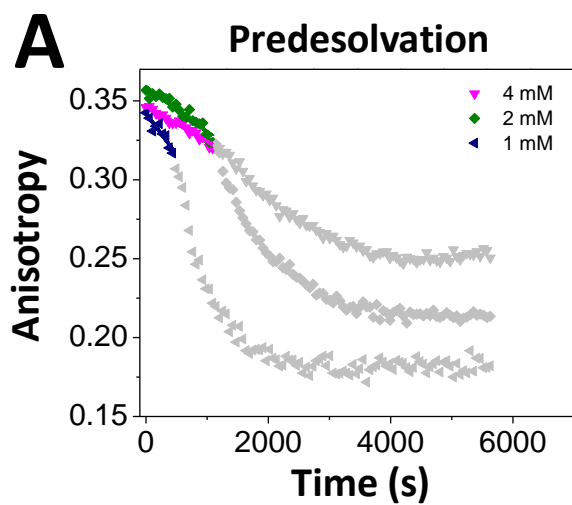


**Figure S16: Time-dependent predesolvation and desolvation of OmpG and FhuA  $\Delta C/\Delta 5L$  incubated with CYMAL-4 at pH 8.2.** (A) Predesolvation of OmpG from CYMAL-4; (B) Predesolvation of FhuA  $\Delta C/\Delta 5L$  from CYMAL-4. (C) Desolvation of OmpG from CYMAL-4; (D) Desolvation of FhuA  $\Delta C/\Delta 5L$  from CYMAL-4. The solubilized protein concentration was 28 nM. Detergent dilutions were conducted using an incubation concentration of 50 mM CYMAL-4. The other experimental conditions were the same as in **Fig. S1**.

# pH 10.0

CYMAL-4 - OmpG

## Desolvation

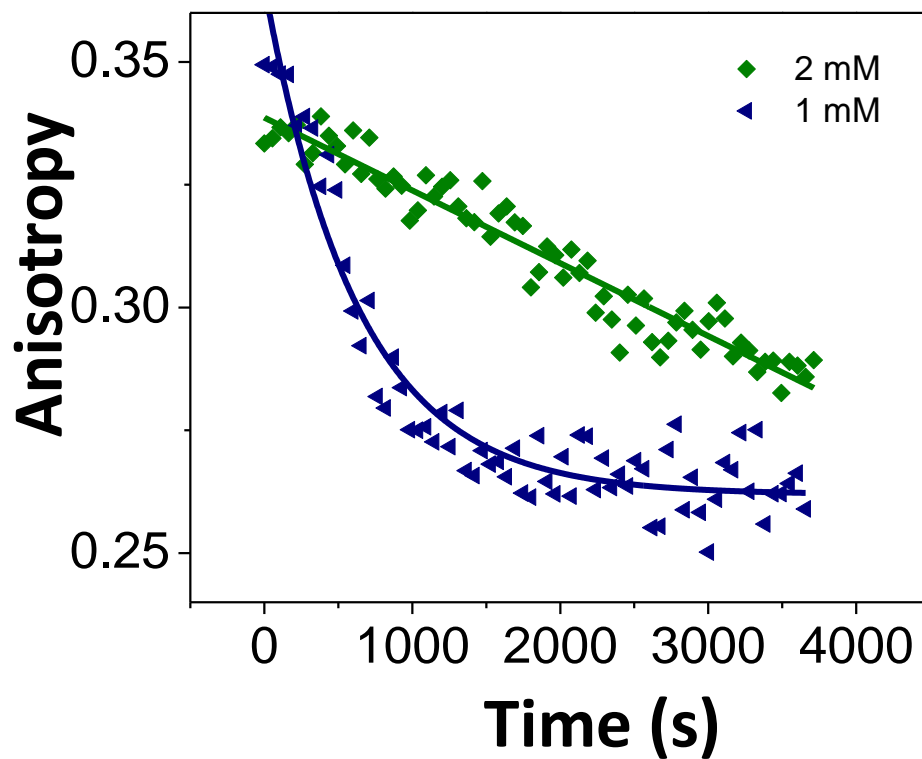


**Figure S17: Time-dependent desolvation of OmpG incubated with CYMAL at pH 10.0.**

Desolvation of OmpG and CYMAL. The solubilized protein concentration was 28 nM.

Detergent dilutions were conducted using an incubation concentration of 50 mM CYMAL-4.

The other experimental conditions were the same as in **Fig. S1**.

# pH 5.6

CYMAL-4 - FhuA DC/D5L\_25N

CYMAL-4 - FhuA DC/D5L\_30N

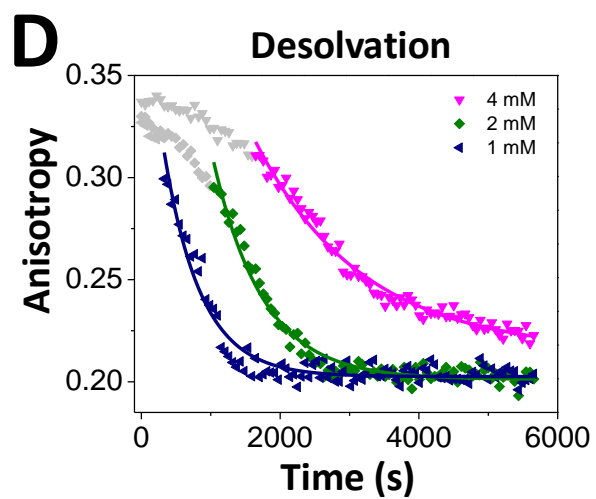
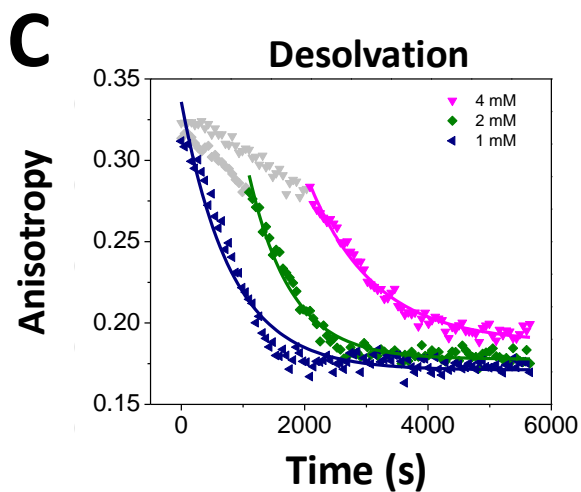
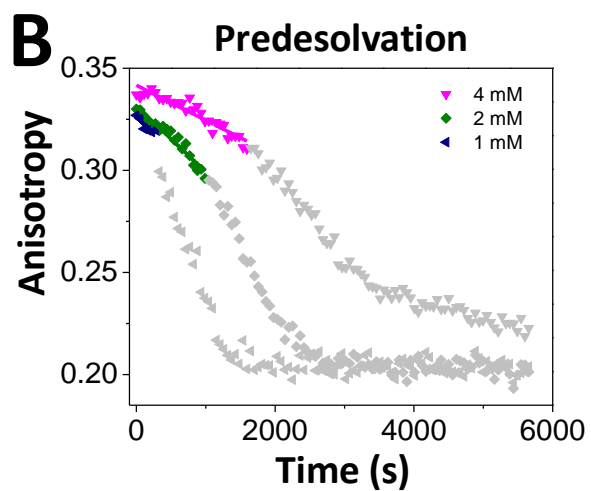
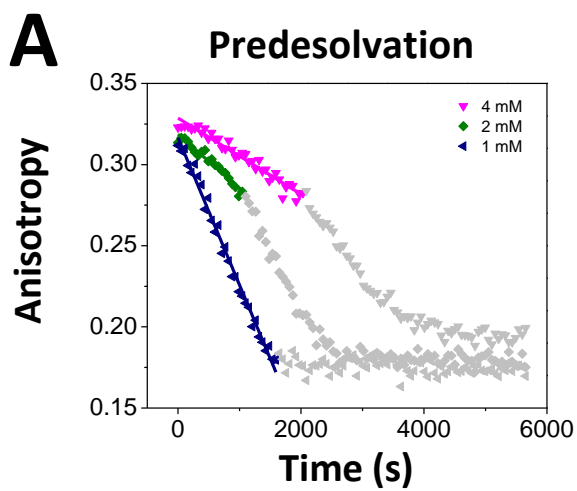


**Figure S18: Time-dependent predesolvation and desolvation of FhuA  $\Delta C/\Delta 5L_{25N}$  and FhuA  $\Delta C/\Delta 7L_{30N}$  incubated with CYMAL-4 at pH 5.6. (A) Predesolvation of FhuA  $\Delta C/\Delta 5L_{25N}$  from CYMAL-4; (B) Predesolvation of FhuA  $\Delta C/\Delta 7L_{30N}$  from CYMAL-4. (C) Desolvation of FhuA  $\Delta C/\Delta 5L_{25N}$  from CYMAL; (D) Desolvation of FhuA  $\Delta C/\Delta 7L_{30N}$  from CYMAL-4. The solubilized protein concentration was 28 nM. Detergent dilutions were conducted using an incubation concentration of 50 mM CYMAL-4. The other experimental conditions were the same as in **Fig. S1**.**

# pH 6.8

CYMAL-4 - FhuA DC/D5L\_25N

CYMAL-4 - FhuA DC/D5L\_30N

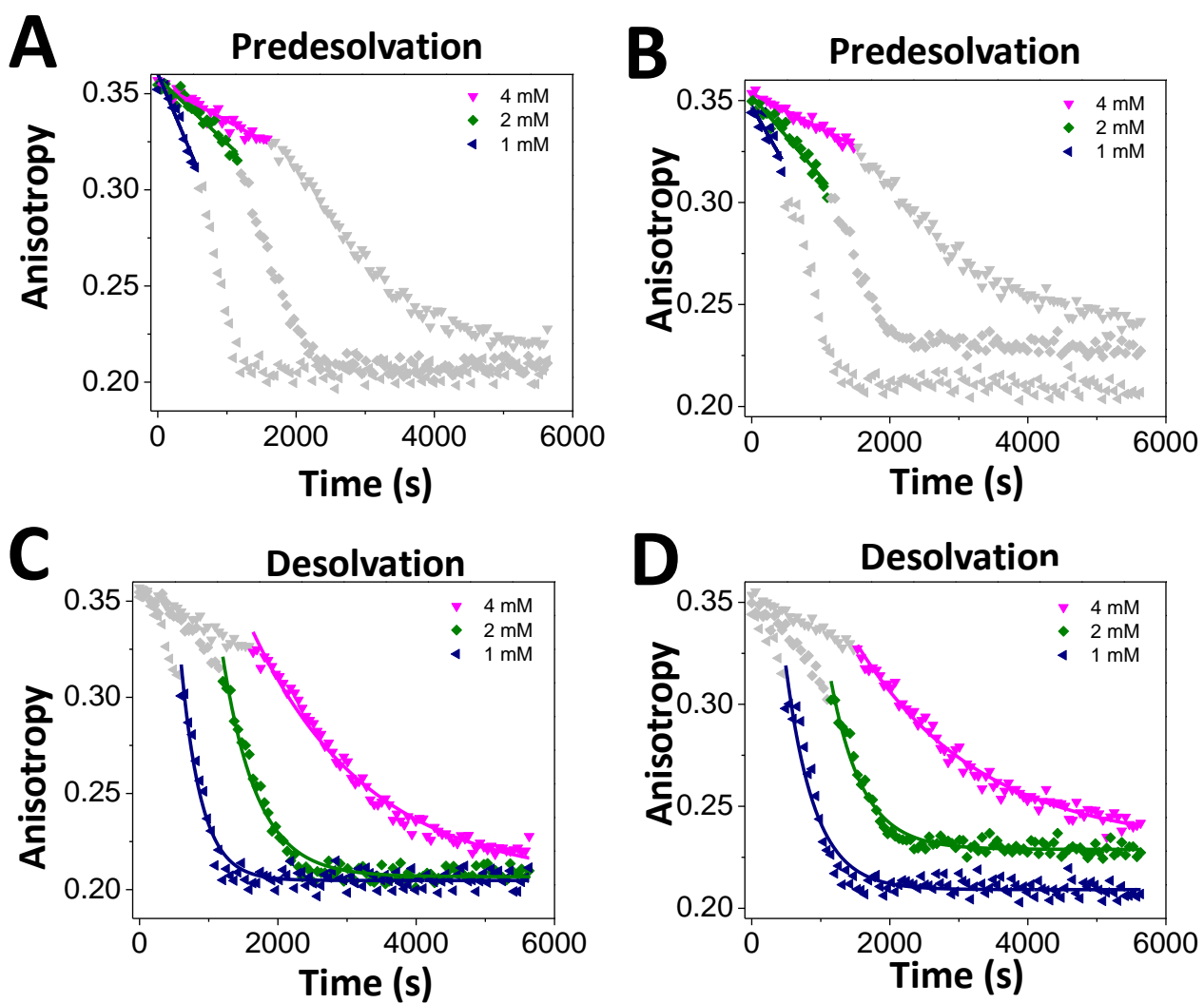


**Figure S19: Time-dependent predesolvation and desolvation of FhuA  $\Delta C/\Delta 5L_{25N}$  and FhuA  $\Delta C/\Delta 7L_{30N}$  incubated with CYMAL-4 at pH 6.8. (A) Predesolvation of FhuA  $\Delta C/\Delta 5L_{25N}$  from CYMAL-4; (B) Predesolvation of FhuA  $\Delta C/\Delta 7L_{30N}$  from CYMAL-4. (C) Desolvation of FhuA  $\Delta C/\Delta 5L_{25N}$  from CYMAL-4; (D) Desolvation of FhuA  $\Delta C/\Delta 7L_{30N}$  from CYMAL-4. The solubilized protein concentration was 28 nM. Detergent dilutions were conducted using an incubation concentration of 50 mM CYMAL-4. The other experimental conditions were the same as in **Fig. S1**.**



# pH 8.2

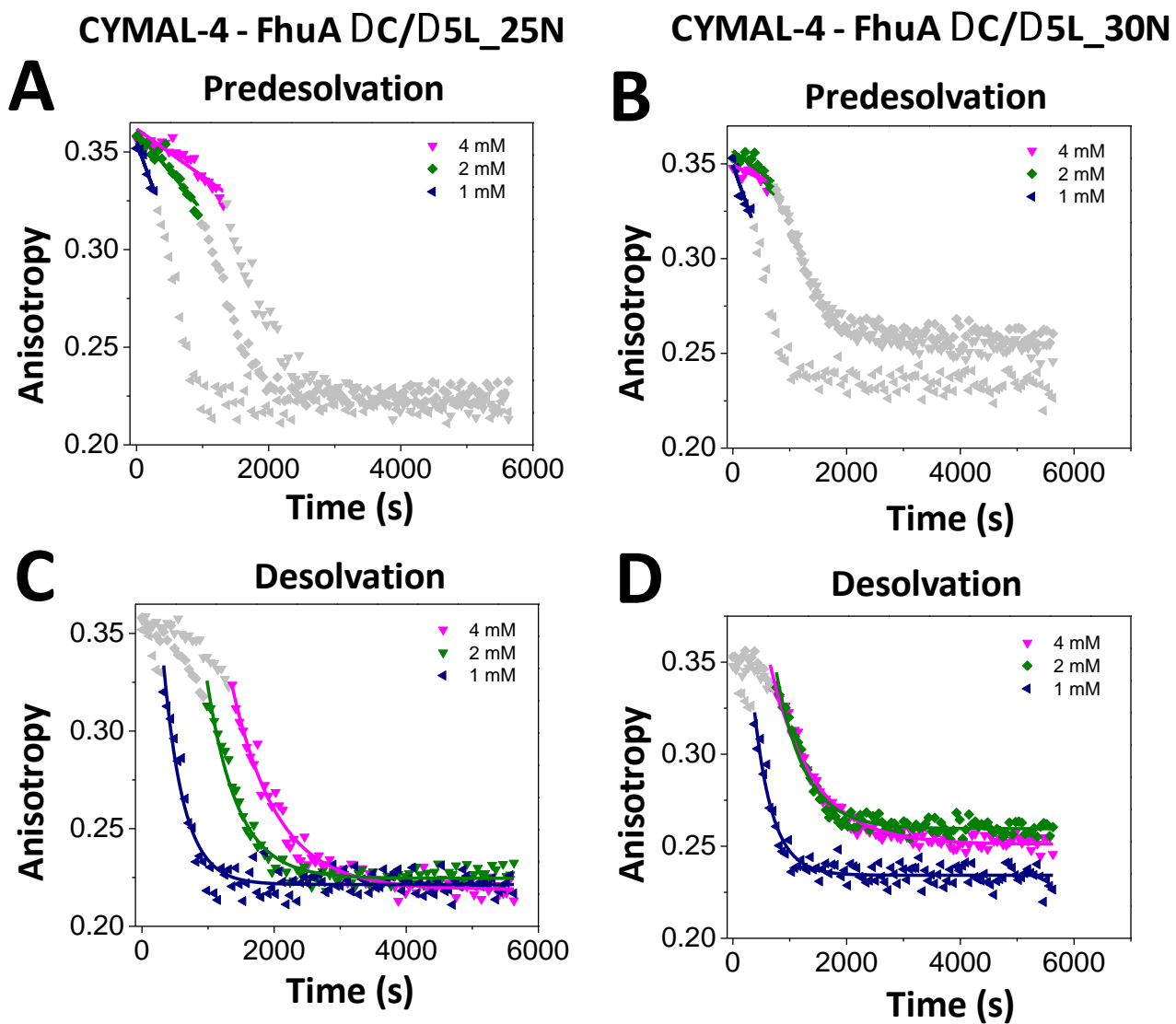


**Figure S20: Time-dependent predesolvation and desolvation of FhuA  $\Delta C/\Delta 5L_{25N}$  and FhuA  $\Delta C/\Delta 7L_{30N}$  incubated with CYMAL-4 at pH 8.2.** (A) Predesolvation of FhuA  $\Delta C/\Delta 5L_{25N}$  from CYMAL-4; (B) Predesolvation of FhuA  $\Delta C/\Delta 7L_{30N}$  from CYMAL-4. (C) Desolvation of FhuA  $\Delta C/\Delta 5L_{25N}$  from CYMAL-4; (D) Desolvation of FhuA  $\Delta C/\Delta 7L_{30N}$  from CYMAL-4. The solubilized protein concentration was 28 nM. Detergent dilutions were conducted using an incubation concentration of 50 mM CYMAL-4. The other experimental conditions were the same as in **Fig. S1**.

# pH 10.0

CYMAL-4 - FhuA DC/D5L\_25N

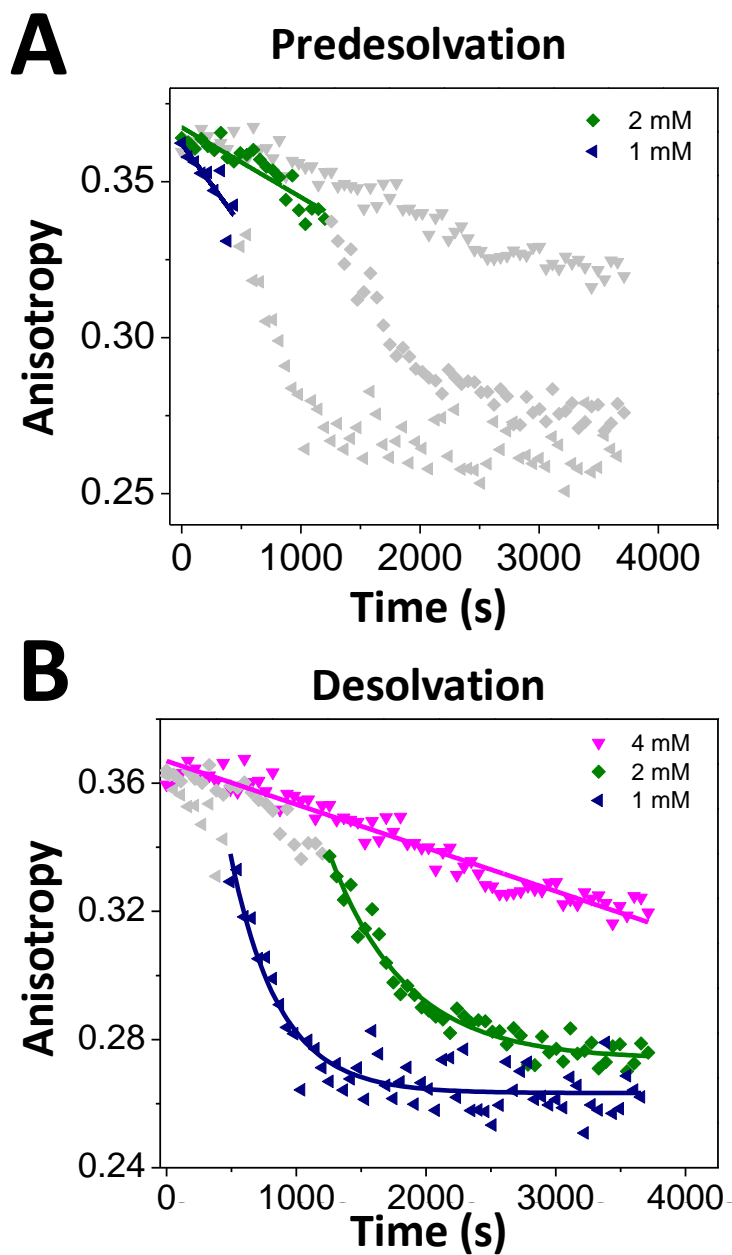


**Figure S21: Time-dependent predesolvation and desolvation of FhuA  $\Delta C/\Delta 5L_{25N}$  incubated with CYMAL-4 at pH 10.0. (A) Predesolvation of FhuA  $\Delta C/\Delta 5L_{25N}$  from CYMAL-4; (B) Desolvation of FhuA  $\Delta C/\Delta 5L_{25N}$  from CYMAL-4. The solubilized protein concentration was 28 nM. Detergent dilutions were conducted using an incubation concentration of 50 mM CYMAL-4. The other experimental conditions were the same as in **Fig. S1**.**

**3. Determination of the predesolvation rates of protein nanopores of varying pI, at detergent concentrations below the CMC, and in buffers of varying pH.**

**Table S1: Determination of the observed predesolvation rates,  $k_{obs}^{pre}$ , of OmpG when was incubated in 5 mM DM.** The predesolvation rates were determined at various pH values. The solubilized protein concentration was 28 nM. The FP measurements were carried out using a solution that contained 200 mM NaCl at room temperature. The buffer was either 50 mM HEPES (pH 6.8, pH 7.4, pH 8.2), 50 mM NaOAc (pH 4.6, pH 5.6) or 50 mM sodium borate (pH 10.0). All data were derived as averages  $\pm$  SDs of three independent data acquisitions. The  $k_{obs}^{pre}$  rate constants were inferred from the approximated linear decline in the FP anisotropy upon the incubation of the proteomicelle samples at detergent concentrations below the CMC. This was accomplished using the equation:  $r(t) = -k_{obs}^{pre}t + r_{max}$ , where  $t$ ,  $r(t)$ , and  $r_{max}$  denote the elapsed time, time-dependent FP anisotropy, and maximum FP anisotropy value, which is reached at detergent concentrations much greater than the CMC.  $T^{pre}$  is the average total duration of the predesolvation phase. [D] is the detergent concentration within the sample well.

pH	[D] (mM)	$k_{obs}^{pre} \times 10^6 (s^{-1})$	$T^{pre} (s)$
4.6	1	$19 \pm 1$	~1680
	0.85	$20 \pm 1$	~1470
	0.45	$52 \pm 4$	~737
5.6	1	$12 \pm 1$	~1340
	0.85	$19 \pm 2$	~1147
	0.45	$22 \pm 3$	~268
6.8	1	$9 \pm 1$	~1220
	0.85	$21 \pm 1$	~1560
	0.45	$42 \pm 7$	~476
8.2	1	$16 \pm 1$	~1070
	0.85	$17 \pm 2$	~737
	0.45	$91 \pm 1$	~201
10.0	1	$11 \pm 2$	~1540
	0.85	~1.5	~1270
	0.45	~1.7	~804

**Table S2:** Determination of the predesolvation observed rates of FhuA  $\Delta C/\Delta 5L$  when was incubated in 5 mM DM. The predesolvation rates were determined at various pH values. The other experimental conditions and data analysis details were the same as in **Table S1**.

pH	[D] (mM)	$k_{obs}^{pre} \times 10^6 (s^{-1})$	$T^{pre} (s)$
4.6	2	$8 \pm 1$	~1270
	1	~0.2	~648
5.6	1	$10 \pm 2$	~1140
	0.85	$19 \pm 1$	~1270
	0.45	$57 \pm 3$	~670
6.8	1	$11 \pm 2$	~1020
	0.85	$12 \pm 1$	~1220
	0.45	$35 \pm 3$	~748
8.2	1	~0.3	~1070
	0.85	$7 \pm 2$	~1070
	0.45	$15 \pm 5$	~603

**Table S3: Determination of the predesolvation observed rates of FhuA  $\Delta$ C/ $\Delta$ 5L\_25N when was incubated in 5 mM DM.** The predesolvation rates were determined at various pH values. The other experimental conditions and data analysis details were the same as in **Table S1**.

pH	[D] (mM)	$k_{obs}^{pre} \times 10^6$ (s <sup>-1</sup> )	$T^{pre}$ (s)
4.6	2	20 ± 1	~720
	1	39 ± 6	~288
5.6	1	25 ± 1	~1610
	0.85	32 ± 1	~1340
	0.45	55 ± 1	~469
6.8 <sup>a</sup>	1	11 ± 1	~1630
	0.85	40 ± 1	~1560
8.2	1	15 ± 2	~1340
	0.85	61 ± 2	~1210
	0.45	61 ± 5	~402

<sup>a</sup>Recorded data at a DM concentration of 0.45 mM exhibited an increased optical noise, precluding accurate determinations of the observed desolvation rates (**Fig. S11A**).

**Table S4: Determination of the predesolvation observed rates of FhuA  $\Delta C/\Delta 7L_{30N}$  when was incubated in 5 mM DM.** The predesolvation rates were determined at various pH values. The other experimental conditions and data analysis details were the same as in **Table S1**.

pH	[D] (mM)	$k_{obs}^{pre} \times 10^6$ (s <sup>-1</sup> )	$T^{pre}$ (s)
5.6	1	$15 \pm 1$	~1610
	0.85	$19 \pm 1$	~1470
	0.45	$63 \pm 5$	~670
6.8	1	$22 \pm 1$	~1470
	0.85	$24 \pm 1$	~1360
	0.45	$12 \pm 5$	~476
8.2	1	$18 \pm 2$	~871
	0.85	$27 \pm 1$	~1340
	0.45	$67 \pm 4$	~536



**Table S5: Determination of the predesolvation observed rates of OmpG when was incubated in 50 mM CYMAL-4.** The predesolvation rates were determined at various pH values. The other experimental conditions and data analysis details were the same as in **Table S1**.

pH	[D] (mM)	$k_{obs}^{pre} \times 10^6$ (s <sup>-1</sup> )	$T^{pre}$ (s)
5.6	4	20 ± 1	~2580
	2	34 ± 2	~1370
	1	58 ± 3	~384
6.8	4	17 ± 1	~2630
	2	27 ± 1	~1260
	1	30 ± 6	~328
8.2	4	28 ± 2	~1090
	2	22 ± 1	~1090
	1	52 ± 8	~437
10.0	2	N/A*	N/A
	1	N/A	N/A

\*N/A stands for predesolvation was not noted.

**Table S6: Determination of the predesolvation observed rates of FhuA  $\Delta C/\Delta 5L$  when was incubated in 50 mM CYMAL-4.** The predesolvation rates were determined at various pH values. The other experimental conditions and data analysis details were the same as in **Table S1**.

pH	[D] (mM)	$k_{obs}^{pre} \times 10^6$ (s <sup>-1</sup> )	$T^{pre}$ (s)
4.6	2	$20 \pm 5$	~2966
	1	$51 \pm 3$	404
5.6	4	N/A*	N/A
	2	N/A	N/A
	1	N/A	N/A
6.8	4	N/A	N/A
	2	N/A	N/A
	1	N/A	N/A
8.2	2	$22 \pm 3$	~874
	1	~31	~383

\*N/A stands for predesolvation was not noted.

**Table S7: Determination of the predesolvation observed rates of FhuA  $\Delta$ C/ $\Delta$ 5L\_25N**

when was incubated in 50 mM CYMAL-4. The predesolvation rates were determined at various pH values. The other experimental conditions and data analysis details were the same as in Table S1.

pH	[D] (mM)	$k_{obs}^{pre} \times 10^6$ (s <sup>-1</sup> )	$T^{pre}$ (s)
5.6	4	23 ± 1	1592
	2	33 ± 1	1043
	1	N/A*	N/A
6.8	4	20 ± 1	~1590
	2	34 ± 2	~1150
	1	86 ± 8	~547
8.2	4	24 ± 2	~1310
	2	41 ± 3	~929
	1	93 ± 14	~273
10.0	2	26 ± 2	~1200
	1	52 ± 13	~437

\*N/A stands for predesolvation was not noted.

**Table S8: Determination of the predesolvation observed rates of FhuA  $\Delta$ C/ $\Delta$ 7L\_30N when was incubated in 50 mM CYMAL-4.** The predesolvation rates were determined at various pH values. The other experimental conditions and data analysis details were the same as in **Table S1**.

pH	[D] (mM)	$k_{obs}^{pre} \times 10^6$ (s <sup>-1</sup> )	$T^{pre}$ (s)
5.6	4	17 ± 1	~1590
	2	32 ± 2	~988
	1	30 ± 8	~274
6.8	4	17 ± 1	~1480
	2	40 ± 2	~1090
	1	59 ± 12	~437
8.2	4	14 ± 5	~601
	2	23 ± 5	~765
	1	85 ± 16	~328

*4. Determination of the desolvation rate and time constants of protein nanopores of varying pI, at detergent concentrations below the CMC, and in buffers of varying pH.*

**Table S9: The observed desolvation rate constants,  $k_{obs}^{des}$ , of OmpG refolded in 5 mM**

**DM.** The desolvation rates were determined at various pH values. The solubilized protein concentration was 28 nM. The FP measurements were carried out using a solution that contained 200 mM NaCl at room temperature. The buffer was either 50 mM HEPES (pH 6.8, pH 7.4, pH 8.2), 50 mM NaOAc (pH 4.6, pH 5.6) or 50 mM sodium borate (pH 10.0). All data were derived as averages  $\pm$  SDs of three independent data acquisitions. The  $k_{obs}^{pre}$  values were inferred using a single-exponential decay of the FP anisotropy upon the incubation of proteomicelle samples at detergent concentrations below the CMC. This was accomplished using the equation:

$$r(t) = r_d e^{-\frac{t}{\tau}} + r_{min}, \quad (S1)$$

$$\text{where } k_{obs}^{des} = \frac{1}{\tau} \quad (S2)$$

Here,  $t$ ,  $r(t)$ , and  $r_{min}$  denote the elapsed time during the detergent desolvation phase, time-dependent FP anisotropy, and minimum FP anisotropy value, which is reached at infinity and at detergent concentrations below the CMC.  $r_d$  is a FP anisotropy constant. The standard error of the mean for  $r_{min}$  was always lower than 0.001.

<b>pH</b>	<b>[D] (mM)</b>	<b><math>k_{obs}^{des} \times 10^5 \text{ (s}^{-1}\text{)}</math></b>	<b><math>r_{min}</math></b>	<b><math>r_d</math></b>	<b><math>\tau \text{ (s)}</math></b>
4.6	1	260 ± 29	0.14	~3.3	385 ± 43
	0.85	300 ± 29	0.09	~7.6	333 ± 32
	0.45	452 ± 45	0.09	3.0 ± 1.2	221 ± 22
5.6	1	114 ± 8	0.15	0.56 ± 0.06	876 ± 61
	0.85	256 ± 10	0.12	~0.14	390 ± 16
	0.45	224 ± 8	0.11	0.38 ± 0.01	447 ± 16
6.8	1	133 ± 14	0.26	0.25 ± 0.05	750 ± 80
	0.85	202 ± 12	0.18	2.6 ± 0.6	494 ± 32
	0.45	236 ± 17	0.15	0.39 ± 0.04	423 ± 31
8.2	1	146 ± 8	0.23	0.40 ± 0.04	685 ± 35
	0.85	269 ± 13	0.17	1.3 ± 0.2	372 ± 18
	0.45	556 ± 38	0.16	0.79 ± 0.10	180 ± 12
10.0	1	235 ± 16	0.24	4.5 ± 1.2	426 ± 30
	0.85	267 ± 18	0.21	3.8 ± 0.9	375 ± 26
	0.45	505 ± 24	0.18	8.6 ± 1.8	198 ± 9

**Table S10:** The observed desolvation rate constants,  $k_{obs}^{des}$ , of FhuA  $\Delta C/\Delta 5L$  refolded in 5 mM DM. Details about other experimental conditions and data analysis were the same as in Table S9.

pH	[D] (mM)	$k_{obs}^{des} \times 10^5$ (s <sup>-1</sup> )	$r_{min}$	$r_d$	$\tau$ (s)
4.6	2	149 ± 26	0.29	0.44 ± 0.16	672 ± 117
	1	236 ± 14	0.21	0.76 ± 0.09	423 ± 25
5.6	1	159 ± 10	0.21	0.84 ± 0.11	628 ± 40
	0.85	323 ± 14	0.21	7.8 ± 1.5	310 ± 13
	0.45	476 ± 32	0.20	3.1 ± 0.8	210 ± 14
6.8	1	117 ± 11	0.26	0.32 ± 0.04	857 ± 80
	0.85	266 ± 18	0.22	3.4 ± 0.8	376 ± 25
	0.45	403 ± 29	0.21	2.4 ± 0.6	248 ± 18
8.2	1	191 ± 18	0.29	0.47 ± 0.10	523 ± 50
	0.85	157 ± 11	0.24	0.60 ± 0.08	636 ± 50
	0.45	319 ± 28	0.23	0.66 ± 0.14	314 ± 28

**Table S11:** The observed desolvation rate constants,  $k_{obs}^{des}$ , of FhuA  $\Delta C/\Delta 5L\_25N$  refolded in 5 mM DM. Details about other experimental conditions and data analysis were the same as in Table S9.

pH	[D] (mM)	$k_{obs}^{des} \times 10^5$ (s <sup>-1</sup> )	$r_{min}$	$r_d$	$\tau$ (s)
4.6	2	115 ± 16	0.19	0.18 ± 0.02	866 ± 117
	1	199 ± 10	0.15	0.23 ± 0.01	503 ± 26
5.6	1	340 ± 16	0.18	28 ± 8	294 ± 14
	0.85	337 ± 14	0.16	12 ± 3	297 ± 12
	0.45	403 ± 22	0.16	1.2 ± 0.2	248 ± 14
6.8 <sup>a</sup>	1	292 ± 23	0.22	10 ± 4	342 ± 27
	0.85	336 ± 16	0.16	23 ± 6	298 ± 14
8.2	1	344 ± 23	0.19	11 ± 4	291 ± 20
	0.85	437 ± 31	0.17	13 ± 5	229 ± 16
	0.45	641 ± 32	0.16	2.3 ± 0.4	156 ± 8

<sup>a</sup>Recorded data at a DM concentration of 0.45 mM exhibited an increased optical noise, precluding accurate determinations of the observed desolvation rates (**Fig. S11C**).



**Table S12:** The observed desolvation rate constants,  $k_{obs}^{des}$ , of FhuA  $\Delta C/\Delta 7L\_30N$  refolded in 5 mM DM. Details about other experimental conditions and data analysis were the same as in Table S9.

pH	[D] (mM)	$k_{obs}^{des} \times 10^5$ (s <sup>-1</sup> )	$r_{min}$	$r_d$	$\tau$ (s)
5.6	1	111 ± 12	0.19	0.84 ± 0.16	899 ± 103
	0.85	217 ± 8	0.19	3.09 ± 0.41	461 ± 18
	0.45	377 ± 19	0.19	1.44 ± 0.22	265 ± 13
6.8	1	263 ± 21	0.23	2.63 ± 0.90	380 ± 31
	0.85	280 ± 11	0.19	5.15 ± 0.92	357 ± 18
	0.45	378 ± 20	0.18	0.90 ± 0.11	265 ± 14
8.2	1	259 ± 24	0.23	0.47 ± 0.12	386 ± 36
	0.85	394 ± 23	0.18	13.7 ± 4.67	254 ± 15
	0.45	595 ± 52	0.18	1.76 ± 0.59	168 ± 15

**Table S13:** The observed desolvation rate constants,  $k_{obs}^{des}$ , of OmpG refolded in 50 mM

CYMAL-4. Details about other experimental conditions and data analysis were the same as in

Table S9.

pH	[D] (mM)	$k_{obs}^{des} \times 10^5$ (s <sup>-1</sup> )	$r_{min}$	$r_d$	$\tau$ (s)
5.6	4	108 ± 4.7	0.15	1.87 ± 0.23	922 ± 40
	2	171 ± 5.6	0.13	1.52 ± 0.14	586 ± 19
	1	202 ± 9.5	0.13	0.39 ± 0.02	495 ± 23
6.8	4	96 ± 5.2	0.23	1.16 ± 0.16	1040 ± 56
	2	200 ± 7.5	0.20	1.63 ± 0.18	499 ± 19
	1	235 ± 8.4	0.19	0.38 ± 0.02	426 ± 15
8.2	4	82 ± 3.6	0.25	0.21 ± 0.01	1220 ± 53
	2	112 ± 2.6	0.21	0.39 ± 0.01	889 ± 21
	1	190 ± 5.8	0.18	0.34 ± 0.01	525 ± 16
10.0	2	~1.48	N/A	N/A	N/A
	1	158 ± 12.0	0.26	0.10 ± 0.00	632 ± 48

NA stands for not applicable. In this case, the desolvation phase followed an almost linear time-dependent decrease with an observed desolvation constant,  $k_{obs}^{des}$ .

**Table S14:** The observed desolvation rate constants,  $k_{obs}^{des}$ , of FhuA  $\Delta C/\Delta 5L$  refolded in 50 mM CYMAL-4. Details about other experimental conditions and data analysis were the same as in Table S9.

pH	[D] (mM)	$k_{obs}^{des} \times 10^5$ (s <sup>-1</sup> )	$r_{min}$	$r_d$	$\tau$ (s)
4.6	2	$7.8 \pm 0.4$	N/A*	N/A	N/A
	1	$185 \pm 10$	$0.18 \pm 0.01$	$0.33 \pm 0.02$	$542 \pm 30$
5.6	4	$2.7 \pm 0.1$	N/A	N/A	N/A
	2	$4.4 \pm 0.1$	N/A	N/A	N/A
	1	$7.7 \pm 0.1$	N/A	N/A	N/A
6.8	4	$1.5 \pm 0.1$	N/A	N/A	N/A
	2	$3.6 \pm 0.1$	N/A	N/A	N/A
	1	$6.1 \pm 0.1$	N/A	N/A	N/A
8.2	4	$40 \pm 3$	0.27	$0.09 \pm 0.01$	$2504 \pm 161$
	2	$135 \pm 7$	0.24	$0.31 \pm 0.02$	$742 \pm 38$
	1	$156 \pm 11$	0.24	$0.20 \pm 0.02$	$643 \pm 45$

\*NA stands for exponential decay of the detergent desolvation was not applicable. In this case, the desolvation phase followed an almost linear time-dependent decrease with an observed desolvation constant,  $k_{obs}^{des}$ .

**Table S15:** The observed desolvation rate constants,  $k_{obs}^{des}$ , of FhuA  $\Delta C/\Delta 5L_{25N}$  refolded in 50 mM CYMAL-4. Details about other experimental conditions and data analysis were the same as in Table S9.

pH	[D] (mM)	$k_{obs}^{des} \times 10^5$ (s <sup>-1</sup> )	$r_{min}$	$r_d$	$\tau$ (s)
5.6	4	94 ± 5	0.19	0.70 ± 0.08	1060 ± 59
	2	146 ± 6	0.18	0.56 ± 0.04	686 ± 28
	1	124 ± 5	0.17	0.16 ± 0.01	807 ± 35
6.8	4	59 ± 3	0.20	0.34 ± 0.02	1702 ± 92
	2	201 ± 9	0.21	1.3 ± 0.2	497 ± 22
	1	339 ± 20	0.20	0.86 ± 0.12	295 ± 17
8.2	4	147 ± 6	0.22	0.77 ± 0.08	680 ± 30
	2	216 ± 10	0.22	0.85 ± 0.10	463 ± 22
	1	326 ± 22	0.22	0.33 ± 0.03	307 ± 21
10.0	2	171 ± 15	0.27	0.55 ± 0.11	585 ± 50
	1	269 ± 29	0.26	0.28 ± 0.05	372 ± 40

**Table S16:** The observed desolvation rate constants,  $k_{obs}^{des}$ , of FhuA  $\Delta C/\Delta 5L\_30N$  refolded in 50 mM CYMAL-4. Details about other experimental conditions and data analysis were the same as in Table S9.

pH	[D] (mM)	$k_{obs}^{des} \times 10^5$ (s <sup>-1</sup> )	$r_{min}$	$r_d$	$\tau$ (s)
5.6	4	65 ± 4	0.21	0.30 ± 0.02	1542 ± 88
	2	139 ± 6	0.20	0.45 ± 0.03	718 ± 30
	1	188 ± 9	0.20	0.20 ± 0.01	531 ± 27
6.8	4	56 ± 3	0.23	0.23 ± 0.01	1786 ± 106
	2	218 ± 10	0.23	1.0 ± 0.1	458 ± 21
	1	240 ± 14	0.21	0.36 ± 0.03	417 ± 25
8.2	4	133 ± 5	0.25	0.23 ± 0.01	753 ± 28
	2	196 ± 9	0.26	0.38 ± 0.03	509 ± 24
	1	309 ± 21	0.23	0.29 ± 0.03	324 ± 22

**5. Initial rates of detergent desolvation determined for acidic and basic  $\beta$ -barrel membrane proteins.**

**Table S17: Initial desolvation rates,  $R_{in}^{des}$ , of the DM- and CYMAL-4-containing proteomicelles that include acidic and basic  $\beta$ -barrel membrane proteins.<sup>a,b,c</sup>**

Detergent	CMC (mM)	Protein	Charge state	pI	Total protein length (residues)	Initial desolvation rate, $R_{in}^{des} \times 10^{12}$ (Ms <sup>-1</sup> ) <sup>d</sup>
DM	1.8	OmpG	Acidic	4.4	281	41 ± 2
		FhuA $\Delta$ C/ $\Delta$ 5L	Acidic	5.7	505	54 ± 5
		FhuA $\Delta$ C/ $\Delta$ 5L_25N	Basic	9.3	473	96 ± 6
		FhuA $\Delta$ C/ $\Delta$ 7L_30N	Basic	9.6	426	73 ± 7
CYMAL-4	7.6	OmpG	Acidic	4.4	281	23 ± 1
		FhuA $\Delta$ C/ $\Delta$ 5L	Acidic	5.7	505	11 ± 1
		FhuA $\Delta$ C/ $\Delta$ 5L_25N	Basic	9.3	473	41 ± 2
		FhuA $\Delta$ C/ $\Delta$ 7L_30N	Basic	9.6	426	37 ± 1

<sup>a</sup>The final detergent concentrations for DM and CYMAL-4 were 1 and 4 mM, respectively.

<sup>b</sup>The isoelectric point was determined using the total number of residues of each protein. The truncation FhuA proteins include a 33-residue signal peptide at the N-terminus and a Cys-containing, Gly/Ser-rich containing polypeptide loop engineered on the T7  $\beta$ -turn.

<sup>c</sup>All proteins include a 6 $\times$ His<sup>+</sup> at the C terminus.

<sup>d</sup>The initial desolvation rates were determined using a solution that contained 200 mM NaCl, 50 mM HEPES, pH 8.2.

**6. Calculation of the association ( $k_{on}$ ) and dissociation ( $k_{off}$ ) rate constants using detergent-desolvation curves.**

In this work, the detergent concentration-dependent desolvation curves were acquired when the

detergent concentration was lower than the CMC. Assuming a simplified bimolecular reaction



where  $[P]$  and  $[D]$  are time-dependent concentrations of free proteins and detergent micelles, respectively.

$$\frac{d[PD]}{dt} = k_{on}[P][D] - k_{off}[PD] \quad (S4)$$

where  $k_{on}$  and  $k_{off}$  are the association and dissociation rate constants, respectively. Here,  $[PD]$  indicates the concentration of proteomicelles. Then,

$$[P] = [P]_{tot} - [PD] \quad (S5)$$

Here,  $[P]_{tot}$  denotes the total solubilized protein in solution (e.g.,  $[P]_{tot} = 28$  nM),

$$[D] = [D]_{tot} - [PD] \quad (S6)$$

Because, the concentration of detergent micelles,  $[D]$ , is much greater than the protein concentration,  $[P]$ ,

$$[P] \ll [D], \text{ then } [PD] \ll [D] \quad (S7)$$

and

$$[D] \cong [D]_{tot} \quad (\text{S8})$$

Therefore,

$$\frac{d[PD]}{dt} = k_{on}[P]_{tot}[D] - (k_{on}[D] + k_{off})[PD] \quad (\text{S9})$$

To solve this differential equation, we will denote the main variable  $[PD]$  by  $x$ , and

$$\alpha = k_{on}[P]_{tot}[D] \quad (\text{S10})$$

$$\beta = (k_{on}[D] + k_{off}) \quad (\text{S11})$$

Thus,

$$\frac{dx}{dt} = \alpha - \beta x \quad (\text{S12})$$

or

$$\int_{x_{max}}^x \frac{dx}{\alpha - \beta x} = \int_0^t dt \quad (\text{S13})$$



where  $x_{max}$  is the concentration of the proteomicelles,  $[PD]_{max}$ , at the beginning of the detergent-

desolvation reaction. The integral equation has the following solution:

$$\ln \left( x - \frac{\alpha}{\beta} \right)_{x_{max}} = -\beta t \quad (\text{S14})$$

$$\frac{x - \frac{\alpha}{\beta}}{x_{max} - \frac{\alpha}{\beta}} = e^{-\beta t} \quad (\text{S15})$$

$$x(0) = x_{max} \text{ at } t = 0 \quad (\text{S16})$$

and

$$x(\infty) = \frac{\alpha}{\beta} \text{ at } t = \infty \quad (\text{S17})$$

$$x_{\infty} = \frac{k_{on}[P]_{tot}[D]}{k_{on}[D] + k_{off}} \quad (\text{S18})$$

In between these values:

$$x(t) = \frac{\alpha}{\beta} + \left( x_{max} - \frac{\alpha}{\beta} \right) e^{-\beta t} \quad (\text{S19})$$

This is an exponential curve, but it has a constant in front of the exponential term

$$x \text{ at } \infty = \frac{\alpha}{\beta} \quad (\text{S20})$$

In order to operate linear-regression fittings of the desolvation curve domains at detergent concentrations comparable with or below CMC'c, we always need to subtract that constant from  $x(t)$ . Of course, the main assumption is that the changes in the FP anisotropy are proportional to the detergent exchange between solution and proteomicelles.

The equation (S19) can be re-written as:

$$\ln \left[ x(t) - \frac{\alpha}{\beta} \right] = \ln \left( x_{max} - \frac{\alpha}{\beta} \right) - \beta t \quad (\text{S21})$$

From the linear fit, one extracts detergent concentration-dependent  $\beta [D]$

$$\beta([D]) = (k_{on}[D] + k_{off}) = k_{obs}^{des} \quad (\text{S22})$$

where  $k_{obs}^{des}$  indicates the observed rate constant of desolvation. Here, we monitor an FP anisotropy decrease, so a dominantly dissociation process, the fitting function (S22) becomes the following:<sup>1</sup>

$$k_{obs}^{des} = -k_{on}[D] + k_{off} \quad (\text{S23})$$

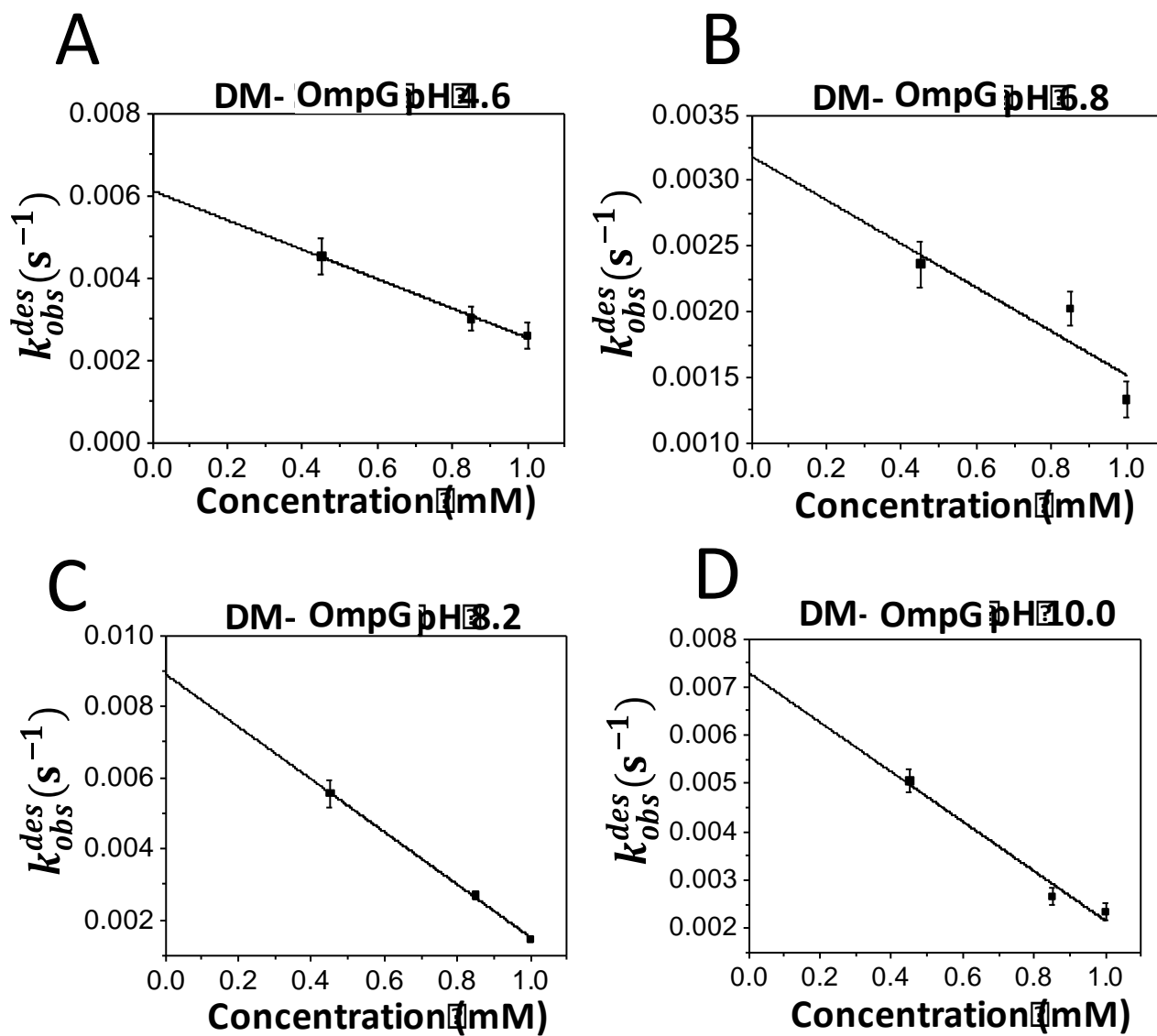
Because the desolvation occurs below the CMC,  $[D]$  is the actual detergent concentration in the sample well. We observed fast desolvation rates when there is little detergent in the well. The intercept with the vertical axis ( $[D]=0$ ) is the kinetic rate constant of dissociation of the proteomicelles,  $k_{off}$ . The intercept with the horizontal axis ( $k_{obs}^{des}=0$ ) is the equilibrium

dissociation constant,  $K_d$ . For a positive value of  $k_{on}$ , an increase of  $[D]$  produces a decrease in  $k_{obs}^{des}$ . Because of an exponential dependence in equation (S21), then

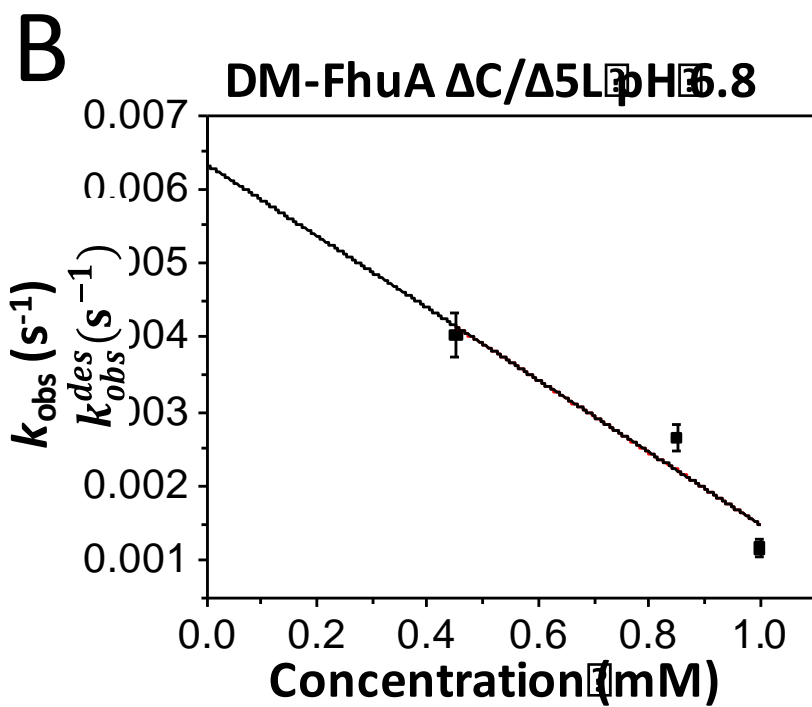
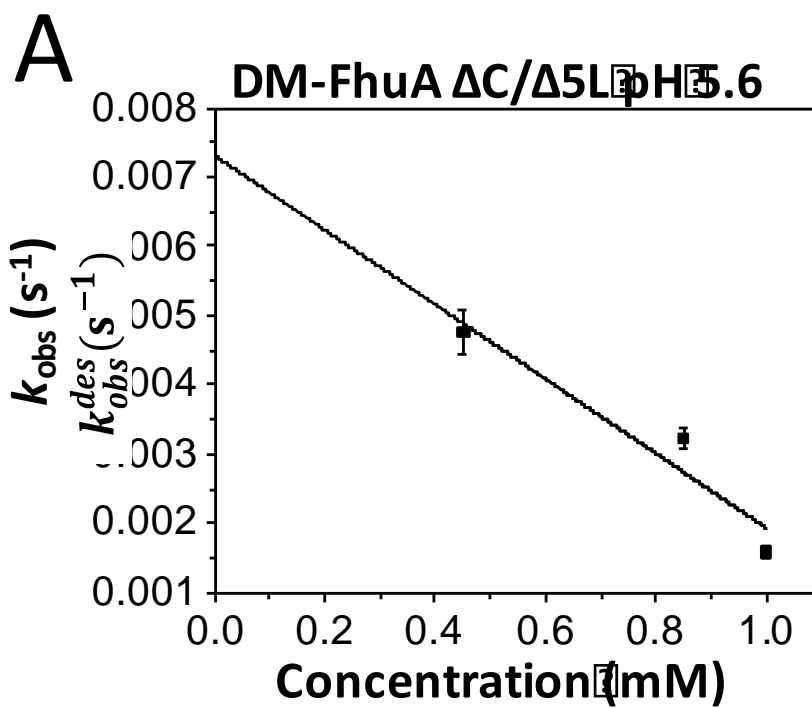
$$k_{obs}^{des} = \frac{\ln 2}{T_{1/2}} = \frac{0.693}{T_{1/2}} \quad (\text{S24})$$

where  $T_{1/2}$  is the half-time of the detergent desolvation reaction, namely the time at which the FP anisotropy reaches 50% out of the value that corresponds to the beginning of the desolvation phase, or the end of the predesolvation phase.

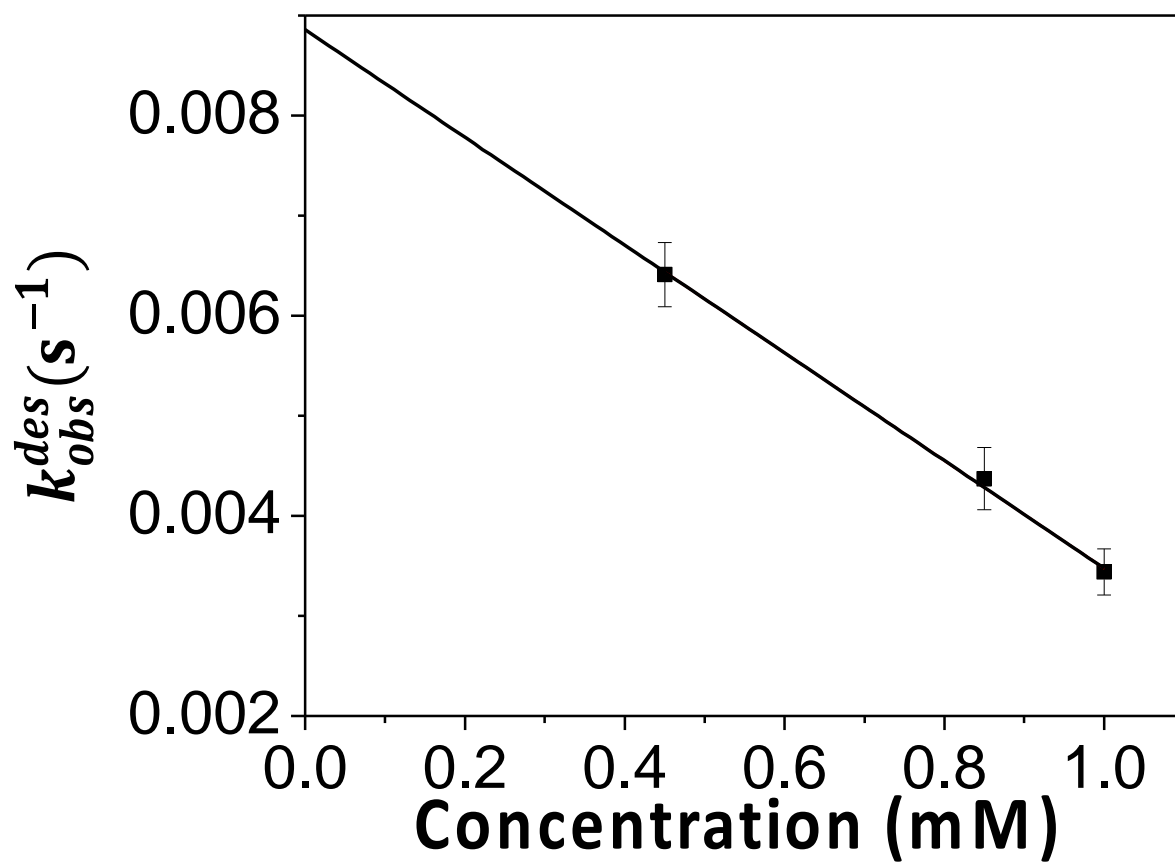
7. Scaling of the observed desolvation rates of the protein nanopores with the detergent concentrations at values below the CMC.



**Figure S22:** The observed kinetic rates of desolvation of OmpG scale linearly with the DM detergent concentrations at values below the  $\text{CMC}^{\text{DM}} = 1.8 \text{ mM}$ . (A) pH 4.6; (B) pH 6.8; (C) pH 8.2; (D) pH 10.0. The other experimental conditions were the same as those stated in the figure caption of **Fig. S1**.

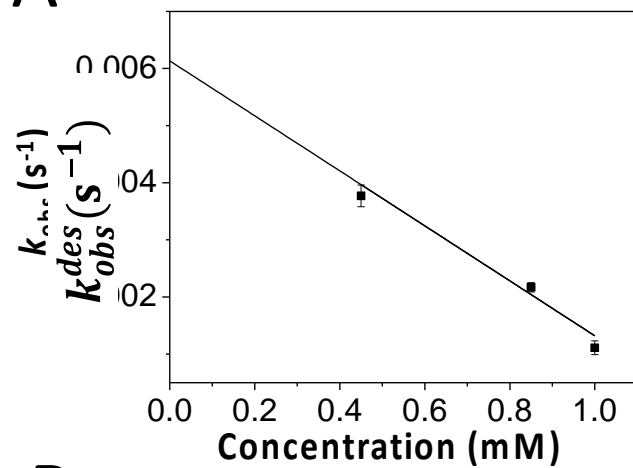
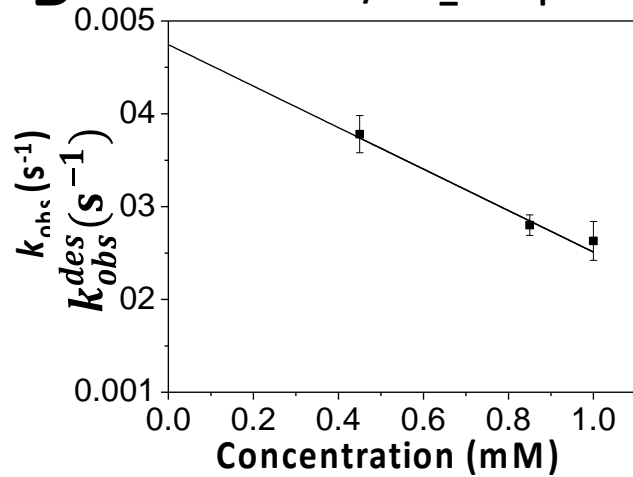
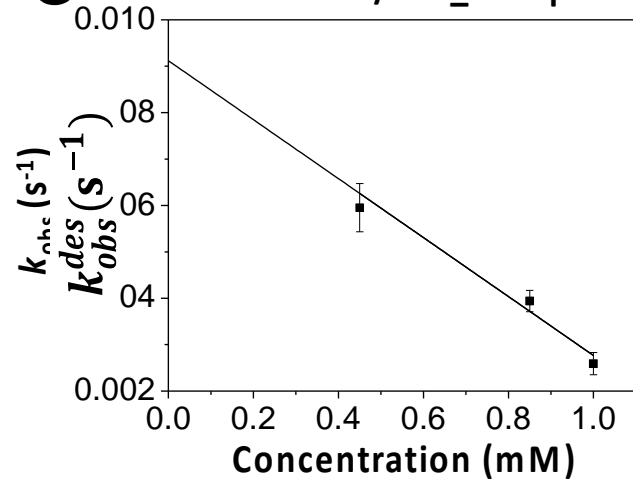


**Figure S23:** The observed kinetic rates of desolvation of FhuA  $\Delta C/\Delta 5L$  scale linearly with the DM detergent concentrations at values below the  $CMC^{DM} = 1.8$  mM. (A) pH 5.6; (B) pH 6.8. The other experimental conditions were the same as those stated in the figure caption of **Fig. S1**.

**DM-FhuA  $\Delta C/\Delta 5L_{25N}$  pH 8.2**



**Figure S24:** The observed kinetic rate constants of desolvation of FhuA  $\Delta C/\Delta 5L_{25N}$  scale linearly with the DM detergent concentrations at values below the  $CMC^{DM} = 1.8$  mM at pH 8.2. The other experimental conditions were the same as those stated in the figure caption of **Fig. S1**.

**A** DM- FhuA  $\Delta C/\Delta 7L_{30N}$  pH 5.6**B** DM- FhuA  $\Delta C/\Delta 7L_{30N}$  pH 6.8**C** DM- FhuA  $\Delta C/\Delta 7L_{30N}$  pH 8.2

**Figure S25:** The observed kinetic rates of desolvation of FhuA  $\Delta C/\Delta 7L_{30N}$  scale linearly with the DM detergent concentrations at values below the  $CMC^{DM} = 1.8$  mM. (A) pH 5.6; (B) pH 6.8; (C) pH 8.2. The other experimental conditions were the same as those stated in the figure caption of **Fig. S1**.

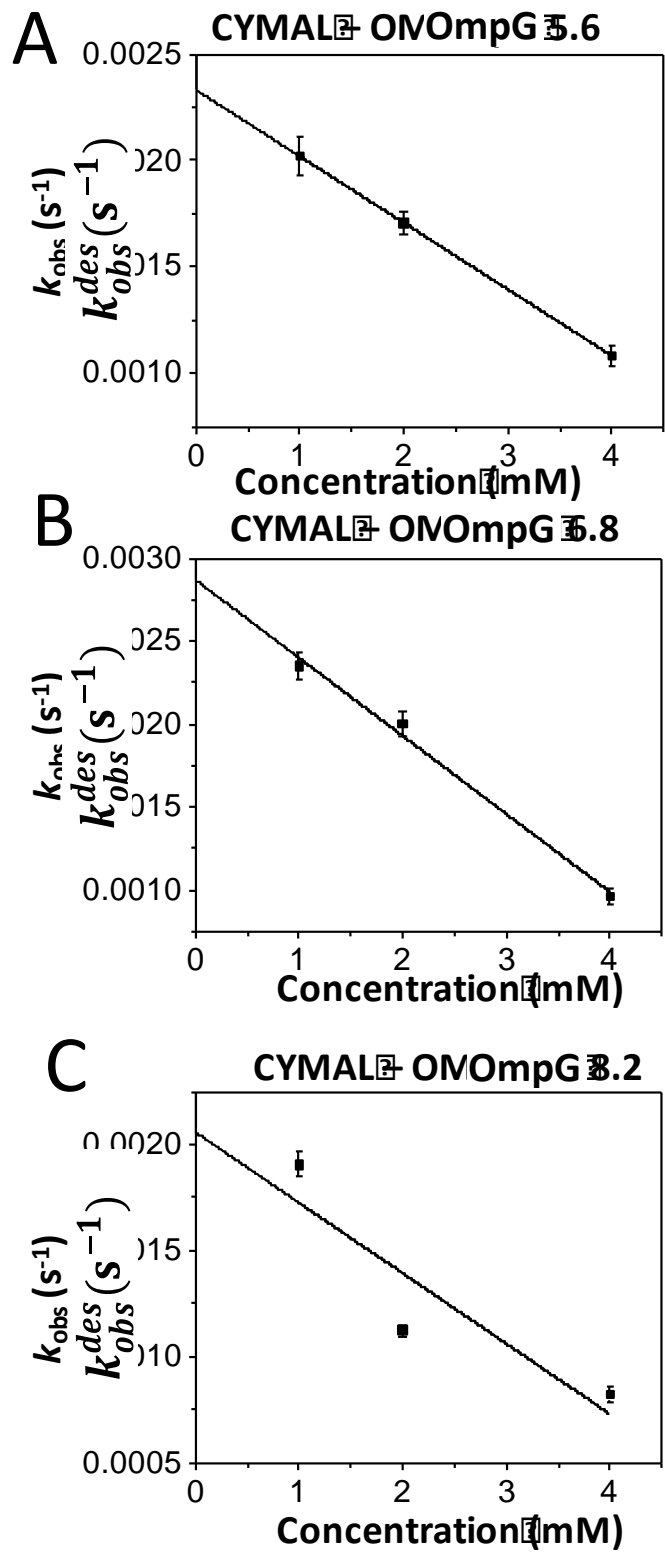


**Figure S26** The observed kinetic rates of desolvation of OmpG scale linearly with the CYMAL-4 detergent concentrations at values below the  $\text{CMC}^{\text{CYMAL-4}} = 7.6 \text{ mM}$ . (A) pH 5.6; (B) pH 6.8; (C) pH 8.2. The other experimental conditions were the same as those stated in the figure caption of **Fig. S1**.

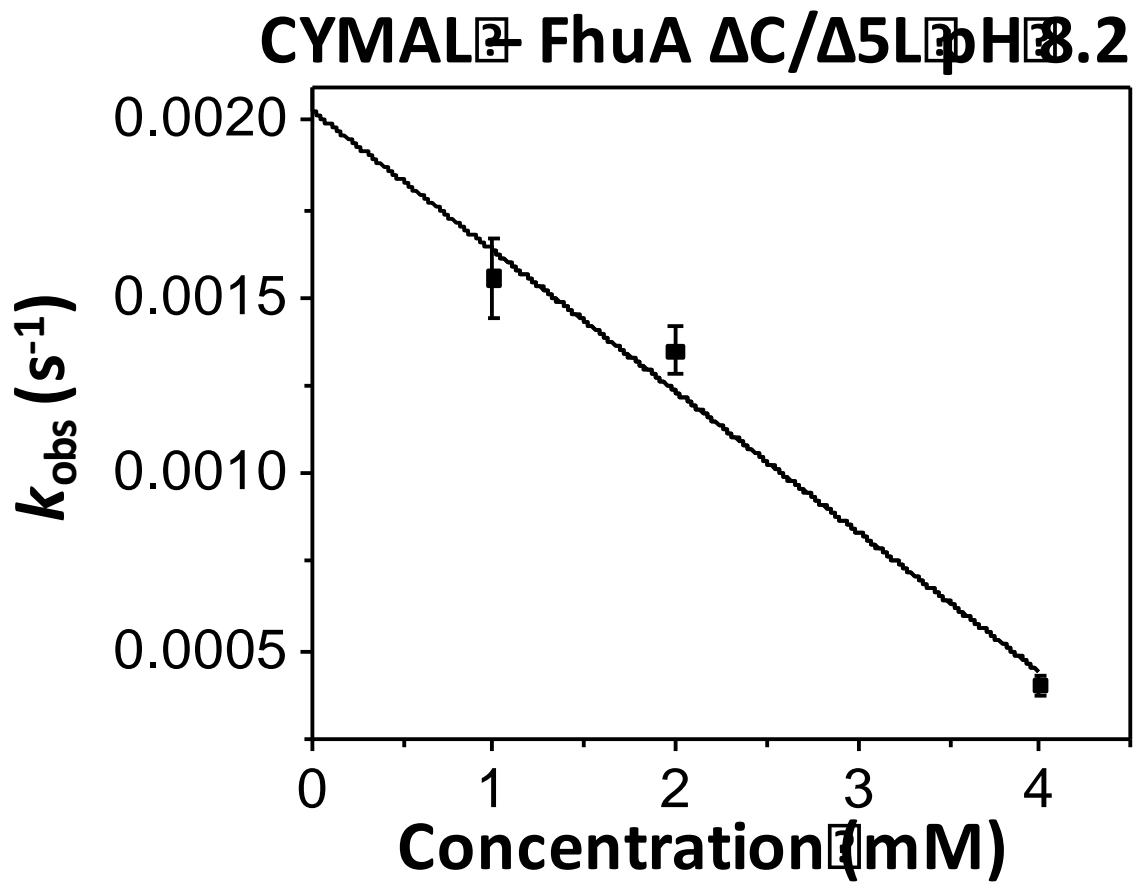
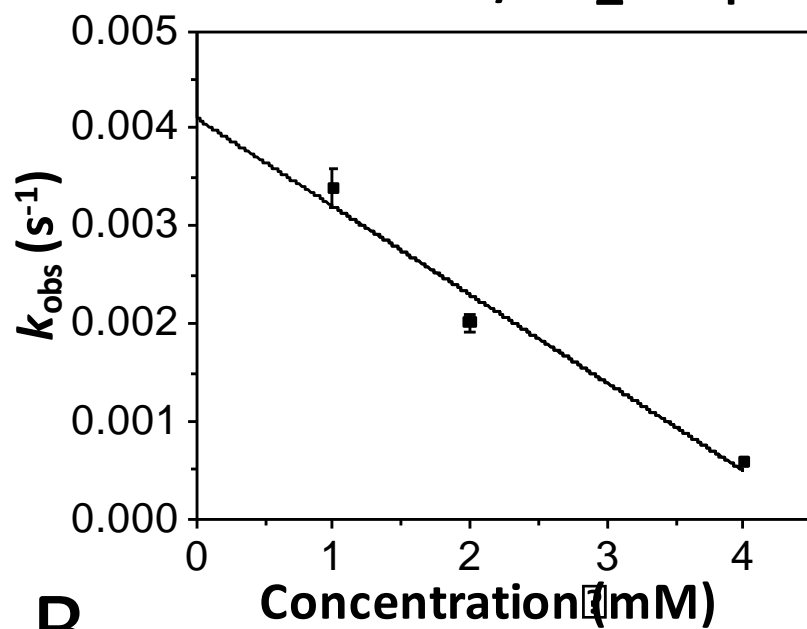


**Figure S27:** The observed kinetic rates of desolvation of FhuA  $\Delta C/\Delta 5L$  scale linearly with the CYMAL-4 detergent concentrations at values below the  $CMC^{CYMAL-4} = 7.6$  mM. The buffer pH was 8.2. The other experimental conditions were the same as those stated in the figure caption of **Fig. S1**.

**A** CYMAL<sup>+</sup> FhuA  $\Delta$ C/ $\Delta$ 5L\_25N pH 6.8



**B** CYMAL<sup>+</sup> FhuA  $\Delta$ C/ $\Delta$ 5L\_25N pH 8.2

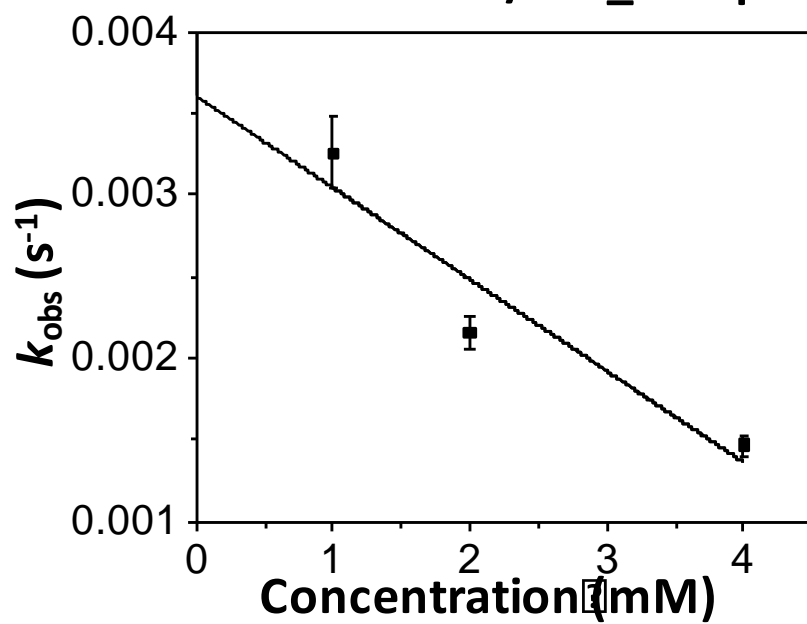
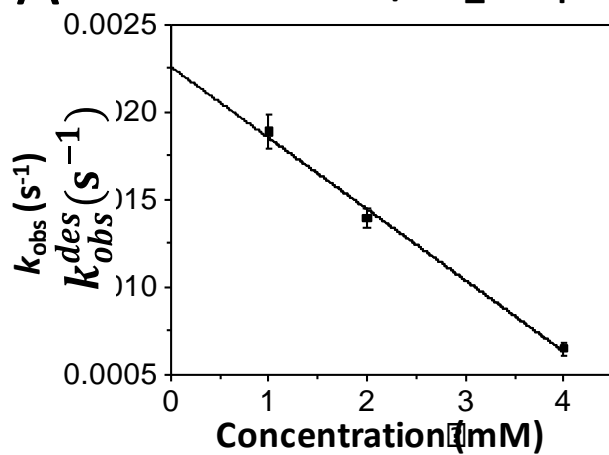


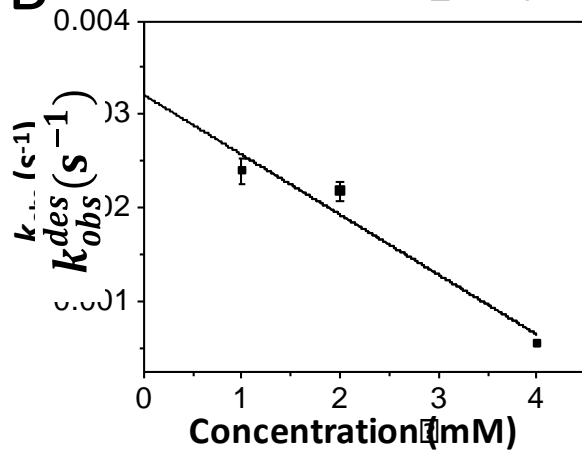


**Figure S28:** The observed kinetic rates of desolvation of FhuA  $\Delta C/\Delta 5L_{25N}$  scale linearly with the CYMAL-4 detergent concentrations at values below the  $CMC^{CYMAL-4} = 7.6$  mM. (A) pH 6.8; (B) pH 8.2. The other experimental conditions were the same as those stated in the figure caption of **Fig. S1**.

**A** CYMAL<sup>+</sup> FhuA  $\Delta$ C/ $\Delta$ 7L\_30N<sup>+</sup> pH 5.6



**B** CYMAL<sup>+</sup> FhuA  $\Delta$ C/ $\Delta$ 7L\_30N<sup>+</sup> pH 5.8



**C** CYMAL<sup>+</sup> FhuA  $\Delta$ C/ $\Delta$ 7L\_30N<sup>+</sup> pH 3.2

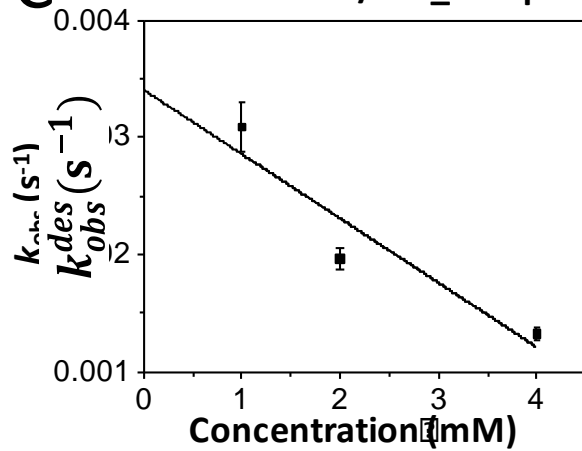


**Figure S29:** The observed kinetic rates of desolvation of FhuA  $\Delta C/\Delta 7L_{30N}$  scale linearly with the CYMAL-4 detergent concentrations at values below the  $CMC^{CYMAL-4} = 7.6$  mM. (A) pH 5.6; (B) pH 6.8; (C) pH 8.2. The other experimental conditions were the same as those stated in the figure caption of **Fig. S1**.

**8. Kinetic rate constants of association and dissociation of proteomicelles using time-dependent FP anisotropy changes.**

**Table S18: Determination of kinetic rate constants of association and dissociation of DM-based proteomicelles as well as the equilibrium dissociation constant,  $K_d$ .** The experimental conditions were the same as those stated in the figure caption of **Fig. S1**.

<b>Protein</b>	<b>pH</b>	$k_{on}$ ( $M^{-1}s^{-1}$ )	$k_{off} \times 10^3$ ( $s^{-1}$ )	$K_d$ (mM) <sup>a</sup>	$K_d$ (mM) <sup>b</sup>
OmpG	4.6	$36 \pm 2$	$61 \pm 2$	$1.7 \pm 0.1$	$1.6 \pm 0.5$
OmpG	6.8	$17 \pm 8$	$32 \pm 6$	$1.9 \pm 0.4$	$1.5 \pm 0.4$
OmpG	8.2	$74 \pm 2$	$89 \pm 2$	$1.2 \pm 0.1$	$1.5 \pm 0.4$
OmpG	10.0	$51 \pm 8$	$73 \pm 7$	$1.4 \pm 0.2$	$1.3 \pm 0.1$
FhuA $\Delta C/\Delta 5L$	5.6	$54 \pm 15$	$73 \pm 12$	$1.4 \pm 0.2$	$1.6 \pm 0.2$
FhuA $\Delta C/\Delta 5L$	6.8	$48 \pm 14$	$63 \pm 11$	$1.3 \pm 0.3$	$1.7 \pm 0.1$
FhuA $\Delta C/\Delta 5L$ 25N	8.2	$53 \pm 2$	$88 \pm 2$	$1.6 \pm 0.1$	~1.7
FhuA $\Delta C/\Delta 7L$ 30N	5.6	$48 \pm 11$	$61 \pm 1$	$1.3 \pm 0.3$	$1.8 \pm 0.3$
FhuA $\Delta C/\Delta 7L$ 30N	6.8	$22 \pm 3$	$47 \pm 3$	$2.1 \pm 0.3$	$1.8 \pm 0.4$
FhuA $\Delta C/\Delta 7L$ 30N	8.2	$63 \pm 14$	$91 \pm 12$	$1.4 \pm 0.3$	~3.2

<sup>a</sup>These model-dependent equilibrium dissociation constants were derived in this work using the values of the association ( $k_{on}$ ) and dissociation ( $k_{off}$ ) rate constants of the proteomicelles. These constants were determined using the linear fits of the observed desolvation rates,  $k_{obs}^{des}$  as follows:

$$k_{obs}^{des} = -k_{on}[D] + k_{off} \quad (\text{S25})$$

The relationships of the observed predesolvation rates,  $k_{obs}^{des}([D])$ , to the association and dissociation constants are closely similar to the equation (S23). The “-“ sign in front of  $k_{on}$  shows that the overall observed rate is a dissociation (not association) rate of the proteomicelles. This is the reason why the observed rate decreases by increasing the detergent concentration within the sample well at values approaching the CMC. Therefore, the  $k_{off}$  and  $k_{on}$  values were inferred using the intercepts with the vertical  $k_{obs}^{des}$  axes ( $[D]=0$ ) and the linear slopes, respectively (**Figs. S22-S29**). At the same time, the  $K_d$  values were derived as intercepts of the linear fits with the horizontal axes ( $k_{obs}^{des}=0$ ).

<sup>b</sup>These equilibrium dissociation constants were derived previously using the endpoints of the desolvation reaction.<sup>2</sup>

**Table S19: Determination of kinetic rate constants of association and dissociation of CYMAL-4-based proteomicelles as well as the equilibrium dissociation constant,  $K_d$ .** The experimental conditions were the same as those stated in the figure caption of **Fig. S1**.

<b>Protein</b>	<b>pH</b>	$k_{on}$ ( $M^{-1}s^{-1}$ )	$k_{off} \times 10^3$ ( $s^{-1}$ )	$K_d$ (mM) <sup>a</sup>
OmpG	5.6	$3 \pm 1$	$23 \pm 1$	$7.5 \pm 0.1$
OmpG	6.8	$5 \pm 1$	$29 \pm 1$	$6.1 \pm 0.1$
OmpG	8.2	$3 \pm 2$	$21 \pm 4$	$6.2 \pm 1.2$
FhuA $\Delta C/\Delta 5L$	8.2	$4 \pm 1$	$20 \pm 2$	$5.1 \pm 1.0$
FhuA $\Delta C/\Delta 5L$ 25N	6.8	$9 \pm 2$	$41 \pm 4$	$4.5 \pm 1.1$
FhuA $\Delta C/\Delta 5L$ 25N	8.2	$6 \pm 2$	$36 \pm 5$	$6.4 \pm 0.9$
FhuA $\Delta C/\Delta 7L$ 30N	5.6	$4 \pm 1$	$23 \pm 1$	$5.6 \pm 0.3$
FhuA $\Delta C/\Delta 7L$ 30N	6.8	$6 \pm 1$	$32 \pm 4$	$5.0 \pm 0.6$
FhuA $\Delta C/\Delta 7L$ 30N	8.2	$5 \pm 2$	$34 \pm 5$	$6.2 \pm 0.9$

<sup>a</sup>These model-dependent equilibrium dissociation constants were derived in this work using the values of the association ( $k_{on}$ ) and dissociation ( $k_{off}$ ) rate constants of the proteomicelles. Other data analysis details are provided in the footnotes of **Table S18**.

**REFERENCES**

1. Stoddart, L. A.; White, C. W.; Nguyen, K.; Hill, S. J.; Pflieger, K. D., Fluorescence- and bioluminescence-based approaches to study GPCR ligand binding. *Br. J. Pharmacol.* **2016**, *173* (20), 3028-3037.
2. Wolfe, A. J.; Si, W.; Zhang, Z.; Blanden, A. R.; Hsueh, Y. C.; Gugel, J. F.; Pham, B.; Chen, M.; Loh, S. N.; Rozovsky, S.; Aksimentiev, A.; Movileanu, L., Quantification of membrane protein-detergent complex interactions. *J. Phys. Chem. B* **2017**, *121* (44), 10228-10241.

## Chapter 7. Concluding Remarks

**Aaron J. Wolfe**

<sup>1</sup>Department of Physics, Syracuse University, 201 Physics Building, Syracuse, New York 13244-1130, USA

<sup>2</sup>Structural Biology, Biochemistry, and Biophysics Program, Syracuse University, 111 College Place, Syracuse, New York 13244-4100, USA

Here I present the general conclusions for this thesis. If the reader desires a more nuanced look at the conclusions for any of the five papers presented within this thesis, I kindly direct them to the discussions and conclusion sections at the end of each chapter.



In the past decades, there have been tremendous advances in the structural and biophysical understanding of membrane proteins[1][2]. The adaption of high throughput methods for determining solubilization conditions is driving the recent advances in the number of membrane protein structures being solved[3]. Even these high throughput techniques are still selecting detergents by trial and error[4] and the reason why one detergent works while another fails for any given protein is ill-defined. The continued use of trial and error for detergent selection may be due to the lack of a descriptive methodology to map the kinetic fingerprint of the protein detergent complex, which may be a fundamental limitation in membrane protein structural biology and biophysics. In this thesis, I describe the development of an assay which uses steady state fluorescence polarization anisotropy to measure the change of hydrodynamic radius caused by stripping of detergent from the membrane protein. This change in signal is due to the physical change of the size of the protein as the detergent torus is depleted. The unique feature of fluorescence anisotropy is that it measures this change in a concentration independent manner. Therefore, as protein aggregates form and proteins fall out of solution, they stop contributing to the overall signal in a meaningful way. This allows the remaining labeled proteins still in solution to report on their size via relative tumbling rate as measured by anisotropy. Unlike most detergent solubilization high throughput assays which report primarily on solubilization[5]–[7], the method I described within this thesis allows for the semiquantitative description of the kinetics of the association and dissociation of the detergents from the protein of interest. So, not only are we able to determine detergents with favorable solubilization features, we are able to identify detergents where the adhesive force to the protein is much tighter than the cohesive force to other detergent monomers.

This is fundamentally important, as we will be able to focus on detergent profiles that show long desorption kinetics and tight adhesive interactions highlighting extremely tight binding detergents that can potentially be used at much lower concentrations, while still imparting huge benefits to protein stability, such as the tight binding of LPPG to FhuA  $\Delta C/\Delta 5L$  described in **Chapter 3**. As more data becomes available on more protein detergent complex mixtures, the analysis may be able to shine some light on the various characteristics driving these not so obvious interactions, such as the finding in **Chapter 6** that the kinetics, but not the energetics, of the adhesive interaction between the protein and detergent depend on protein charge even with neutral detergents. This type of information may be used to further understand the elements of the protein-detergent complex that are driving strong interactions. Due to the complexities of membrane proteins and the interactions governing the protein detergent-complex, a complete and informative description of the forces driving these interactions is still far off. Hopefully, this methodology will be broadly adapted to many membrane proteins. The accumulated information could allow chemists to have a powerful tool, that in the future, would allow the informed tuning of novel detergent structures to specific membrane proteins based on simple findings, such as charge density or other biophysical characteristics of the complex.

## Expanding possibilities beyond detergents

The next step in understanding and working with membrane proteins after they are well solubilized in detergents, is determining how they insert from that detergent solubilized state into lipids. The study of proteoliposomes is important in understanding transport kinetics [8] and is the next step in understanding structure in a native-like environment [9]. However, the transition from detergent solubilized state to liposomal associated state is ill defined and wrought with trial and error.

It may be possible to adapt the previously described method to determine detergent solubilized protein insertion kinetics into liposomes. The main technical hurdle in employing fluorescence polarization to a large complex, such as a proteoliposome, is the fluorescence lifetime of the fluorophore. The effect on measured anisotropy ( $r$ ) of rotation is the strongest when the when the lifetime of fluorescence emission is on the same time scale as the molecular rotation of the target. If the rotation is too slow because the complex is large, the emission will be over before the target rotates enough and will approach the fundamental limit of anisotropy,  $r$  0.4. For complexes >100 kDa, longer lifetimes of approximately >20 ns would be preferable [10]. For the work highlighted in this thesis, Texas Red was the fluorophore of choice, as it is bright and environmentally robust, but it has a relatively short fluorescent lifetime of ~4.5 ns [11]. This was sufficient for the complexes of proteomicelles examined in this work, primarily because the anisotropy signal was decreasing as desorption took place, which is easier to measure than small changes in intensity. However, Texas Red's lifetime was too short to study assembly of the proteomicelles to the larger liposomes. As the anisotropy level of many of the proteomicelles examined in this thesis was between 0.32-0.37, which is close to the theoretical anisotropy limit

of  $r=0.4$ , this short fluorescence lifetime gives little room to measure signal for assembling into larger complexes such as a liposome. A fluorophore that would emit a signal for  $>20$  ns would strongly increase the chances of measuring the assembly kinetics of the labeled protein to a liposome. In the search for longer emitting fluorophores, we identified Dr. Laursen's group out of Denmark. Dr. Laursen and his colleagues manufactured a new type of dye, ADOA+, that emits red and has a lifetime of  $\sim 20$  ns [12]–[14]. It is my belief that, armed with the well characterized engineered FhuA beta-barrel described within this thesis orthogonally labeled with the ADOA fluorophores, the complex assembly kinetics into liposomes can be measured. I think that this would have a great impact on the field of membrane biophysics broadly but would also allow my fellow single molecule electrophysiology brethren to know if the long waits in measuring insertions are due to insoluble proteins or poor kinetics, which if the reader recalls, was the impetus for the line of thinking and body of work that resulted in this thesis.

## References

- [1] D. Hardy, R. M. Bill, A. Jawhari, and A. J. Rothnie, "Overcoming bottlenecks in the membrane protein structural biology pipeline," *Biochem. Soc. Trans.*, vol. 44, no. 3, pp. 838–844, 2016.
- [2] L. Anson, "Membrane protein biophysics," *Nature*, vol. 459, p. 343, May 2009.
- [3] E. P. Carpenter, K. Beis, A. D. Cameron, and S. Iwata, "Overcoming the challenges of membrane protein crystallography," *Current Opinion in Structural Biology*, vol. 18, no. 5, pp. 581–586, Oct-2008.
- [4] J. M. Vergis, M. D. Purdy, and M. C. Wiener, "A high-throughput differential filtration assay to screen and select detergents for membrane proteins," *Anal. Biochem.*, vol. 407, no. 1, pp. 1–11, Dec. 2010.
- [5] J. Fan *et al.*, "An efficient strategy for high throughput screening of recombinant integral membrane protein expression and stability," *Protein Expr. Purif.*, vol. 78, no. 1, pp. 6–13, 2011.
- [6] P. Champeil *et al.*, "A robust method to screen detergents for membrane protein stabilization, revisited," *Anal. Biochem.*, vol. 511, pp. 31–35, 2016.
- [7] A. E. Rawlings, "Membrane proteins: always an insoluble problem?," *Biochem. Soc. Trans.*, vol. 44, no. 3, pp. 790–795, 2016.
- [8] M. Scalise, L. Pochini, N. Giangregorio, A. Tonazzi, and C. Indiveri, "Proteoliposomes as Tool for Assaying Membrane Transporter Functions and Interactions with Xenobiotics," *Pharmaceutics*, vol. 5, no. 3, pp. 472–497, Sep. 2013.
- [9] J.-L. Rigaud, "Membrane proteins: functional and structural studies using reconstituted proteoliposomes and 2-D crystals," *Brazilian Journal of Medical and Biological Research*, vol. 35, pp. 753–766, 2002.
- [10] H. Zhang, Q. Wu, and M. Y. Berezin, "HHS Public Access," vol. 10, no. 11, pp. 1145–1161, 2016.
- [11] T. Isothiocyanate, H. Brismar, O. Trepte, and B. Ulfhake, "Environmental Factors Recorded with a Confocal Laser Scanning Microscope ' I \ TexanRed," vol. 43, no. 7, pp. 699–707, 1995.
- [12] T. J. Sorensen *et al.*, "Azadioxatriangulenium (ADOTA(+)): A long fluorescence lifetime fluorophore for large biomolecule binding assay.," *Methods Appl. Fluoresc.*, vol. 1, no. 2, p. 25001, 2013.
- [13] R. Chib *et al.*, "Fluorescent biosensor for the detection of hyaluronidase: intensity-based ratiometric sensing and fluorescence lifetime-based sensing using a long lifetime azadioxatriangulenium (ADOTA) fluorophore.," *Anal. Bioanal. Chem.*, vol. 408, no. 14, pp. 3811–3821, May 2016.
- [14] I. Bora, S. A. Bogh, M. Santella, M. Rosenberg, T. J. Sørensen, and B. W. Laursen, "Azadioxatriangulenium: Synthesis and Photophysical Properties of Reactive Dyes for

Bioconjugation,” *European J. Org. Chem.*, vol. 2015, no. 28, pp. 6351–6358, Oct. 2015.



## Vita

NAME OF AUTHOR: Aaron J Wolfe

PLACE OF BIRTH: Lockport, New York, USA

DATE OF BIRTH: November, 6, 1983

DEGREES AWARDED: Bachelors of science in Biotechnology from the State university of New York Enviromental Science and Forestry

### PROFESSIONAL EXPERIENCE:

#### **Co-Founder and CEO of RecombiPure Inc.**

March 2017- Current

A biotechnology research tool company spun out of Finger Lakes Bio LLC.

- Manage daily operations and corporate strategy
- Craft and Implement IP strategy

#### **COO of Ichor Therapeutics**

Sept 2016- Current

A biotechnology company that develops large molecule biologic drugs for Age related Macular degeneration

- Manage daily operations of 12 person research staff
- Craft and implement IP strategy

#### **Chair IACUC for Ichor Therapeutics**

March 2016- Current

The IACUC is a committee that examines the ethical treatment of research animals

#### **Co-Founder and CEO of Finger Lakes Bio LLC.**

June 2015- Current

A biotechnology startup drug and biologic development company that develops screening and drug testing platforms for pre-IND drug discovery programs focusing on p53.

- Biologics manufacturing
- Pre-clinical drug discovery

#### **Private Equity Biotechnology Consultant for Axiom Equity Partners**

Jan 2011- May 2013

A private Investment Company looking to fund early stage medical device and biotechnology companies.

- Identified and vetted opportunities in the biotechnology space by locating and communicating with early stage companies
- Performed technology based due diligence on perspective investment targets

#### **Vice President and Co-founder of Design Concepts of Niagara Ltd.**

Dec.2007- March 2016

A New York corporation founded to develop proprietary products in consumer markets